Edited by Hongwei Han, Michael Grätzel, Anyi Mei, and Yue Hu

Printable Mesoscopic Perovskite Solar Cells
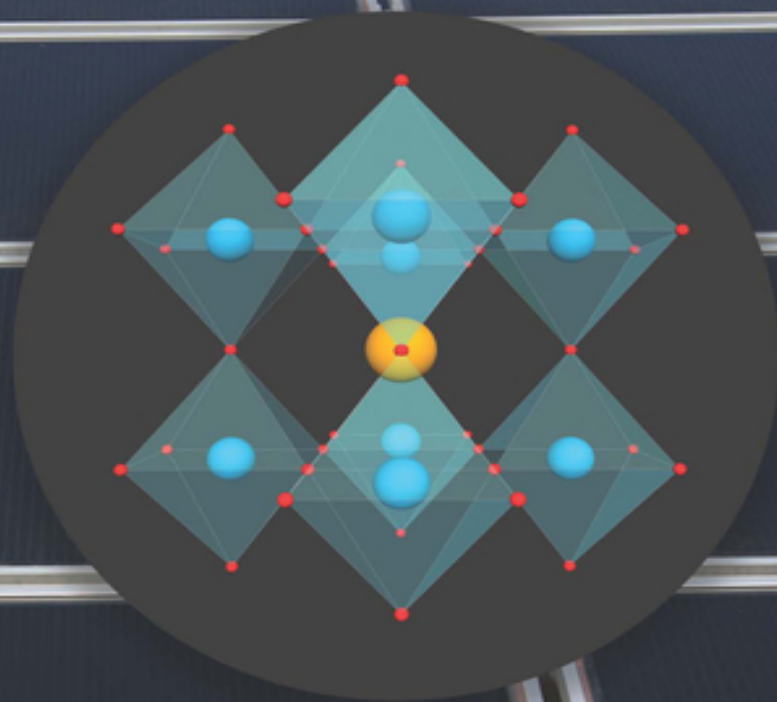
Table of Contents

List of Tables

List of Illustrations

Chapter 3

Chapter 4

Printable Mesoscopic Perovskite Solar Cells

Edited by Hongwei Han, Michael Grätzel, Anyi Mei, and Yue Hu

WILEY-VCH

Editors

Prof. Hongwei Han

Huazhong Univ. of Science & Technology

National Laboratory for Optoelectronics

1037 Luoyu Road

430074 Wuhan

China

Prof. Michael Grätzel

Ecole Polytechnique Federale de Lausann

Institute of Chemical Science

Station 6

CH-1015 Lausanne

Switzerland

Prof. Anyi Mei

Huazhong Univ. of Science & Technology

National Laboratory for Optoelectronics

1037 Luoyu Road

430074 Wuhan

China

Prof. Yue Hu

Huazhong Univ. of Science & Technology

National Laboratory for Optoelectronics

1037 Luoyu Road

430074 Wuhan

China

Biography

Hongwei Han is a Professor at Wuhan National Laboratory for Optoelectronics, Huazhong University of Science and Technology. He is a pioneer in printable mesoscopic perovskite solar cells.

Michael Grätzel is a Professor at Ecole Polytechnique Federale de Lausanne. He is a pioneer in the field of molecular photovoltaics and the development of perovskite solar cells.

Anyi Mei, PhD, is a Professor at Wuhan National Laboratory for Optoelectronics, Huazhong University of Science and Technology. His research is focused on printed mesoscopic solar cell materials and devices.

Yue Hu, PhD, is an Associate Professor at Wuhan National Laboratory for Optoelectronics, Huazhong University of Science and Technology. Her research interest is dye-sensitized solar cells and perovskite solar cells.

Preface

The sudden outbreak of COVID-19 disrupted the normal life of people around the world in 2020. We were combating the virus in the most primitive way of staying at home to fight against the pandemic. Out of sheer boredom, I was thinking maybe we could make full use of the spare time to summarize the research achievements and insights on printable mesoscopic perovskite solar cells (PSCs) (referred to simply as p-MPSC, also honored to be known as "Han cells" or "Wuhan cells") since we can't go out to continue our research. By doing so, we can set sail for our work again in a shift manner once the pandemic is over. Therefore, after a quick discussion with our team, I emailed Prof. Michael Grätzel at École Polytechnique Fédérale de Lausanne (EPFL, Swiss Federal Institute of Technology in Lausanne) in Switzerland. He is a pioneer in dye-sensitized solar cells (DSSCs) and we invited him to compile the book with us. Prof. Michael Grätzel readily accepted our invitation and recommended us to invite other internationally recognized scholars to participate in the work.

Human beings are fragile in face of nature. Any sign of slight disturbance in the environment can impact people's life. Over the past century, the greenhouse effect caused by the excessive emission of carbon dioxide from overexploitation and usage of fossil fuels has tipped the balance and led to global warming, glacier and permafrost melting, and sea level rising, which not only endanger the balance of natural ecosystems, but also pose threats on the survival of mankind. COVID-19 reminds us that humankind should launch a green revolution and move faster to create a green way of development and life, preserve the

environment, and make Mother Earth a better place for all. On September 22, 2020, Chinese president Xi Jinping had announced at General Debate of the 75th Session of the General Assembly of the United Nations, "China will scale up its Intended Nationally Determined Contributions by adopting more vigorous policies and measures. We aim to have CO_2 emissions peak before 2030 and achieve carbon neutrality before 2060. We call on all countries to pursue innovative, coordinated, green and open development for all, seize the historic opportunities presented by the new round of scientific and technological revolution and industrial transformation, achieve a green recovery of the world economy in the post-COVID era and thus create a powerful force driving sustainable development."

The new generation of ultra-low-cost photovoltaic (PV) technology will be the key to drive carbon neutrality, to fundamentally reduce the proportion of coal power, and to advance the development of the "ultimate power source in twenty-first century" – hydrogen energy. As the leading technology of PV industry, p-MPSC has received widespread attention from scientific research and business sectors because of its simple fabrication process, excellent performance, low-cost materials constituents, and enormous commercial value since its invention. p-MPSC is based on triple-layer mesoporous films and takes halide materials as its light-absorbing materials and mesoporous carbon as electrode. All components can be fabricated by screen printing or slot coating method which shows great advantages over industrial production and upscaling module fabrication. This whole process can meet the demand of ultra-low-cost solar cells for PV industry.

The development history of organic–inorganic metal halide perovskite materials can be traced back to 1893. H.L. Wells in America was the first to successfully synthesize the

perovskite material based on $CsPbX_3$. In 1958, C.K. Møller in Denmark took a further step to confirm that $CsPbX_3$ is a perovskite structure. In 1978, D. Weber in Germany fabricated organic–inorganic hybrid perovskite materials for the first time. Subsequently, D.B. Mitzi and C.R. Kagan from IBM Corporation in America applied this organic–inorganic perovskite material into LED and TFT devices in 1994 and in 1999, respectively. However, the materials couldn't be widely used because of their poor stability. The perovskite material was firstly used in solar cells as liquid perovskite-sensitized solar cells by T. Miyasaka Group in Japan in 2009. But unfortunately, it didn't draw much attention since it can only work for dozens of seconds under light-soaking conditions. Nam-Gyu Park Group in South Korea and Michael Grätzel Group in Switzerland applied this perovskite materials into solid-state DSSCs for the first time until 2012, and the device showed a good stability after 500 hours of preservation in the dark conditions. Since then, there has been a wave of research on PSCs.

The first PSC to show promising light-soaking stability was obtained by the p-MPSC based on a triple-layer mesoporous films structure and carbon counter electrode. Aided by the natural strengths in triple mesoscopic films structure like inhibiting ionic immigration and thermal expansion mismatch and by introducing the bifunctional organic molecular, Han Group in China obtained a stability of 1000 hours in ambient air and successfully passed the main items of IEC61215:2016 qualification tests. Meanwhile, the device fabricated by the team has been working for more than 13 000 hours at a maximum power point of 55 ± 5 °C under the standard sunlight without obvious decay. M.K. Nazeeruddin Group in Switzerland also gained p-MPSCs with a stability of 10 000 hours at short-circuit conditions. Furthermore, WonderSolar LLC. in China has made

tremendous efforts to upscale p-MPSCs toward commercialization, both of which have shown wide application prospect of p-MPSCs. So far, the instability of perovskite materials has been satisfactorily solved through the design of device structure with triple-mesoscopic layers.

Compared with conventional p–n junction devices, the mesoscopic structure with nano-size pores favors charge extraction among various dynamic competitive processes due to the micron-scale charge diffusion length of perovskite. When the incident light is fully absorbed by the perovskite material in ETL, only holes will remain in the perovskite medium in the part of mesoscopic ZrO_2 layer and carbon layer, so far as there is no need for conventional hole transport layer within p-MPSCs. The hole-conductor-free character and the carbon electrode help reduce the cost of solar cells. Meanwhile, all functional layers including the back electrode in p-MPSCs are fabricated via solution-processed methods while evaporation is excluded, which reduces the device fabrication cost. The inexpensive components and the full solution-processable character minimize the cost and make p-MPSC a great choice for low-cost photovoltaics.

This book consists of 10 chapters and the lead authors of each chapter are the experts on the front line in MSPC industry. We introduce the structure characteristics and application on PV device of perovskite materials combining physical and chemical basic principles and the research achievements of the lead authors and industry professors. We focus on the characteristics of p-MPSCs. Starting from inorganic framework materials and perovskite materials, we summarize the characterizations of p-MPSCs and analyze the kinetics of carriers in solar cells under mesoscale conditions. Based on that, we put up with the

strategies of enhancing the efficiency and stability of p-MPSCs and make prospect of p-MPSC commercialization.

The authors sought to express accurately in words with clear illustrations during the compiling, and the editors reviewed and proofread each chapter carefully. However, due to limited time and knowledge, errors and omissions are inevitable. Advice and corrections from readers and peers will be deeply appreciated for our future reprint.

In HUST, Feb. 2021
Hongwei Han

1
Background and Basic Knowledge of Perovskite Solar Cells

Maria Vasilopoulou[1], Abd Rashid B. Mohd Yusoff[2], and Mohammad K. Nazeeruddin[3]

[1] National Centre for Scientific Research Demokritos, Institute of Nanoscience and Nanotechnology, Agia Paraskevi, 15341 Attica, Greece

[2] Pohang University of Science and Technology(POSTECH), Department of Chemical Engineering, Pohang, Gyeongbuk, 37673, Republic of Korea

[3] École Polytechnique Fédérale de Lausanne (EPFL), Institute of Chemical Sciences and Engineering, Group for Molecular Engineering of Functional Materials, Rue de l'Industrie 17,, CH-1951, Sion, Switzerland

1.1 Background

The deployment of renewable energy sources lies within the context of prohibiting climate change and achieving greenhouse gas reduction targets [1]. Solar energy is clean and abundant; therefore, its usage can fulfill the need for sustainable development in order to protect the environment by limiting the consumption of fossil fuels. Photovoltaic systems convert the sun's energy directly into electricity through the application of semiconductor materials that utilize the so-called photovoltaic effect or photovoltaic phenomenon.

The photovoltaic phenomenon was first reported in 1839 by 19-year-old Edmund Becquerel, who was able to produce

weak electrical current in a prototype cell by employing a silver-coated platinum electrode immersed in certain electrolytes, which was exposed to sunlight. He called this phenomenon the "photovoltaic effect," which is the basic principle that governs solar cell operation that converts sunlight into electricity [2]. However, it was about forty years later, in 1876, when the first solid-state photovoltaic cell was demonstrated by William Adams and Richard Day [3]. It employed a junction formed between selenium (Se) and platinum (Pt) which produced electricity without having moving parts and led to the development of modern solar cell systems. Adams and Day also found that "the ultra-red or the ultraviolet rays have little or no effect on the production of energy." They also observed that the produced electricity was highly dependent on the illuminating power of the light, "being directly related to the square root of that illuminating power" [4]. A few years later, in 1883, Charles Fritts fabricated the first large-area solar cell by pressing a selenium layer between two thin gold metal foils [5].

In the following years, photovoltaic effects were also observed in other semiconductor materials such as copper–copper oxide (Cu:CuO) thin-film heterostructures, lead sulfide (PbS), and thallium sulfide (TlS). In these early devices, a thin semi-transparent metal layer was deposited on the semiconductor material to provide an asymmetric Schottky junction without prohibiting light from reaching the semiconductor. The discovery of silicon (Si) p–n junction in the 1950s offered a significant boost to the development of solar cells as these p–n junction structures exhibited better rectifying ability than the Schottky ones and hence delivered better photovoltaic behavior. The first Si solar cell was reported by Chapin, Fuller, and Pearson in 1954 and converted sunlight to electricity with an efficiency of 6% [6]. These pioneers used their solar panels

to power a small toy Ferris wheel and a solar-powered radio transmitter. A few years later, in 1957, they increased the efficiency to 8% [7]. Notably, a solar cell based on cadmium sulfide (CdS) p–n junction was demonstrated in 1954, also producing electricity with an efficiency of 6%.

During the next decades, interest in photovoltaics expanded to other semiconductor materials such as gallium arsenide (GaAs), indium phosphide (InP), and cadmium telluride (CdTe), which, unlike Si, possess a direct bandgap, and theoretical work indicated that they could offer higher efficiency. Afterward, the growing awareness of the need to make use of an alternative to fossil fuel sources of electricity led photovoltaic production to be expanded at a rate of 15–25% per year. This has also driven a sufficient cost reduction which made photovoltaics competitive for increase in supply in grid-connected loads at peak use and in contexts where the conventional electricity supply was quite expensive, for example, in remote low-power applications such as telecommunications, navigation, and rural electrification. However, new markets have opened up such as building integrated photovoltaics, where besides the efficiency and cost of the photovoltaic system, its easy integration in building facades and roofs can be facilitated by using alternative solution-based materials and fabrication methods.

1.2 The Principle of Solar Cells

1.2.1 Silicon Solar Cells

A solar cell is an optoelectronic device based on a p–n junction formed between two oppositely doped regions of a single semiconductor material, a p–type which has an excess of free holes and n-type having an excess of free

electrons [2]. The p-type and n-type regions in a Si p–n junction are created by using appropriate trivalent (acceptor, having three valence electrons like boron, B; aluminum, Al; gallium, Ga; and indium, In) and pentavalent (donor, like phosphorus, P; antimony, Sb; and arsenic, As) impurities (dopants), respectively, via ion implantation, epitaxy, or diffusion of dopants. Because the Si semiconductor owns four valence electrons, doping with acceptors creates an excess of holes, while doping with donors results in the formation of nearly free electrons. Consequently, the concentration of free holes is much higher in the p-type region compared to the n-type region and *vice versa* (free electrons are much more in the n-type region), which creates a high concentration gradient of charge carriers across the junction line.

Considering the energy diagram, the Fermi level (E_F) shifts toward the valence band (VB) maximum in the p-type region and toward the conduction band (CB) minimum in the n-type region, hence creating a discontinuity in energy across the p–n junction. As a result, free holes (majority carriers) diffuse from the p-type region toward the junction line, while electrons diffuse from the n-type region and cross the p–n junction where they subsequently recombine with holes leaving negatively charged acceptor and positively charged donor ions at the p-type and n-type regions, respectively. These charged ions continue to increase and, because they are immobile, they build an electric field which is directed from the n-type to p-type region of the junction.

Due to this internal electric field, minority carriers (which are holes from the n-type region and electrons from the p-type region) drift toward the opposite region and eventually balance and stop the diffusive flow of majority carriers. At this stage of equilibrium, the two charged ionic

"layers" on either side of the p–n junction form the so-called space charge region of the diode. This central region is also called as "depletion region" because it is depleted of free carriers; holes have left the space $-x_{p0} \leq x < 0$ in the p-type region and electrons have left the space $0 \leq x \leq x_{n0}$ in the n-type region, where $x = 0$ corresponds to p–n junction line. As a result, for $x_{p0} \leq x \leq x_{n0}$, we have $np < n_i^2$, where n, p are the concentration of free electrons and holes in the doped semiconductor, and n_i (equal to p_i) is the concentration of electrons (holes) in the intrinsic material before doping. The width of the depletion region is $W = x_{n0} + x_{p0}$. Note that, deep in the p-type and in the n-type regions, the semiconductor remains quasi-neutral, having a concentration of free holes $p = N_A$ and of free electrons $n = N_D$ in these quasi-neutral p and n regions, where N_A and N_D are the concentrations of acceptor and donor dopants, respectively.

The internal electric field of the p–n junction defines a voltage barrier which is called the device's "built-in" potential, V_{bi}, that prohibits further movement of free carriers, and the diode enters an equilibrium phase where the drift current of the minority carriers becomes equal to the diffusion current of majority carriers, hence eliminating each other. This potential is defined by the following equation:

(1.1)

$$V_{bi} = E_{Fn0} - E_{Fp0} = E_i + k_B T \ln \left(\frac{N_D}{n_i} \right) - E_i + k_B T \ln \left(\frac{N_A}{n_i} \right)$$

$$= k_B T \ln \left(\frac{N_D N_A}{n_i^2} \right)$$

If we consider the band diagram of the semiconductor just before the p–n region is formed, the conduction and VB edges will line up at both sides, while the Fermi level will exhibit a discontinuity at the junction (due to different positioning between E_{Fp} and E_{Fn} that correspond to the Fermi levels of p-type and n-type semiconductors and lie near the VB maximum and CB minimum, respectively, while E_{Fi} corresponds to the Fermi level of an intrinsic semiconductor and lies at the middle of the bandgap, Figure 1.1a). Statistical mechanics demands that at equilibrium where the diffusion of opposite carriers is prohibited by the internal electric field, the Fermi level of the system is unique and becomes aligned at both sides of the p–n junction (Figure 1.1b). If we apply an external forward bias with the positive voltage, V_{a}, applied to the p-region, as illustrated in Figure 1.1c, the field in the depletion region decreases by V_{a}, so that it will not balance anymore the diffusion of the majority of holes and electrons flowing toward the opposite directions of the p–n junction with the drift current of the minority carriers. This will result in an increased majority hole and electron flow toward opposite directions that both contribute to a net current density (J_{tot}) flowing from the p-type to the n-type regions of the junction. On the contrary, if we apply a negative voltage, V_{a}, (reverse bias) to the p-type region, the electric field in the depletion region will be strengthened and the associated drift current of the minority carriers will be larger than the diffusion current. As a result, the diode is flowed by a small (because the concentration of minority carriers is extremely low) reverse current (also called as reverse saturation current, J_{s}). Figure 1.1d illustrates the qualitative behavior of the diode current density, J_{total}, as a function of applied bias, V_{a}, and shows that diodes based on p–n junctions rectify the current flow as follows:
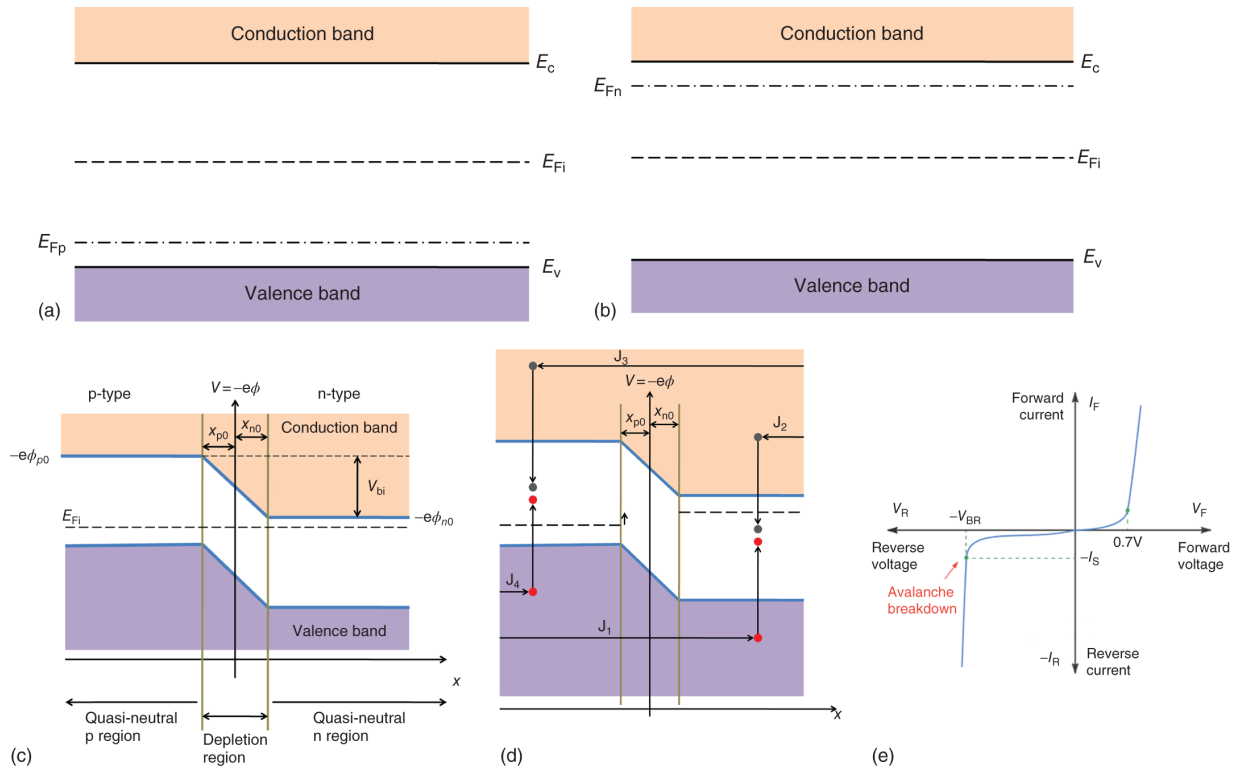
Figure 1.1 The conduction and valence band edges of the p-type and n-type regions of a semiconductor (a) before contact and (b) at the equilibrium when p–n junction is formed. (c and d) The illustration of current generation under forward bias of a p–n junction and (e) the current density–voltage characteristic of a rectifying diode.

$$J_{\text{total}} = J_{\text{S}} \left[e^{eV_a/(k_B T)} - 1 \right] \tag{1.2}$$

where e is the elemental charge, k_B is the Boltzmann constant, and T is the absolute temperature. Equation (1.2) is known as "Shockley" (or diode) equation.

In a Si photovoltaic cell, when a photon is absorbed from the semiconductor material, it creates a free electron in the CB, hence leaving a free hole in the VB (Figure 1.2a). Due to the presence of the "internal" electric field of the p–n junction, the photogenerated holes in the crystal are forced to drift toward the direction of the electric field and accumulate on the p-type region, whereas the

photogenerated electrons drift to the opposite direction and accumulate on the n-type region, thereby producing a potential difference termed as open-circuit voltage (V_{OC}) of the photovoltaic cell. Under reverse bias, the accumulated photogenerated holes and electrons flow toward the respective electrodes (the hole selective and electron selective contact, respectively), and thus a significant reverse current (termed as photocurrent, J_{photo}) (Figure 1.2b) flows through the device. A representative current density–voltage (J–V) characteristic of a solar cell operating in the dark and under illumination is shown in Figure 1.2c. In the operation in the dark, we obtain the rectifying behavior of a diode based on the p–n junction. The curve lying beneath the dark curve shows what happens under illumination where a reverse saturation current is obtained even in the absence of an external voltage. This current is called short-circuit current (J_{SC}). If we apply a forward bias, it will compensate the internal electric field, and we will reach a point where it becomes zero and thus there is no current flow within the device. At this point, we obtain the V_{OC} because it is as if the electric circuit is open.

For efficient solar cell operation, both J_{SC} and V_{OC} should be maximized. Moreover, the so-called fill factor (FF) should approach unity. It is the product of the current and voltage, according to the following equation:

$$\text{FF} = \frac{J_{MAX}V_{MAX}}{J_{SC}V_{OC}}, \tag{1.3}$$

where $J_{MAX} V_{MAX}$ gives the maximum power.
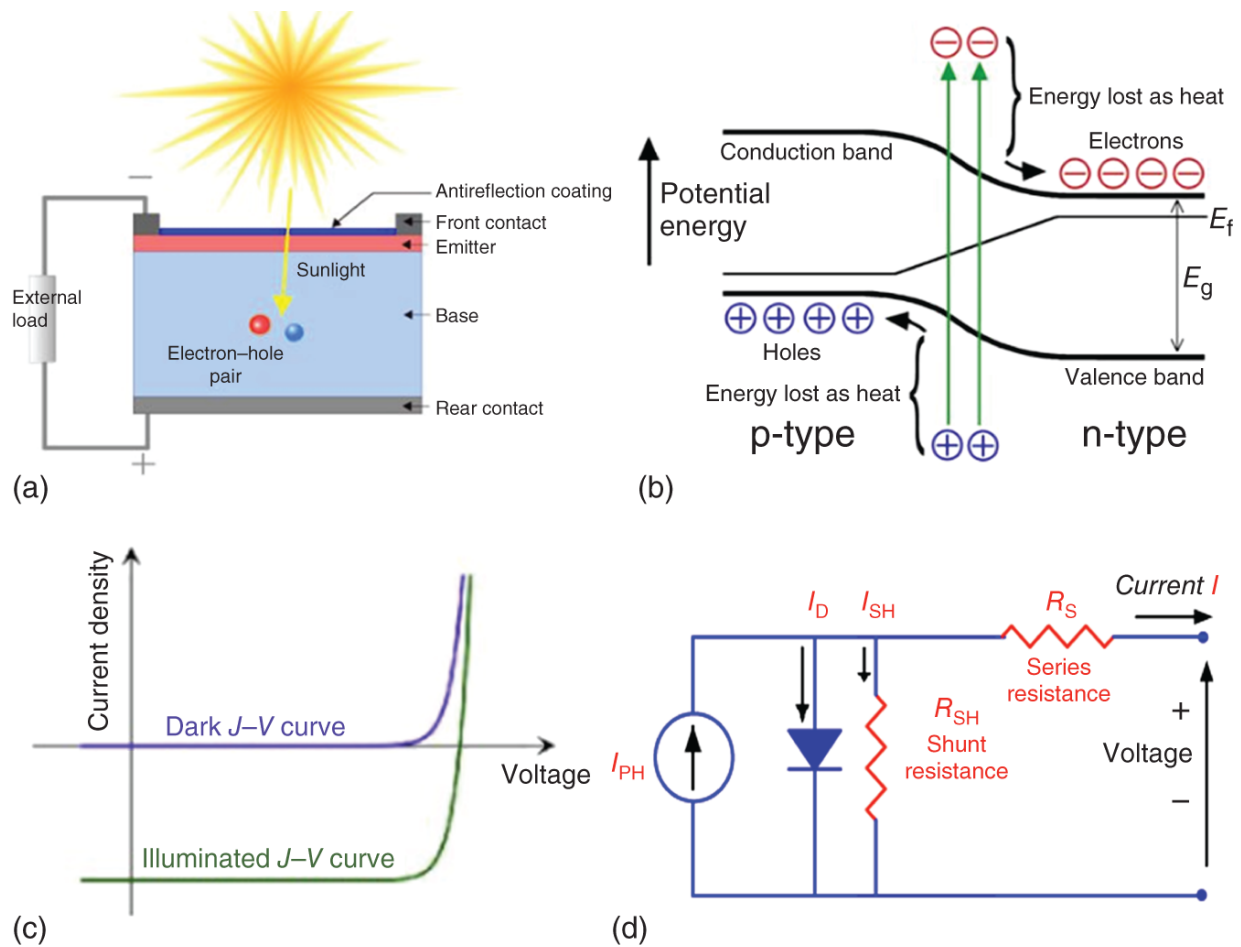
Figure 1.2 (a) The PV cell and (b) the production of electrical current due to the photovoltaic phenomenon taking place in a p–n junction. (c) The J–V characteristics of a solar cell in dark and under illumination and (d) the equivalent electrical circuit of a solar cell.

Finally, the obtained power conversion efficiency (n or PCE) is calculated according to the following equation:

$$n = \frac{P_{\text{MAX}}}{P_{\text{solar}}} = \text{FF}\frac{J_{\text{SC}}V_{\text{OC}}}{P_{\text{solar}}} \tag{1.4}$$

A photovoltaic cell can be represented by an equivalent electrical circuit presented in Figure 1.2d. By applying Kirchhoff's law, we obtain the device current:

$$I = I_L - I_0 \left[\exp \left(\frac{V + IR_s}{nV_T} \right) - 1 \right] - \frac{V + IR_s}{R_{sh}} \qquad (1.5)$$

where I_L is the photocurrent, I_0 is the reverse saturation current of the diode, R_s is the series, R_{sh} is the shunt resistance, and n is the so-called ideality factor. For optimum operation, R_s should be minimized, whereas R_{sh} should be maximized.

Using the sun as the photon source (the energy of solar photons ranges from 0.3 to over 4.0 eV), a high-efficiency solar cell can be produced only if we overcome the compromise between photocurrent and photovoltage: a high photocurrent device harvests the majority of the sunlight, whereas a high photovoltage solar cell only harvests the high-energy (UV) photons. There is, hence, a limit in the maximum theoretically achieved efficiency in a single junction device, which is called the Shockley and Queisser limit and is equal to 30% [8]. This can be only achieved by an ideal solar cell harvesting UV to near-infrared (IR) photons up to 1.1 eV. Silicon solar cells have progressed considerably over the five decades of their existence, and the to-date efficiency record of 26.7% for single-crystal-based Si photovoltaics [9] is approaching the theoretical limit.

1.2.2 Dye-sensitized Solar Cells

Dye-sensitized solar cells (DSSCs) are much different in their architecture and working principle compared to the p–n junction Si photovoltaics. They were first demonstrated in 1972, after the discovery that organic dyes (i.e. chromophores) coated on the zinc oxide (ZnO) electrode of an electrochemical cell could produce electricity upon illumination [10]. Regarding the working mechanism, it was based on the observation that the absorbed photons

with energy above the bandgap of the chromophore formed electron–hole (i.e. exciton) pairs in the excited molecule followed by exciton dissociation and electron injection into the wide bandgap metal oxide semiconductor, hence producing electricity (Figure 1.3a). The first demonstration was followed by intense study on ZnO-single crystal electrodes aiming to increase efficiency of these premature DSSCs. However, due to the limited absorption within the visible range of commonly used chromophores and small surface area of ZnO electrode, the PCE remained as low as 1% [12]. Higher efficiencies were obtained upon increasing the porosity of ZnO electrode to enhance the absorption of dye over electrode and, subsequently, the light-harvesting efficiency (LHE) of the system. However, large improvements were obtained in 1991 at Ecole Polytechnique Fédèrale de Lausanne (EPFL), when Michael Grätzel replaced the ZnO electrode with a titanium dioxide (TiO_2) nanoporous layer with a roughness factor of c. 1000; this skyrocketed the DSSCs efficiency up to 7% [13]. These cells, also known as Grätzel cells, were originally co-invented in 1988 by Brian O'Regan and Michael Grätzel at UC Berkeley but were highly optimized by Grätzel's team during the next years [14].

The main constituent of the DSSC cell is a thick (of the order of a few micrometers, µm) mesoporous network of TiO_2, which consists of nanoparticles around 10–30 nm in diameter, prepared as paste in ethanol or water solutions. The paste can be deposited via spin coating, screen printing, or doctor blade onto a glass substrate coated with fluorinated tin oxide (FTO) that serves as the anode electrode (electron selective contact or anode); afterward, the TiO_2 layer is sintered at 400 °C to avoid decomposition. In this "mesoporous" layer, the particles form a network with a high porosity of 40–60%. The mesoporous TiO_2 is

sensitized with the organic dye (D) and infiltrated with a redox-active electrolyte [15, 16]. During the next years, this electrolyte was replaced by a solid-state hole transport material (HTM) to avoid device failure due to electrolyte leakage. The photogenerated electrons (produced when dye is photoexcited with sunlight) are transferred from the excited states of the dye into the TiO_2 and then to the front contact (FTO). The oxidized dye (D^+) is subsequently regenerated by the redox active electrolyte through a multi-charge-transfer process; generally, four iodide molecules as well as two holes take place in the regeneration of dye by creating one triiodide and one iodide species (i.e. I_3^-/I^- redox couple, Figure 1.3b) [11, 17]. The triiodide then transfers holes to the counter electrode (platinum, Pt), where it is reduced to three iodide species. Hence, the circuit is complete and current flows through the device. In the case of solid-state hole transport-based DSSCs, the regeneration of dye occurs via initial hole transfer to the highest occupied molecular orbital (HOMO) or VB of the hole transporter and then to the cathode electrode to complete the circuit [18].
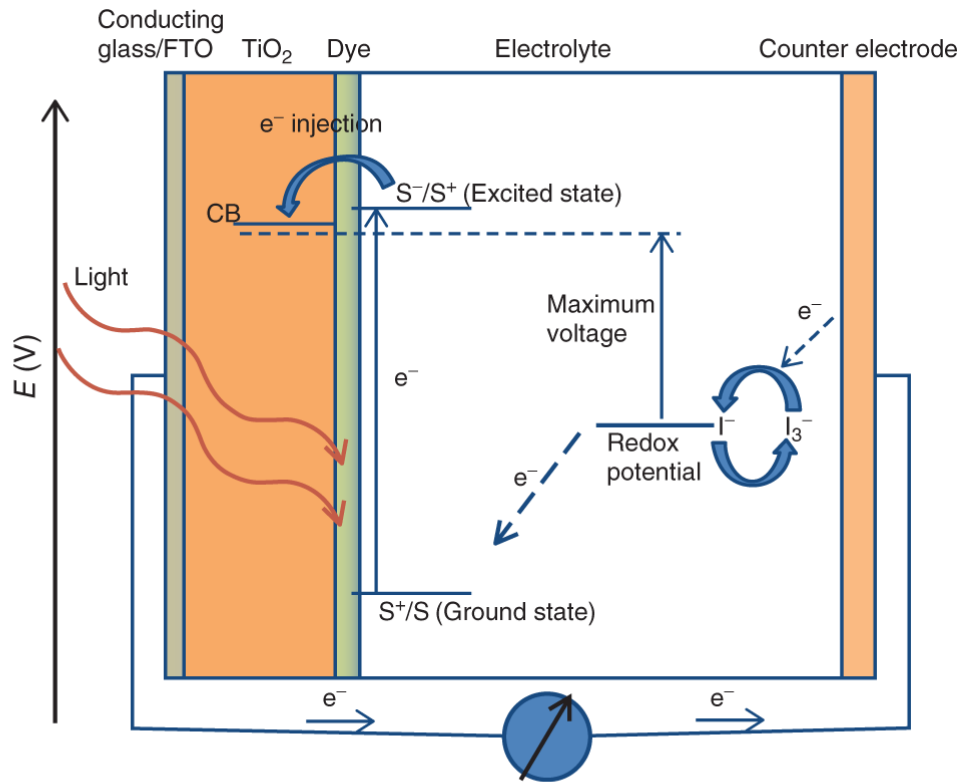
(a)
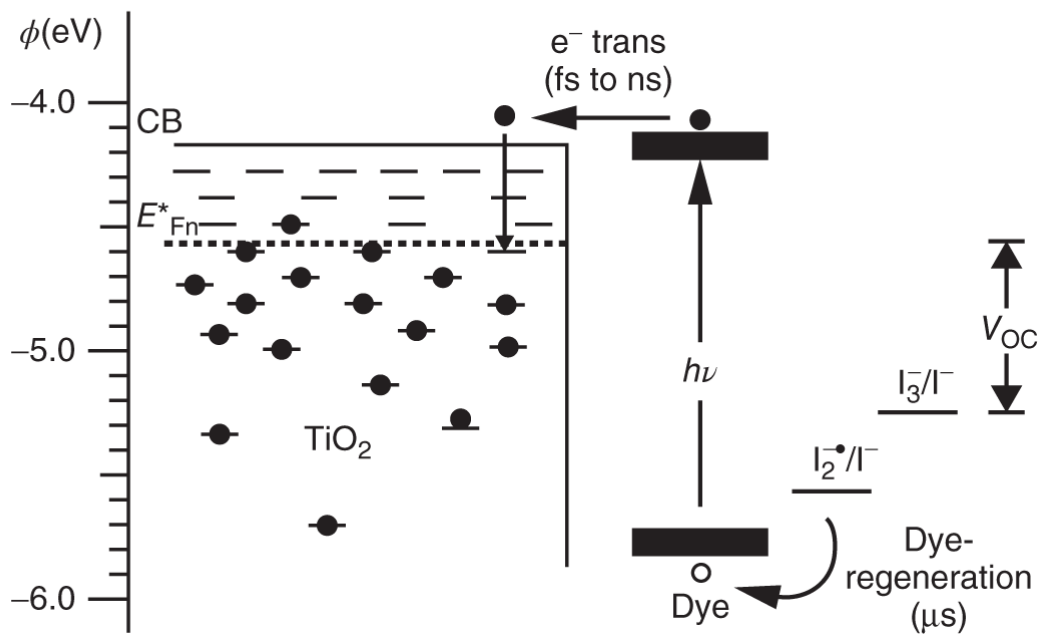
(b)

Figure 1.3 (a) The DSSC device architecture and the working mechanism of dye-sensitized solar cell. (b) Illustration of the energy levels at the photoactive heterojunction in a dye-sensitized solar cell. Light is absorbed in the dye at energies higher than the optical bandgap. The open-circuit voltage (V_{OC}) is set by the difference in the quasi-Fermi level for electrons $E_{Fn}*$ in the TiO$_2$ and the equilibrium redox potential of the electrolyte, I$_3^-$/I$^-$. The loss-in-potential from going from the optical bandgap (hv) to the open-circuit voltage is clearly illustrated. Source: Reproduced with permission from Snaith et al. [11]/John Wiley & Sons.

Grätzel's cell was based on a 10-µm-thick, optically transparent, and colorless with high surface area TiO$_2$ nanoparticle consisting of film. Deposition of a monolayer of a trimeric ruthenium complex, $RuL_2(\mu\text{-}(CN)Ru(CN)L_2')_2$, where L is 2,2′bipyridine-4,4′-dicarboxylic acid and L′ is 2,2′bipyridine resulted in a significant coloration of TiO$_2$ film due to the strong absorption of the ruthenium complex within the visible (absorption onset at 750 nm and extinction coefficient at 478 nm of $1.88 \times 10^7 \, \mathrm{cm^2 \, mol^{-1}}$). As a result, the device harvested a high portion of nearly 46% of the incident solar light energy flux and yielded PCE values between 7.1% and 7.9% in simulated solar light (due to a large J_{SC} above $12 \, \mathrm{mA \, cm^{-2}}$) as well as 12% in diffuse daylight. It also exhibited an exceptional stability by sustaining at least five million turnovers without decomposition. In 1993, Nazeeruddin et al. achieved a record efficiency of 10% by using m-X2Bis (2,2,-bipyridyl-4, 4/-dicarboxylate) ruthenium (II) complexes as dye sensitizers with absorption onsets up to 800 nm [19]. Further improvements were reported by the EPFL team in 2011 when they demonstrated 12.3% efficient DSSCs that

incorporated a cobalt Co$^{(II/III)}$ tris(bipyridyl)–based redox electrolyte in conjunction with a custom synthesized donor–π-bridge–acceptor zinc porphyrin dye as sensitizer [20]. These authors later demonstrated the record efficiency of 13% holding DSSC, featuring a prototypical structure of a donor–π-bridge–acceptor porphyrin sensitizer that maximized electrolyte compatibility and improved light-harvesting properties [21].

1.2.3 Organic Solar Cells

Organic solar cells (OSCs) are layered structures consisting of an organic photoactive layer sandwiched between two opposite electrodes (Figure 1.4a) [22]. The photoactive layer is based on a blend of a polymer donor with either a fullerene or a non-fullerene acceptor (NFA), hence forming the so-called bulk heterojunction (BHJ) architecture. This is because of the large Coulombic attraction between electron and hole pairs, the so-called Frenkel excitons, due to the low dielectric constants (about 3.5) of common organic semiconductors [23].

For these excitons to dissociate into free carriers, the presence of a two-component system containing the electron donor (D) and the electron acceptor (A) that is similar to that of a p–n junction is necessary [24, 25]. The electron donor should possess a large ionization energy (I_E), whereas the electron acceptor should have a high electron affinity (E_A) for the following reason: Upon photon absorption, an electron is excited from the HOMO to the lowest unoccupied molecular orbital (LUMO) of the donor, hence forming a Frenkel exciton (Figure 1.4b). This exciton then diffuses toward the D:A heterointerface where it dissociates via an energy gradient into a hole and an electron; the latter transfers to the LUMO of the acceptor

material and forms a charge transfer (CT) complex, which will be favorable to occur when:
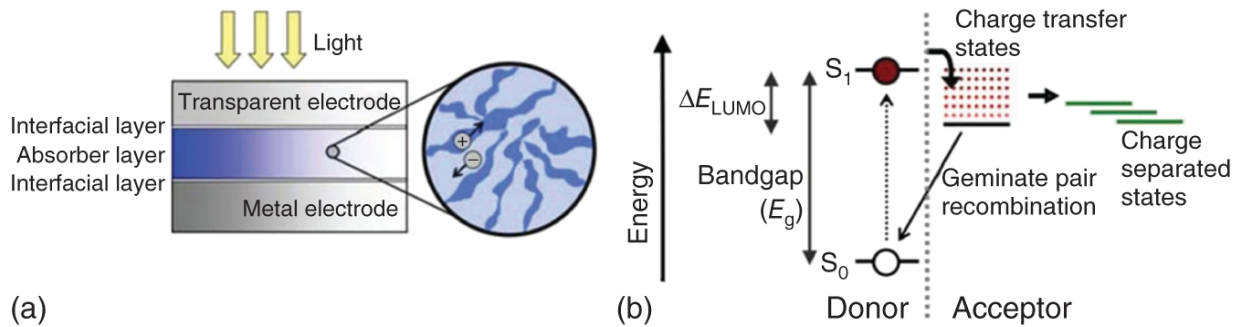
(a)   (b)   Donor : Acceptor

Figure 1.4 (a) Schematic representation of the bulk heterojunction OSC. (b) Organic solar cell energy-level diagram depicting the HOMO and LUMO levels of donor and the formation of charge-transfer states between the donor and acceptor. The process of geminate recombinations is also illustrated. Source: Reproduced with permission from Servaites et al. [22]/Royal Society of Chemistry.

$$E_A^A - E_A^D > U_D \qquad (1.6)$$

where E_A^A and E_A^D is the electron affinity of the acceptor and the donor, respectively, and U_D is the binding energy of the exciton (of the order of few hundreds of meV). This sets a theoretical maximum for the attainable voltage output in these cells as being the difference between the donor HOMO and acceptor LUMO, given by the following formula:

$$V_{bi} = E_{LUMO\ (acceptor)} - E_{HOMO\ (donor)} \qquad (1.7)$$

representing important material design considerations. The electron/hole pair forming the CT state can also be referred to as geminate pair and is highly dependent on the Coulombic attraction between opposite carriers and on the distance that separates these species [26]. If the latter

becomes larger than the coulomb capture radius, the geminate pair dissociates into free carriers; otherwise, the geminate pair will recombine across the donor:acceptor interface, the so-called geminate recombination, which constitutes a common loss mechanism in OSCs [27, 28]. The dissociated electrons and holes can then be transported through the acceptor and donor domains, respectively, to the respective electrodes, with electrons being collected at the cathode and holes at the anode.

In the most efficient OSC architecture, the BHJ one, an interpenetrating network of pure donor and acceptor domains, forms the active layer because it strikes a balance between promoting exciton dissociation at D:A interfaces and transports charges through the bulk. This implies that the final and leading loss mechanism in OSCs is charge recombination during charge transport to the electrodes. Key objectives in OSCs are the minimization of energy and charge losses both upon exciton dissociation and through transport within the BHJ device (the latter is crucial due to the low carrier mobility and low diffusion length of the order of 10 nm in organic semiconductors) [1] in order to enhance the efficiency of devices.

A challenging step that contributes to efficient OSCs operation is the charge transport and collection at the electrodes. As most photoactive materials exhibit large energetic differences of their molecular levels, i.e. the HOMO of the donor and the LUMO of the acceptor with the corresponding electrodes, a typical OSC device configuration, fabricated on a transparent rigid (e.g. glass) or flexible substrate, usually comprises a hole transport/extraction layer (HTL/HEL) and an electron transport/extraction layer (ETL/EEL), which are all sandwiched between a high work-function (W_F) (anode, the hole-selective contact) and a low W_F (cathode, the electron-

selective contact) electrode aiming at reducing these differences. In principle, the cathode electrode should have a sufficiently low W_F (lower than the LUMO of the acceptor in the active layer), whereas the anode electrode should have a sufficiently high W_F (higher than the HOMO of the active layer). An energetic mismatch at any device interface may lead to barriers for charge extraction, to high contact resistance, and to space charge formation and undesirable recombination, thus severely reducing device performance. Other issues that may influence charge transport/extraction, even when interfacial energetic alignment is excellent, are the surface energy mismatch between the various layers and poor interfacial compatibility/morphology.

Examples of electron donor materials used in the photoactive layer of BHJ OSCs are the poly(3-hexylthiophene-2,5-diyl) (P3HT), poly[[9-(1-octylnonyl)-9H-carbazole-2,7-diyl]-2,5-thiophenediyl-2,1,3-benzothiadiazole-4,7-diyl-2,5-thiophenediyl] (PCDTBT), and poly((4,8-bis[(2-ethylhexyl)oxy] benzo[1,2-b,4,5-b']dithiophene-2,6-diyl)(3-fluoro-2-[(2-ethylhexyl)carbonyl] thieno [3,4-b] thiophenediyl)) (PTB7). Materials for electron acceptors are either fullerene such as [6,6]-phenyl C_{71} butyric acid methyl ester ($PC_{71}BM$) and 1′,1″,4′,4″-tetrahydro-di[1,4]methanonaphthaleno[5,6]fullerene-C_{60}($IC_{60}BA$) or NFAs such as 3,9-bis(2-methylene-((3-(1,1-dicyanomethylene)-6,7-difluoro)-indanone))-5,5,11,11-tetrakis(4-hexylphenyl)-dithieno[2,3-d,2′,3′-d']-s-indaceno[1,2-b,5,6-b']dithiophene (ITIC-2F). Although the first OSCs reported in 1984 by Tang exhibit very low efficiency of 1% (they were two-layer structures based on a phthalocyanine/perylene carboxylic derivative bilayer absorber) [29], recent developments on NFAs have led to a rapid increase in PCEs, with values of ~17.1% in ternary

blend single-junction cells [30] and ~17.3% in double-junction tandem OSCs [31].

1.2.4 Perovskite Solar Cells

Organometallic halide perovskites are materials with a general formula ABX_3 ([Figure 1.5a](#)) [34]. Typical examples of A-site substitution are monovalent cations such as organic methylammonium (CH_3NH_3, MA) and formamidinium ($CH(NH_2)_2$, FA) or an inorganic cation such as cesium (Cs) and rubidium (Rb), for B-site occupation, a heavy divalent metal such as lead (Pb) or tin (Sn) and X is a halogen anion (i.e. Cl, Br, and I). The first reported perovskite solar cells (PSCs) had adopted the mesoporous configuration of their DSSC counterparts, and they were hence termed mesoscopic PSCs (MPSCs). They were considered as solid-state DSSCs in which the dye sensitizer has been replaced by an organic–inorganic lead halide perovskite. These first demonstrations of PSCs were based on the 3-dimensional (3D) methylammonium lead iodide ($MAPbI_3$) perovskite, and yielded in mid-2012 PCEs between 6% and 10% [35–37], which were doubled within a few subsequent years only. Immense research to improve device performance by combining novel perovskite materials and their processing techniques led to a remarkable certified PCE of 27.7% in a tandem configuration [38].

In a typical mesoscopic device architecture ([Figure 1.5b](#)), a thin (~50 nm) compact TiO_2 layer is first coated on the FTO on glass substrate [32]. Subsequently, the mesoporous TiO_2 layer is deposited on top of the compact layer to serve as the electron transport material (ETM) as well as the scaffold for the infiltration of the perovskite absorber. After its post-annealing at 450 °C, the deposition of the perovskite absorber layer (300–500 nm thick) takes place.

The device is completed by the deposition of a thin HTM capped with a metal electrode, such as gold (Au) or silver (Ag). The working principle of these devices is quite similar to those of DSSC counterparts and can be split into three steps, i.e. light absorption by perovskite absorber, charge dissociation and separation, and charge transport to respective electrodes. In the first step, light is absorbed by a thin perovskite layer. An optimum bandgap of perovskite (~1.55–1.6 eV) and a high absorption coefficient (~10^5 cm^{-1}) ensure that maximum visible light is absorbed by the perovskite layer [39]. High-efficiency PSCs require negligible light absorption by the TCO and charge transport/extraction layers such that most absorbed light reaches the perovskite absorber layer. Next is charge dissociation and separation. Herein, the low exciton binding energy of MAPbI$_3$, in the range of a few eV only [40], suggests that photon absorption leads to the generation of free charge carriers. This is extremely desired for a high-efficiency solar cell operation as no external force is required to separate the photogenerated electron–hole pair. The low binding energy and generation of free charge carriers are among the key reasons for high-efficiency PSCs [41]. In other excitonic solar cells, where photogenerated charge pairs (excitons) are bound with higher binding energy (300–500 meV), losses during exciton dissociation and migration account for significant losses [42].
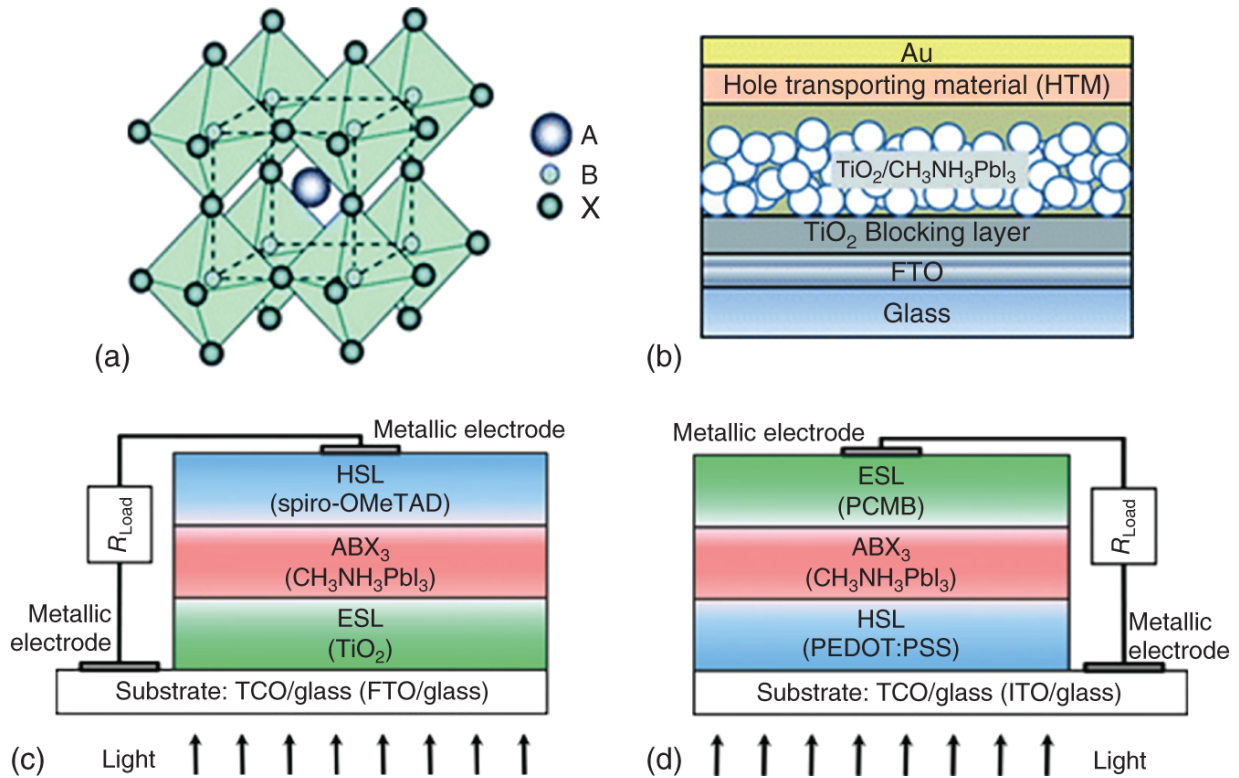
Figure 1.5 (a) Crystal structure of cubic perovskite with general chemical formula ABX_3. Typical device architecture of perovskite solar cells. (b) Device architecture of mesoscopic PSCs. (c) The regular planar (n-i-p) PSC configuration where electrons are collected at the conducting substrate and (d) the inverted planar (p-i-n) architecture where holes are collected at the FTO substrate. Source: (a) and (b) Reproduced with permission from Krishna et al. [32]/Royal Society of Chemistry. (c) and (d) Reproduced with permission from Lopez-Varo et al. [33]/John Wiley & Sons.

The third step that completes the photovoltaic operation in PSCs is charge extraction toward respective electrodes. This requires the injection of at least one type of charge carriers from the perovskite absorber layer into the transport material (and blocking of the other type). Charge selective layers that allow only one type of charge carriers to be extracted are hence employed alongside the

perovskite layer to facilitate their extraction. These selective contacts heavily influence interfacial recombination, charge accumulation and extraction, and consequently play a critical role in determining photovoltaic parameters in PSCs.

Other architectures besides the mesoscopic cells are the regular planar (n-i-p) or inverted planar (p-i-n) structures (Figure 1.5c,d) in which the mesoporous TiO_2 layer is omitted and the perovskite planar absorber is deposited directly either on the electron transport (n-i-p) or the hole transport (p-i-n) material, which guides photogenerated charges toward their respective electrode [33, 43]. These planar devices can be processed at temperature below 150 °C and, therefore, are advantageous for mass production.

An interesting aspect while designing a PSC is its tunable electrical properties. From a typically intrinsic perovskite, their electrical conductivity can be tuned to n- or p-type by manipulating its defects density. Typical 3D halide perovskite, for example, $MAPbI_3$ or $FAPbI_3$, shows an optimum direct bandgap (E_g) of ~1.6 and 1.5 eV, respectively [2–4]. Theoretical calculations predict that an optimized single junction $MAPbI_3$ PSC can deliver PCE of ~31%. This efficiency corresponds to a photocurrent density (J_{SC}) of 26 mA cm^{-2}, an open-circuit voltage (V_{OC}) of 1.3 V, and FF of 91% [44]. However, this requires that there be no non-radiative losses within the bulk of the perovskite as well as the device interfaces. The PSCs still have to overcome losses due to bulk and interfacial defects to reach their Shockley Queisser limit.

Another important device architecture with triple-mesoscopic layer, which replaces expensive metal contacts such as Au or Ag with carbon (C), is printable MPSCs, also called as Han Cells or Wuhan Cells [45–47]. Such

structures, even though lagging in performance compared to their mesoporous or planar counterparts, provide improved operational stability and also are cost-effective . Moreover, carbon composite electrodes can offer an affordable, conductive alternative with abundant sources and blends of carbon black (CB) and graphite (G) being also chemically resistant toward oxidation/reactions and can be printed in batch or continuous roll-to-roll processing, hence offering the possibility for fully printable large area devices [48, 49].

1.3 The Typical Structures of PSC

1.3.1 Mesoscopic Structure

MPSCs are based on a mesoporous ETL such as TiO_2 and SnO_2 or an insulating scaffold like Al_2O_3 and ZrO_2 [50]. The perovskite absorber is then infiltrated in the mesoporous metal oxide scaffold layer, followed by a solid-state hole conductor, which is deposited on top of the perovskite layer (Figure 1.6a). The reader is referred to Section 1.2.4 for more details about the MPSC architecture. Notably, the most efficient PSCs are the mesoscopic ones as they allow larger portion of the incident light to be absorbed while also exhibiting a high surface area between the perovskite absorber and the bottom ETL. Even though in early years high-temperature sintering of the metal oxide layer was generally applied, it was later revealed that using metal oxides alternative to TiO_2 such as SnO_2 that demand post-treatment at lower temperatures can lead to the possibility of MPSCs fabrication upon flexible substrates and multifunctional device architectures [51].
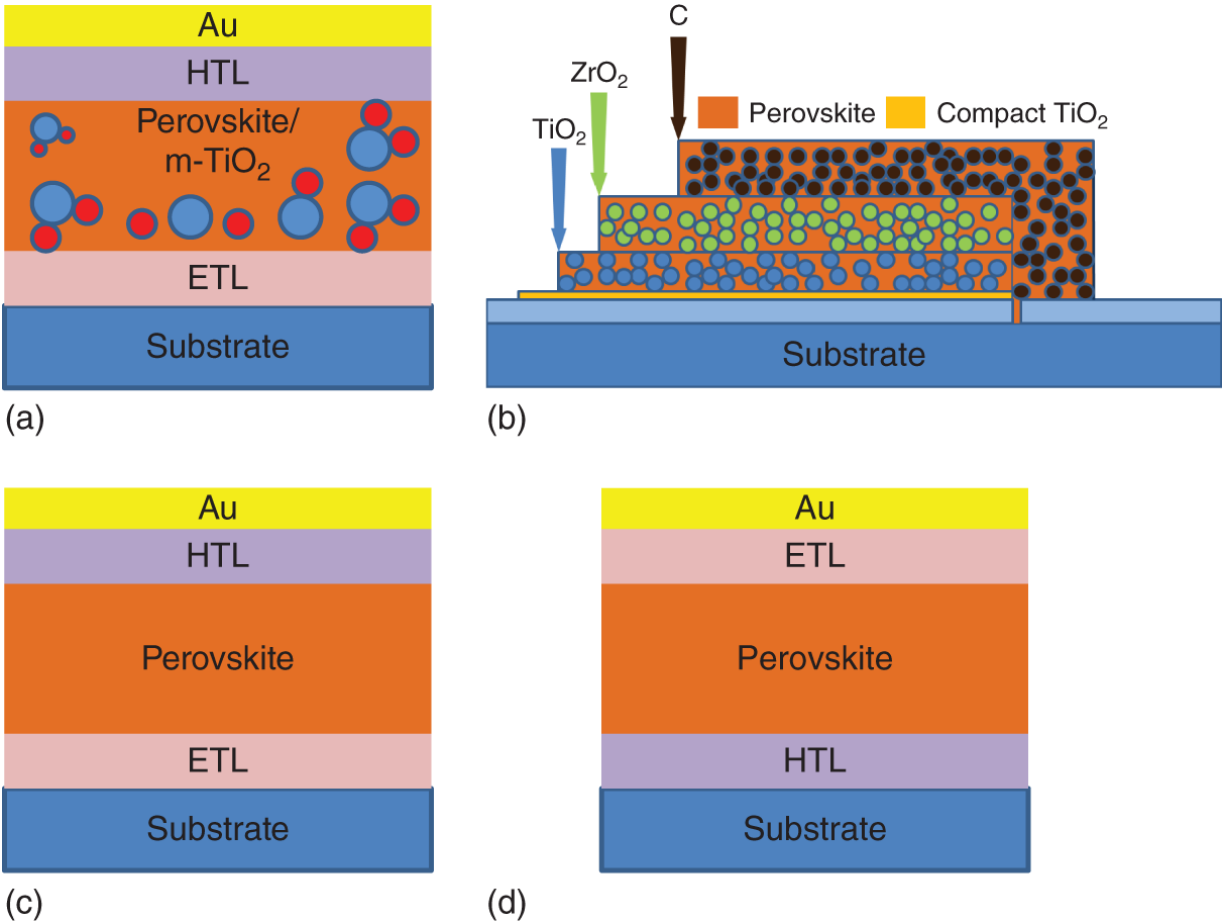
Figure 1.6 Device architecture for (a) mesoscopic (b) triple layer, (c) regular planar n-i-p, and (d) inverted planar p-i-n structure.

1.3.2 Triple-mesoscopic Layer Structure

Besides the mesoscopic structure using a single mesoporous metal oxide at the bottom electrode, solar cells with a double layer consisting of mesoporous oxides such as TiO_2 and ZrO_2, where the perovskite film is infiltrated, have been successfully demonstrated (Figure 1.6b) [46]. In the first demonstration of this device structure, which was printable, the metal halide perovskite was infiltrated into the mesoporous TiO_2/ZrO_2 scaffold by drop-casting a solution through the printed porous carbon (C) layer, which served as the top cathode electrode [46]. The perovskite

precursor solution contained PbI_2 in g-butyrolactone mixed with MA and 5-aminovaleric acid (5-AVA) cations that formed a mixed-cation $(5\text{-AVA})_x(MA)_{1-x}PbI_3$ perovskite. The hole-conductor–free cell with the simple mesoscopic $TiO_2/ZrO_2/C$ triple layer as a scaffold to host the perovskite absorber yielded a PCE of 12.84% and good long-term stability.

However, for these printable cells, it is difficult to control the crystallization mechanism of perovskite owing to the complicated triple-layer mesoporous structure. Recently, a solvent evaporation-controlled crystallization method has been reported that enabled ideal crystallization of the perovskite absorber in the mesoscopic structure [52]. It was based on the adjustment of the evaporation rate of solvent during annealing in the mesoporous structures. The FP–MPSCs exhibited a homogeneous pore filling in the triple-layer structure without any additives and achieved a stabilized PCE of 16.26% using ternary-cation perovskite absorber.

1.3.3 Regular Planar n-i-p Structure

This structure is quite similar to thin-film inorganic and OSCs. It consists of a bottom transparent electron selective electrode (anode), an n-type thin compact ETL, the perovskite absorber layer, the p-type HTL, and the top high W_F metal cathode (hole selective electrode) (Figure 1.6c). This configuration is based on the mesoscopic structure, but it does not include the mesoporous metal oxide layer. One of the maximum efficiencies achieved in this architecture (PCE of 21.6%) was based on an EDTA-modified SnO_2 instead of TiO_2 as the ETL and Cs-doped $FAPbI_3$ as the perovskite absorber, along with a Spiro-OMeTAD as the HTL [53]. Notably, PSCs with the n-i-p structure undergo severe degradation when using organic

HTLs while those with inorganic HTMs not only achieve good PCE but also show comparatively better device stability.

1.3.4 Inverted Planar p-i-n Structure

This device architecture was borrowed from the OSCs technology where it is considered as the regular structure. It has a reverse sequence of ETLs and HTLs compared to the n-i-p structure (Figure 1.6d). The bottom HTL is commonly an organic p-type semiconductor, whereas the top ETL is based on fullerene derivatives [54]. However, appropriate p-type metal oxides such as NiO have been also applied as HTMs with sufficient success in terms of efficiency but, most importantly, stability to ambient air-induced degradation [54].

References

1 Saidel, M.A., Reis, T.M., and Prado, F.A.A. (2009). Carbon credits and energy efficiency. *International Journal of Green Energy* 6 (3): 312–322.

2 Luque, A. and Hegedus, S. (2011). *Handbook of Photovoltaic Science and Engineering*. Wiley.

3 Adams, W.G. and Day, R.E. (1877). V. The action of light on selenium. *Proceedings of the Royal Society of London* 25 (171–178): 113–117.

4 Chen, T., Qiu, L., Yang, Z., and Peng, H. (2013). Novel solar cells in a wire format. *Chemical Society Reviews* 42 (12): 5031–5041.

5 Fritts, C.E. (1883). ART. LII.--On a new form of selenium cell, and some electrical discoveries made by its use. *American Journal of Science (1880–1910)* 26 (156): 465.

6 Chapin, D.M., Fuller, C.S., and Pearson, G.L. (1954). A new silicon p-n junction photocell for converting solar radiation into electrical power. *Journal of Applied Physics* 25 (5): 676–677.

7 Chapin, D. M., Fuller, C. S.,and Pearson, G. L. (1957), inventors Google Patents US2780765A, assignee. Solar energy converting apparatus.

8 Shockley, W. and Queisser, H.J. (1961). Detailed balance limit of efficiency of p-n junction solar cells. *Journal of Applied Physics* 32 (3): 510–519.

9 Green, M.A., Hishikawa, Y., Dunlop, E.D. et al. (2018). Solar cell efficiency tables. *Progress in Photovoltaics: Research and Applications* 26: 427.

10 Tributsch, H. and Calvin, M. (1971). Electrochemistry of excited molecules: photo-electrochemical reactions of chlorophylls. *Photochemistry and Photobiology* 14 (2): 95–112.

11 Snaith, H.J. (2010). Estimating the maximum attainable efficiency in dye-sensitized solar cells. *Advanced Functional Materials* 20 (1): 13–19.

12 Tsubomura, H., Matsumura, M., Nomura, Y., and Amamiya, T. (1976). Dye sensitised zinc oxide: aqueous electrolyte: platinum photocell. *Nature* 261 (5559): 402–403.

13 O'Regan, B. and Grätzel, M. (1991). A low-cost, high-efficiency solar cell based on dye-sensitized colloidal TiO_2 films. *Nature* 353 (6346): 737–740.

14 Nazeeruddin, M.K., Baranoff, E., and Grätzel, M. (2011). Dye-sensitized solar cells: a brief overview. *Solar Energy*

85 (6): 1172–1178.

15 Altobello, S., Bignozzi, C., Caramori, S. et al. (2004). Sensitization of TiO_2 with ruthenium complexes containing boronic acid functions. *Journal of Photochemistry and Photobiology A: Chemistry* 166 (1–3): 91–98.

16 Kunzmann, A., Valero, S., Sepúlveda, Á.E. et al. (2018). Hybrid dye-titania nanoparticles for superior low-temperature dye-sensitized solar cells. *Advanced Energy Materials* 8 (12): 1702583.

17 Peter, L.M. (2007). Dye-sensitized nanocrystalline solar cells. *Physical Chemistry Chemical Physics* 9 (21): 2630–2642.

18 Montanari, I., Nelson, J., and Durrant, J.R. (2002). Iodide electron transfer kinetics in dye-sensitized nanocrystalline TiO_2 films. *Journal of Physical Chemistry B* 106 (47): 12203–12210.

19 Nazeeruddin, M.K., Kay, A., Rodicio, I. et al. (1993). Conversion of light to electricity by cis-X2bis(2,2'-bipyridyl-4,4'-dicarboxylate)ruthenium(II) charge-transfer sensitizers (X = Cl-, Br-, I-, CN-, and SCN-) on nanocrystalline titanium dioxide electrodes. *Journal of the American Chemical Society* 115: 6382.

20 Yella, A., Lee, H.-W., Tsao, H.N. et al. (2011). Porphyrin-sensitized solar cells with cobalt (II/III)–based redox electrolyte exceed 12 percent efficiency. *Science* 334 (6056): 629–634.

21 Mathew, S., Yella, A., Gao, P. et al. (2014). Dye-sensitized solar cells with 13% efficiency achieved

through the molecular engineering of porphyrin sensitizers. *Nature Chemistry* 6 (3): 242–247.

22 Servaites, J.D., Ratner, M.A., and Marks, T.J. (2011). Organic solar cells: a new look at traditional models. *Energy & Environmental Science* 4 (11): 4410–4422.

23 Ameri, T., Khoram, P., Min, J., and Brabec, C.J. (2013). Organic ternary solar cells: a review. *Advanced Materials* 25 (31): 4245–4266.

24 Kniepert, J., Schubert, M., Blakesley, J.C., and Neher, D. (2011). Photogeneration and recombination in P_3HT/PCBM solar cells probed by time-delayed collection field experiments. *Journal of Physical Chemistry Letters* 2 (7): 700–705.

25 Ran, N.A., Roland, S., Love, J.A. et al. (2017). Impact of interfacial molecular orientation on radiative recombination and charge generation efficiency. *Nature Communications* 8 (1): 1–9.

26 Elumalai, N.K. and Uddin, A. (2016). Open circuit voltage of organic solar cells: an in-depth review. *Energy & Environmental Science* 9 (2): 391–410.

27 Weickert, J., Dunbar, R.B., Hesse, H.C. et al. (2011). Nanostructured organic and hybrid solar cells. *Advanced Materials* 23 (16): 1810–1828.

28 Brabec, C., Scherf, U., and Dyakonov, V. (2011). *Organic Photovoltaics: Materials, Device Physics, and Manufacturing Technologies*. Wiley.

29 Tang, C.W. (1986). Two-layer organic photovoltaic cell. *Applied Physics Letters* 48 (2): 183–185.

30 Lin, Y., Firdaus, Y., Nugraha, M.I. et al. (2020). 17.1% efficient single-junction organic solar cells enabled by n-type doping of the bulk-heterojunction. *Advanced Science* 7 (7): 1903419.

31 Meng, L., Zhang, Y., Wan, X. et al. (2018). Organic and solution-processed tandem solar cells with 17.3% efficiency. *Science* 361 (6407): 1094–1098.

32 Krishna, A. and Grimsdale, A.C. (2017). Hole transporting materials for mesoscopic perovskite solar cells–towards a rational design? *Journal of Materials Chemistry A* 5 (32): 16446–16466.

33 Lopez-Varo, P., Jiménez-Tejada, J.A., García-Rosell, M. et al. (2018). Device physics of hybrid perovskite solar cells: theory and experiment. *Advanced Energy Materials* 8 (14): 1702772.

34 Saparov, B. and Mitzi, D.B. (2016). Organic–inorganic perovskites: structural versatility for functional materials design. *Chemical Reviews* 116 (7): 4558–4596.

35 Alsulami, A., Griffin, J., Alqurashi, R. et al. (2016). Thermally stable solution processed vanadium oxide as a hole extraction layer in organic solar cells. *Materials* 9 (4): 235.

36 Burschka, J., Pellet, N., Moon, S.-J. et al. (2013). Sequential deposition as a route to high-performance perovskite-sensitized solar cells. *Nature* 499 (7458): 316–319.

37 Kim, H.-S., Lee, C.-R., Im, J.-H. et al. (2012). Lead iodide perovskite sensitized all-solid-state submicron thin film mesoscopic solar cell with efficiency exceeding 9%. *Scientific Reports* 2 (1): 1–7.

38 Pham, H., Kho, T.C., Phang, P. et al. (2020). High efficiency perovskite-silicon tandem solar cells: effect of surface coating versus bulk incorporation of 2D perovskite. *Advanced Energy Materials* 10 (32): 2002139.

39 De Wolf, S., Holovsky, J., Moon, S.-J. et al. (2014). Organometallic halide perovskites: sharp optical absorption edge and its relation to photovoltaic performance. *Journal of Physical Chemistry Letters* 5 (6): 1035–1039.

40 Chen, W., Zhou, Y., Chen, G. et al. (2019). Alkali chlorides for the suppression of the interfacial recombination in inverted planar perovskite solar cells. *Advanced Energy Materials* 9 (19): 1803872.

41 Collavini, S., Völker, S.F., and Delgado, J.L. (2015). Understanding the outstanding power conversion efficiency of perovskite-based solar cells. *Angewandte Chemie International Edition* 54 (34): 9757–9759.

42 Bai, Y., Chen, H., Xiao, S. et al. (2016). Effects of a molecular monolayer modification of NiO nanocrystal layer surfaces on perovskite crystallization and interface contact toward faster hole extraction and higher photovoltaic performance. *Advanced Functional Materials* 26 (17): 2950–2958.

43 Im, J.-H., Lee, C.-R., Lee, J.-W. et al. (2011). 6.5% efficient perovskite quantum-dot-sensitized solar cell. *Nanoscale* 3 (10): 4088–4093.

44 Sha, W.E., Ren, X., Chen, L., and Choy, W.C. (2015). The efficiency limit of $CH_3NH_3PbI_3$ perovskite solar cells. *Applied Physics Letters* 106 (22): 221104.

45 Ku, Z.L., Rong, Y.G., Xu, M. et al. (2013). Full printable processed mesoscopic $CH_3NH_3PbI_3/TiO_2$ heterojunction solar cells with carbon counter electrode. *Scientific Reports* 3.

46 Mei, A.Y., Li, X., Liu, L.F. et al. (2014). A hole-conductor-free, fully printable mesoscopic perovskite solar cell with high stability. *Science* 345 (6194): 295–298.

47 Rong, Y.G., Hu, Y., Mei, A.Y. et al. (2018). Challenges for commercializing perovskite solar cells. *Science* 361 (6408).

48 Han, H., Bach, U., Cheng, Y.-B. et al. (2009). A design for monolithic all-solid-state dye-sensitized solar cells with a platinized carbon counterelectrode. *Applied Physics Letters* 94 (10): 103102.

49 He, Q., Yao, K., Wang, X. et al. (2017). Room-temperature and solution-processable Cu-doped nickel oxide nanoparticles for efficient hole-transport layers of flexible large-area perovskite solar cells. *ACS Applied Materials & Interfaces* 9 (48): 41887–41897.

50 Etgar, L., Gao, P., Xue, Z. et al. (2012). Mesoscopic $CH_3NH_3PbI_3/TiO_2$ heterojunction solar cells. *Journal of the American Chemical Society* 134 (42): 17396–17399.

51 Ball, J.M., Lee, M.M., Hey, A., and Snaith, H.J. (2013). Low-temperature processed meso-superstructured to thin-film perovskite solar cells. *Energy & Environmental Science* 6 (6): 1739–1743.

52 Wang, Q., Zhang, W., Zhang, Z. et al. (2020). Crystallization control of ternary-cation perovskite

absorber in triple-mesoscopic layer for efficient solar cells. *Advanced Energy Materials* 10 (5): 1903092.

53 Yang, D., Yang, R., Wang, K. et al. (2018). High efficiency planar-type perovskite solar cells with negligible hysteresis using EDTA-complexed SnO_2. *Nature Communications* 9 (1): 1–11.

54 Tang, J., Jiao, D., Zhang, L. et al. (2018). High-performance inverted planar perovskite solar cells based on efficient hole-transporting layers from well-crystalline NiO nanocrystals. *Solar Energy* 161: 100–108.

2
Characterization Methods and Technologies for Halide Perovskite Materials and Devices

Lukas Wagner[1,2], Dmitry Bogachuk[1], Cheng Qiu[3], Gayathri Mathiazhagan[1], Salma Zouhair[1], and Andreas Hinsch[1]

[1] Fraunhofer Institute for Solar Energy Systems ISE, Heidenhofstraße 2, 79110 Freiburg, Germany

[2] University Marburg, Solar Energy Conversion Group, Department of Physics, Renthof 7, 035037 Marburg, Germany

[3] Huazhong University of Science and Technology, Wuhan National Laboratory for Optoelectronics, 1037 Luoyu Road, Wuhan, 430074, P.R. China

2.1 Introduction

Characterization techniques are fundamental to enhance the basic understanding of solar cells and indispensable for providing a feedback loop that enables device optimization. In this chapter, a range of characterization methods that facilitate a deeper understanding of mesoscopic perovskite solar cells (PSCs) are discussed. Following the order of the device processing steps, the chapter begins with methods to study the layer quality of the mesoscopic contact cell before perovskite filling. Here layer thicknesses, porosity, and resistances are considered. Then, the necessary methods to study chemical–physical material and crystal properties are introduced and their applicability to mesoscopic PSC is presented. This is followed by discussion

of spatially-resolved photophysical methods such as photoluminescence (PL) imaging, which are typically carried out when the system is in steady-state. Transient photophysical methods complete this picture. Finally, the investigation on current–voltage (*I–V*) performance includes transient and steady-state characterization methods, as well as certified efficiency measurements and device stability estimations.

2.2 Printing Layer Quality

2.2.1 Thickness Measurement

The layer thickness, constituting any type of solar cell, plays an essential role in the efficiency of the PV device. In mesoscopic cells, the thickness of the carbon-based back contact has a direct influence on the electrical series resistance, where larger thicknesses are desired for achieving lower resistance losses for high fill factor of the carbon electrode based perovskite solar cells (C-PSCs) under full sun illumination. However, if the thickness of the carbon-based contact layer is too large, the perovskite solution infiltration through such a thick layer becomes challenging, reducing the number of photogenerated charge carriers in the underlying photo absorber. The thickness of the space layer (e.g. ZrO_2) also has to be sufficient to avoid any direct electrical contact between graphite and m-TiO_2, yet, it cannot be too thick, otherwise, the solution might not penetrate as well, and/or the photogenerated holes might not be able to reach the back contact due to limited hole diffusion length. The thickness of m-TiO_2 layer also has to be carefully optimized to facilitate efficient electron extraction and transport. Finally, the thickness of the ultrathin c-TiO_2 can not only influence the electron conduction and recombination at the

front contact, but also alter the ion accumulation at the perovskite/c-TiO$_2$ interface leading to unwanted hysteresis effects. All these considerations point out that the layer thickness in C-PSCs has to be precisely controlled and measured, to develop highly efficient perovskite photovoltaic devices. In the following, a range of techniques to determine the layer thicknesses are discussed.

2.2.1.1 Profilometry

One of the measurement tools commonly employed to evaluate layer thickness is contact profilometry. In a profilometer, a stylus (e.g. made of diamond) is moved across a sample to measure the surface height profile, where the vertical position of the stylus is recorded during the movement. The analog input from the stylus is converted into a digital format and can be used to analyze surface roughness and morphology. Compared to the measurement obtained on a reference substrate (on which the layer is deposited), the thickness of a layer under investigation can be easily calculated. There are also noncontact profilometers based on confocal microscopy, optical triangulation, and interferometry, which can actively slow down the wear process, require less maintenance, and can sometimes be more accurate, although may also be limited by the acquisition speed.

2.2.1.2 SEM

The versatile tool scanning electron microscopy (SEM) can be used for a wide range of applications, including layer thickness measurement. The advantage of SEM is that it can acquire highly resolved images with up to nm-sized features, making it possible to detect the presence of even the thinnest layers such as c-TiO$_2$ (typically around 20 nm). Taking SEM images at the C-PSCs cross section provides

an accurate picture of how thick the layers are, how well they are stacked on top of each other, the homogeneity of deposited layers, presence of shunts, agglomerates, etc. Although SEM is a powerful tool to analyze the sub-micrometer objects, it cannot provide a broad overview of the layer thickness and its homogeneity in the entire solar cell.

2.2.1.3 Ellipsometry

Ellipsometry is an analytical technique in which the change in the polarization (namely s- and p-components) of light reflected from or transmitted through the sample surface is measured. When light is reflected at the surface of a material, it experiences a difference in polarization. By analyzing the reflected light beam, polarization change can be obtained from which information about the refractive index of the material and the geometrical structure of the sample surface is found.

When the incident circular polarized light (which can have a single or multiple wavelengths, depending on the application) is reflected by the sample, a change in the amplitude and phase shift of the p and s components of light is caused. With a compensator, the reflected light is again linearly polarized, and this polarization is detected with an analyzer. The p component, in this case, is the polarization of light parallel to the plane of incidence and the s component is for the polarization of light perpendicular to the plane of incidence.

In ellipsometry, the ratio of complex Fresnel reflection coefficients of p- and s-components is measured, which is also given by:

$$\rho = \frac{R_p}{R_s} = \tan \Psi \cdot e^{i\Delta} \qquad (2.1)$$

From the measurement, Ψ and Δ coefficients are extracted, which represent the amplitude ratio and phase-shift of the *s*- and *p*-components of the reflected light, respectively. After obtaining the coefficients, typically, a model is used to fit the results to the calculated response based on Fresnel equations of the specific material and optical parameters. Therefore, often ellipsometry requires an estimation of the expected result before the measurement takes place. The fitting of experimental data to the model results is usually done by regression with a mean square error (MSE) estimator quantifying the difference between the model and the measurement. Once the measurement is well-fitting to the model, the material thickness can be obtained.

Ellipsometry is a convenient characterization tool as it is accurate, nondestructive, quick, and does not require high vacuum conditions (unlike SEM). Moreover, ellipsometry can also be used for evaluating pore size and their distribution in the layer. However, the disadvantage of ellipsometry is the necessity of having an accurate model describing the optical parameters of the layer under investigation.

2.2.2 Porosity Estimation

Since all the layers in standard C-PSCs are porous, the porosity of each layer plays a crucial role. For example, if the pores are too small, only small volumes of perovskite solution can infiltrate the C-PSC stack. On the other hand, layers with different pore sizes can have various effects on the photovoltaic properties of the cell. Thus, the porosity evaluation is sometimes necessary to understand the behavior and improve performance of C-PSCs.

2.2.2.1 Gas Adsorption (BET Method)

One method that is often used for evaluating the effective surface area of the porous substances (e.g. for fuel cell applications) is the *Brunauer–Emmet–Teller* (BET) method [1]. It is based on the theory of multilayer adsorption of gases (e.g. N_2) on a material surface as an extension of Langmuir theory for the monolayer physisorption process [2]. A specific volume of a gas, which is continuously measured by a volume flow meter, is supplied to the sample at a temperature of 77 K, which is the boiling temperature of nitrogen. At such temperature, the nitrogen gas will condense on the porous media, forming adsorbed multilayers, as described by the BET theory. As the volume and pressure of the supplied gas are measured, an isotherm is obtained.

The BET equation to describe the behavior of an adsorption isotherm is derived as:

$$\frac{p}{v(p_0 - p)} = \frac{1}{v_m c} + \frac{c-1}{v_m c}\left(\frac{p_0}{p}\right) \tag{2.2}$$

where v is the measured volume of adsorbed gas, p_0 and p are the saturation and equilibrium pressures, respectively, v_m is the volume required to form a complete unimolecular monolayer of adsorbed gas, and c is the BET constant related to the heat of adsorption and heat of gas liquefaction/vaporization.

Plotting $p/v(p_0 - p)$ against p_0/p gives a straight line, where the intercept yields $\frac{1}{v_m c}$ and the slope is $\frac{c-1}{v_m c}$. The linear part of the isotherm is maintained only in the $0.05 < p_0/p < 0.35$ region, therefore only this isotherm part is used to obtain the surface area of the adsorbent. From the slope and the intercept of the BET plot, the v_m and c can be found, which

are used to extract the total surface area S, given by the equation:

$$S = \frac{v_m N_A s}{V_m} \tag{2.3}$$

where N_A is the Avogadro number, s is the cross-sectional area of the adsorbed molecules, and V_m is the molar volume of the adsorbing gas. Furthermore, the specific surface area can be easily found by dividing the total surface area S by the mass of the adsorbent (i.e. the porous media), which can later be used to find the pore volume as well.

2.2.2.2 SEM/FIB 3D Nanotomography

Besides the BET characterization method based on physisorption, the sample porosity can also be determined by imaging techniques. Scanning electron microscopy can give an approximate idea of the pore size (with appropriate magnification), but cannot produce a quantitative comparison. As the pores are three-dimensional objects, their size cannot be captured by a single microscopy scan as it gives information about the pore size only in two dimensions (e.g. x and y). However, the information about the pore dimensions along z axis, can be obtained by "cutting out" slices of the sample and scanning the investigated area again. Such accurate layer removal can be achieved by a focused ion-beam (FIB), where after each ablation a new microscopy image/scan is obtained [3]. The ion beam is produced by heating metal ions (typically gallium) at the tip of a tungsten needle, forming a Taylor cone, which leaves the tip by field-enhanced thermal emission in a rounded shape with an end radius of approximately 5 nm. Applying a large voltage field (e.g. 10 kV) causes the field emission of the ions in the desired

direction, which are further accelerated and focused by electrostatic lenses [4]. Once the highly energetic gallium atoms hit the sample, the surface atoms will be sputtered away from the surface (Figure 2.1). Repeating this process produces a 3D image of the layer under investigation and can be afterward analyzed by an image software to perform particle/pore segmentation analysis. This SEM/FIB 3D nanotomography is particularly interesting for pore-size engineering, where the pore volumes can be accurately determined and quantitatively compared.
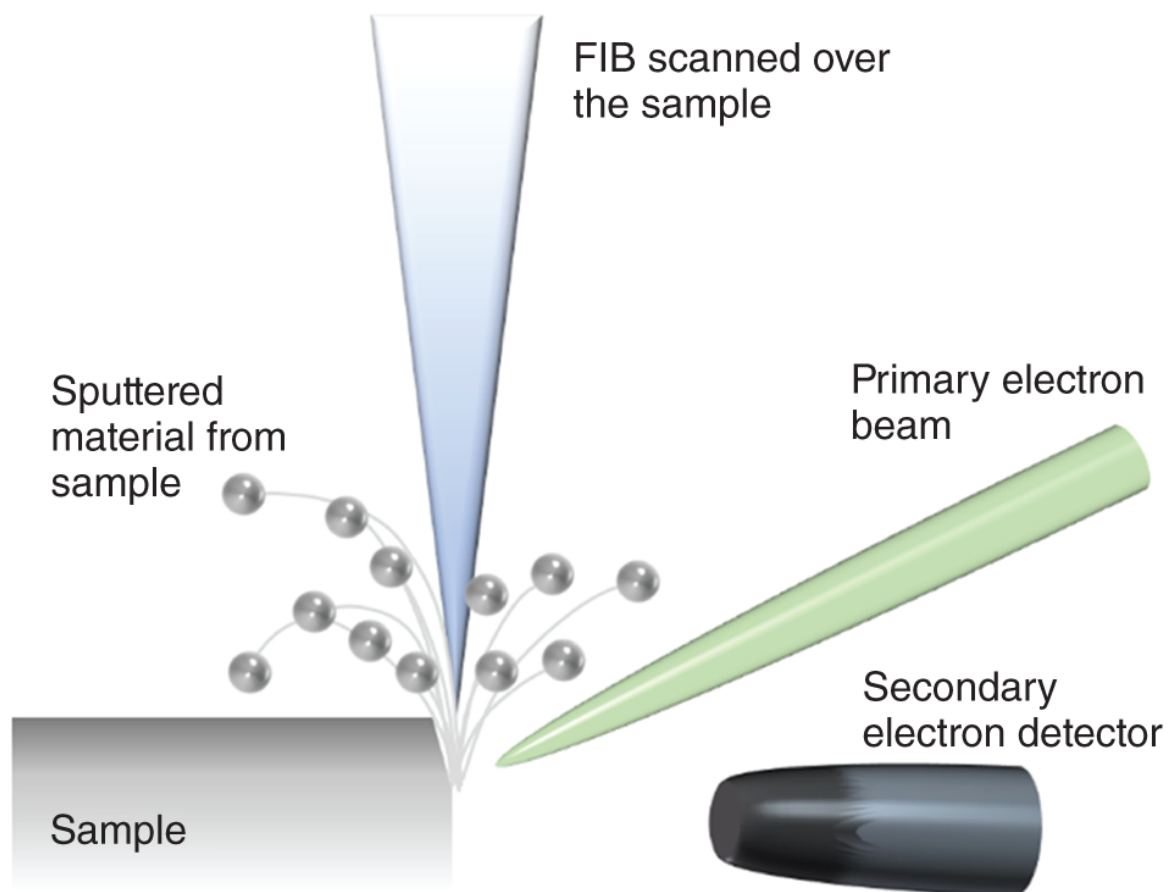
Figure 2.1 Illustration of focused ion beam (FIB) milling process.

2.2.3 Sheet Resistance

2.2.3.1 Four-point Probe Measurement

As the transparent conducting oxide and the carbon-based layer of the perovskite solar cell act as a front- and back-contact, respectively, both of them should have as low series resistance (R_s) as possible to ensure efficient conduction of charge carriers to the corresponding electrode of the PV device. To optimize the resistivity of the layer, an accurate measurement of the sheet resistance (also known as surface resistance) is essential, which represents lateral resistance through a thin square-shaped layer (with homogeneous thickness). The main difference between the standard resistance measurement of material between two probes and the sheet resistance measurement is the independency of sheet resistance on the square size under consideration, providing an accurate and simple comparison between different conductive materials.

As R_s depends on the cross-sectional area (A) of the conductor, the thickness (t) of conducting films also has an impact on it according to Eq. (2.4):

$$R_s = \frac{\rho \cdot l}{A} = \frac{\rho \cdot l}{t \cdot W} \tag{2.4}$$

where ρ is material bulk resistivity, l is the length of the conductor, and W is the width of the conducting film. The sheet resistance R_{sq} is defined as:

$$R_{sq} = \frac{\rho}{t} = \frac{R_s \cdot W}{l} \tag{2.5}$$

As seen from Eq. (2.2), R_{sq} can be expressed in Ohms, but only because it is a particular case for the resistance of the "square" surface. Hence, a more commonly used unit of R_{sq} is Ohm-per-square (Ω/sq or Ω/□) and therefore represents sheet resistance of the layer regardless of the size of the

square under investigation, satisfying the conditions of $W = l$ and $R_{sq} = R_s$.
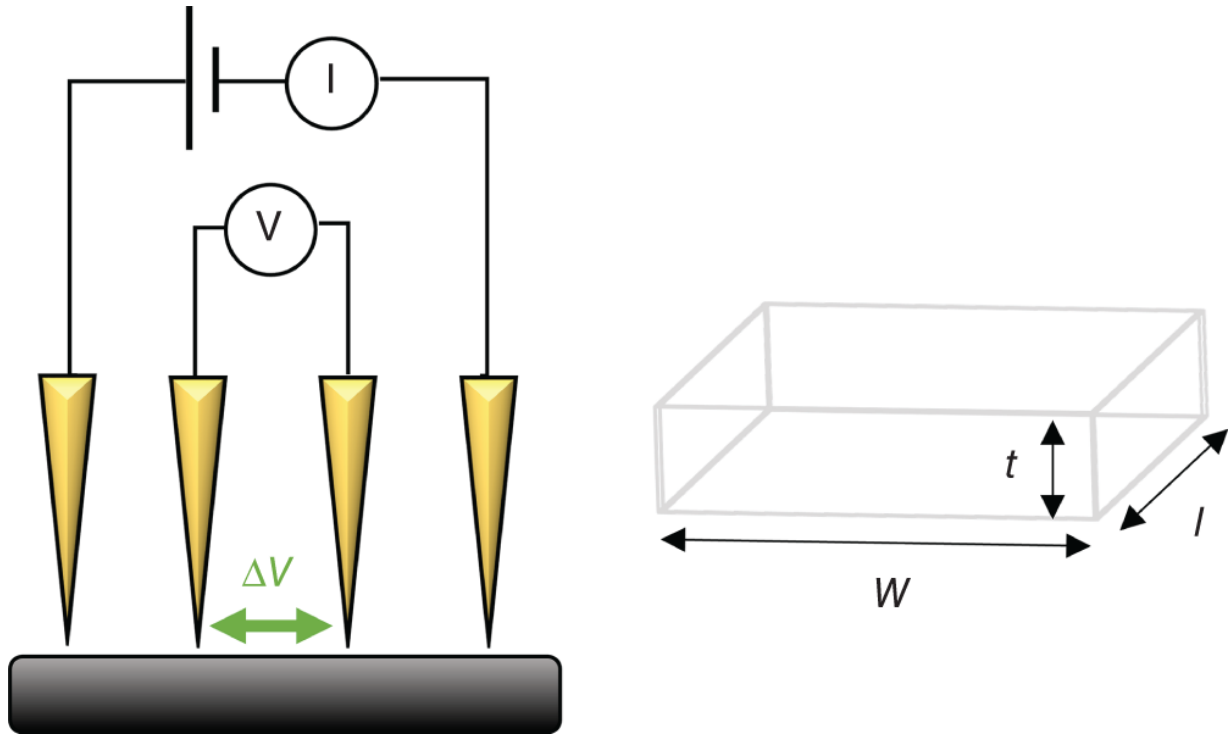
Figure 2.2 Schematic of four-point probe sheet resistivity measurements setup.

One of the methods to measure sheet resistance of thin conducting films (e.g. in PSCs) is a four-point probe method, consisting of four electrical probes arranged in line with an equal distance between each probe (Figure 2.2). When the current is applied between the outer two probes (sometimes referred to as force connections), the voltage drop ΔV between the two inner probes (also known as sense connections) is measured. The separation between the force and sense connections allows to eliminate any additional resistance of the voltage probes and displays only the voltage drop due to sample resistance.

Most of the fabricated PSCs employ doped transparent conductive oxides as front electrodes, due to their low

parasitic absorption and low sheet resistance (usually 7–20 $\Omega\,sq^{-1}$). Often in conventional PSCs, the cell's back contact is made out of a metal, such as gold, silver, copper, or aluminum with meager sheet resistance (reaching <1 Ω sq^{-1}). Naturally, the conductivity of layers made of such metals is higher than that of the carbon-based ones, although effective strategies to reduce their sheet resistivity down to <5 $\Omega\,sq^{-1}$ have been demonstrated.

It has to be noted, that during the four-probe measurement of thin and fragile carbon-based layers, the probe might penetrate through the layer and reach the substrate, on which it is deposited. Therefore, for an accurate sheet resistance measurement, an insulating substrate (e.g. glass) under the carbon-based film has to be used.

2.2.4 Shunt Resistance of Unfilled Cell

Electrical shunts between the graphite and TCO layer can represent a severe source for performance losses in mesoscopic PSCs. A straightforward but powerful method to assess if there are shunts in the printed layer scaffold is to measure the ohmic resistance of the unfilled contact structure. Thereby, the anode and cathode are connected to a multimeter. If the resistance ranges around or beyond 100 kΩ, the structures can be assessed as "shunt free" and used for perovskite filling.

2.3 Material and Crystal Properties

2.3.1 X-Ray Diffraction (XRD) Analysis

X-ray diffraction (XRD) technique is one of the widely used nondestructive techniques in PSCs for analyzing the physical and structural properties of elements and compounds. Depending on the XRD system, it is possible to analyze the samples in powder form or in layered form. In

PSCs, the opportunity to examine the layered form helps in the detailed investigation of the perovskite layer after its fabrication. For PSCs, the photoactive layer and the charge transport layer (CTL) can be analyzed using XRD as a separate entity or collectively. The characteristic properties analyzed through XRD are atomic spacing, phase identification, and crystalline size.

XRD diffractograms at different incidence angles can be acquired. The mode preferred for layers is grazing incidence and referred to as grazing incidence XRD (GIXRD). The higher the incidence angle, the deeper is the layer under investigation. For a multilayered device like PSCs, it facilitates the analysis of the complete device through all the layers. The resultant diffraction pattern has peaks at different 2θ values that correspond to the phases of crystal. Apart from phase identification and crystal size analysis, different computation of the resultant diffractograms helps in the further interpretation of PSCs. For example, Mathiazhagan et al. showed a comparison of percentage composition of the area under the peaks corresponding to PbI_2 ($2\theta = 12.6°$) and perovskite ($2\theta = 14°$) to see the influence of UV treatment of SnO_2/perovskite interface in perovskite degradation [5]. A similar comparison of PbI_2: perovskite percentage to analyze the effect of various electron transport layers (ETLs) on perovskite degradation composition has been carried out by Boldyreva et al. [6].

Even though XRD is a nondestructive technique, in the case of carbon–graphite-based perovskite solar cells (CG-PSCs), the sample preparation plays a vital role. The presence of a micrometer-thick carbon–graphite (CG) counter electrode absorbs the entire incidence/reflected X-rays making it challenging to record the diffraction patterns of the perovskite embedded into the cell. Thus, it becomes

essential to remove the CG electrode from a complete device before analyzing the underlying layers. For this reason, sample preparation for the XRD analysis of CG-PSCs poses a challenge to remove graphite without destroying the layer of interest. For two-step perovskites, the graphite could be easily removed by a Kapton tape [7].

2.3.2 UV–Vis–NIR Spectroscopy

Absorption spectra show which wavelength of light is absorbed by the layer(s) under investigation. The spectra can further be evaluated to determine the optical bandgap of the material. Knowing the absorption spectra of perovskite and the charge transport layers (CTLs) (individually and collectively) provides the key to evaluate the light-harvesting efficiency and respective optical losses of the device. Ultraviolet-to-near-infrared range (UV–NIR) spectroscopy is a technique used to determine the absorption spectra of single or combined layers. The layers are excited using monochromatic light. The ratio between the input and the output intensity can be calculated using Beer–Lambert's law to determine the absorption spectra. Note that the sample configuration needs to fulfill the conditions allowing the approximation with this equation. If this is the case, the absorption A can be calculated from the logarithm of the ratio between the reference light intensity I_0 and the light intensity after passing through the sample I, $A = \log \frac{I_0}{I}$.
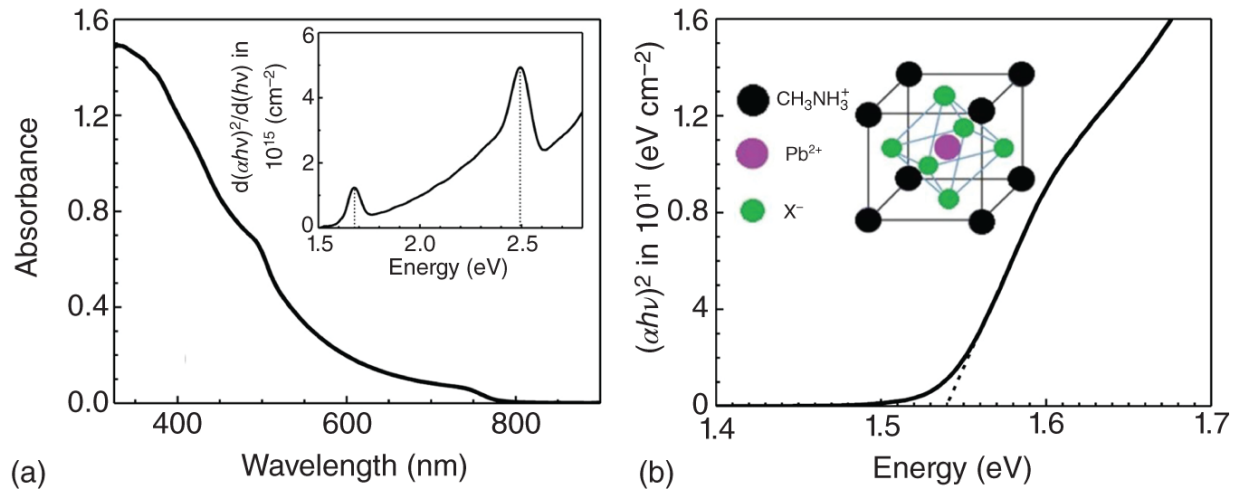
Figure 2.3 (a) UV–vis absorption spectrum of MAPbI$_3$. Inset shows the d[$(\alpha h\nu)^2$]/d($h\nu$) for a better view of the peak. (b) Tauc plot. Source: Chatterjee and Pal [8]/American Chemical Society.

Figure 2.3 shows the absorption spectra of MAPbI$_3$. The peak wavelength absorbed by the layer can be visibly seen (Figure 2.3a). It represents the peak transition from the valance band maximum to the conduction band minimum, as seen at 740 nm. The second peak at 498 nm is also a characteristic peak of MAPbI$_3$ perovskite [8] as a result of the two-valance-band model. d[$(\alpha h\nu)^2$]/d($h\nu$) was plotted in the inset of Figure 2.3a to see these peaks clearly. Here, α is the absorption coefficient, h is Planck's constant (6.626 × 10^{-34} Js), and ν is the frequency of light. 1.67 eV corresponds to 740 nm, and 2.5 eV corresponds to 498 nm.

The optical energy bandgap (E_g) can be determined from the Tauc plot [$(\alpha h\nu)^2$ vs. energy in eV] plotted using the data from the absorption spectra (Figure 2.3a,b). A tangent is drawn from where the curve peaks in the Tauc plot. It gives the E_g value in eV. However, it is advised to take more than one tangent line to determine the E_g correctly.

It is essential to note from which side the device or sample is excited. Usually, it is excited from the glass side. Thus, for the processing of efficient solar cells, it is significant to have a CTL (electron transport layer (ETL) in the n-i-p configuration and a hole transport layer (HTL) in p-i-n configuration), which is transparent to the visible spectrum, i.e. none of the visible wavelengths are absorbed by this layer.

2.3.3 Raman Shift Spectroscopy

An example of a powerful optical tool to analyze the molecular vibrations and interatomic bonding of the substance is Raman shift spectroscopy. Unlike vibrational transitions seen from the Fourier-transform infrared (FTIR) measurements, Raman shifts originate from the electronic polarization of the molecule induced by the incident light (usually monochromatic). In this case, the light beam with frequencies ν and $\nu \pm \nu_i$ is scattered, where the vibrational frequency of a molecule ν_i is detected and presents a Raman shift (i.e. a deviation from the photon energy of incident light). Therefore, each molecule has a set of unique Raman shifts, associated with specific vibrational interatomic bonds.

According to the elementary classical theory, the dipole P of a diatomic molecule under illumination (represented by fluctuating electric field) can be expressed as [9]:

(2.6)

$$P = \alpha_0 E_0 \cos 2\pi\nu t + \frac{1}{2}\left(\frac{\partial\alpha}{\partial q}\right)_0 q_0 E_0 \{\cos 2\pi[\nu + \nu_i]t + \cos 2\pi[\nu - \nu_i]t\}$$

where α is the polarizability of the molecule (α_0 is polarizability at the equilibrium position), E_0 is the amplitude of the applied electric field, $(\partial\alpha/\partial q)_0$ is the rate

of polarizability change with respect to nuclear displacement at equilibrium position and q_0 is the amplitude of the molecular vibrations. This equation describes an oscillating dipole emitting photons with a frequency ν, resulting in Rayleigh scattering of the incident light, whereas the second term of the equation describes the emission of photons with frequencies $\nu - \nu_i$ (Stoke shift) and $\nu + \nu_i$ (anti-Stoke shift), which constitutes Raman scattering. In such a way, by simulating atomic motions in the bonds (e.g. using density-functional theory) it is possible to obtain Raman shift frequencies/bands for complex molecules (with the condition that the polarizability changes during the vibration) and correlate them with the experimentally obtained spectra.

In theory, Raman shift spectroscopy can be used to analyze all the layers of the PSC to understand the bonding environment and how it affects the optoelectronic properties of the cell. However, perovskite films tend to quickly degrade under the strong incident light (even at intensities $<1\,\mathrm{mW\,cm^{-2}}$) [10] of the laser, which is customarily used for Raman shift measurement. It can result in misinterpretation of the vibrational bands of the perovskite and may compromise the measurement. Nevertheless, it is often used to characterize perovskite precursor solutions, CTLs, and electrodes (including carbon-based ones).

Structural characterization of compact and mesoporous TiO_2 layers, which have a hole-blocking and electron-transporting role in C-PSCs, can also be done by Raman shift spectroscopy. The number of vibrational bands observed in the Raman spectra depends on the polymorph type of m-TiO_2. For example, in rutile titanium(IV) dioxide, only four vibrational modes can be observed, whereas, in the anatase phase, six vibrational modes (with motions

including Ti atom) are present. Additionally, doping the TiO_2 with foreign atoms will result in changes in vibrational frequencies, arising from the change in polarizability. In such a way, it is possible to confirm the integration of dopants and detect changes in the molecular arrangement and their influence on the optoelectronic properties of the final C-PSC.

An accurate evaluation of the graphite crystallite properties can also be done via Raman shift spectroscopy, as it is a fast and nondestructive characterization method for such applications. Typically, in graphite crystals, Raman shift bands at 1380, 1580, 1620, and $2720\,cm^{-1}$ can be observed, which are commonly attributed to D, G, D′, and 2D bands, respectively. The G band is always found in the graphitic carbon, arising from a doubly degenerate E_{2g} vibrational mode, caused by an in-plane vibration of the hexagonally structured crystalline graphite. The D band is often observed in disordered carbon structures with crystal imperfections and symmetry loss and is associated with an in-plane A_{1g} vibrational mode. The intensity of the D band can be correlated with the type and density of structural defects in a crystal. Therefore, a common method to evaluate the graphite lattice disorder is by looking at the ratio of intensities of D and G bands (I_D/I_G). Naturally, the graphite crystallites with a lower I_D/I_G possess a lower density of structural defects (e.g. pyrolytic graphite), whereas amorphous and non-graphitic carbon has a higher I_D/I_G ratio, as can be seen from the [Figure 2.4](#). For large crystallite size (L_a), where the sheet edge as the only defect type present, an approximation $I_D/I_G \propto 1/L_a$ given by Tuinstra and Koenig can be used for comparing crystallite lateral dimensions. The crystal defect density, type, and crystallite size can have a direct influence on the charge

carrier mobility and, therefore, series resistance and FF of the PSC. Thus, Raman shift spectroscopy can be very beneficial for evaluating properties of carbon-based layers and developing highly conductive back contacts for enhancing the efficiency of C-PSCs.

2.3.4 Scanning Electron Microscopy (SEM) and Energy Dispersive X-Ray Spectroscopy (EDX)

2.3.4.1 Scanning Electron Microscopy (SEM)

Electrons are the negatively charged particles of an atom, orbiting around a nucleus. They can be released by heat or through an applied electric field. They have 2000 times less mass as compared to a proton and can reach wavelengths that are 100 000 times smaller compared to light while being able to reach high energy levels. Hence, electron microscopes, among which scanning electron microscopes, are capable of producing high-resolution magnified images – up to 2 million times magnification – through the principle of electron–matter interactions.

The working principle of an electron microscope is comparable to that of an optical microscope. The source of light used to illuminate the sample in an optical microscope would be replaced by an electron gun – a tungsten filament is commonly used as the electron source, and electromagnetic lenses and apertures would replace the glass lenses used to focus and control the path of the incident electron beam.

The free electrons are generated by heating the tungsten filament to temperatures that can reach up to 2700 °C. A voltage is then applied to the electrons, which allows their acceleration through the microscope's vacuum-filled column and passes through several electromagnetic lenses and apertures to create a focused beam that hits and scans

the surface of the sample. Depending on the depth of interaction of the incident electron beam with the inspected device, different signals would be emitted allowing for high-resolution images that can be obtained through the different detectors that capture the diffused electrons namely, auger electrons that are emitted at an interaction depth of 1 nm providing surface-sensitive information, secondary electrons (SE) that are low-energy electrons that provide information on the morphology of the sample resulting from inelastic interactions at a depth that ranges from 5 to 50 nm, and backscattered electrons (BSE) that are high-energy electrons that result from elastic interaction of the beam with the sample and give more in-depth morphological and structural information on the sample [12] (cf. Figure 2.5).
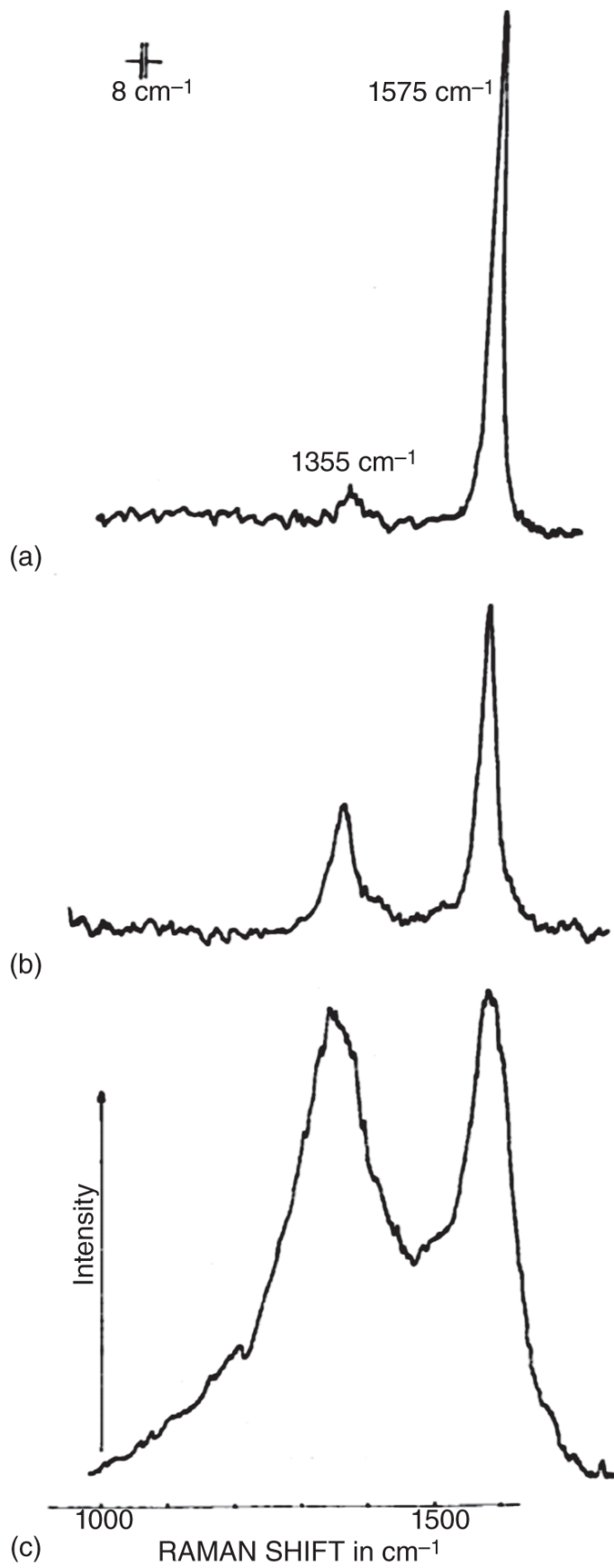
Figure 2.4 Raman shift spectra of the (a) stress-annealed pyrolytic graphite, (b) commercial graphite, and (c) activated charcoal, showing the difference in ratio between intensities of D and G bands – I_D/I_G. Source: Tuinstra and Koenig [11] with permission of AIP Publishing.

Scanning electron microscopy (SEM) provides information on the topography, morphology, composition, and crystallography of the investigated mesoscopic PSCs. The quality of the structural stack forming the mesoporous layers along with the quality of infiltration of the perovskite and its homogeneous embedment into the mesoscopic layers is fundamental to establishing optimal electronic contact with the layers, and thus obtaining highly efficient devices. For that matter, SEM allows to inspect and provide information on the surface, the side view, and the cross sections of the monolithic mesoporous PSCs. As illustrated in Figure 2.6 [13], the thickness of the deposited stack (can reach up to several micrometers for specific mesoscopic layers), the structural porosity of the mesoporous layers, the size of its pores, the morphology of the back contact i.e. carbon layer (flaky or porous or a combination of both for carbon/graphite composites), and the homogeneity of the filling of the perovskite are the primary information that is investigated for monolithic mesoscopic PSCs through SEM.
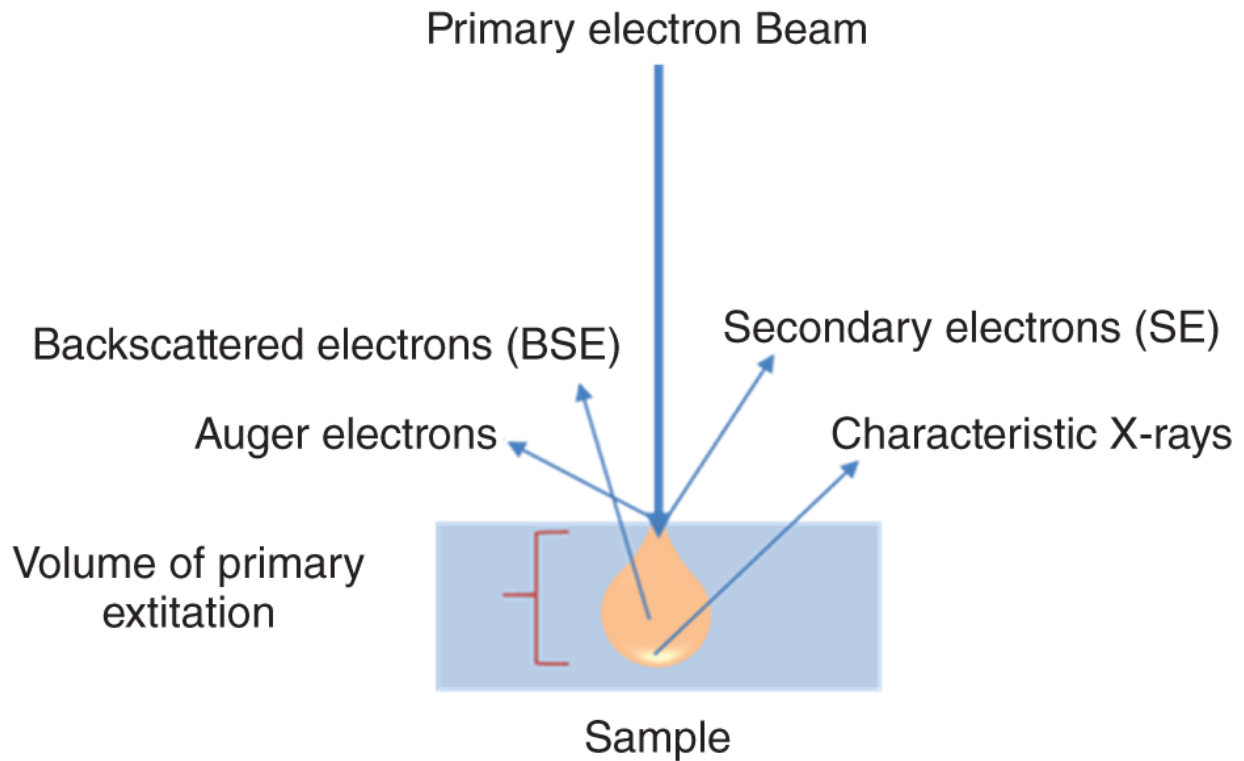
Figure 2.5 Principle of electron beam interaction.
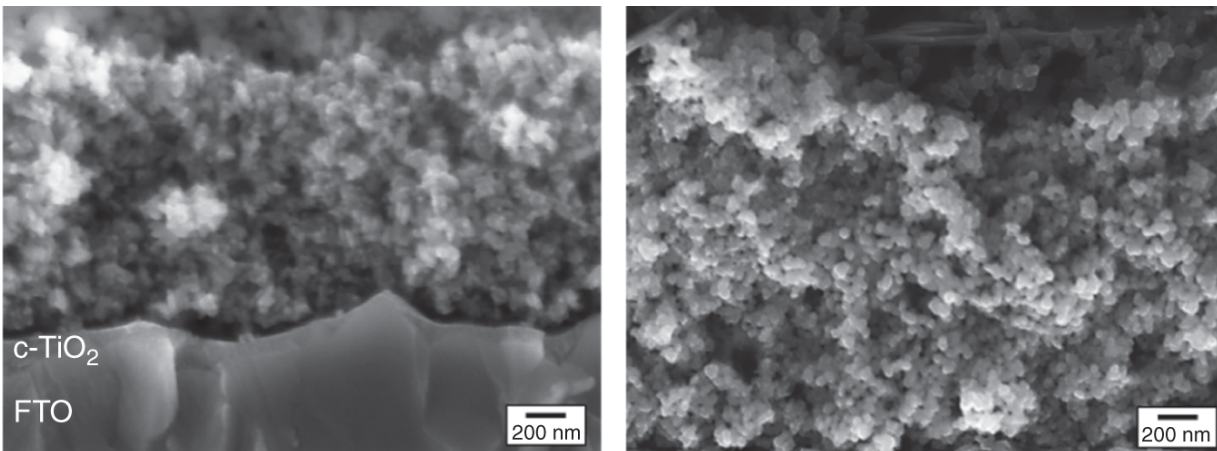
Figure 2.6 SEM images of FTO/c-TiO$_2$/m-TiO$_2$ of unfilled PSC stack (left) m-ZrO$_2$ layer (right). Source: Yasaroglu [13].

2.3.4.2 Energy Dispersive X-Ray Spectroscopy (EDX)

As a complement to SEM, energy dispersive X-ray spectroscopy (EDX or EDS) is a characterization tool that

provides elemental information on different types of materials in the sample. Among the various detectors equipped in a scanning electron microscope, an energy dispersive spectrum detector would typically be featured. These detectors allow to obtain information on the elemental composition of a sample through an electron microscope rather than just obtaining an image of that sample.
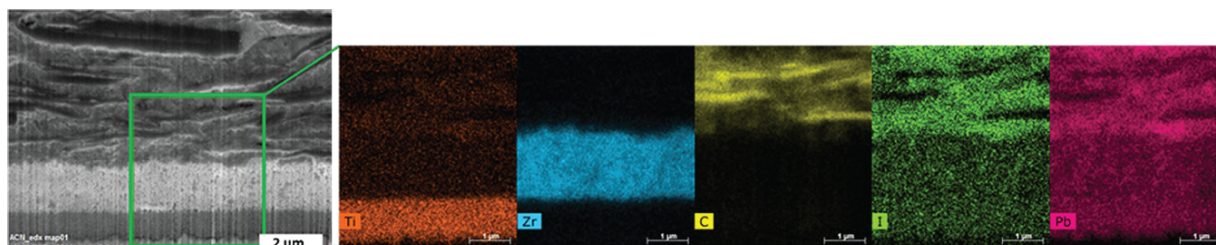
Figure 2.7 SEM image and EDX maps of a mesoporous cell cross section, indicating the dense distribution of perovskite (MAPbI$_3$) throughout the mesoporous TiO$_2$/ZrO$_2$/graphite-carbon stack. Source: Wagner et al. [15], American Chemical Society.

EDX uses the emitted characteristic X-ray of materials, diffused after the incident electron beam hits the inner shell of the in-depth atoms in the scanned surface, to identify the various compounds present in a sample [14].

Figure 2.7 [15] provides an example of the use of EDX characterization for mesoscopic PSCs. EDX is especially effective to examine the homogeneity and the distribution density of the infiltrated perovskite throughout the mesoscopic stack. It is also a practical tool to observe the uniformity of the deposition of doped or functionalized layers.

2.3.5 Atomic Force Microscopy (AFM)

Atomic force microscopy (AFM) is another nondestructive microscope technology fundamental to characterizing and

obtaining information on the topography of the thin film surface of a solar cell at the nanoscale. It allows obtaining 3D magnified images of the investigated samples with the help of an applied force – either originating from an applied voltage or an external magnetic field. Thus, allowing the possibility to also investigate the roughness and surface quality of nonconductive insulating thin film layers [16].

As sketched in Figure 2.8, the concept of AFM consists of moving a cantilever across the sample, where a detector records its vertical displacements due to morphological differences. In this case, the cantilever should have a lower spring constant than that found between atoms. By scanning the cantilever, a 3D image of the surface is obtained. The resonance of the spring frequency is given by $f_0 = \frac{\sqrt{k/m_0}}{2\pi}$, where f_0 is the resonant frequency of the cantilever spring, k is the spring constant which Binning et al. [18]. established needs to be as low as possible to ensure a soft spring, and m_0 is the given effective mass of the spring. The displacement of the cantilever tip over the investigated surface is driven by force applied on it, and three-dimensional images can be obtained through a photodiode that detects the force exerted by the closeness of the tip to the surface of thin film.
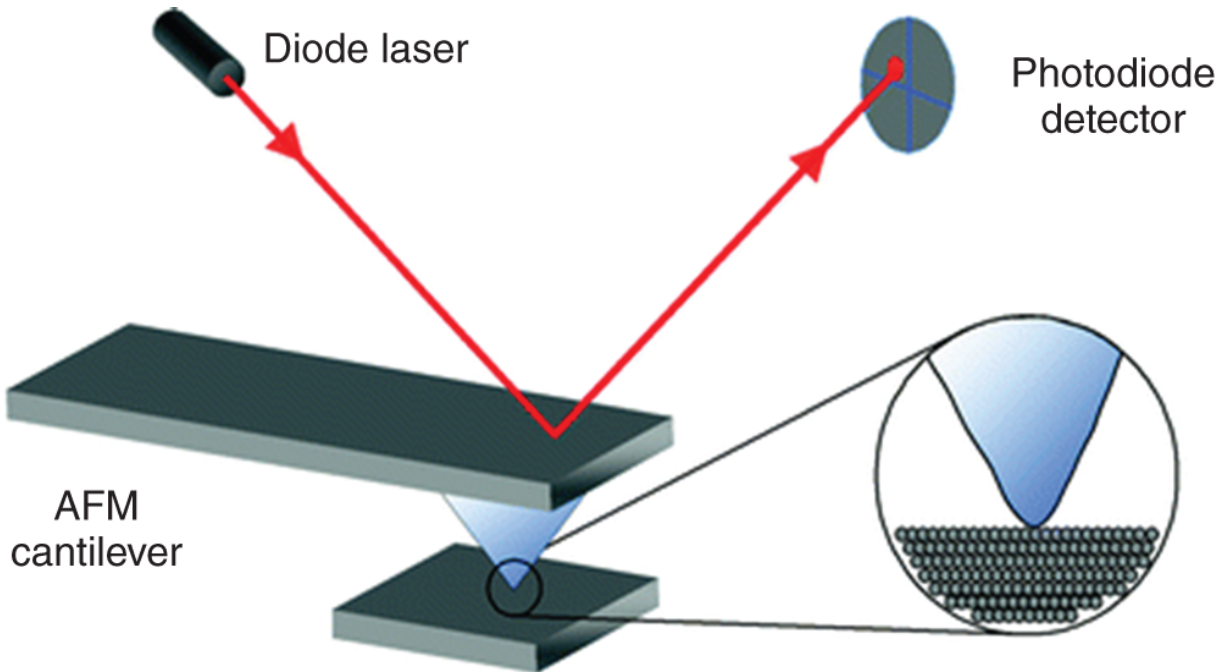
Figure 2.8 Schematic diagram of the basic setup of an atomic force microscope. Source: Grobelny et al. [17] with permission of Springer Nature.

Depending on the nature of the interaction between the cantilever tip and the surface, atomic force microscopes can operate following three different modes, contact mode, noncontact mode, and tapping or otherwise known as intermittent contact mode [17].

- **Contact mode**: The cantilever tip is in direct contact with the surface. This scan mode is selected when the interaction between the probe and the sample would be repulsive.

- **Noncontact mode**: This mode allows the topographical scanning of surfaces with little or no contact between the tip and the surface. The tip interacts with the investigated surface through an atomic force of attraction.

- **Tapping mode**: The cantilever tip is intermittently in contact with the investigated surface. The tip oscillates

at a close range to its resonance frequency. As the tip is brought at a proximity to the sample, the nature of the interaction forces would vary from attraction to repulsion.

For mesoscopic PSCs, AFM is an effective and fundamental tool to study the roughness, uniformity, and morphology of various deposited thin layers namely the compact hole-blocking layers (HBL). The compact HBL, c-TiO$_2$ is typically used as HBL for monolithic mesoscopic PSCs. As previously mentioned, is required to be 20–30 nm thick to attune to the rough fluorine doped tin oxide (FTO) layer surface. Additionally, tapping mode or contact mode would most commonly be used to study the topography of the deposited thin films in PSCs. It would mainly be used to complement other imaging characterization tools such as SEM. AFM can also be useful to study the grain structure as well as analyze the electrical response and charge transport of perovskite layers through high-resolution electrical mapping of the investigated surface. Figure 2.9 shows AFM images of c-TiO$_2$ layers.

2.3.6 Contact Angle Measurement

Contact angle (CA) measurement, in general, is used to analyze the surface properties of the interested layer under investigation. The surface tension of a solid layer is analyzed using a testing liquid (commonly deionized water). The higher the surface tension of a layer, the higher is the CA measured. As PSCs are multilayered devices, the wettability of each layer plays a vital role in its adhesion onto the other layer. It affects the contact between layers and, eventually, the charge transport in the complete devices.

In the case of mesoporous layers in PSCs, the wettability of a layer further affects the infiltration. Considering the case

of graphite-based PSCs, the infiltration of perovskite solution comes in as the final step in the device fabrication. Thus, an excellent wettability is required to result in complete pore filling of the underlying layer with perovskite solution. In graphite-based PSCs, CA measurement can be measured in unfilled devices. It gives an idea about the quality of infiltration in the PSCs later. It can be done by analyzing the change in the CA and the bubble height H over time [19]. While interpreting the CA and bubble height over time, care has to be taken to notice that the base diameter BD of the drop doesn't change drastically as this could mean evaporation of the drop rather than infiltration into the pores (Figure 2.10).
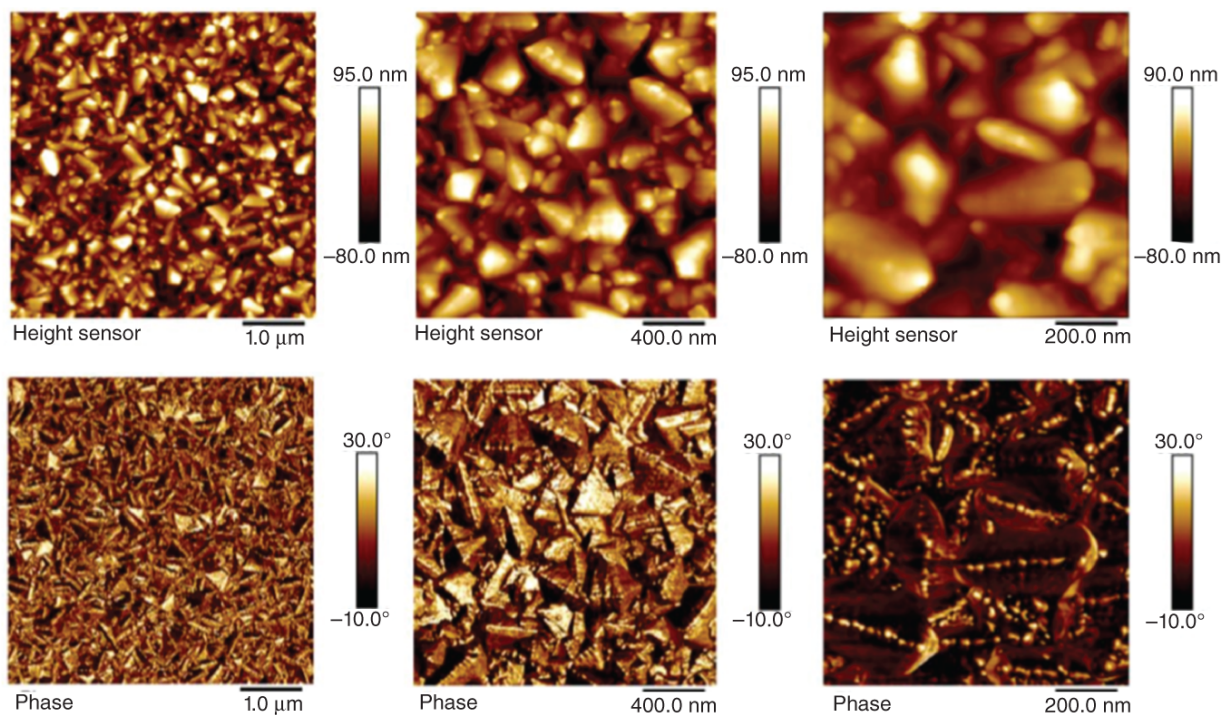
Figure 2.9 AFM images of spray-coated compact TiO$_2$ layers on FTO scanned through tapping mode. Top images: Surface topography at different scale bars, the dark spots refer to depth. Bottom images: Phase images at different scale bars helping to determine surface. Source: Yasaroglu [13].

The literature shows various methods to improve the wettability of the underlying layer. A popular way is to treat the surface at a higher temperature. In the direction of a low-temperature solution to improve surface wettability, UV–ozone treatment [20, 21] and plasma treatments [22] are widely suggested methods. Another technique is the use of additives to the corresponding precursor solutions [23], which forms hydrogen bonds to reduce the surface tension of the liquid, thereby improving the wettability. Thus, CA measurement is one of the quality control methods that can be used to assess how well the perovskite precursor can infiltrate into the mesoscopic layers.

2.4 Spatially Resolved Steady-state Photophysical Methods

Microscopically resolved optoelectronic methods provide spatial information on the fundamental physical properties of the solar cell. It is typically achieved by a recording of different photons emitted by the sample by processes such as luminescence due to radiative recombination or infrared light emitted due to joule heating.

(a)

CA°(R)   H   CA°(L)

BD

H: Height (mm)
CA: Contact angle (°)
BD: Base Diameter (mm)

(b)

Droplet height (mm)

0.40
0.35
0.30
0.25
0.20
0.15

- w/o SL
- 10 nm Al_2O_3
- 40 nm Al_2O_3
- 100 nm Al_2O_3

0   20   40   60   80   100   120   140

Time (s)

(c)

0 s   30 s   60 s   90 s

30.7°   28.2°   26.1°   24.4°

120 s   150 s   180 s   240 s

21.4°   16.9°   10.8°
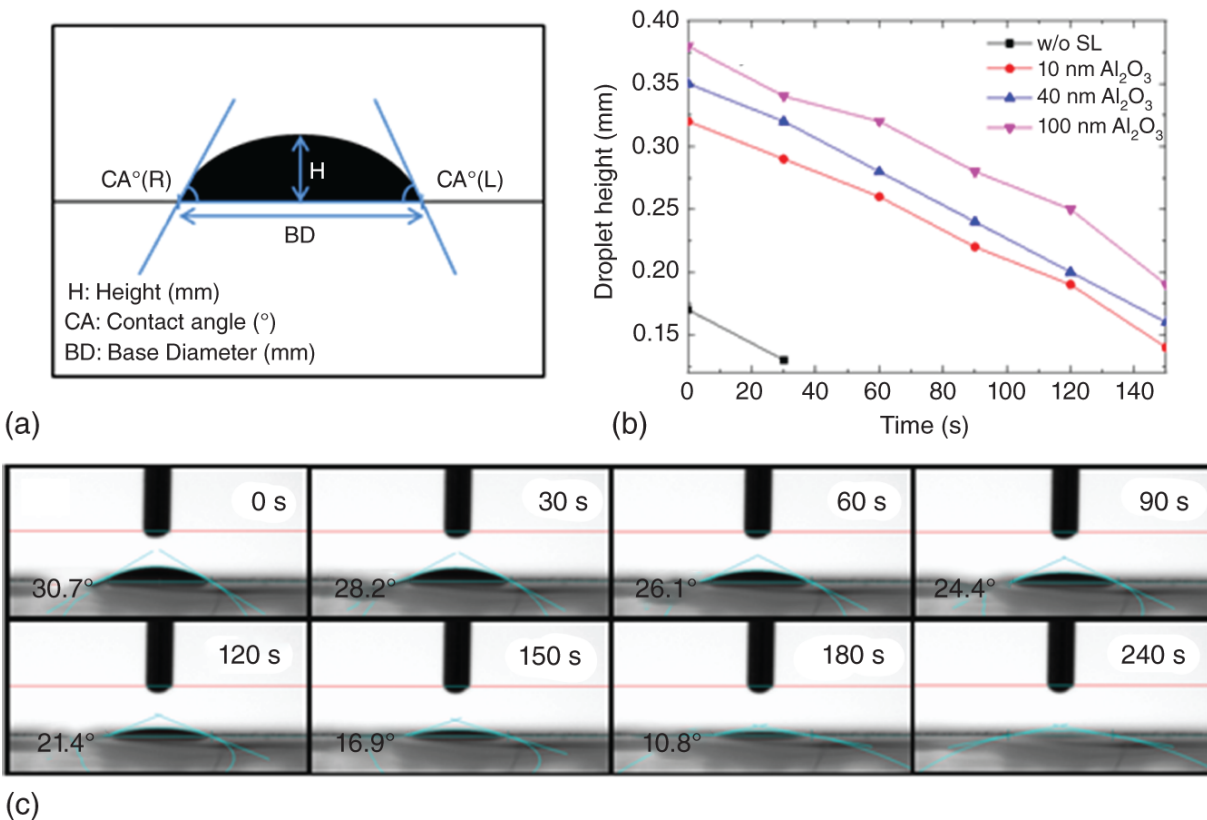
Figure 2.10 (a) Representative image of a drop on the layer of investigation through CA measurement. (b) Change in the drop height over time for varying thickness of Al_2O_3 in FTO/mp-TiO$_2$/sputtered Al_2O_3 sample (c) Series of images taken during the CA measurement for a cell with 40 nm of sputtered Al_2O_3. Source: Mathiazhagan et al. [19], American Chemical Society.

Focusing first on radiative emission, the generalized Planck's law tells us that the photon current density, i.e. the (photo)luminescence intensity, is exponentially proportional to the difference of the Fermi energies [24]. The quasi fermi level splitting (QFLS) can be regarded as internal photovoltage, and, non-surprisingly, in ideal solar cells the PL intensity correlates with the V_{oc} [25]. However, as demonstrated by Würfel's group for organic PV [26] and by Nehers' group for perovskite PV [27], for nonideal devices there is an offset between the QFLS in the

perovskite bulk and the externally measured V_{oc} that can be assigned to surface recombination losses at the contact layers. In the following, a range of steady-state luminescence imaging techniques is introduced that also enable spatially resolved analysis of perovskite layers and the respective interfaces to contact layers.

2.4.1 Photoluminescence Microscopy Imaging

Optical microscopes are a powerful tool for quality control e.g. after perovskite filling. Camera-based microscopes can be employed to measure the PL image by choosing a monochromatic light source (e.g. with an LED) and adding an optical low band pass filter in front of the camera. Thereby, the light source excites charge carriers in the perovskite to the conduction band. Upon recombination, photons with a corresponding wavelength at or below the bandgap are emitted. As they have a wavelength larger than the photons from the excitation light, these photons are able to travel through the longpass filter and can be recorded with the camera while the excitation light is blocked.
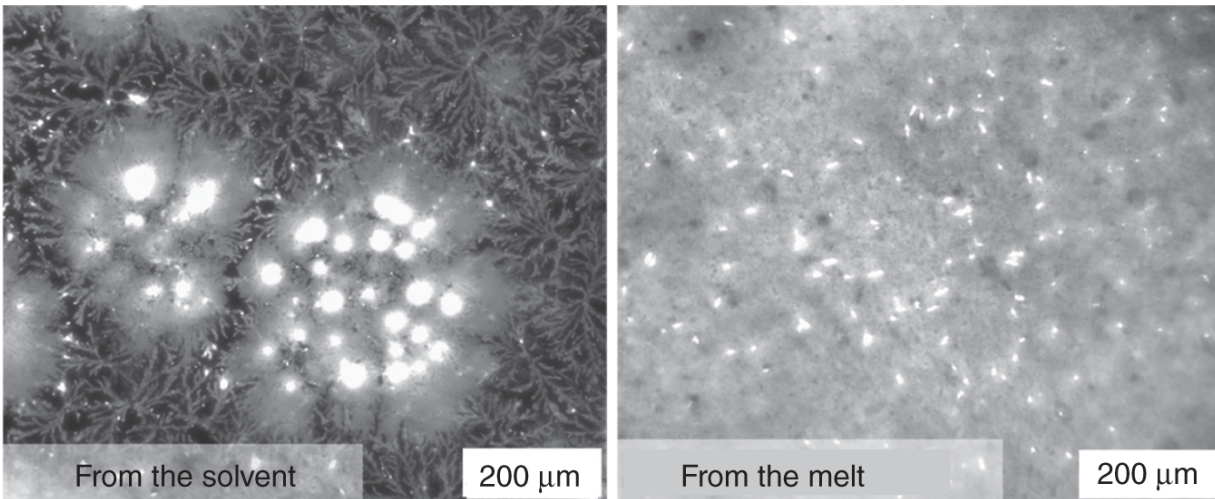
Figure 2.11 Microscopic PL images of two mesoscopic PSC (top view from the glass side), comparing devices process by a DMF-based (left) and a "molten-salt"-based precursor. The scale bar represents 200 µm.

Thereby, the homogeneity of the filling of C-PSCs can be studied with a microscopic resolution as the presence of perovskite is indicated by its PL emission and can be sharply distinguished from unfilled spots where no perovskite and hence no PL is seen. As discussed in the section on real-time PL measurement, this approach can also be employed to visualize the perovskite crystallization in real-time. Furthermore, as discussed below, the coupling to the contact layers can be visualized by recording the PL images at different electrical biases.

A common artifact from unwanted inhomogeneous crystallization are bush-like structures, as displayed in Figure 2.11. Such structures emerge, e.g. in dimethylformamide (DMF)-based precursor solution as this can lead to the formation and precipitation of intermediate DMF complexes during crystallization (left image). The right image shows a homogeneous crystallization with a high PL signal, as obtained by crystallization from a "molten salt" precursor [15].

2.4.2 Microscopic Photoluminescence Spectroscopy Mapping

While the advantages of the above-described camera-based imaging technique lie in its easy implementation and the real-time observation, the image does not contain any spectral information. In contrast, in microscopic photoluminescence (µ-PL) spectroscopy, a map of highly-resolved PL spectra is produced when scanned along the probe of the sample. Therefore, the sample is excited by a microscopically focused excitation laser, and the PL signal is recorded through a confocal microscope in a grating spectrometer.

It needs to be noted that due to the intensely focused laser beam in this method, the excitation photon flux density can easily exceed that of one sun. Secondly, the sample is only excited on a small spot, and charge carriers might migrate to the surrounding and unilluminated areas.

As a general note, PL spectra can also be recorded in a simpler PL spectrometer without obtaining spatial information.

2.4.3 Electroluminescence Imaging

Electroluminescence (EL) imaging is closely related to the PL imaging method. However, here the charge carriers are not excited optically but electrically. Therefore, an electrical bias of $V > V_{oc}$ is applied. Figure 2.12 shows the comparison of an EL and PL image of a spot on an "in situ" type mesoscopic PSC. The EL image was recorded under a bias of 1.1 V, while the PL was obtained under blue (405 nm) LED illumination at an intensity close to one sun at an open circuit. Note that a different scale for signal intensity was used. In the PL image recorded at open circuit, the highest signal is outside of the active area (on the upper

and lower edges of the image) while in the EL image, only spots that are electrically coupled to the contact layers are luminescing. As discussed in the next section, this discrepancy can be overcome by bias-dependent PL measurements.

While EL imaging can provide insightful information on charge carrier dynamics, it is essential to note that for perovskite PV, this method needs to be treated with caution. As demonstrated by Soufiani and coworkers, the PL image changes strongly after application of a bias voltage, which mandates a profound choice of the time at which the sample is considered to be in a steady-state [28]. Similar can be observed for PL imaging and the choice of the stabilization time after turning on the excitation light. While for both methods, irreversible degradation cannot be excluded. Regarding that the devices are optimized for operation under solar illumination, it could be assumed that in the optical excitation, the PL method is less detrimental than the operation in the dark under forward bias. In our own experience, the required sampling time to obtain comparable signal-to-noise ratios is significantly longer for the EL methods (several 10 seconds for a bias of e.g. 1.1 V) in comparison to the PL method (in the range of 0.1 second for excitation equivalent to one sun).
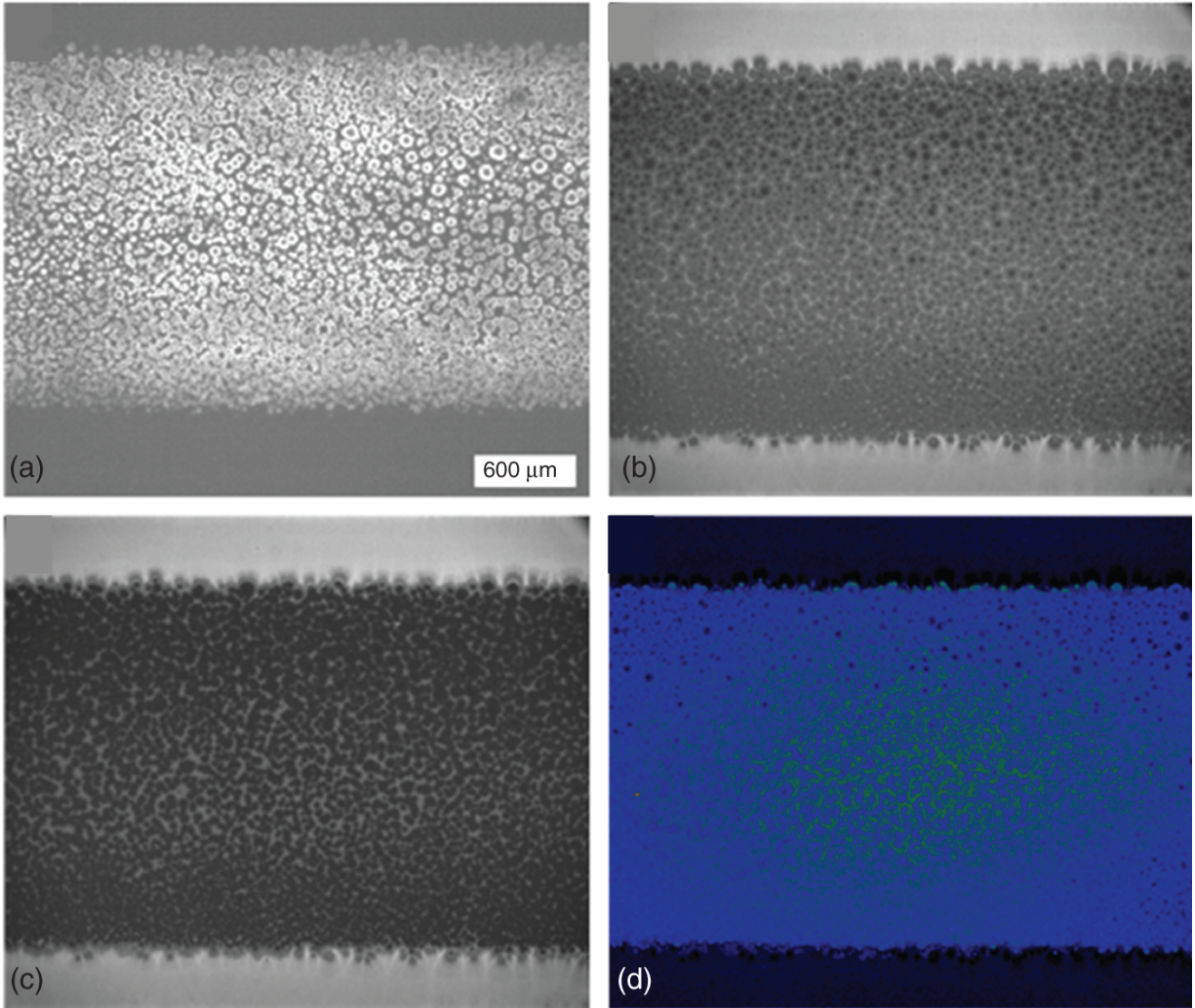
Figure 2.12 EL image (a) as well as PL image under open circuit (b) and short circuit (c) of an "in situ" type mesoscopic PSC. (d) is the subtraction of PL_{SC} from the PL_{OC} image.

2.4.4 Bias-dependent Photoluminescence Imaging

PL imaging is typically carried out in an open circuit (PL_{oc}). As discussed above, thereby only information on the presence of perovskite can be obtained. In fact, the highest PL_{oc} signal is observed outside the active area on the bare perovskite, where no "quencher layers" is present. PL_{oc} is

not a satisfying indicator to assess device performance. While outside the active area, high PL_{oc} indicates that charge carriers are effectively photogenerated, they do not contribute to the photocurrent. It is informative to record a PL image under short circuit condition (PL_{sc}), as shown in [Figure 2.12c](#), to assess charge extraction of photogenerated charge carriers. We observe a strong quenching of the PL in the active area while outside the active area, the PL intensity remains unaltered. [Figure 2.12d](#) shows an image where the PL_{sc} image was subtracted from the PL_{oc} image. Thereby, we obtain an image that indicates the regions where charge carriers are both efficiently generated and extracted [29]. The charge extraction image (d) resembles – although not exactly – that of the EL (a). Yet, it needs to be kept in mind that the direction of the current flowing through the device is inverse in the two methods.

2.4.5 Real-time Photoluminescence Measurement

In addition to steady-state PL measurement, allowing to quantify radiative recombination and excess charge carrier density, PL can also be used to analyze different crystallization stages of perovskite. When the precursor solution is deposited on a substrate, it exists in a liquid form, having no perovskite crystal structure, and hence do not display perovskite-type PL. However, as soon as the perovskite nucleation starts, photoactive perovskite crystals begin to grow, facilitating charge carrier generation and recombination processes. In this way, it is possible to evaluate the nucleation behavior, crystallization dynamics, and to quantify the crystallization rate.

A key advantage of the mesoscopic structure is that the cell anode and cathode are both already present at the time of

perovskite crystallization. This allows monitoring the evolution of the photocurrent during crystallization in parallel to the PL measurement and hence enables to link the PV performance with the crystallization process directly [7].

Several reports have shown how such real-time PL can be employed to understand the perovskite crystallization stages in standard layer-by-layer deposited cells as well as in mesoscopic C-PSCs. Fundamentally the crystallization of planar films is different from the one happening inside the mesoporous scaffolds, as crystals are constrained by the pore size. Therefore, it can be expected that heterogeneous nucleation starts easily due to the abundance of the nucleation sites inside the mesoporous layers. Naturally, the perovskite crystal size within the mesoporous scaffold is also much smaller as for free-standing perovskite films as it is confined by the pore size, which is typically 5–20 nm in radius. Despite large differences in the crystallization dynamics, its stages are similar following the classical growth mechanisms from precursors:

(1) Increase in precursor concentration.

(2) Supersaturation leading to nucleation.

(3) Perovskite crystal growth.

Looking at the PL signal during these stages, several stages can be observed. Firstly, the increase of precursor concentration (e.g. by the evaporating solvent) cannot be observed from PL, as no solid-state constituents have been formed yet. But as soon as the concentration of precursors reaches supersaturation, the nuclei start to form by several precursor molecules (in classical nucleation model referred to as monomers) clustering together. As soon as a specific (critical) nucleus radius is reached, the crystal growth starts. Under incident light, it would generate electron–

hole pairs, the radiative recombination of which can be seen from PL measurement. Therefore, the real-time PL measurement can provide information on the perovskite crystallization dynamics only starting from the beginning of the nucleation.

In Figure 2.13a, one can see a time evolution of the PL intensity and its spectral position as well as the evolution of the photocurrent external quantum efficiency (EQE) during the 2-step deposition where perovskite is converted of PbI_2 to $CH_3NH_3PbI_3$ upon introduction of CH_3NH_3I. In the first stage, the increase in PL intensity is affiliated with the continuous nucleation and formation of perovskite crystallites after the supersaturation. Interestingly, little amounts of PbI_2 at the perovskite grain boundaries can passivate the perovskite crystals, which is reflected in a high PL intensity. During the second stage, as all the precursors are converted into perovskite, the PbI_2 passivation is removed, introducing additional energy traps. Additionally, the bulk non-radiative recombination also increases during crystal growth, reducing the PL further.

In stage three, the PL signal does not change, indicating a complete conversion to perovskite. Surprisingly, however, most of the photocurrent does only emerge at this third stage, highlighting that more processes happen even after the crystals are formed. The experimental data suggest that in this third phase, the perovskite material rearranges inside the mesoscopic contact scaffold. It establishes efficient electric contact between anode and cathode to allow the extraction of the photogenerated charge carriers.

An example of real-time PL monitoring of one-step perovskite deposition is the methylamine-induced $CH_3NH_3PbI_3$ liquefaction and recrystallization. Here the

collapse of the ABX_3 structure does not happen immediately after the introduction of CH_3NH_2 gas (also referred to as MA^0). First, methylamine binds to the surface of perovskite and diffuses through grain boundaries, isolating them from each other. As the perovskite crystal size and number of dangling bonds (due to CH_3NH_2 passivation) gets continuously reduced, the non-radiative recombination becomes lower, causing a sharp peak in PL. However, once a certain amount of methylamine is reached, the perovskite crystal structure ceases to exist, leading to a complete loss of PL. Once methylamine is removed from perovskite, a reverse process happens that resembles the crystallization stages discussed earlier: (i) nucleation and formation of perovskite (PL rises), (ii) growth of perovskite crystals and formation of multiple energy trap states due to increased surface and bulk non-radiative recombination (PL decreases). (iii) Finally, strain-induced perovskite grain coarsening causes a decrease in number of grain boundaries and consequentially the number of surface trap states (PL increases) [30] (Figure 2.14).
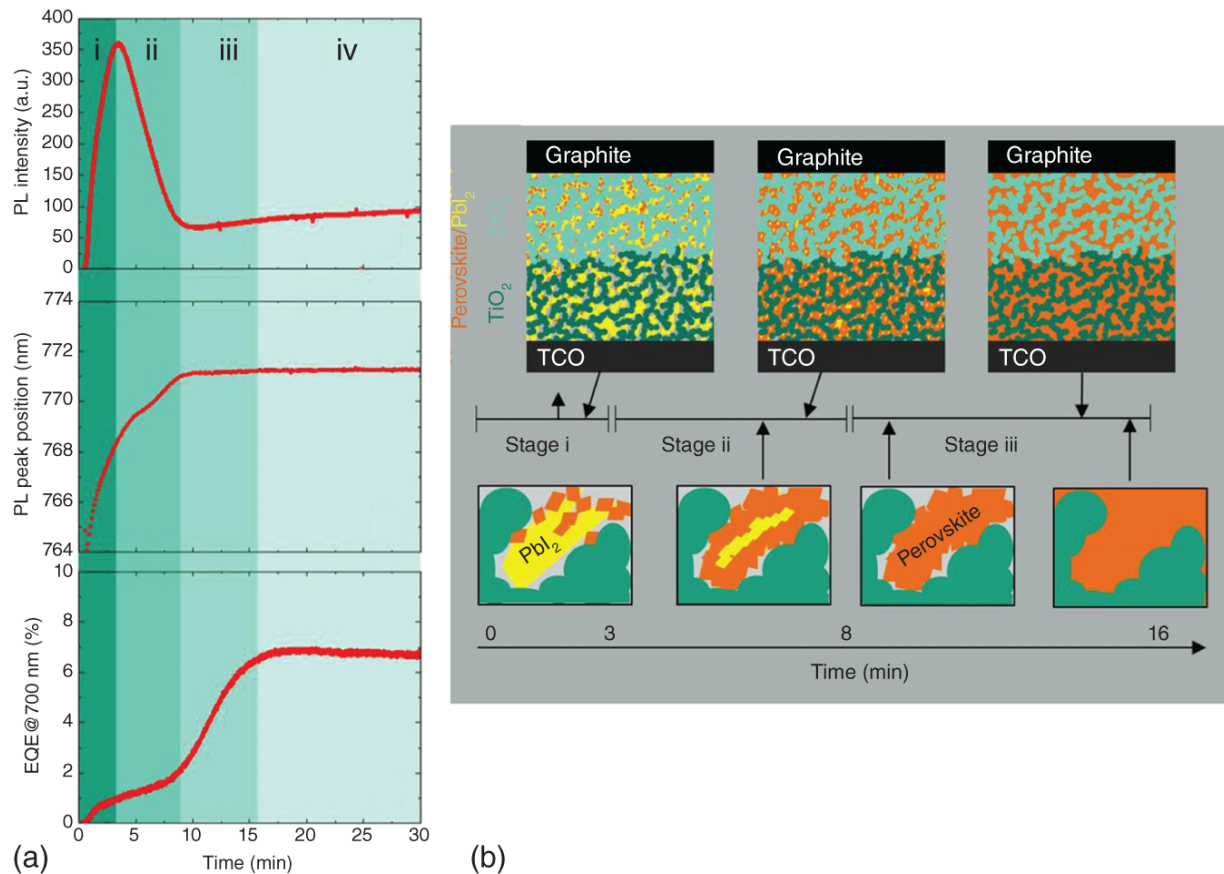
Figure 2.13 (a) Real-time monitoring of PL intensity and spectral peak position as well as photocurrent (EQE). (b) Derived crystallization stages for 2-step crystallization. Source: Wagner et al. [7] Springer Nature/CC BY-4.0.

2.4.6 Dark Lock-in Thermography (DLIT)

Dark lock-in thermography () is a camera-based nondestructive tool to detect the shunt spots in the solar cell. An infrared camera is used to acquire the thermal output signals from a solar device. Figure 2.15 shows the block diagram of the DLIT setup. DLIT characterization technique works on the principle of lock-in. The infrared camera captures all the signals, including the noise signals from the device that is triggered through input bias voltage. It is essential to remove all unwanted noise signals

to see the defect spots clearly. Thus, a lock-in principle is used. It is mathematically expressed as:
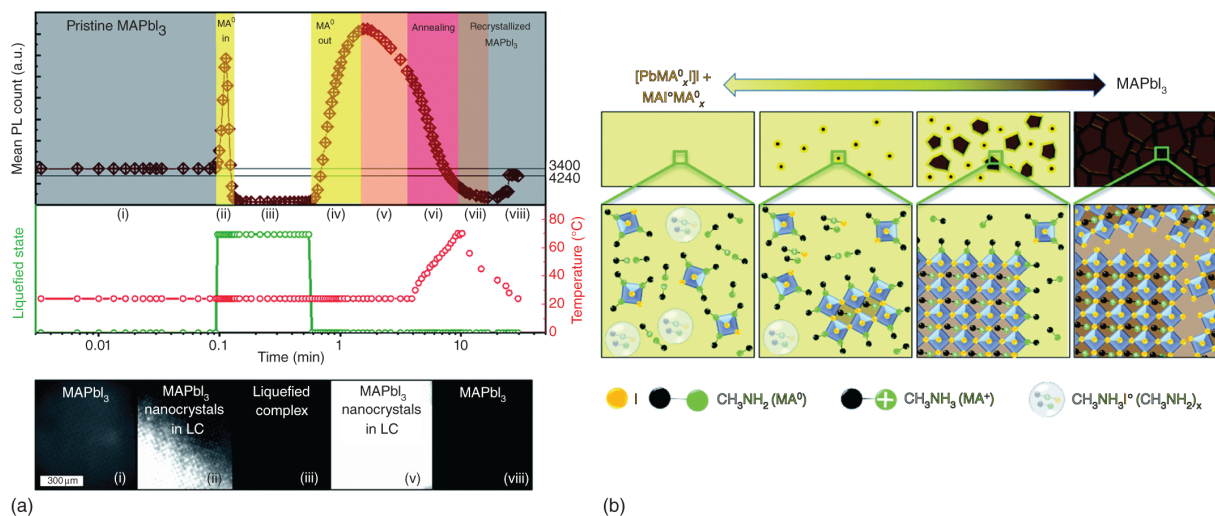
Figure 2.14 (a) The PL measurement in real-time on the glass/ZrO$_2$/graphite device. When the MA^0 is supplied through to a device, the layer turns pale-yellow, causing a drop in the PL signal due to the collapse of the ABX$_3$ structure. Once the MA^0 gas is removed the methylamine-perovskite complex it recrystallizes into perovskite and causes a rise in PL. When the sample is heated up to ~70 °C, it induces a more rapid leave of MA^0 and the subsequent crystallization. The PL images of corresponding stages are presented below (LC refers to liquefied methylamine-perovskite complex). (b) Illustration of MAPbI$_3$ perovskite recrystallization during desorption of MA^0 from the methylamine-perovskite complex (also referred to as MAPbI$_3$ × MA^0) or crystalline [PbMA$^0_4$I]I + MAI·MA^0_x. The double-sided arrow highlights that the reaction and mechanisms are reversible. The upper row depicts the crystal morphology change, while the bottom row illustrates the interaction of PbI$_6$ octahedra with MA^0 and the by-products in the solution such as MAI-MA^0_x and MA$^+$·MA^0. Source: Bogachuk et al. [30], Royal Society of Chemistry, CC BY 3.0.
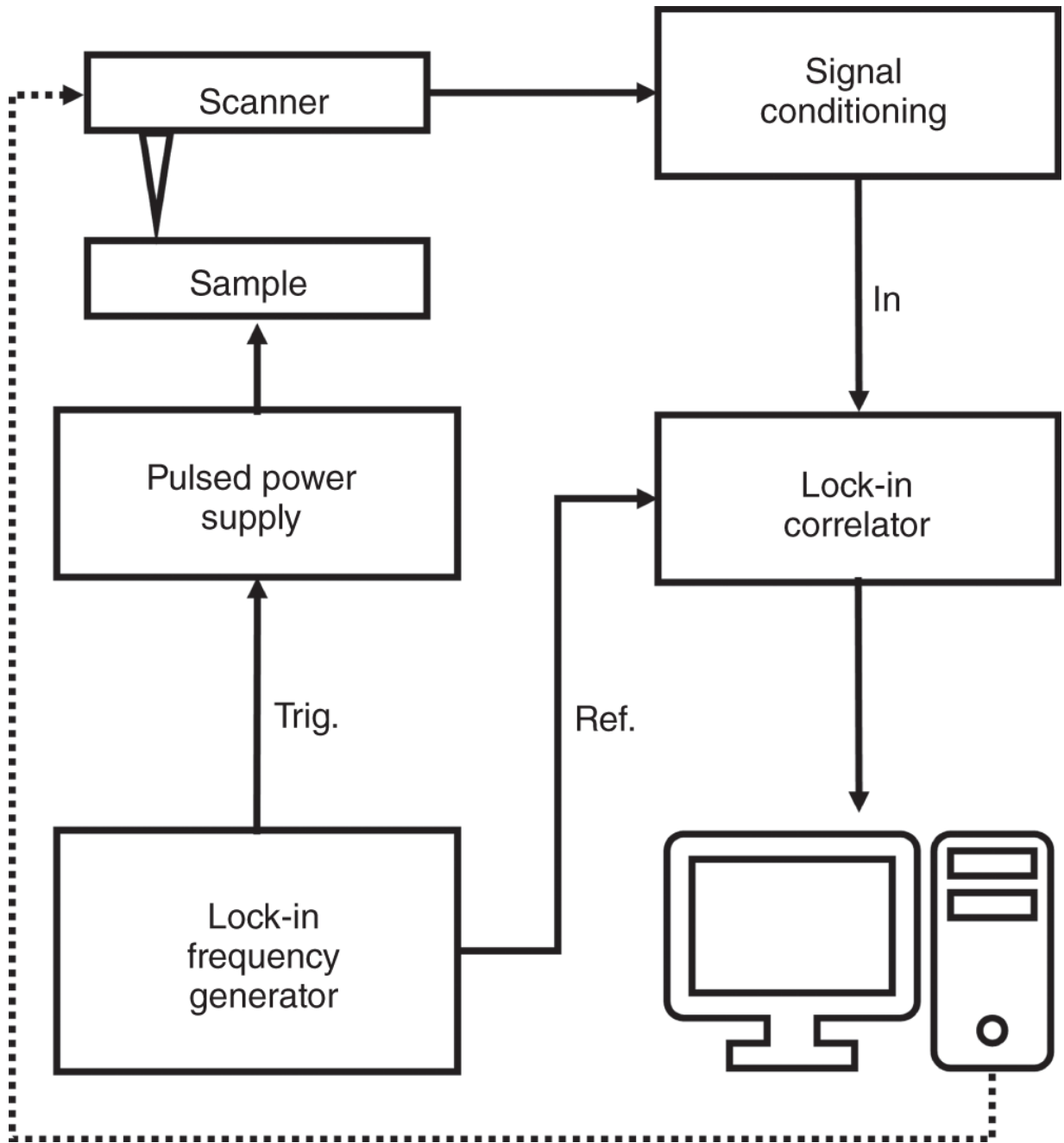
Figure 2.15 Block diagram of LIT system.

$$\text{Resultant signal, } R(t) = \frac{1}{T} \int_0^T F(t) \cdot G(t)\, dt \qquad (2.7)$$

where,

Input signal is $G(t) = G\sin(\omega_g t + \varphi)$ (2.8)

Reference signal is $F(t) = F\sin(\omega_f t + \theta)$ (2.9)

when $\omega_g = \omega_f$, $R_1(t) \sim G\cos\delta$ where, $\delta = \varphi - \theta$. This signal gives the phase difference between the input and the reference signal.

In general, two-channel lock-in is used to get the signals from $\delta = 0°$ and $\delta = 90°$. They result in an in-phase component [$R(0°)$], and phase-shifted component [$R(90°)$], respectively. These two signals are processed for further interpretation of the resulting measurement.

Another critical parameter is the lock-in frequency. It is calculated based on the framerate (f_s) of the IR camera and the number of frames during lock-in. It is given by the formula, $f_{\text{lock-in}} = \frac{f_s}{n}$. Thus, for a two-channel lock-in, $n = 4$ is used.

The spatially resolved DLIT can be used on PSCs to detect the spots of power loss in the devices such as pinholes that introduce ohmic shunts. When a forward input bias voltage is higher, electrical current passes through these spots, resulting in high local heat dissipation. This dissipated heat is captured via the IR camera. Thus, in a DLIT image, high-intensity regions correspond to high current flow. With known voltage and the corresponding global current, the power dissipated can be calculated using the formula $J \propto \sqrt{I_{\text{DLIT}}}$.

DLIT images can also be obtained with reverse bias voltage. However, in PSCs, owing to potential cell damage, it is often avoided.

2.4.7 Light-Beam-Induced Current (LBIC)

Another technique to estimate the performance homogeneity of the PV device is light-beam-induced current (LBIC), where a monochromatic light can be focused on the specific point of the cell, and the resulting current under short-circuit condition is measured. The LBIC resolution can reach up to 1 µm, allowing to build a well-resolved map of the spatial distribution of carrier generation and transport if the light spot is scanned over the sample. By knowing the incident irradiation and sample reflection, the internal and external quantum efficiencies (EQEs) at specific wavelengths can be obtained. Furthermore, if one correlates the integral from the complete EQE curve in the absorption wavelength range with the EQE obtained from LBIC at several specific wavelengths, an approximation of the spatial distribution of cell's J_{sc} can be obtained. Such a J_{sc} map can be used to assess the qualities of the photoabsorber and charge-selective layers. It is noted that careful adjustment of the laser intensity to 1 sun is required to avoid problems with charge-limited current transport.

2.5 Transient Optoelectronic Methods

2.5.1 Intensity-modulated Photocurrent/Photovoltage Spectroscopy (IMPS/IMVS)

For intensity-modulated photocurrent spectroscopy (IMPS) and intensity-modulated photovoltage spectroscopy (IMVS) measurements, small light disturbances are applied to the cell in a static state, and the modulated photocurrent or photovoltage is measured. The output electrical signal of the solar cell has the same frequency as the applied optical signal. Still, its phase might be shifted, and the amplitude altered depending on the excitation frequency. By

sweeping the frequency of the optical signal, information about the carrier transmission and recombination inside the device can be obtained.

In fully printable mesoscopic solar cells, IMPS can be used to characterize the mean transit time of the photoinjected charge carriers in solar cells under short-circuit conditions. IMVS provides information about the electron–hole recombination time at an open circuit. The time constant can be calculated by the equation $\tau = \frac{1}{2\pi f}$, where f is the frequency corresponding to the characteristic peak in the Bode plot.

To illustrate this by an example, Figure 2.16a,b show the recombination and transit time of fully printable mesoscopic solar cells prepared based on oxygen-deficient carbon black (ODC) and oxygen-rich carbon black (ORC). The time constant extracted from the IMVS and IMPS measurements effectively distinguishes the difference in charge recombination and charge transport between the two kinds of devices.
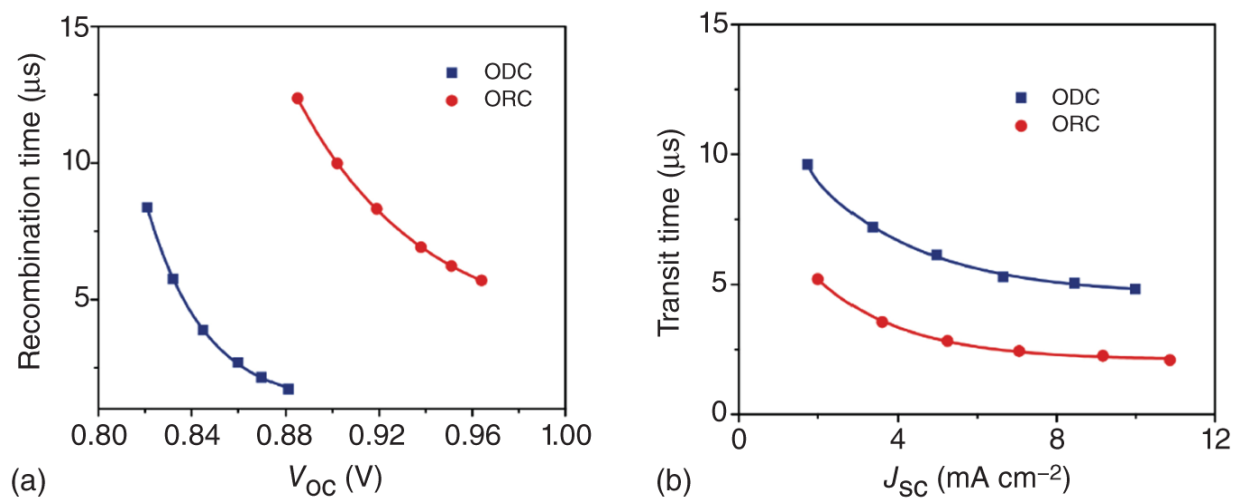
Figure 2.16 (a) The plot of the charge recombination lifetime and (b) mean electron transit times for ODC- and ORC-based PMPSCs. Source: Tian et al. [31] with permission of Elsevier.

In conclusion, IMPS/IMVS measurement can be a useful tool to study charge transport and recombination phenomena and to qualitatively compare the respective properties of different CTL materials.

2.5.2 Transient Photocurrent/Photovoltage (TPC/TPV)

Transient photocurrent (TPC) and transient photovoltage (TPV) technologies can be used to measure the charge extraction time and charge recombination life of complete solar cell devices. Here, first, the response to pulsed light is discussed. In the next section, the V_{oc} decay from steady state is treated. In the measurement of TPC and TPV, the oscilloscope records the response of the solar cell to pulsed light. When the device is connected in series with high resistance (e.g. by setting the oscilloscope input resistance to 1 MΩ), the device is essentially under open circuit, in that case the measurement is referred to as TPV. TPV is generally used to characterize the charge recombination processes in a device. When a small resistance is connected in series at both ends of the device (e.g. by setting the input resistance of the oscilloscope to below 10 Ω), the external circuit can be regarded as a short-circuit state, which is referred to as TPC measurement. TPC is generally used to characterize the transport process of the device.

In the transient photoelectric measurement process, under the excitation of the incident pulse light, the light-absorbing layer generates free carriers. The migration of the charge carriers is fundamentally governed by drift and diffusion mechanisms. The charge collection time (τ_j) can be obtained by converting the TPC decay time (τ_c) and the photovoltage recombination time (τ_r): $\frac{1}{\tau_j} = \frac{1}{\tau_c} - \frac{1}{\tau_r}$. The charge collection efficiency (η_c) can be further calculated

using the charge collection time (τ_j) and the photovoltage recombination time (τ_r): $\eta_c = 1 - (\tau_j/\tau_r)/(1 + \tau_j/\tau_r)$ [32].

The ratio of the amount of charge collected at the electrode to the amount of charge extracted into the CTL is charge collection efficiency (η_c), which is primarily dependent on charge transport and interfacial recombination within the CTL. η_E is the ratio of the amount of charge drawn into the CTL to the total amount of photogenerated charge, mainly depending on charge transport and bulk phase recombination within the light-absorbing layer. η_E can be calculated from EQE and η_C, $\eta_E = \text{EQE}/\eta_C$. The most significant benefit of TPC/photovoltage measurement is the ability to directly measure the charge transport, recombination, and charge storage characteristics of complete devices. The traditional TPC/photovoltage method can only measure the device characteristics in the short circuit or open state. In contrast, the opto-electro-modulated TPC/photovoltage (M-TPC/M-TPV) configuration developed by Shi et al. [33]. allows to characterize the transmission and recombination processes in the device under arbitrary bias and light conditions. It is enabled by introducing a low-pass filter into the conventional TPC/TPV system.

2.5.3 Open-circuit Voltage Decay (OCVD) Analysis for Shunt Detection

Similar to TPV discussed above, the open-circuit voltage decay analysis is a technique used to analyze the electron lifetime in solar cells. The cells under open circuit are initially under illumination in steady state, which is then switched off. The V_{oc} decay provides insights to track the kinetics of charge recombination. Contrary to the observation in silicon solar cells, PSCs show longer

electron lifetime under dark, particularly in mesoscopic architecture. Thus, it is vital to understand the interpretation of OCVD analysis made especially for PSCs.

A typical OCVD graph consists of three phases:

- **Phase A**: The device is under illumination. The open-circuit voltage value corresponds to the photogenerated charges.

- **Phase B**: As the light is switched off, fast radiative and non-radiative recombination (due to defects in the bulk) occur in the pure perovskite. Under phase A, certain charges are stored in the shallow and deep traps of the mesoporous ETLs. In phase B, non-radiative charge recombination is also contributed at the interface between the ETL and the perovskite (i.e. electrons in the shallow traps from the ETL recombination with the holes in the perovskite).

- **Phase C**: The V_{oc} decay is further monitored as the device remains in the dark for many seconds. Here, the reduction in the V_{oc} is often contributed by the charges in the deep trap states of ETL. A slow recombination trend is frequently reported under dark (i.e. V_{oc} under dark is >0 V).

The behavior in phase C could be explained by the presence of charges with a very long lifetime in the deep traps of the mesoporous CTLs [34, 35]. Yet, this is still under debate why such charge storage effect is observed under dark in mesoporous PSCs. In any case, such an observation of long-lived photovoltages indicates that there are no ohmic shunt pathways through which the charges are immediately lost. The electron lifetime is calculated from this phase using the formula [36, 37]

$$\tau_n = \frac{k_B T}{q} \left(\frac{dV_{OC}}{dt} \right)^{-1},$$ where τ_n is the electron lifetime and $\frac{k_B T}{q}$ the thermal energy.
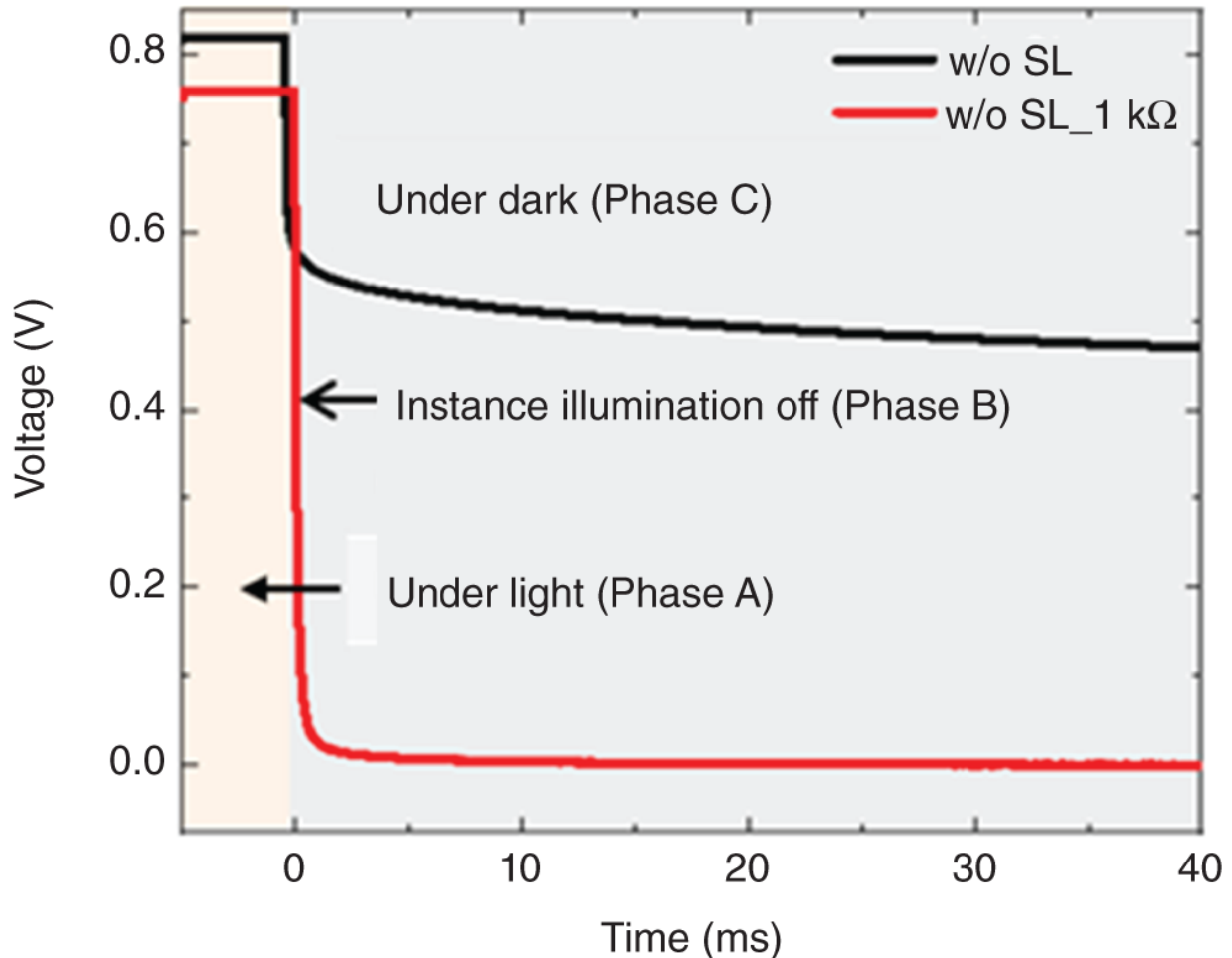
Figure 2.17 OCVD analysis on FTO/mp-TiO$_2$/carbon-graphite (referred to as without space layer – w/o SL) filled with perovskite [19].

Figure 2.17 shows a graphite-based PSC without any insulation layer (FTO/mp-TiO$_2$/carbon-graphite) filled with perovskite where the ETL and counter electrode is in direct electric contact. While at first sight, this looks like a shunt. Surprisingly, the OCVD analysis showed that the voltage of ~500 mV still remained under dark conditions after 40 ms. A 1 kΩ resistor was connected in parallel to verify the

absence of a shunt. In this case, the V_{oc} immediately dropped to 0 V after the light was switched off. It shows that in mesoscopic graphite-based PSCs, in the absence of an insulation layer, more non-radiative recombination but not ohmic shunts is the cause for low V_{oc} values [19]. To reduce the non-radiative recombination further, an insulating layer needs to be placed between ETL and graphite [19].

2.5.4 Transient Absorption Spectroscopy (TAS)

Transient absorption spectroscopy (TAS) is also known as time-resolved pump–probe spectroscopy. In a typical TAS test, a laser pulse is split into two beams of light into the pump beam path and the probe beam path through a splitting wedge before being introduced into the test system. Among them, the frequency-converted pump light excites a small portion of the sample from the ground state to the excited state. In the probe optical path, the fundamental light is converted into a broad-spectrum super-continuous white light through the optical path and then divided into two almost identical beams by the optical wedge as the probe light and the reference light, respectively, which are focused at different positions on the sample, wherein the probe light and the pump light are spatially coincident. Finally, two beams of light passing through the sample are collected by the detector through an optical fiber. Since the probe light contains light of different wavelengths, the detector can receive information of all wavelengths at the same time. Besides, it is also possible to obtain information about the sample at different times by adjusting the optical path difference between the pump light and the probe light. Therefore, a three-dimensional spectrum of signal-time-wavelength can be obtained by TAS. TAS can monitor the transient state and change trend of carriers in the photophysical process in

real-time, so that the photophysical characteristics and behavior of internal carriers before the sample reaches equilibrium can be studied from the time scale.

2.5.5 Time-resolved Photoluminescence (TRPL)

Perovskite photoabsorbers can be manufactured with comparably low effort to an astonishingly high degree of purity. To obtain high-performing solar cells, minimizing interface recombination and optimizing charge extraction of photoexcited charge carriers at the charge extraction layers (CELs) are a major leverage point. Steady-state PL and time-resolved photoluminescence (TRPL) decay measurements yield insightful mechanisms on these mechanisms.

2.5.5.1 Typical Setup: Pulsed (Transient) Excitation

TRPL setups measure the time between optical excitation and the emission of photons by radiative recombination. Typical commercially available TRPL systems operate under the following working principle: the light emitted by a short laser pulse is divided into two pulses, one strong and one weak, by a beam splitter, as depicted in [Figure 2.18](#). The weak pulse light is received by detector A and converted into a reference pulse to start the time-to-amplitude converter. The second intense pulse is used as excitation light to excite the sample. An optical filter or monochromator in front of detector B blocks the excitation light and allows the PL of the sample to pass. The first photon emitted by the sample that reaches the highly sensitive detector B is converted into an electrical pulse signal to terminate the time-to-amplitude converter. In the time-to-amplitude converter, the time difference between the two signals is converted into an electrical signal with an amplitude corresponding to the specific time difference and then stored in the multi-channel analyzer. These

signals are sequentially stored in different channels in order of magnitude, and the number of signals for each channel is counted. Since the probability of detecting a photon at a specific moment is proportional to the fluorescence intensity at that moment, the distribution curve of the cumulative number of pulses vs. the number of channels in the multichannel analyzer represents the PL decay curve of the sample.

2.5.5.2 Alternative Setup: Steady-state Excitation

Suppose the system is in steady state, then any reduction of the PL indicates that charge carriers are lost by non-radiative emission. Hence, as a general rule, in steady state, a lower PL intensity is unfavorable for the photovoltage. In the above-described pulsed setup, the sample is not necessarily in steady state, and the energy states in the absorber and contact layers are not filled accordingly. For a short, excitation of relatively low intensity, the environment for the photoexcited charge carriers might thus resemble more that of a device in a short circuit than under V_{oc}. Therefore, a reduction in PL intensity e.g. by the addition of a CEL, might indicate an improved charge extraction of charge carriers into the empty energy states of the CEL and hence higher device performance.
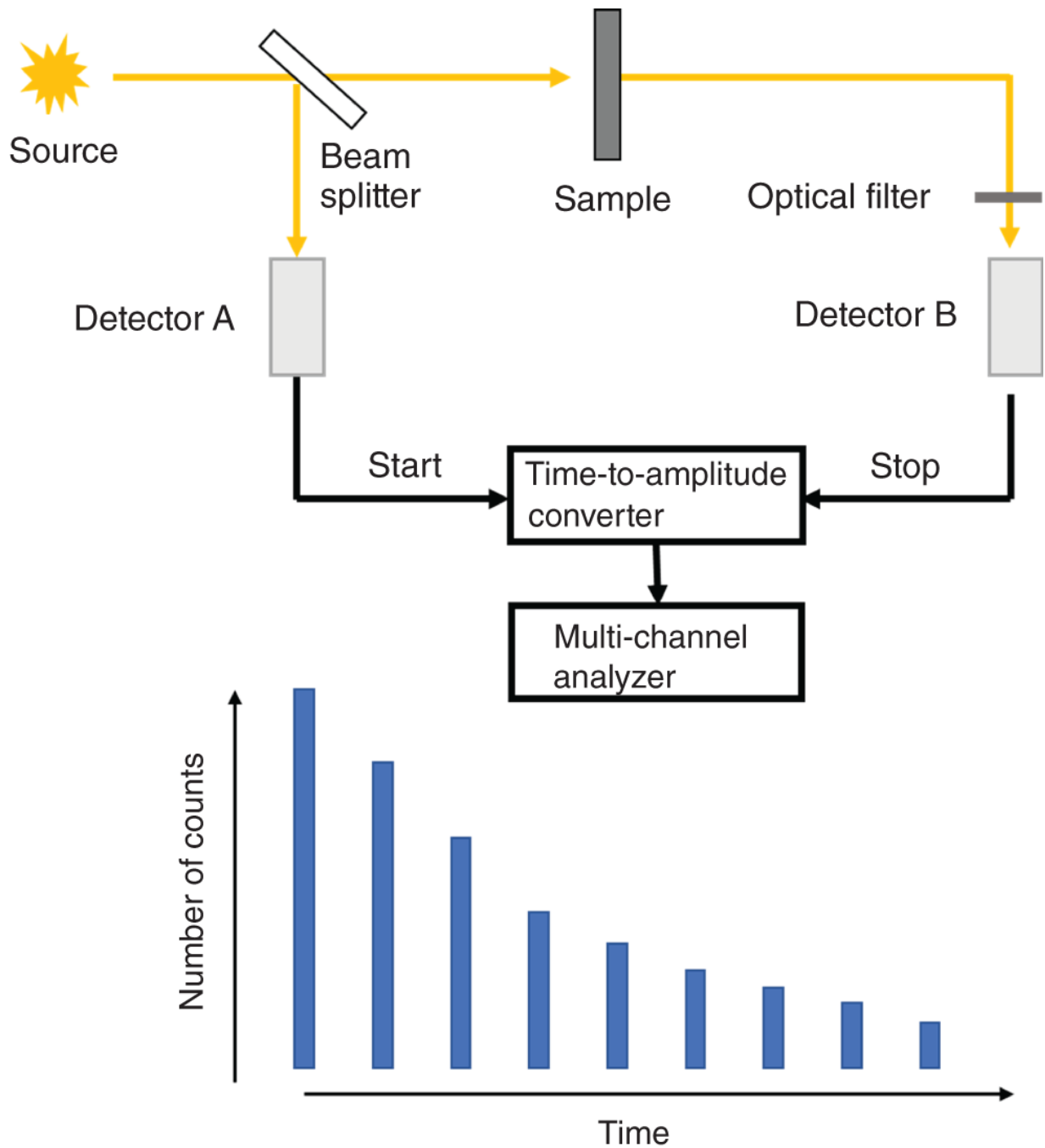
Figure 2.18 Schematic setup of a pulse-based TRPL setup.

While this transient approach can yield insightful information on charge extraction, the involved physical processes are challenging to describe. Even more so, to gain insights on charge carrier recombination, it is insightful to study the PL decay from the stabilized state. In

recent years, the availability of fast measurement electronics such as oscilloscope cards has enabled an alternative TRPL setup that enabled to measure the PL decay in real-time. It has the advantage that the sample can be excited for a long time until a steady state is reached. Thus, in contrast to the excitation by a short laser pulse, it can be ensured that all electronic states are filled as in the case of constant one-sun illumination under V_{oc}. As shown in Figure 2.19, the sample is excited by a laser beam that is widened to ensure homogeneous illumination, ideally at an excitation power close to one sun. The radiatively emitted light of the sample is spectrally separated by an optical filter and measured by a sensitive detector. In this setup, it is essential that the laser has a shortfall time when switched off. As the photodetector is constantly illuminated, it needs to be fast and sensitive. At the same time, it should not go into saturation. The signal from the photodetector (photomultiplier) is amplified and transferred to an oscilloscope. When the sample has been illuminated long enough to reach steady state, the laser is switched off. It triggers the measurement at the oscilloscope, which records the decay of the PL signal in real-time. To improve the signal-to-noise ratio, the measurement can be repeated to average over several measurements.
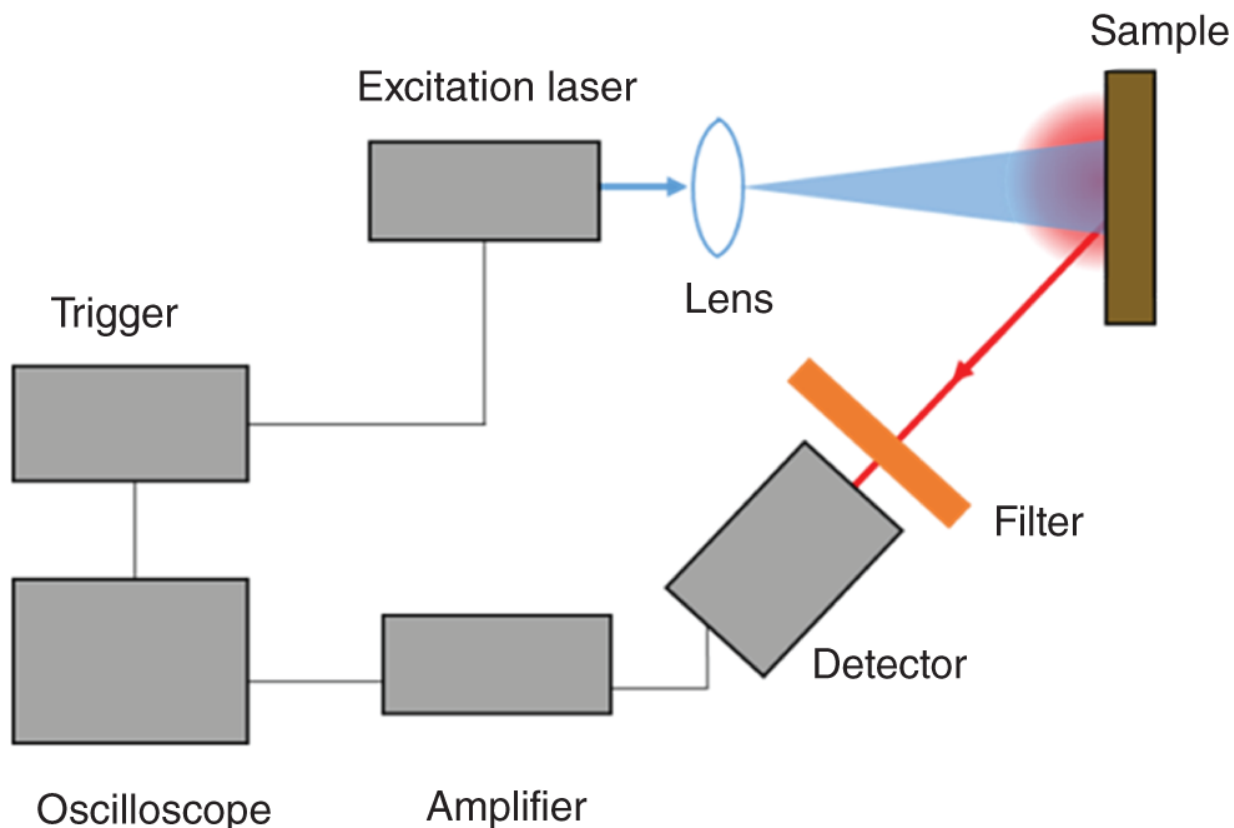
Figure 2.19 Alternative TRPL setup to measure the PL decay from the excitation at steady state.

A common application of TRPL measurements is to study the effect of CELs on the charge carriers in the perovskite. As this typically leads to a reduction of PL intensity, in this context, these layers are also referred to as "quenching layer." In the following, the measurements are discussed relating to the pulsed, transient TRPL setup. Note that in the steady-state setup, some arguments do not apply.

In the simplest sample configuration, a bare perovskite layer is deposited onto a dielectric substrate, such as glass. Ideally, the surface recombination at the interface with the substrate and air is low enough to allow the assumption that the TRPL curve represents the recombination in the "bulk" perovskite. However, in practice, this assumption needs to be treated with care. The perovskite layer can be deposited by spin-coating or by drop-casting into a

mesoporous dielectric film such as ZrO_2. By comparing the TRPL decay curves of samples without the quenching layer, the defect concentration and crystallinity of different perovskite samples can be compared.

Accordingly, devices with quenching layers can be studied. It includes "half-cells" where the perovskite is in contact with only the electron- or hole-selective layer, as well as "full-cells" with the complete solar cell device stack. For the samples with a quenching layer, the PL attenuation includes charge transfer and non-radiative recombination components. Due to the electron selective layer or the hole selective layer, photogenerated carriers will be extracted by the selective layer, resulting in quenching of the PL intensity. In addition, the interface between the selective layer and the perovskite will introduce some defects, which will increase the possibility of non-radiative recombination. In hole-conductor-free, fully printable mesoscopic solar cells, Han's group has performed a wide range of measurements on the TRPL of mesoporous double-layer half-cells, such as TiO_2/perovskite and graphite/perovskite samples. [31,38–42]The curve of TRPL is usually fitted with a double exponential function. It is generally believed that the fast process corresponds to the charge extraction effect, and the slow process corresponds to the process of slow radiation decay. (The latter could be (non-radiative) surface recombination as well as (non-radiative or radiative) recombination in the perovskite bulk.)
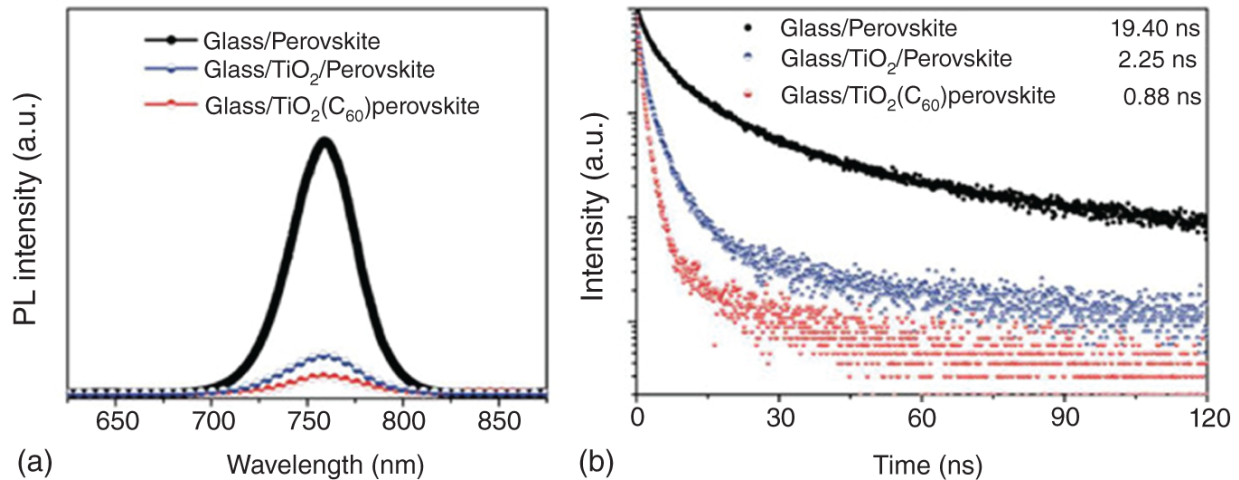
Figure 2.20 PL spectrum (a) and PL decay (b) of perovskite layers deposited on different quenching layers. Source: Tian et al. [40] John Wiley & Sons.

Accordingly, the TRPL decay curve of a complete solar cell device mainly includes the following information: (i) The extraction or recombination of electrons at the TiO_2 interface. (ii) The extraction or recombination of holes by the porous graphite layer. (iii) Radiative recombination in the bulk perovskite. (iv) Non-radiative recombination in bulk. However, as these processes influence each other and are not independent, it is challenging to fit such multi-exponential functions and extract the time constants corresponding to each individual process. Based on literature and experimental results, the fast process of the double exponential fitting results can be attributed to the charge extraction process, and the slow process can be attributed to the interface recombination process.

In addition to the simple analysis under a single excitation light intensity, the researchers found that as the excitation light intensity increases, the PL decay curve of the perovskite material will change from a single exponential to a double exponential [43–46]. This method of changing the intensity of excitation light can be used to assess the concentration of trap states.

To illustrate the TRPL method by an example, <u>Figure 2.20</u> shows the PL spectrum (a) and the TRPL (b) of a perovskite film on the bare glass as well as on TiO_2 and $TiO_2(C_{60})$ layers. The TRPL lifetimes are 19.4, 2.25, and 0.88 ns, respectively. Due to the quenching effect of the ETL, the perovskite film formed on the glass/TiO_2 and glass/$TiO_2(C_{60})$ substrates exhibit lower PL intensity and shorter TRPL lifetime. In addition, the curve of the glass/$TiO_2(C_{60})$/perovskite delays faster than glass/TiO_2/perovskite, which proves that $TiO_2(C_{60})$ can transport electrons more efficiently.

2.5.5.3 Some Notes on Sample Preparation

Different from planar solar cells, in the sample preparation of incomplete mesoporous device structures, there will be some problems that will not exist in the process of preparing complete devices. For example, when the perovskite precursor is filled on the non-graphite layer, a capping layer will be formed on the upper surface of the "half cell." To reduce the effect of this capping layer on the measurement, it can be helpful to increase the thickness of the mesoporous material or reduce the amount of precursor liquid.

2.5.6 Note on the Extension to Spatially Resolved Measurements

While the methods mentioned in this section (and some in the section on material and crystal properties) were discussed without considering spatial information, the methods themselves do not necessarily exclude to be integrated into imaging or mapping techniques. By doing so, a deep understanding of the homogeneity of the probe can be gained. For large-area devices, such as mesoscopic graphite-based perovskite modules, evaluation of

performance homogeneity over the device area becomes essential to identify and resolve potential issues during upscaling.

2.6 *I–V* Performance: Transient and Steady State

2.6.1 *I–V* Characterization

The *I–V* characteristic represents the most important measured property of a solar cell from the application point of view. For this measurement, the device is placed under simulated solar light (AM1.5G spectrum) as provided by class A illumination sources. The optical power density for such solar simulators is defined as $P_{in} = 1000\,\mathrm{W\,m^{-2}}$. The cell is contacted, and an electrical bias is applied while the photocurrent is measured. By sweeping the voltage between the open-circuit voltage (V_{oc}) and 0 V, the *I–V* curve is recorded.

Figure 2.21 shows a *J–V* curve measured from a mesoscopic PSC. For better comparison, the current density *J* is plotted as calculated from the measured current divided by the illuminated active cell area. The curve resembles a typical exponential behavior as described by Shockley's diode equation, shifted by the photocurrent. From this, the *J–V* parameters J_{sc}, V_{oc}, *FF*:

- The open-circuit voltage (V_{oc}) or photovoltage represents the voltage at $J = 0$.
- The short-circuit current density (J_{sc}) or photocurrent density represents the current density at $V = 0$.
- The maximum power point P_{mpp} describes the point of highest output power density.

- The fill factor FF serves as a coefficient to express P_{mpp} by J_{sc} and V_{oc}. It represents the ratio between the rectangles spanned by J_{mpp} and V_{mpp} (marked in green) and by J_{sc} and V_{oc}:

$$FF = \frac{J_{mpp}V_{mpp}}{J_{sc}V_{oc}} \tag{2.10}$$
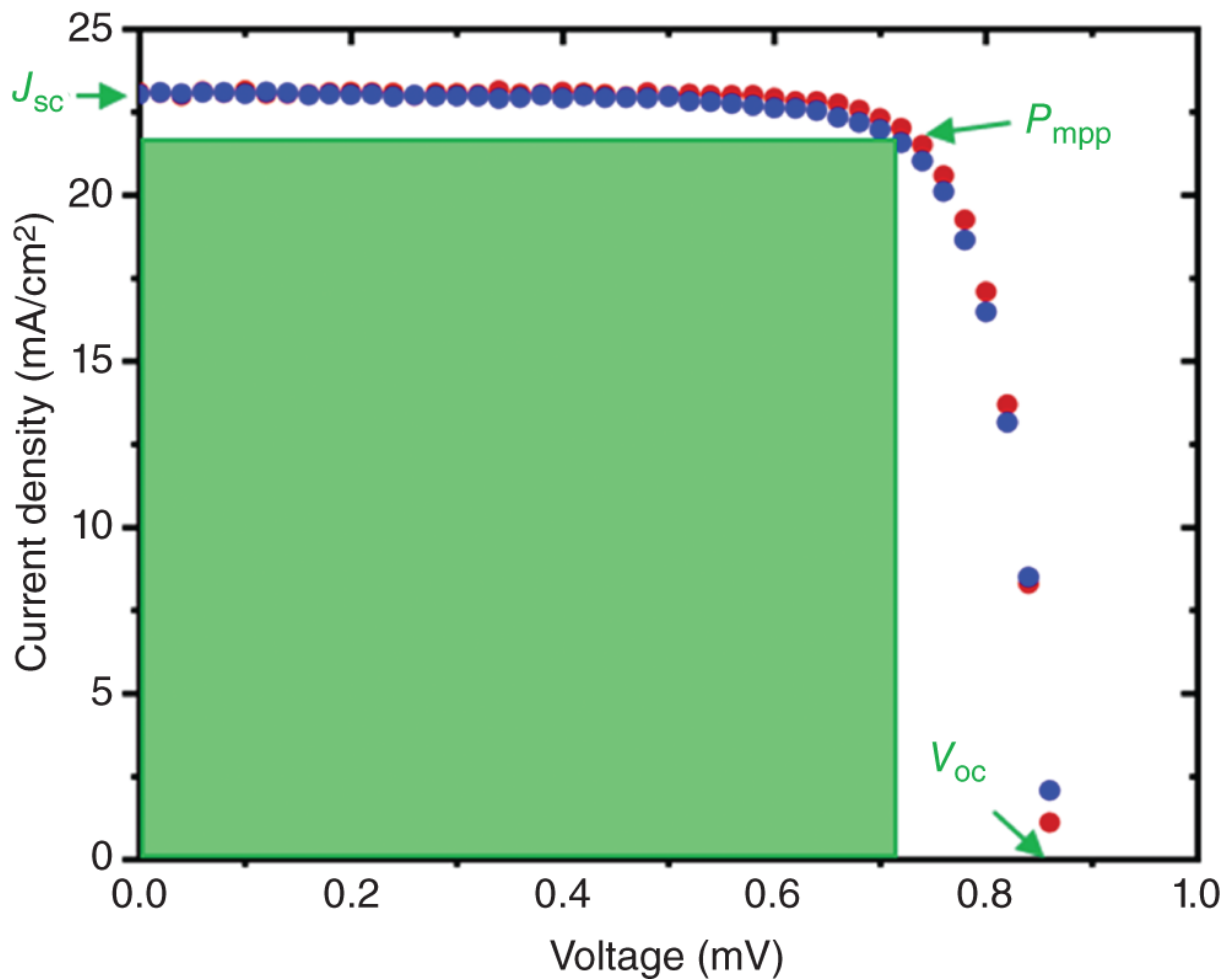
Figure 2.21 *J–V* curve of a mesoscopic PSC curve, measured in reverse (red) and forward (blue) scan direction. In green, the V_{oc}, J_{sc}, and P_{mpp} are marked.

- From this, the optical-to-electrical power conversion efficiency (PCE) of the cell is calculated by the equation:

$$PCE = \frac{P_{\text{mpp}}}{P_{\text{in}}} = \frac{V_{\text{oc}} J_{\text{sc}} FF}{P_{\text{in}}} \qquad (2.11)$$

2.6.2 *I–V* Hysteresis

Hysteretic behavior is a distinct feature of PSCs. A hysteresis in general means that an effect arises with a retardation to the cause. In other words, the system "remembers" its own history. The most prominent hysteresis in PSC is commonly observed in *I–V* scans. There can be a significant difference between the *I–V* scan carried out in "forward direction" (from 0 V to V_{oc}) and in "reverse direction" (from V_{oc} to 0 V). This shows that the system is in a different state when kept under short circuit (0 V) or open circuit and the aftereffects last for at least several seconds (the time of an *I–V* scan). While a range of sources for this behavior has been debated, such as ferroelectricity and capacitive effects, there is strong evidence that ionic movement plays a vital part in this effect. In consequence, we can conclude that,

- the preconditioning has a strong influence on the shape of the scanned *I–V* curve.

- the *I–V* curve recorded from an *I–V* scan does not necessarily resemble a unique feature of the device, but its shape depends on the measurement conditions.

This makes it difficult to compare *I–V* curves reported in the literature. If several devices are compared within one experiment in an un-stabilized *I–V* scan, it needs to be at least assured that the preconditioning needs to be the same

and it should be reported if the devices have been kept illuminated or in the dark at which bias for which time before measurement.

Clearly, the scan speed, measured in millivolts per seconds, is a key influence on the hysteresis. Ideally, I–V scans should thus be recorded in a way that, at each voltage point, the photocurrent is measured long enough to stabilize completely. On the downside, this can imply very long measurement times for each sample and might not be practical when large numbers of devices are to be measured.

Finally, the sampling procedure of the measurement system needs to be taken into account. For each voltage step, typically the bias voltage is applied and the current is measured. It can make a difference if the reported current is the average over the time span of the bias step or the last measurement value at the end of this time span. To give another example of a potential error source, it needs to be ensured that the measurement system does not go into an "idle mode" between the measurement steps where the bias voltage is not applied.

For a quantitative comparison of the hysteresis, a hysteresis index can be employed for I–V parameters such as J_{sc}, V_{oc}, FF, or PCE. Habisreutinger et al. [47]. suggested the following definition for the PCE:

$$\text{Hysteresis index} = \frac{\text{PCE}_{rev} - \text{PCE}_{for}}{\text{PCE}_{rev}} \qquad (2.12)$$

2.6.3 Stabilized Efficiency Measurement

The PCE is the key of merit by which solar cells are compared. However, if efficiency values are taken from the I–V measurement, the outcome can be strongly influenced

by the hysteresis effect. Revealingly, Dunbar and coworkers even found that the PCE determined from a hysteresis-free *I–V* scan does not necessarily represent the stabilized PCE [48] which makes it difficult to compare PCE values obtained by *I–V* measurement. Additionally, *I–V* measurements also do not represent the final solar cell working conditions for outdoor power conversion, where the cell will be continuously operated in steady state at the maximum power point. For a reliable and comparable measurement in PSCs, Zimmermann et al. suggest analyzing stabilized power conversion efficiencies by tracking it for at least 60 seconds [49]. Analyzing the stabilized values not only provides reliable efficiencies at standard working conditions but also provides information on the effects of light soaking and device degradation over continuous illumination conditions.

In practice, the simplest way to stabilize PCE measurements is the so-called "PCE at fixed voltage" method. Therefore, voltage close to the actual (but unknown) steady-state V_{mpp} is chosen, e.g. by a *J–V* sweep, and the cell current is recorded while the cell is biased at this voltage. Further, advanced methods are discussed below in the section dealing with long-term stability.

2.6.4 Spectral Response/External Quantum Efficiency (SR/EQE)

EQE is a parameter used to express the sensitivity of a solar cell to the spectrum of solar radiation. It defines the ratio of electrons extracted from the solar cell under illumination, with regard to the incident photons. Ideally, each incident photon would generate an electron–hole pair that would have enough energy to travel toward the respective cell terminals. EQE measurements allow, therefore, quantifying the amount of generated photo

carriers that have contributed to the overall photocurrent running through the solar cell [50].
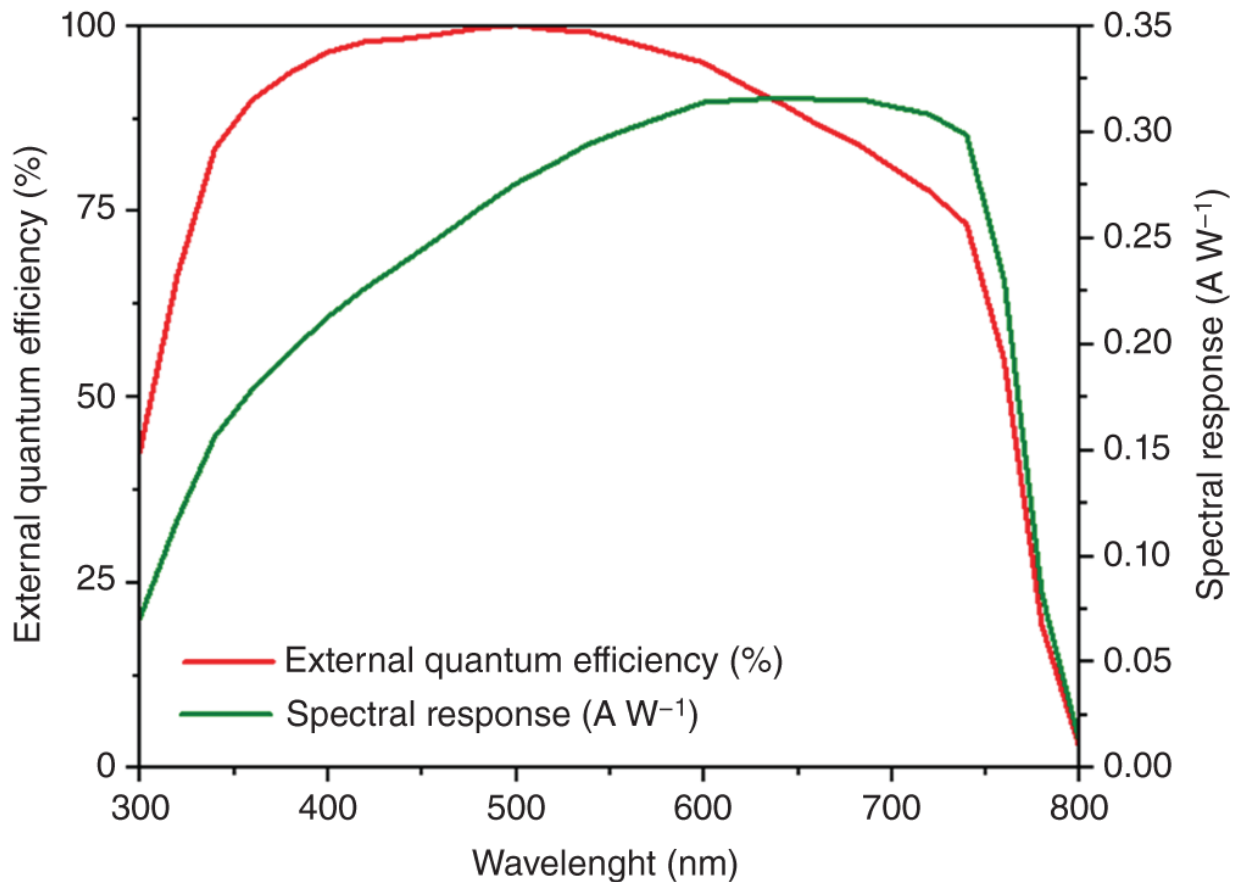
Figure 2.22 External quantum efficiency and spectral response patterns of 12% certified mesoscopic PSC reported by Wagner et al. [15].

Fundamentally, spectral response (SR) provides similar information to the aforementioned EQE measurement. While EQE describes the number of electrons extracted by the solar cell relative to the number of photons absorbed by it, SR represents a ratio of current generated by the solar cell at a specific wavelength to the incident power at that wavelength. The equation linking EQE to SR is as follows [51]:

$$\text{EQE} = \frac{hc}{q\lambda} \times \text{SR} \qquad (2.13)$$

where h stands for Planck's constant, c is the speed of light, q describes the electron charge (As), λ is the wavelength (nm), and the spectral response (SR) is given by A/W.

Notably, the shape of the SR is different from the EQE as seen in Figure 2.22. At low wavelengths, the highly energetic photons will be absorbed by the semiconductor. Still, the energy difference between the incident photon and the electron energy, which was excited to the conduction band by it, will be lost as heat. Therefore, as the energy of incoming photons gets closer to the bandgap, the "utilization" of the incoming light improves, as the power loss becomes reduced. Therefore, at wavelength, corresponding to the photoabsorber bandgap, the SR is the highest. At longer wavelengths, SR sharply decreases, since the photon absorption becomes possible only due to low number of shallow states close to the conduction band minimum and valence band maximum that can facilitate the charge carrier generation.

Measuring SR/EQE in PSCs with a carbon-based back contact can provide additional information on the efficiency of charge collection at different wavelengths, which could partially be attributed to the difference in the light-penetration depth (e.g. long-wavelength light can excite electrons in deeper regions of the cell than the short-wavelength light). Thus, the photogeneration profile influences the charge collection efficiency and, therefore SR and EQE of the cell. These measurements can also provide information on photoinduced degradation in PSCs as well as provide an estimate of the optical bandgap of the perovskite absorber. Furthermore, SR and EQE would typically be measured for PSCs at a wavelength range of 300–900 nm [52]. Moreover, considering the time scale

required to measure SR/EQE, it is essential to keep in mind the sensitivity and temperature dependence [53] of PSCs, consequently, measurements need to be carried out following a well-established protocol under a standard test temperature of 25 °C and a global standard spectrum of AM1.5G. Another factor that needs to be taken into consideration is the frequency dependence of EQE originating from the modulation frequency of the monochromatic light source applied to the sample. PSCs have been found to show slow response time which ranges from milliseconds to seconds on longer timescale measurements, which can be problematic for EQE, causing perturbations when estimating the current density (J_{sc}) of the investigated devices. For that matter, characterization setups with different optical chopper frequencies are recommended to obtain reliable measurements [54].

2.6.5 V_{oc} vs. Light Intensity Measurement

"V_{oc} vs. light intensity" is an insightful measurement to study recombination mechanisms and investigate the shunt resistance. Therefore, the V_{oc} for different light intensities is measured. In comparison to other PV technologies, in PSC, the V_{oc} typically needs to be stabilized for long timescales in the range of seconds to minutes. It prohibits the use of flashlamps as typically used, e.g. for silicon PV. To avoid disturbing effects of heating and thermal degradation, it is advisable to measure the stabilized V_{oc} under intensities that do not exceed one sun. A criterion that the V_{oc} is stabilized could be that it is not changing by 10 mV over 30 seconds. It can make sense to use optical filters to change the light intensities. If it can be ensured that the illumination remains homogeneous and the spectrum of the light source does not change, alternative ways are changing the height or input power of the light.

The light intensity needs to be measured by a suited reference cell or luxmeter, which in turn needs to be calibrated to one sun intensity.

The obtained V_{oc} values can then be plotted against the logarithmic axis of the light intensities. In the following, the theoretical device behavior is discussed, provided that the cell can be represented by the two-diode model ([Figure 2.23](#)). In this case, the J–V characteristic follows the equation:

(2.14)

$$J(V) = J_{01}\left(e^{q\left(V - \frac{J(V)R_S}{k_B T}\right)} - 1\right) + J_{02}\left(e^{q\left(V - \frac{J(V)R_S}{k_B T}\right)} - 1\right) + \left(V - J(V)R_s\right)/R_p - J_{ph}$$

Herein, J_{01} and J_{02} are the dark saturation currents of the respective diode; R_s is the series and R_p the parallel or shunt resistance, and J_{ph} is the photocurrent. q is the elementary charge and $k_B T$ the thermal energy (25.8 meV at room temperature). Note that diode two (J_{02}) accounts for the "ideality factor $n = 2$"-component of the single-diode model.
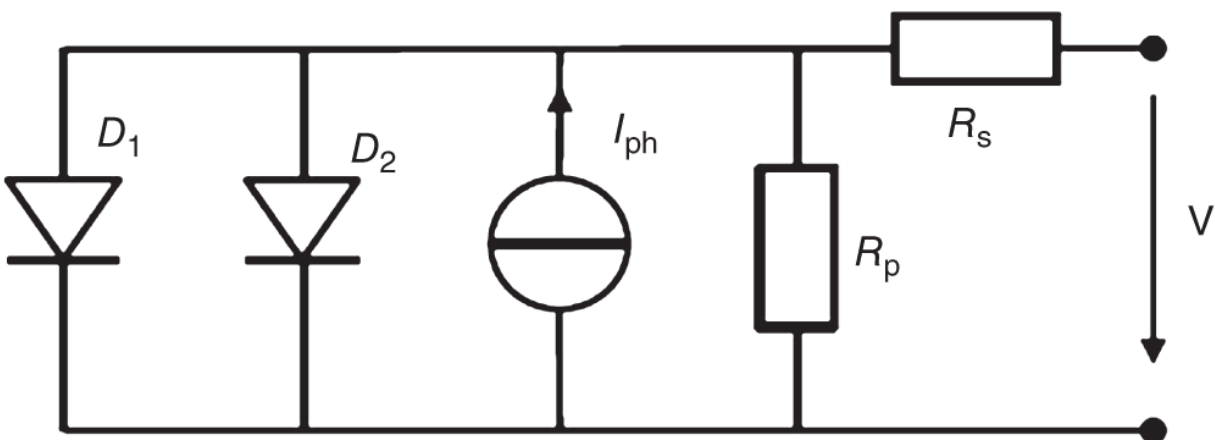
Figure 2.23 Equivalent circuit of the two-diode model.

As there is no general analytical solution of the two-diode equation for V_{oc} in the following, the influence of the different parameters is explored through an example numerically calculated from theoretical values.

2.6.6 Effect of Parallel and Series Resistance R_p

The parallel resistance R_p accounts for "external recombination," i.e. shunt paths of carriers which have already been extracted to the contacts (here: graphite and TCO). In [Figure 2.24](#) we see how the V_{oc} depends on R_p. If we assume that J_{ph} linearly follows the light intensity, then the two-diode equation tells us that V_{oc} generally follows the logarithm of the light intensity. As R_p is reduced (i.e. more shunts are introduced), there is a "breakdown" of V_{oc} at lower intensities. This breakdown point shifts proportionally to higher light intensities with lower R_p: 10 times lower R_p shifts the breakdown up by 10 times higher light intensity.
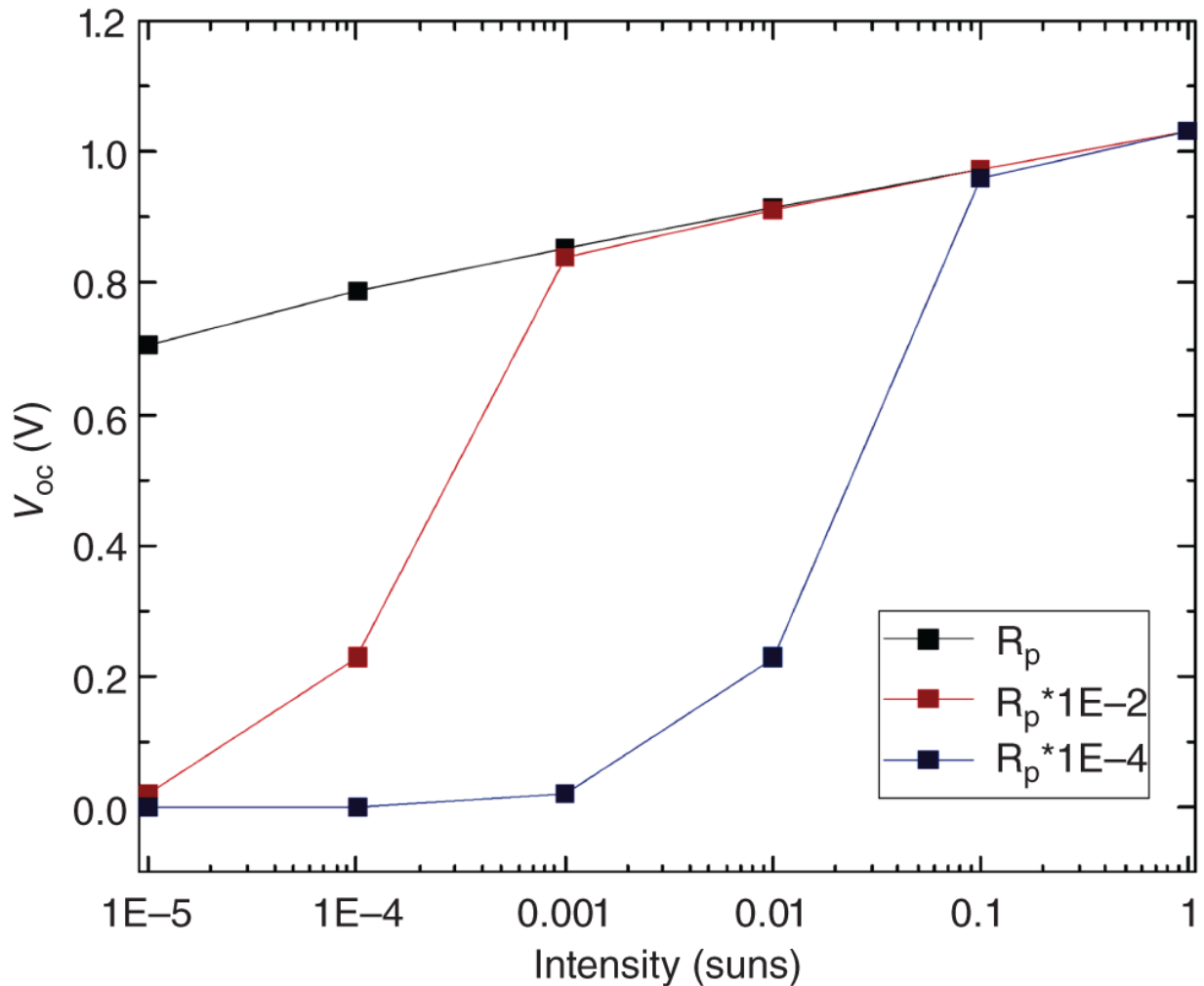
Figure 2.24 Effect of parallel resistance R_{p} on the V_{oc} vs. light intensity curve as calculated from the two-diode equation from theoretical values. Source: Wagner [55] Reproduced with permission from Lukas Wagner.

In the model, R_{s} has no effect on the V_{oc}, since $J(V_{\mathrm{oc}}) = 0$.

2.6.7 Effect of Saturation Current J_{01} and J_{02}

J_{01} and J_{02} account for carrier recombination in the solar cell. Essentially, J_{01} represents recombination mechanisms "limited by one carrier type" (usually by minority carriers), while J_{02} represents recombination mechanisms "limited by two (inversely charged) carrier types." Which

recombination mechanisms this implies for perovskite is quite difficult to say. We refer to Tress et al. for an insightful discussion of this question [56].

As can be seen from the two-diode equation, beyond the R_p-breakdown point, we can derive from the slope of the V_oc vs. light intensity curve if the device is dominated by J_{01} or J_{02}. In the parameter regime where J_{01} is dominating, the two-diode equation can be simplified to $V_\text{oc} \cong \frac{k_\text{B}T}{e} \ln \left(\frac{J_{ph}}{J_{01}} \right)$. At room temperature, we expect a slope of 60 mV per decade whereas a slope of 100 mV per decade signifies that the device is dominated by J_{02}.

As can be seen in Figure 2.25a, if the device is J_{01}-dominated, an increase of J_{01} leads to a shift down of the V_oc at a constant slope.

In Figure 2.25b, we start from a point where the device is dominated by J_{01} (black line). As J_{02} is increased, we shift to a regime where the curve is increasingly dominated by J_{02}. First, the slope changes to is 100 mV per decade (leaving V_oc at 1 sun unaffected), then the V_oc shifts down at constant slope, similar to the behavior in Figure 2.25a for J_{01}.

In the one-diode equation, the domination by J_{01} or J_{02} is expressed by the diode ideality factor n_id, ranging between 1 and 2.

The diode ideality factor is given by the formula, $n_{iD} = \frac{q}{k_\text{B}T} \frac{\text{d}V_\text{OC}}{\text{d} \ln \frac{I}{1\ \text{mW cm}^{-2}}}$ where, $\frac{q}{k_\text{B}T}$ is the thermal energy. A straightforward understanding of the diode ideality factor for PSCs is still under discussion. Contrary to the common

belief that high n_{iD} values result in low photovoltage, high V_{oc} values along with $n_{iD} = 2$ have been reported [57]. In parallel, low V_{oc} values (<1 V) with low n_{iD} values have also been published [58]. The effect is believed to be caused by the difference in the work function because of the electrodes resulting in low built-in potential. This effect also reduces the charge separation in PSCs.
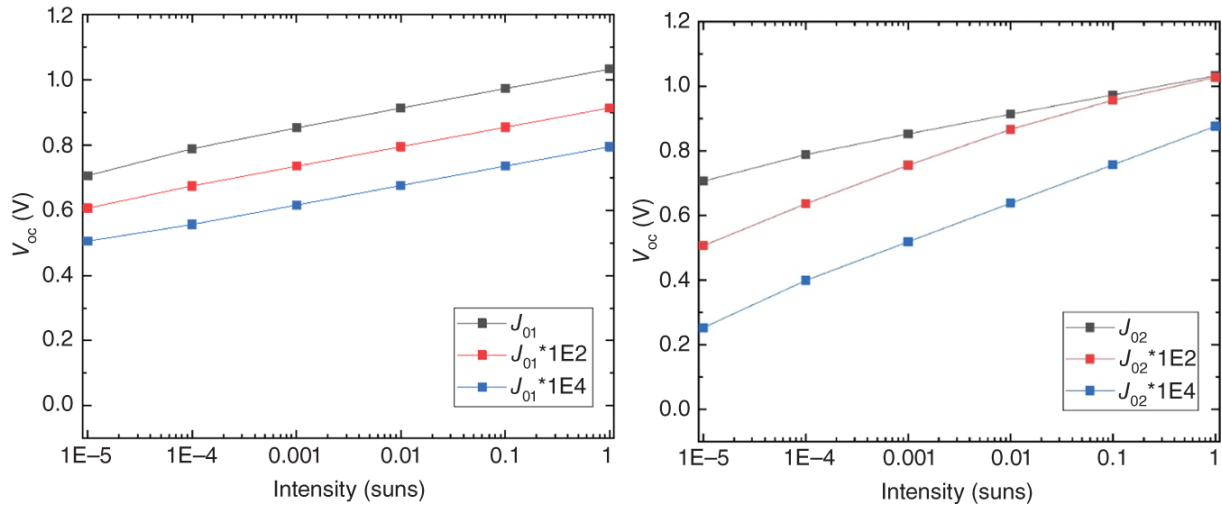
Figure 2.25 Effect of saturation current J_{01} (a) and J_{02} (b) on the V_{oc} vs. light intensity curve as calculated from the two-diode equation from theoretical values.

PSCs have different and specific layers for electron and hole transportation. Thereby, the electrons and holes could follow different recombination orders. One could follow the trap-assisted monomolecular recombination having $n_{iD} = 2$, and others could follow bimolecular recombination with $n_{iD} = 1$ [57]. The presence of various CTLs could also be a cause for the vague understanding of n_{iD} in PSCs. It is still unclear whether a high or low ideality factor is ideal for high device performance in PSCs. However, most PSCs report n_{iD} values of 1.5, which is a combination of both recombination orders [57].

2.6.8 Certification of PV Performance

Certified efficiency measurements are the "gold standard" for the determination of comparable solar cell performance values. The highest certified values for different PV technologies are reported in prestigious tables such as the "solar cell efficiency tables" issued bi-annually by Green et al. [59]. or the NREL efficiency tables [60]. Certificates are issued by accredited test centers such as the ones of NREL (USA), AIST (Japan), Fraunhofer ISE (Germany), Newport (USA), or CSIRO (Australia).

The measurement procedure to determine a calibrated efficiency value as issued by the calibration laboratory at Fraunhofer ISE is as follows:

(1) Determination of the designated area. This is typically defined by the manufacturer through an aperture mask.

(2) Measurement of the spectral response (SR) at J_{sc} conditions (approximate for 30 minutes). This is used to determine the spectral mismatch for accurate measurement in the next step.

(3) Determination of stabilizing temperature (25 °C) under one sun by stabilizing V_{oc} or by tactile temperature measurement.

(4) Under simulated solar light (AM1.5G, 1000 W m^{-2}), the *I–V* curve is measured in both sweeping directions.

(5) Right after this, the devices are biased close to V_{mpp} (as determined from the *I–V* sweep) and the output power is iteratively maximized by variation of the voltage. At the point of highest output power, both the voltage and current are recorded over 300 seconds. The average over 300 seconds is referred to as "steady-state

P_{mpp}" in the calibration report where also the evolution of the output power over the 300 seconds is reported.

(6) Right after this, the *I–V* curve is measured again in both scan directions again and this scan is reported in the calibration report.

(7) If the cell performance improves, the procedure is repeated from step 4 on.

Further details on the measurement procedure can be found under reference [61] and in the exemplary calibration reports as provided in the SI of these publications [15, 62].

Hence, there are a range of criteria that the solar cell should fulfill before it can be sent to a certification lab:

(1) The device must not degrade during the shipping.

(2) The device must not degrade during the measurement procedure. This means that the device needs to be stable for an operation of approximately 30 minutes under J_{sc} (during the SR measurement) and V_{oc} (for the adjustment of the steady-state temperature).

PSC are typically deposited on a so-called superstrate configuration, i.e. the light passes through the rigid glass support on which the actual solar cell is deposited. This poses two challenges for the measurement: first, the devices need to be contacted appropriately. This is typically achieved by a contact chuck. Second, the test standard requires that the cell is operated at 25 °C under one sun illumination. This requires a thermal sink to cool the cell during illumination. Therefore, the cell is fixed by vacuum on a temperature-controlled table. Hence, the contacting chuck needs to provide thermal coupling between the cell and the table.

2.6.9 Long-term Stability Measurement

International Electrotechnical Commission (IEC) test conditions (# IEC61646) have to be met for thin-film solar cell technology to be commercialized. However, the test conditions mentioned are related to the silicon solar cells, the working principles of which are well-known. The physics of perovskite and other organic photovoltaics (OPVs) are different from silicon solar cells. Hence, the same test conditions cannot be followed to test and approve PSCs and OPVs. In 2011, Krebs and team renewed test conditions for short- and long-term stability analysis of OPVs [63] and also for PSCs [64]. The time taken by the device to reduce to 80% of its initial PCE (referred to as T_{80}) is the main parameter to compare between devices to analyze its stability. For PSCs, International Summit on Organic Photovoltaic Stability (ISOS) test conditions are suggested to be followed instead of IEC61646 as they concentrate more on the environmental aspects [65]. These test conditions are required to reliably compare the efficiencies of various device architectures, different working groups, etc. Following the test conditions, T_{80} values as high as 10 000 hours under one sun illumination have been reported for carbon-based PSCs [66].

As discussed above, the simplest way to measure the stabilized efficiency is the "PCE at fixed voltage" method, where the cell is biased at a constant voltage close to V_{mpp}.

A related alternative represents the "PCE at fixed resistance" method. Here, instead of applying an external bias, a variable resistor (potentiometer) in series with a fixed resistor can be attached to the cell. By measuring the voltage drop over both resistors, the output power from the solar cell can be determined. Now the P_{mpp} can manually be adjusted by varying the potentiometer. This simple setup

has the advantage that one does not need to care if the electronics apply the electrical bias constantly or only during the measurement interval (which could falsify the measurement due to hysteretic effects). Moreover, as long as the light source is turned on, the cell remains at the working point even if the measurement electronic fails during a long time of recording.

The disadvantage of these two methods is that they do not react optimally in case there is a change of the maximum power point in case the cell degrades. This can be ensured by employing an MPP tracker. The design of such a system for PSC can be challenging. Different approaches to determine the MPP are discussed by Rakocevic et al. [67].

References

1 Brunauer, S., Emmett, P.H., and Teller, E. (1938). Adsorption of gases in multimolecular layers. *Journal of the American Chemical Society* 60 (2): 309–319.

2 Langmuir, I. (1918). The adsorption of gases on plane surfaces of glass, mica and platinum. *Journal of the American Chemical Society* 40 (9): 1361–1403.

3 Uchic, M.D., Holzer, L., Inkson, B.J. et al. (2007). Three-dimensional microstructural characterization using focused ion beam tomography. *MRS Bulletin* 32 (5) Focused Ion Beam Microscopy and Micromachining: 408–416, https://doi.org/10.1557/mrs2007.64.

4 Orloff, J., Swanson, L., and Utlaut, M. (2003). *High Resolution Focused Ion Beams: FIB and its Applications: FIB and its Applications: The Physics of Liquid Metal Ion Sources and Ion Optics and their Application to Focused*

Ion Beam Technology. Springer Science & Business Media.

5 Mathiazhagan, G., Seeber, A., Gengenbach, T. et al. (2020). Improving the stability of ambient processed, SnO_2-based, perovskite solar cells by the UV-treatment of sub-cells. *Solar RRL* 4 (9): 2000262.

6 Boldyreva, A.G., Akbulatov, A.F., Elnaggar, M. et al. (2019). Impact of charge transport layers on the photochemical stability of $MAPbI_3$ in thin films and perovskite solar cells. *Sustainable Energy & Fuels* 3 (10): 2705–2716.

7 Wagner, L., Mundt, L.E., Mathiazhagan, G. et al. (2017). Distinguishing crystallization stages and their influence on quantum efficiency during perovskite solar cell formation in real-time. *Scientific Reports* 7 (1): 14899.

8 Chatterjee, S. and Pal, A.J. (2016). Introducing Cu_2O thin films as a hole-transport layer in efficient planar perovskite solar cell structures. *Journal of Physical Chemistry C* 120 (3): 1428–1437.

9 Nakamoto, K. (2009). *Infrared and Raman Spectra of Inorganic and Coordination Compounds, Part B: Applications in Coordination, Organometallic, and Bioinorganic Chemistry*. Wiley.

10 Ledinský, M., Löper, P., Niesen, B. et al. (2015). Raman spectroscopy of organic–inorganic halide perovskites. *Journal of Physical Chemistry Letters* 6 (3): 401–406.

11 Tuinstra, F. and Koenig, J.L. (1970). Raman spectrum of graphite. *Journal of Chemical Physics* 53 (3): 1126–1130.

12 Joseph, I.G., Dale, E., Joseph, R.M. et al. (2018). *Scanning Electron Microscopy and X-Ray Microanalysis*. Springer.

13 Yasaroglu, U.K. (2019). *Preparation of a TiO_2 Porous Layer by Molding of Polymer Beads for Perovskite Solar Cells Application: Préparation de couche poreuse de TiO_2 par moulage de billes de polymères pour des applications dans des cellules solaires à base de perovskites: Strasbourg; Albert-Ludwigs-Universität*. Allemagne: Fribourg-en-Brisgau.

14 Abd Mutalib, M., Rahman, M.A., Othman, M.H.D. et al. (2017). Chapter 9 – Scanning electron microscopy (SEM) and energy-dispersive X-ray (EDX) spectroscopy. In: *Membrane Characterization* (ed. N. Hilal, A.F. Ismail, T. Matsuura, and D. Oatley-Radcliffe), 161–179. Elsevier.

15 Wagner, L., Chacko, S., Mathiazhagan, G. et al. (2018). High photovoltage of 1 V on a steady-state certified hole transport layer-free perovskite solar cell by a molten-salt approach. *ACS Energy Letters* 3 (5): 1122–1127.

16 Rugar, D. and Hansma, P. (1990). Atomic force microscopy. *Physics Today* 43 (10): 23–30.

17 Grobelny, J., DelRio, F.W., Pradeep, N. et al. (2011). Size measurement of nanoparticles using atomic force microscopy. In: *Characterization of Nanoparticles Intended for Drug Delivery* (ed. S.E. McNeil), 71–82. Totowa, NJ: Humana Press.

18 Quate, C., Gerber, C., and Binnig, C. (1986). Atomic force microscope. *Physical Review Letters* 56 (9): 930–933.

19 Mathiazhagan, G., Wagner, L., Bogati, S. et al. (2020). Double-mesoscopic hole-transport-material-free perovskite solar cells: overcoming charge-transport limitation by sputtered ultrathin Al_2O_3 isolating layer. *ACS Applied Nano Materials* 3 (3): 2463–2471.

20 Méndez, P.F., Muhammed, S.K.M., Barea, E.M. et al. (2019). Analysis of the UV–ozone-treated SnO_2 electron transporting layer in planar perovskite solar cells for high performance and reduced hysteresis. *Solar RRL* 3 (9): 1900191.

21 Xu, X., Ma, C., Cheng, Y. et al. (2017). Ultraviolet-ozone surface modification for non-wetting hole transport materials based inverted planar perovskite solar cells with efficiency exceeding 18%. *Journal of Power Sources* 360: 157–165.

22 Nishihara, Y., Chikamatsu, M., Kazaoui, S. et al. (2018). Influence of O_2 plasma treatment on NiO_x layer in perovskite solar cells. *Japanese Journal of Applied Physics* 57 (4S): 04FS7.

23 Wei, J., Guo, F., Wang, X. et al. (2018). SnO_2-in-polymer matrix for high-efficiency perovskite solar cells with improved reproducibility and stability. *Advanced Materials* 30 (52): 1805153.

24 Würfel, P. and Würfel, U. (2016). *Physics of Solar Cells: From Basic Principles to Advanced Concepts*. Wiley.

25 Hameiri, Z., Mahboubi Soufiani, A., Juhl, M.K. et al. (2015). Photoluminescence and electroluminescence imaging of perovskite solar cells. *Progress in Photovoltaics: Research and Applications* 23 (12): 1697–1705.

26 Spies, A., List, M., Sarkar, T., and Würfel, U. (2017). On the impact of contact selectivity and charge transport on the open-circuit voltage of organic solar cells. *Advanced Energy Materials* 7 (5): 1601750.

27 Caprioglio, P., Stolterfoht, M., Wolff, C.M. et al. (2019). On the relation between the open-circuit voltage and quasi-fermi level splitting in efficient perovskite solar cells. *Advanced Energy Materials* 9 (33): 1901631.

28 Soufiani, A.M., Kim, J., Ho-Baillie, A. et al. (2018). Luminescence imaging characterization of perovskite solar cells: a note on the analysis and reporting the results. *Advanced Energy Materials* 8 (12): 1702256.

29 Lukas, W., Schygulla, P., Herterich, J. et al. (2021). Revealing fundamentals of charge extraction in photovoltaic devices through potentiostatic photoluminescence imaging. *Matter* 5 (7): 2352–2364, https://doi.org/10.1016/j.matt.2022.05.024.

30 Bogachuk, D., Wagner, L., Mastroianni, S. et al. (2020). The nature of the methylamine–$MAPbI_3$ complex: fundamentals of gas-induced perovskite liquefaction and crystallization. *Journal of Materials Chemistry A* 8 (19): 9788–9796.

31 Tian, C., Mei, A., Zhang, S. et al. (2018). Oxygen management in carbon electrode for high-performance printable perovskite solar cells. *Nano Energy* 53: 160–167.

32 Qiu, C., Wagner, L., Liu, J. et al. (2022). Probing charge carrier dynamics in metal halide perovskite solar cells. *EcoMat* 5: e12268.

33 Shi, J., Li, D., Luo, Y. et al. (2016). Opto-electro-modulated transient photovoltage and photocurrent system for investigation of charge transport and recombination in solar cells. *Review of Scientific Instruments* 87 (12): 123107.

34 Gao, X., Li, J., Baker, J. et al. (2014). Enhanced photovoltaic performance of perovskite $CH_3NH_3PbI_3$ solar cells with freestanding TiO_2 nanotube array films. *Chemical Communications* 50 (48): 6368–6371.

35 Liu, Z., Sun, B., Shi, T. et al. (2016). Enhanced photovoltaic performance and stability of carbon counter electrode based perovskite solar cells encapsulated by PDMS. *Journal of Materials Chemistry A* 4 (27): 10700–10709.

36 Zaban, A., Greenshtein, M., and Bisquert, J. (2003). Determination of the electron lifetime in nanocrystalline dye solar cells by open-circuit voltage decay measurements. *ChemPhysChem* 4 (8): 859–864.

37 Di Giacomo, F., Zardetto, V., Lucarelli, G. et al. (2016). Mesoporous perovskite solar cells and the role of nanoscale compact layers for remarkable all-round high efficiency under both indoor and outdoor illumination. *Nano Energy* 30: 460–469.

38 Sheng, Y., Mei, A., Liu, S. et al. (2018). Mixed $(5\text{-}AVA)_xMA_{1-x}PbI_{3-y}(BF_4)_y$ perovskites enhance the photovoltaic performance of hole-conductor-free printable mesoscopic solar cells. *Journal of Materials Chemistry A* 6 (5): 2360–2364.

39 Wang, Q., Liu, S., Ming, Y. et al. (2018). Improvements in printable mesoscopic perovskite solar cells via thinner

spacer layers. *Sustainable Energy & Fuels* 2 (11): 2412–2418.

40 Tian, C., Zhang, S., Li, S. et al. (2018). A C60 modification layer using a scalable deposition technology for efficient printable mesoscopic perovskite solar cells. *Solar RRL* 2 (10): 1800174.

41 Jiang, X., Xiong, Y., Zhang, Z. et al. (2018). Efficient hole-conductor-free printable mesoscopic perovskite solar cells based on SnO_2 compact layer. *Electrochimica Acta* 263: 134–139.

42 Hu, Y., Zhang, Z., Mei, A. et al. (2018). Improved performance of printable perovskite solar cells with bifunctional conjugated organic molecule. *Advanced Materials* 30 (11): 1705786.

43 Yamada, Y., Nakamura, T., Endo, M. et al. (2014). Photocarrier recombination dynamics in perovskite $CH_3NH_3PbI_3$ for solar cell applications. *Journal of the American Chemical Society* 136 (33): 11610–11613.

44 Stranks, S.D., Burlakov, V.M., Leijtens, T. et al. (2014). Recombination kinetics in organic-inorganic perovskites: excitons, free charge, and subgap states. *Physical Review Applied* 2 (3): 034007.

45 Haughn, C.R., Schmieder, K.J., Zide, J.M.O. et al. (2013). Quantification of trap state densities in GaAs heterostructures grown at varying rates using intensity-dependent time resolved photoluminescence. *Applied Physics Letters* 102 (18): 182108.

46 Sum, T.C., Chen, S., Xing, G. et al. (2015). Energetics and dynamics in organic–inorganic halide perovskite

photovoltaics and light emitters. *Nanotechnology* 26 (34): 342001.

47 Habisreutinger, S.N., Noel, N.K., and Snaith, H.J. (2018). Hysteresis index: A figure without merit for quantifying hysteresis in perovskite solar cells. *ACS Energy Letters* 3 (10): 2472–2476.

48 Dunbar, R.B., Duck, B.C., Moriarty, T. et al. (2017). How reliable are efficiency measurements of perovskite solar cells? The first inter-comparison, between two accredited and eight non-accredited laboratories. *Journal of Materials Chemistry A* 5 (43): 22542–22558.

49 Zimmermann, E., Wong, K.K., Müller, M. et al. (2016). Characterization of perovskite solar cells: towards a reliable measurement protocol. *APL Materials* 4 (9): 091901.

50 Markvart, T. and McEvoy, A. (2003). *Practical Handbook of Photovoltaics: Fundamentals and Applications*. Elsevier.

51 Ananda, W. (2017). External quantum efficiency measurement of solar cell. 2017 15th International Conference on Quality in Research (QiR) : International Symposium on Electrical and Computer Engineering, (24–27 July 2017), https://doi.org/10.1109/QIR.2017.8168528.

52 Wang, Y., Liu, X., Zhou, Z. et al. (2019). Reliable measurement of perovskite solar cells. *Advanced Materials* 31 (47): 1803231.

53 Mundus, M., Venkataramanachar, B., Gehlhaar, R. et al. (2017). Spectrally resolved nonlinearity and temperature

dependence of perovskite solar cells. *Solar Energy Materials and Solar Cells* 172: 66–73.

54 Ravishankar, S., Aranda, C., Boix, P.P. et al. (2018). Effects of frequency dependence of the external quantum efficiency of perovskite solar cells. *Journal of Physical Chemistry Letters* 9 (11): 3099–3104.

55 Wagner, L. (2021). Perovskite photovoltaic modules with a very low CO_2-eq footprint: the in-situ technology.

56 Tress, W., Yavari, M., Domanski, K. et al. (2018). Interpretation and evolution of open-circuit voltage, recombination, ideality factor and subgap defect states during reversible light-soaking and irreversible degradation of perovskite solar cells. *Energy & Environmental Science* 11 (1): 151–165.

57 Sarritzu, V., Sestu, N., Marongiu, D. et al. (2017). Optical determination of Shockley-Read-Hall and interface recombination currents in hybrid perovskites. *Scientific Reports* 7 (1): 44629.

58 Tress, W., Leo, K., and Riede, M. (2013). Dominating recombination mechanisms in organic solar cells based on ZnPc and C60. *Applied Physics Letters* 102 (16): 163901.

59 Green, M.A., Dunlop, E.D., Hohl-Ebinger, J. et al. (2019). Solar cell efficiency tables (Version 55). *Progress in Photovoltaics*; 28(NREL/JA-5900-75827).

60 Best Research-Cell Efficiency Chart. (2022). https://www.nrel.gov/pv/cell-efficiency.html (accessed 13 February 2023).

61 Fraunhofer, I.S.E. CalLab, P.V. (2022) Cells changes to new spectral distribution in IEC 60904-3 standard.

https://www.ise.fraunhofer.de/content/dam/ise/de/down loads/service/callab/IEC60904_3Ed1vs2_V2.pdf (accessed 13 February 2023).

62 Wagner, L., Mastroianni, S., and Hinsch, A. (2020). Reverse manufacturing enables perovskite photovoltaics to reach the carbon footprint limit of a glass substrate. *Joule* 4 (4): 882–901.

63 Reese, M.O., Gevorgyan, S.A., Jørgensen, M. et al. (2011). Consensus stability testing protocols for organic photovoltaic materials and devices. *Solar Energy Materials and Solar Cells* 95 (5): 1253–1267.

64 Khenkin, M.V., Katz, E.A., Abate, A. et al. (2020). Consensus statement for stability assessment and reporting for perovskite photovoltaics based on ISOS procedures. *Nature Energy* 5 (1): 35–49.

65 Urbina, A. (2020). The balance between efficiency, stability and environmental impacts in perovskite solar cells: a review. *Journal of Physics: Energy* 2 (2): 022001.

66 Grancini, G., Roldán-Carmona, C., Zimmermann, I. et al. (2017). One-year stable perovskite solar cells by 2D/3D interface engineering. *Nature Communications* 8 (1): 15684.

67 Rakocevic, L., Ernst, F., Yimga, N.T. et al. (2019). Reliable performance comparison of perovskite solar cells using optimized maximum power point tracking. *Solar RRL* 3 (2): 1970024.

3
Printable Processing Technologies for Perovskite Solar Cells

Daiyu Li, Anyi Mei, Yue Hu, and Hongwei Han
Wuhan National Laboratory for Optoelectronics,
Huazhong University of Science and Technology, 1037
Luoyu Road, Wuhan, 430074, P.R. China

3.1 Introduction

Commercialization of perovskite solar cells (PSCs) relies on three critical factors: performance, stability, and cost. Recently, the performance and stability of laboratory-scale PSCs ($<1.0\,cm^2$) are gradually improved through material research and fabrication processes, approaching that of silicon solar cells [1, 2]. However, when the device area is increased to prepare perovskite solar modules (PSMs), the performance and stability tend to decrease [3, 4]. These upscaling losses are due to the inhomogeneous fabrication of all functional layers with a large area, including perovskite layer, electron-transport layer (ETL), hole-transport layer (HTL), and back electrodes [5]. Hence, the fabrication technologies to prepare high-quality large-area thin films become crucial. In addition, the cost, such as levelized cost of electricity and life-cycle assessment [6, 7], is used to assess PSMs' competitiveness when compared with other photovoltaic technologies. The cost can be lowered by establishing industrial production lines for PSMs. Hence, the fabrication technologies with higher and faster throughputs toward industrial-scale production should be considered.

Currently, various fabrication technologies have been developed [5]. Figure 3.1 shows a timeline of fabrication technologies for the deposition of perovskite layers [8], which can be divided into solution-based methods (e.g. spin coating, blade coating, slot-die coating, etc.) and vacuum-based methods (e.g. chemical vapor deposition, etc.). As the pioneering reports are shown in the timeline, it is interesting to find that most researchers have mainly focused on solution-based methods than vacuum-based methods. This is because solution-based methods have attractive low costs. In comparison, the vacuum-based methods require specific vacuum pressures and precise evaporation processes, causing high operating costs and low reproducibility [5, 9]. In addition to depositing perovskite layers, the solution-based methods are also commonly used to deposit ETL, HTL, and back electrodes. For example, the chemical bath deposition (CBD) is used to deposit ETL, such as TiO_2 and SnO_2 [10, 11]; the screen printing is used to deposit a triple-layer scaffold of mesoporous TiO_2 (m-TiO_2)/mesoporous ZrO_2 (m-ZrO_2)/carbon electrode [12].
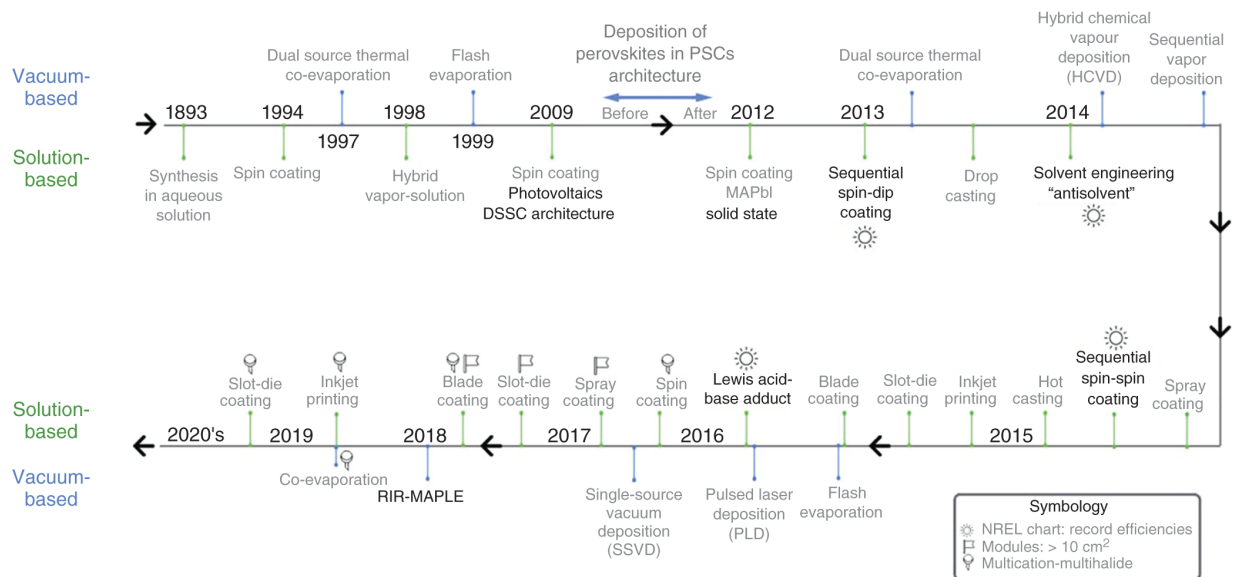
Figure 3.1 Timeline of fabrication methods for PSCs and PSMs. The methods are divided into solution-based and vacuum-based methods. The symbology indicates that the methods are applied to modules, multi-cation/multi-halide compositions, or achieve NREL record efficiency. Source: Soto-Montero et al. [8]/AIP Publishing/CC BY-4.0.

In this chapter, we provide an overview of the solution-based technologies for PSCs. These technologies include traditional technologies (spin coating, blade coating, slot-die coating, and bar coating), patternable technologies (spray coating, inkjet printing, and screen printing), specific technologies (CBD), and emerging technologies (soft-cover deposition and brush painting). We will introduce these solution-based technologies from several following aspects: fundamental principles, deposition areas, universality, material utilization, production capacity, and reproducibility.

3.2 Solution-Based Technologies

3.2.1 Spin Coating

As the most efficient method to fabricate PSCs in lab-scale, spin coating is a procedure that can effectively deposit thin films on flat substrates. The coating material is usually dissolved or dispersed in solvents to prepare a precursor solution. After applying the precursor at the center of the substrate, the substrate is rotated at a high spin speed/rate (revolutions per minute, RPM) to spread the coating material by centrifugal force (Figure 3.2a). The solvents in the precursor are usually volatile and simultaneously evaporate during the rotation. Typically, the higher the spin rate, the thinner the deposited film. The thickness of the film also depends on the viscosity and concentration of the precursor, and the solvent [16]. The spin coating could easily obtain pinhole-free perovskite layer, ETL, and HTL with good morphology and crystallization [17]. Hence, most laboratory-scale PSCs with record efficiencies are prepared by spin coating [18, 19].
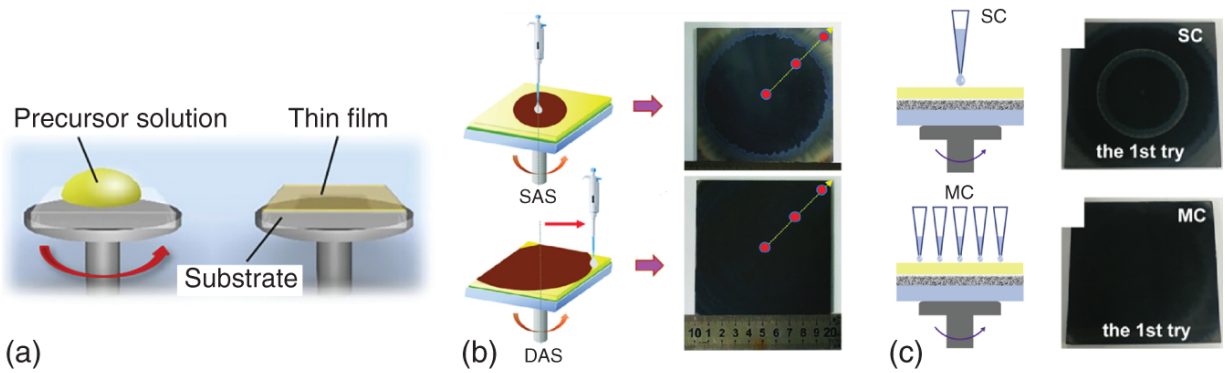
Figure 3.2 (a) Schematic diagram of spin coating. Source: Rong et al. [13] Reproduced with permission of American Chemical Society. (b) Schematic diagram of static antisolvent (SAS) process and dynamic antisolvent quenching (DAS), and photographs of the SAS-processed and DAS-processed $10 \times 10 \, cm^2$ perovskite film. Source: Bu et al. [14], Reproduced with permission from John Wiley & Sons. (c) Schematic diagram of single-tip pipette (SC) process and multi-tip pipette (MC), and photographs of the SC-processed and MC-processed $10 \times 10 \, cm^2$ perovskite film. Source: Wang et al. [15], Reproduced with permission from Elsevier.

However, spin coating is not a suggested commercial method for PSMs now. Firstly, since most of the precursor spins off the substrate as the rotation proceeds, the material utilization ratio of spin coating is as low as 1%, increasing costs and making it feasible only for fabrication on lab-scale [20]. Secondly, spin coating is not able to deposit uniform films on a large scale. This unevenness will be magnified when the scale enlarges and thus causes efficiency loss [14, 15]. To solve the above problems, two optimized spin-coating methods are reported, which are called a dynamic antisolvent quenching (DAS) process and multi-tip pipette (MC) process [14, 15]. In DAS process, a moving pipette continuously dropped the antisolvent from the center to the edge (Figure 3.2b) [14]. Compared with static antisolvent (SAS) process, DAS process allowed

antisolvent to interact with the whole perovskite wet film almost simultaneously to form homogenous nucleation, thus forming an even and pinhole-free perovskite films. The principle of MC process was similar to that of DAS process, but the operation was relatively simpler (Figure 3.2c) [15]. Both methods were successful in fabricating PSMs. A DAS-processed $10 \times 10 \, cm^2$ PSM obtained a certified PCE of 17.4% under a certified aperture area of $53.64 \, cm^2$. An average PCE of 60 MC-processed $5 \times 5 \, cm^2$ modules was 15.71% with a standard deviation of 0.42%, showing a higher reproducibility. DAS and MC processes suggest that it is possible to adapt spin coating to industrial fabrication by optimizing the dropping method of solutions. If the movement of the pipette and the volume of solutions could be dynamically adjusted by machine, large-area films with high quality and good reproducibility could be obtained and the cost could be reduced at the same time.

Moreover, as the most widely used deposition method on lab-scale, spin-coating is almost compatible with any kind of solution and possesses quite a high reproducibility. Thus, it can always be used to fabricate control devices and compare the influence of the precursors on the formation of films and device performance. Besides, the crystal growth kinetics of perovskite and other materials can be investigated by spin-coating prepared samples, promoting the understanding of the deposition and formation process of the desired films. Therefore, continuous research on spin coating is also very essential for other solution-based methods.

3.2.2 Blade Coating

Great effort has been devoted to developing industrial-scale deposition technologies, and meniscus coating is the main one of them. The meniscus coating is a noncontact

processing method for the deposition of homogeneous wet films with high cross-directional uniformity and reproducibility. In the coating process, the solution takes on a meniscus shape under the guidance of coating tools. Meniscus-coated films will be affected by the shape of the meniscus and coating process. According to the type of coating tool, meniscus coating methods contain blade coating, slot-die coating and bar coating (Figure 3.3) [5]. These three coating methods have already been used to deposit perovskite films and other functional layers of PSMs and can be integrated into a roll-to-roll (R2R) process on flexible substrate [5, 21].
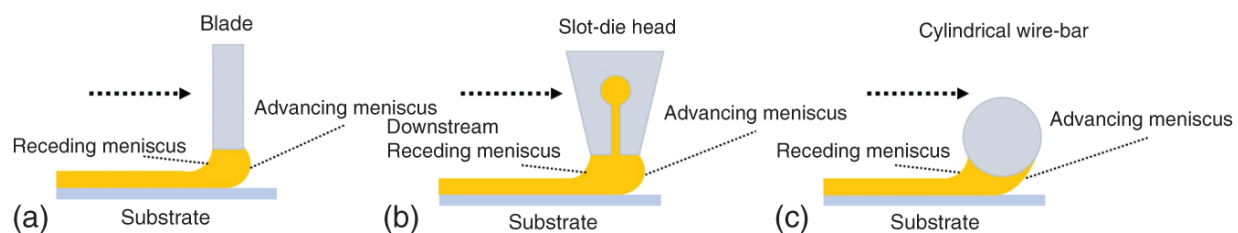
Figure 3.3 Schematic diagram of meniscus coatings. (a) Blade coating; (b) Slot-die coating; (c) Bar coating. Source: Li et al. [5]. Reproduced with permission of Wiley-VCH.

The blade coating is the earliest and relatively simple method to be used to produce large-area PSMs [22]. In blade coating, a knife-type coating tool moves linearly across the substrate, spreading the solution and forming a thin liquid film (Figure 3.4a). After annealing, a solid thin film is fabricated. Compared with spin coating, blade coating has a wider precursor-processing window (up to ~8 minutes), which provides more fault tolerance for industrial production. In addition, a slow solvent-drying process of wet films in blade coating resulted in perovskite layer with higher coverage and better quality [26].

In blade coating, there are two regimes, which are called evaporation regime and Landau–Levich regime (Figure 3.4b). These two regimes have different properties

that affect the thickness of perovskite films. As shown in [Figure 3.4c], when the coating speed increases, the film thickness first decreases and then increases [25]. This is because, in evaporation regime, faster coating speed causes shorter residence time per unit length, resulting in a reduced amount of accumulated solute [24]. On the contrary, in Landau–Levich regime, liquid film is pulled out by viscous forces and then dried [24]. Obviously, a high-throughput blade coating method in Landau–Levich regime is required for industrial production. It has been reported that an optimal surfactant called l-α-phosphatidylcholine could reduce the surface tension and suppress the flows, thus obtaining a smooth perovskite layer ([Figure 3.4d]) [25]. With the surfactant, an estimated annual production capacity of 236 MW with a 1 m-wide production line was expected to achieve. In addition, the coating and annealing processes also influence film thickness, uniformity, and crystallinity, such as solution volume, coating speed, gap between blade and substrate, and substrate/airflow temperature [22, 23].

At present, a champion PCE of 15.3% for a PSM with an aperture area of 205 cm^2 was achieved by blade coating perovskite layer and HTL [27]. This PCE was higher than previously reported for comparable sizes and printing technologies. Moreover, an all-layer blade except the metal electrode PSM was achieved by overcoming the challenges of blading a thin ETL on a rough perovskite layer [28]. This PSM with an area of 25.03 cm^2 had an aperture PCE of 19.3%, which was the highest efficiency of inverted PSMs by blade coating.

3.2.3 Slot-Die Coating

Different from blade coating, slot-die coating delivers solutions through a fixed slot gap onto the substrate ([Figure 3.5a]). The solutions are filling the gap between the

die and the substrate and form the coating bead. Notably, slot-die coating belongs to pre-metered coating processes, whereby all the supplied solution is steadily and continuously deposited on the substrate with no waste. It can handle a broad range of viscosities for the coated solution and coating speed [31]. The thickness of the coated solution layer or the wet film can be preset and precisely controlled by adjusting the flow rate of the solution fed into the die and the coating speed [29]. The quality of slot-die-coated film can be affected by many complex factors, including coating speed, flow rate coating gap, and liquid viscosity. These factors have been reviewed in detail [29], which has high theoretical guiding significance for slot-die coating in PSMs. Currently, the slot-die-printed PSMs achieve champion PCE of 20.42% and 19.54% with an active area of 17.1 and 65.0 cm^2, respectively [32].

(a)

Blade direction

Perovskite film
Substrate

Elevated support
Doctor blade
Precursor liquid
Hot plate
Base plate and speed control unit

(b)

Evaporation

Q_{evap}

h J_{film}

$Q_{solvent}$
J_{solute}

ν

Landau–Levich

Static meniscus z Back meniscus

Dynamic meniscus

h d θ_2 l θ_1

ν

(c)

Evaporation   Landau–Levich

Slope = −0.99   Slope = 0.64

Film thickness (µm)

2.5
2
1.5
1
0.5

1   10   100

Coating speed (mm s^{-1})

(d)

Solution flow   Surface tension gradient   Marangoni flow   Surfactant

$\nabla\gamma$ $\nabla\gamma$

Hydrophobic

Hydrophilic

Figure 3.4 (a) Schematic diagram of blade coating. Source: Mallajosyula et al. [23] Reproduced with permission of Elsevier. (b) Schematic diagram of evaporation regime and Landau–Levich regime. Source: Le Berre et al. [24]. Reproduced with permission of American Chemical Society. (c) The thickness of a MAPbI$_3$ film as a function of coating speed on a 145 °C preheated substrate. Linear fitting determines the evaporative and the Landau–Levich regimes. Source: Deng et al. [25]. Reproduced with permission of Springer Nature. (d) Schematic diagram of the directional microscale solution flow toward perovskite island during ink drying and the suppressed solution flow dynamics in the presence of surfactant. Source: Deng et al. [25]. Reproduced with permission from Springer Nature.
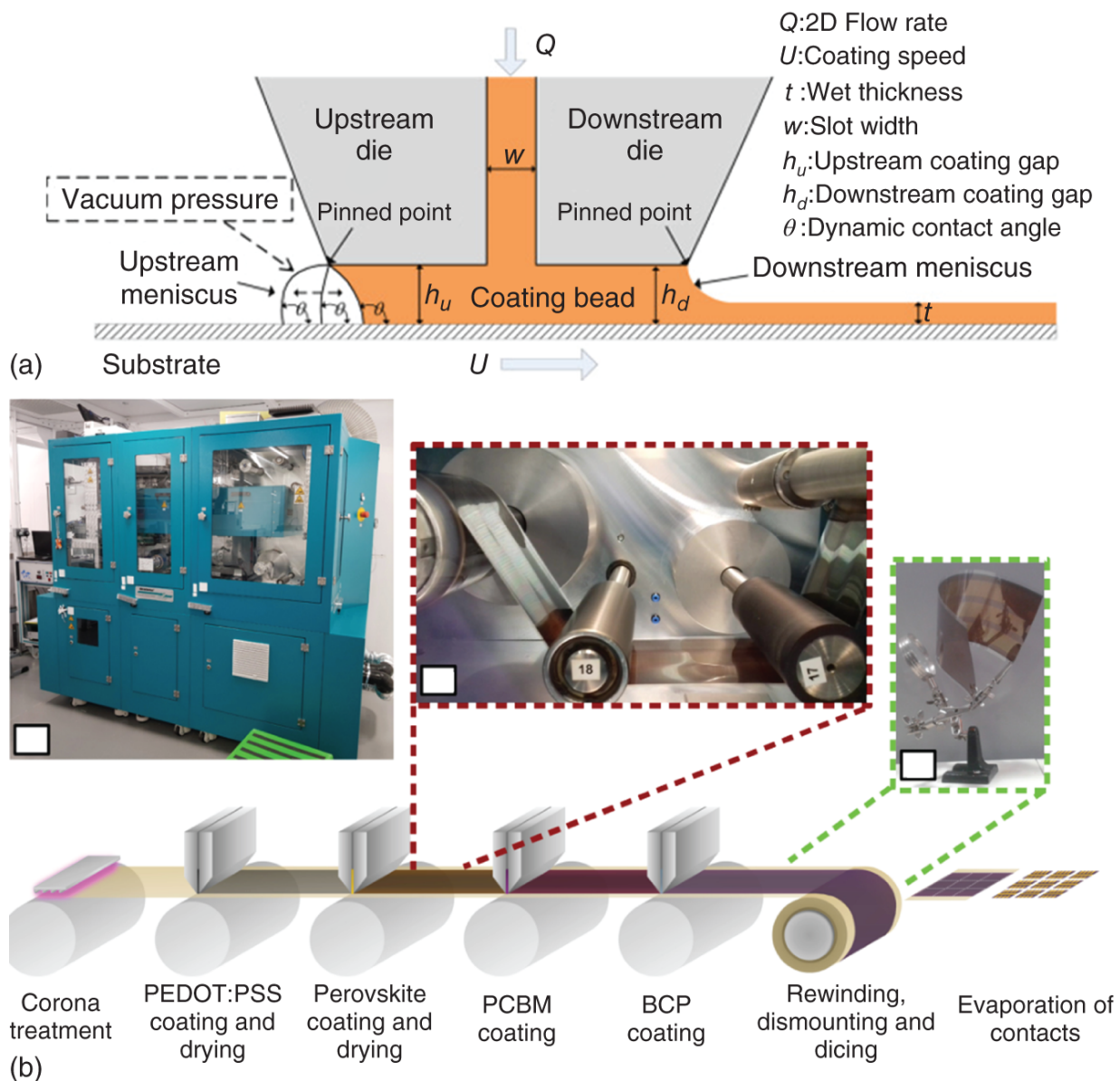
Figure 3.5 (a) Schematic diagram of slot-die coating. Source: Ding et al. [29]. Reproduced with permission of Wiley-VCH. (b) Schematic diagram and photographs of R2R slot-die coating process. Source: Burkitt et al. [30]. Reproduced with permission from Royal Society of Chemistry.

Due to the advantages of rapid deposition, well-controlled areas, and little solution waste, slot-die coating is widely considered to be compatible with continuous R2R technology. As Figure 3.5b shows, a R2R slot-die coating

process was developed [30]. The appropriate length meniscus guides were used as part of the coating head for each ink rheology. Four R2R slot-die coated layers, including PEDOT:PSS, perovskite, PCBM, and BCP, were fabricated at the same continuous speed to avoid bottlenecks in production rate and an overall slowing of process speed or needing to perform large amounts of parallel processing. Finally, the back electrode was evaporated and the entire device were divided into small cells. After optimizing drying conditions for perovskite layer and developing multi-solvent blend systems for electron collection layers, a stabilized PCE of 12.2% under an illuminated area of $0.09\,cm^2$ was obtained. Although the area and PCE were far away from those of the champion PSMs, this work demonstrated the feasibility of a R2R fabrication process for PSCs. With R2R process, a closed loop for production, deployment, operation, and decommissioning was generated, reducing the costs of materials, and speeding and simplifying fabrication processes [30]. It is very meaningful for PSCs' industrial production.

3.2.4 Bar Coating

Bar coating is a well-known scalable method to deposit thin films for various optoelectronic devices [33]. It uses a cylindrical wirebar (or D-bar) as the coater, while the solutions are filled in the gap of the wire, which is similar to the feed slot in the slot-die coating (Figure 3.6a). During spreading the solutions over the substrate, the solutions within the gap of the wire are drawn by the rod owing to the meniscus force upon moving the bar at a constant speed [35]. The thickness of a wet film is directly proportional to the gap of wire with passing a little solution through it. Therefore, bar coating deposit thin films with high reproducibility and material utilization [33].

In 2017, bar coating was first used to deposit laboratory-scale perovskite layers [36]. In 2018, Toshiba Corporation (Tokyo) reported a PSM with 802 cm^2 and a certified PCE of 11.6%, which is still the largest certified module until now [1]. According to public information, its perovskite layer was prepared by two-step bar-coating process (Figure 3.6b) [5]. However, more detailed information is not disclosed.

In the past three years, more works are focused on bar coating in PSMs with good results [35, 37], but there are still challenges to understand the complex fluid dynamics in the gap of the wire. Recently, Yoo et al. theoretically investigated the effect of the contact angle of the perovskite precursor solution on the substrate during bar coating from the perspective of nucleation kinetics. They concluded that a small contact angle provided a wettable interface to the perovskite, leading to a better crystallinity and full surface coverage [35]. After solvent engineering and surface passivation, a 31 cm^2 aperture area PSM with PCE of >20% was fabricated. This is the best-performing PSM prepared by bar coating to date. In addition to the perovskite layer, bar coating could also be used to deposit ETL. Mandati et al. achieved a uniform and conformally covered compact TiO_2 layer followed by uniform and desirable thick mesoporous TiO_2 layer on 5×5 cm^2 substrate by bar coating (Figure 3.6c) [34]. Because bar-coated TiO_2 layers had high uniformity, the bar-coated devices had better spatial homogeneity than spin-coated devices. The results show that bar coating has potential to be applicable to the fabrication of larger-area PSMs.

(a)

(b)

Dropping and moving

Wet film

Heating

Bar coated TiO$_2$

Dropping and spinning

Wet film

Heating

Spin coated TiO$_2$

(b)
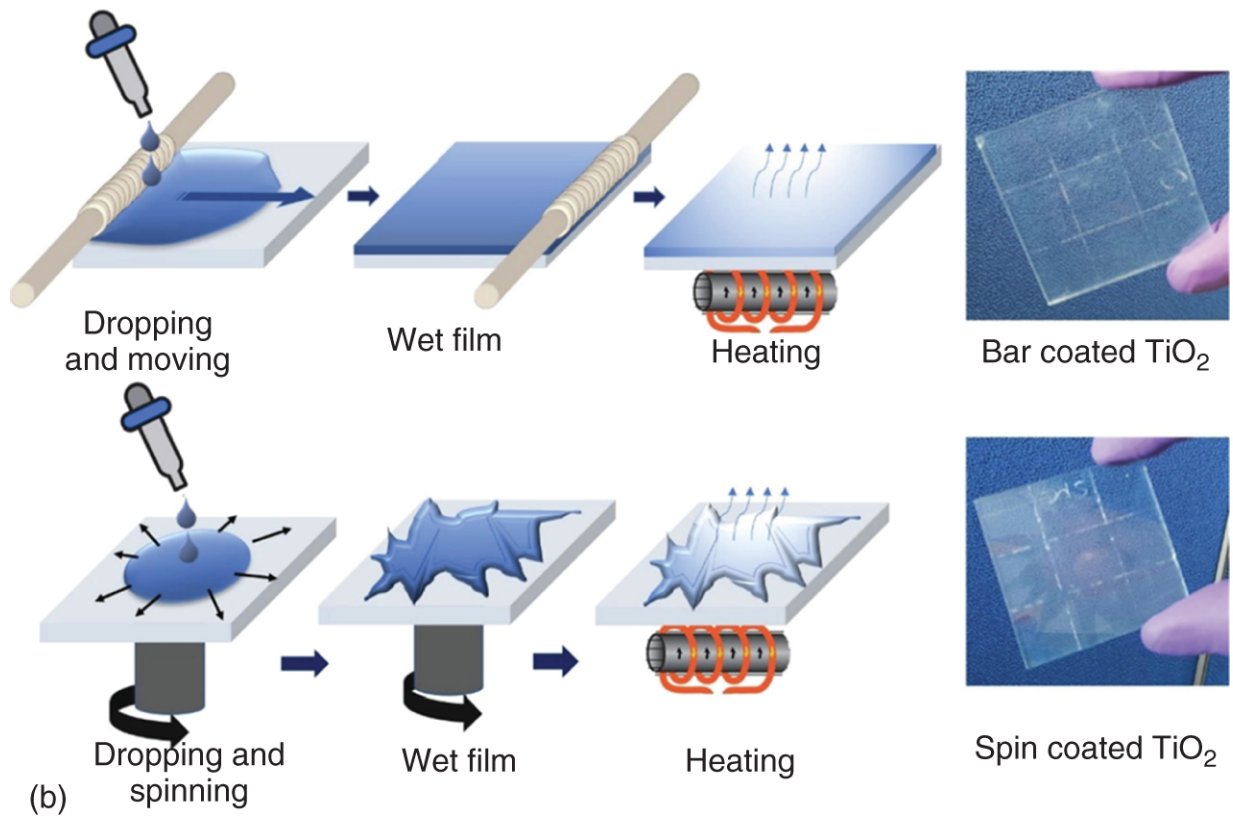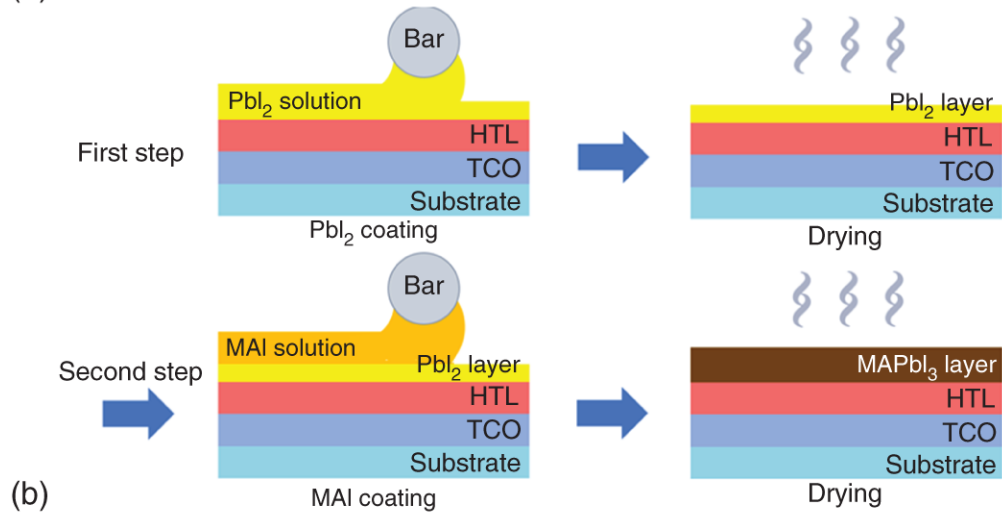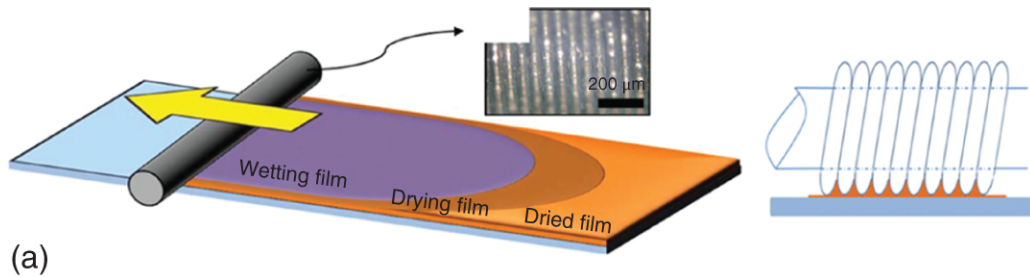
Figure 3.6 (a) Schematic diagram of bar coating with optical microscope image and illustration of the coating bar. Source: Khim et al. [33]. Reproduced with permission from John Wiley & Sons. (b) Schematic diagram of bar coating with two-step process. Source: Li et al. [5]. Reproduced with permission of Wiley-VCH. (c) Schematic diagram and photographs of bar coating and spin coating employed for the large-area TiO_2 layer deposition. Source: Mandati et al. [34]. Reproduced with permission from Elsevier.

3.2.5 Spray Coating

Spray coating can be classified into four steps (Figure 3.7a) [40]. (i) precursor solutions are sheared into a mist of micrometer-sized droplets and sprayed through a nozzle. (ii) The spray mist is guided to the substrate with the assistance of a shaping gas. (iii) The droplets arrive at the substrate and converge to form a wet film. (iv) The solvents evaporate by heating to form a solid film. According to the methods of generating mist, spray coating can be divided into pneumatic spraying and ultrasonic spraying. Pneumatic spray coating is achieved by forcing a solution through a narrow aperture or nozzle, which is simple and easy to implement. The compact TiO_2 layer was often deposited by this method [5]. Later, it is found that the size and uniformity of the droplets have great impact on the sprayed perovskite layer. Hence, ultrasonic spray coating is developed by using more sophisticated ultrasonic coaters equipped with piezoelectric transducers to break up the solution (Figure 3.7b). Ultrasonic spray coating could obtain smaller and more uniform droplets to deposit smooth perovskite films. According to the calculation, using frequency under 1 MHz generates over 10 µm droplets with broad size distribution [41]. Further, a megasonic spray coating with 1.7 MHz megasonic nebulizer was developed

and could generate droplets with sizes of 2–4 μm [39]. With small droplets and narrow size distribution, Park et al. were able to fabricate a large-area ($7.5 \times 7.5 \, \text{cm}^2$) perovskite layer with high quality.
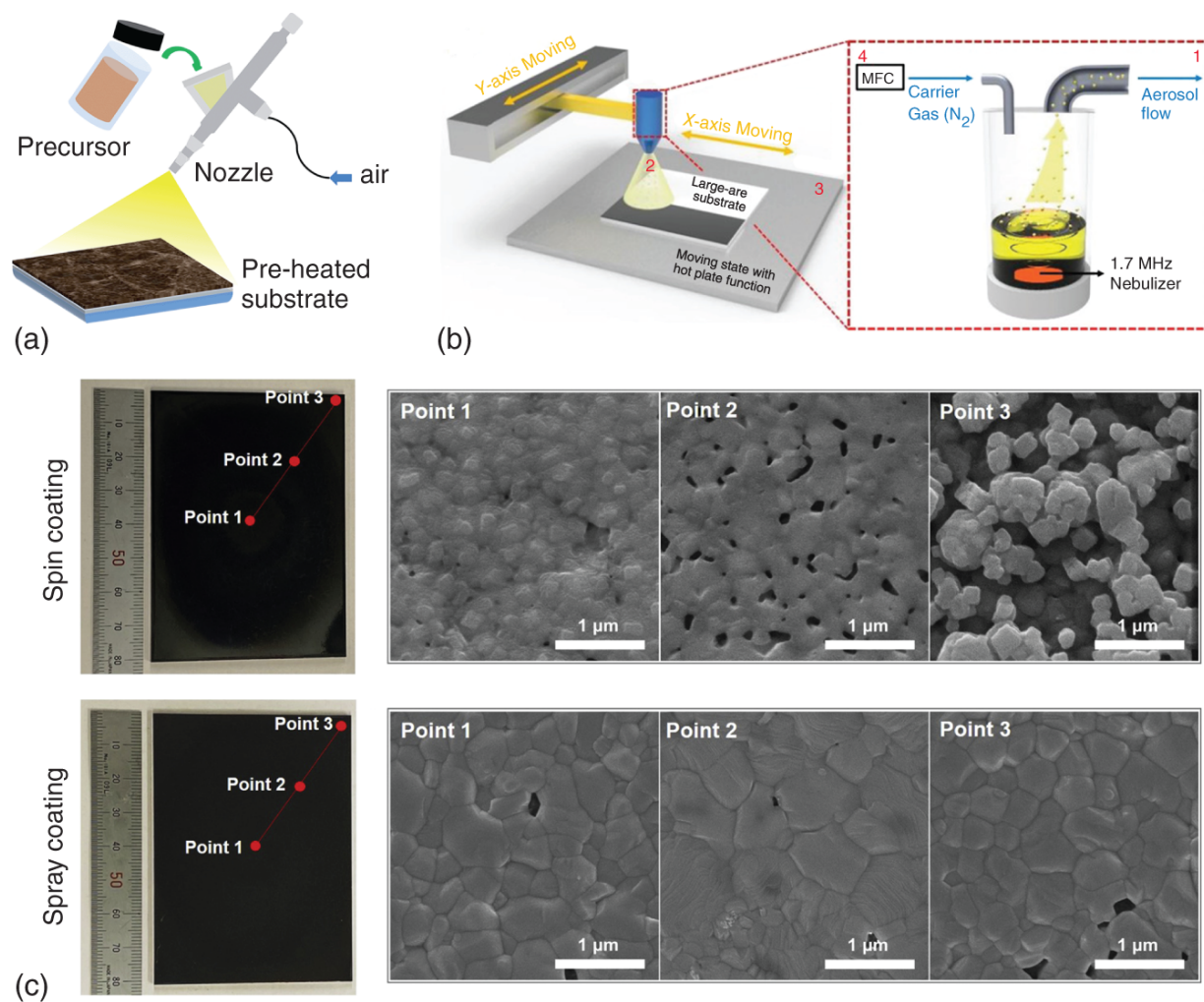
Figure 3.7 (a) Schematic diagram spray coating. Source: Swartwout et al. [38]. Reproduced with permission from John Wiley & Sons. (b) Schematic diagram ultrasonic spray coating. Source: Park et al. [39]. Reproduced with permission of Wiley-VCH. (c) Photographs and SEM images of large-area spin-coated and spray-coated $CsPbI_2Br$ perovskite films. Source: Park et al. [39]. Reproduced with permission from John Wiley & Sons.

Besides the methods of generating mist, the solvents affect the quality of the spray-coated films. For example, the boiling point (b.p.) of the solvent in the precursor significantly influences the quality of the spray-deposited films. If the b.p. of the solvent (such as chloroform with b.p. 63 °C) is too low, the sprayed solution will dry before reaching the substrate, obtaining films with abundant pinholes and significant variation in film thickness. If the b.p. of the solvent is relatively high (such as dimethylsulfoxide (DMSO) with b.p. 189 °C), the sprayed solution may need a relatively prolonged drying/annealing process to obtain dry films, which will cause shrinkage of the wet films on the substrate and variations of the thickness in large area.

Recently, Heo et al. reported an effective, orthogonal processable spray-coating approach to fabricate graded, inorganic $CsPbI_{3-x}Br_x$ perovskite layer (Figure 3.7c) [42]. This graded structure broadened the absorption wavelength range and increases carrier lifetime. With this method, they obtained a $112 \, cm^2$ PSM with 13.82%. In addition, some studies have shown that large-area spray-coated ETL and HTL had better performance than spin-coated ones, such as TiO_2, SnO_2, NiO_x, and Spiro-OMeTAD [43–46]. This is because spray coating could deposit a dense and uniform layer on the substrate, allowing the fabrication of efficient PSCs. Generally, spray coating can provide high production capacity, precise control over directional deposition, efficient utilization of materials, and compatibility with a variety of substrates.

3.2.6 Inkjet Printing

Similar to spray coating, the inkjet printing directly drops miniscule ink volumes onto substrates from the nozzle. With fine control of droplet size and trajectory, inkjet

printing has the freedom of printing arbitrary design patterns at low material consumption [47, 48]. This feature means inkjet printing removes the necessity for laser etching of photoactive films as required in common PV module fabrication [9], which is beneficial to reduce production processes and thus reduce the cost. Inkjet printing enables intricate cell shapes for particular functions, such as small and portable power supplies and building-integrated photovoltaic, which were more compared to those obtained from the standard screen-printing route [49]. According to the method used to generate ink droplets, inkjet printing can be classified as continuous inkjet printing (CIP, by surface tension) and drop-on-demand inkjet printing (DOD, by pressure pulse) (Figure 3.8a) [47]. DOD is more commonly used than CIP because it enables more material saving.

By using homogeneous molecular or colloidal liquid phase inks, inkjet printing can achieve versatile deposition. For example, Schackmar et al. fabricated inverted planar PSCs with inkjet-printed NiO_x, perovskite layer, PCBM, and BCP (Figure 3.8b) [50]. Verma et al. achieved triple mesoscopic PSCs by inkjet printing all of the oxide layers in the stack and perovskite precursor (Figure 3.8c) [49]. Pendyala et al. inkjet-printed arrays of inert transparent pillars to provide digital control of both the transparency and efficiency of the cells, thus fabricating semitransparent PSCs (Figure 3.8d) [51]. These results are a promising next step on the way to fully inkjet-printed PSCs, including both electrodes as well.
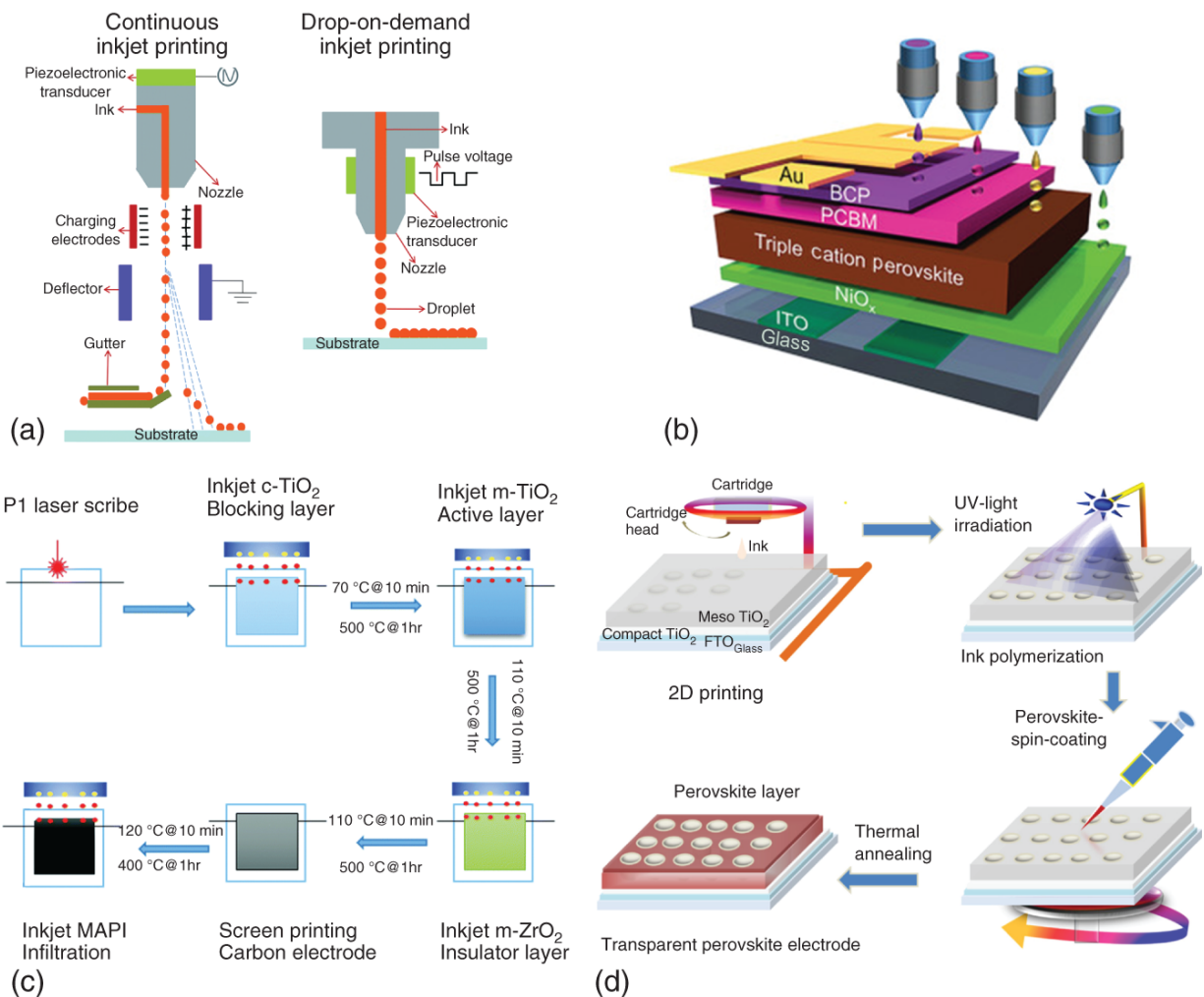
Figure 3.8 (a) Schematic diagram of two main inkjet-printing methods: continuous inkjet printing and drop-on-demand inkjet printing. Source: Karunakaran et al. [47]. Reproduced with permission of Royal Society of Chemistry. (b) Schematic diagram of inverted planar PSCs with inkjet-printed absorber and extraction layers. Source: Schackmar et al. [50]/John Wiley & Sons/CC BY-4.0. (c) Schematic diagram of triple mesoscopic PSCs with inkjet-printed oxide layers in the stack and perovskite precursor. Source: Verma et al. [49]/Royal Society of Chemistry/CC BY-3.0. (d) Schematic diagram of semitransparent PSCs with inkjet-printed arrays of inert transparent pillars. Source: Pendyala et al. [51]. Reproduced with permission of American Chemical Society.

However, inkjet printing has not been able to prepare large-area PSMs, and the largest inkjet-printed PSCs were only 4.04 cm^2 with a PCE of 14.5% [52]. This is because there are still challenges to achieve precise control over the nozzle jetting and strict requirements for ink composition [5, 53]. During the printing, the ink crystallizes quickly and the printed perovskite film becomes discontinuous with increasing defects. Hence, ink engineering for inkjet printing is very important.

3.2.7 Screen Printing

Inspired by the work on DSSCs, PSCs made breakthroughs based on the mesoscopic structure with mesoporous TiO$_2$ as the scaffold for hosting perovskite absorber. Previously, screen-printing technique has been widely used to fabricate large-area DSSCs toward practical applications [54, 55]. Now, it is commonly utilized to deposit mesoporous scaffolds and carbon electrodes in PSCs [12].
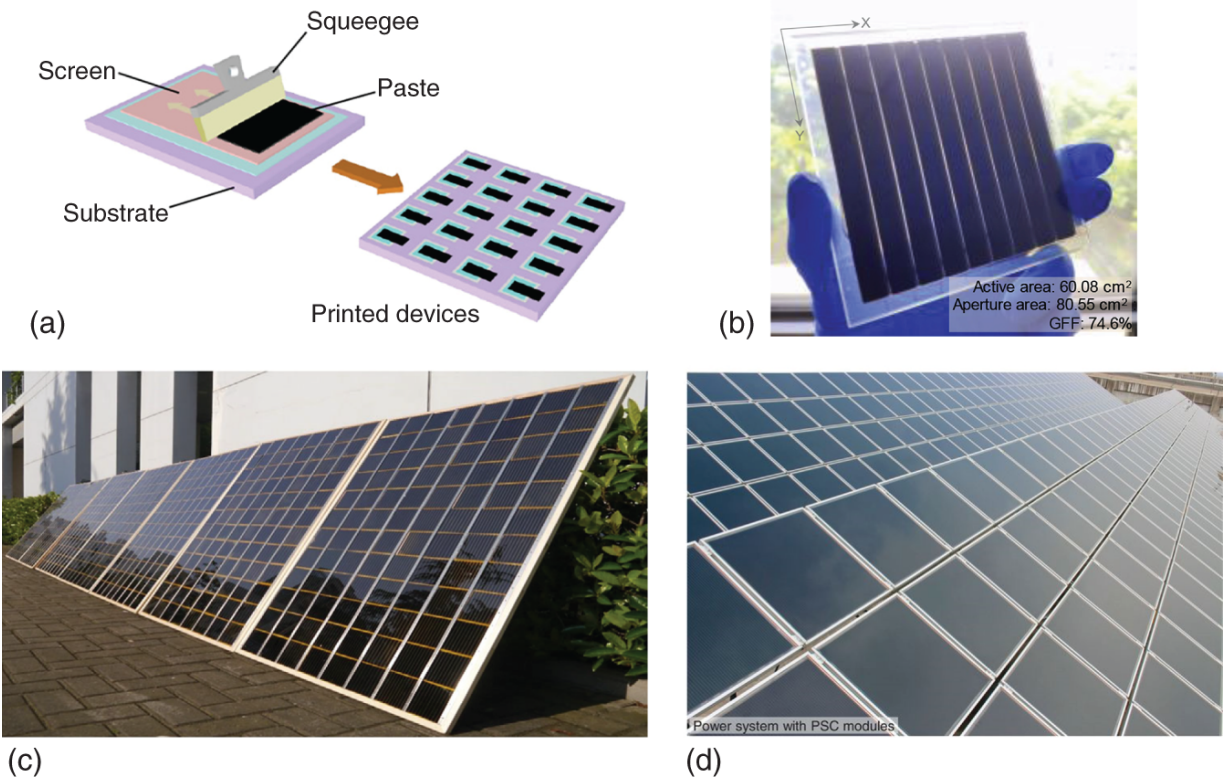
Figure 3.9 (a) Schematic diagram of screen printing. Source: Rong et al. [13]. Reproduced with permission of American Chemical Society. (b) Photograph of a screen-printed $10 \times 10\,cm^2$ triple mesoscopic PSM. Source: Xu et al. [56]. Reproduced with permission from Elsevier. (c) Photograph of a $7\,m^2$ fully printable perovskite solar panel. Source: Hu et al. [57]. Reproduced with permission from John Wiley & Sons. (d) Photograph of a $110\,cm^2$ power system with triple mesoscopic PSMs. Source: Rong et al. [58]. Reproduced with permission from American Association for the Advancement of Science - AAAS.

Screen printing is a widely used film deposition technique, for which a mesh (screen) is used to transfer paste (ink) onto a flat substrate (Figure 3.9a). The printed patterns are determined by the open mesh apertures of the screen. The non-printed areas are made impermeable to the paste by a blocking stencil. The paste is placed on the non-printed areas, and a printing squeegee is moved across the surface

of the screen to fill the open mesh apertures with paste. The paste that is in the mesh apertures is pumped or squeezed by capillary action to the substrate in a controlled and prescribed amount (the printed wet film is proportional to the thickness of the mesh and or stencil). As the squeegee moves toward the rear of the screen, the tension of the mesh pulls the mesh up away from the substrate (called snap-off) leaving the paste upon the substrate surface. The thickness of the printed films is determined by the mesh size, the thickness of the mesh screen, and the material ratio of pastes.

For screen printing, the deposition area can be as large as several square meters. At first, Han and coworkers developed triple mesoscopic PSCs with $0.8\,cm^2$ active area by screen printing [12]. Because scaling up the perovskite layer actually means scaling up the triple-layer scaffold, triple mesoscopic PSCs can be easily scaled up via screen printing [5]. Soon after, they developed $10 \times 10\,cm^2$ triple mesoscopic PSMs and used them to assemble a $7\,m^2$ fully printable perovskite solar panel, showing high reproducibility of screen printing (Figure 3.9b,c) [57]. Further, WonderSolar (China) launched a $110\,m^2$ perovskite PV system with screen-printed triple mesoscopic PSMs ($3600\,cm^2$ for each PSM) (Figure 3.9d) [58]. These reports demonstrate the unique advantage of screen printing in scaling up PSMs.

Moreover, the production capacity might be determined by the following drying and/or sintering process, not limited by the screen-printing process. And the material utilization can be as high as 100% for continuous process. To sum up, screen printing has great potential on the road to mass production and commercialization for PSCs.

3.2.8 Chemical Bath Deposition

CBD could also be used to fabricate perovskite films. However, one-step CBD process is difficult to obtain thickness-controllable, uniform, and high-quality perovskite thin films. Hence, sequential CDB processes, including two-step and three-step deposition methods, are developed. In two-step method, a PbI_2 layer is first coated by other deposition methods, such as spin coating and thermal evaporation (Figure 3.10a) [17, 62]. Then the PbI_2-coated substrate is dipped into in MAI solution. During dipping process, MAI intercalates into crystallized PbI_2 lattice to start perovskite formation, where the intercalation starts at grain boundaries and defect sites in PbI_2 [63]. After annealing, a $MAPbI_3$ perovskite film is obtained. Yaghoobi Nia et al. fabricated a 10.1 cm^2 PSM with a PCE of 13% through two-step CBD [64]. In three-step method, water-based metal precursors (M) are first deposited followed by iodination leading to MI_2. Then, the MI_2 is chemically converted to $MAPbI_3$ perovskite films (Figure 3.10b) [65]. Using water-based metal precursors is to solve the problems of poor solubility of PbI_2 and utilization of toxic solvents in two-step method. Gozalzadeh et al. employed a toxic solvent-free route based on CBD to deposit PbS as the lead metal precursor film and fabricated perovskite layers [65]. However, less studies have focused on depositing perovskite layer through CDB due to the lower improvement in device efficiency.
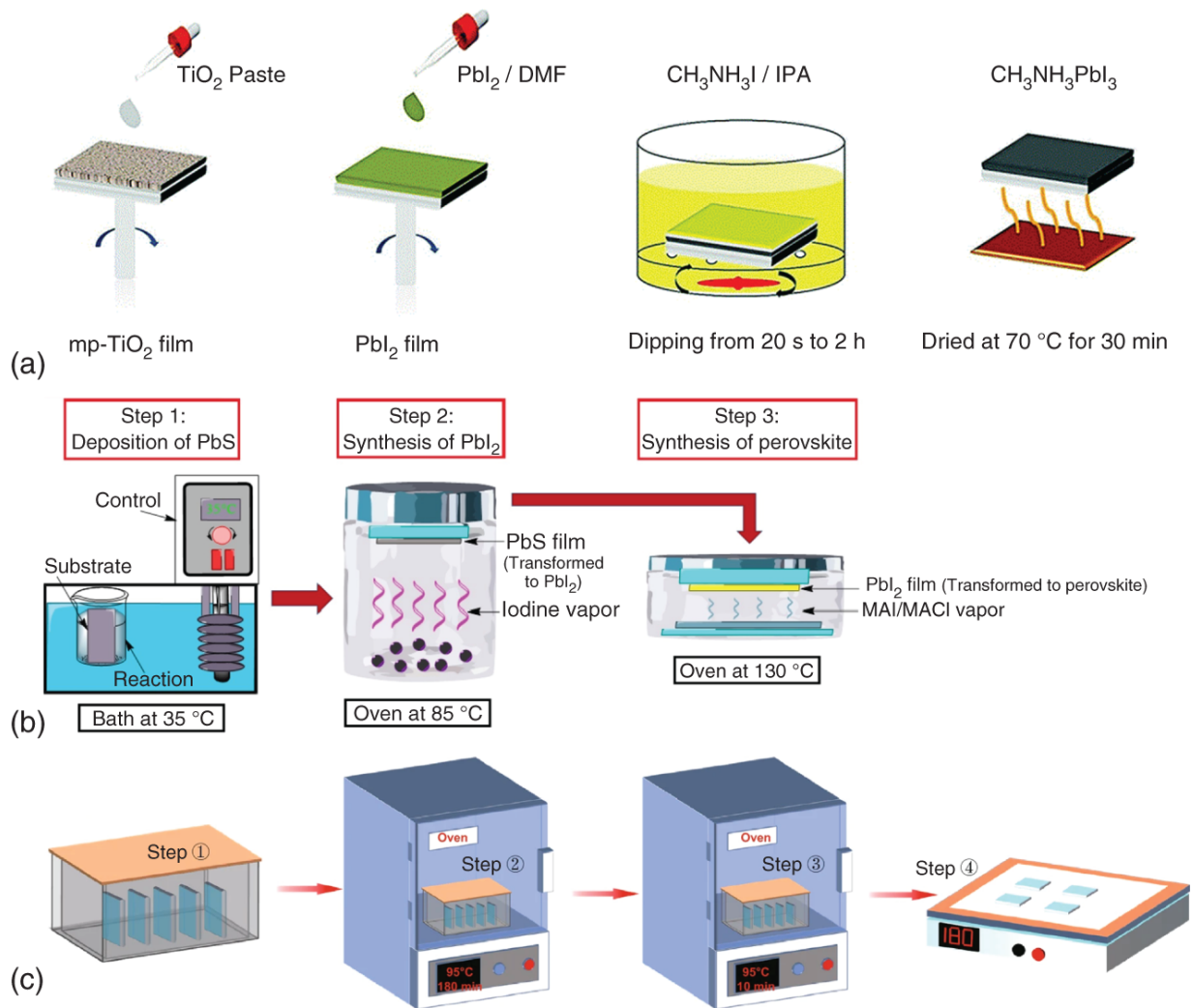
Figure 3.10 (a) Schematic diagram of the perovskite films by a two-step CBD method. Source: Zhao et al. [59]. Reproduced with permission of Royal Society of Chemistry. (b) Schematic diagram of the perovskite films by a three-step CBD method. Source: Cota-Leal et al. [60]. Reproduced with permission of Elsevier. (c) Schematic diagram of the SnO_2 films fabricated by CBD. Source: Tong et al. [61]/Springer Nature/CC BY-4.0.

Unlike perovskite layer, CBD is widely used to deposit metal oxide (Figure 3.10c), such as TiO_2, SnO_2, and NiO_x [10, 11, 66]. In CBD, there are two critical steps, namely, nucleation and particle growth [67]. (i) The substrate is

immersed in an aqueous solution containing the metal ion, such as $TiCl_4$, $SnCl_2$, and $NiSO_4$. (ii) The oxide is grown on the surface via hydrolysis of the cations, which are then precipitated onto the substrate as an oxide. The composition of aqueous solutions is usually complex because some additives are needed to initiate the hydrolysis of the cation and aid nucleation at the substrate. For example, using urea, acids, and glycerol as a binder, stabilizer, and retarding agent, respectively, could improve the morphology of CBD-processed SnO_2 films [19, 68].

Because CBD can uniformly and completely deposit a dense and conformal layer on the underlying substrate [11], the PSCs with CBD-processed SnO_2 have achieved a certified PCE of 25.5% [19]. Moreover, CBD can be easily applied to deposit large-area films, as reflected in a rapidly growing number of large-area CBD-processed PSMs with high performance [14, 61]. However, the size of the film deposited by CBD is less than $100\,cm^2$ at present [14, 69], which is still far from industrial scale. This might be due to the low uniformity of CBD-processed large-area films, or the limitation of other functional layers, so more research is needed. In addition, the necessity of frequent bath replacement and the large volume of solution waste are key challenges to consider when applying CBD in large-scale fabrication.

3.2.9 Soft-Cover Deposition

Soft-cover deposition is an emerging solution-based technology. This deposition used a soft cover with high surface wettability cover on the top of wet perovskite films. Then the substrate is heated and the soft cover is peeled off. After exposure to ambient air, the solvent in the precursor starts to evaporate and the perovskite crystallization simultaneously occurs (Figure 3.11a) [59,

[70]. The crystallization process is mainly affected by the heating temperature, peeling speed, and precursor compositions. Polyimide and polytetrafluoroethylene were chosen as the soft covers due to their high heat deflection temperature. In addition, the deposition system mainly consists of a computer-controlled mechanical hand to peel off the soft cover at a certain speed. With soft-cover deposition, the perovskite films exhibit superior uniformity and excellent quality.
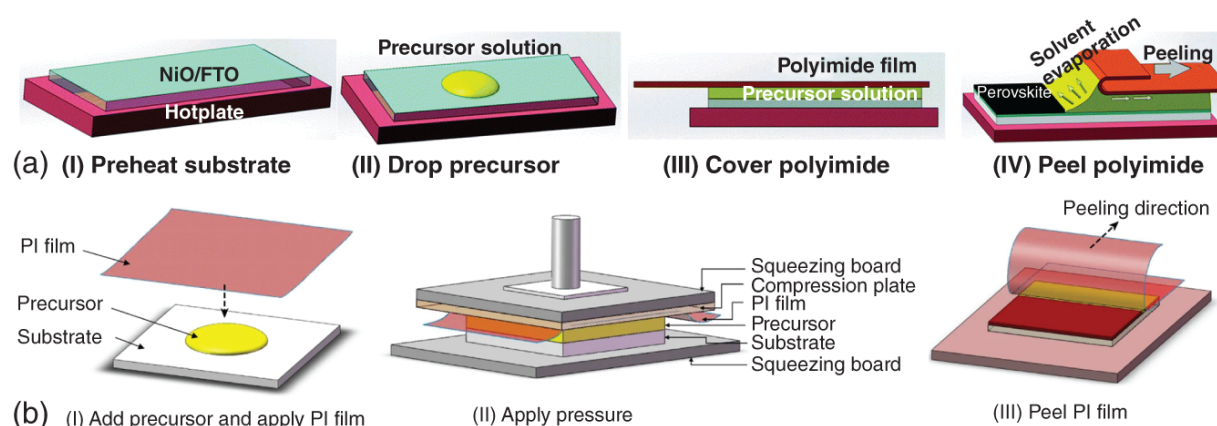
Figure 3.11 (a) Schematic diagram of soft-cover deposition. Source: Ye et al. [20]. Reproduced with permission of Royal Society of Chemistry. (b) Schematic diagram of soft-cover deposition with the assistance of pressure treatment. Source: Chen et al. [70]. Reproduced with permission of Springer Nature.

Ye et al. first developed soft-cover deposition and kept optimizing it. From the very beginning, they could already obtain 51 cm^2 high-quality perovskite films and fabricated a PSC with a PCE of 17.6% upon an active area of 1 cm^2 [20]. Moreover, the material utilization ratio was up to ~80%. Later, they developed a low-temperature soft-cover deposition [71]. Following this idea, an improved soft-cover deposition with the assistance of a pressure treatment was developed (Figure 3.11b) [70]. As a result, an orthorhombic perovskite crystal structure with good crystallinity and

large grains was formed in air at room temperature. Correspondingly, a certified PCE of 12.1% with an aperture area of 36.1 cm^2 was obtained. Recently, they extended soft-cover deposition to fabricate large-scale, compact and homogeneous TiO$_2$ layers, and a 16 cm^2 PSM exhibited a PCE of 14.01% [72].

These results show that soft-cover deposition has the potential to relatively enlarge the device area and fabricated modules with much higher material utilization ratio. But at current level, it is still challenging for these methods to further increase the area of PSCs from mini-modules to modules. For example, more studies are needed to further enlarge the device area, such as soft-cover wettability, solution viscosity, and the selection of a soft cover.

3.2.10 Brush Painting

Recently, a brush painting method which was inspired by an old Chinese calligraphy tradition was developed to deposit solution-processable thin films (Figure 3.12a) [73]. The Chinese ink brush of "Maobi" was employed to coat active layers and polymer electrodes with tunable thickness from nanometers to micrometers for organic solar cells and modules, which may also be able to deposit the perovskite active layers and various charge transport layers for PSCs and modules. Maobi is usually made from animal hairs (mainly goat, weasel, and rabbit hairs). Dipping into the ink, the ink is firstly absorbed and stored inside/between the hairs. When the hairs are pressed upon the surface of the substrate, the ink slides to the tip and is delivered to the substrate. As the painting direction and pressure change, continuous and patterned handwriting is thus formed under shear stress and capillary force [77]. Lee et al. first fabricated a fully brush-painted PSCs with the

exception of an evaporated metal electrode on flexible substrates (Figure 3.12b) [74]. They used a purchasable flat paint brush with nylon synthetic hair to coat perovskite and electron acceptor layers. The thickness and morphology of brush-painted films can be controlled by the concentration and substrate temperature.
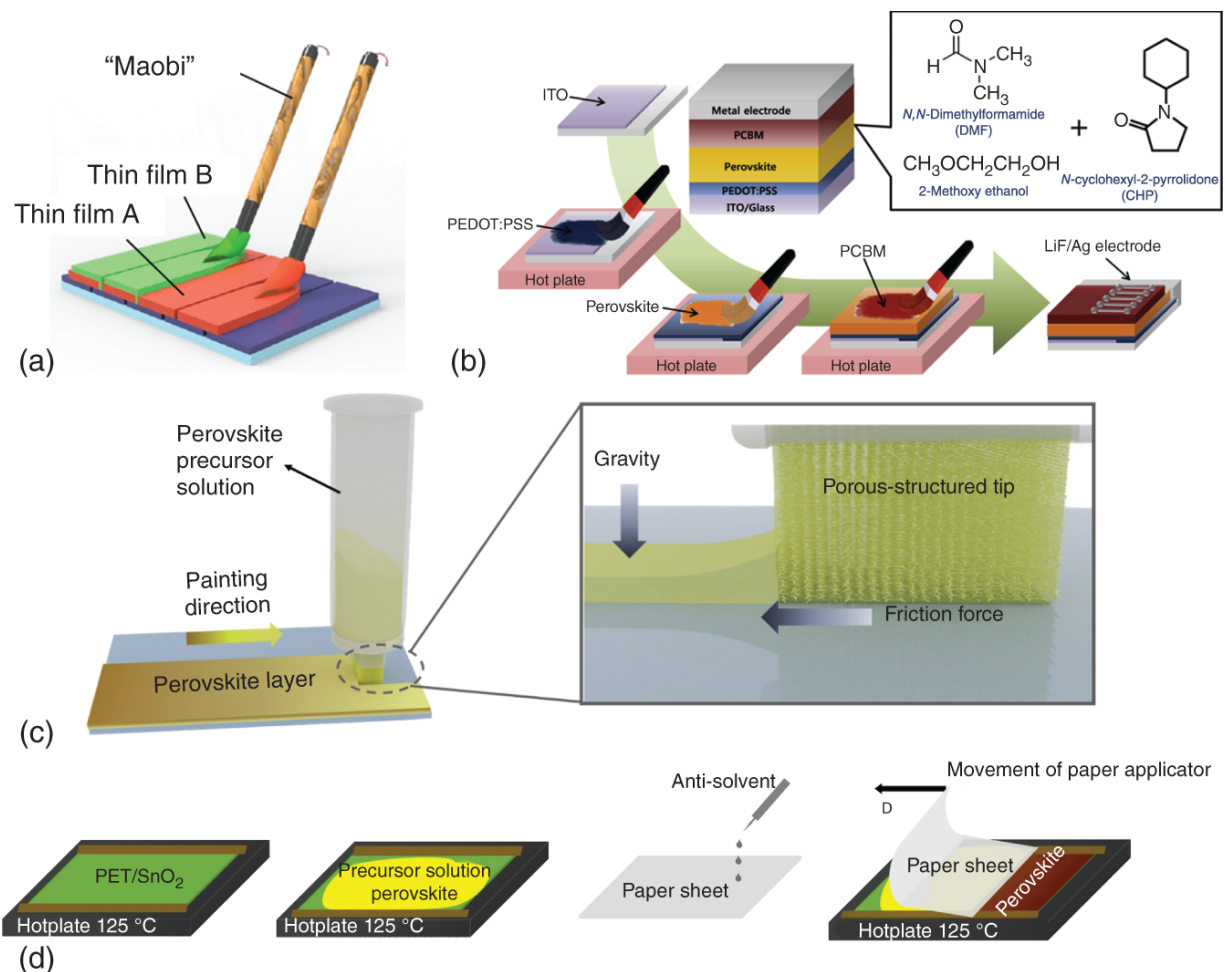
Figure 3.12 (a) Schematic diagram of brush painting by "Maobi." Source: Mao et al. [73] Reproduced with permission of Royal Society of Chemistry. (b) Schematic diagram of fully brush-painted PSCs. Source: Lee et al. [74]. Reproduced with permission of Elsevier. (c) Schematic diagram of brush painting by liquid chalk. Source: Zhu et al. [75]. Reproduced with permission of Elsevier. (d) Schematic diagram of brush painting by a sheet of paper. Source: Zarabinia et al. [76]/Elsevier/CC BY 4.0.

Besides "Maobi," a liquid chalk and a sheet of paper were also developed for brush painting. Zhu et al. demonstrated a liquid chalk, which had a cuboid made of polyester fibers as the tip of liquid chalk (Figure 3.12c) [75]. The porous

structure in a liquid chalk could hold solution steadily in it. Moreover, the large-scale and flat tip allowed liquid-chalk release solution onto the substrate uniformly. Recently, Zarabinia et al. used a sheet of paper as an antisolvent-soaked applicator for coating the perovskite films (Figure 3.12d) [76]. In this process, a precursor solution was first dropped on a preheated substrate. Then a sheet of paper, which was soaked in antisolvent, was pulled manually from one side to the other of the substrate with no additional pressure apart from that exerted by the weight of the paper applicator. The paper absorbed parts of precursor solutions and left a thin wet film at the trailing end of the paper. After the remaining solvent evaporated, a solid thin film was formed. The solvent-absorbing capacity of the paper affected the quality of perovskite films.

Brush painting has many technical advantages, such as ease of patterning, high material utilization ratio, processability on various substrates, and good compatibility with large-area production. However, the quality and thickness of a painted film are difficult to control accurately, so the brush painting is still hard to realize mass production on account of little storage of solution and small uniform area. In addition, although brush painting is an inexpensive method, these different brushes may not be reusable, thus raising the cost.

3.3 Conclusion and Outlook

In this chapter, present progresses of solution-based technologies are reviewed. Most solution-based technologies already have the ability to prepare large-area films and PSMs. Among them, spin coating could fabricate laboratory-scale PSMs with the best performance. Blade coating, slot-die coating, and bar coating could deposit >100 cm^2 perovskite films. Spray coating and CBD could

deposit $>100\,cm^2$ electron collection layers. Screen printing could deposit $3600\,cm^2$ triple mesoscopic scaffolds. Obviously, there is still a certain distance from the fabrication of industrial-scale PSMs. The good thing is that more and more researchers are focusing on large-scale fabrication and many companies have invested in building $>100\,MW$ mass production line for PSCs.

Although the industrialization of PSCs has a promising future, more work should be done to reduce performance degradation, improve the stability and reduce the cost of PSMs. Significantly, for solution-processed technologies, after depositing the wet films, the drying or annealing process play an essential role in controlling the morphology and obtaining high-quality dry films. Besides the drying temperature, atmosphere, vapor pressure et al., this process is also influenced by the compositions of the precursor, such as the solvents, and the crystal growth kinetics. Compared with obtaining uniform wet films, it is more complicated and challenging to obtain homogeneous and compact dry films. Notably, this process can be hardly tuned by adjusting the depositing parameters, which only affect the deposition of wet films, not the dry films. Thus, in the next step, besides developing more industrial-scale methods to deposit films for the fabrication of PSMs, a deeper understanding of the crystal growth kinetics and tuning strategies of perovskite are also required. In addition, the characteristics of the substrates, such as F-doped tin oxide (FTO) or indium tin oxide (ITO), have limited discussion, therefore, researchers commonly use commercially supplied standard materials. However, the morphology of substrates directs that of the deposited thin films [78]. A too-rough surface tends to lead to FTO spikes or pinholes into the absorbers and lower adhesion between functional layers, resulting in fast electron/hole recombination and lower efficiencies [78]. The FTO

roughness also affects the wettability of the deposited solution, thereby affecting the solid surface coverage and crystallinity [79]. It can be inferred that the effect of substrate roughness is greater for larger-area devices, so the substrate also needs to be studied.

References

1 Green, M.A., Dunlop, E.D., Hohl-Ebinger, J. et al. (2022). Solar cell efficiency tables (version 60). *Progress in Photovoltaics: Research and Applications* 30 (7): 687–701.

2 Wang, R., Mujahid, M., Duan, Y. et al. (2019). A review of perovskites solar cell stability. *Advanced Functional Materials* 29 (47): 1808843.

3 Li, Z., Klein, T.R., Kim, D.H. et al. (2018). Scalable fabrication of perovskite solar cells. *Nature Reviews Materials* 3 (4): 18017.

4 Rakocevic, L., Mundt, L.E., Gehlhaar, R. et al. (2019). Loss analysis in perovskite photovoltaic modules. *Solar RRL* 3 (12): 1900338–1900347.

5 Li, D., Zhang, D., Lim, K.-S. et al. (2020). A review on scaling up perovskite solar cells. *Advanced Functional Materials* 31 (12): 2008621–2008647.

6 Alberola-Borràs, J.-A., Baker, J.A., De Rossi, F. et al. (2018). Perovskite photovoltaic modules: life cycle assessment of pre-industrial production process. *iScience* 9: 542–551.

7 Ludin, N.A., Mustafa, N.I., Hanafiah, M.M. et al. (2018). Prospects of life cycle assessment of renewable energy

from solar photovoltaic technologies: a review. *Renewable & Sustainable Energy Reviews* 96: 11–28.

8 Soto-Montero, T., Soltanpoor, W., and Morales-Masis, M. (2020). Pressing challenges of halide perovskite thin film growth. *APL Materials* 8 (11): 110903.

9 Hamukwaya, S.L., Hao, H., Zhao, Z. et al. (2022). A review of recent developments in preparation methods for large-area perovskite solar cells. *Coatings* 12 (2): 252.

10 Ding, B., Huang, S.-Y., Chu, Q.-Q. et al. (2018). Low-temperature SnO_2-modified TiO_2 yields record efficiency for normal planar perovskite solar modules. *Journal of Materials Chemistry A* 6 (22): 10233–10242.

11 Yoo, J.J., Seo, G., Chua, M.R. et al. (2021). Efficient perovskite solar cells via improved carrier management. *Nature* 590 (7847): 587–593.

12 Mei, A., Li, X., Liu, L. et al. (2014). A hole-conductor–free, fully printable mesoscopic perovskite solar cell with high stability. *Science* 345 (6194): 295–298.

13 Rong, Y., Ming, Y., Ji, W. et al. (2018). Toward industrial-scale production of perovskite solar cells: screen printing, slot-die coating, and emerging techniques. *Journal of Physical Chemistry Letters* 9 (10): 2707–2713.

14 Bu, T., Liu, X., Li, J. et al. (2019). Dynamic antisolvent engineering for spin coating of $10 \times 10\ cm^2$ perovskite solar module approaching 18%. *Solar RRL* 4 (2): 1900263.

15 Wang, C., Tan, G., Luo, X. et al. (2020). How to fabricate efficient perovskite solar mini-modules in lab.

Journal of Power Sources 466: 228321.

16 Scriven, L.E. (1988). Physics and applications of DIP coating and spin coating. *MRS Proceedings* 121: 717.

17 Burschka, J., Pellet, N., Moon, S.-J. et al. (2013). Sequential deposition as a route to high-performance perovskite-sensitized solar cells. *Nature* 499 (7458): 316–319.

18 Li, X., Zhang, W., Guo, X. et al. (2022). Constructing heterojunctions by surface sulfidation for efficient inverted perovskite solar cells. *Science* 375 (6579): 434–437.

19 Min, H., Lee, D.Y., Kim, J. et al. (2021). Perovskite solar cells with atomically coherent interlayers on SnO_2 electrodes. *Nature* 598 (7881): 444–450.

20 Ye, F., Chen, H., Xie, F. et al. (2016). Soft-cover deposition of scaling-up uniform perovskite thin films for high cost-performance solar cells. *Energy & Environmental Science* 9 (7): 2295–2301.

21 Benitez-Rodriguez, J.F., Chen, D., Gao, M. et al. (2021). Roll-to-roll processes for the fabrication of perovskite solar cells under ambient conditions. *Solar RRL* 5 (9): 2100341.

22 Razza, S., Di Giacomo, F., Matteocci, F. et al. (2015). Perovskite solar cells and large area modules (100 cm^2) based on an air flow-assisted PbI_2 blade coating deposition process. *Journal of Power Sources* 277: 286–291.

23 Mallajosyula, A.T., Fernando, K., Bhatt, S. et al. (2016). Large-area hysteresis-free perovskite solar cells via

temperature controlled doctor blading under ambient environment. *Applied Materials Today* 3: 96–102.

24 Le Berre, M., Chen, Y., and Baigl, D. (2009). From convective assembly to Landau−Levich deposition of multilayered phospholipid films of controlled thickness. *Langmuir* 25 (5): 2554–2557.

25 Deng, Y., Zheng, X., Bai, Y. et al. (2018). Surfactant-controlled ink drying enables high-speed deposition of perovskite films for efficient photovoltaic modules. *Nature Energy* 3 (7): 560–566.

26 Kim, J.H., Williams, S.T., Cho, N. et al. (2015). Enhanced environmental stability of planar heterojunction perovskite solar cells based on blade-coating. *Advanced Energy Materials* 5 (4): 1401229.

27 Bu, T., Ono, L.K., Li, J. et al. (2022). Modulating crystal growth of formamidinium–caesium perovskites for over 200 cm^2 photovoltaic sub-modules. *Nature Energy* 7: 528–536.

28 Uddin, M.A., Rana, P.J.S., Ni, Z. et al. (2022). Blading of conformal electron transport layers in p-i-n perovskite solar cells. *Advanced Materials* 2202954.

29 Ding, X., Liu, J., and Harris, T.A.L. (2016). A review of the operating limits in slot die coating processes. *AIChE Journal* 62 (7): 2508–2524.

30 Burkitt, D., Patidar, R., Greenwood, P. et al. (2020). Roll-to-roll slot-die coated P–I–N perovskite solar cells using acetonitrile based single step perovskite solvent system. *Sustainable Energy & Fuels* 4 (7): 3340–3351.

31 Romero, O.J., Scriven, L.E., and Carvalho, M.S. (2006). Slot coating of mildly viscoelastic liquids. *Journal of Non-*

Newtonian Fluid Mechanics 138 (2): 63–75.

32 Bu, T., Li, J., Li, H. et al. (2021). Lead halide–templated crystallization of methylamine-free perovskite for efficient photovoltaic modules. *Science* 372 (6548): 1327–1332.

33 Khim, D., Han, H., Baeg, K.-J. et al. (2013). Simple bar-coating process for large-area, high-performance organic field-effect transistors and ambipolar complementary integrated circuits. *Advanced Materials* 25 (31): 4302–4308.

34 Mandati, S., Dileep, K.,.R., Veerappan, G. et al. (2022). Large area bar coated TiO_2 electron transport layers for perovskite solar cells with excellent performance homogeneity. *Solar Energy* 240: 258–268.

35 Yoo, J.W., Jang, J., Kim, U. et al. (2021). Efficient perovskite solar mini-modules fabricated via bar-coating using 2-methoxyethanol-based formamidinium lead tri-iodide precursor solution. *Joule* 5 (9): 2420–2436.

36 Liu, X., Xia, X., Cai, Q. et al. (2017). Efficient planar heterojunction perovskite solar cells with weak hysteresis fabricated via bar coating. *Solar Energy Materials and Solar Cells* 159: 412–417.

37 Lim, K.-S., Lee, D.-K., Lee, J.-W. et al. (2020). 17% efficient perovskite solar mini-module via hexamethylphosphoramide (HMPA)-adduct-based large-area D-bar coating. *Journal of Materials Chemistry A* 8 (18): 9345–9354.

38 Swartwout, R., Hoerantner, M.T., and Bulović, V. (2019). Scalable deposition methods for large-area

production of perovskite thin films. *Energy & Environmental Materials* 2 (2): 119–145.

39 Park, M., Cho, W., Lee, G. et al. (2019). Highly reproducible large-area perovskite solar cell fabrication via continuous megasonic spray coating of $CH_3NH_3PbI_3$. *Small* 15 (1): 1804005.

40 Bishop, J.E., Smith, J.A., and Lidzey, D.G. (2020). Development of spray-coated perovskite solar cells. *ACS Applied Materials & Interfaces* 12 (43): 48237–48245.

41 Tsai, S.C., Song, Y.L., Tsai, C.S. et al. (2004). Ultrasonic spray pyrolysis for nanoparticles synthesis. *Journal of Materials Science* 39 (11): 3647–3657.

42 Heo, J.H., Zhang, F., Xiao, C. et al. (2021). Efficient and stable graded $CsPbI_3-xBrx$ perovskite solar cells and submodules by orthogonal processable spray coating. *Joule* 5 (2): 481–494.

43 Paik, M.J., Lee, Y., Yun, H.-S. et al. (2020). TiO_2 colloid-spray coated electron-transporting layers for efficient perovskite solar cells. *Advanced Energy Materials* 10 (39): 2001799.

44 Taheri, B., Calabrò, E., Matteocci, F. et al. (2020). Automated scalable spray coating of SnO_2 for the fabrication of low-temperature perovskite solar cells and modules. *Energy Technology* 8 (5): 1901284.

45 Scheideler, W.J., Rolston, N., Zhao, O. et al. (2019). Rapid aqueous spray fabrication of robust NiO_x: a simple and scalable platform for efficient perovskite solar cells. *Advanced Energy Materials* 9 (19): 1803600.

46 Bishop, J.E., Read, C.D., Smith, J.A. et al. (2020). Fully spray-coated triple-cation perovskite solar cells. *Scientific Reports* 10 (1): 6610.

47 Karunakaran, S.K., Arumugam, G.M., Yang, W. et al. (2019). Recent progress in inkjet-printed solar cells. *Journal of Materials Chemistry A* 7 (23): 13873–13902.

48 Zhang, L., Chen, S., Wang, X. et al. (2021). Ambient inkjet-printed high-efficiency perovskite solar cells: manipulating the spreading and crystallization behaviors of picoliter perovskite droplets. *Solar RRL* 5 (5): 2100106.

49 Verma, A., Martineau, D., Abdolhosseinzadeh, S. et al. (2020). Inkjet printed mesoscopic perovskite solar cells with custom design capability. *Materials Advances* 1 (2): 153–160.

50 Schackmar, F., Eggers, H., Frericks, M. et al. (2021). Perovskite solar cells with all-inkjet-printed absorber and charge transport layers. *Advanced Materials Technologies* 6 (2): 2000271.

51 Pendyala, N.K., Magdassi, S., and Etgar, L. (2021). Fabrication of perovskite solar cells with digital control of transparency by inkjet printing. *ACS Applied Materials & Interfaces* 13 (26): 30524–30532.

52 Li, Z., Li, P., Chen, G. et al. (2020). Ink engineering of inkjet printing perovskite. *ACS Applied Materials & Interfaces* 12 (35): 39082–39091.

53 Liang, C., Li, P., Gu, H. et al. (2018). One-step inkjet printed perovskite in air for efficient light harvesting. *Solar RRL* 2 (2): 1700217.

54 Rong, Y., Li, X., Ku, Z. et al. (2012). Monolithic all-solid-state dye-sensitized solar module based on mesoscopic carbon counter electrodes. *Solar Energy Materials and Solar Cells* 105: 148–152.

55 Hinsch, A., Veurman, W., Brandt, H. et al. (2012). Worldwide first fully up-scaled fabrication of 60×100 cm^2 dye solar module prototypes. *Progress in Photovoltaics: Research and Applications* 20 (6): 698–710.

56 Xu, M., Ji, W., Sheng, Y. et al. (2020). Efficient triple-mesoscopic perovskite solar mini-modules fabricated with slot-die coating. *Nano Energy* 74 (2020): 104842.

57 Hu, Y., Si, S., Mei, A. et al. (2017). Stable large-area (10 $\times 10\,cm^2$) printable mesoscopic perovskite module exceeding 10% efficiency. *Solar RRL* 1 (2): 1600019–1600024.

58 Rong, Y., Hu, Y., Mei, A. et al. (2018). Challenges for commercializing perovskite solar cells. *Science* 361 (6408): eaat8235.

59 Zhao, J.J., Wang, P., Liu, Z.H. et al. (2015). Controlled reaction for improved $CH_3NH_3PbI_3$ transition in perovskite solar cells. *Dalton Transactions* 44 (40): 17841–17849.

60 Cota-Leal, M., García-Valenzuela, J.A., Cabrera-German, D. et al. (2019). Synthesis of $CH_3NH_3PbI_3$–xClx perovskite by the three-step route consisting of chemical solution deposition followed by gas–solid reaction transformations: film quality and photodetector performance evaluation. *Organic Electronics* 73: 76–86.

61 Tong, G., Ono, L.K., Liu, Y. et al. (2021). Up-scalable fabrication of SnO_2 with multifunctional interface for high performance perovskite solar modules. *Nano-Micro Letters* 13 (1): 155.

62 Leyden, M.R., Jiang, Y., and Qi, Y. (2016). Chemical vapor deposition grown formamidinium perovskite solar modules with high steady state power and thermal stability. *Journal of Materials Chemistry A* 4 (34): 13125–13132.

63 Ummadisingu, A. and Grätzel, M. (2018). Revealing the detailed path of sequential deposition for metal halide perovskite formation. *Science Advances* 4 (2): e1701402.

64 Yaghoobi Nia, N., Zendehdel, M., Cinà, L. et al. (2018). A crystal engineering approach for scalable perovskite solar cells and module fabrication: a full out of glove box procedure. *Journal of Materials Chemistry A* 6 (2): 659–671.

65 Gozalzadeh, S., Nasirpouri, F., and Seok, S.I. (2021). Towards environmental friendly multi-step processing of efficient mixed-cation mixed halide perovskite solar cells from chemically bath deposited lead sulphide. *Scientific Reports* 11 (1): 18561.

66 Sun, J., Lu, J., Li, B. et al. (2018). Inverted perovskite solar cells with high fill-factors featuring chemical bath deposited mesoporous NiO hole transporting layers. *Nano Energy* 49 (2018): 163–171.

67 Calnan, S. (2014). Applications of oxide coatings in photovoltaic devices. *Coatings* 4 (1).

68 Kim, S., Yun, Y.J., Kim, T. et al. (2021). Hydrolysis-regulated chemical bath deposition of tin-oxide-based

electron transport layers for efficient perovskite solar cells with a reduced potential loss. *Chemistry of Materials* 33 (21): 8194–8204.

69 Tian, S., Li, J., Li, S. et al. (2019). A facile green solvent engineering for up-scaling perovskite solar cell modules. *Solar Energy* 183: 386–391.

70 Chen, H., Ye, F., Tang, W. et al. (2017). A solvent- and vacuum-free route to large-area perovskite films for efficient solar modules. *Nature* 550: 92.

71 Ye, F., Tang, W., Xie, F. et al. (2017). Low-temperature soft-cover deposition of uniform large-scale perovskite films for high-performance solar cells. *Advanced Materials* 29 (35): 1701440.

72 He, J., Bi, E., Tang, W. et al. (2018). Low-temperature soft-cover-assisted hydrolysis deposition of large-scale TiO_2 layer for efficient perovskite solar modules. *Nano-Micro Letters* 10 (3): 49.

73 Mao, L., Luo, B., Sun, L. et al. (2018). Writable and patternable organic solar cells and modules inspired by an old Chinese calligraphy tradition. *Materials Horizons* 5 (1): 123–130.

74 Lee, J.-W., Na, S.-I., and Kim, S.-S. (2017). Efficient spin-coating-free planar heterojunction perovskite solar cells fabricated with successive brush-painting. *Journal of Power Sources* 339: 33–40.

75 Zhu, J.-Y., Lou, Y.-H., Li, M. et al. (2019). Liquid-chalk painted perovskite films toward low-cost photovoltaic devices. *Organic Electronics* 75: 105371.

76 Zarabinia, N., Lucarelli, G., Rasuli, R. et al. (2022). Simple and effective deposition method for solar cell

perovskite films using a sheet of paper. *iScience* 25 (2): 103712.

77 Bico, J., Roman, B., Moulin, L. et al. (2004). Elastocapillary coalescence in wet hair. *Nature* 432 (7018): 690–690.

78 Yates, H.M., Afzaal, M., Walter, A. et al. (2016). Progression towards high efficiency perovskite solar cells via optimisation of the front electrode and blocking layer. *Journal of Materials Chemistry C* 4 (47): 11269–11277.

79 Chen, P., Wang, Y., Wang, M. et al. (2015). TiO_2 nanoparticle-based electron transport layer with improved wettability for efficient planar-heterojunction perovskite solar cell. *Journal of Energy Chemistry* 24 (6): 717–721.

4
Mesoscopic Anodes and Cathodes for Printable Perovskite Solar Cells

Seigo Ito and Ryuki Tsuji
University of Hyogo, Graduate School of Engineering, Department of Materials and Synchrotron Radiation Engineering, 2167 Shosha, Himeji, Hyogo, 671-2280, Japan

4.1 Introduction

Commercialization of photovoltaic module requires three characteristics, which are "high stability," "low cost," and "high efficiency." Thin-film-type organo-lead halide perovskite solar cells (PSCs) recorded a high photoenergy conversion efficiency (*Eff*) of over 25% [1, 2]. However, expensive Au back contacts have been utilized for normal PSCs. Hence, it should be replaced with cost-effective materials, which would be carbon ink printed on perovskite-crystal layer, as a fully printed PSC (over 16% *Eff*) [3]. Moreover, Au must be coated by vacuum deposition, which can also rise up the processing cost. And Au can dissolve into perovskite, resulting in low stability [4]. Regarding the stability, scientists have improved it to pass the industrial standard tests (durability at 85 °C and 85%RH) [5]. For the real commercialization and 25 years guarantee of photovoltaic modules, industrial companies have adopted much through durability tests on solar cells (e.g. over 100 °C test, in private communication). For the outer-space application on satellite and space ship, the stability test has been performed at 120 °C (in conference information from JAXA). Hence, more severe tests are quite important for the commercialization of solar modules.

As such ultra-durable PSCs, multiporous-layered-electrode perovskite solar cells (MPLE-PSCs) have been investigated by the group of Hongwei Han (Huazhong University of Science and Technology: HUST) [6, 7] (illustrated in Figure 4.1a,c). Afterward, NiO-cathode MPLE-PSC has been introduced by the group of Mingkui Wang (Figure 4.1b,d) [8]. The super stability of MPLE-PSC has been confirmed with 1100 hours at 85 °C and 85%RH [9], 4500 hours stability at 100 °C [10], and 10 000 hours stability at 60 °C [11]. However, the highest photoenergy conversion efficiency of MPLE-

PSC is just 16–17% [8, 12, 13]. Hence, the studies of MPLE-PSC to improve the *Eff* are quite important due to the ultrahigh stability and the low cost for the real commercialization. Of course, the photoenergy conversion efficiency should be improved by over 20% in the near future. At present, without NiO HTM, the photovoltaic characteristics of the best MPLE-PSC are 17.01% of *Eff*, $23.9\,\mathrm{mA\,cm^{-2}}$ of J_{sc}, 981 mV of V_{oc}, and 0.73 of *FF* [13]. With NiO HTM, the photovoltaic characteristics were 17.02% of *Eff*, $23.40\,\mathrm{mA\,cm^{-2}}$ of J_{sc}, 1008 mV of V_{oc}, and 0.72 of *FF* [8].
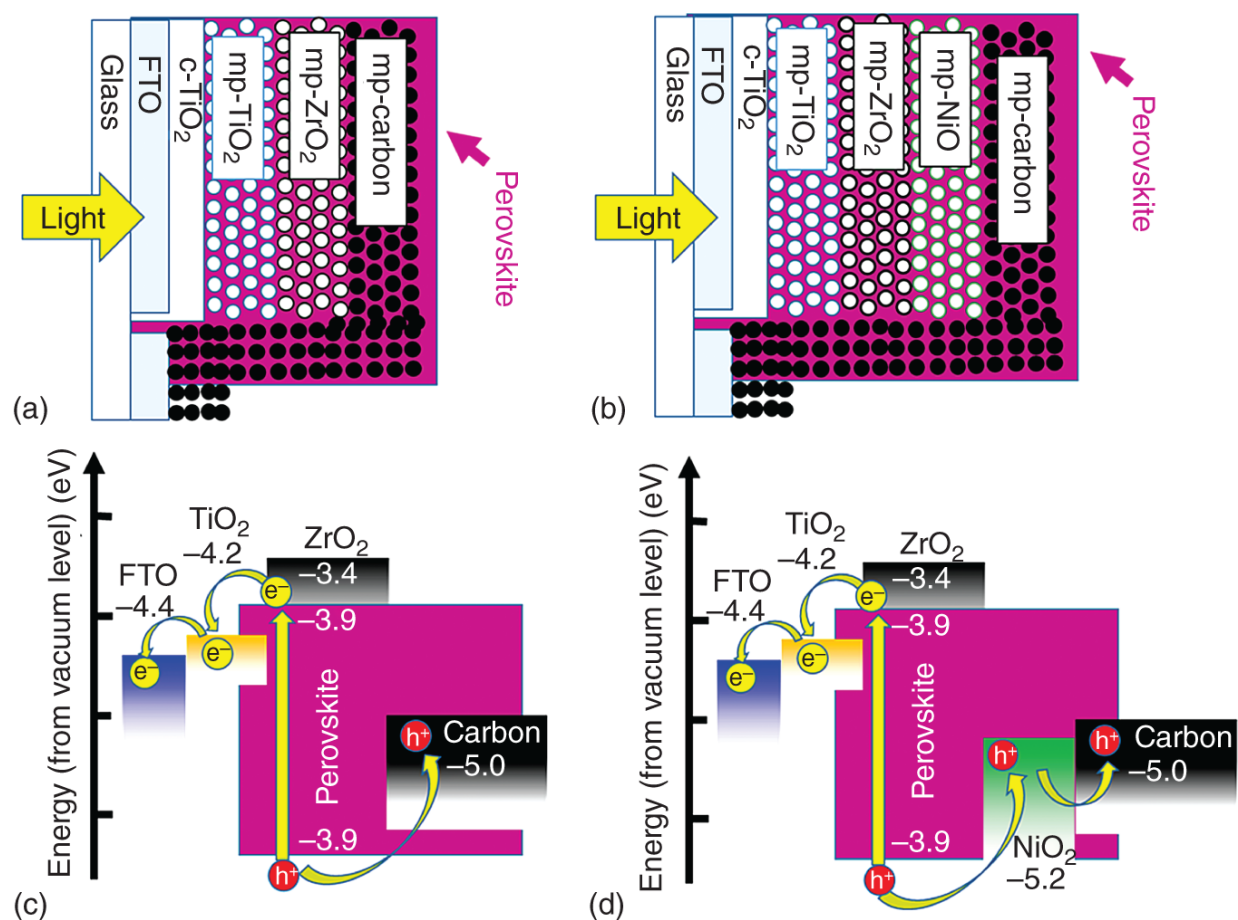
Figure 4.1 Cross-sectional illustration of multi-porous-layered electrodes perovskite solar cells (MPLE-PSC) with (a) and without (b) porous hole conducting layer, and the energy diagram with (c) and without (d) porous hole conducting layer.

In this chapter, the information of anode and cathode materials in MPLE is explained (Figure 4.1). The anode has been n-type semiconductor, TiO_2 (in our knowledge, we couldn't find another material in publication). The cathodes are carbon (Figure 4.1c) or p-

type semiconductors (NiO and so on) ([Figure 4.1d](#)). At first, the fabrication methods are illustrated, and the information of each material is described. The detailed information of spacer layer <mesoporous-ZrO_2 (shown in [Figure 4.1](#) as, "mp-ZrO_2")>, which can be replaced with Al_2O_3, will be described in another chapter.

4.2 Fabrication Methods

[Figure 4.2](#) illustrates the fabrication scheme of MPLE-PSC. The electrode is composed of <glass/fluorine-doped tin oxide (written as, "FTO")> substrate, <compact TiO_2 (written as "c-TiO_2")> layer, <mesoporous TiO_2 (written as "mp-TiO_2")> layer, <mesoporous TiO_2 (written as "mp-TiO_2")> layer, <mp-ZrO_2> layer, and <mesoporous carbon (written as, "mp-carbon)> layer. The <glass/FTO> can be purchased from Glass Company (Nippon Sheet Glass Co. Ltd. [Pilkington Group Limited], etc.). The <c-TiO_2>can be prepared by spray-pyrolysis deposition (SPD), basically. But, ALD, CBD, CVD, and spin coating may work for it. The mesoporous layers have been fabricated by screen printing and annealing. As a typical method to fabricate mesoporous layers, the mesoporous TiO_2 layer ($\approx$800 nm) was screen printed onto the compact TiO_2 layer and sintered at 773 K for 40 minutes (TiO_2 paste (30NR-T) was purchased from Greatcell Solar (Australia) and dispersed in terpineol with a weight ratio of 1: 4.5). And then, the ZrO_2 layer ($\approx$2.5 µm) and the carbon electrode layer ($\approx$10 µm) were subsequently screen printed on the mesoporous TiO_2 layer and sintered at 673 K for 40 minutes (ZrO_2 paste and carbon paste were purchased from WonderSolar Co. Ltd.) [13]. Perovskite crystal is inserted in the mesoporous layers by drip-casting of the precursor solution and annealing.
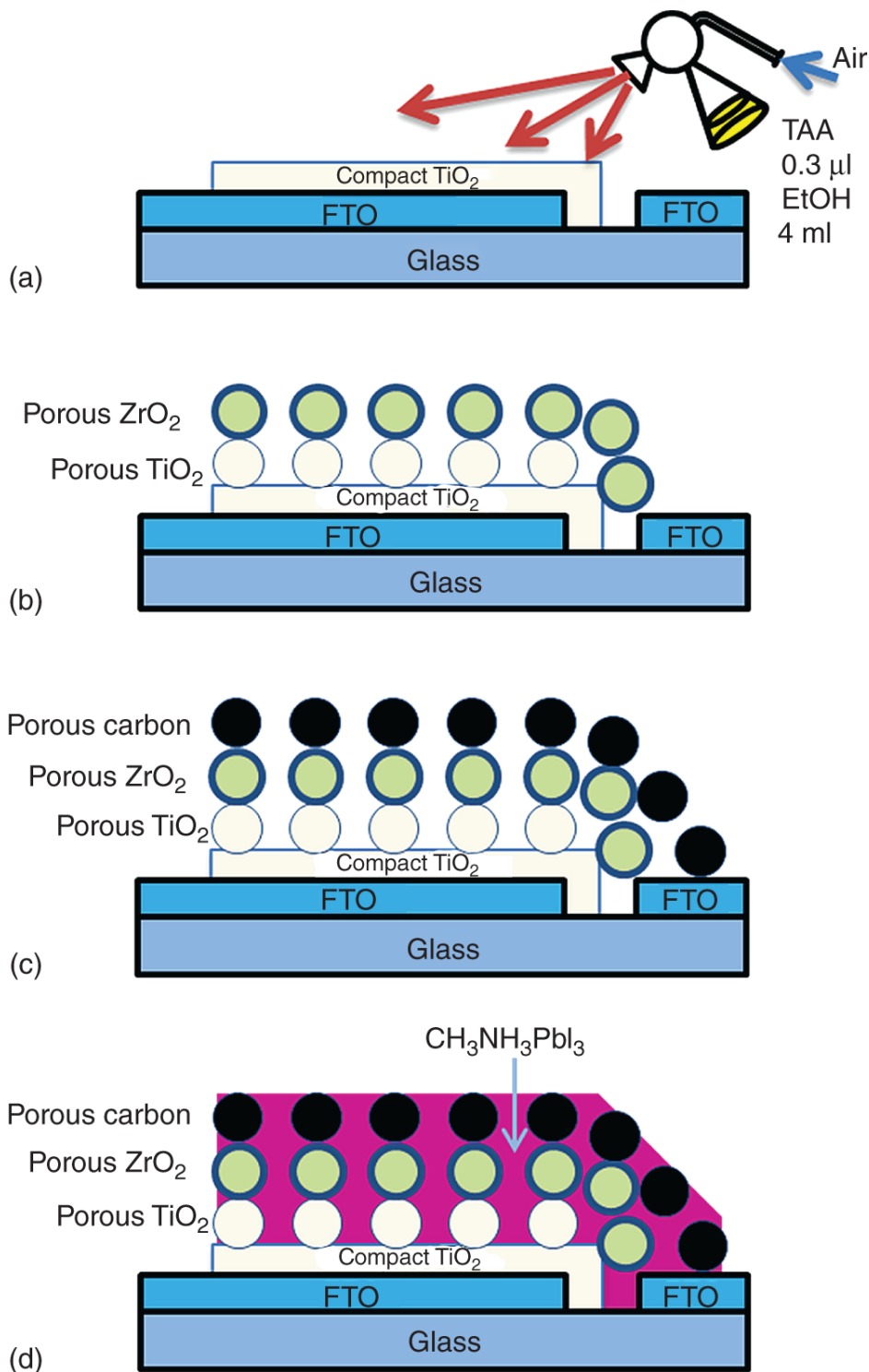
Figure 4.2 Fabrication scheme of multi-porous-layered electrodes perovskite solar cells (MPLE-PSC); (a) coating of compact n-type layer; (b) coating of mesoporous n-type layer and coating of mesoporous insulating spacer layer; (c) coating of mesoporous carbon back-contact layer; and (d) coating of perovskite.
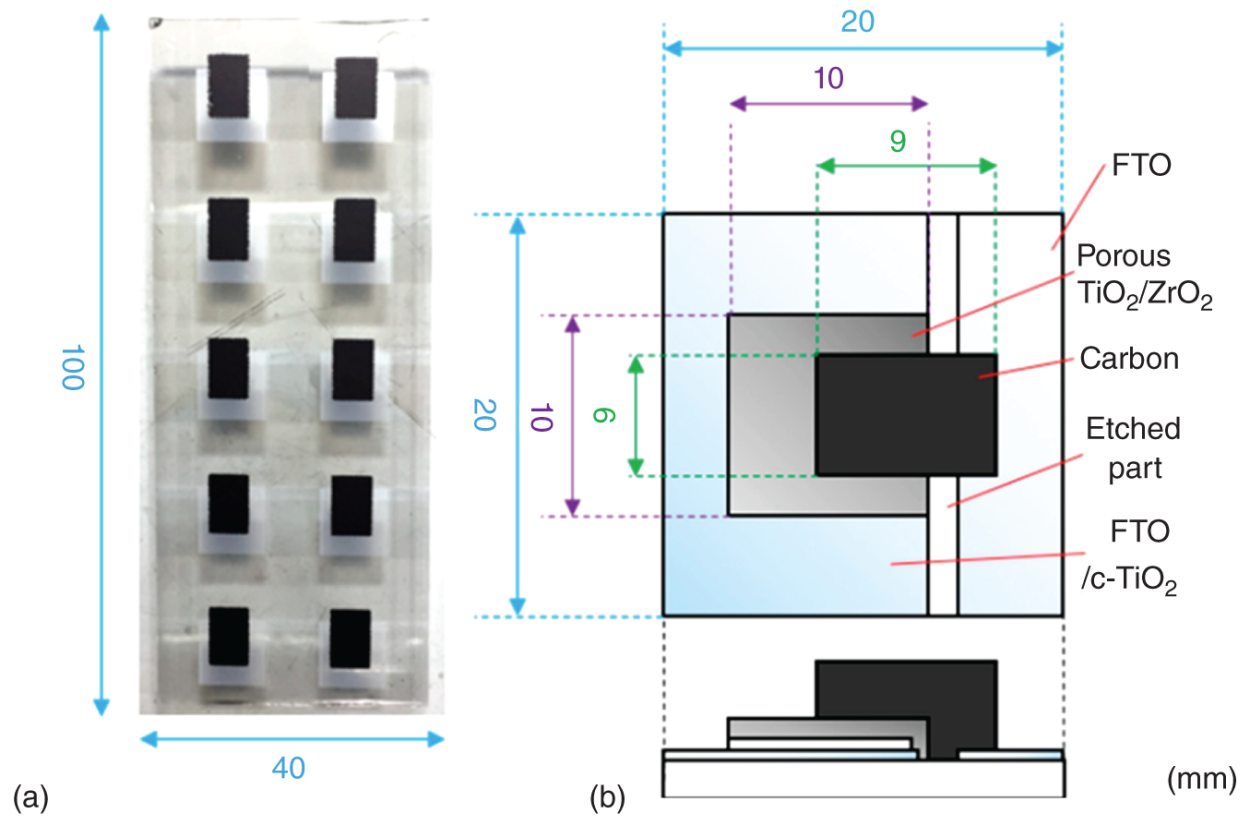
Figure 4.3 Structure of laboratory cells; (a) a single MPLE; (b) MPLEs on a substrate, which can be cut into 10 single cells. Source: Tsuji et al. [14], MDPI, CC BY 4.0.

Figure 4.3a shows a lab-scale MPLE, which can be cut out from a substrate (Figure 4.3b) to be 10 single MPLE [14]. For the fabrication of MPLE, the FTO layer has to be etched by chemical reduction or a laser scriber. The chemical-reductive etching can be performed by putting zinc powder on aimed FTO area, dripping 10% HCl aqueous solution, and scribing by a cotton bar. The aimed FTO area can be regulated by sealing material such as adhesive tape. This small cell is for research works in laboratory. For the outdoor application, large photovoltaic panels are necessary. Figure 4.4 is a screen-printing design example of MPLE-PSC sub-module for University's laboratory and/or student demonstration. Due to the cell separation by chemical etching and screen printing, the cell gap is 3-mm wide, which is too large for the real application. For real applications, the cell can be separated by laser scribing, resulting in 0.4-mm wide separation [15]. In the next section, the fabrication schemes of each layer are described one by one.

4.3 Comact Layer (TiO$_2$)

In order to prevent the hole carrier flow from perovskite crystal to FTO layer, a compact anode TiO$_2$ layer (called as "c-TiO$_2$," "blocking TiO$_2$ layer," "TiO$_2$ under layer," etc.) should be coated on FTO (Figure 4.1). Mostly, it has been prepared by SPD, but can be fabricated by spin coating [16], chemical bath deposition [17], and atomic layer deposition (ALD) [18]. Although the basic material has been TiO$_2$ for the MPLE-PSC, SnO$_2$ also can work for the compact layer with 13.77% of photoenergy conversion efficiency [19]. In order to improve the conductivity, Nb^{5+}-doped SnO$_2$ and zinc tin oxide (ZTO) have been utilized to be 13.5% and 15.86% of *Eff*, respectively [20, 21].
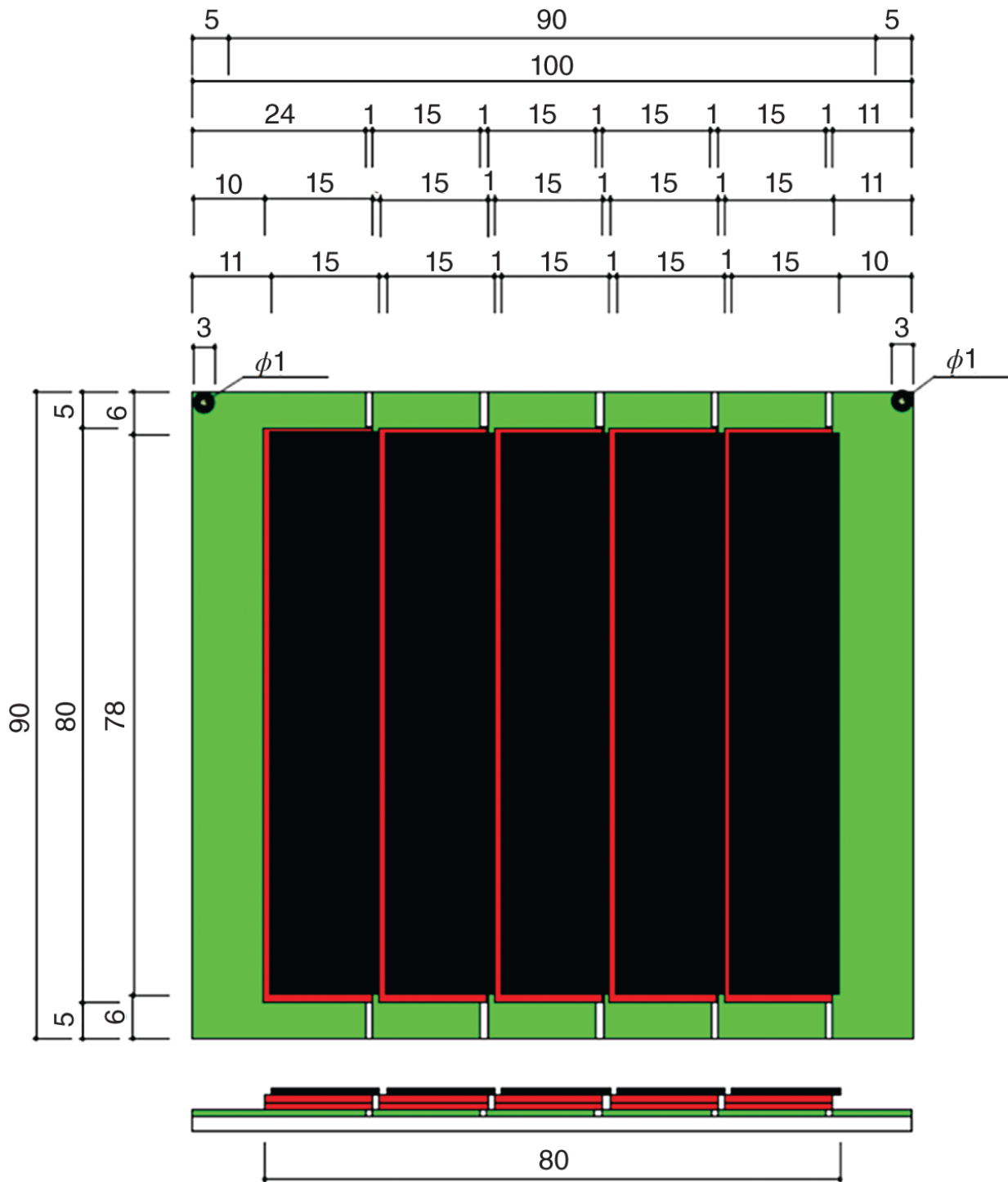
Figure 4.4 Screen-printing design example of MPLE-PSC submodules for university laboratory and/or student demonstration (the number of unit is "mm.").

Figure 4.5 shows the schematic image of SPD for the compact TiO$_2$ layer. The FTO substrate should be set at hot temperature of 350–

550 °C. The temperature should be set higher than the pyrolysis reaction temperature of source material (c. 300 °C) (titanium isopropoxide acetylacetonate [TAA] for c-TiO_2) but lower than the deterioration temperature of FTO conductivity (c. 600 °C). Basically, it can be around 450 °C. The typical SPD source solution has been TAA in ethanol, which can be splayed on the hot FTO substrates using atomizer as mist (small droplet) (Figures 4.2a and 4.5a). Near the substrate, the solvent (ethanol) in small droplets can be evaporated, and the solution in droplet can be denser (Figure 4.5b). If the substrate temperature is quite high, all of the solvent can be evaporated and the droplet can't reach to the FTO surface for SPD. When the droplet can attach to FTO surface, the solvent (ethanol) can evaporate, explosively (Figure 4.5c). The TAA can be remained on the hot FTO substrate and react with oxygen in the air (Figure 4.5d), resulting in the TiO_2 layer (Figure 4.5e). If the temperature is too low, the amount of ethanol can be large and the FTO temperature can't be high enough for the oxidative pyrolysis reaction, resulting in the not smooth TiO_2 layer.
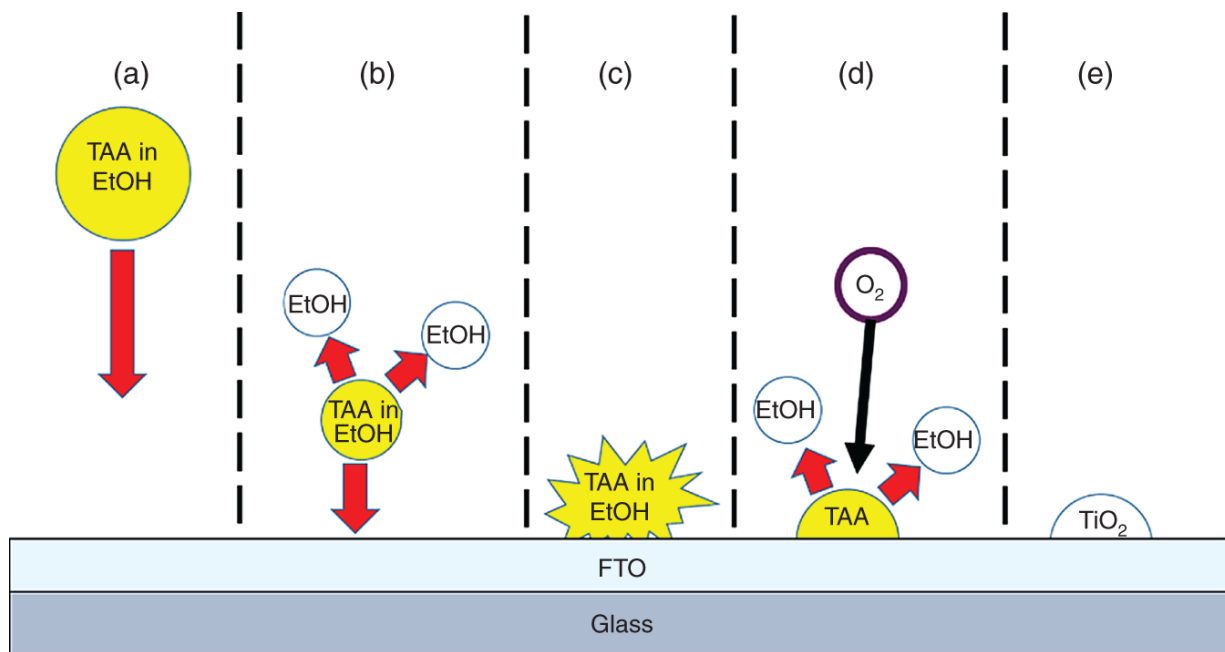
Figure 4.5 Schematic image of spray-pyrolysis deposition of compact TiO_2 layer: (a) splayed droplet of TAA in ethanol approaching the hot substrates; (b) evaporation of solvent from the droplet; (c) explosive evaporate; (d) reaction with oxygen; and (e) formation of TiO_2.
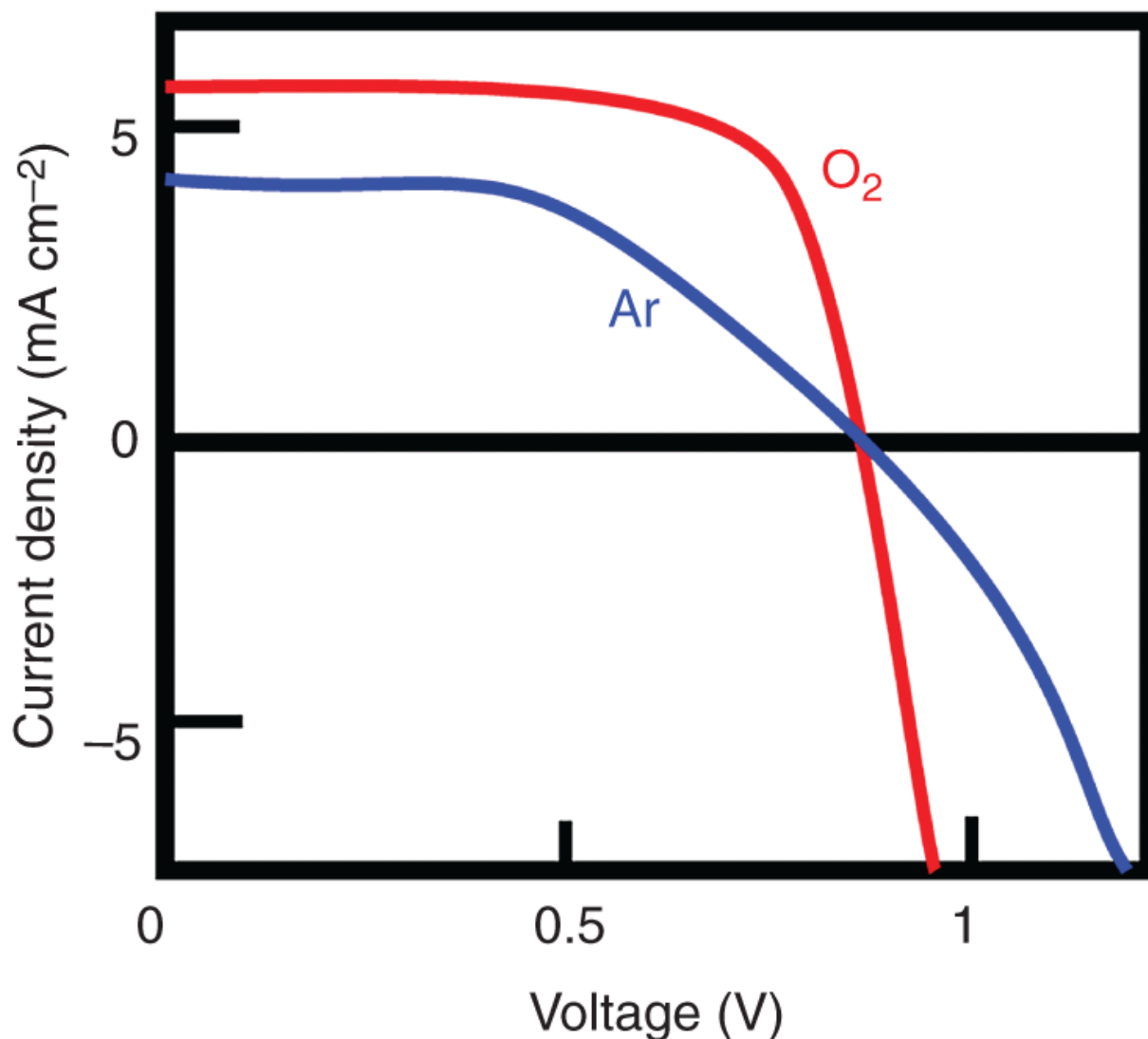
Figure 4.6 Photocurrent density–voltage (J–V) curves of solid-state dye-sensitized solar cells using different deposition atmosphere for c-TiO_2. Source: Adapted from Snaith and Grätzel [22].

The carrier gas should be air or oxygen gas in order to remove the carbon contamination and the defects in c-TiO_2 layer. If it may be deposited using argon or nitrogen, the c-TiO_2 layer will have significant defects in it and will deteriorate the photovoltaic performance [22] (as Figure 4.6).

4.4 Mesoporous Anodes (n-Type Semiconductor: TiO$_2$, etc.)

In order to fabricate the mesoporous anodes, we have to prepare the aiming screen-printing paste. We can buy the screen-printing anatase-TiO$_2$ paste from companies specialized for PSCs (Solaronix SA (Switzerland) and Greatcell Solar (Australia)). They can provide several types of screen-printing anatase-TiO$_2$ pastes, and we have to select the material based on the research works. In order to control the thickness of mesoporous anode, we have to change the screen-printing mesh and dilute the screen-printing anatase-TiO$_2$ paste by adding solvent (α-terpineol) to be the aiming thickness.

We have to think about the particle size to control the physical phenomena, listed in Figure 4.7a [23]. The physical phenomena of mesoporous TiO$_2$ layer such as "pore size (geometry)" and "light diffraction and penetration (photonics)" can be changed by variation of the TiO$_2$ particle size.

Effects	Particle size	Large	>	Small
Geometry	Pore size	Large	>	Small
Photonics	Light diffraction	Large	>	Small
	Light transmission	Small	<	Large

(a)

(b) Pore size (R_p) (nm)

(c) Wavelength (nm)
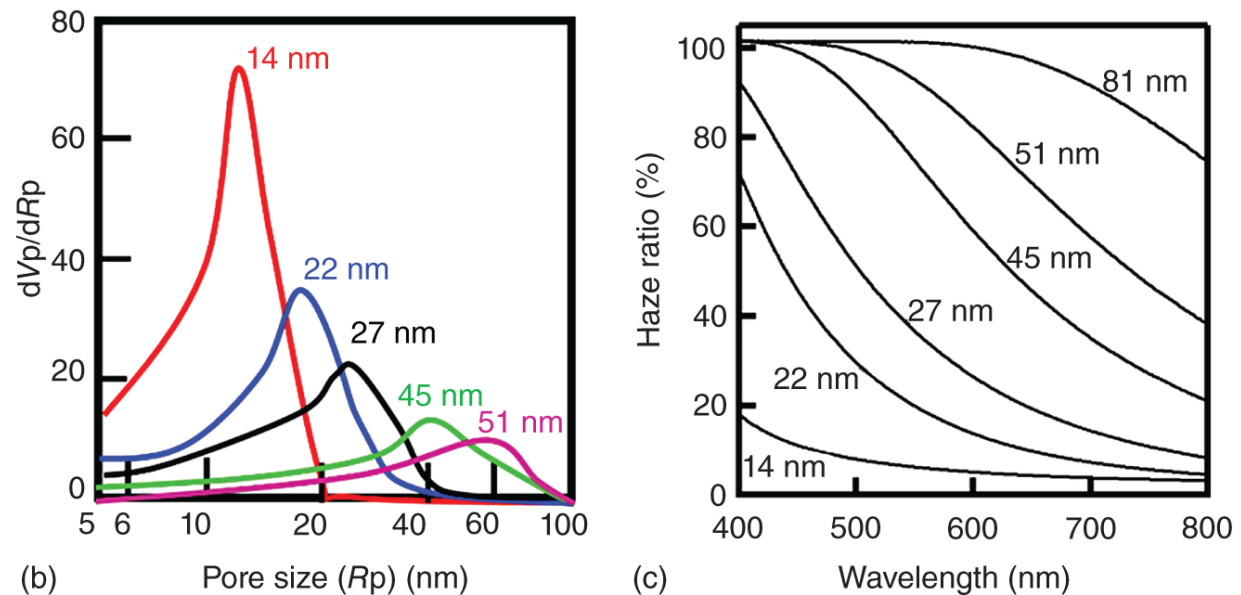
Figure 4.7 (a) Photonic–electronic-materials effects of anode particle size on photovoltaics of multi-porous-layered-electrodes perovskite solar cells (MPLE-PSCs); (b) variation of porosity with different particle-sized TiO$_2$ anode layer; and (c) variation of optical diffusion with different particle-sized TiO$_2$ anode layer. The numbers (nm) show the TiO$_2$ particle sizes. Source: Adapted from Ito et al. [23].

Figure 4.7b shows the relationship between TiO$_2$ particle size (from 14 to 54 nm) and the mesoscopic geometry (pore size and volume) [23]. It can be noticed that the pore diameter projects the particle size. It looks that the smaller TiO$_2$ nanoparticle has larger pore volume, but the volume ratio of pores can be calculated by the integration of the multiplied value of x-axis (pore size [R_p]/nm) and y-axis (dV_p/dR_p), resulting in the similar value. The pore volume can be related to the amount of organic binder (ethyl cellulose), resulting in 40–80%. The pore size can also be changed with the amount of organic binder [24].

The photonics in a nanocrystalline-TiO_2 electrode, the light diffraction and the light transmission (penetration), are dominated by the Mie-scattering theory, which follows the photonics law that the effective light diffraction can occur in particles that are half the size of the incident wavelength [25]. Figure 4.7c shows the haze (light-scattering) ratios of the mesoporous-TiO_2 layers with different particle sizes [23]. It can be noticed that the layer using larger particles scatters visible light effectively but can pass longer wavelength light (in the red region). Contrary, the layer using smaller particles can pass visible light effectively, but shorter wavelength light (in the blue region) is scattered.

For the optimization of TiO_2 nanoparticles, we have to synthesize them to change the particle size. There are two ways for the TiO_2 synthesis, acidic and basic routes, shown in Figures 4.8 and 4.9, respectively. The particle size of acidic route can be 15–20 nm with round shape [26]. Contrary, the particle size of basic route can be ca. 30 nm with angular shape [27]. If you can get TiO_2 powders in several sizes, you can prepare the TiO_2 paste using the powders using mortar, ultrasonic horn, and evaporator (Figure 4.10) [28].

In order to improve the photoenergy conversion efficiency further, another new material to replace mesoporous TiO_2 should be considered. In our knowledge, however, no other material has been published for MPLE-PSC. For the flexible thin-film PSCs by spin-coating and low-temperature processing, Zn_2SnO_4 anode has been utilized with 14.85% of *Eff* [29]. The Zn_2SnO_4 nanoparticles can be synthesized under low temperature at 90 °C. However, it needs hydrazine, which is quite toxic material and should be very much careful for the health of researchers and students.

```
┌─────────────────────────────────────────────────────────────────────┐
│ White precipitation by hydrolysis of Ti(OCH(CH₃)₂)₄ with acetic acid  │
└─────────────────────────────────────────────────────────────────────┘
                                    ↓
┌─────────────────────────────────────────────────────────────────────────┐
│ Semi transparent colloidal solution by poetization at 80°C for 8 h with HNO₃ │
└─────────────────────────────────────────────────────────────────────────┘
                                    ↓
┌───────────────────────────────────────────────────────────────────┐
│ Crystallization by hydrothermal autoclaving at 250°C for 12 h       │
└───────────────────────────────────────────────────────────────────┘
                                    ↓
┌───────────────────────────────────────────────────────────────────────┐
│ Sonication using 200 W ultrasonic horn by 15 times (2 s work and 2 s rest) │
└───────────────────────────────────────────────────────────────────────┘
                                    ↓
┌─────────────────────────────────────────────────────────────────────┐
│ Exchange of the solvent water to ethanol by centrifugation (3 times)  │
└─────────────────────────────────────────────────────────────────────┘
                                    ↓
┌───────────────────────────────────────────────────────────────────────┐
│ Addition of terpineol and ethyl cellulose (10% solution in ethanol) and │
│ dispersion by sonication and stirring with a magnet tip.                │
└───────────────────────────────────────────────────────────────────────┘
                                    ↓
┌───────────────────────────────────────────────────────┐
│ Evaporate the ethanol with a rotary evaporator          │
└───────────────────────────────────────────────────────┘
```
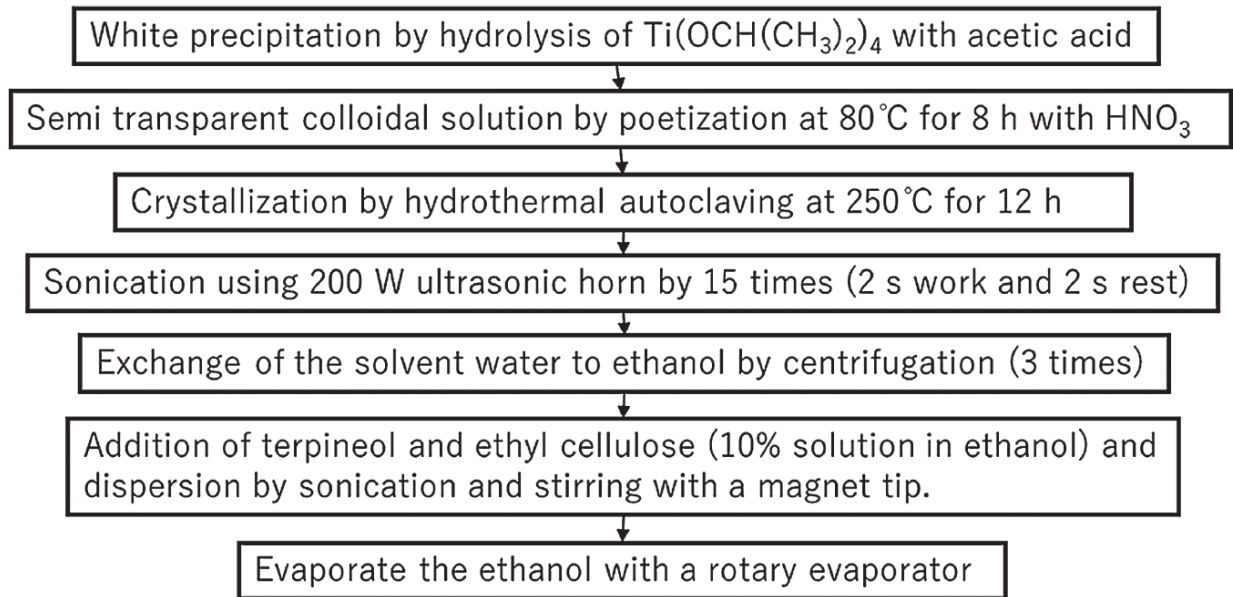
Figure 4.8 Acidic-route synthesis scheme of nano-TiO_2 colloid (d = c. 18 nm) for mesoporous TiO_2 layer. Source: Adapted from Ito et al. [26].

titanium(IV) isopropoxide (162 ml/0.5 mol) was rapidly added to distilled water (290 ml/15.5 mol), stirred for 1 h, filtered using a glass frit, and washed three times with 50 ml distilled water.

The resulting filter cake was added to a Teflon-lined titanium autoclave containing 30 ml of 0.6 M tetramethylammonium hydroxide (Fluka) to form a white slurry with a pH of 13.

Peptization in the presence of tetramethylammonium hydroxide occurred after heating the product at 100 °C for 6 h.

Crystallization by hydrothermal autoclaving at temperatures around 240 °C for 4.5 h, resulting in pH 13.5.

Sonication using 200 W ultrasonic horn by 15 times (2 s work and 2 s rest)

Exchange of the solvent water to ethanol by centrifugation (3 times)

Addition of terpineol and ethyl cellulose (10% solution in ethanol) and dispersion by sonication and stirring with a magnet tip.

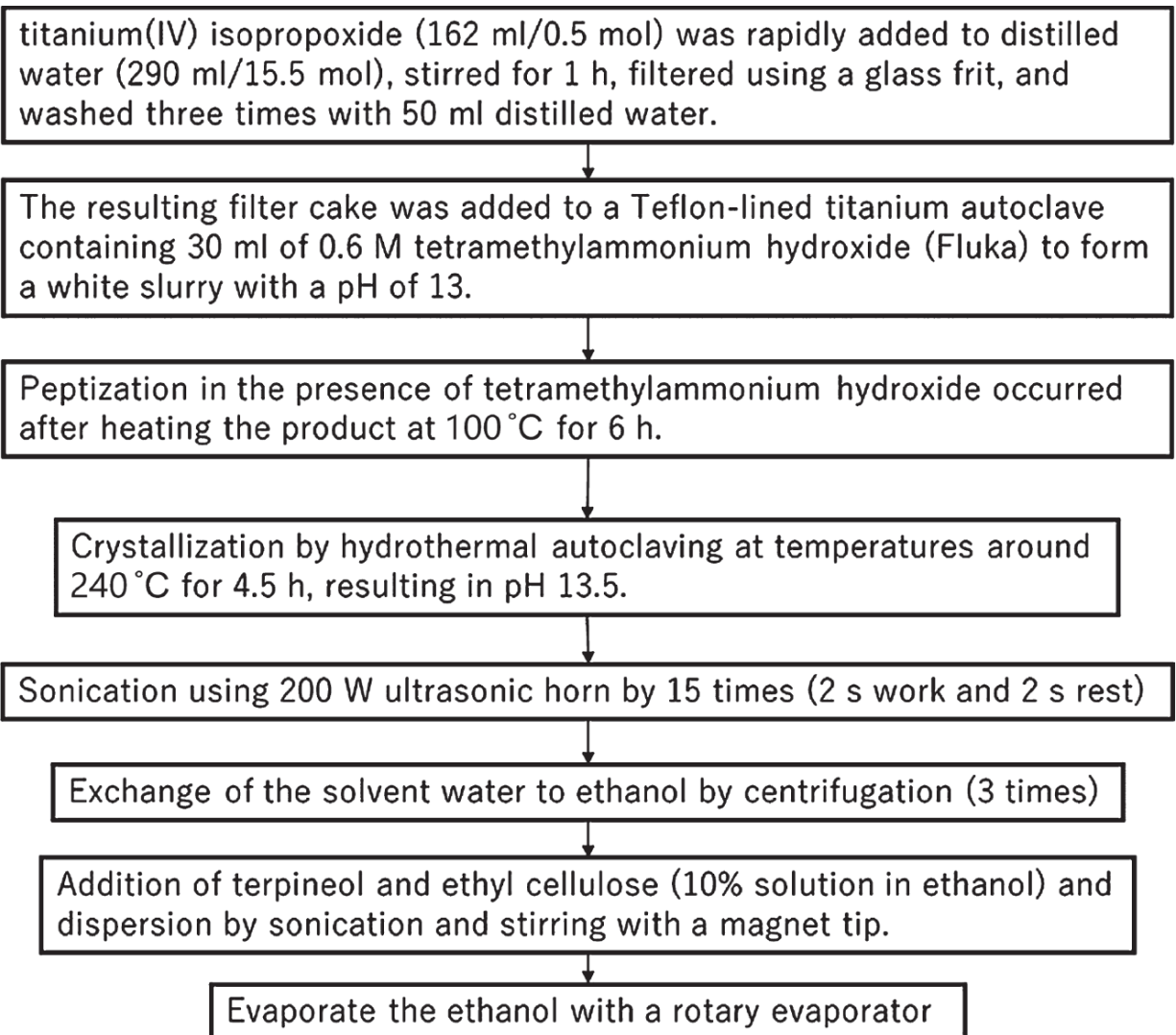Evaporate the ethanol with a rotary evaporator

Figure 4.9 Basic-route synthesis scheme of nano-TiO_2 colloid (d = c. 30 nm) for mesoporous TiO_2 layer. Source: Adapted from Ito et al. [27].

Figure 4.11 shows the picture of hand-processed screen-printing, which is good system for the number of devices less than 200 pieces, but it can be changed by the technique of printing persons (students). Hence, for the larger number of screen printing more than 200, and/or in order to avoid the technical variation of printing person, semi-automation screen-printing system can also be used.

Figure 4.12 shows the scheme of screen printing. At first, the screen-printing mesh should be set above the aiming substrate (an etched-FTO glass with c-TiO_2 layer). For the polyester mesh, the gap between the screen-printing mesh and the substrate would be 2–4 nm,

and the squeegee angle would be close to normal (80°–85°). For stainless mesh, contrary, the gap between the screen-printing mesh and the substrate would be 1–2 nm, and the squeegee angle would be lower (60°–75°). Next, the substrate is removed, and the TiO_2 paste is set on the printing mesh (Figure 4.12a) and filled in the patterned mesh using the squeegee (Figure 4.12b,c). Afterward, the aiming substrate is set below the printing mesh (Figure 4.12d), and the TiO_2 paste in the printing mesh is transferred to the substrate with keeping the designed patterns (Figure 4.12d–f). The TiO_2-printed substrate is removed from the screen-printing stage (Figure 4.12f) and transferred on a hot plate at 125 °C to evaporate the solvent (α-terpineol) to fix the structure [26]. Again, TiO_2 paste should be set in the printing mesh for the next printing.
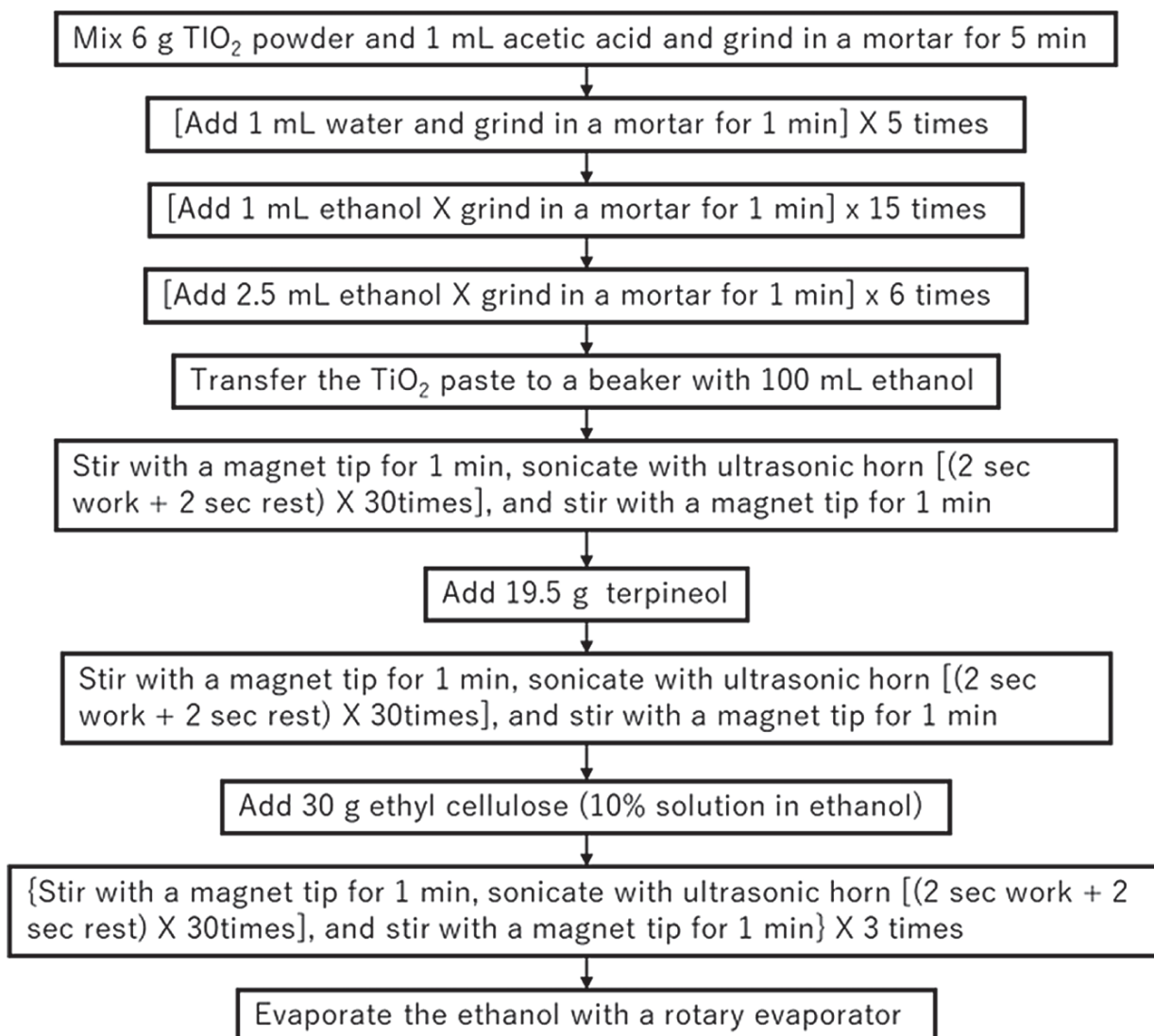
Mix 6 g TlO$_2$ powder and 1 mL acetic acid and grind in a mortar for 5 min

↓

[Add 1 mL water and grind in a mortar for 1 min] X 5 times

↓

[Add 1 mL ethanol X grind in a mortar for 1 min] x 15 times

↓

[Add 2.5 mL ethanol X grind in a mortar for 1 min] x 6 times

↓

Transfer the TiO$_2$ paste to a beaker with 100 mL ethanol

↓

Stir with a magnet tip for 1 min, sonicate with ultrasonic horn [(2 sec work + 2 sec rest) X 30times], and stir with a magnet tip for 1 min

↓

Add 19.5 g terpineol

↓

Stir with a magnet tip for 1 min, sonicate with ultrasonic horn [(2 sec work + 2 sec rest) X 30times], and stir with a magnet tip for 1 min

↓

Add 30 g ethyl cellulose (10% solution in ethanol)

↓

{Stir with a magnet tip for 1 min, sonicate with ultrasonic horn [(2 sec work + 2 sec rest) X 30times], and stir with a magnet tip for 1 min} X 3 times

↓

Evaporate the ethanol with a rotary evaporator

Figure 4.10 Powder-based preparation of TiO$_2$ screen-print paste for mesoporous TiO$_2$ layer. Source: Ito et al. [28]/with permission of John Wiley & Sons.
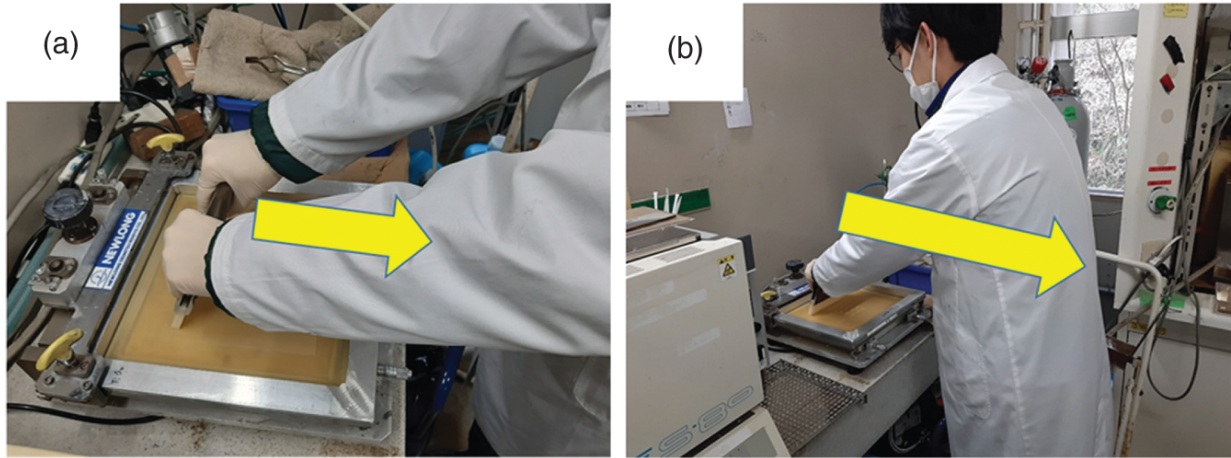
Figure 4.11 A picture of screen print procedure: (a) hands with squeegee on the printing mesh; (b) standing Figure 4 in front of the printing stage. The arrows in the pictures show the direction of printing movement.
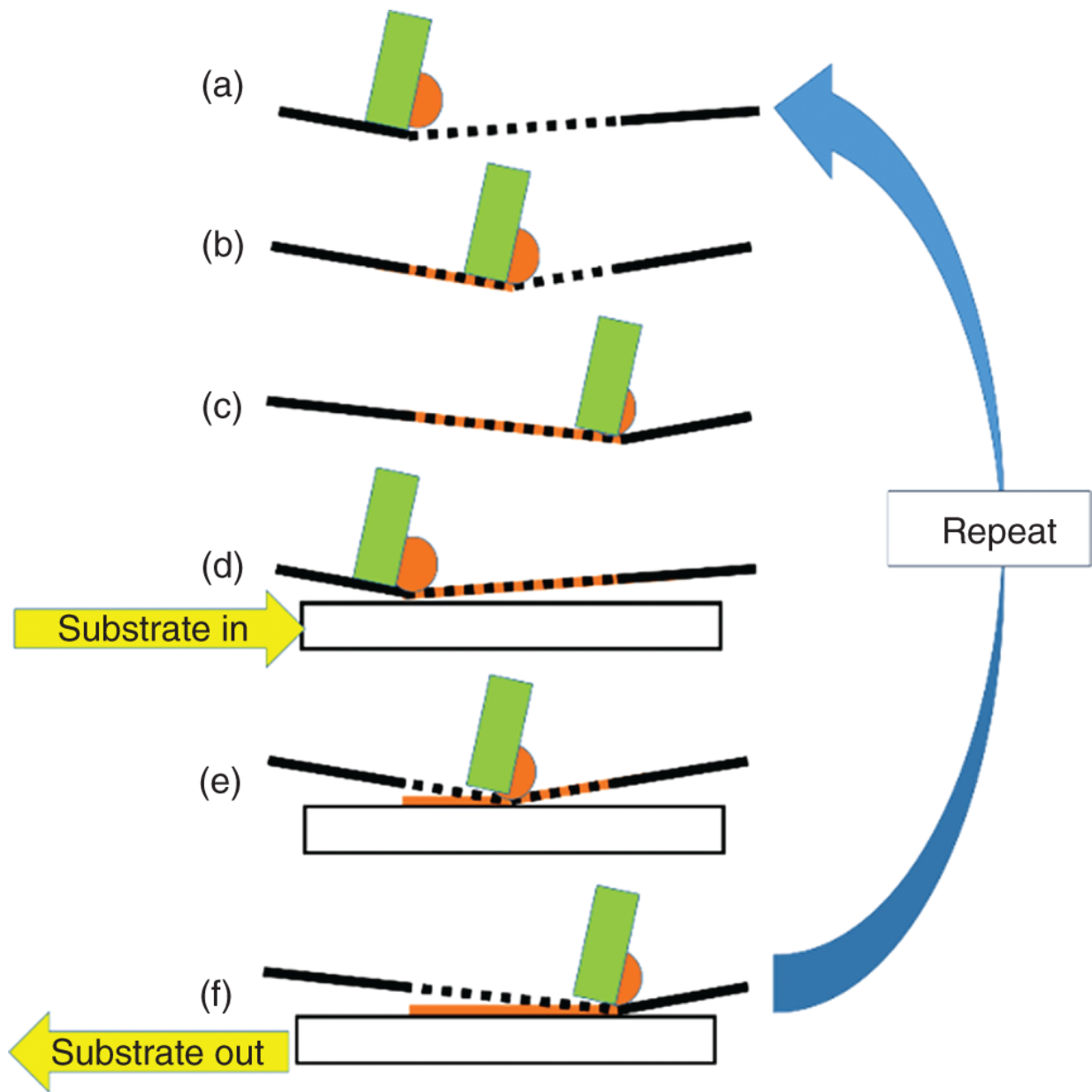
Figure 4.12 Screen print procedure: (a) setting printing mesh, squeegee, and paste; (b and c) filling in the paste in the patterned mesh; (d) inserting the substrate for printing; (e) printing; (f) finishing print and taking out the substrate.

4.5 Mesoporous Cathodes (NiO and Co$_3$O$_4$)

One of the best performing MPLE-PSC contains mesoporous-NiO cathode (Figure 4.1b,d) with 17.02% of *Eff*. [8]. Basically, V_{oc} with HTM layer can be larger than that without it.

In order to improve the *Eff* using NiO-HTM MPLE-PSCs, Cu was doped in NiO, resulting in the improvement of *Eff* by 2% (from 10.49% *Eff* (reverse scan) to 12.79% *Eff* (reverse scan)) (Table 4.1) [30]. In place of NiO, Co_3O_4 can also be used for HTM [31]. The *Eff* with Co_3O_4 can improve by 2% from that without it (Table 4.2).

Table 4.1 Solar cell parameters for carbon-based cells with and without Cu:NiOx with an aperture of $0.8\,cm^2$ under 1 Sun ($100\,mW\,cm^{-2}$) light illumination.

Parameters	Standard carbon		With NiO		With Cu:NiO	
	Reverse	Forward	Reverse	Forward	Reverse	Forward
V_{oc} (V)	0.89	0.89	0.95	0.94	1.00	0.98
J_{sc} (mA cm^{-2})	21.13	21.75	22.09	21.98	22.15	22.65
FF	0.49	0.49	0.50	0.51	0.57	0.57
PCE (%)	9.21	9.48	10.49	10.53	12.79	12.65

Source: Bashir et al. [30]/with permission of Elsevier.

Table 4.2 Solar cell parameters for standard carbon cell without and with Co_3O_4 layer with an active area of $0.09\,cm^2$ under 1 Sun ($100\,mW\,cm^{-2}$) light illumination.

Parameters	Without Co_3O_4		With Co_3O_4	
	Reverse	Forward	Reverse	Forward
V_{oc} (V)	0.86	0.85	0.88	0.85
J_{sc} (mA cm^{-2})	21.64	21.78	23.43	23.52
FF	0.60	0.57	0.64	0.65
PCE (%)	11.25	10.62	13.27	13.11

Source: Bashir et al. [31]/with permission of Royal Society of Chemistry.

4.6 Back-Contact Porous Carbon

From the first investigation of MPLE-PSCs [6], the back-contact porous carbon has been studied intensively, which is the key material to improve the photoenergy conversion efficiency. The group of Hongwei Han (HUST) reported 17.01% photoenergy conversion

efficiency without HTM using porous carbon layer [13]. From their publication, the fabrication method of carbon layer is, "2 g carbon black powders (particle size: 30 nm) was mixed with 6 g graphite powders in a 30 ml terpineol solution, and then 1 g of 20 nm ZrO_2 nanopowders and 1 g of ethyl cellulose were added into the solution, followed by stirring vigorously using ball milling for two hours" [32].

In our group, the infiltration effects of perovskite precursor solution between two types of graphite (amorphous and pyrolytic) were compared for the mesoporous-carbon electrodes [14]. It was confirmed that the amorphous graphite can soak up the perovskite precursor solution, which can't reaches enough to the mesoporous TiO_2/ZrO_2 layers (Figure 4.13a, left), resulting in the lower incident photon-to-current efficiency (IPCE) value in the blue light region (Figure 4.13b). This low IPCE in the blue light region is due to the blue light scattering and the red light penetration by the mesoporous TiO_2/ZrO_2 layers without perovskite crystal (as Figure 4.7c). Contrary, the pyrolytic graphite can pass the perovskite precursor solution, effectively (Figure 4.13a, right), and showed a higher IPCE value (Figure 4.13b). Hence, the transportation effect of perovskite solution through the mesoporous-carbon layer is quite important.

By the collaborations between ISE (Germany) and our group, different types of graphite particles were compared for mesoporous-carbon electrodes in MPLE-PSCs [33]. Figure 4.14 shows that the pyrolytic graphite performed the best FF value (74%) due to the high conductivity (4 Ω sq.$^{-1}$) and low charge transfer resistance. However, scaly graphite performed the best *Eff* of 14.63%, which may be due to the transportation properties of perovskite precursor solution through the mesoporous-carbon electrodes (see Figure 4.13).
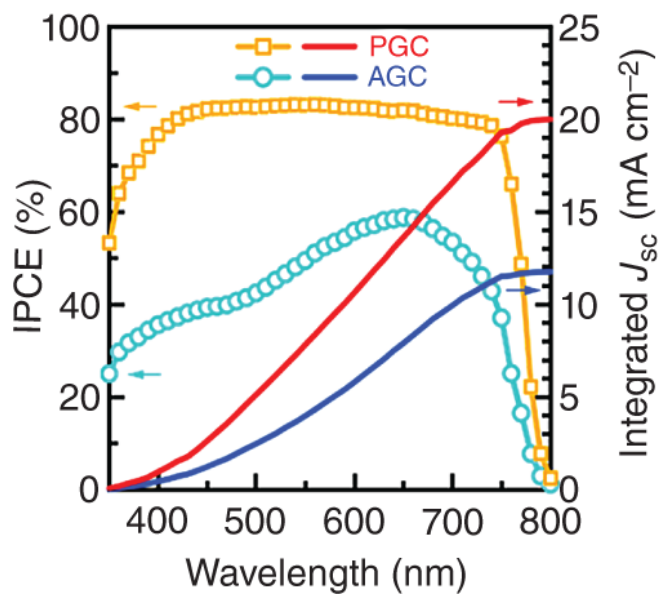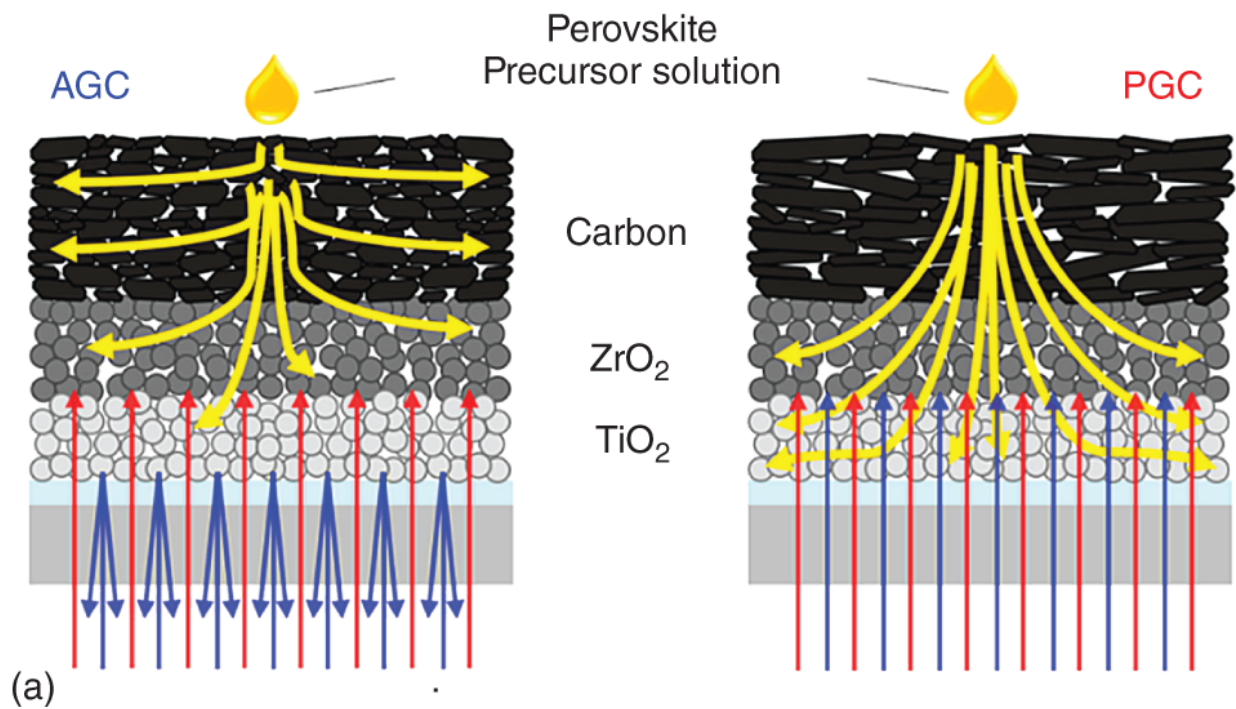
Figure 4.13 Schematic soaking image of perovskite precursor solution (a) and variation of IPCE (b) with different carbon (amorphous or pyrolytic). Source: Tsuji et al. [14]/MDPI/CC BY-4.0.
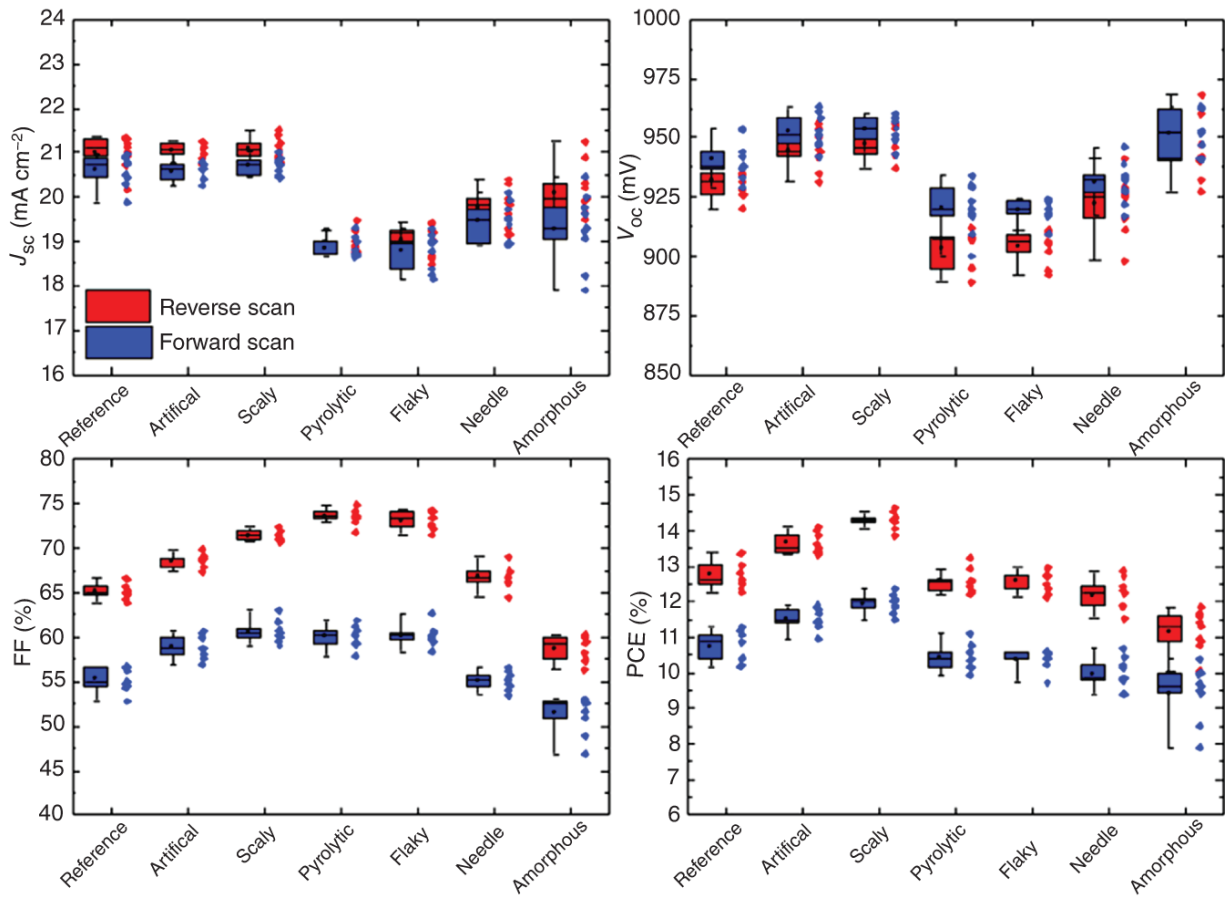
Figure 4.14 Photovoltaic characteristics of reverse (red) and forward (blue) voltage sweeps of MPLE-PSCs with mesoporous-carbon electrodes made of different graphite types. Source: Bogachuk et al. [33]/Elsevier/CC BY 4.0.

4.7 Photovoltaic Measurements

For the accurate photovoltaic analysis of MPLE-PSCs, we show two important points in this section [34]. The first point is about J–V measurements under 1 sun (AM 1.5) irradiation. Although the short-circuit photocurrent density under 1 sun (written as J_{sc}(1 sun) below) is almost constant from the initial stage (0 minute), the *FF* and V_{oc} can be activated with light activation (Figure 4.15). Hence, MPLE-PSC requires several measurements for the *Eff* analysis.

The second point is about IPCE measurements. In order to perform accurate photovoltaic measurements of solar cells, IPCE should be measured, and simulated J_{sc} should be calculated by integration of IPCE multiplied with AM 1.5 spectrum (shown as "J_{sc}(IPCE)" below).

However, due to the mismatching between J_{sc}(IPCE) and J_{sc}(1 sun) of MPLE-PSCs, several papers have been published without IPCE results. In this section, we have introduced the accurate measurement method and analysis of IPCE for MPLE-PSCs [34]. Figure 4.16 shows the set-up of weak-light activation for IPCE measurements (a), variation of IPCE (b), and light-activation time course of J_{sc}(1 sun) and J_{sc}(IPCE) (c). It can be noticed that saturation timing for light activation is different between J_{sc}(1 sun) and J_{sc}(IPCE).

For Figure 4.16c, we have used enough-light-activated devices (12 minutes-activated in Figure 4.16b) for IPCE measurements. But, J_{sc}(1 sun) and J_{sc}(IPCE) shows still a big difference without weak-light activation (Figure 4.16a) at 0 minute. Hence, 1-sun activation for J–V measurements and weak-light irradiation for IPCE activation are different. Please be careful about the IPCE measurements.
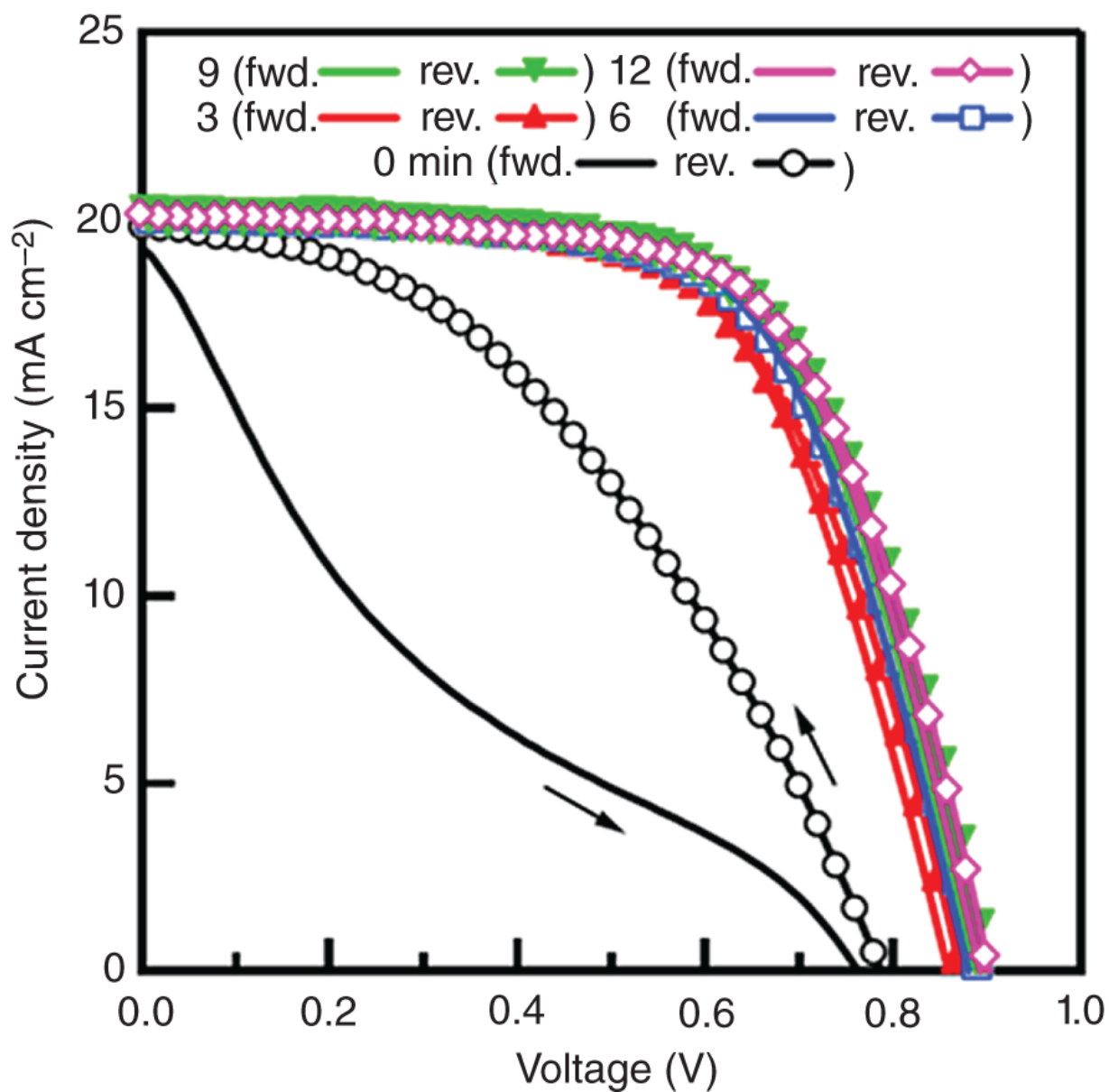
Figure 4.15 Repeated *J–V* measurements of MPLE-PSC with time interval. Source: Tsuji et al. [34]/ECSJ/CC BY-4.0.
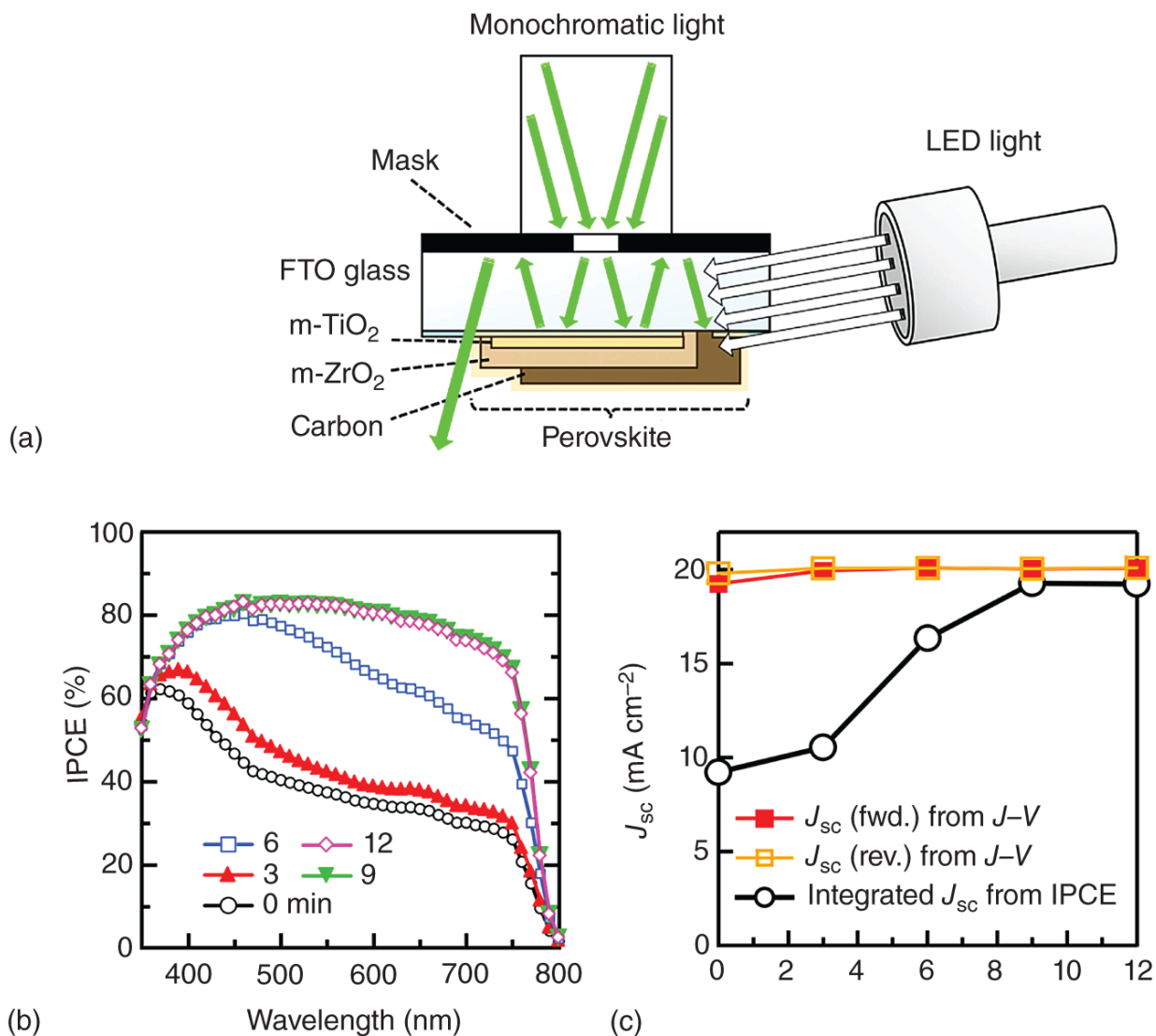
Figure 4.16 IPCE activation effects: (a) activation setup; (b) IPCE spectra with different activation times; and (c) time course of J_{sc}(1 sun) and J_{sc}(IPCE). Source: Tsuji et al. [34]/ECSJ/CC BY-4.0.

4.8 Conclusion

This chapter is about electrode materials in MPLE-PSCs for students and researchers who are starting their research works. The basis of knowledge has been progressed in the field of dye-sensitized solar cells with 30 years of history. Although we may have missed some information due to the rapid progress of this field, we have tried to show the details of important information that can't be written in a normal scientific paper. The progress of PSC is still rapidly ongoing. I

hope that students and researchers can obtain the progress of PSCs based on the knowledge in this book.

References

1 Yoo, J.J., Seo, G., Chua, M.R. et al. (2021). *Nature* 590: 587–593.

2 NREL. Best research-cell efficiency chart. https://www.nrel.gov/pv/cell-efficiency.html

3 Zhang, F., Yang, X., Cheng, M. et al. (2016). *Nano Energy* 20: 108–116.

4 Domanski, K., Correa-Baena, J.-P., Mine, N. et al. (2016). *ACS Nano* 10: 6306–6314.

5 Shi, L., Bucknall, M.P., Young, T.L. et al. (2020). *Science* 368: 1328.

6 Ku, Z., Rong, Y., Xu, M. et al. (2013). *Scientific Reports* 3: 3132.

7 Mei, A., Li, X., Liu, L. et al. (2014). *Science* 345: 295.

8 Liu, S., Huang, W., Liao, P. et al. (2017). *Journal of Materials Chemistry A* 5: 22952–22958.

9 Mei, A., Sheng, Y., Ming, Y. et al. (2020). *Joule* 4: 1–15.

10 Baranwal, A.K., Kanda, H., Shibayama, N. et al. (2019). *Energy Technology* 7: 245–252.

11 Grancini, G., Roldán-Carmona, C., Zimmermann, I. et al. (2017). *Nature Communications* 8: 15684.

12 Yang, K., Liu, S., Du, J. et al. (2021). *Solar RRL* 2000825.

13 Liu, C., Liu, S., Wang, Y. et al. (2021). *Advanced Functional Materials* 2010603.

14 Tsuji, R., Bogachuk, D., Martineau, D. et al. (2020). *Photonics* 7: 133.

15 Palma, A.L., Matteocci, F., Agresti, A. et al. (2017). *IEEE Journal of Photovoltaics* 7: 1674–1680.

16 Im, J.-H., Kim, H.-S., and Park, N.-G. (2014). *APL Materials* 2: 081510.

17 Yella, A., Heiniger, L.-P., Gao, P. et al. (2014). *Nano Letters* 14: 2591–2596.

18 Kim, B.J., Kim, D.H., Lee, Y.-Y. et al. (2015). *Energy & Environmental Science* 8: 916–921.

19 Jiang, X., Xiong, Y., Zhang, Z. et al. (2018). *Electrochimica Acta* 263: 134.

20 Wang, S., Shen, W., Liu, J. et al. (2021). *Nanotechnology* 32: 145403.

21 Zhao, J., Zhang, Y., Zhao, X. et al. (2019). *ACS Applied Energy Materials* 2: 2034–2042.

22 Snaith, H.J. and Grätzel, M. (2006). *Adv. Mater.* 18: 1910.

23 Ito, S., Murakami, T.N., Zakeeruddin, S.M. et al. (2014). *NANO: Brief Reports and Reviews* 9: 1440010.

24 Saito, Y., Kambe, S., Kitamura, T. et al. (2004). *Solar Energy Materials and Solar Cells* 83: 1–13.

25 Jochen, W. (2003). *Titanium Dioxide*. Hannover, Vincents: European Coating Literature.

26 Ito, S., Murakami, T.N., Comte, P. et al. (2008). *Thin Solid Films* 516: 4613.

27 Ito, S., Zakeeruddin, S.M., Comte, P. et al. (2008). *Nature Photonics* 2: 693.

28 Ito, S., Chen, P., Comte, P. et al. (2007). *Progress in Photovoltaics: Research and Applications* 15: 603.

29 Shin, S.S., Yang, W.S., Noh, J.H. et al. (2015). *Nature Communications* 6: 7410.

30 Bashir, A., Haur, L.J., Shukla, S. et al. (2019). *Solar Energy* 182: 225–236.

31 Bashir, A., Shukla, S., Haur, L.J. et al. (2018). *Nanoscale* 10: 2341.

32 Wu, J., Zhang, W., Wang, Q. et al. (2020). *Journal of Materials Chemistry A* 8: 11148–11154.

33 Bogachuk, D., Tsuji, R., Martineau, D. et al. (2021). *Carbon* 178: 10–18.

34 Tsuji, R., Bogachuk, D., Luo, B. et al. (2020). *Electrochemistry* 88: 418.

5
Insulating Layers for Printable Mesoscopic Perovskite Solar Cells

Jian Zhang[1], Dongjie Wang[1], and Yuli Xiong[2]

[1] Guilin University of Electronic Technology, Department of Materials Science and Engineering, Guangxi Key Laboratory of Information Materials, Engineering Research Center of Electronic Information Materials and Devices of Ministry of Education, No.1 Jinji Road, Dongjiang Street, Guilin, 541004, PR China

[2] Wuhan University of Technology, Department of Materials Science and Engineering, State Key Laboratory of Advanced Technology for Materials Synthesis and Processing, No. 122 Luoshi Road, Luonan Street, Wuhan, 430070, PR China

5.1 Introduction

Insulating layers, also known as "spacer layers," refer to the material that separates the anode and cathode in mesoscopic perovskite solar cells (MPSCs). The insulating layer is an important component of printable MPSCs, which plays a crucial role in obtaining high-performance devices. The insulating layer mainly performs three important functions in efficient printable MPSCs. First, the core mission of the insulating layer is to prevent the direct transport of electrons from the electron transport layer (ETL) to the hole transport layer (HTL). This requires the insulating layer to have a wide bandgap without cracking. Second, the perovskite confined in the mesopores of the insulating layer can absorb photons transmitted through the perovskite/TiO_2 composite layer and contribute to the

photocurrent. Furthermore, holes generated in the perovskite/TiO$_2$ layer should go through the perovskite/insulating layer to reach the carbon electrode, while the electrons generated in the perovskite/insulating layer need to go through the perovskite/insulating layer to reach the TiO$_2$ ETL. The results demonstrate that compared with printable MPSCs without the insulating layer, printable MPSCs with the insulating layer have significantly improved photovoltaic performance.

The most widely used materials for insulating layers include ZrO$_2$ [1–3], Al$_2$O$_3$ [4–6], SiO$_2$ [7–9], and their composites [10]. Figure 5.1 presents the crystal models of monoclinic ZrO$_2$, α-Al$_2$O$_3$ and cristobalite SiO$_2$, which are all indirect bandgap semiconductors with high lowest unoccupied molecular orbitals (LUMO). Among them, ZrO$_2$ and Al$_2$O$_3$ possess wide bandgaps of 4.14 and 5.57 eV, respectively, and SiO$_2$ is also a wide bandgap insulator with an E_g range of 9–11 eV. Based on these, electrons are difficult to inject and can only be transported within the perovskite active layer, thereby reducing charge recombination and providing printable MPSCs with enhanced photovoltaic performance, especially in terms of open-circuit voltage (V_{oc}) and fill factor (FF).
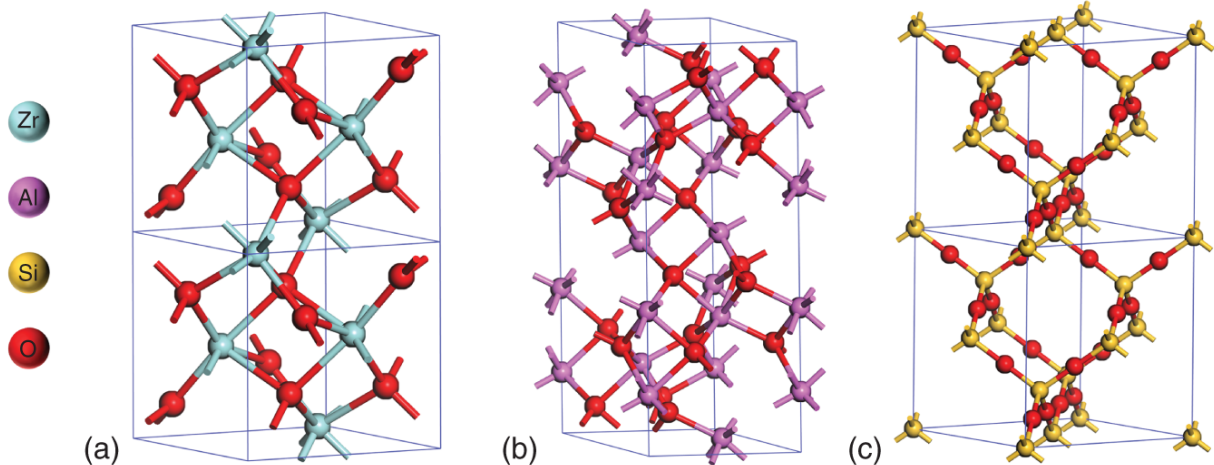
Figure 5.1 The crystal model of (a) monoclinic ZrO_2, (b) α-Al_2O_3, and (c) cristobalite SiO_2.

5.2 ZrO_2-Insulating Mesoscopic Layers

Zirconium dioxide, chemical formula ZrO_2, is the main oxide of zirconium. As shown in Figure 5.2, ZrO_2 is usually a white, odorless, and tasteless crystal, which is difficult to dissolve in water, hydrochloric acid, and dilute sulfuric acid. Due to its stable chemical properties, high melting point, high resistivity, high refractive index, and low thermal expansion coefficient, ZrO_2 has been widely applied in the fields of optics, electronics and optoelectronics, ceramic insulating material, and high-temperature resistant material.

Dash et al. [11] calculated the energy bands and density of states (DOS) of ZrO_2 in cubic, tetragonal, monoclinic, and rutile crystal systems using the first-principle calculation method. According to the calculation results, all structures of ZrO_2 have a wide bandgap near the Fermi level, and the bandgap is larger than 4 eV, so ZrO_2 belongs to the

category of insulators. In addition, both high-purity ZrO_2 and doped ZrO_2 exhibit high insulating properties at room temperature, and their resistivity is greater than $1010\,\Omega$ cm. In conclusion, ZrO_2 is an excellent insulating material because of its large bandgap and high conduction band (CB) energy level, which can effectively prevent the recombination of electrons and holes. Therefore, ZrO_2 has been widely used as the insulating layer in the field of next-generation solar cells, such as dye-sensitized solar cells (DSSCs) and emerging perovskite solar cells (PSCs).

Figure 5.2 (a) High-purity ZrO_2 powders, (b) High-purity ZrO_2 beads.

In monolithic DSSCs, to improve the absorption capacity of sunlight, Kay et al. [12] used a mixture of rutile TiO_2 and ZrO_2 to prepare an astigmatic spacer layer, which achieved a PCE of 6.67%. Thompson et al. [13] studied the role of spacer layer in monolithic DSSCs, and they used ZrO_2 and TiO_2 as spacer materials, respectively. Experiments proved that a higher V_{oc} had been obtained when ZrO_2 was used as the spacer material, mainly derived from the fact that ZrO_2 effectively inhibits the recombination pathway of electrons

from TiO_2 to carbon electrode. Hinsch et al. [14] studied the influence of the thickness of spacer layer on the limiting current of DSSCs and found that the limiting current value increased with the decrease in the thickness of spacer layer.

In 2013, Ku et al. [15] developed a carbon-based, hole-conductor-free, fully printable mesoscopic perovskite solar cells (FP-MPSCs), which is a new type of PSCs based on the triple-mesoscopic scaffold of mp-TiO_2/mp-ZrO_2/mp-Carbon (mp: mesoscopic), as illustrated in Figure 5.3. Soon after, in 2014, Mei et al. [16] innovatively introduced 5-aminovaleric acid (5-AVA) iodide as an effective bifunctional additive into the $MAPbI_3$-based perovskite to form the new mixed-cation perovskite $(5\text{-}AVA)_x MA_{1-x} PbI_3$ with better pore filling and lower defect concentration as well as more compact contact with the triple-mesoscopic scaffold. Most notably, a certified PCE of 12.84% was obtained with excellent light and thermal stability, and the initial PCE remained undecayed after >1000 hours under full illumination in the atmospheric environment. Inspired by the study of ZrO_2 in DSSCs, the authors employed ZrO_2 as the spacer layer to prevent short circuits in FP-MPSCs (see Figures 5.3 and 5.4). The invention of FP-MPSCs marks the milestone progress of PSCs toward industrial application [17].
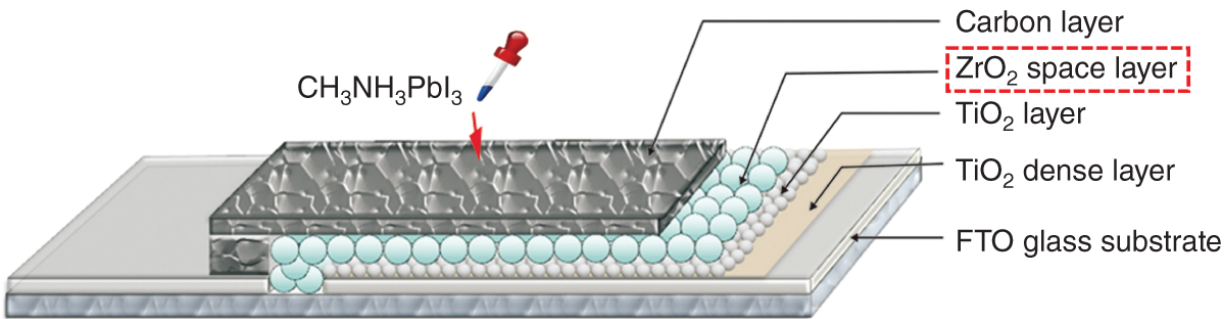
Figure 5.3 Schematic structure of carbon-based, hole-conductor-free FP-MPSCs (utilizing ZrO_2 as spacer layer). Source: Reproduced with permission from Ku et al. [15]. Copyright 2013, Springer Nature.
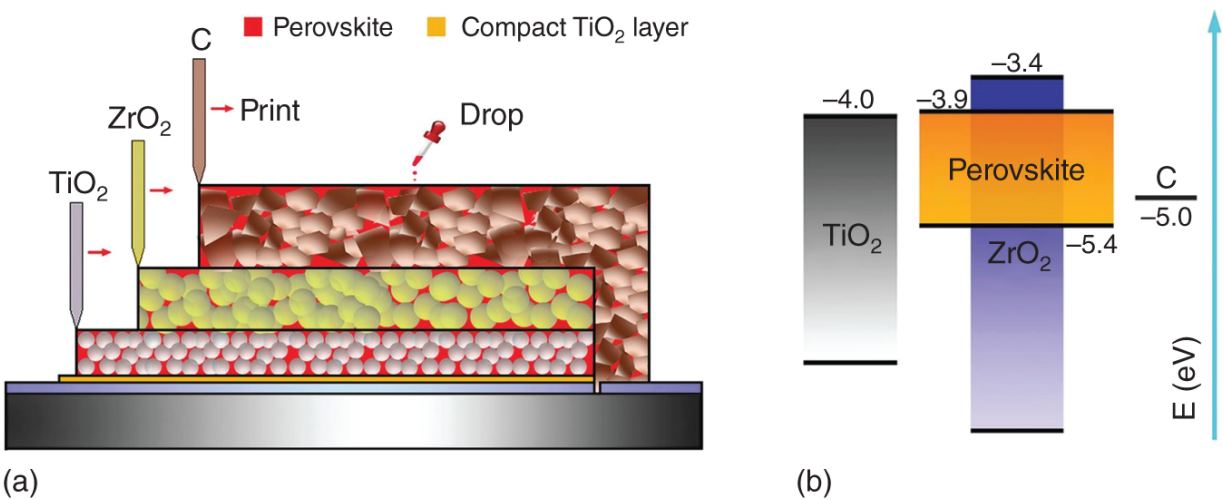

Figure 5.4 (a) Cross section of the triple-mesoscopic FP-MPSCs. (b) Energy level diagram of the triple-mesoporous FP-MPSCs. Source: Reproduced with permission from Mei et al. [16]. Copyright 2014, American Association for the Advancement of Science.

ZrO_2 slurry is generally prepared by mixing commercial ZrO_2 nanopowders or nanoparticles with ethyl cellulose and α-terpineol, followed by vigorous stirring by ball milling for several hours. Then, the mixture was evaporated at 50 °C using a rotary evaporator to obtain ZrO_2 slurry. Subsequently, ZrO_2 slurry is first printed on top of the mesoscopic TiO_2 layer by screen printing technique, and

then the ZrO_2 wet film is sintered in air at 450 °C for 30 minutes to burn the organics. Finally, a mesoscopic ZrO_2 layer is fabricated on top of the mesoscopic TiO_2 layer as an insulating layer to prevent electrons in the TiO_2 ETL from reaching the carbon electrode.

On the basis of the above research, a series of studies have been carried out on the effects of the thickness [18, 19] and morphology of the spacer layer [2, 20], nanoparticle size [19], spacer material type [1], and the ratio of ZrO_2 nanoparticles to ethyl cellulose [2] on the photovoltaic performance of FP-MPSCs. For instance, in view of the problem of uneven ZrO_2 spacer layer caused by the agglomeration of ZrO_2 nanoparticles, highly dispersed $TiO_2@ZrO_2$ nanoparticles were designed as building blocks for ultra-flat and crack-free ZrO_2 spacer layer in FP-MPSCs [20]. A flat and crack-free spacer layer is preferred to achieve better insulating properties and to form defect-free and intimate interfacial contact between perovskite film and carbon electrode for efficient hole extraction and avoiding the short-circuit.

Meng et al. [1] conducted systematic research on spacer layer to compare the effects of ZrO_2 and Al_2O_3 on printable MPSCs. As shown in Figure 5.5a,b, the authors used the field emission scanning electron microscopy (SEM) to observe the effect of the morphology of different insulating layers on the infiltration and crystallization process of perovskite. Comparing with Al_2O_3 spacer layer, ZrO_2 spacer layer shows a relatively large particle size and pores, which is favorable for the permeation of perovskite precursor solution in the interstitial space and the crystallization and growth of $(5\text{-AVA})_x MA_{1-x} PbI_3$ perovskite in the pores, facilitating the transport of photogenerated charge. In addition, as can be seen from the cross-sectional

SEM images of the printable MPSCs based on Al_2O_3 (Figure 5.5c) and ZrO_2 (Figure 5.5d) insulating layers, TiO_2 layer, and carbon electrode are completely separated by Al_2O_3 or ZrO_2 insulating layers. Especially, compared with small pores in the Al_2O_3 insulating layer, larger pores can be formed by the ZrO_2 insulating layer, which is beneficial to the infiltration of perovskite precursor solution into the triple-mesoscopic architecture.
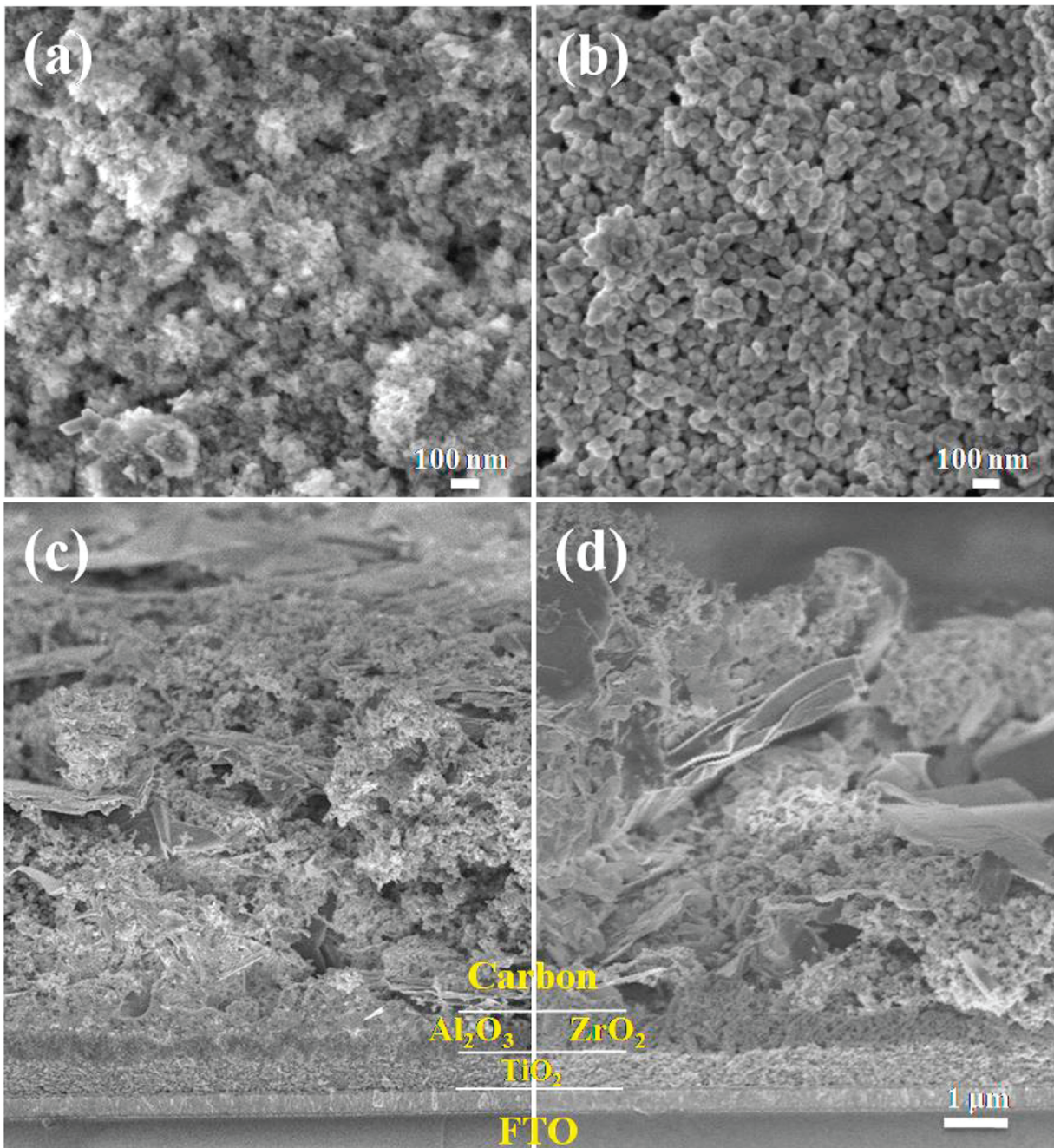
Figure 5.5 SEM images of (a) Al_2O_3 and (b) ZrO_2 mesoscopic layers; cross-sectional SEM images of FP-MPSCs based on (c) Al_2O_3 and (d) ZrO_2 insulating layers, respectively. Source: Meng et al. [1]/Reproduced with permission from Elsevier.

They also measured the nitrogen adsorption–desorption isotherms to analyze the Brunauer–Emmett–Teller (BET) surface area and pore size distribution of ZrO_2 and Al_2O_3, respectively (Figure 5.6). Both isotherms show relatively high adsorption at the high relative pressure, indicating the existence of large mesopores. The pore size distributions (inset of Figure 5.6) of ZrO_2 and Al_2O_3 samples have a wide distribution range of 2–100 nm with a peak pore diameter of 53 nm for ZrO_2 and 18 nm for Al_2O_3. Obviously, the larger pores of ZrO_2 insulating layer could provide sufficient space for the permeation of $(5\text{-}AVA)_x MA_{1-x} PbI_3$ perovskite. Moreover, BET surface areas were obtained to be $21 \, m^2 g^{-1}$ for ZrO_2 and $152 \, m^2 \, g^{-1}$ for Al_2O_3, respectively. Although Al_2O_3 insulating layer possesses larger specific surface areas, however, its small pores hinder the filling of perovskite into the mesoporous architecture. Therefore, the larger pores of ZrO_2 insulating layer are favorable for the infiltration and crystallization of $(5\text{-}AVA)_x MA_{1-x} PbI_3$ perovskite, generating large grains to reduce the crystal boundaries. Hence, ZrO_2 owns superior insulating ability than Al_2O_3 as insulating layer for FP-MPSCs.
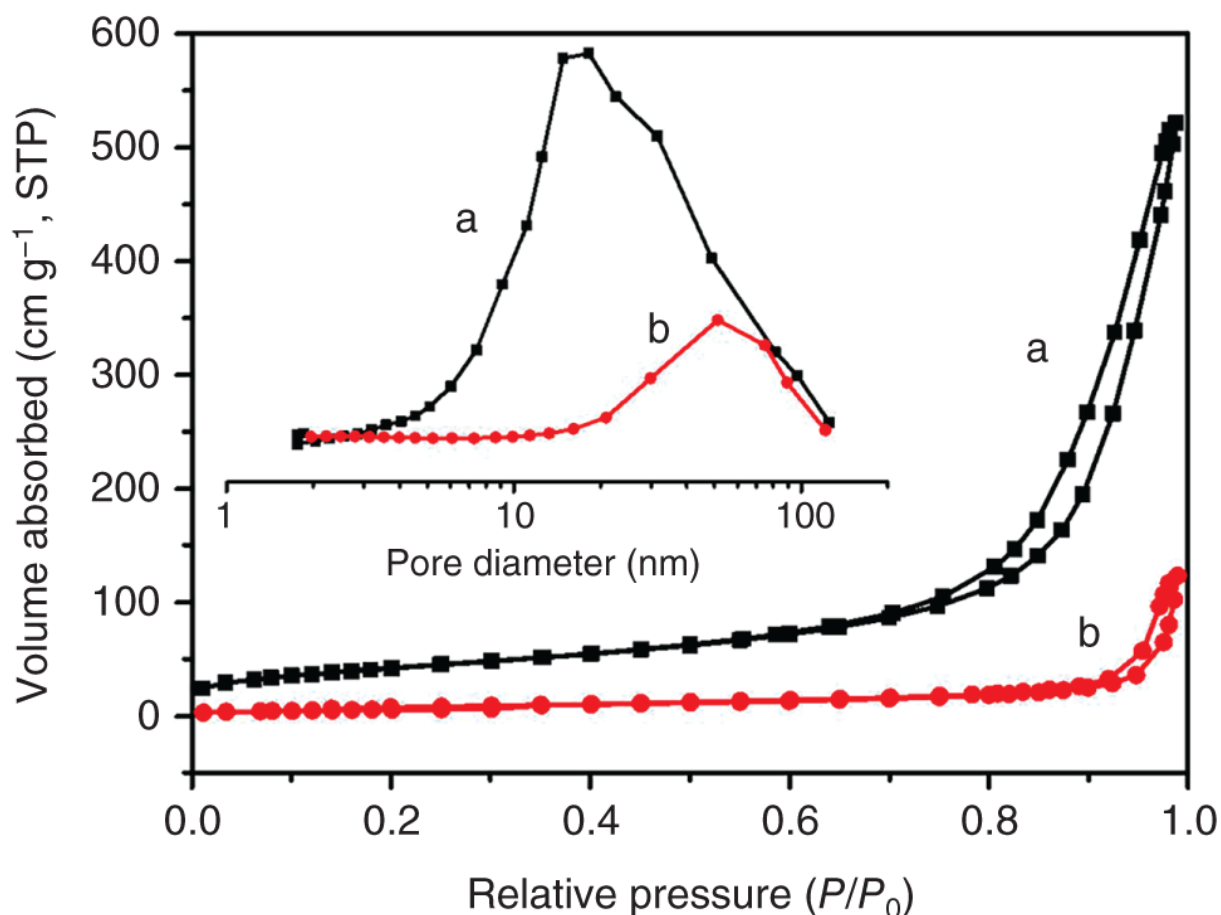
Figure 5.6 Nitrogen adsorption–desorption isotherms and pore-size distribution curves (inset) of Al_2O_3 (a) and ZrO_2 (b) insulating layers. Source: Reproduced with permission from Meng et al. [1]. Copyright 2018, Elsevier Ltd.

For the effect of the thickness of ZrO_2 on the device performance of FP-MPSCs, Liu et al. [2] optimized the thickness of ZrO_2 to enhance the light-harvesting ability and reduce the hole transporting resistance. Figure 5.7a presents characteristic parameters from the typical photocurrent density–voltage (J–V) curve of FP-MPSCs with different ZrO_2 thicknesses and device parameters are listed in Table 5.1. The device without ZrO_2 presents rather poor photovoltaic performance, delivering a PCE of only 1.56%. Here, electrons in the CB of TiO_2 may directly leak to the

carbon electrode, leading to large undesirable energy losses. In contrast, even with a thin 0.3 µm thick ZrO_2, device performance is improved markedly to 5.92%. When the thickness of ZrO_2 increases to 1 µm, the short-circuit photocurrent density (J_{sc}) of the device is significantly enhanced, resulting in a higher PCE of 10.30%. However, when the thickness of ZrO_2 is much larger than 1 µm, V_{oc} and FF of the device decreased, which could be attributed to the limit of the carrier diffusion length. Moreover, conventional MPSCs (e.g. the structure of TiO_2/MAPbI$_3$/Au or TiO_2/MAPbI$_3$/Carbon) show a depletion layer due to the charge transfer between MAPbI$_3$ and TiO_2. Mott–Schottky analysis was conducted in FP-MPSCs (Figure 5.7b). The junction capacitance indicates the existence of a built-in electric potential that is conducive to the separation of carrier. The authors concluded that there is an optimal thickness of ZrO_2 because of balancing factors, such as needs of light harvesting by MAPbI$_3$ confined in spacer layer, width of built-in electric field, and quality of spacer layer.
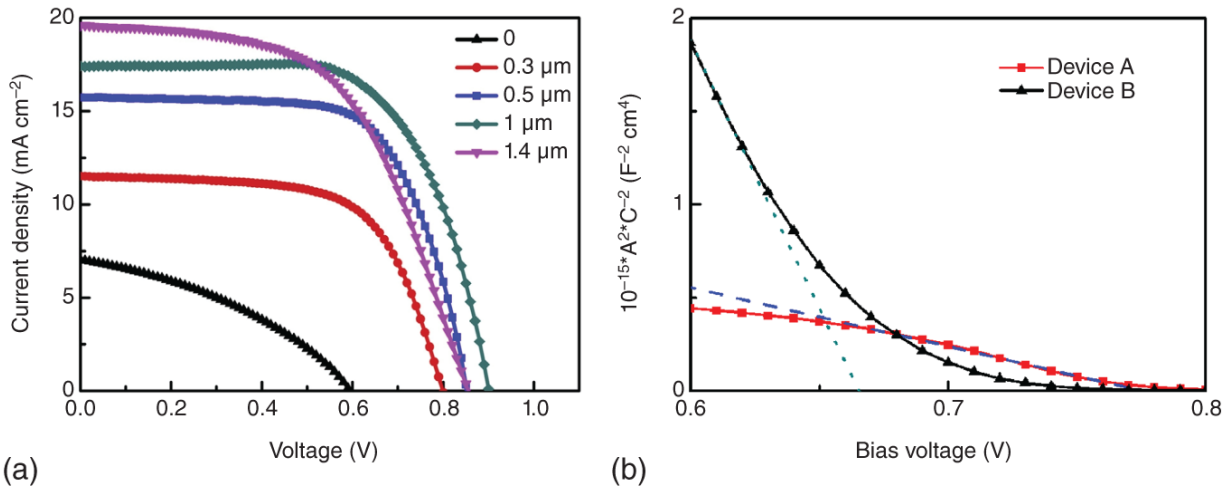
Figure 5.7 (a) Typical J–V curves for FP-MPSCs with different thickness of ZrO_2 insulating layers measured at a simulated AM1.5G solar irradiation. (b) Mott–Schottky analysis of device A (high pore filling and uniform morphology prepared by two-step method) and device B (low pore filling and uncontinuous morphology prepared by one-step method) measured at 1 kHz. The built-in potentials of device A and device B are calculated to be 0.77 and 0.67 V, respectively.

Table 5.1 Photovoltaic parameters of FP-MPSCs based on ZrO_2 with different thickness.

Thickness (μm)	J_{sc} (mA cm^{-2})	V_{oc} (mV)	FF (%)	PCE (%)
0	7.03	594	37	1.56
0.3	11.52	799	64	5.92
0.5	15.74	852	67	9.02
1.0	17.42	901	66	10.30
1.4	19.60	856	55	9.29

Liu et al. [19] conducted a systematic study on the effects of nanoparticle size and layer thickness on insulating properties of ZrO_2 spacer layer and device performance of

FP-MPSCs. They adopted five sizes of ZrO_2 particles with 5, 10, 20, 60, and 100 nm, respectively (referred to S5, S10, S20, S60, and S100 spacer, respectively), as spacer building blocks to construct ZrO_2 spacer layer. Figure 5.8a–e present that there is a large difference in surface morphology with different nanoparticle sizes. As can be seen from Figure 5.8a–e, there are many cracks in S5 and S10 spacers and micrometer scale pore in S100 spacer, while the surface of S20 and S60 is uniform, no obvious defects are observed. Figure 5.8f shows XRD patterns of ZrO_2 insulating layer with different particle sizes, indicating that the majority phase of five insulating layers is tetragonal crystal phase.

As observed by the high-resolution transmission electron microscope (TEM) image (Figure 5.9a), the mesopores of ZrO_2 spacer layer are fully filled with perovskite crystals, providing continuous channels for charge carriers. The crystal size of perovskite in insulating layers is strongly influenced by the mesopore size of ZrO_2. As seen in XRD patterns (Figure 5.9b), there is a clear trend that the peak intensity of (110) crystal plane increased with the increase in particle size of ZrO_2. The infiltrated perovskite precursor started to nucleate onto the heterogeneous surface of ZrO_2 nanoparticles with high surface area, resulting in multiple nucleation centers and small crystal size. The calculated sizes of perovskite from XRD spectra are 4.3, 3.9, 6.2, 11.5, and 12.6 nm, for the S5, S10, S20, S60, and S100 insulating layers, respectively. The band-edge emission spectra of perovskite film deposited on ZrO_2 spacer layer were exhibited in Figure 5.9c to evaluate the effect of ZrO_2 nanoparticle size on physicochemical properties of perovskite films. Apparently, as the particle size of ZrO_2 decreased, a blue shift of the band-edge photoluminescence

(PL) occurred, and line width is broadened. The peak position of perovskite emission spectra can be tuned in the range of 33 nm through varying the pore size of ZrO_2. The increase in emission line width at grain boundaries can be attributed to the disorder and defects in perovskite films, which also decreased lifetime in time-resolved PL (Figure 5.9d). Perovskite films grown on bare glass show a lifetime of 141.9 ns. However, perovskite films grown in different ZrO_2 decreased to 0.5, 8.4, 24.1, 37.2, and 53.7 ns, for S5, S10, S20, S60, and S100, respectively.
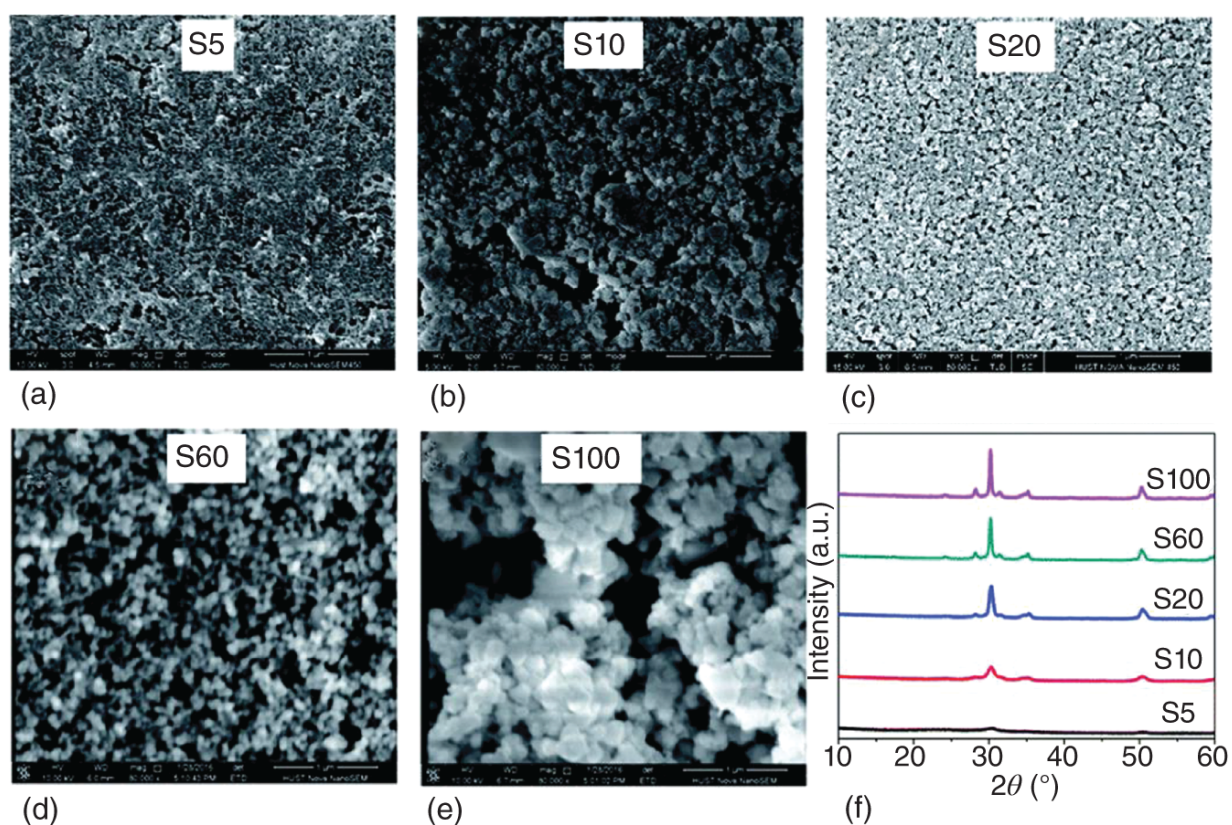
Figure 5.8 SEM images of ZrO_2 insulating layers with particle size of (a) 5 nm, (b) 10 nm, (c) 20 nm, (d) 60 nm, and (e) 100 nm, respectively. (f) XRD patterns of insulating layers with different ZrO_2 building block sizes. Source: Liu et al. [19]/Reproduced with permission from Royal Society of Chemistry/CC BY-NC 3.0.
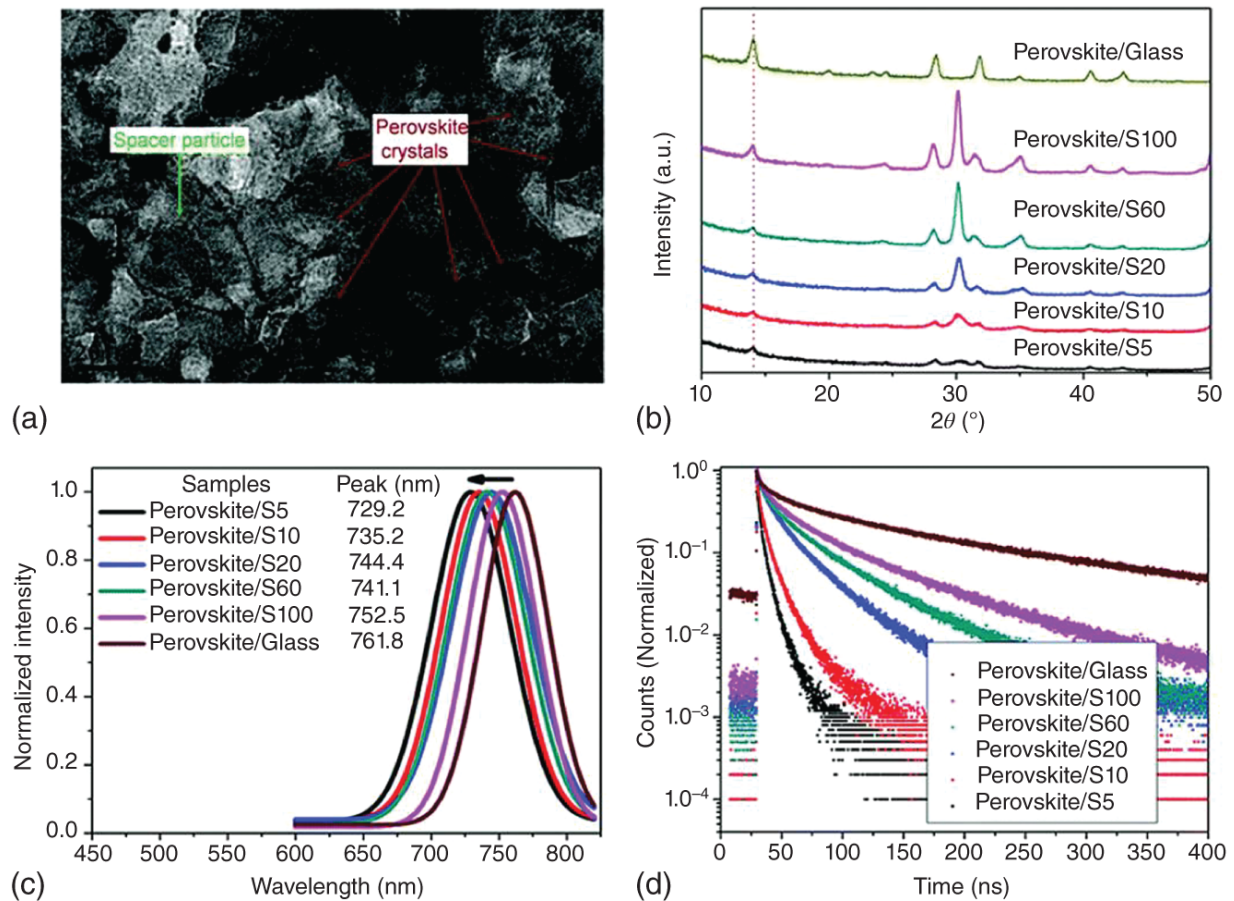
Figure 5.9 (a) High-resolution TEM image of perovskite/S20 spacer film composite. (b) XRD patterns of perovskite/spacer film composite. (c) Steady PL spectra and (d) Time-resolved PL of perovskite/spacer film composite. Source: Liu et al. [19]/Reproduced with permission from Royal Society of Chemistry/CC BY-NC 3.0.

The size of ZrO_2 nanoparticles also has a remarkable effect on insulating ability of ZrO_2 spacer layer. The authors designed FTO/ZrO_2 spacer/carbon configuration to measure the insulating ability of ZrO_2 insulating layers with the same thickness. Under ideal conditions, the resistance between carbon and FTO, defined as insulating resistance (R_I), should be infinite, indicating that there is not any leakage current from ideal-insulating spacer. However, all the R_I has finite values from $300\,\Omega$ to $1.5\,K\Omega$ for ZrO_2 space

layers with the same thickness but different nanoparticle size that is summarized in Table 5.2. Obvious trends of R_I changing with different ZrO_2 nanoparticle sizes are observed. It was found that the S100 spacer layer has the lowest R_I, indicating the poorest insulating ability. In addition, the S100 spacer layer was very loosely packed even after sintering at 500 °C for one hour. The authors speculated that the difference of R_I in ZrO_2 insulating layers originated from the quantum size effect dominated by surface to bulk atom ratio of ZrO_2 nanoparticles.

Figure 5.10a shows the cross-sectional SEM image of carbon-based, hole-conductor-free FP-MPSCs with ZrO_2 as spacer layer. The influence of ZrO_2 nanoparticle sizes on J–V curves of FP-MPSCs based on $(5\text{-}AVA)_x MA_{1-x} PbI_3$ perovskite with and without ZrO_2 spacer layer is illustrated in Figure 5.10b and photovoltaic parameters are summarized in Table 5.2. The device without ZrO_2 spacer layer has a low PCE of 6.52%, featuring a low V_{oc} of 605 mV. The V_{oc} increased significantly to above 808 mV when ZrO_2 spacer layers were introduced into the devices. The perovskite films in devices with S100 ZrO_2 spacer layers have the best crystallinity and longest time-resolved PL lifetime, are expected to have excellent performance. However, S100 device has a particularly low V_{oc} of 808 mV and low PCE of 10.10%. This resulted from the poorest insulating ability of S100 ZrO_2 spacer layers. Due to the balance between perovskite films confined in ZrO_2 spacer layers and insulating properties of ZrO_2 spacer layers, FP-MPSCs with S20 ZrO_2 spacer layers had the best photovoltaic performance with PCE of 11.86%. It is common sense that FP-MPSCs with large perovskite
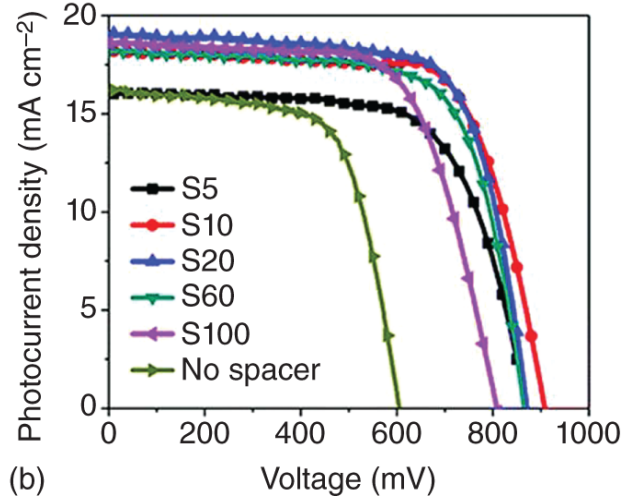
crystals with low trap density may achieve a V_{oc} approaches to the limit of theoretical value [21, 22]. The blueshift of the band-edge PL and decreased lifetime of perovskite in ZrO_2 spacer layers may explain the relatively low V_{oc} in FP-MPSCs (less than 1.0 V) relative to the V_{oc} of conventional planar PSCs (more than 1.1 V), because the size of perovskite crystals was larger than 500 nm in conventional planar PSCs. Therefore, ZrO_2 spacer layers with large pore sizes and excellent insulating properties are expected to further improve V_{oc} of FP-MPSCs.

Table 5.2 Photovoltaic parameters of FP-MPSCs based on ZrO_2 with different building block sizes.

Spacer layer	Time-resolved PL lifetime (ns)	R_I (Ω)	J_{sc} (mA cm^{-2})	V_{oc} (mV)	FF (%)	PCE (%)
No spacer	—	30	16.21	605	66	6.52
S5	0.5	1500	16.06	871	67	9.42
S10	8.4	970	18.26	908	71	11.77
S20	24.1	960	19.10	871	71	11.86
S60	37.2	800	18.19	865	70	11.08
S100	53.7	300	18.62	808	67	10.10
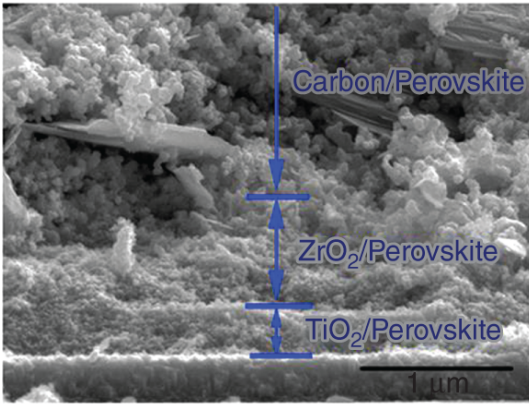
Figure 5.10 (a) Cross-sectional SEM image of FP-MPSCs with ZrO$_2$ as spacer layer. Source: Liu et al. [2]/Reproduced with permission from Elsevier. (b) *J–V* curves of FP-MPSCs based on ZrO$_2$ spacer layer with different building block sizes. Source: Reproduced with permission from Liu et al. [19]. Copyright 2019, Royal Society of Chemistry.

Hereafter, a detailed study from the points of insulating ability and impedance was conducted to clarify the mechanism on how thickness of ZrO$_2$ spacer layers affects the photovoltaic performance of FP-MPSCs. In monolithic DSSCs, the thickness of ZrO$_2$ spacer layers usually exceeds 4 µm, while in FP-MPSCs, due to the high absorption coefficient of perovskite, 1 µm-thick perovskite can completely absorb all visible light, and a thicker spacer layer will only increase the probability of carrier recombination. Figure 5.11a exhibits photovoltaic parameters depending on the thickness of ZrO$_2$ spacer layer in FP-MPSCs. Dark current (Figure 5.11b) is suppressed by increasing the thickness of ZrO$_2$ spacer layers, which agrees well with that V_{oc} reached a maximum value and remained stable when the thickness is above 2.64 µm. The V_{oc} has coincident trends with R_I. Therefore,

V_{oc} has a strong relationship with insulating properties of ZrO_2 spacer layers when other conditions are the same. J_{sc} reached a maximum value and remained stable when the thickness is above 3.31 µm. J_{sc} decreased with more than 5 µm-thick ZrO_2 spacer layer resulting from recombination, and PCE reached a maximum value when the thickness is about 4.84 µm. There is no doubt that the device without ZrO_2 spacer layers has the poorest V_{oc} due to the severe recombination of electrons and holes. The dependence of J_{sc} on thickness of ZrO_2 spacer layers and different trends between J_{sc} and V_{oc} indicates that perovskite confined in ZrO_2 spacer layers can generate charge carriers, playing a similar role in perovskite-capping layers in conventional mesoporous/planar bilayer PSCs. The FF was not linearly decreased with the increase of the thickness of ZrO_2 spacer layers, although the transport distance of charge carriers was increased. This result was different from DSSCs, where FF decreased linearly when the thickness of the spacer layer was increased.

(a)

(b)

(c)
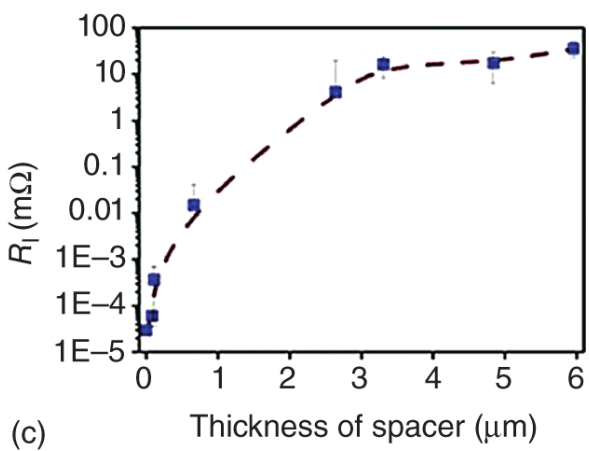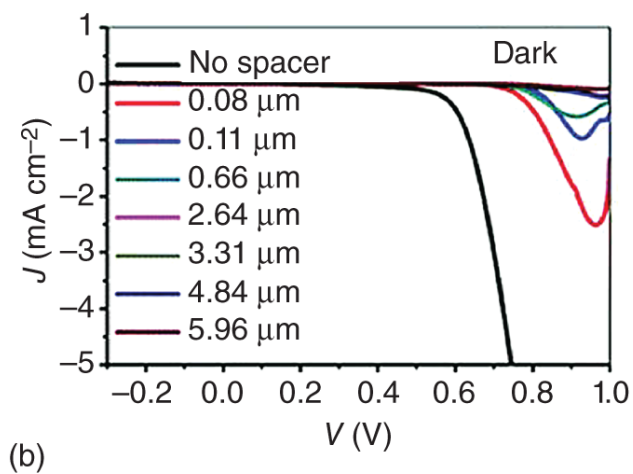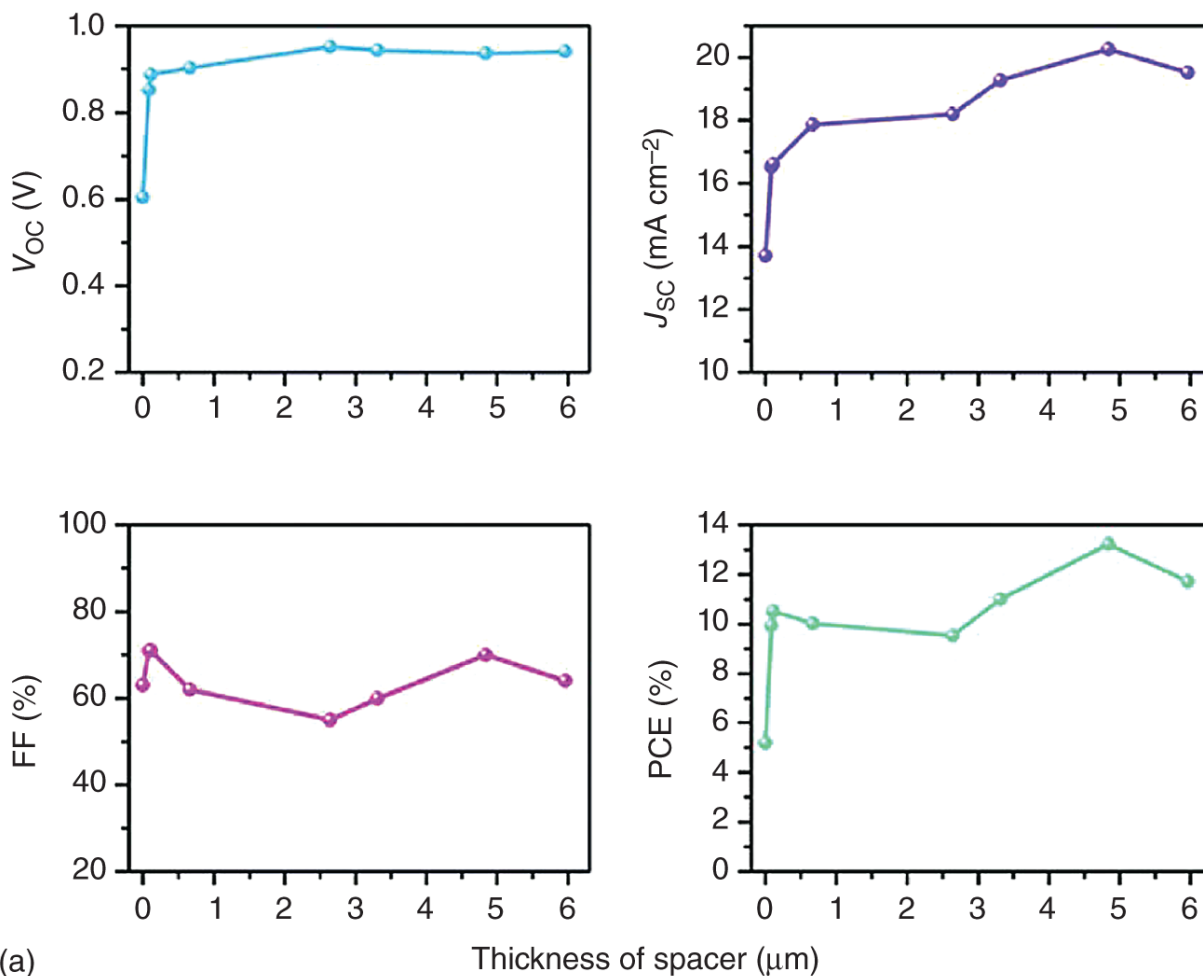
Figure 5.11 (a) Photovoltaic parameters and (b) dark current of FP-MPSCs based on different thickness of ZrO_2. (c) Insulating resistance (R_I) of ZrO_2 spacer layer with different thicknesses. Source: Reproduced with permission from Liu et al. [19]. Copyright 2019, Royal Society of Chemistry.

Impedance spectra (IS) were used to elucidate the relationship between the thickness of ZrO_2 spacer layer and the photovoltaic performance of FP-MPSCs, as well as the charge transport in ZrO_2 spacer layer. To assure reliability, IS were characterized by varying the thickness of ZrO_2 spacer layer, with or without mp-TiO_2 layers. The typical Nyquist plot and Bode plot of FP-MPSCs with different thicknesses of ZrO_2 spacer layer measured at 0.3 V, under weak illumination is plotted in Figure 5.12. Figure 5.13a–d presents the fitting resistance and capacitance, which was normalized with active area. Under the condition of weak light (0.1 sun), series resistances (R_S) are between 10 and 15 $\Omega\,cm^2$, remaining constant in the whole bias voltage range while high-frequency resistances ($R_{Perovskite}$) increased with increasing the thickness of ZrO_2 spacer layer and associating capacitance decreased with increasing the thickness of ZrO_2 spacer layer. Integrating IS features, the authors concluded that the high-frequency semicircle is related to both perovskites confined in ZrO_2 spacer layer and carbon/perovskite interface, and the change in high-frequency semicircle originates from the thickness varying of ZrO_2 spacer layer. It can be concluded that the thick ZrO_2 spacer layer of more than 2.5 μm with enough insulating ability would increase the charge carrier transport length through the spacer layer and cause severe recombination, considering the relatively smaller perovskite nanocrystals.
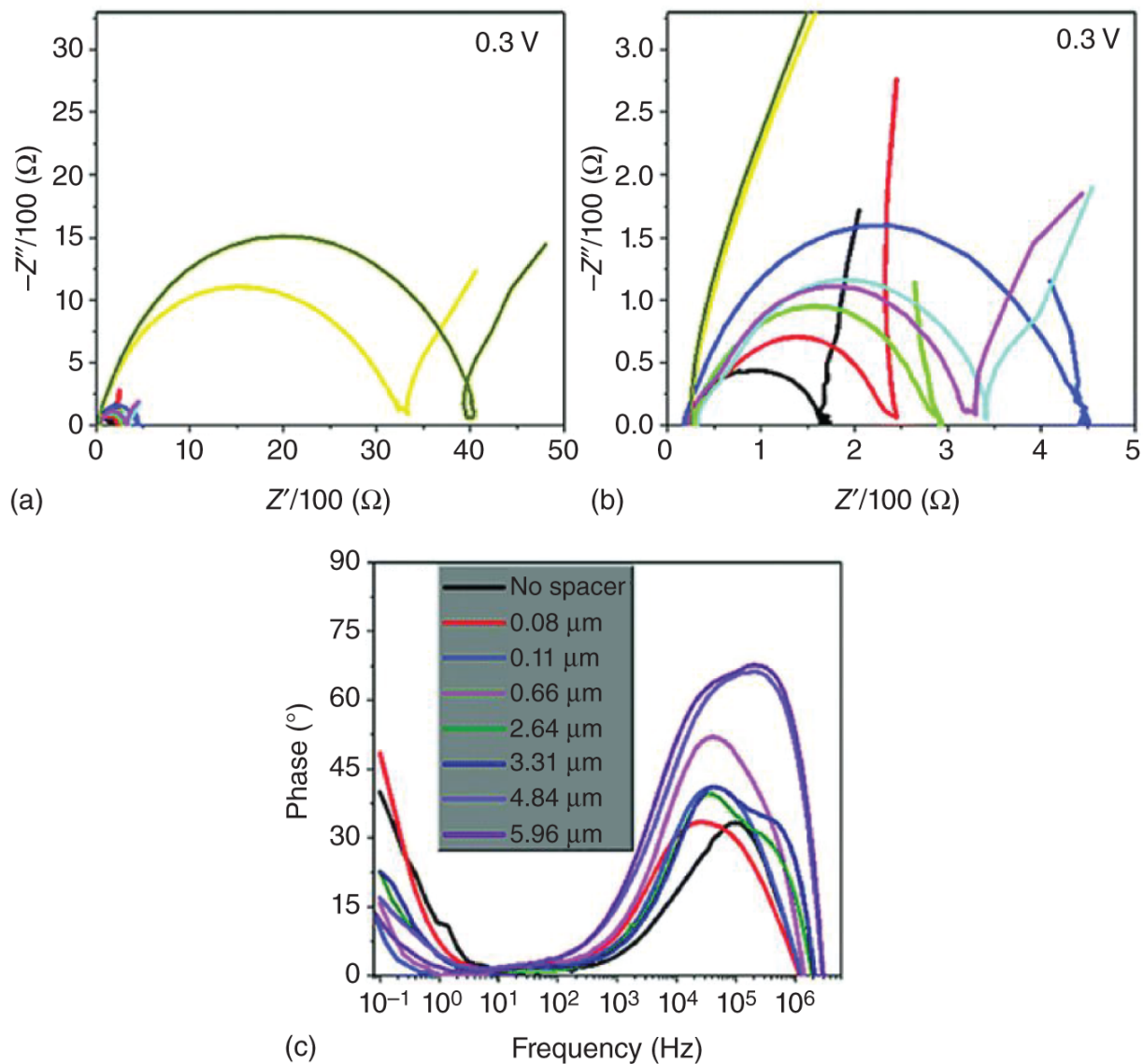
Figure 5.12 Nyquist plot (a, b) and Bode plot (c) of FP-MPSCs with different ZrO_2 spacer layer thickness measured at 0.3 V, under weak illumination (0.1 sun). Source: Reproduced with permission from Liu et al. [19]. Copyright 2019, Royal Society of Chemistry.
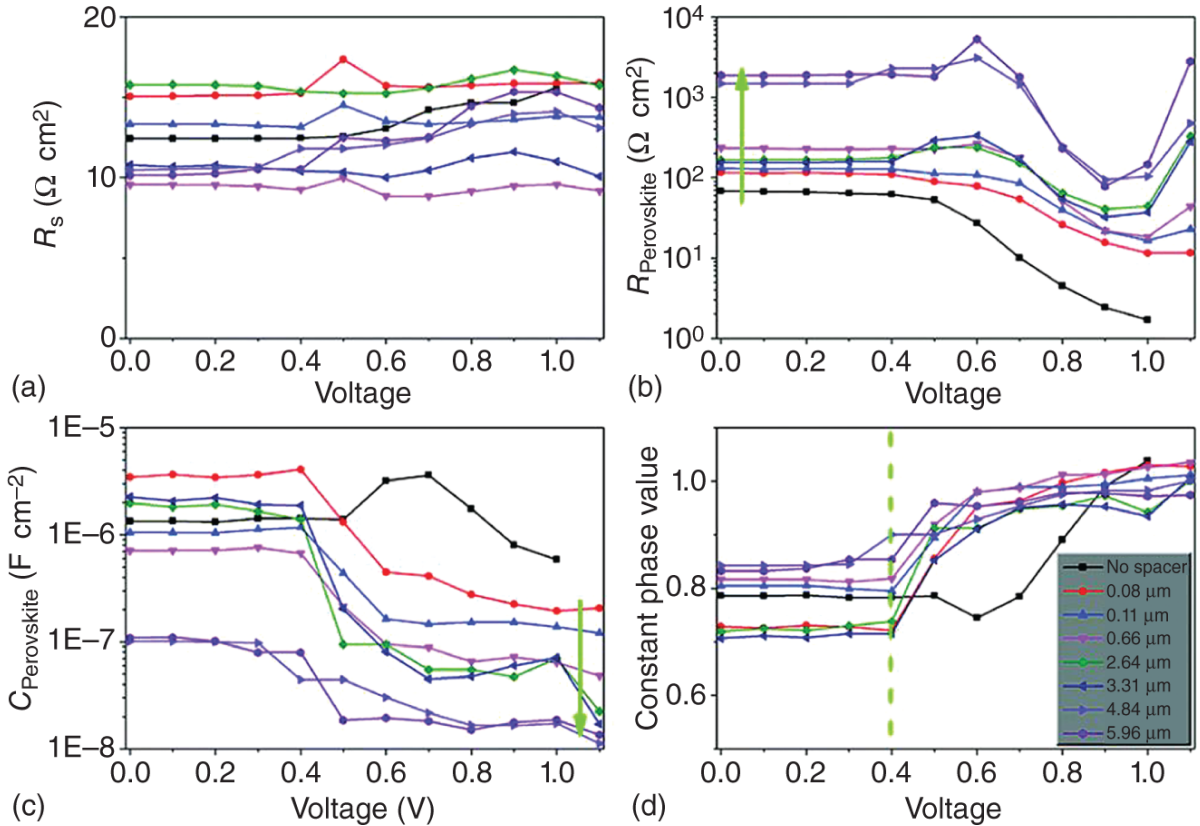
Figure 5.13 Parameters obtained from high frequency ($\sim 10^2$–10^6 Hz) semicircle IS analysis of FP-MPSCs with different ZrO_2 spacer layer thickness measured at between 1.1–0 V, under weak illumination (0.1 sun). (a) Series resistance (R_s). (b) Resistance related to perovskite ($R_{Perovskite}$). (c) Capacitance related to perovskite ($C_{Perovskite}$) and (d) associated constant phase value. Source: Reproduced with permission from Liu et al. [19]. Copyright 2019, Royal Society of Chemistry.

Combined with the exploration and analysis of the effect of the nanoparticle size and the layer thickness of ZrO_2, it can be concluded that the advanced insulating layer features pore size larger than 100 nm, high porosity, and simultaneously ideal insulating ability with layer thickness as thin as possible. In addition, the melting point of ZrO_2 is about 2700 °C, therefore, the particle size of ZrO_2 must be

small enough to be sintered at the allowable temperature, because the FTO glass substrates will soften when $T > 550$ °C.

5.3 Al$_2$O$_3$-Insulating Mesoscopic Layers

Alumina (Al$_2$O$_3$) is widely applied in electrolytic aluminum, ceramics, electronics, machinery, medicine, and many other applications. Al$_2$O$_3$ has many isomorphous crystals, mainly including three crystal configurations, namely α-Al$_2$O$_3$, β-Al$_2$O$_3$, γ-Al$_2$O$_3$, the properties of different crystal structures are completely different, in which α-Al$_2$O$_3$ is the most stable phase structure. In particular, α-Al$_2$O$_3$ is a wide bandgap insulator ($E_g \sim$ 9–11 eV) with excellent stability. Therefore, α-Al$_2$O$_3$ can be employed as an alternative insulating layer in hole-conductor-free FP-MPSCs. Similar to ZrO$_2$ spacer, Al$_2$O$_3$ spacer in FP-MPSCs is usually prepared from Al$_2$O$_3$ slurry through various deposition methods. The Al$_2$O$_3$ slurry could be commercially available or made from Al$_2$O$_3$ nanoparticles with ethyl cellulose as the binder and alpha-terpineol/ethanol as the solvent [23–26]. For example, Li et al. [27] applied Al$_2$O$_3$ as the spacer layer in FP-MPSCs by screen printing with the device structure of c-TiO$_2$/mp-TiO$_2$/mp-Al$_2$O$_3$/Carbon/single-walled carbon nanotubes (SWCNTs) (as shown in Figure 5.14), which is similar to the device structure used by Han's group. By doping the graphite/carbon counter electrode with a certain amount of SWCNTs, CH$_3$NH$_3$PbI$_3$-based FP-MPSCs achieved an improved PCE of 14.7% with a V_{oc} up to 1 V.
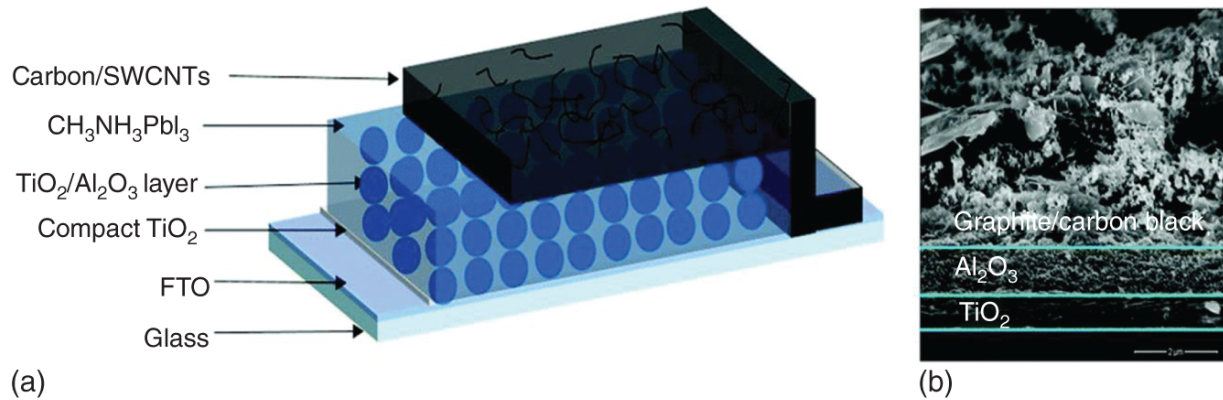
Figure 5.14 (a) Schematic architecture of FP-MPSCs based on Al_2O_3 as spacer layer and SWCNT-added graphite/Carbon as counter electrode. (b) Typical cross-sectional SEM image of Al_2O_3-based FP-MPSCs. Source: Li et al. [27]/Reproduced with permission from Royal Society of Chemistry.

In 2016, Chan et al. [28] adopted a mesoporous device configuration based on FTO/c-TiO_2/TiO_2/Al_2O_3/Carbon, in which Al_2O_3 was also used as spacer layer (see Figure 5.15). Notably, they developed a simple drop-casting method to grow dense and uniform perovskite nanocrystals via solvent extraction at room temperature without annealing. Then in 2017, Tsai et al. [24] fabricated FP-MPSCs with different precursor solvents, in which the device with N-methyl-2-pyrrolidone solvent achieved the best PCE of 15.0% with slow crystallization.

Commercial Al_2O_3 slurry was used by Huang et al. [26], and the Al_2O_3 layer was deposited by spin-coating a commercial Al_2O_3 slurry (Figure 5.16a). They investigated FP-MPSCs with different mesoporous spacer layers to understand the role of mesoporous materials in the performance of different devices, including mesoporous TiO_2 (mp-TiO_2), mesoporous Al_2O_3 (mp-Al_2O_3), mp-TiO_2 and mp-Al_2O_3 (mp-TiO_2 + Al_2O_3), mp-TiO_2, and mp-ZrO_2(mp-

$TiO_2 + ZrO_2$). As shown in Figure 5.16b, the characteristic diffraction peaks of $FA_{0.4}MA_{0.6}PbI_3$ perovskite do not change, indicating that different insulating mesoporous materials do not affect the crystal structure of mixed-cation perovskite. Also note that perovskite films deposited on the mp-$TiO_2 + Al_2O_3$ insulating mesoporous layer have better crystallinity than that of the other structures, which is more favorable for solar energy absorption and conversion.
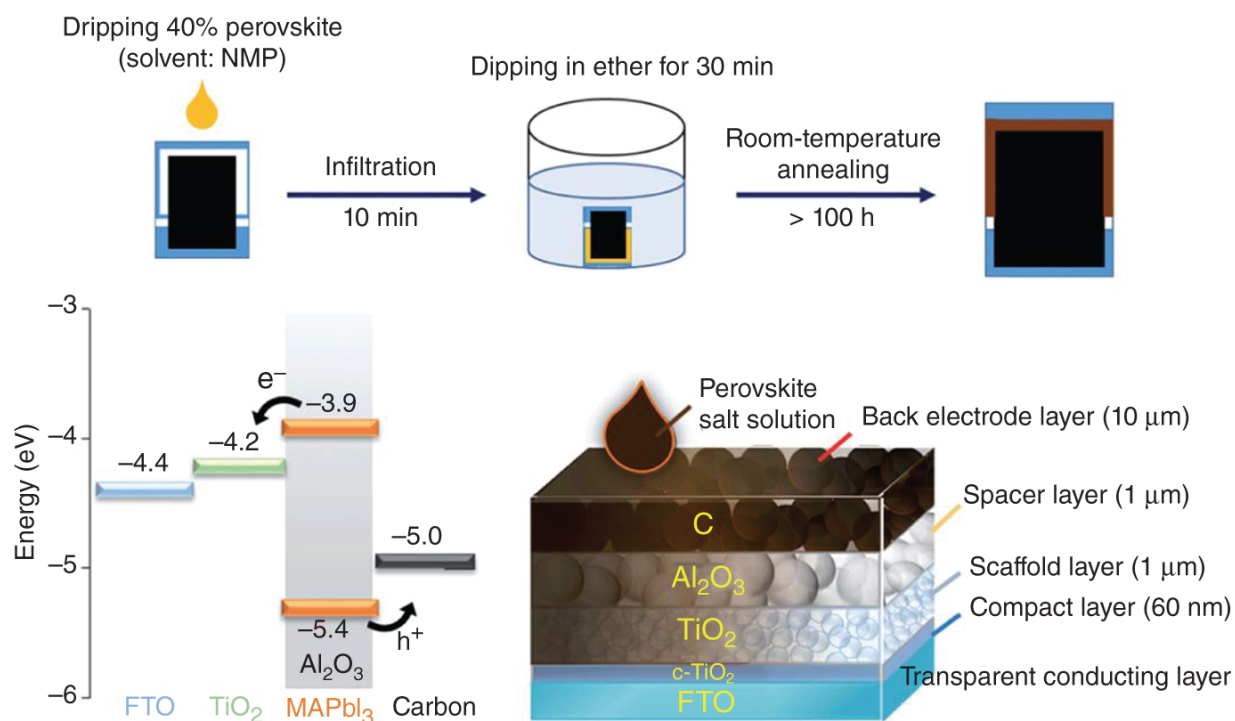

Figure 5.15 Schematic illustration to fabricate a carbon-based, hole-conductor-free FP-MPSCs using solvent-extraction crystal growth: the corresponding device configuration with Al_2O_3 as spacer layer and the energy level diagram of each functional layer. Source: Reproduced with permission from Chan et al. [28]. Copyright 2016, Royal Society of Chemistry.

Time-resolved PL was measured for FP-MPSCs with different mesoporous spacer layers (Figure 5.16c). The device (bl-TiO_2) shows the longest electron lifetime of

97.24 ns, indicating the charge carriers cannot be effectively transferred, resulting in inferior photovoltaic performance. The electron lifetime for devices with a spacer layer is shorter than those with a single-layer structure. The device with mp-TiO$_2$ + Al$_2$O$_3$ is 77.98 ns, which is shorter than that with mp-TiO$_2$ + ZrO$_2$ (87.11 ns), suggesting the employment of Al$_2$O$_3$ as the mesoporous spacer layer is more favorable for extracting electrons from perovskite. These are correspond with the device performance. Compared with the device (bl-TiO$_2$), the performances of devices with mesoporous scaffolds were significantly improved and the device performance with insulating layers (mp-TiO$_2$ + Al$_2$O$_3$ and mp-TiO$_2$ + ZrO$_2$) are better than that with single-layer mesoporous structures (mp-Al$_2$O$_3$ and mp-TiO$_2$), as shown in [Figure 5.16d]. This is because the mesoporous layers improve electron exaction and hinder the photogenerated electrons from recombining with holes, while the ZrO$_2$ or Al$_2$O$_3$ are insulating layers that separate the carbon cathode from the ETL. The performances of devices with mp-TiO$_2$ + Al$_2$O$_3$ and mp-TiO$_2$ + ZrO$_2$ are similar, although the device with the mp-TiO$_2$ + Al$_2$O$_3$ frame structure has the highest PCE of 11.3%, with V_{oc} of 0.97 V, and a J_{sc} of 23.77 mA cm^{-2}.

The mp-Al$_2$O$_3$ layer could be deposited by spin-coating diluted Al$_2$O$_3$ slurry. Instead of the conventional carbon electrode, Li et al. [29] fabricated Au: NiO$_x$ electrode that serves as HTM and conductive electrode ([Figure 5.17]). With the optimization of the annealing parameter and the modification of the mesoporous layer thickness (mp-TiO$_2$ and mp-Al$_2$O$_3$), a PCE of 10.25% was delivered. The mp-Al$_2$O$_3$ layer with a thickness in the order of micrometers always has an effective insulating ability, serving as the

spacer layer in FP-MPSCs, while it is in nanometers, it shows a blocking effect that could be served as a buffer layer or an interface modification film between the perovskite and electron transport material (ETM) [30–32]. This is because Al_2O_3 is an insulating material, which can hinder the photogenerated electrons from recombining with holes and reduce the electron–hole recombination rate.
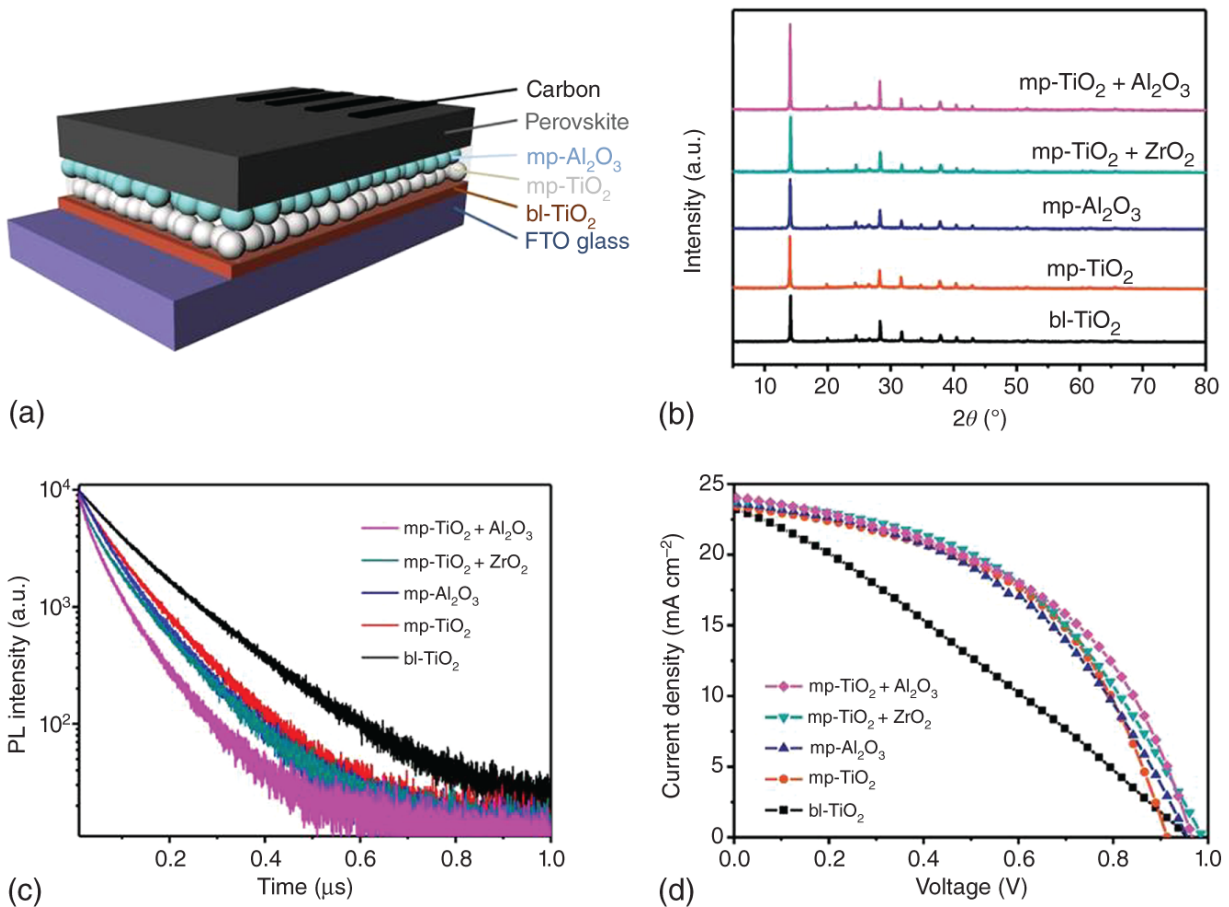
Figure 5.16 (a) Carbon-based, hole-conductor-free FP-MPSCs based on the device structure of FTO/bl-TiO$_2$/mp-TiO$_2$/mp-Al$_2$O$_3$/Perovskite/Carbon. (b) XRD patterns and (c) Time-resolved PL spectra of perovskite films fabricated on various spacer layers. (d) *J–V* curves of FP-MPSCs based on various spacer layers. Source: Reproduced with permission from Huang et al. [26]. Copyright 2019, Elsevier Ltd.
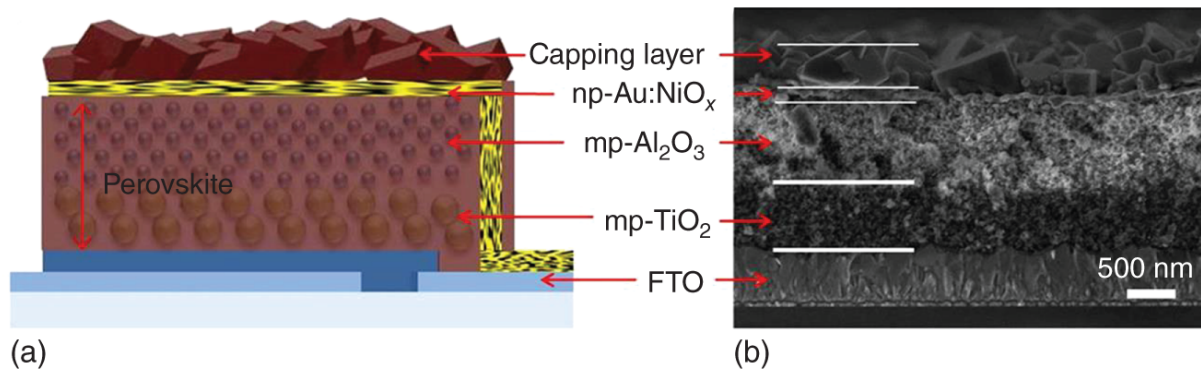
Figure 5.17 The schematic structure and cross-sectional SEM image of PSCs with Au:NiO$_x$ electrode. Source: Li et al. [29]/Reproduced with permission from American Chemical Society.

5.4 SiO$_2$-Insulating Mesoscopic Layers

SiO$_2$ is another wide bandgap insulator ($E_g \sim 9$–11 eV) and exhibits excellent optical transmittance in the visible-light range (400–800 nm). Therefore, SiO$_2$ could be employed as an alternative insulating layer in hole-conductor-free FP-MPSCs. In addition, SiO$_2$ is abundant on earth, where Si element is more than 1000 times of Zr element. The cost of FP-MPSCs could be further reduced if ZrO$_2$ is replaced by SiO$_2$.

In 2016, Cheng et al. [8] successfully introduced a mesoporous SiO$_2$ layer into FP-MPSCs by spin-coating method. The SiO$_2$ slurry was prepared by ball milling SiO$_2$ nanoparticles, ethyl cellulose, terpineol, and ethanol together for 24 hours. The as-prepared SiO$_2$ slurry was further diluted using single, double, triple, and quadruple amounts of ethanol to fabricate 1/2, 1/3, 1/4, and 1/5 SiO$_2$ slurry, respectively. As shown in Figure 5.18, (i) corresponds to electron transfer from CB of CH$_3$NH$_3$PbI$_3$ perovskite to TiO$_2$, (ii) corresponds to hole transfer from

valence band of $CH_3NH_3PbI_3$ perovskite to carbon electrode, (iii) charge recombination process from CB of TiO_2 to carbon electrode, when pinholes exist in the perovskite film. When FP-MPSCs are fabricated on double-layered TiO_2/SiO_2 layers, the insulating SiO_2 layer will separate the electron-conducting TiO_2 layer from the hole-conducting carbon electrode, thereby suppressing the charge recombination.

The variation of PCE with the thickness of SiO_2 layer is studied. The thickness of the SiO_2 film is about 190 nm for the 1/5 SiO_2 slurry and gradually increases with higher concentration of SiO_2 slurry. The maximum thickness of the SiO_2 film is 630 nm for the 1/2 SiO_2 slurry, but the film quality is not excellent. As the perovskite infiltrated into the mesoporous TiO_2 and SiO_2 layers, the thickness of the perovskite layer will increase with the thicker SiO_2 layer, inducing better light absorption. As shown in Figure 5.19, the device performance of FP-MPSCs with SiO_2 spacer layer is better than that without SiO_2 spacer layer, because the insulating SiO_2 layer separates the hole-conducting carbon electrode from the electron-conducting TiO_2 layer and reduces the charge recombination, leading to a larger V_{oc} and FF. However, the V_{oc} and FF decreased in FP-MPSCs with 1/2 SiO_2 slurry, probably due to the too-thick perovskite layer, which increases the charge recombination rate. When 1/3 SiO_2 slurry is employed, the insulating SiO_2 layer with a thickness of ~370 nm and device shows a superior PCE of ~12% and exhibits good long-time stability for 30 days.
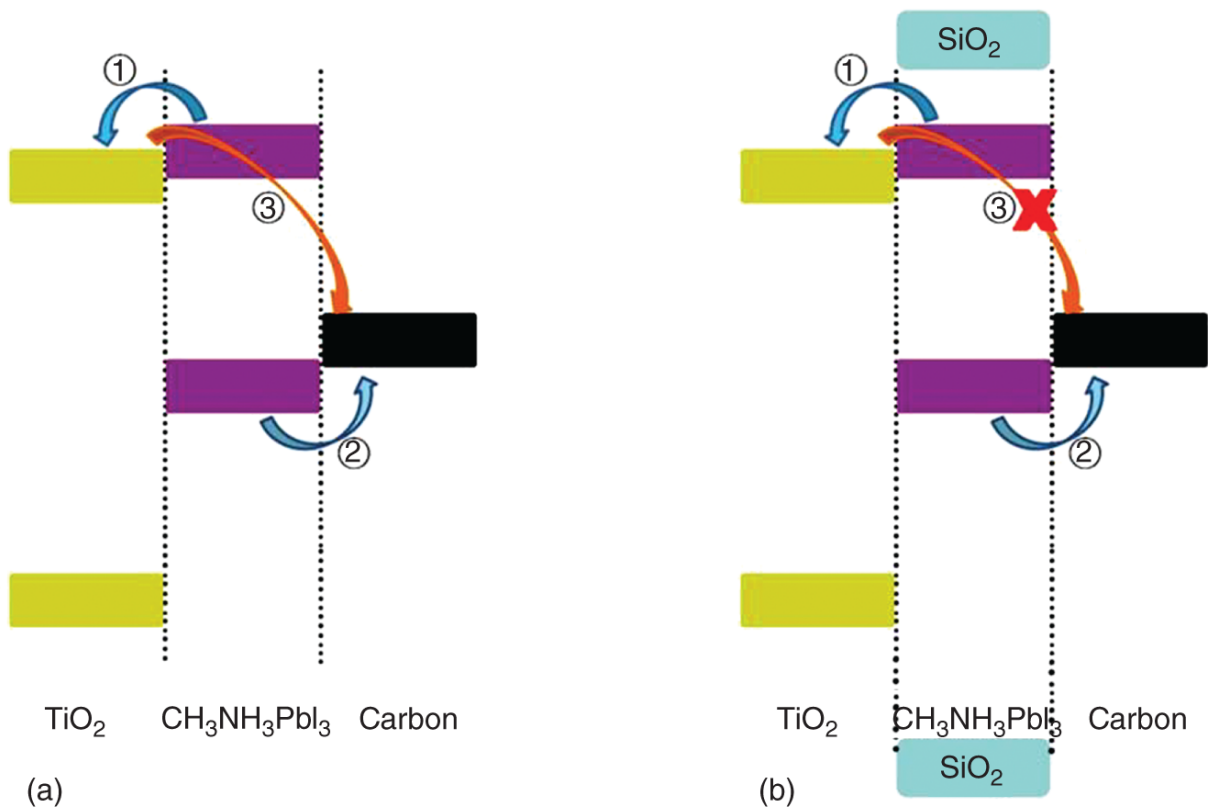
Figure 5.18 Schematic diagram showing the transfer process of electron and hole in hole-conductor-free FP-MPSCs fabricated on (a) TiO_2, and (b) TiO_2/SiO_2, respectively. Source: Reproduced with permission from Cheng et al. [8]. Copyright 2016, Elsevier Ltd.
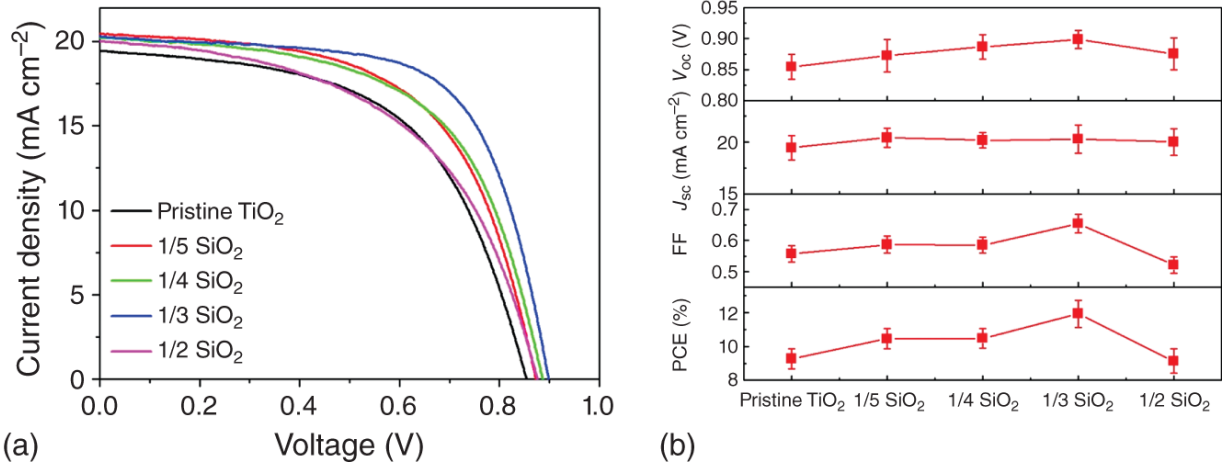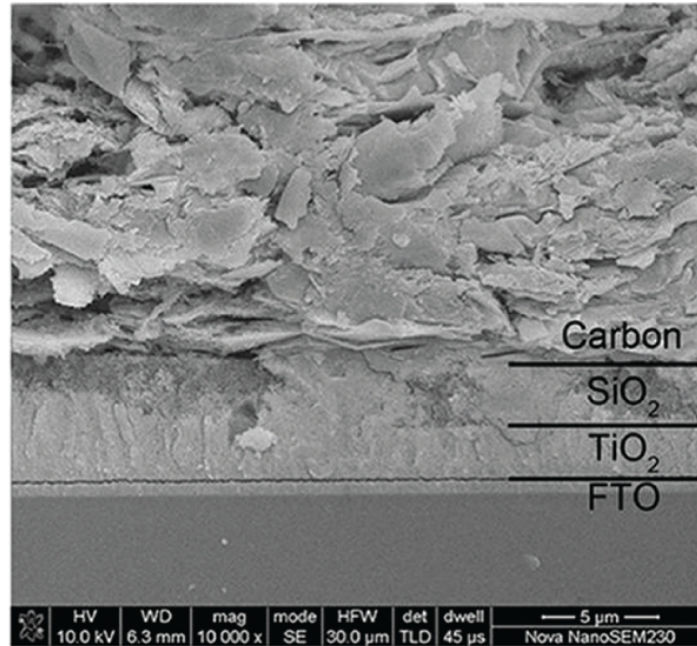
Figure 5.19 (a) *J–V* curves and (b) corresponding photovoltaic parameters of FP-MPSCs with pristine SiO_2 and TiO_2/SiO_2 spacer layers with different concentrations of SiO_2 paste. Source: Reproduced with permission from Cheng et al. [8]. Copyright 2016, Elsevier Ltd.

In 2018, Liu et al. [9] also used mesoporous SiO_2 layer in FP-MPSCs and discussed the effects of SiO_2 layer thickness on the device performances, while they used (5-AVA)$_x$MA$_{1-x}$PbI$_3$ perovskite. The schematic structure and the cross-sectional SEM image are described in Figure 5.20. The SiO_2 slurry was fabricated by ball-milling SiO_2 powders in ethanol with ethylene glycol (5% in volume ratio) as binder, which is a little different from Cheng's work [8]. In addition, they regulated the thickness of the SiO_2 layer by adjusting the concentration of the SiO_2 slurry.

From Figure 5.21a, without SiO_2 spacer, the device shows the worst performance (PCE ~ 5%) because of the direct contact between TiO_2 ETL and carbon electrode. After the introduction of SiO_2 spacer, device performance is boosted in all four parameters due to the retarded charge recombination contributed by the SiO_2 spacer. Besides, the relationship between device performance and the

concentration of SiO_2 slurry is displayed in [Figure 5.21b](#). The device performance is worse and disperses from 5% to 10% when the SiO_2 concentration is relatively higher (1.26 or 1.68 M). This is because the concentration of SiO_2 slurry determines the thickness of SiO_2 films. When the concentration of SiO_2 is 1.26 or 1.68 M, the SiO_2 film thickness is thicker than 2 µm and the films become uneven and crack (see [Figure 5.22](#)). At higher concentrations, SiO_2 spacer cracks and direct contact are possible between carbon electrode and TiO_2 ETL, which will cause charge recombination and deteriorate device performance. However, at relatively lower concentrations, uniform SiO_2 layer is obtained, which leads to a narrowed distribution of device performances. So, according to the device performance, the concentration of 0.84 M with a thickness of ~1.5 µm is optimum for SiO_2 spacer in this work.

(a)

(a) c-TiO$_2$ (b) mp-TiO$_2$ (c) mp-SiO$_2$

PVSK

(d) Carbon film   (e) Infiltration of PVSK precursor   (f) Device architecture
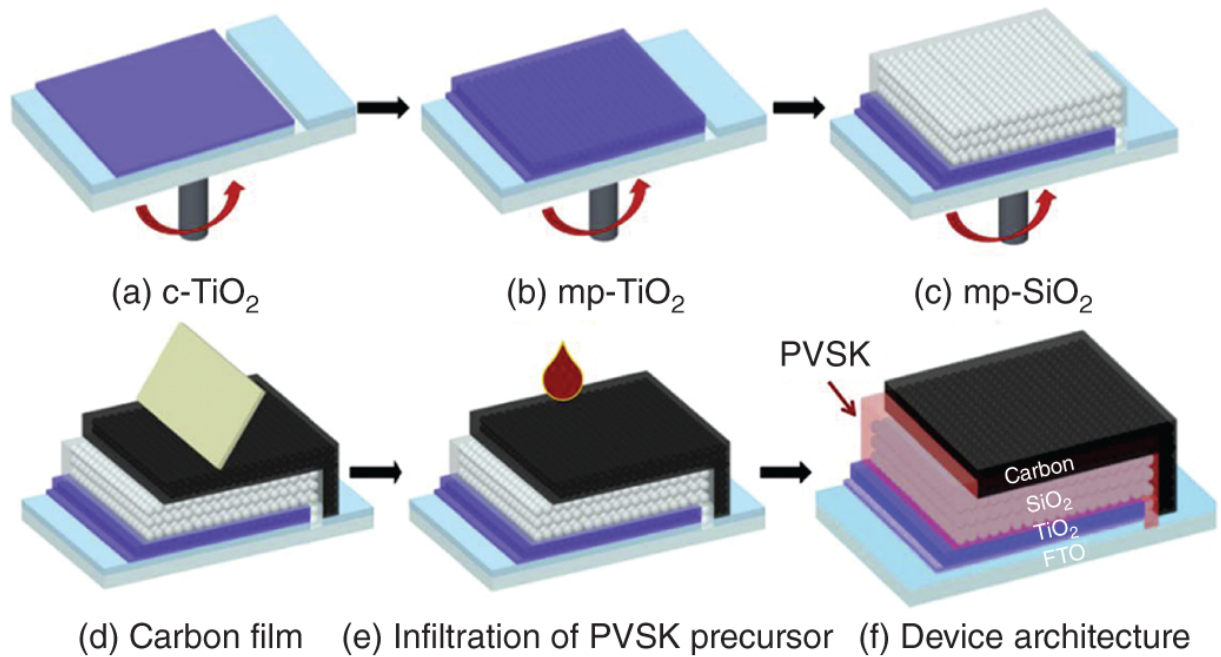
(b)

Figure 5.20 (a) Cross-sectional SEM image of FP-MPSCs based on SiO$_2$ spacer layer. (b) Preparation process of carbon-based, hole-conductor-free FP-MPSCs using SiO$_2$ as spacer layer. Source: Liu et al. [9]/Reproduced with permission from Elsevier.
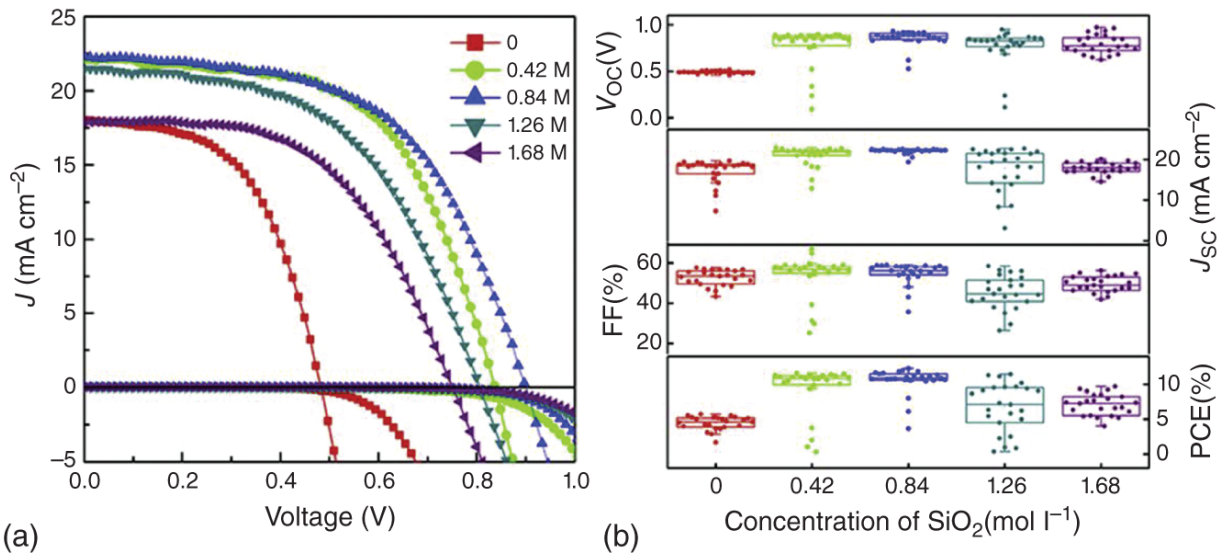
Figure 5.21 (a) *J–V* curves and (b) key photovoltaic parameters of FP-MPSCs with respect to different concentrations of SiO$_2$. Source: Reproduced with permission from Liu et al. [9]. Copyright 2018, Elsevier Ltd.
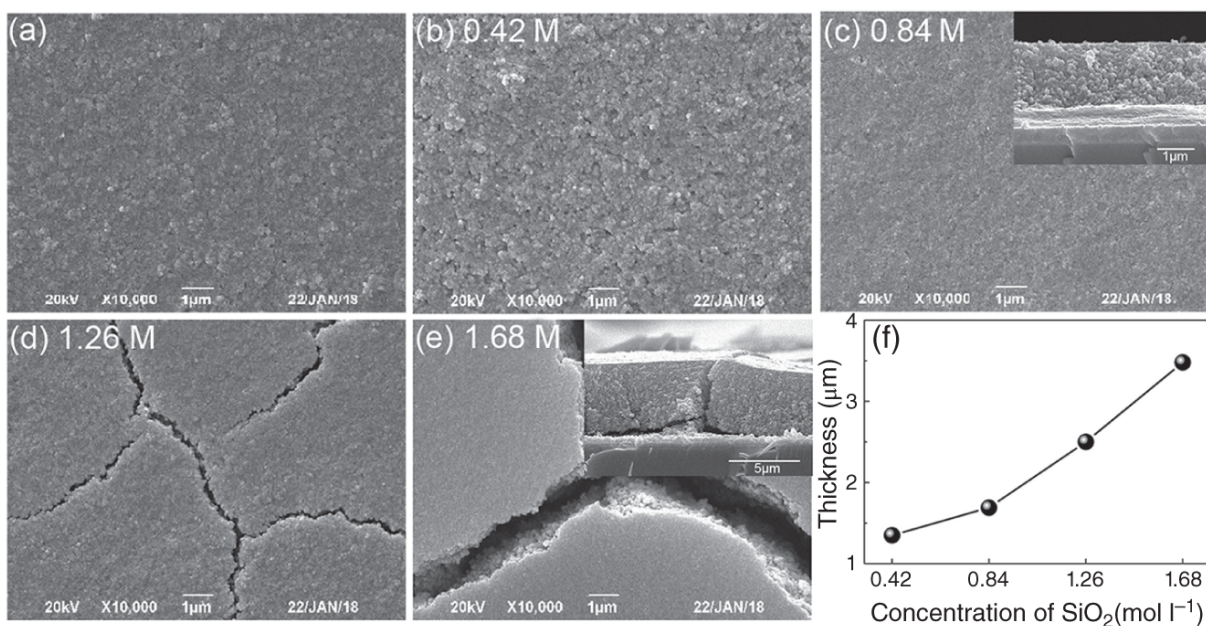
Figure 5.22 SEM images of (a) mp-TiO$_2$ film, SiO$_2$ layers prepared from slurry with a SiO$_2$ concentration of (b) 0.42 M, (c) 0.84 M, (d) 1.26 M, and (e) 1.68 M. Insets in (c) and (e) depict corresponding cross-section images. (f) Relationship between film thickness of SiO$_2$ layer and concentration of SiO$_2$. Source: Liu et al. [9]/Reproduced with permission from Elsevier.

Additionally, they compared the FP-MPSCs using SiO$_2$ or ZrO$_2$ as spacer layer. FP-MPSCs using either SiO$_2$ or ZrO$_2$ display similar PCE but with a slight difference in V_{oc}. SiO$_2$-based devices show a relatively higher V_{oc} than those based on ZrO$_2$ spacer. The stability of SiO$_2$-based FP-MPSCs (without encapsulation) had been tested. After being stored for 104 days (relative humidity 50~70%), 94.19% of the initial PCE was maintained. Moreover, operational stability was tested for 10 hours illumination, the PCE decreased to 86.93% for the first 1 hour, then remained unchanged for the afterward 9 hours. After being stored in the dark for 2 days, the PCE is recovered. The stability results indicate that SiO$_2$-based FP-MPSCs exhibit good stability.

5.5 Multilayer Insulating Mesoscopic Layers

5.5.1 Al_2O_3 + ZrO_2

In 2018, Xiong et al. [10] inserted an Al_2O_3 interlayer between TiO_2 ETL and ZrO_2 spacer layer. The Al_2O_3 interlayer not only serves as an insulating layer along with ZrO_2 but also modifies the interface between the ETM and perovskite, and thus effectively retards the recombination at ETM/perovskite and perovskite/carbon electrode interfaces simultaneously. Figure 5.23a displays the fabrication processes of bifunctional Al_2O_3 interlayer. Al thin film was deposited on mp-TiO_2 layers by vacuum evaporation. After the removal of organics in calcination, the Al film became porous Al_2O_3 film and some of Al_2O_3 went into the mesopore channels of TiO_2 layer to form a modification layer of TiO_2 ($TiO_2(Al_2O_3)$). Figure 5.23b,c show the schematic structure and energy level diagram of Al_2O_3 interlayer-based FP-MPSCs, respectively. It is worth noting that both the Al_2O_3 capping layer and the ZrO_2 film serve as spacer layers to separate the ETM and carbon electrode, while the Al_2O_3 interlayer modified the interface of ETM/perovskite.
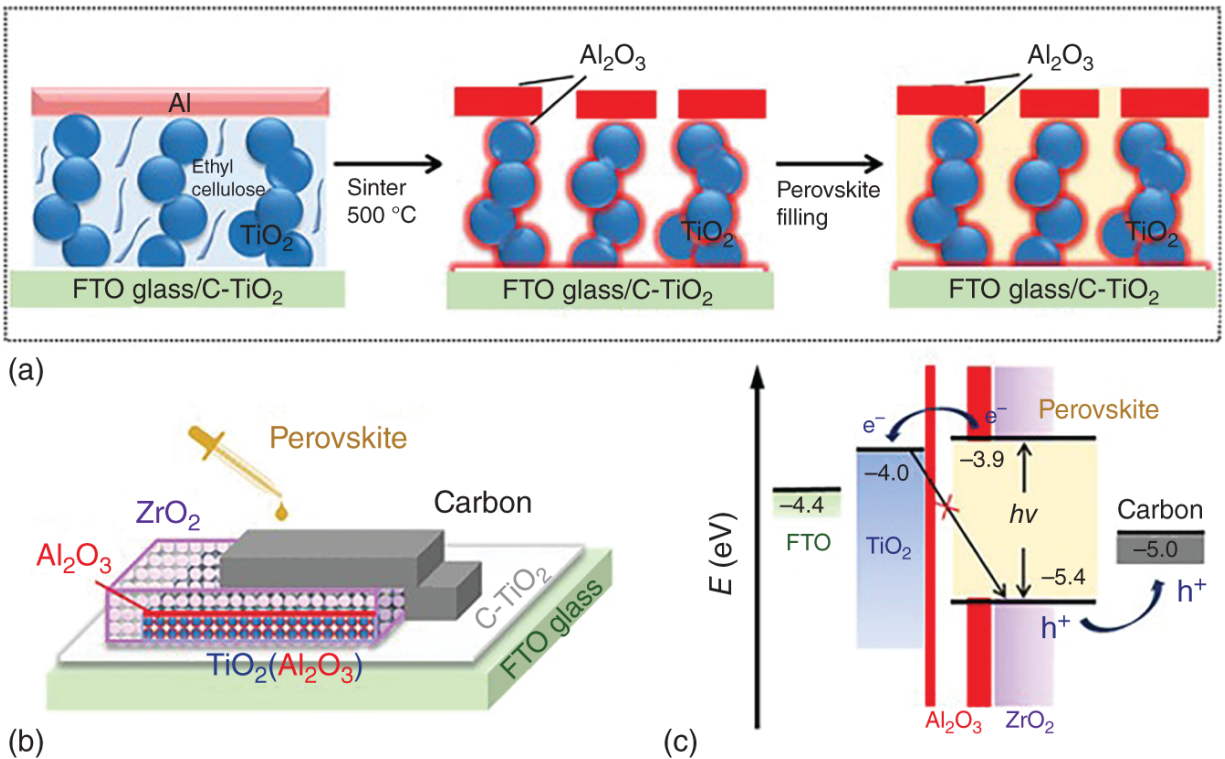
Figure 5.23 (a) Formation processes of bifunctional Al_2O_3 interlayer; schematic structure (b) and energy band diagram (c) of FP-MPSCs with Al_2O_3 interlayer. Source: Reproduced with permission from Xiong et al. [10]. Copyright 2018, Wiley-VCH.

From the XPS and XRD results in Figure 5.24a–d, the Al_2O_3-modified TiO_2 ETM did not affect the crystallization of perovskite. However, the charge transport character at ETM/perovskite was influenced, as suggested by time-resolved and steady-state PL results (Figure 5.24e,f).

By varying the thickness of Al_2O_3 and ZrO_2 films, the device performance was discussed (Figure 5.25a). With the introduction of an Al_2O_3 interlayer, the V_{oc} increased, then decreased a little with the increase of ZrO_2 thickness. This is because the increase of ZrO_2 thickness will improve the insulating ability to retard recombination at the perovskite/carbon interface, however, the transport

distance of carriers will increase which adds the possibility of recombination if the ZrO_2 thickness is too large. Alternatively, with the increase of Al_2O_3 thickness, the V_{oc} increased quickly and then decreased sharply. This is because the insulating ability boosts with the increase of Al_2O_3 thickness, but the thicker Al_2O_3 makes the device difficult to be infiltrated by perovskite. The cross-sectional images of a typical FP-MPSCS with Al_2O_3 interlayer are displayed in Figure 5.25b. It is easily found that the Al_2O_3 interlayer is much more compact than the mesoporous ZrO_2 layers, which is conducive to the improvement of device performance. *J–V* curves of FP-MPSCs based on various architectures were taken, as shown in Figure 5.25c. Without the spacer layer, the FP-MPSCs shows the worst performance due to the quick recombination at perovskite/carbon interface and device performance booted after the introduction of the spacer layer, which reveals the critical role of spacer in hole-conductor-free FP-MPSCs. Specifically, the device with 10 nm Al_2O_3 interlayer (60 nm in real thickness) shows the same V_{oc} as 1 μm ZrO_2 spacer, indicating the excellent insulating ability of Al_2O_3 interlayer. The highest V_{oc} of 950 mV is obtained for FP-MPSCs with 10 nm Al_2O_3 interlayer and 1 μm ZrO_2, as it has the most insulated spacer layer with the modified TiO_2 surface.
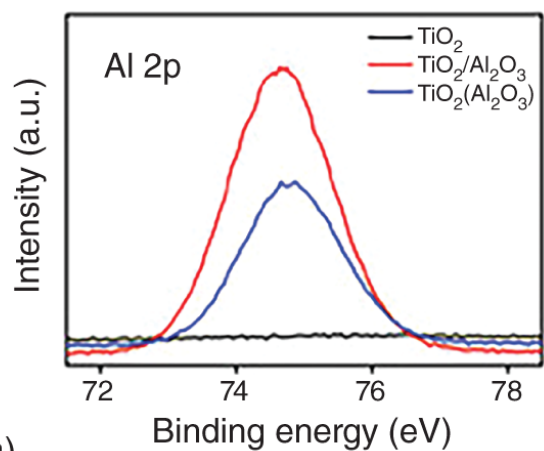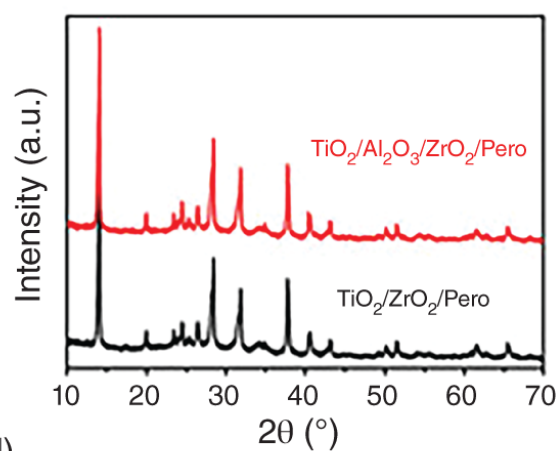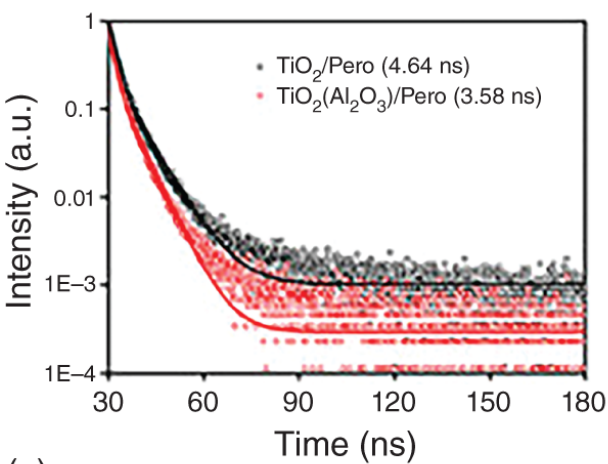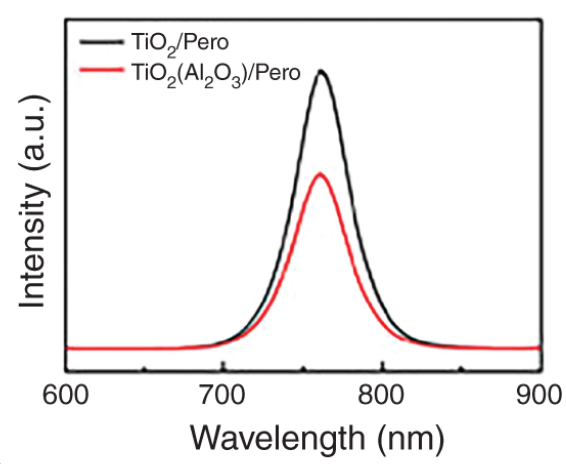
(a)
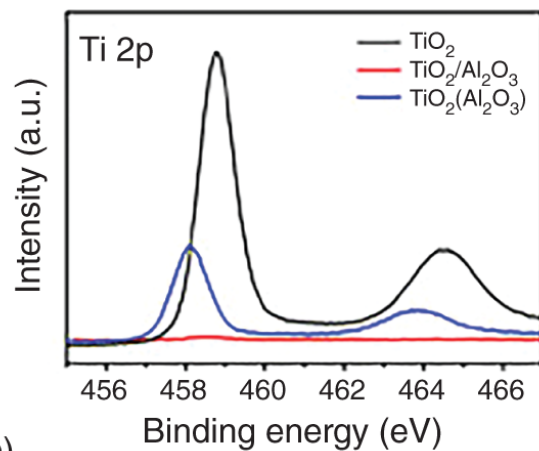
(b)
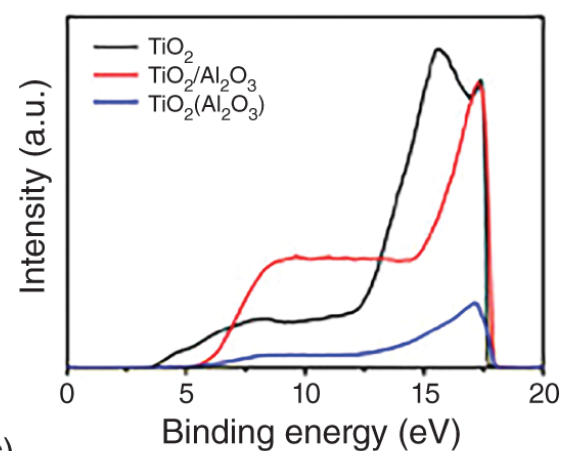
(c)

(d)

(e)

(f)

Figure 5.24 XPS spectra of Al 2p (a) and Ti 2p (b) and UPS spectra (c) for TiO_2, TiO_2/Al_2O_3, and $TiO_2(Al_2O_3)$ films; (d) XRD spectra of $TiO_2/Al_2O_3/ZrO_2/Pero$ and $TiO_2/ZrO_2/Pero$ films; (e) time-resolved PL decays and (f) steady-state PL spectra of $TiO_2/Pero$ and $TiO_2(Al_2O_3)/Pero$ films. Source: Reproduced with permission from Xiong et al. [10]. Copyright 2018, Wiley-VCH.

5.5.2 Al_2O_3 + NiO

Nickel oxide (NiO), a p-type semiconductor with wide bandgap, favorable thermal, and chemical stability, is widely employed as an electron blocking layer due to its high CB (−1.8 eV). Wang et al. [5] prepared FP-MPSCs with the structure of $TiO_2/Al_2O_3/NiO/carbon$ (Figure 5.26). Both NiO and Al_2O_3 films serve as the spacer layer to separate the TiO_2 and carbon electrode, while NiO film also plays a role of the HTL in the system. The device based on $TiO_2/Al_2O_3/NiO/carbon$ (device B) achieves a J_{sc} of 21.62 mA cm^{-2}, FF of 0.76, V_{oc} of 915 mV, achieving a PCE of 15.03%. For comparison, the device with $TiO_2/Al_2O_3/carbon$ (device A) shows a lower PCE of 11.20% (J_{sc} = 17.59 mA cm^{-2}, FF = 0.71, and V_{oc} = 896 mV). In FP-MPSCs, the V_{oc} can be ascribed to the energy level difference between the electronic Fermi level in the TiO_2 and the hole Fermi level in the excited $MAPbI_3$ formed at the $MAPbI_3/TiO_2$ junction. The NiO spacer layer effectively accelerates the charge extraction to the external circuit, which improves the cell performance. Additionally, the PCE of unsealed device B lowered to 93.2% of the initial value when they were stored in ambient atmosphere at room temperature (relative humidity 40%) without light for 1000

hours. It also exhibited good stability in an oven at 60 °C in the dark (relative humidity 10%).
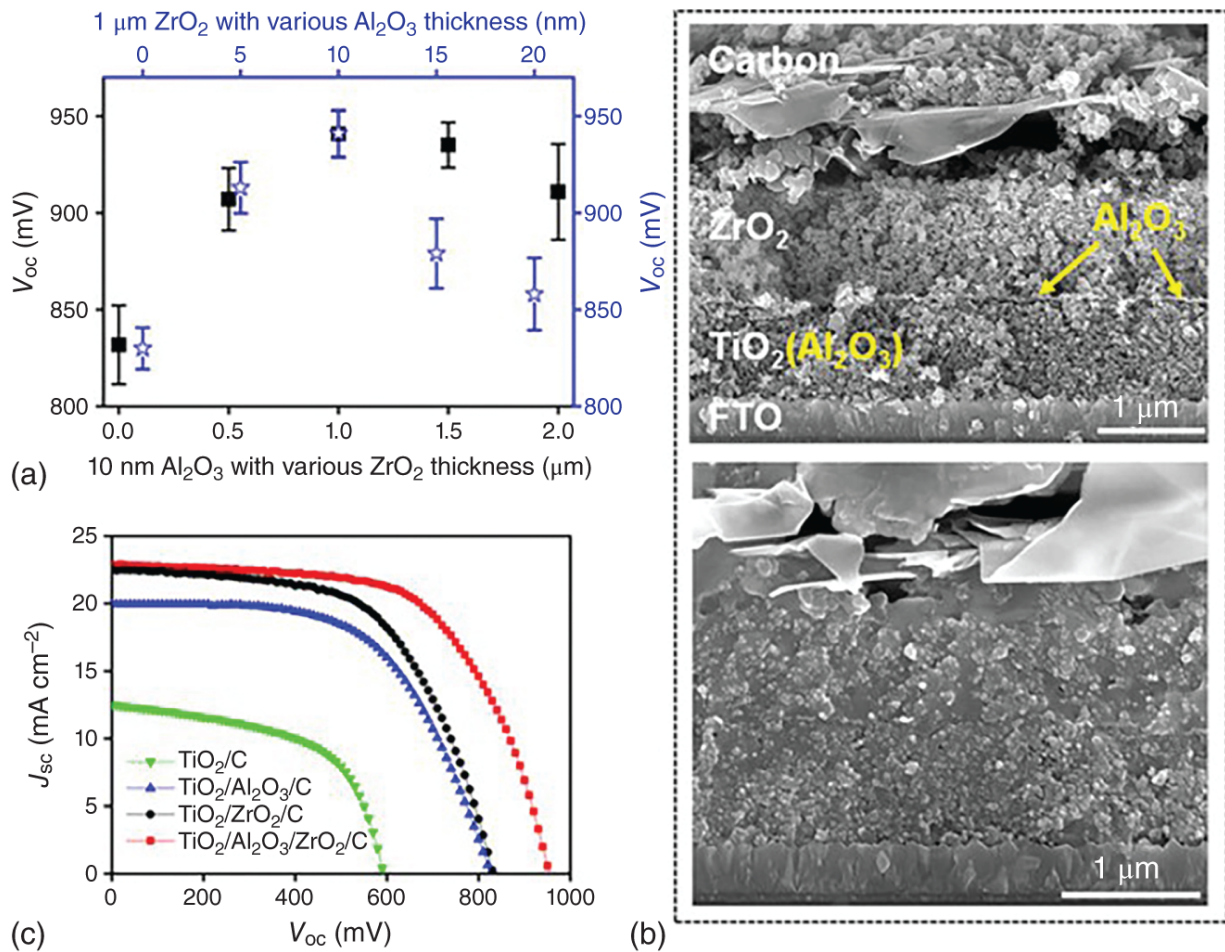

Figure 5.25 (a) V_{oc} as a function of various Al_2O_3/ZrO_2 thickness. (b) Cross-sectional SEM images of FP-MPSCs with Al_2O_3 interlayer before and after perovskite infiltration. (c) J–V curves of FP-MPSCs with various spacer layers. Source: Xiong et al. [10]/Reproduced with permission from John Wiley & Sons, Inc.
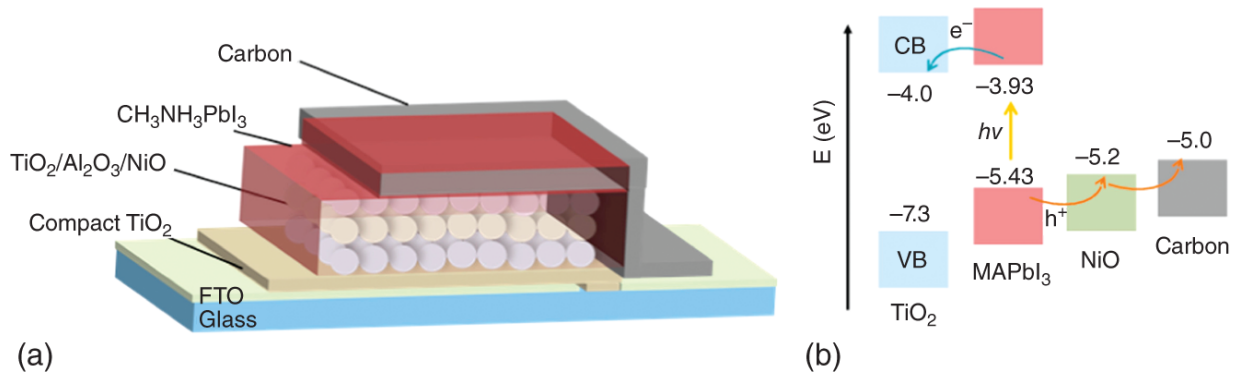
Figure 5.26 (a) Schematic structure of FP-MPSCs based on the structure of $TiO_2/Al_2O_3/NiO/carbon$ ($CH_3NH_3PbI_3$). (b) Energy band diagram of the fabricated FP-MPSCs. Source: Reproduced with permission from Cao et al. [5]. Copyright 2015, Elsevier Ltd.
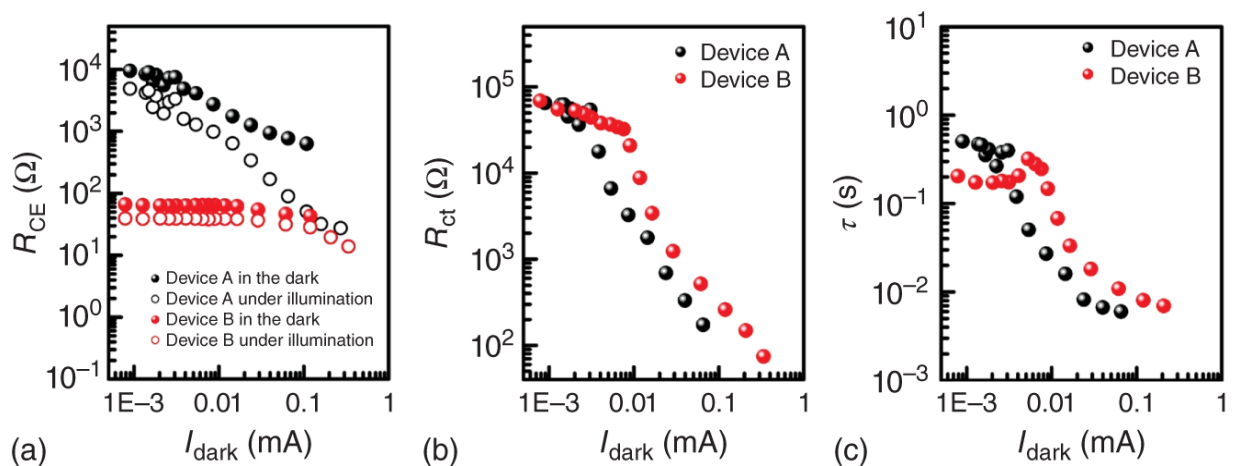

Figure 5.27 (a) R_{CE} at the counter electrode interface, (b) R_{ct}, and (c) the apparent electron lifetime (τ) at the $TiO_2/MAPbI_3$ interface obtained from impedance measurements on $TiO_2/Al_2O_3/carbon$ ($MAPbI_3$) (device A, black) and $TiO_2/Al_2O_3/NiO/carbon$ ($MAPbI_3$) (device B, red) in the dark. Source: Reproduced with permission from Cao et al. [5]. Copyright 2015, Elsevier Ltd.

In Figure 5.27a, device B presents a smaller charge transfer resistance (R_{CE}) at the counter electrode interface, indicating a faster transport of holes from perovskite and

NiO to carbon electrode, which contributed by a better interfacial connection between NiO/carbon than Al_2O_3/carbon. In [Figure 5.27b](#), device B presents a larger interfacial charge recombination resistance (R_{ct}) at the TiO_2/MAPbI$_3$ junction. The clear electron lifetime τ shows an exponential decrease with increasing current in [Figure 5.27c](#). An increased lifetime was observed when the interlayer of NiO was adopted compared to the device structure without the NiO layer. Therefore, it is concluded that the performance enhancement of device B could be mainly derived from the higher carrier lifetime in the device.

Two years later, Liu et al. [25] applied the triple-cation perovskite $Cs_{0.05}(FA_{0.4}MA_{0.6})_{0.95}\, PbI_{2.8}Br_{0.2}$ instead of $CH_3NH_3PbI_3$ in FP-MPSCs based on the TiO_2/Al_2O_3/NiO/carbon structure. Notably, they found that partial substitution of FA/MA with Cs increased the bandgap and exciton binding energy of $Cs_x(FA_{0.4}MA_{0.6})_{1-x}PbI_{2.8}Br_{0.2}$ perovskite, and an optimal PCE of 17.02% could be obtained. This work once again demonstrates the potential of Al_2O_3/NiO based mesoporous layered structures to fabricate highly efficient FP-MPSCs.

5.5.3 ZrO$_2$ + NiO

Wang et al. [33] investigated efficient FP-MPSCs with a device structure of TiO_2/ZrO_2/NiO/carbon and an appreciated PCE of 14.9% ([Figure 5.28](#)). Similar to the device structure based on mesoscopic TiO_2/Al_2O_3/NiO/carbon, both NiO and ZrO_2 serve as insulating layers separating the TiO_2 and carbon electrode, while the NiO layer also functions as a HTL. The PCE of the unsealed device maintained over 93% of its initial value when the device was stored in ambient atmosphere at room

temperature (relative humidity ~40%) without light for 1000 hours, while lowered to 80% of its initial value after thermal aging over 1000 hours at 60 °C in the dark. Additionally, in this study, three devices were investigated to obtain a systematic comparison of interfacial recombination. Devices A, B, and C are based on $TiO_2/ZrO_2/carbon$, $TiO_2/NiO/carbon$, and $TiO_2/ZrO_2/NiO/carbon$, respectively. This study indicates that the p-type semiconductor NiO possesses the capability as a hole selective contact in FP-MPSCs with perfect photovoltaic performance.
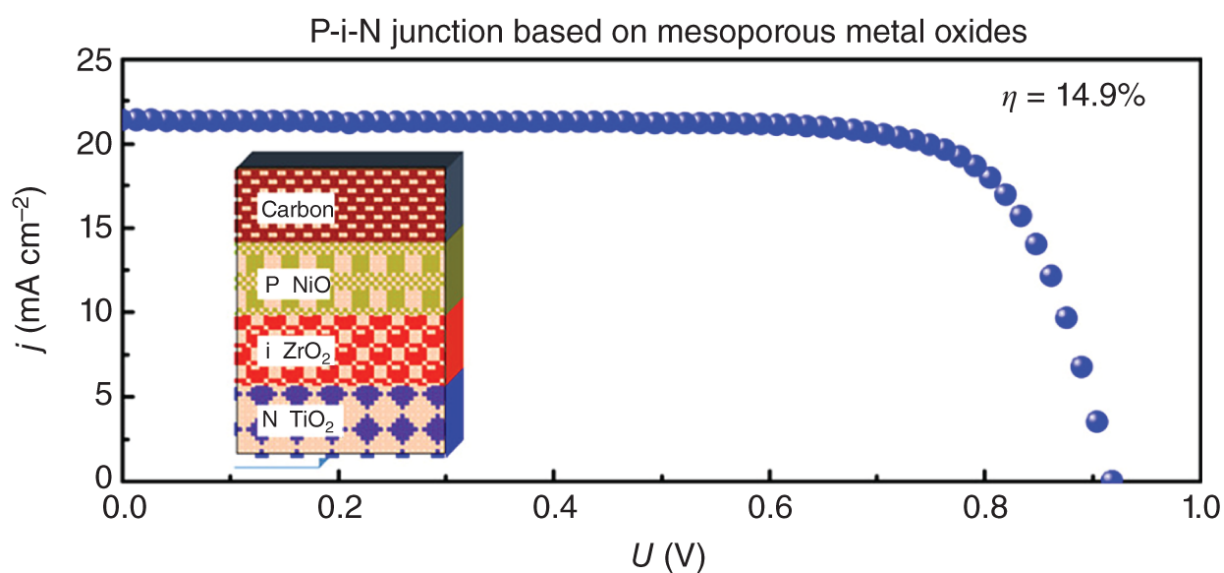

Figure 5.28 *J–V* curve and schematic structure of FP-MPSCs based on $TiO_2/ZrO_2/NiO/Carbon$ device structure. Source: Reproduced with permission from Xu et al. [33]. Copyright 2015, American Chemical Society.

Impedance measurements are conducted, and the parameters are shown in Figure 5.29. From Figure 5.29a, the interfacial recombination resistance $\boldsymbol{R_{ct}}\boldsymbol{1}$ shows little change for all devices when the applied bias is less than −0.75 V, while it decreases exponentially with bias after −0.75 V, because of the elimination of the depleted region

width by increasing the bias on devices. [Figure 5.29b](#) shows the calculated charge recombination lifetime $\tau_e 1$ as a function of the applied bias and the interfacial recombination at the $MAPbI_3/TiO_2$ interface shows a millisecond time scale. In [Figure 5.29c](#), the relation between the recombination resistance $\boldsymbol{R_{ct}}2$ at the $MAPbI_3/NiO$ interface and the applied potential shows similar characteristics as that at $TiO_2/MAPbI_3$ interface, although the value of $\boldsymbol{R_{ct}}2$ is about 10 times larger than that of $\boldsymbol{R_{ct}}1$. [Figure 5.29d](#) presents the calculated lifetime $\tau_e 2$ for the recombination process at the $MAPbI_3/NiO$ interface. We observed that the recombination lifetime $\tau_e 2$ was about 2 orders of magnitude larger than the lifetime $\tau_e 1$ at the $MAPbI_3/TiO_2$ interface. This result indicates that the recombination at the $MAPbI_3/TiO_2$ interface largely determines the interfacial recombination of devices. The mesoporous NiO layer is believed to efficiently accelerate charge extraction to external circuits.
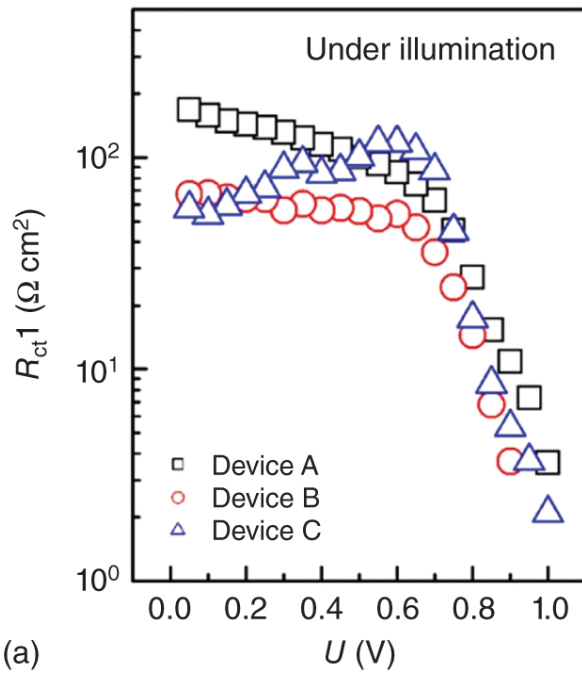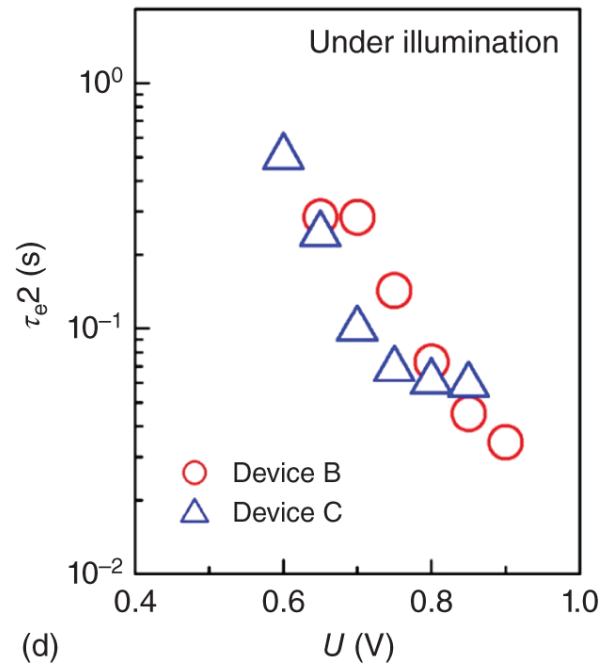
(a)
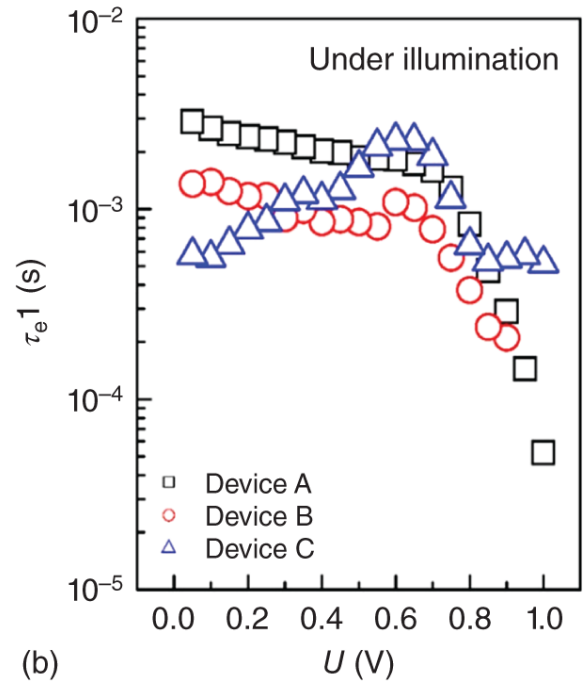
(b)
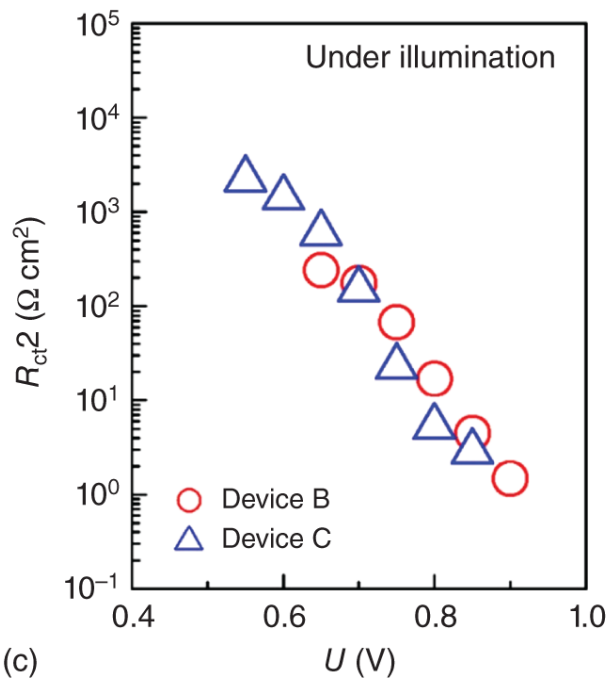
(c)

(d)

Figure 5.29 Derived equivalent circuit components obtained from impedance under light for different devices: (a) the recombination resistance $R_{ct}1$ at the MAPbI$_3$/TiO$_2$ interface, (b) the charge recombination lifetime τ_e1. Derived equivalent circuit components obtained from impedance under dark for different devices: (c) The recombination resistance $R_{ct}2$ at the MAPbI$_3$/TiO$_2$ interface and (d) the charge recombination lifetime τ_e2. Source: Reproduced with permission from Xu et al. [33]. Copyright 2015, American Chemical Society.

5.6 Conclusion and Perspective

Since the advent of carbon-based hole-conductor-free FP-MPSCs, great progress has been made in the research and application of insulating layers. Based on above deep understanding of different insulating materials applied in FP-MPSCs, the bottlenecks of current insulating layers and infiltrated perovskite are summarized in the left picture of Figure 5.30. Perovskite embedded in mesoscopic insulating layers are composed of crystals with the size of tens of nanometers. The limited charge transport capacity in quantum dots will damage the high performance of FP-MPSCs due to the serious charge recombination. Furthermore, the thickness of the insulating layer must be several micrometers to guarantee the insulating ability, which further hinders the charge transport to the charge-selective layer. These two disruptive factors severely restrict the potential performance of hole-conductor-free FP-MPSCs.
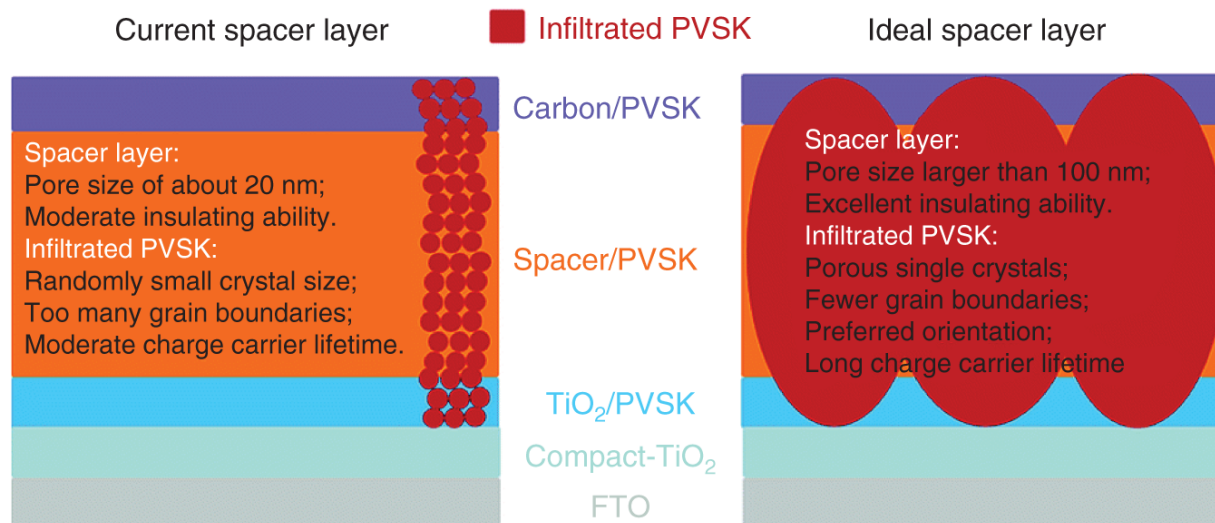
Figure 5.30 Illustration to show problems of current spacer layer and perovskite (PVSK) infiltrated in spacer layer, and proposed features of ideal spacer layer and infiltrated PVSK. Source: Reproduced with permission from Liu et al. [19]. Copyright 2019, Royal Society of Chemistry.

Based on above discussion, the proposed characteristics of ideal spacer layer and infiltrated perovskite are illustrated in the right picture of Figure 5.30. For infiltrated perovskite, porous single-crystal perovskite films grown in mesoscopic spacer layers are more favorable for obtaining high-performance FP-MPSCs. For example, Kollek et al. [34] realized the preparation of porous single-crystal $CH_3NH_3PbI_3$ perovskite by adding triethylene glycol (TEG) additive into $CH_3NH_3PbI_3$ perovskite precursors (Figure 5.31). Therefore, exploring feasible methods to grow porous single-crystal perovskite films with few defects and high mobility in mesoscopic ordered spacer layers will help to further improve the photovoltaic performance of FP-MPSCs.

For ideal insulating layers of efficient FP-MPSCs, future research directions are summarized in the following three aspects. First, there is unquestionable that the photovoltaic performance of FP-MPSCs has close connection with

insulating ability of spacer layers. The ideal insulating property depends mainly on high porosity, appropriate pore size, interparticle connection, uniform morphology without cracking, and simultaneously thickness as thin as possible. Second, although stable insulating materials such as ZrO_2, Al_2O_3, SiO_2, and their complexes have been widely used in FP-MPSCs in previous studies, it is urgent to explore more excellent insulating materials for efficient FP-MPSCs. Third, to further reduce the cost of FP-MPSCs and improve their operational stability for large-scale applications, it is a smart strategy to design new device configuration (e.g. developing efficient FP-MPSCs without the spacer layer) and optimize fabrication procedure (e.g. introducing multilayer structure that serves as the spacer layer and hole conductor to improve the hole extraction, etc.)
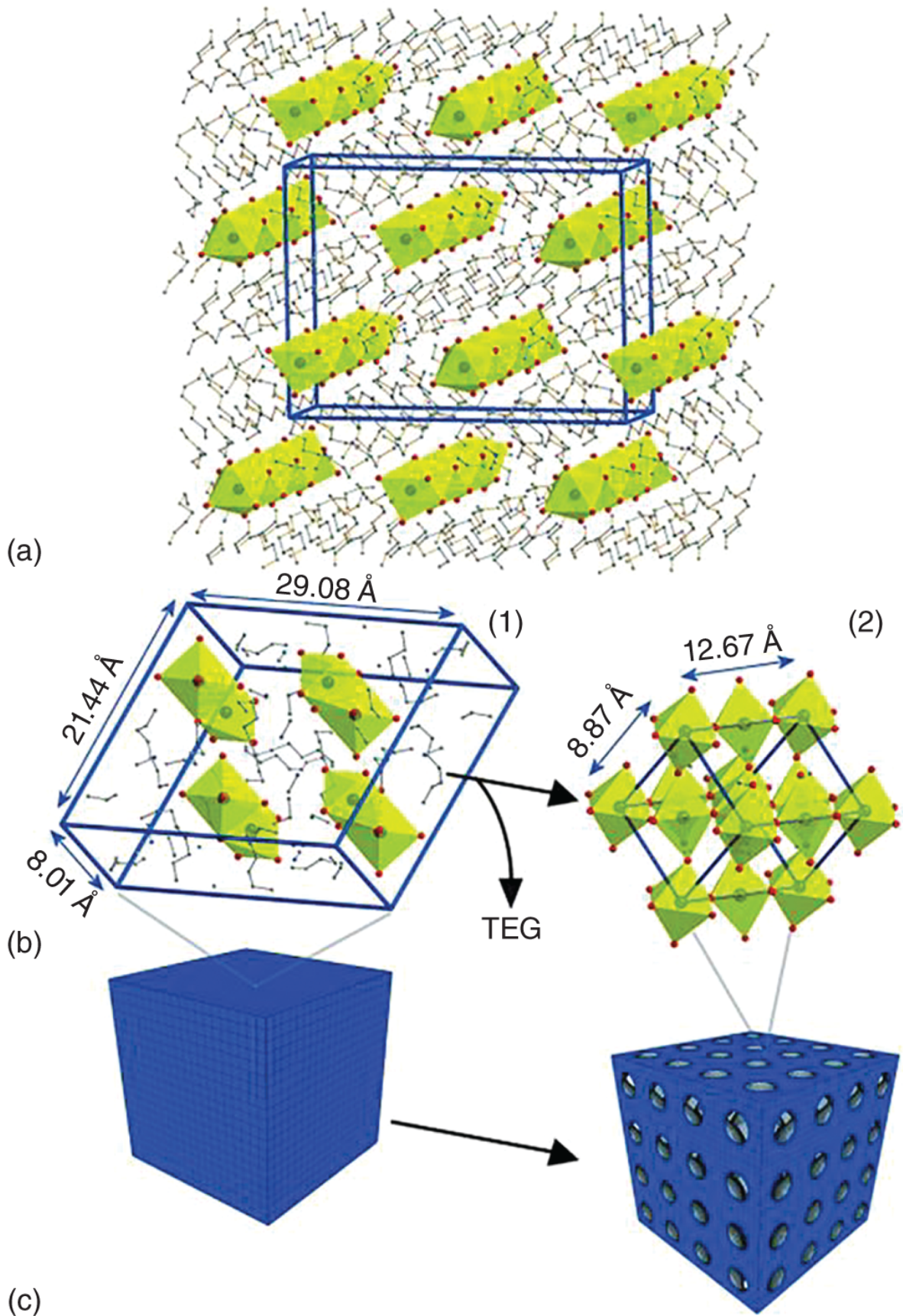
(a)

(b)

29.08 Å

(1)

(2)

21.44 Å

12.67 Å

8.87 Å

8.01 Å

TEG

(c)

Figure 5.31 (a) The novel $(TEG)_2(CH_3NH_3)PbI_3$ perovskite precursor phase (1) Pb: black, I: red, N: blue, carbon: dark gray, oxygen: light gray, $[PbI_6]$ octahedra: yellow faces, unit cell: blue lines. (b) Crystal-to-crystal transition into the $CH_3NH_3PbI_3$ perovskite (2) accompanied by the loss of TEG additive. (c) Formation of porous perovskite single crystals. Source: Reproduced with permission from Kollek et al. [34]. Copyright 2014, Wiley-VCH.

References

1 Meng, Z., Guo, D.P., Yu, J.G., and Fan, K. (2018). Investigation of Al_2O_3 and ZrO_2 spacer layers for fully printable and hole-conductor-free mesoscopic perovskite solar cells. *Applied Surface Science 430*: 632–638.

2 Liu, T.F., Liu, L.F., Hu, M. et al. (2015). Critical parameters in TiO_2/ZrO_2/carbon-based mesoscopic perovskite solar cell. *Journal of Power Sources 293*: 533–538.

3 Priyadarshi, A., Bashir, A., Gunawan, J.T. et al. (2017). Simplified architecture of a fully printable perovskite solar cell using a thick zirconia layer. *Energy Technology 5* (10): 1866–1872.

4 Wang, Q.F., Liu, S., Ming, Y. et al. (2018). Improvements in printable mesoscopic perovskite solar cells via thinner spacer layers. *Sustainable Energy & Fuels 2* (11): 2412–2418.

5 Cao, K., Zuo, Z., Cui, J. et al. (2015). Efficient screen printed perovskite solar cells based on mesoscopic TiO_2/Al_2O_3/NiO/carbon architecture. *Nano Energy 17*: 171–179.

6 Liu, S., Cao, K., Li, H. et al. (2017). Full printable perovskite solar cells based on mesoscopic $TiO_2/Al_2O_3/NiO$ (carbon nanotubes) architecture. *Solar Energy 144*: 158–165.

7 Yu, X., Chen, S., Yan, K. et al. (2016). Enhanced photovoltaic performance of perovskite solar cells with mesoporous SiO_2 scaffolds. *Journal of Power Sources 325*: 534–540.

8 Cheng, N., Liu, P., Bai, S. et al. (2016). Application of mesoporous SiO_2 layer as an insulating layer in high performance hole transport material free $CH_3NH_3PbI_3$ perovskite solar cells. *Journal of Power Sources 321*: 71–75.

9 Liu, H., Yang, B.C., Chen, H. et al. (2018). Efficient and stable hole-conductor-free mesoscopic perovskite solar cells using SiO_2 as blocking layer. *Organic Electronics 58*: 69–74.

10 Xiong, Y.L., Zhu, X.T., Mei, A.Y. et al. (2018). Bifunctional Al_2O_3 interlayer leads to enhanced open-circuit voltage for hole-conductor-free carbon-based perovskite solar cells. *Solar RRL 2* (5): 1800002.

11 Dash, L.K., Vast, N., Baranek, P. et al. (2004). Electronic structure and electron energy-loss spectroscopy of ZrO_2 zirconia. *Physical Review B 70* (24): 245116.

12 Kay, A. and Grätzel, M. (1996). Low cost photovoltaic modules based on dye sensitized nanocrystalline titanium dioxide and carbon powder. *Solar Energy Materials & Solar Cells 44* (1): 99–117.

13 Thompson, S.J., Duffy, N.W., Bach, U., and Cheng, Y.-B. (2010). On the role of the spacer layer in monolithic dye-sensitized solar cells. *The Journal of Physical Chemistry C 114* (5): 2365–2369.

14 Hinsch, A., Behrens, S., Berginc, M. et al. (2008). Material development for dye solar modules: results from an integrated approach. *Progress in Photovoltaics: Research and Applications 16* (6): 489–501.

15 Ku, Z., Rong, Y., Xu, M. et al. (2013). Full printable processed mesoscopic $CH_3NH_3PbI_3/TiO_2$ heterojunction solar cells with carbon counter electrode. *Scientific Reports 3* (1): 3132.

16 Mei, A., Li, X., Liu, L. et al. (2014). A hole-conductor-free, fully printable mesoscopic perovskite solar cell with high stability. *Science 345* (6194): 295–298.

17 Rong, Y., Hu, Y., Mei, A. et al. (2018). Challenges for commercializing perovskite solar cells. *Science 361* (6408): eaat8235.

18 Li, Y.Y., Zhao, L., Wei, S.B. et al. (2018). Effect of ZrO_2 film thickness on the photoelectric properties of mixed-cation perovskite solar cells. *Applied Surface Science 439*: 506–515.

19 Liu, T.F., Xiong, Y.L., Mei, A.Y. et al. (2019). Spacer layer design for efficient fully printable mesoscopic perovskite solar cells. *RSC Advances 9* (51): 29840–29846.

20 Liu, T.F., Rong, Y.G., Xiong, Y.L. et al. (2017). Spacer improvement for efficient and fully printable mesoscopic perovskite solar cells. *RSC Advances 7* (17): 10118–10123.

21 Chen, H., Ye, F., Tang, W. et al. (2017). A solvent- and vacuum-free route to large-area perovskite films for efficient solar modules. *Nature 550* (7674): 92–95.

22 Bi, C., Wang, Q., Shao, Y. et al. (2015). Non-wetting surface-driven high-aspect-ratio crystalline grain growth for efficient hybrid perovskite solar cells. *Nature Communications 6*: 7747.

23 Cao, K., Cui, J., Zhang, H. et al. (2015). Efficient mesoscopic perovskite solar cells based on the $CH_3NH_3PbI_2Br$ light absorber. *Journal of Materials Chemistry A 3* (17): 9116–9122.

24 Tsai, C.-M., Wu, G.-W., Narra, S. et al. (2017). Control of preferred orientation with slow crystallization for carbon-based mesoscopic perovskite solar cells attaining efficiency 15%. *Journal of Materials Chemistry A 5* (2): 739–747.

25 Liu, S., Huang, W., Liao, P. et al. (2017). 17% efficient printable mesoscopic PIN metal oxide framework perovskite solar cells using cesium-containing triple cation perovskite. *Journal of Materials Chemistry A 5* (44): 22952–22958.

26 Huang, Y.M., Zhao, L., Li, Y.Y. et al. (2019). Comparison of mesoporous materials based on mixed-organic-cation hole-conductor-free perovskite solar cells. *Applied Surface Science 493*: 975–981.

27 Li, H., Cao, K., Cui, J. et al. (2016). 14.7% efficient mesoscopic perovskite solar cells using single walled carbon nanotubes/carbon composite counter electrodes. *Nanoscale 8* (12): 6379–6385.

28 Chan, C.-Y., Wang, Y., Wu, G.-W., and Wei-Guang Diau, E. (2016). Solvent-extraction crystal growth for highly efficient carbon-based mesoscopic perovskite solar cells free of hole conductors. *Journal of Materials Chemistry A 4* (10): 3872–3878.

29 Li, M.H., Yang, Y.S., Wang, K.C. et al. (2017). Robust and recyclable substrate template with an ultrathin nanoporous counter electrode for organic-hole-conductor-free monolithic perovskite solar cells. *ACS Applied Materials & Interfaces 9* (48): 41845–41854.

30 Yang, Z.-L., Zhang, Z.-Y., Fan, W.-L. et al. (2019). High-performance g-C_3N_4 added carbon-based perovskite solar cells insulated by Al_2O_3 layer. *Solar Energy 193*: 859–865.

31 Marin-Beloqui, J.M., Lanzetta, L., and Palomares, E. (2016). Decreasing charge losses in perovskite solar cells through mp-TiO_2/MAPI interface engineering. *Chemistry of Materials 28* (1): 207–213.

32 Liang, Z., Bi, Z., Gao, K. et al. (2019). Interface modification via Al_2O_3 with retarded charge recombinations for mesoscopic perovskite solar cells fabricated with spray deposition process in the air. *Applied Surface Science 463*: 939–946.

33 Xu, X., Liu, Z., Zuo, Z. et al. (2015). Hole selective NiO contact for efficient perovskite solar cells with carbon electrode. *Nano Letters 15* (4): 2402–2408.

34 Kollek, T., Gruber, D., Gehring, J. et al. (2015). Porous and shape-anisotropic single crystals of the semiconductor perovskite $CH_3NH_3PbI_3$ from a single-

source precursor. *Angewandte Chemie (International Ed. in English) 54* (4): 1341–1346.

6
Perovskite Materials and Perovskite Solar Cells

Maria Vasilopoulou[1], Abd Rashid B. Mohd Yusoff[2], and Mohammad K. Nazeeruddin[3]

[1] National Centre for Scientific Research Demokritos, Institute of Nanoscience and Nanotechnology, Agia Paraskevi, 15341, Attica, Greece

[2] Pohang University of Science and Technology (POSTECH), Department of Chemical Engineering, Pohang, Gyeongbuk, 37673, Republic of Korea

[3] École Polytechnique Fédérale de Lausanne (EPFL), Institute of Chemical Sciences and Engineering, Group for Molecular Engineering of Functional Materials, Rue de l'Industrie 17, CH-1951, Sion, Switzerland

6.1 Perovskite Materials

6.1.1 3D Halide Perovskites

Three-dimensional (3D) halide perovskites (HPs) crystallize in the ABX_3 perovskite structure, where A and B are monovalent and divalent cations, respectively, and X is a halide anion. The A^+ cations, in particular, are larger than B^{2+} ones and function as structural templates with their shape, size, and charge distribution to be crucial factors for the stabilization of the perovskite structure. More specifically, A^+ is usually an organic ($CH_3NH_3^+$, methylammonium, MA, $CH_3(NH_2)_2^+$, formamidinium, FA, $CH_6N_3^+$, guanidinium, Gua) or inorganic (cesium, Cs^+) cation, B^{2+} is a large atomic number metal (such as lead,

Pb^{2+}, tin, Sn^{2+}, and germanium, Ge^{2+}) and X^- is a halogen (Cl^-, Br^-, I^-).

The simplest possible ABX_3 perovskite consists of a high-symmetry cubic structure belonging to the space group $Pm\bar{3}m$. In this structure the halogen anions X^- occupy the vertices in $[BX_6]_4^-$ octahedra, which share corners in all three orthogonal directions to generate infinite 3D $[BX_3]^-$ frameworks, while the divalent metal cations B^{2+} are placed at the centers of these octahedra [1]. The smallest volume enclosed by neighboring octahedra defines a cuboctahedral cavity and hosts the monovalent cation A^+ [1]. Different possible perovskite structures can be regarded as obtained by rotating or distorting the BX_6 octahedra, displacing the B^{2+} metal cations off-center and rotating the A^+ cations within the cuboctahedral cavity. More than one structure is usually found for a perovskite material with a given chemical composition, depending on the temperature and preparation methods. For example, methylammonium lead triiodide ($MAPbI_3$), a prototypical hybrid organic–inorganic metal HP, can undergo phase transformations from tetragonal to cubic at the temperature of 54 °C and from tetragonal to orthorhombic at −111 °C during cooling (Figure 6.1a–c) [2].
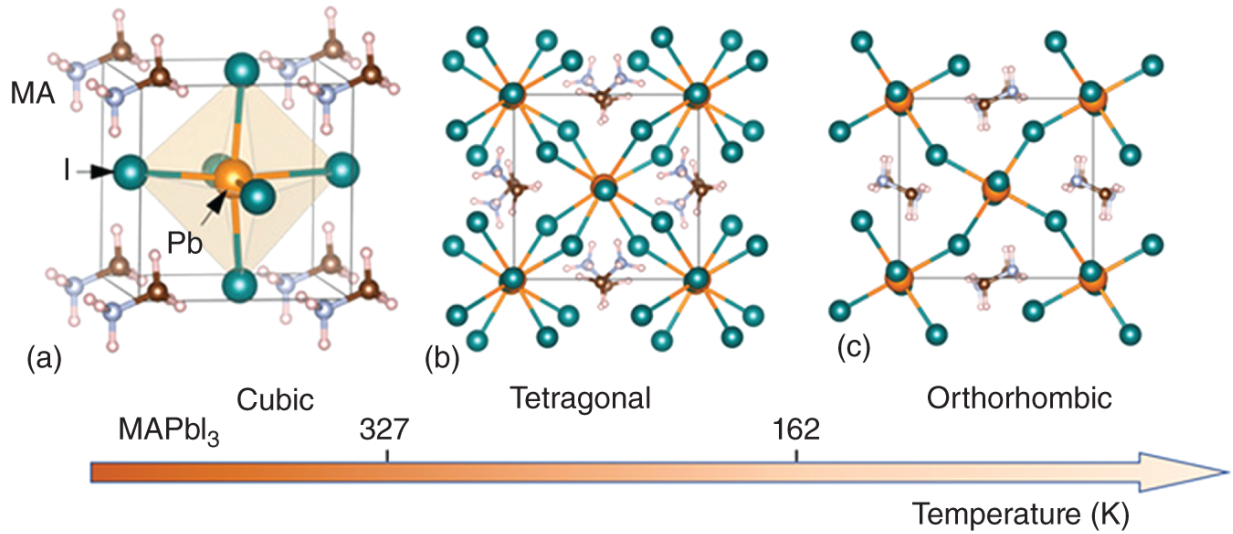
Figure 6.1 Crystal structures of the three different MAPbI$_3$ phases. (a) Cubic, (b) tetragonal, and (c) orthorhombic phases. The crystal structures of the three phases differ by rotation of the inorganic octahedral cages. The critical temperatures of the phase transitions are marked on the temperature axis. Source: Reproduced with permission from Zhang et al. [2]. John Wiley & Sons.

The crystal structure stability of HPs can be predicted by calculating the tolerance factor, t, a geometrical parameter introduced in 1926 by V. M. Goldschmidt [3–5]. It gives an estimate of the ionic size mismatches that a perovskite structure can tolerate until a different structure type is formed (Eq. (6.1)):

$$t = \frac{r_A + r_X}{\sqrt{2}(r_B + r_X)} \tag{6.1}$$

with r_i being the radii of $i = $ A, B, and X ions in the perovskite ABX$_3$.

Both the performance and stability of inorganic–organic perovskite solar cells are limited by the size of the cations required for forming a proper lattice. It has been found that

compounds with a tolerance factor of $t = 0.9$–1.0 have an ideal cubic structure; $t = 0.8$–0.9 results in a distorted perovskite structure with tilted octahedra (usually orthorhombic), while when the tolerance factor is higher than 1 or lower than 0.8 non-perovskite structures are formed ([Figure 6.2a](#)) [7]. It is common in HP literature to denote the phase with cubic structure as α-phase and the phase with non-perovskite structures as δ-phase [1]. Based on the above considerations, only three A^+ cations known to date have tolerance values between 0.8 and 1 and are thus able to form a stabilized perovskite, namely Cs^+, $CH_3NH_3^+$ (MA), and $HC(NH_2)_2^+$ (FA).

However, each one of the commonly used single-cation HPs presents limitations that arise from their thermal or structural instabilities. $MAPbI_3$, for example, the prototypical HP studied in PSCs, degrades fast upon light and moisture (the latter is due to the hygroscopic nature of the methylammonium cation) while also decomposed during annealing at 85 °C even in inert atmosphere [8–10]. $FAPbI_3$, on the other hand, despite being advantageous concerning its bandgap (1.48 vs. 1.57 eV for $MAPbI_3$) [11] and thermal stability (it is relatively stable up to 150 °C in air), suffers from severe structural instability at room temperature as it commonly crystallizes into the photoinactive, non-perovskite hexagonal δ-phase ("yellow phase") instead of the photoactive perovskite α-phase ("black phase"); in addition, it is sensitive to solvents or humidity [12].
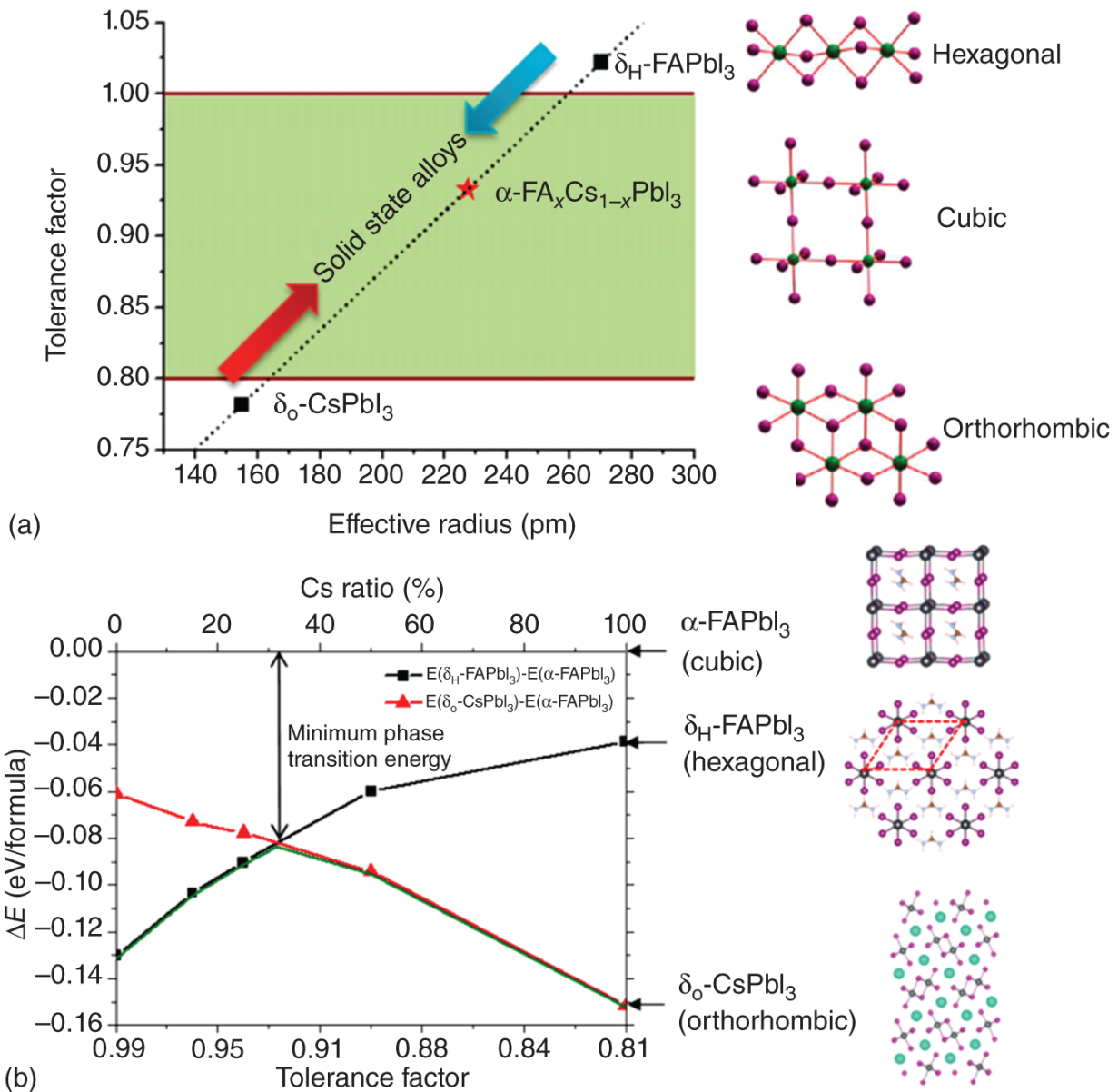
Figure 6.2 (a) Correlations between tolerance factor and crystal structure of perovskite materials. (b) Calculated energy difference between α-phase and different δ-phases for $FA_{1-x}Cs_xPbI_3$ alloys with different Cs ratios. Source: Reproduced with permission from Li et al. [6]. American Chemical Society.

A reasonable way to overcome the limitations of single-cation (and anion) HPs is the compositional engineering approach by mixing cations as well as halides to achieve

perovskite compounds with improved thermal and structural stability [7]. Intermixing different cations can combine the advantages of the constituents while avoiding their drawbacks. Mixed cation 3D perovskites of the composition $(MA)_x(FA)_{1-x}PbI_3$ where $x = 0.6$ delivered superior device performance when used as light-harvesting layers in mesoscopic solar cells [13]. The optimized stoichiometry of $MA_{0.6}FA_{0.4}PbI_3$ outperformed the single-cation compositions $MAPbI_3$ and $FAPbI_3$, while it also completely avoided the undesirable formation of the δ-phase while maintaining the redshifted bandgap of $FAPbI_3$. The superior carrier-collection efficiency was related to the longer exciton lifetime of more than 130 ns in the $MA_{0.6}FA_{0.4}PbI_3$ material. These results showed that even a small amount of MA is sufficient to induce a preferable crystallization into the photoactive phase of FA perovskite resulting in a more thermally and structurally stable composition than the pure MA or FA compounds. This illustrates that the MA can be thought of as a "crystallizer" (or stabilizer) of the black phase FA perovskite. The fact however that MA is only slightly smaller than FA still permits a large fraction of the yellow phase to exist. Furthermore, alloying $FAPbI_3$ with $CsPbI_3$, the effective tolerance factor can be effectively tuned, and the stability of the photoactive α-phase of the mixed $FA_{1-x}Cs_xPbI_3$ perovskite is significantly enhanced (Figure 6.2b) [7]. These mixed cation perovskite films demonstrate much-improved stability in a high-humidity environment and better solar cell performance and device stability than the $FAPbI_3$ counterparts.

Moreover, the substitution of the larger I atoms with smaller Br ones in the mixed halide structure, $MAPb(I_{1-x}Br_x)_3$, for $x > 0.2$, leads to the reduction of the lattice constant and a transition from a distorted tetragonal

perovskite structure of pure $MAPbI_3$ to the cubic perovskite structure of $MAPbBr_3$ hence inducing advanced optoelectronic properties and superior PSC performance [14, 15]. Further intermixing both MA/FA cations as well as I/Br anions in an optimized $(FAPbI_3)_{0.85}(MAPbBr_3)_{0.15}$ perovskite structure stabilizes the perovskite phase and increases its crystallinity [16]. As a step forward, intermixing Cs^+, which has a considerably smaller ion than both MA^+ and FA^+, in a triple cation configuration $Cs_x(MA_{0.17}FA_{0.83})_{(100-x)}Pb(I_{0.83}Br_{0.17})_3$ provides additional versatility in fine-tuning high-quality perovskite films that can yield stabilized *PCEs* [17]. Incorporation of optimum amounts of Cs^+ reduces trap density by one order of magnitude, which was responsible for the increased V_{OC} and FF, eventually leading to enhancement in PCE. The triple cation perovskite films are less affected by temperature for a fixed halide ratio, while increased Br content also contributes considerably to thermal stability. Cs^+ induces the black phase of FA-based HPs at room temperature and better morphology as more uniform grains are formed that enable better charge transport, which in turn endows the fabricated devices with higher *FF*.

Furthermore, incorporation of traces of the small radius rubidium (Rb) ($r_{Rb+} = 152$ pm vs. $r_{Cs+} = 167$ pm) has been recently found to stabilize the black phase of FA perovskites. Whereas it is clear from the tolerance factor discussion above that Cs^+ is the only elemental cation that is large enough to sustain the perovskite structure, Rb^+ can still be integrated into PSCs, despite not being suitable as a pure $RbPbI_3$ compound. PSCs based on perovskite materials bearing the rubidium cation along with cesium and/or organic cations have reached reasonable device performances [17]. The outstanding maximum V_{OC} of 1240

mV indicates a "loss in potential" (difference between V_{OC} and bandgap) of only ~0.39 V, which is one of the lowest recorded for any perovskite material, implying very small non-radiation recombination losses owing to very low bulk and surface defect density. Moreover, it was observed that the charge transport within the RbCsMAFA perovskite layer is substantially faster than in CsMAFA, which is already much more defect-free than MAFA.

HPs exhibit a direct bandgap which can be effectively tuned through compositional adjustment to allow absorption reaching the high-energy frontier of the near-infrared spectral region. The change in bandgap observed with compositional adjustment such as tailoring of halide concentration can be explained as follows: The electronic states at the top of the valence band (VB) are mainly of halide p-character with a small contribution from metal s-orbitals (i.e. Pb 5s orbitals); those at the bottom of the conduction band (CB) are mainly derived from the metal p states (i.e. Pb 6p) [5]. The fully occupied 5s orbital of Pb^{2+} has strong antibonding coupling with I 5p, making upper valence bands (VBs) dispersive. The strong s–p antibonding coupling results in the small hole effective mass, which is comparable with electron effective mass, making $MAPbI_3$-based perovskite an ideal candidate for thin-film solar cells with a p-i-n configuration. The replacement of I^- by Cl^- or Br^- leads to an increase in the bandgap, due to the lower-lying Br-4p and Cl-3p electronic states that populate the top of the VB [18]. In addition, the smaller dielectric constant associated with the larger bandgap in $MAPbBr_3$ results in larger binding energy (BE), smaller Bohr radius, larger effective g-factor (that is a quantity that characterizes the magnetic moment and angular momentum of an atom or particle), and larger oscillator

strength of the lowest-energy excitons in $MAPbBr_3$ compared to those in $MAPbI_3$ [19].

Due to the antibonding character and mixing of s and p orbitals to form the bands extrema, perovskites present only shallow defects – primarily A- and X-site vacancies, while interstitial and antisite defects, which would form detrimental deep trap states in the electronic structure, are almost absent [20]. However, several types of extrinsic surface defects caused by unsaturated surface bonds and/or the surrounding environment are a major issue in the grainy, polycrystalline HP films. For instance, X-terminating surfaces form traps due to a lack of local stoichiometric composition and improper surface bonding, which can be mitigated by introducing an appropriate passivation agent (PA). In an effective passivation scheme, new chemical bonds formed at the perovskite surface, and the derived orbitals shift the defect level either toward or into the band edges, hence suppressing the detrimental influence of the defect [21].

In a similar manner, substitution of Pb by Sn lowers the CB bottom hence reducing the bandgap due to the lower-lying Sn-p states (1.2–1.4 eV in Sn-based iodide perovskites as compared to 1.45–1.7 eV in Pb–iodide perovskites) [1]. This arises from the greater instability of the Sn^{2+} lone pair of electrons (residing in the s orbital), which in the octahedral coordination environment is pushed up in energy creating broader bands than the corresponding Pb lone pair. In a first approximation, the MA cations do not contribute to the optical absorption, and their role is to act as a structural filler and to ensure the charge neutrality of the unit cell. However, they can affect the bandgap energetics through steric, hydrogen bonding, and Coulombic interactions, which may deform the perovskite lattice in a cation-specific way. On the other hand, such mixed HPs were found to be

prone to photoinstability as photoexcitation during light-soaking was suggested to cause halide segregation into two crystalline phases, namely iodide-rich minority, and bromide-enriched majority domains, the former having a lower bandgap and acting as a recombination trap centers, limiting thus the photovoltage attainable with these materials.

6.1.2 2D Halide Perovskites

Two-dimensional (2D) HPs can be generally described by the general formula $L_2A_{n-1}M_nX_{3+1}$, where L is a large aliphatic or aromatic ammonium cation of the chemical type R–NH$_3$, such as 2-phenylethylammonium (PEA) and n-butylammonium (n-BA) [22, 23]. They are also known as Ruddlesden–Popper (RP) layered perovskites because they consist of alternative organic spacer and perovskite layers. They are hence quite similar with conventional 2D materials having a van der Waals layered crystal structure. The $(A_{n-1}M_nX_{3n+1})^{2-}$ part of their formula denotes the conductor layer that derives from the parent 3D (AMX$_3$) perovskite. As illustrated in Figure 6.3a, the MX$_6$ octahedrons form the perovskite sub-layers that are sandwiched by the insulating organic spacers formed by the long-chain molecular cations. The number of the BX$_6$ octahedrons and, thus, the thickness of each perovskite layer is defined by the n value ($n = 1$, 2, 3, 4, ...) and can be adjusted by careful control of the stoichiometry [24].

The incorporation of large organic spacers within their structure endows this class of HP materials with superior structural, thermal, and moisture stability [23]. Their structural stability is due to the strong van der Waals forces among the organic layers [25]. Notably, the formation even of a small amount of a 2D perovskite

structure can successfully inhibit the low-temperature phase transition of $FAPbI_3$ and $CsPbI_3$ perovskites, hence rendering α-$FAPbI_3$ and α-$CsPbI_3$ stable at room temperature [26]. The moisture stability is due to the hydrophobic nature of the organic spacers, typically ammonium cations, that prohibit the water molecules' penetration into the perovskite crystal lattice [27]. In addition, ion migration, which is a severe limitation in PSCs based on 3D HPs, is not a great issue in the 2D RP perovskites due to the higher activation energy of ion migration in 2D perovskites compared to 3D ones with similar compositions [28]. Moreover, "edge states" that existed in perovskite layers when $n > 2$ can provide a direct pathway for dissociating excitons into longer-lived free carriers.
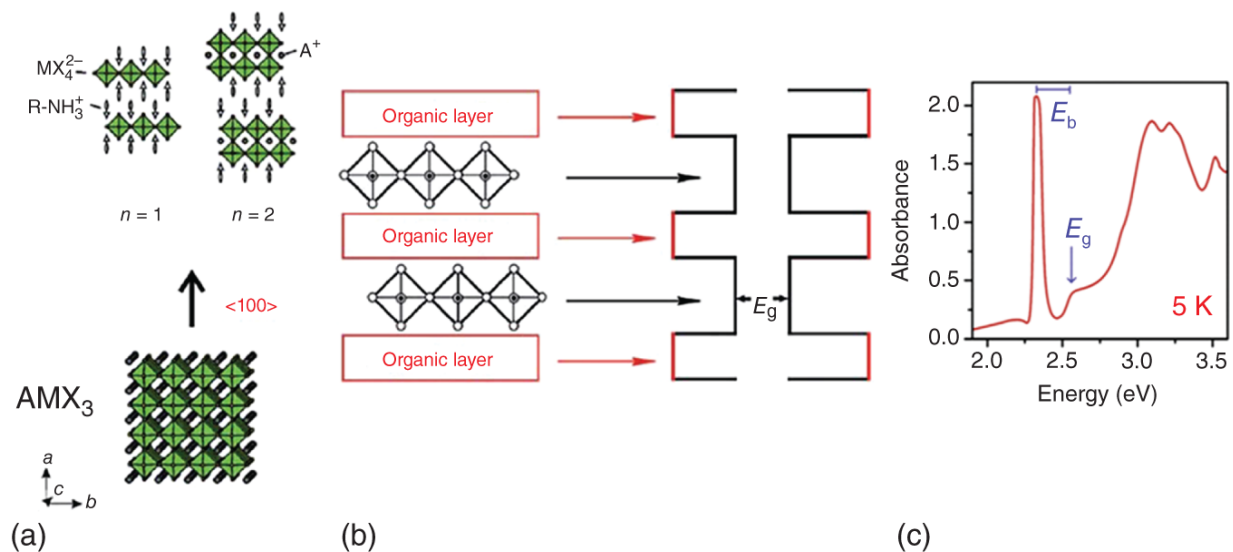
Figure 6.3 (a) Schematic of [100] oriented families of layered organic–inorganic perovskites. R is an organic group and defines the thickness of the perovskite sheets. (b) The quantum well structure, formed by alternating semiconductor inorganic sheets with organic layers having a wider bandgap. Source: Reproduced with permission from Yan et al. [23]. Copyright © 2018 The Royal Society of Chemistry. (c) The absorption spectrum of a representative RP perovskite. The exciton BE (E_b) is determined by the energy difference between the excitonic absorption peak and the onset of the absorption spectrum (E_g). Source: Reproduced with permission from Lan et al. [24]. Copyright © 2018 Elsevier Ltd.

However, besides their exceptional overall stability, 2D HPs also present some not very appealing characteristics regarding their application in PSCs. The electrically insulating nature of the organic spacer and high conductivity of the perovskite conductor layers give rise to the natural multiple-quantum-well structure: the perovskite layers serve as the potential "well" while the organic spacer layers play the role of the potential "wall" (Figure 6.3b). This results in weaker absorption of RP 2D perovskites within the visible spectrum due to their larger

bandgap values compared to their 3D counterparts. For example, the bandgap (E_g) values of $BA_2MA_{n-1}Pb_nI_{3n+1}$ and $PEA_2MA_{n-1}Pb_nI_{3n+1}$ RP perovskites are 2.24 and 2.35 eV (for $n = 1$), respectively, [29, 30] while that of $MAPbI_3$ is only 1.54 eV [31]. Moreover, they present higher exciton binding energies (BEs), which make it more difficult for exciton dissociation to photogenerated carriers to occur [32]. The excitons in 2D are generally considered as the Wannier type and their BEs in a single layer ($n = 1$) RP perovskite is in the range of 170–480 meV (depending on the organic spacer) [33]. This large exciton BE is much higher than the thermal energy at room temperature ($k_B T$ = 25.7 meV). Therefore, the photogenerated electron and hole pairs in RP HPs are strongly bound together by Coulombic attraction. This is why the so-called excitonic absorption can be easily observed even at room temperature in these 2D perovskites in the form of a sharp peak below the bandgap onset. However, in most cases the excitonic absorption is merged with the absorption onset at room temperature, while in low temperatures this sharp peak is quite distinct (Figure 6.3c).

In addition, the insulating organic spacer largely prohibits carrier transport, hence inducing charge accumulation and non-radiative recombination at the interface conductor/insulator. Moreover, the charge extraction can also be hindered by the insulation of the organic spacers. The charge mobility is much higher in the direction along the perovskite slabs than in the direction perpendicular to the orientation of these slabs. To this end, for efficient 2D PSCs, it is important to have perovskite slabs with the out-of-plane orientation, such that thicker films with balanced charge transport and light absorption can be used to achieve a high PCE.

Because of these unfavorable characteristics, RP perovskite-based PSCs lag behind in efficiency compared to their 3D counterparts with the goal of current research efforts to maximize the efficiency without compromising the stability. For example, huge research efforts have been devoted to alter the composition of 2D perovskites aiming to improve their optoelectronic properties. These also include molecular design of the spacer cations, such as altering alkyl chain length [34], revealing ammonium dications [35], and inserting p-conjugated segments [36]. Thus, a much wider range of optoelectronic properties can be tuned for 2D perovskites than for 3D analogs.

An attractive approach to tackle the limitations of lower absorption and limited charge transport of 2D HPs is their combination with the parent 3D structure. In fact, as the value of n in the perovskite formula increases above 10, HPs with properties resampling those of their corresponding 3D counterparts are obtained; yet these materials present features of 2D perovskites [37]. Typically, the absorption onset of such perovskite materials combining the 2D and 3D structure is close to that of the corresponding 3D counterparts. Moreover, as the bandgap values of 2D perovskite phases are much larger than those of the 3D ones, charges are highly confined to the 3D phase hence overcoming the limitation of trapping and recombination at the interfaces between layers in the 2D phase, resulting in longer carrier lifetime [38]. Nevertheless, the presence of the 2D component endows their devices with exceptional stability and ultrahigh V_{OC} values resulting in PCEs comparable to the 3D ones, indicating them to be highly attractive candidates for PSCs. Finally, due to their highly hydrophobic nature and resilience to moisture thin 2D perovskite films are also inserted as protective interlayers at either the bottom or top side of a 3D perovskite absorber [39].

6.1.3 Synthesis of Halide Perovskites

The structural and optoelectronic properties of HPs are highly related with the synthetic procedure adopted for their preparation. This is because only high-quality films can enable the excellent intrinsic perovskite material characteristics to be fully exploited. A variety of synthetic procedures for 3D perovskites has been reported aiming to achieve high-quality perovskite films. They can be categorized into vacuum vapor deposition and solution processes. With the vacuum deposition method, high-quality perovskite films and, consequently, high-efficiency PSCs can be obtained. The perovskite films are prepared by co-evaporation of the two precursors, the inorganic metal halide (MX_2 such as PbI_2) and the organic/inorganic halide salt (i.e. MAX, FAX, CsX, where $X = I$, Br, Cl). With this technique high-quality perovskite films that exhibit satisfactory substrate coverage and uniformity within expectations can be constructed; such thin films are highly appropriate for planar junctions. For example, in 2013 Snaith and coworkers succeeded to achieve a record efficiency of 15% in planar PSCs by using a dual-source vapor deposition system to deposit $MAPbI_{3-x}Cl_x$ perovskite films of superior quality through evaporating lead chloride ($PbCl_2$) and methylammonium iodide (MAI) precursors simultaneously [40]. However, this method requires the use of expensive vacuum facilities, thus increasing the device manufacturing cost. Moreover, it is not appropriate for the fabrication of mesoscopic PSCs, which required the infiltration of perovskite pigment onto mesoporous metal oxide.

In the early attempts, this was sufficiently accomplished in a single step using a common solution of PbI_2 and MAI precursors [41]. However, the lack of suitable solvents that can dissolve both components and the high perovskite

reaction rate resulted in large morphological variations and therefore large deviations in the achieved efficiencies. In 2013, Grätzel and coworkers described a sequential deposition method for the successful infiltration of the perovskite pigment within the porous TiO$_2$ film [42]. In particular, lead iodide (PbI$_2$) was first introduced via spin coating from solution into the nanoporous TiO$_2$ film and subsequently dipped into a solution of MAI to synthesize the resultant MAPbI$_3$ perovskite film. It was found that the conversion to perovskite occurred within the nanoporous oxide as soon as the two precursors came into contact, hence allowing for better control over the morphology and reproducibility of perovskite films. As a result, solid-state mesoscopic PSCs with a high efficiency of 15% were obtained, thus providing new opportunities for the fabrication of solution-processed mesoscopic PSCs [43]. However, this method is not very convenient for the preparation of planar devices because it often results in films with significant surface roughness that frequently peel off from the substrate.

Several other methods based on solution processes, such as the vapor-assisted solution process (VASP) [44], the solid-state reaction [45], and the precipitation reaction [46], offer the advantage of facile and low-cost manufacturing. In the vapor-assisted solution method (Figure 6.4a) [44], PbX$_2$ films are initially deposited on the bottom electrode, which is covered with the suitable charge transport interlayer (i.e. a TiO$_2$ layer). Subsequently, it follows an annealing step in the vapors of the organic halide salt (i.e. MAX) at appropriate temperature (i.e. 150 °C). During this step, the inorganic perovskite framework is formed in the film. This process takes advantage of the kinetic reactivity of the organic vapors and thermodynamic stability of perovskite during the in situ growth process. As a result, pinhole free

perovskite films with full substrate coverage, small surface roughness, and well-defined grain sizes up to microscale are formed.
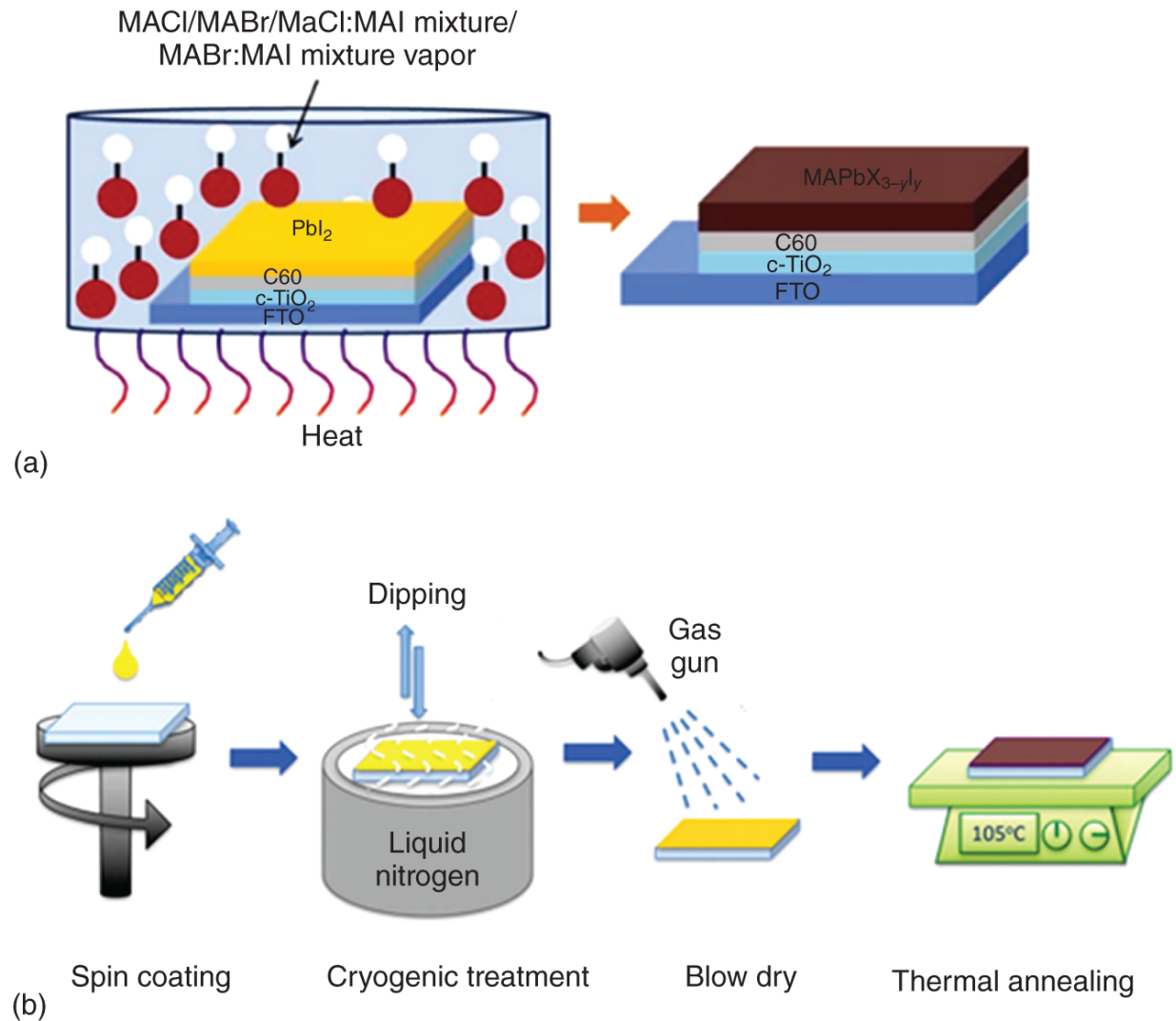

(a)

(b)

Figure 6.4 (a) VASP synthesis of perovskite films. Source: Reproduced with permission from Xiao et al. [44]. Elsevier. (b) Schematic diagram showing the cryogenic controlled nucleation technique for perovskite film deposition along with optical microscopy images of the precursor and the formed perovskite film. Source: Reproduced with permission from Ng et al. [47]. John Wiley & Sons.

In the solid-state reaction method, the PbX_2 and organic halide (i.e. MAX) films are deposited on two independent substrates. Then, the MAX film is placed on top of the PbX_2 one and annealed at a certain temperature (i.e. 140 °C) to vaporize and drive MAX molecules into PbX_2 to form the $MAPbX_3$ perovskite through a solid-state chemical reaction; then, the top substrate is removed. However, this method does not allow precise control on the perovskite stoichiometry because the mass exchange between PbX_2 and MAX during the annealing step is rather random.

Room-temperature processing has recently been exploited to fabricate, among others, inorganic lead halide PSCs that demonstrate increased potential for greater thermal stability compared with hybrid organic perovskites. A characteristic example is $CsPbI_2Br$ PSCs which, even though generally require a high annealing temperature for conversion from the non-perovskite phase to the cubic perovskite phase, were prepared by a vacuum-assist method under room temperature conditions in air and achieved promising PCEs up to 8.67% and improved moisture resistance [47, 48].

Furthermore, Ng et al. proposed a novel cryogenic process instead of the conventional antisolvent method to control the crystallization of perovskite layers with different compositions and demonstrated its application on three types of HP-based PSCs [47] (Figure 6.4b). This process enabled decoupling of the nucleation and the crystallization phases by inhibiting chemical reactions in as-cast precursor films rapidly cooled down by immersion in liquid nitrogen. The cooling is followed by blow-drying with nitrogen gas, which induces uniform precursor precipitation due to their supersaturation in the residual solvents at very low temperatures, while at the same time enhancing the residual solvent evaporation and preventing the ordered

precursors/perovskite from redissolution. Hence, the crystallization process is initiated after the formation of a uniform precursor seed layer, resulting in a champion PCE of 21.4%, highlighting its potential for wider applicability for various perovskites and device structures.

In addition, the conventional hydrothermal and solvothermal synthesis are of particular interest for the preparation of homogeneous perovskite films [49, 50]. In hydrothermal synthesis, perovskite crystals are prepared in hot water (around 150 °C). Variation of the reaction temperature and time results in precise control of the nucleation and crystallization of perovskite materials. In the solvothermal synthesis, the precursors are fully mixed together at room temperature and then transferred into an autoclave where a solvothermal reaction takes place and perovskite crystals are obtained. All the operations are completed in ambient atmosphere. The shape and size of perovskite crystals can be tuned by simply adjusting the reaction times or temperatures.

Recently, novel synthetic procedures such as an ultrasound-assisted synthesis of the perovskite material by the irradiation of MAI and PbI_2 precursors, which were dissolved in isopropanol without any catalyst, have been reported [51]. Moreover, microwave-assisted synthesis has also been applied to allow for better control of the properties of perovskite by facile temperature tuning through adjusting the microwave power [52]. The microwave irradiation process needs a specific material to have appropriate dipolar polarization and ionic conductivity to absorb microwave energy. It is expected that higher nucleation rates can be reached by accelerating the temperature [53]. Therefore, microwave radiations are suitable to accelerate the temperature at the atomic level to get better crystallization. Mechanochemically synthesized HP powders from a solvent-free ball milling

approach have also been recently employed to fabricate a variety of lead HPs with exceptional intrinsic stability [54].

6.2 Compositional and Interfacial Engineering of Perovskite Solar Cells

Organic–inorganic HPs exhibit significant tolerance to defects attributed to the antibonding character of valence and CB extrema. In lead HPs, in particular, the upper states of the VB are mainly of halogen p character (Cl 3p, Br 4p, I 5p) with a small contribution from the Pb 6s orbitals, while the bottom of the CB consists mainly of Pb 6p orbitals with a slight contribution from the halogen p* [55]. However, they present a variety of defects that are accommodated in their surface and at grain boundaries (GBs) [56]. These can be summarized as follows: halide anion (such as Cl^-, Br^-, and I^-) and organic cation (such as MA^+ and FA^+) vacancies, under-coordinated lead cations (Pb^{2+}) and halide anions, lead halide antisite defects, mobile halide, and MA ions, Pb clusters, halide excess, and Pb–halogen antisites (Figure 6.5) [56].

The majority of such defects are vacancies (such as X^- or MA^+ vacancies) that form shallow traps that can act as non-radiative recombination centers hence being detrimental to solar cell performance. Therefore, surface and GB defect passivation are generally applied following various approaches aiming to decrease defect density and, accordingly, charge trapping at these defects [57]. In the following sections, different approaches to achieve defect passivation in HPs are thoroughly presented.

6.2.1 Solvent Engineering

Solvent engineering is a widely applied method that enables morphology control and defect passivation in

perovskite thin films. Its main principle is that while it removes excess solvent, it also leaves behind solvent to assist in the formation of chemical adducts with the perovskite precursors that regulate nucleation, grain size, and crystallization [58]. Common solvents used in this engineering approach are isopropyl alcohol (IPA), acetone (ACE), diethyl ether (DEE), dichloromethane (DCM), and triethylenetetramine (TETA). After the photoactive perovskite film is deposited onto the bottom charge transport interlayer (i.e. onto the TiO_2 scaffold for MPSCs) the solvent treatment process is carried out to complete the formation of perovskite film. Compact and smooth films, pinhole-free and with full substrate coverage with sufficiently larger grains compared to the reference samples (not subjected to the solvent engineering step) are usually obtained with this method [59–62]. Furthermore, the residual PbI_2 is removed and converted to a crystalline perovskite film.
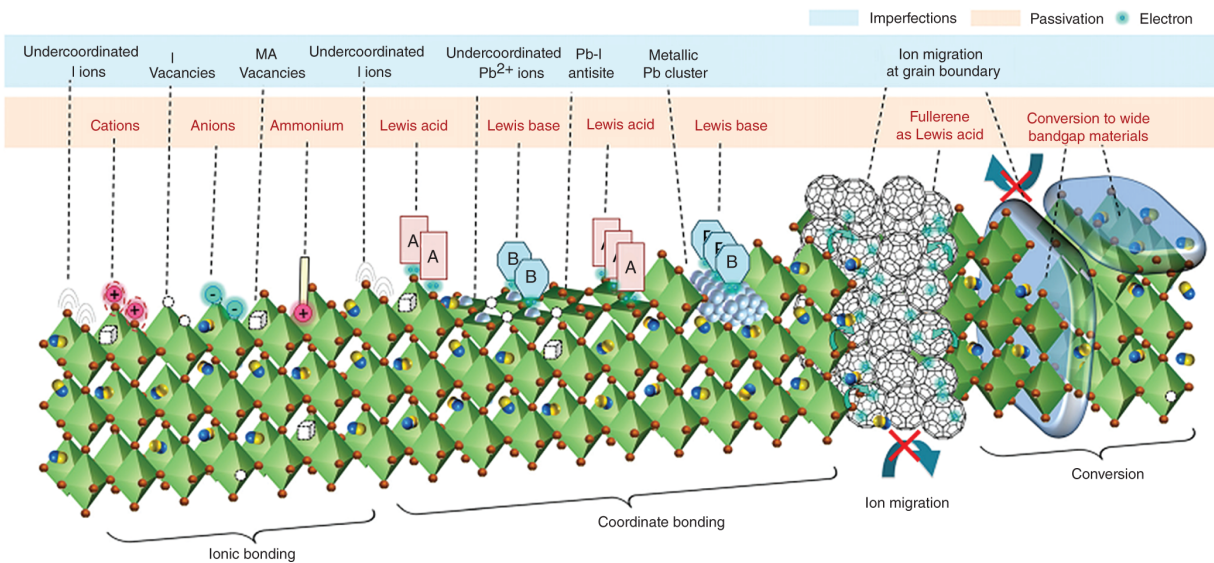
Figure 6.5 The different defects present at surface and grain boundaries of the perovskite film. Examples of their passivation by ionic or coordinate bonding and conversion to wide bandgap perovskites are also illustrated. Source: Reproduced with permission from Chen et al. [56]. Royal Society of Chemistry.

A two-step sequential solvent engineering method has been exploited to prepare a high-quality perovskite absorber layer for carbon CE-based MPSCs [63]. Specifically, in the first step a PbI_2 solution was prepared in IPA and the solvent was changed in the second step where a mixture of IPA and cyclohexane was used for dissolving MAI. This change largely facilitated the conversion of PbI_2 to $MAPbI_3$ but also suppressed the Ostwald ripening process resulting in a smooth, compact, perovskite layer.

The efficient and complete conversion of PbI_2 to perovskite involving different steps such as diffusion, infiltration, contact, and reaction is crucial as their simultaneous optimization would facilitate high-quality film formation. As a result, a significant enhancement in device performance and reproducibility with a record PCE value of 14.38% was obtained in solvent-engineered carbon CE MPSCs owing

mainly to the lower trap density, improved interfacial contact, and faster charge transport [37]. Moreover, in a three-step sequential coating method based on solvent (IPA) substitution instead of annealing treatment Stonehenge-like PbI_2 films due to the volume expansion with controllable porosity and crystallinity were formed allowing the complete conversion of PbI_2 to $MAPbI_3$. These high-quality $MAPbI_3$ films enabled the fabrication of PSCs with high reproducibility and a PCE of 17.78%.

A generally common solvent combination for this engineering approach also includes N,N-dimethylformamide (DMF) and dimethyl sulfoxide (DMSO) [64, 65]. This binary solvent system has resulted in the formation of dense, compact, pinhole-free $MAPb(I_{1-x}Br_x)_3$ ($x = 0.1$) perovskite films with few grain boundaries and large grains with an average size of 450 nm and to the demonstration of PSCs with high PCEs and reproducibility [64]. An optimal composition (volume ratio of $3:2$) and precursor concentration led also to improved crystallization and pinhole-free film formation of inorganic $CsPbI_2Br$ perovskite, thus enhancing the device PCE with good stability under 100 °C stress and continuous light soaking [65].

Solvent engineering was also applied to prepare high-performance planar 2D PSCs with efficiencies beyond 10% (up to 11.8%) and outstanding stability [66]. In this method, the crystallization process includes two distinct steps. The first step is the formation of the flaky capping layer at the air/liquid interface, where heterogeneous nucleation primarily occurs driven by fast DMF volatilization, with an intermediate product forming that retards crystallization. In the second step, the capping layer serves as a seed layer that forces the subsequent vertically growth and its crystallization.

6.2.2 Cation Optimization

$MAPbI_3$perovskite with a bandgap of 1.55 eV has been unambiguously the most extensively utilized absorber in PSCs. However, it suffers from severe instability issues due to a phase transition at 55 °C and thermal degradation at 85 °C and also [67]. The instability issues were successfully addressed through the replacement of MA^+ cation with the larger FA^+ one; $FAPbI_3$ exhibits superior thermal stability and narrower bandgap of 1.48 eV compared to $MAPbI_3$ counterpart [68]. However, the large size of FA^+ results in lattice distortion with a yellow non-photoactive δ-phase to be formed at room temperature while the black perovskite α-phase is only present at elevated temperature [69]. To enhance phase stability mixed MA/FA cation perovskites are hence synthesized.

Moreover, the chemically stable, monovalent alkali cations have been used for the preparation of multi-cation perovskites [70]. It was found that the formation energies for alkali cations in A-site substitution are significantly lower those that of the B-site substitution [71]. However, the ionic radius has to meet the requirement of Goldschmidt's empirical tolerance factor ($0.8 < t < 1$) to maintain the 3D perovskite framework (see Section 3.1). Among all alkali cations, only Cs^+ exhibits suitable ionic radius and has been hence hybridized with either MA^+ or FA^+ or a mixture of both at the A-site in multi-cation perovskites along, with the aim to inhibit the undesired phase transition and enhance their photo- and moisture stability. Furthermore, substituting Cs^+ at the A-site has been shown to shrink the cubo-octahedral volume of the perovskite lattice while also strengthening the chemical interaction between FA^+ and I^-. The latter results in significant reduction in trap density and suppresses halide

segregation (*vide infra*) in parallel with making the devices more reproducible and thermally stable. Notably, the tolerance factor of fully inorganic $CsPbX_3$ (where X is Br^- and I^-) is appropriate to attain a black α-phase with a bandgap of 1.73 eV which makes this perovskite suitable for dual-junction tandem PSCs [72].

Besides Cs^+, Rb^+ has also been used to engineer the cation in A-sire in multi-cation perovskites despite the fact that it possesses small ionic radius which leaves $RbPbI_3$ out of the tolerance factor range [73]. Small amounts of Rb^+ have been shown to significantly impact the optoelectronic properties as a consequence of structural variations in the mixed cation perovskites. It was also demonstrated that Rb^+ can increase the conductivity of $(CsFAMA)Pb(IBr)_3$ and reduce capacitive current [74]. Furthermore, the functions of Rb^+ in improving the device performance, thermal and photo stability were confirmed in many cases, which were attributed to reduced non-radiative recombination's and enlarged grain size of the perovskite films along with entropic gains and small internal energy input required for the formation of mixed perovskite in terms of thermodynamics [75].

The findings about Rb^+ motivated a surge of interest for other alkali cations which, however, have proven insufficient in terms of tolerance factor to provide stable perovskite phases. An exception is potassium (K^+), which has been shown to improve the photovoltaic performance of PSCs. K^+ incorporation can increase the crystallinity due to the decreased activation energy for crystallization, and enlarge the grain size thereby leading to fewer defects at grain boundaries, longer carrier lifetime, and enhanced conductivity [76]. Incorporation of K^+ in $CsPbI_2Br$ resulted in smaller lattice spacing as a result of Cs substitution [77].

On the other hand, for the mixed perovskites (such as $FA_{0.85}MA_{0.15}Pb(I_{0.85}Br_{0.15})_3$, K^+ incorporation has expanded the crystal lattice and decreased the bandgap due to both occupation of A-site and/or interstitial ion in the lattice [78]. Due to the sequestration of K^+, excess halide is immobilized at the grain boundaries and surfaces, thereby inhibiting halide migration in parallel with suppressing hysteresis and photoinduced ion segregation.

6.2.3 Halide Optimization

Another approach used to tune the optoelectronic properties of perovskites is through substitution in the halide anion X^- position. Engineering of the halide anion changes the Pb X bond distance and, therefore, the angle between X–Pb–X. With this approach effective bandgap tuning can be achieved. The compounds with I^- have the smaller bandgap (in the range of 1.55–1.61 eV) harvesting light up to near infrared, while those with chlorides exhibit the highest bandgap (2.88–3.13 eV); perovskites with bromine anions (Br^-) exhibit modest bandgap values (2.0–2.44 eV) [79]. The bandgap values of the mixed HPs range between those of the single halide ones.

Mixed-HPs are bandgap-tunable materials which are considered ideal ingredients for use in tandem solar cells where the overall efficiency of the double-junction cells is highly sensitive to the bandgap of the two composite layers [80, 81]. Accordingly, mixed-HPs are already being implemented with great success as absorber layers in perovskite-silicon [82], as well as in perovskite–perovskite tandem cells [83]. The successful mixing of halide ions on the X-site of the perovskite structure represents key factor to the versatility of this exciting class of materials, and will likely be integral for the future commercialization of the perovskite photovoltaic technology.

6.2.4 Stoichiometric and Nonstoichiometric Compositions

For a given perovskite, irrespective of its composition, i.e. single or mixed cation and/or mixed halide, the precise stoichiometry is an important factor governing the optoelectronic properties of the perovskite film and, subsequently, the performance of the fabricated PSC. For instance, a slight excess (no more than 5%) of PbI_2 precursor in the perovskite film has been shown to be beneficial for the device performance and stability [84]. However, larger excess is detrimental, as it deteriorates the attained V_{OC} and hence the overall performance.

In a two-step perovskite synthesis, a PbI_2 film is initially deposited and subsequently exposed to solutions of the organic salts such as methyl ammonium or formamidinium iodide (MAI/FAI) to form the perovskite film. The stoichiometry of the resultant material strongly depends on both the stoichiometry of the reactants and the duration of the second step. Sub-stoichiometric PbI_2 and short duration of the second step may result in uncompleted conversion with some excess PbI_2 to remain in the perovskite film. As the reaction between lead iodide and the organic salt begins from the top side of the already-formed PbI_2 film, in short duration second steps the excess PbI_2 is usually accumulated at the bottom charge transport layer resulting in electronic insulation and inferior device performance if remains in a large excess [85].

However, a small excess of PbI_2 has proven beneficial as it simultaneously passivates surface defects of the electron transport layer (in a forward cell architecture), blocks hole leakage, and facilitates electron transport toward anode. In the inverted devices, accumulation of PbI_2 at the

perovskite/hole transport layer interface could, accordingly, act as an electron blocking layer, facilitate hole injection, and thereby decrease recombination. However, if the formed PbI_2 layer is very thick it may instead insulate and block charge transfer toward the bottom electrode (Figure 6.6a–d). Recent studies indicate that significant deficiency in PbI_2 used for the synthesis of perovskite films leads to loss in J_{SC}, whereas large excess results in a loss in V_{OC}, with the optimal performance to be achieved for a small 5% excess of PbI_2.

In addition, excess of PbI_2 can be also formed when the duration of the second step is higher than that required for complete conversion of the precursors into perovskite. This PbI_2 is formed as a consequence of perovskite degradation and could be beneficial in small amounts. However, very long duration of the second step results in severe perovskite degradation and device failure [86, 87]. One-step methods provide a higher degree of control on the resultant perovskite stoichiometry and generally leave smaller amounts of unreacted PbI_2 in the synthesized perovskite films.
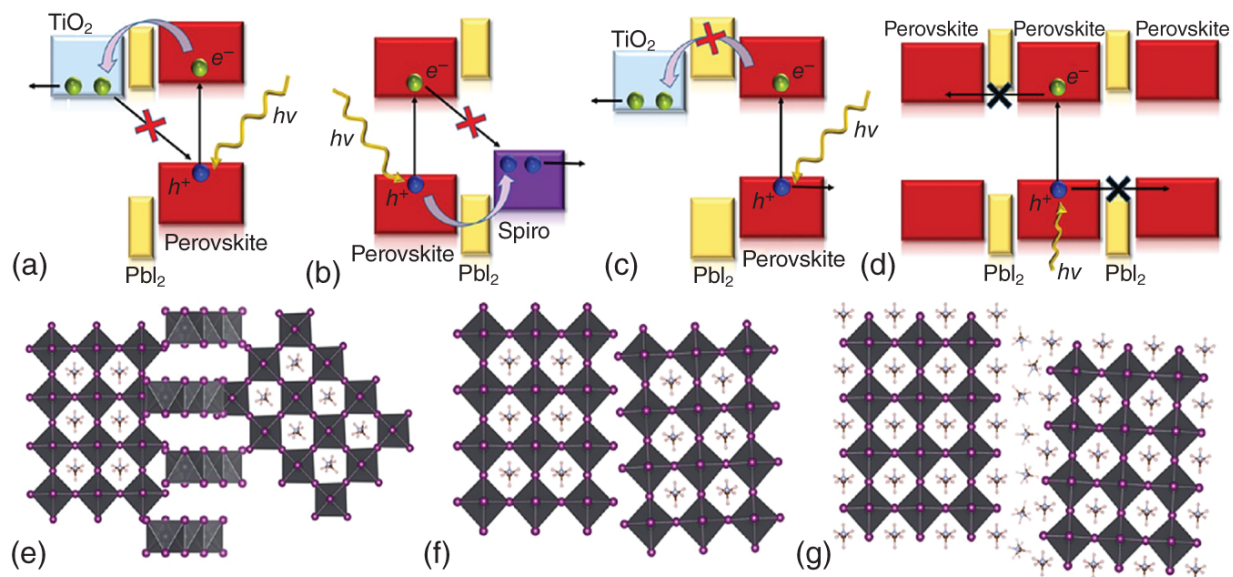
Figure 6.6 Consequences of the formation of excess PbI$_2$ in the perovskite film related to possible energy level alignment suggested in the literature and an artistic illustration of different grain boundary character as a function of overall stoichiometry. (a) PbI$_2$ as a passivating layer at the back contact. (b) PbI$_2$ as a passivation layer next to the hole-selective layer. (c) PbI$_2$ as an electron-blocking layer next to the back contact. (d) PbI$_2$ as charge carrier barrier between perovskite grains. (e) Grain boundary with a large surplus of PbI$_2$. (f) Grain boundary with a small deficiency of organic species. (g) Grain boundary with a large surplus of organic species. Source: Reproduced with permission from Jacobsson et al. [84]. American Chemical Society.

Another important implication concerns the grain boundaries of the perovskite film that are more prone to stoichiometry variations compared to the center of the grains, which are rather insensitive toward small changes in overall stoichiometry. The grain boundaries as well as the regions between the perovskite grains are hence significantly sensitive to the overall composition

([Figure 6.6e–g](#)). This may have a profound impact on the perovskite optoelectronic properties such as density of defects, conductivity, dangling bonds, doping, and ion migration. Some results indicate that PbI_2 acts as passivation interlayer between grains as its presence reduces the recombination rate within grain boundaries rich in PbI_2 [88, 89]. Theoretical calculations indicate that grain boundaries PbI_2-rich exhibit good termination with fewer intra-bandgap states, which would act as possible recombination centers [90]. Other computations predict that perovskite synthesis under poor halide conditions may lead to less bulk defects, which are related to detrimental deep traps [91]. In general, there is a strong correlation between the synthetic procedure followed and the formation of bulk defects [92], which has important implication in the fabricated PSCs.

6.2.5 The Influence of Inorganic Cations on the Formation of Different Phases

Addition of an inorganic cation such as cesium (Cs) in HPs (i.e. $MAPbI_3$, $FAPbI_2$, or mixed cation) has been shown to have a minor effect on the bandgap of the perovskite, hence not altering the absorption spectrum of the resultant material [93]. However, mixed perovskites such as $Cs_{0.2}FA_{0.8}PbI_3$ and $Cs_{0.2}FA_{0.8}PbI_{2.84}Br_{0.16}$ have been found to be extremely stable in temperatures ranging from 20 to 250 °C, contrary to pure $FAPbI_3$ which is unstable and undergoes a phase transition from the hexagonal yellow δ_H-phase to the black perovskite structure at about 156 °C [79].

According to Goldschmidt's rule, stable perovskite phases are formed when the tolerance factor, t, for a structure lies between 0.8 and 1. Due to the large size of FA, the

tolerance factor for hexagonal δ_H-phase of FAPbI$_3$ is higher than 1 [94]. However, the small-size Cs$^+$ cation results in a tolerance factor very small to obtain a stable cubic perovskite structure at room temperature. The photoactive α-phase of CsPbI$_3$ can be attained at temperatures above 300 °C [67, 94]. At room temperature, CsPbI$_3$ forms an orthorhombic yellow phase (δ_O-phase) because it exhibits t < 0.8. Solid-state alloying FA with Cs is a common tool for tailoring the chemical instability of the α-phase of FAPbI$_3$.

The alloying compositions would have smaller t than pure FAPbI$_3$, so the effective tolerance factor is potentially reduced and the perovskite α-phase of FAPbI$_3$ is stabilized. The remarkable stabilization of the perovskite phase over the non-perovskite one upon Cs/FA mixing can be explained on the basis of significant structural and thermodynamic differences between the δ_H-phase of FAPbI$_3$ and δ_O-phase of CsPbI$_3$ perovskite. In particular, the δ_H-phase of the former perovskite consists mainly of 1D pillars made of face-sharing PbI$_6$ octahedra (Figure 6.7a) [75]. These pillars are aligned along the crystallographic direction of c-axis crystallographic but well separated by FA-consisting domains. On the contrary, the δ_O-phase of pure inorganic CsPbI$_3$ crystal is made of 1D pillars consisting of stacked and shifted edge-sharing (not face sharing) PbI$_6$ octahedra surrounded by the Cs$^+$ cation (Figure 6.7b) [73]. This difference also results in different volume per stoichiometric unit of these two systems: for the FAPbI$_3$ δ-phase this is $V \sim 256$ Å^3, whereas for the δ-phase of CsPbI$_3$ it is $V \sim 222$ Å^3 [95, 96].
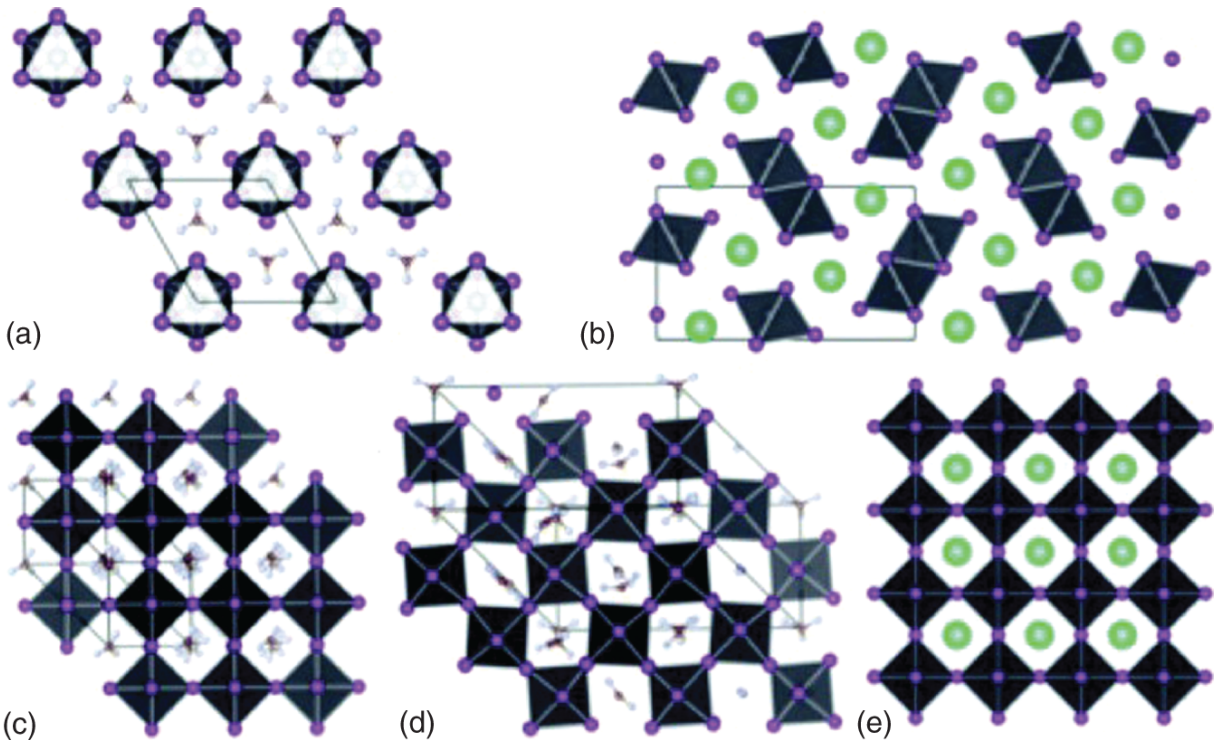
Figure 6.7 Various phases of $FAPbI_3$ and $CsPbI_3$ and variation of internal energy of mixed $Cs_xFA_{1-x}PbI_3$ in different phases. (a) and (b) represent the δ-phase in the FA and Cs perovskites, respectively; (c) and (d) show the α and β $FAPbI_3$, respectively. (e) shows the cubic phase of the $CsPbI_3$ structure. Source: Reproduced with permission from Yi et al. [75]. Royal Society of Chemistry.

However, both α- and β-phases of $FAPbI_3$ are very similar to the perovskite α-phase of $CsPbI_3$ (Figure 6.7c–e), also having nearly identical volumes per stoichiometric unit ($FAPbI_3$: α-phase $V \sim 256\ \text{Å}^3$, β-phase $V \sim 249\ \text{Å}^3$, $CsPbI_3$: α-phase $V \sim 250\ \text{Å}^3$ [97].). This suggests that Cs/FA cation mixing is more favorable for the perovskite α- and β-phases, whereas it is energetically unfavorable in the δ-phase. However, in the δ-phase the unfavorable energetic contribution due to mixing is very large and cannot be compensated by the mixing entropy [73, 75]. In strict difference, the sum of the energetic contribution and

mixing entropy results in a significant reduction of the free energy in the α- and β-perovskite phases, which are stabilized in the formed 3D perovskite over the δ-phase.

Notably, for the mixed FA/Cs perovskite the stable α- and β-phases are formed directly – before the separated δ-phases can prevent mixing – in solutions where Cs and FA are mixed. The free energies have been found of the order of 0.05 and 0.02 eV per stoichiometric unit for the α- and β-phases, respectively. Therefore, the temperature of transition from δ- to α- or β-phase (above 150 °C) is reduced by ~200–300 K when moving from the pure $FAPbI_3$ to the mixed cation $Cs_xFA_{1-x}PbI_3$ perovskite. This explains the stability of the photoactive perovskite phase at room temperature for the mixed compound.

6.2.6 Halide Segregation

Mixed-HPs, such as $MAPb(I_{1-x}Br_x)_3$ ($0 \leq x \leq 1$), are very appealing for photovoltaic applications especially in multi-junction solar cells as they exhibit continuously tunable bandgap values ranging from 1.6–2.3 eV simply by adjusting the ratio of halide precursors [98]. However, when these mixed-HPs are employed at PSCs as the absorber layer, the achieved V_{OC} does not increase monotonically as the bandgap decreases. Hoke et al. have examined the emission properties of $MAPb(I_{1-x}Br_x)_3$ (with $0.2 < x < 1$) perovskites to understand the poor voltage performance of solar cells with the bromide-rich alloys [99]. They found that, upon illumination of these mixed-HP films with light, under illumination intensities of less than 1 sun in less than a minute at room temperature, a strong and reversible photoluminescence (PL) feature appears at around 1.68 eV, which disappears after storing the samples in the dark [99]. They speculated that this emission originates from the halide segregation and the formation of

minority domains having a high iodide content. The emission from these domains can dominate the PL spectra even at low volume fractions because photogenerated carriers relax from the high energy states of the high bandgap Br-rich majority domains into the lower energy states of the I-rich minority ones and predominately emit. In the photovoltaic cell, these domains act as carrier traps, facilitating non-radiative electron–hole recombination, hence inducing voltage loss while also could have implications for the photostability of mixed HPs.

However, the sub-bandgap PL has been found to depend on several factors such as the intensity and duty cycle of illumination [100], the cation on the A-site [101], and the processing conditions as well as the sample pressure [102]. It also depends on the internal light distribution within the material, which is consistent with vertical halide segregation [98]. In particular, the segregation of halide anions is initiated by halide defects in the perovskite structure, which causes the formation of iodide-rich domains near the more defective surface. This segregation is driven by the strong gradient in carrier generation rate through the thickness of these strongly absorbing materials and is dependent on film opacity and therefore thickness.

Overall, halide migration and segregation are promoted by halide defects, such as halide vacancies and interstitials, which provide low-energy migration pathways. The defect-assisted halide migration in $MAPbI_3$ has been also proposed to be initiated by light [103]. Once stored in the dark, entropically driven intermixing of halides returns the system to the initial homogeneous condition. Suppression of the detrimental Hoke effect (which is the light-induced halide segregation [99]) can be achieved in perovskite films engineered to exhibit less density of halide defects and a more homogeneous carrier generation profile.

6.2.7 Interface Engineering

The intrinsic perovskite instability against humidity has been successfully addressed through the application of novel surface/interface engineering approaches such as the formation of a capping or a self-encapsulation layer. The capping layer usually exhibits lower dimensionality and wider bandgap compared to the perovskite absorber and protects the device from moisture penetration while also increasing its tolerance under light or thermal stress. Promising capping/interface layers are those formed by one-dimensional (1D) or 2D HPs which have shown to exhibit superior environmental stability compared with their 3D counterparts. For example, through inserted nitrogen derivatives, such as alkylammonium cations [104], phenylalkylamine [105], and pyrazolyl pyridine compounds [106], at the surface of perovskite films low-dimensionality phases are stabilized through the rapid exchange of protons and subsequent formation of coordination bonds with the perovskite material. For instance, 1D–3D hybrid perovskite material was formed within the whole volume of the perovskite film when 2-(1H-pyrazol-1-yl)pyridine (PZPY) was introduced into 3D HPs [107]. This 1D–3D perovskite structure exhibited a strong thermodynamic self-healing ability as it could effectively block the ion-migration channels of the cations in A-site ions in the 1D perovskite domains with less dense closely packed structure. Moreover, the hybrid 1D–3D structure experienced less density of defects that could form during the crystal growth process, thus enabling a remarkably enhanced PSCs performance and durability under temperature cycling (25–85 °C).

Furthermore, 2D perovskites are also appropriate to form protective (capping) layers on top of the less resilient to moisture 3D ones. For example, a mixed cation 2D

perovskite based on a steric phenyltrimethylammonium (PTA) cation, PTAMAPbI$_4$, has been recently applied as a capping layer on the surface of MAPbI$_3$ by controllable PTAI intercalation via either spin coating or soaking treatment [107]. The 2D PTAMAPbI$_4$ perovskite effectively passivated MAPbI$_3$ while also acting as a locker of volatile MA$^+$ cations hence prohibiting the formation and extraction from the perovskite surface of MAI. By doing so, a highly performing PSC that retained its initial efficiency (above 21%) after 500 hours continuous illumination was fabricated.

An alternative though fascinating approach is the treatment of the perovskite film surface with perovskite quantum dots (QDs) that form a protective layer against moisture penetration [108]. For example, a stable 0D–2D perovskite capping layer was formed on top a 3D perovskite through employing a diammonium porphyrin (ZnPy–NH$_3$Br) to treat CsPbBr$_3$ QDs. That assembly strategy resulted in the formation of large-scale nanocubic perovskite crystals, whereas the capping layer improved charge transport and separation.

Besides low-dimensionality and QD perovskites, effective capping/protective layers of perovskite films have been obtained through inserting hydrophobic species on the surface (or within the bulk) of the perovskite film [109, 110]. For example, hydrophobic bulky tertiary and quaternary alkyl ammonium cations have been assembled via functionalization on the perovskite surface as efficient water-resistive capping layers. The steric effects due to the bulky cations and the change of surface Pb$_5$ I$_{1c}$ bonds effectively hindered water adsorption on the Pb$_{5c}$ sites.

Moreover, aprotic sulfonium cations have recently shown better resilience to humidity compared to protic ammonium

cations [111]. Moreover, coating evaporated MAPI thin films with different hydrophobic molecules, namely trioctyl phosphine oxide and tridodecyl MAI, resulted in a remarkably mitigated degradation of MAPI and formation of PbI_2 and led to high efficiency and enhanced stability single-junction n-i-p PSCs.

6.2.8 Charge Transfer Dynamics

In a PSC, photoexcitation of the perovskite absorber leads to generation of excitons with BEs as low as 50 meV (in some cases it might be even lower ~2 meV) [112, 113], indicating that at room temperature predominately free charges are generated. These photogenerated carriers are then injected toward the charge-transporting layers and, subsequently, the respective electrodes. In the mesoscopic devices, a significant portion of the electrons has been found to be injected into TiO_2 scaffold on the sub-picosecond time scale [114]. This was accomplished by detailed and systematic studies of the ultrafast events related to exciton generation, electron/hole transfer, and ultrafast relaxation using transient absorption spectroscopy (TAS).

In the TAS spectra of $MAPbI_3$, two prominent negative bands and two positive photoinduced absorption (PIA) bands are generally observed [115]. The two negative bands were attributed either to bleaching transitions from two different VBs to a common CB leading to reduced transition probabilities and therefore negative signals in the transient spectra or due to depopulation of the VB [116], or to the existence of a dual excited state composed of a charge transfer band and a charge-separated state [117]. The positive bands contain information about the excited populations, the evolution of excitons and

thermalized charges, as well as hot electrons and holes both at early times and at later times.

The efficient charge transfer toward either a hole or an electron-transporting layer can be monitored through recording the TAS spectra of the perovskite same deposited on the charge-transporting layer of interest. For example, the TAS spectra of a $MAPbI_3$ sample coated on HTM are expected to be dominated by the spectral features of pristine perovskite. However, significant quenching of the negative bands is expected (i.e. faster decay compared to the sample without HTM), if effective hole transfer from the excited $MAPbI_3$ to the HTM occurs. As these bands can be explained by the depopulation of two VBs and the population of the CB, hole transfer from the VBs of the photoexcited perovskite to the HTM would then lead to an increase of the population in the VBs and consequently to a decrease of the amplitudes of these bands.

The electron transfer toward the ETM can be also monitored through a similar manner. TAS studies of the FTO/TiO_2/perovskite samples under excitation at different wavelengths indicated the sub-picosecond electron injection into titania [118]. Moreover, the power-dependent femtosecond TAS measurements showed strong Auger-type multiparticle interactions at early times. They also revealed that the contribution of the bulk perovskite defects in the recombination is small, thus increasing the survival probability of the charges in the excited perovskite film.

References

1 Stoumpos, C.C. and Kanatzidis, M.G. (2015). The renaissance of halide perovskites and their evolution as emerging semiconductors. *Accounts of Chemical Research* 48 (10): 2791–2802.

2 Zhang, X., Shen, J.X., and Van de Walle, C.G. (2020). First-principles simulation of carrier recombination mechanisms in halide perovskites. *Advanced Energy Materials* 10 (13): 1902830.

3 Kieslich, G., Sun, S., and Cheetham, A.K. (2014). Solid-state principles applied to organic–inorganic perovskites: new tricks for an old dog. *Chemical Science* 5 (12): 4712–4715.

4 Goldschmidt, V.M. (1926). Die gesetze der krystallochemie. *Die Naturwissenschaften* 14 (21): 477–485.

5 Bartel, C.J., Sutton, S., Goldsmith, B.R. et al. (2019). New tolerance factor to predict the stability of perovskite oxides and halides. *Science Advances* 5, https://doi.org/10.1126/sciadv.aav0693.

6 Li, Z, Yang, M., Park, J-S et al. (2016). Stabilizing perovskite structures by tuning tolerance factor: formation of formamidinium and cesium lead iodide solid-state alloys. *Chemistry of Materials* 28 (1): 284–292.

7 Zuo, C. and Ding, L. (2015). Solution-processed Cu_2O and CuO as hole transport materials for efficient perovskite solar cells. *Small* 11 (41): 5528–5532.

8 Chatterjee, S. and Pal, A.J. (2016). Introducing Cu_2O thin films as a hole-transport layer in efficient planar perovskite solar cell structures. *Journal of Physical Chemistry C* 120 (3): 1428–1437.

9 Conings, B., Drijkoningen, J., Gauquelin, N. et al. (2015). Intrinsic thermal instability of methylammonium lead

trihalide perovskite. *Advanced Energy Materials* 5 (15): 1500477.

10 Hörantner, M.T., Leijtens, T., Ziffer, M.E. et al. (2017). The potential of multijunction perovskite solar cells. *ACS Energy Letters* 2 (10): 2506–2513.

11 Nejand, B.A., Ahmadi, V., Gharibzadeh, S., and Shahverdi, H.R. (2016). Cuprous oxide as a potential low-cost hole-transport material for stable perovskite solar cells. *ChemSusChem* 9 (3): 302–313.

12 Pellet, N., Gao, P., Gregori, G. et al. (2014). Mixed-organic-cation perovskite photovoltaics for enhanced solar-light harvesting. *Angewandte Chemie* 126 (12): 3215–3221.

13 Guo, Y., Lei, H., Xiong, L. et al. (2018). An integrated organic–inorganic hole transport layer for efficient and stable perovskite solar cells. *Journal of Materials Chemistry A* 6 (5): 2157–2165.

14 Jeon, N.J., Noh, J.H., Kim, Y.C. et al. (2014). Solvent engineering for high-performance inorganic–organic hybrid perovskite solar cells. *Nature Materials* 13 (9): 897–903.

15 Jeon, N.J., Noh, J.H., Yang, W.S. et al. (2015). Compositional engineering of perovskite materials for high-performance solar cells. *Nature* 517 (7535): 476–480.

16 Saliba, M., Matsui, T., Seo, J.-Y. et al. (2016). Cesium-containing triple cation perovskite solar cells: improved stability, reproducibility and high efficiency. *Energy & Environmental Science* 9 (6): 1989–1997.

17 Saliba, M., Matsui, T., Domanski, K. et al. (2016). Incorporation of rubidium cations into perovskite solar cells improves photovoltaic performance. *Science* 354 (6309): 206–209.

18 Yin, W.-J., Shi, T., and Yan, Y. (2014). Unusual defect physics in $CH_3NH_3PbI_3$ perovskite solar cell absorber. *Applied Physics Letters* 104 (6): 063903.

19 Tanaka, K., Takahashi, T., Ban, T. et al. (2003). Comparative study on the excitons in lead-halide-based perovskite-type crystals $CH_3NH_3PbBr_3$ $CH_3NH_3PbI_3$. *Solid State Communications* 127 (9–10): 619–623.

20 Jokar, E., Huang, Z.Y., Narra, S. et al. (2018). Anomalous charge-extraction behavior for graphene-oxide (GO) and reduced graphene-oxide (rGO) films as efficient p-contact layers for high-performance perovskite solar cells. *Advanced Energy Materials* 8 (3): 1701640.

21 Jin, H., Debroye, E., Keshavarz, M. et al. (2020). It's a trap! On the nature of localised states and charge trapping in lead halide perovskites. *Materials Horizons* 7 (2): 397–410.

22 Zheng, Y., Niu, T., Ran, X. et al. (2019). Unique characteristics of 2D Ruddlesden–Popper (2DRP) perovskite for future photovoltaic application. *Journal of Materials Chemistry A* 7 (23): 13860–13872.

23 Yan, J., Qiu, W., Wu, G. et al. (2018). Recent progress in 2D/quasi-2D layered metal halide perovskites for solar cells. *Journal of Materials Chemistry A* 6 (24): 11063–11077.

24 Lan, C., Zhou, Z., Wei, R., and Ho, J.C. (2019). Two-dimensional perovskite materials: from synthesis to energy-related applications. *Materials Today Energy* 11: 61–82.

25 Chowdhury, T.H., Akhtaruzzaman, M., Kayesh, M.E. et al. (2018). Low temperature processed inverted planar perovskite solar cells by r-GO/CuSCN hole-transport bilayer with improved stability. *Solar Energy* 171: 652–657.

26 Eperon, G.E., Paternò, G.M., Sutton, R.J. et al. (2015). Inorganic caesium lead iodide perovskite solar cells. *Journal of Materials Chemistry A* 3 (39): 19688–19695.

27 Smith, I.C., Hoke, E.T., Solis-Ibarra, D. et al. (2014). A layered hybrid perovskite solar-cell absorber with enhanced moisture stability. *Angewandte Chemie International Edition* 53 (42): 11232–11235.

28 Blancon, J.C., Tsai, H., Nie, W. et al. (2017). Extremely efficient internal exciton dissociation through edge states in layered 2D perovskites. *Science* 355 (6331): 1288–1292.

29 Stoumpos, C.C., Cao, D.H., Clark, D.J. et al. (2016). Ruddlesden–Popper hybrid lead iodide perovskite 2D homologous semiconductors. *Chemistry of Materials* 28 (8): 2852–2867.

30 Ishihara, T. (1994). Optical properties of PbI-based perovskite structures. *Journal of Luminescence* 60: 269–274.

31 Yang, Y., Ostrowski, D.P., France, R.M. et al. (2016). Observation of a hot-phonon bottleneck in lead-iodide perovskites. *Nature Photonics* 10 (1): 53–59.

32 Hirasawa, M., Ishihara, T., Goto, T. et al. (1994). Magnetoabsorption of the lowest exciton in perovskite-type compound (CH_3NH_3) PbI_3. *Physica B: Condensed Matter* 201: 427–430.

33 Hong, X., Ishihara, T., and Nurmikko, A.V. (1992). Dielectric confinement effect on excitons in PbI 4-based layered semiconductors. *Physical Review B* 45 (12): 6961.

34 Cho, J., Choi, Y.-H., O'Loughlin, T.E. et al. (2016). Ligand-mediated modulation of layer thicknesses of perovskite methylammonium lead bromide nanoplatelets. *Chemistry of Materials* 28 (19): 6909–6916.

35 Zhang, T., Dar, M.I., Li, G. et al. (2017). Bication lead iodide 2D perovskite component to stabilize inorganic α-$CsPbI_3$ perovskite phase for high-efficiency solar cells. *Science Advances* 3 (9): e1700841.

36 Quan, L.N., Yuan, M., Comin, R. et al. (2016). Ligand-stabilized reduced-dimensionality perovskites. *Journal of the American Chemical Society* 138 (8): 2649–2655.

37 Tu, Y., Wu, J., He, X. et al. (2017). Solvent engineering for forming stonehenge-like PbI_2 nano-structures towards efficient perovskite solar cells. *Journal of Materials Chemistry A* 5 (9): 4376–4383.

38 Wang, Z., Lin, Q., Chmiel, F.P. et al. (2017). Efficient ambient-air-stable solar cells with 2D–3D heterostructured butylammonium-caesium-formamidinium lead halide perovskites. *Nature Energy* 2 (9): 1–10.

39 Li, N., Zhu, Z., Chueh, C.-C. et al. (2017). Mixed cation $FA_xPEA_{1-x}PbI_3$ with enhanced phase and ambient

stability toward high-performance perovskite solar cells. *Advanced Energy Materials* 7 (1): 1601307.

40 Liu, M., Johnston, M.B., and Snaith, H.J. (2013). Efficient planar heterojunction perovskite solar cells by vapour deposition. *Nature* 501 (7467): 395–398.

41 Wong, K.H., Ananthanarayanan, K., Heinemann, M.D. et al. (2012). Enhanced photocurrent and stability of organic solar cells using solution-based NiO interfacial layer. *Solar Energy* 86 (11): 3190–3195.

42 Chen, W., Zhou, Y., Wang, L. et al. (2018). Molecule-doped nickel oxide: verified charge transfer and planar inverted mixed cation perovskite solar cell. *Advanced Materials* 30 (20): 1800515.

43 Chaudhary, N., Chaudhary, R., Kesari, J.P. et al. (2015). Copper thiocyanate (CuSCN): an efficient solution-processable hole transporting layer in organic solar cells. *Journal of Materials Chemistry C* 3 (45): 11886–11892.

44 Xiao, L., Xu, J., Luan, J., et al. (2017). Achieving mixed halide perovskite via halogen exchange during vapor-assisted solution process for efficient and stable perovskite solar cells. *Organic Electronics* 50: 33–42.

45 Park, B.-w., Kedem, N., Kulbak, M. et al. (2018). Understanding how excess lead iodide precursor improves halide perovskite solar cell performance. *Nature Communications* 9 (1): 1–8.

46 LaMer, V.K. and Dinegar, R.H. (1950). Theory, production and mechanism of formation of monodispersed hydrosols. *Journal of the American Chemical Society* 72 (11): 4847–4854.

47 Ng, A., Ren, Z., Hu, H. et al. (2018). A cryogenic process for antisolvent-free high-performance perovskite solar cells. *Advanced Materials* 30 (44): 1804402.

48 Jain, S.M., Qiu, Z., Häggman, L. et al. (2016). Frustrated Lewis pair-mediated recrystallization of $CH_3NH_3PbI_3$ for improved optoelectronic quality and high voltage planar perovskite solar cells. *Energy & Environmental Science* 9 (12): 3770–3782.

49 Xia, H.-R., Sun, W.-T., and Peng, L.-M. (2015). Hydrothermal synthesis of organometal halide perovskites for Li-ion batteries. *Chemical Communications* 51 (72): 13787–13790.

50 Zhai, W., Lin, J., Li, Q. et al. (2018). Solvothermal synthesis of ultrathin cesium lead halide perovskite nanoplatelets with tunable lateral sizes and their reversible transformation into Cs_4PbBr_6 nanocrystals. *Chemistry of Materials* 30 (11): 3714–3721.

51 Kesari, Y. and Athawale, A. (2015). Ultrasound assisted bulk synthesis of $CH_3NH_3PbI_3$ perovskite at room temperature. *Materials Letters* 159: 87–89.

52 Jancik, J., Jancik Prochazkova, A., Scharber, M.C. et al. (2020). Microwave-assisted preparation of organo-lead halide perovskite single crystals. *Crystal Growth & Design* 20 (3): 1388–1393.

53 Dunlap-Shohl, W.A., Zhou, Y., Padture, N.P., and Mitzi, D.B. (2018). Synthetic approaches for halide perovskite thin films. *Chemical Reviews* 119 (5): 3193–3295.

54 Leupold, N., Schötz, K., Cacovich, S. et al. (2019). High versatility and stability of mechanochemically synthesized halide perovskite powders for optoelectronic

devices. *ACS Applied Materials & Interfaces* 11 (33): 30259–30268.

55 Sutton, R.J., Eperon, G.E., Miranda, L. et al. (2016). Bandgap-tunable cesium lead halide perovskites with high thermal stability for efficient solar cells. *Advanced Energy Materials* 6 (8): 1502458.

56 Chen, B., Rudd, P.N., Yang, S. et al. (2019). Imperfections and their passivation in halide perovskite solar cells. *Chemical Society Reviews* 48 (14): 3842–3867.

57 Aydin, E., De Bastiani, M., and De Wolf, S. (2019). Defect and contact passivation for perovskite solar cells. *Advanced Materials* 31 (25): 1900428.

58 Haque, M.A., Sheikh, A.D., Guan, X., and Wu, T. (2017). Metal oxides as efficient charge transporters in perovskite solar cells. *Advanced Energy Materials* 7 (20): 1602803.

59 Timasi, N., Tafazoli, S., Nouri, E. et al. (2019). Solvent engineering based on triethylenetetramine (TETA) for perovskite solar cells processed in ambient-air. *Photochemical & Photobiological Sciences* 18 (5): 1228–1234.

60 Zuo, L., Dong, S., De Marco, N. et al. (2016). Morphology evolution of high efficiency perovskite solar cells via vapor induced intermediate phases. *Journal of the American Chemical Society* 138 (48): 15710–15716.

61 Fang, X., Wu, Y., Lu, Y. et al. (2017). Annealing-free perovskite films based on solvent engineering for efficient solar cells. *Journal of Materials Chemistry C* 5 (4): 842–847.

62 Liu, J., Gao, C., He, X. et al. (2015). Improved crystallization of perovskite films by optimized solvent annealing for high efficiency solar cell. *ACS Applied Materials & Interfaces* 7 (43): 24008–24015.

63 Chen, H., Wei, Z., He, H. et al. (2016). Solvent engineering boosts the efficiency of paintable carbon-based perovskite solar cells to beyond 14%. *Advanced Energy Materials* 6 (8): 1502087.

64 Zheng, Z.-H., Lan, H.-B., Su, Z.-H. et al. (2019). Single source thermal evaporation of two-dimensional perovskite thin films for photovoltaic applications. *Scientific Reports* 9 (1): 1–9.

65 Zhang, S., Wu, S., Chen, W. et al. (2018). Solvent engineering for efficient inverted perovskite solar cells based on inorganic $CsPbI_2Br$ light absorber. *Materials Today Energy* 8: 125–133.

66 Zhang, J., Zhang, L., Li, X. et al. (2019). Binary solvent engineering for high-performance two-dimensional perovskite solar cells. *ACS Sustainable Chemistry & Engineering* 7 (3): 3487–3495.

67 Stoumpos, C.C., Malliakas, C.D., and Kanatzidis, M.G. (2013). Semiconducting tin and lead iodide perovskites with organic cations: phase transitions, high mobilities, and near-infrared photoluminescent properties. *Inorganic Chemistry* 52 (15): 9019–9038.

68 Lee, J.W., Seol, D.J., Cho, A.N., and Park, N.G. (2014). High-efficiency perovskite solar cells based on the black polymorph of $HC(NH_2)_2PbI_3$. *Advanced Materials* 26 (29): 4991–4998.

69 Lee, J.W., Kim, D.H., Kim, H.S. et al. (2015). Formamidinium and cesium hybridization for photo-and moisture-stable perovskite solar cell. *Advanced Energy Materials* 5 (20): 1501310.

70 Johnson, M., Baryshev, S.V., Thimsen, E. et al. (2014). Alkali-metal-enhanced grain growth in Cu_2ZnSnS_4 thin films. *Energy & Environmental Science* 7 (6): 1931–1938.

71 Cao, J., Tao, S.X., Bobbert, P.A. et al. (2018). Interstitial occupancy by extrinsic alkali cations in perovskites and its impact on ion migration. *Advanced Materials* 30 (26): 1707350.

72 Wang, Y., Zhang, T., Kan, M., and Zhao, Y. (2018). Bifunctional stabilization of all-inorganic α-$CsPbI_3$ perovskite for 17% efficiency photovoltaics. *Journal of the American Chemical Society* 140 (39): 12345–12348.

73 Trots, D.M. and Myagkota, S.V. (2008). High-temperature structural evolution of caesium and rubidium triiodoplumbates. *Journal of Physics and Chemistry of Solids* 69 (10): 2520–2526.

74 Yadav, P., Dar, M.I., Arora, N. et al. (2017). The role of rubidium in multiple-cation-based high-efficiency perovskite solar cells. *Advanced Materials* 29 (40): 1701077.

75 Yi, C., Luo, J., Meloni, S. et al. (2016). Entropic stabilization of mixed A-cation ABX_3 metal halide perovskites for high performance perovskite solar cells. *Energy & Environmental Science* 9 (2): 656–662.

76 Nam, J.K., Chai, S.U., Cha, W. et al. (2017). Potassium incorporation for enhanced performance and stability of

fully inorganic cesium lead halide perovskite solar cells. *Nano Letters* 17 (3): 2028–2033.

77 Tang, Z., Bessho, T., Awai, F. et al. (2017). Hysteresis-free perovskite solar cells made of potassium-doped organometal halide perovskite. *Scientific Reports* 7 (1): 1–7.

78 Bu, T., Liu, X., Zhou, Y. et al. (2017). A novel quadruple-cation absorber for universal hysteresis elimination for high efficiency and stable perovskite solar cells. *Energy & Environmental Science* 10 (12): 2509–2515.

79 Crespo, C.T. (2019). The effect of the halide anion on the optical properties of lead halide perovskites. *Solar Energy Materials & Solar Cells* 195: 269–273.

80 Bush, K.A., Palmstrom, A.F., Yu, Z.J. et al. (2017). 23.6%-efficient monolithic perovskite/silicon tandem solar cells with improved stability. *Nature Energy* 2 (4): 1–7.

81 Knight, A.J. and Herz, L.M. (2020). Preventing phase segregation in mixed-halide perovskites: a perspective. *Energy & Environmental Science* 13 (7): 2024–2046.

82 Duong, T., Wu, Y., Shen, H. et al. (2017). Rubidium multication perovskite with optimized bandgap for perovskite-silicon tandem with over 26% efficiency. *Advanced Energy Materials* 7 (14): 1700228.

83 Eperon, G.E., Leijtens, T., Bush, K.A. et al. (2016). Perovskite-perovskite tandem photovoltaics with optimized band gaps. *Science* 354 (6314): 861–865.

84 Jacobsson, T.J., Correa-Baena, J.-P., Halvani Anaraki, E. et al. (2016). Unreacted PbI_2 as a double-edged sword for enhancing the performance of perovskite solar cells.

Journal of the American Chemical Society 138 (32): 10331–10343.

85 Kumar, V., Barbé, J., Schmidt, W.L. et al. (2018). Stoichiometry-dependent local instability in MAPbI$_3$ perovskite materials and devices. *Journal of Materials Chemistry A* 6 (46): 23578–23586.

86 Luo, Y., Aharon, S., Stuckelberger, M. et al. (2018). The relationship between chemical flexibility and nanoscale charge collection in hybrid halide perovskites. *Advanced Functional Materials* 28 (18): 1706995.

87 Ma, Q., Huang, S., Chen, S. et al. (2017). The effect of stoichiometry on the stability of inorganic cesium lead mixed-halide perovskites solar cells. *Journal of Physical Chemistry C* 121 (36): 19642–19649.

88 Chen, Q., Zhou, H., Song, T.-B. et al. (2014). Controllable self-induced passivation of hybrid lead iodide perovskites toward high performance solar cells. *Nano Letters* 14 (7): 4158–4163.

89 Wang, L., McCleese, C., Kovalsky, A. et al. (2014). Femtosecond time-resolved transient absorption spectroscopy of CH$_3$NH$_3$PbI$_3$ perovskite films: evidence for passivation effect of PbI$_2$. *Journal of the American Chemical Society* 136 (35): 12205–12208.

90 Haruyama, J., Sodeyama, K., Han, L., and Tateyama, Y. (2014). Termination dependence of tetragonal CH$_3$NH$_3$PbI$_3$ surfaces for perovskite solar cells. *Journal of Physical Chemistry Letters* 5 (16): 2903–2909.

91 Buin, A., Pietsch, P., Xu, J. et al. (2014). Materials processing routes to trap-free halide perovskites. *Nano Letters* 14 (11): 6281–6286.

92 Song, Z., Watthage, S.C., Phillips, A.B. et al. (2015). Impact of processing temperature and composition on the formation of methylammonium lead iodide perovskites. *Chemistry of Materials* 27 (13): 4612–4619.

93 Choi, H., Jeong, J., Kim, H.-B. et al. (2014). Cesium-doped methylammonium lead iodide perovskite light absorber for hybrid solar cells. *Nano Energy* 7: 80–85.

94 Li, Z., Yang, M., Park, J.-S. et al. (2016). Stabilizing perovskite structures by tuning tolerance factor: formation of formamidinium and cesium lead iodide solid-state alloys. *Chemistry of Materials* 28 (1): 284–292.

95 Collavini, S., Völker, S.F., and Delgado, J.L. (2015). Understanding the outstanding power conversion efficiency of perovskite-based solar cells. *Angewandte Chemie International Edition* 54 (34): 9757–9759.

96 Bai, Y., Chen, H., Xiao, S. et al. (2016). Effects of a molecular monolayer modification of NiO nanocrystal layer surfaces on perovskite crystallization and interface contact toward faster hole extraction and higher photovoltaic performance. *Advanced Functional Materials* 26 (17): 2950–2958.

97 Filip, M.R., Eperon, G.E., Snaith, H.J., and Giustino, F. (2014). Steric engineering of metal-halide perovskites with tunable optical band gaps. *Nature Communications* 5 (1): 1–9.

98 Barker, A.J., Sadhanala, A., Deschler, F. et al. (2017). Defect-assisted photoinduced halide segregation in mixed-halide perovskite thin films. *ACS Energy Letters* 2 (6): 1416–1424.

99 Hoke, E.T., Slotcavage, D.J., Dohner, E.R. et al. (2015). Reversible photo-induced trap formation in mixed-halide hybrid perovskites for photovoltaics. *Chemical Science* 6 (1): 613–617.

100 Slotcavage, D.J., Karunadasa, H.I., and McGehee, M.D. (2016). Light-induced phase segregation in halide-perovskite absorbers. *ACS Energy Letters* 1 (6): 1199–1205.

101 McMeekin, D.P., Sadoughi, G., Rehman, W. et al. (2016). A mixed-cation lead mixed-halide perovskite absorber for tandem solar cells. *Science* 351 (6269): 151–155.

102 Jaffe, A., Lin, Y., Beavers, C.M. et al. (2016). High-pressure single-crystal structures of 3D lead-halide hybrid perovskites and pressure effects on their electronic and optical properties. *ACS Central Science* 2 (4): 201–209.

103 Le Bail, A., Duroy, H., and Fourquet, J.L. (1988). Ab-initio structure determination of $LiSbWO_6$ by X-ray powder diffraction. *Materials Research Bulletin* 23 (3): 447–452.

104 Chen, Y., Sun, Y., Peng, J. et al. (2017). Tailoring organic cation of 2D air-stable organometal halide perovskites for highly efficient planar solar cells. *Advanced Energy Materials* 7 (18): 1700162.

105 Lee, J.-W., Dai, Z., Han, T.-H. et al. (2018). 2D perovskite stabilized phase-pure formamidinium perovskite solar cells. *Nature Communications* 9 (1): 1–10.

106 Fan, J., Ma, Y., Zhang, C. et al. (2018). Thermodynamically self-healing 1D–3D hybrid perovskite solar cells. *Advanced Energy Materials* 8 (16): 1703421.

107 Wang, X., Wang, Y., Zhang, T. et al. (2020). Steric mixed-cation 2D perovskite as a methylammonium locker to stabilize $MAPbI_3$. *Angewandte Chemie* 132 (4): 1485–1489.

108 Feng, X.-X., Lv, X.-D., Liang, Q. et al. (2020). Diammonium porphyrin-induced $CsPbBr_3$ nanocrystals to stabilize perovskite films for efficient and stable solar cells. *ACS Applied Materials & Interfaces* 12 (14): 16236–16242.

109 Yang, S., Wang, Y., Liu, P. et al. (2016). Functionalization of perovskite thin films with moisture-tolerant molecules. *Nature Energy* 1 (2): 1–7.

110 Palazon, F., Perez-del-Rey, D., Marras, S. et al. (2018). Coating evaporated MAPI thin films with organic molecules: improved stability at high temperature and implementation in high-efficiency solar cells. *ACS Energy Letters* 3 (4): 835–839.

111 Kim, B., Kim, M., Lee, J.H., and Seok, S.I. (2020). Enhanced moisture stability by butyldimethylsulfonium cation in perovskite solar cells. *Advanced Science* 7 (3): 1901840.

112 D'innocenzo, V., Grancini, G., MJP, A. et al. (2014). Excitons versus free charges in organo-lead tri-halide perovskites. *Nature Communications* 5 (1): 1–6.

113 Lin, Q., Armin, A., Nagiri, R.C.R. et al. (2015). Electro-optics of perovskite solar cells. *Nature Photonics* 9 (2): 106–112.

114 Piatkowski, P., Cohen, B., Ramos, F.J. et al. (2015). Direct monitoring of ultrafast electron and hole dynamics in perovskite solar cells. *Physical Chemistry Chemical Physics* 17 (22): 14674–14684.

115 Brauer, J.C., Lee, Y.H., Nazeeruddin, M.K., and Banerji, N. (2015). Charge transfer dynamics from organometal halide perovskite to polymeric hole transport materials in hybrid solar cells. *Journal of Physical Chemistry Letters* 6 (18): 3675–3681.

116 Stamplecoskie, K.G., Manser, J.S., and Kamat, P.V. (2015). Dual nature of the excited state in organic–inorganic lead halide perovskites. *Energy & Environmental Science* 8 (1): 208–215.

117 Manser, J.S. and Kamat, P.V. (2014). Band filling with free charge carriers in organometal halide perovskites. *Nature Photonics* 8 (9): 737–743.

118 Hsu, H.Y., Wang, C.Y., Fathi, A. et al. (2014). Femtosecond excitonic relaxation dynamics of perovskite on mesoporous films of Al_2O_3 and NiO nanoparticles. *Angewandte Chemie* 126 (35): 9493–9496.

7
The Efficiency Progress in Printable Mesoscopic Perovskite Solar Cells

Xufeng Xiao[1], Wenhao Zhang[1], Qifei Wang[1], Wenjun Wu[2], and Yue Hu[1]

[1] Huazhong University of Science and Technology, Wuhan National Laboratory for Optoelectronics, 1037 Luoyu Road, Wuhan, 430074, PR China

[2] East China University of Science & Technology, Feringa Nobel Prize Scientist Joint Research Center, School of Chemistry and Molecular Engineering, Key Laboratory for Advanced Materials and Joint International Research Laboratory of Precision Chemistry and Molecular Engineering, 130 Meilong Road, Shanghai, 200237, PR China

7.1 Introduction

Before metal halide perovskites were introduced as a light absorber into the photovoltaic field, dye-sensitized solar cells (DSSCs) has been developed as a potentially low-cost alternative for silicon wafers. Reported by Michael Grätzel and Brian O'Regan in 1991, dye-sensitized solar cell (DSSC) is the only photovoltaic device that mimics natural photosynthesis, which separates the process of light-harvesting and charge carrier transport [1]. The main advantages of this solar cell are the ease of manufacture, non-toxicity of the materials, and the possibility to fabricate solar cells on any substrates. However, the DSSCs still have limitations such as comparatively low efficiency (the record certified efficiency is less than 15%) and poor long-term stability. In 1998, Grätzel group reported a solid-state DSSC type in which the liquid electrolyte was replaced by a hole conductor, which solves the problem of liquid leakage, iodide corrosion, etc. [2]. However, the low molar absorption coefficient of the ruthenium dyes and the narrow light absorption of organic dyes largely limit the further performance improvement of such solid-state DSSCs.

The first application of metal halide perovskite materials in solar cells is realized by Miyasaka group in 2009, based on the same structure of

the liquid-state DSSCs, using mesoporous TiO_2 as the electron transporter and I^-/I_3^- redox couple in acetonitrile (ACN) as the electrolyte [3]. The perovskites actually dissolve in ACN so the device can only last for seconds. However, the incident photo-to-current conversion efficiency spectrum exhibited a very broad absorbance of the $MAPbI_3$ and the $MAPbBr_3$ type resulted in a very high open-circuit voltage, so they are very promising. In 2012, Park and Grätzel tried these perovskite materials in the solid-state DSSC and achieved a PCE of 9.7% [4]. Henry J. Snaith replaced mesoporous TiO_2 with mesoporous Al_2O_3 (Al_2O_3 is not an electron-accepting layer) to obtain 10.9% PCE, which means that the mesoporous oxide layer can be used as a scaffold for perovskite deposition, and perovskite materials can transport electrons on their own in the absence of electron transport materials [5]. It was not until 2013 that the field really took off when Grätzel obtained the first 14.1% certified efficiency of PSCs based on the FTO/compact TiO_2/mesoscopic TiO_2/HTM/Au structure (Figure 7.1) [7]. After a series of improvements such as device structure adjustment, perovskite material morphology, and component regulation, and interface optimization, the current certified efficiency of PSCs has reached 25.7% [12].
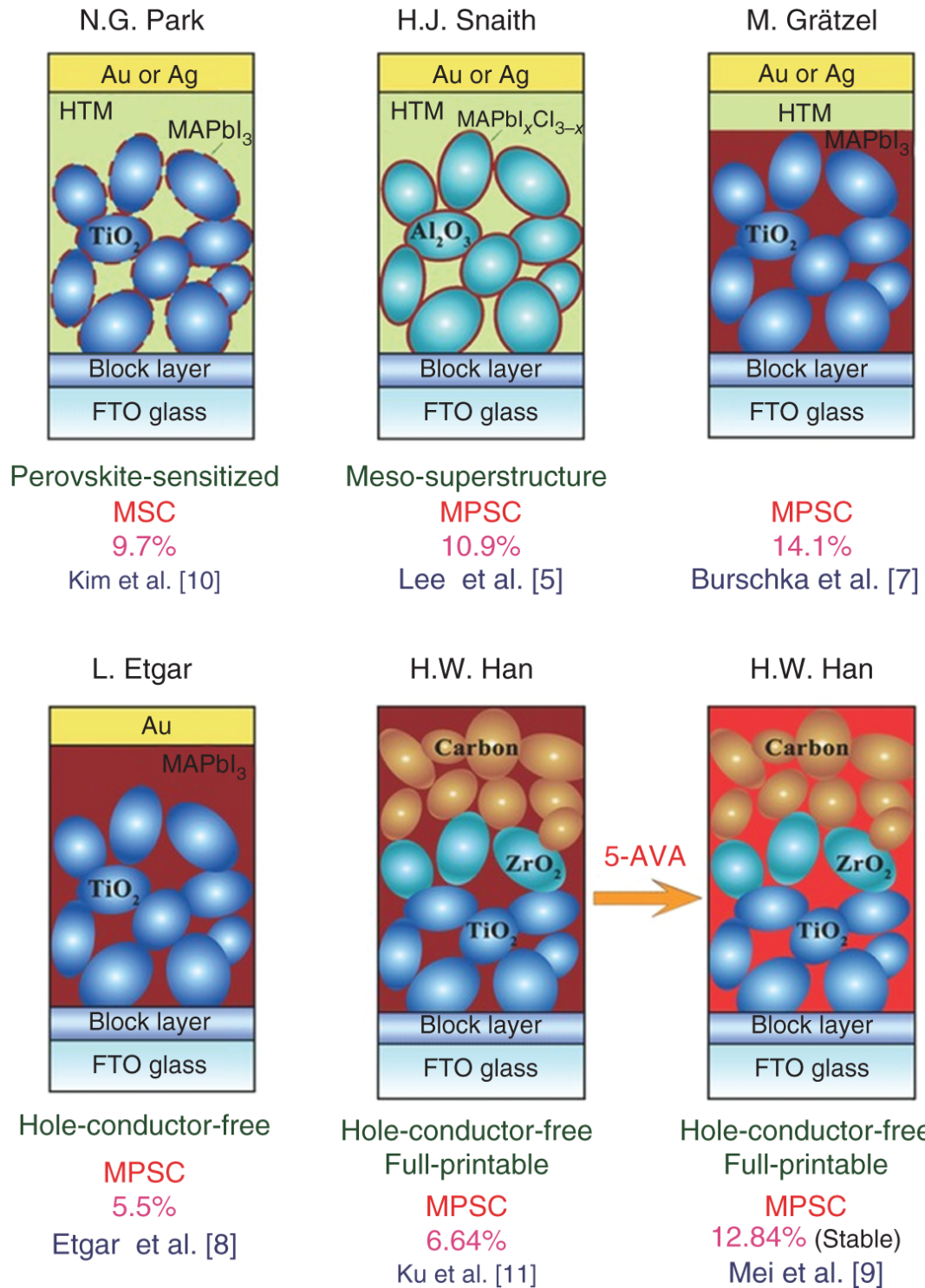
Figure 7.1 Historic architecture evolution of PSCs, starting from dye-sensitized MSC to classical structure of PSC. Source: Rong et al. [6]/With permission of John Wiley & Sons.

Some simplified cell structures are of great interest in the development of PSCs structures, such as electron-transport-free PSCs and hole-conductor-free PSCs with electrodes as electron or hole acceptors. The hole-transport-free PSCs, which first appeared in 2012. At that time, Lioz Etgar showed that the PSCs worked without hole transporting materials and achieved a photovoltaic conversion efficiency of 5.5% [8]. In 2013, Hongwei Han replaced the conventional layer-by-layer deposition with screen-printed mesoscopic TiO_2/ZrO_2/Carbon structure and obtained 6.64% efficiency [13]. Afterwards, they found that the introduction of 5-AVA molecules into perovskite significantly improved the stability of the printable PSCs and obtained a certified PCE of 12.84%, which led to a wider interest in cavity transport layer-free chalcogenide solar cells. which attracted wider attention for the printable hole-conductor-free PSCs [9].

The main challenges in improving the performance of printable mesoscopic PSCs lie in the control of the perovskite crystallization in the mesopores and the separation of carriers in the absence of hole conductor. Different from traditional PSCs which are usually fabricated layer by layer with the spin-coating method, printable mesoscopic PSCs are fabricated by the drop-casting method, in which the perovskite materials go through the in-suit growth in the mesoporous scaffold. Whether the perovskite materials could fill the mesopores densely could directly influence the interface contact among the perovskite and other functional materials, which further determines several properties of devices including carrier transport, defects density, and crystallinity. Due to the unique device structure, some compositions or additives that are suitable for traditional devices may lead to bad pore-filling in printable mesoscopic PSCs. The interface properties are also more complex in the mesoporous scaffold for the large specific surface area of nanoparticles could lead to higher surface energy and bring complex factors to the crystallization of perovskite. There are still many scientific problems that are worth to be explored and solved in printable mesoscopic PSCs.

In this chapter, we introduce the methods of improving the performance of printable mesoscopic PSCs from four aspects, including solvent engineering and annealing, composition engineering, additive engineering, and interface engineering. Detailed differences between traditional PSCs and printable mesoscopic PSCs are compared and some existing and possible

methods could be explored and utilized in printable mesoporous PSCs.

7.2 Solvent Engineering and Annealing

Solvent and annealing process could influence the nucleation and growth of perovskite crystals. In the fabrication of PSCs, the solvent is not only used to assist in dissolving certain precursor components but also to form the intermediate/adduct with PbI_2. To attain dense and uniform morphology as well as high crystallinity, a suitable solvent is of vital importance. As for the annealing process, a proper annealing temperature and time are necessary to get the black phase perovskite with high quality. As a result, choosing the proper strategy of solvent engineering and annealing could assist in optimizing the crystallization process of perovskite.

7.2.1 Solvent Engineering

The crystallization of perovskite materials includes nucleation and crystal growth processes, which can be significantly influenced by the properties of certain solvents. Organic polar solvents are commonly used in preparing the perovskite precursor solutions, including dimethylformamide (DMF), [14] DMSO, [15] γ-butyrolactone (GBL), [16, 17] N-methyl-2-pyrrolidone (NMP), [18] 2-methoxyethanol (2-ME), and acetonitrile (ACN).

For traditional PSCs, the solvent is widely used to form the intermediate, which could be transformed into perovskite through annealing. The formation of MAI·PbI_2·DMF intermediate was reported by Guo et al. In the perovskite precursor solution, DMF, PbI_2, and MAI could form stable intermediate due to the coordination interaction, which could react at 40–80 °C. When the intermediate film is annealed at 100 °C, the intermediate phase could be converted to the perovskite phase [14]. Subsequently, Gao et al. reported that the DMF existing in the intermediates could induce the dissolution–recrystallization process based on Ostwald ripening model during annealing process, resulting in the increased perovskite grain size [19]. Besides the DMF, DMSO is also used in the precursor solution, which has a stronger coordination with PbI_2 compared with DMF. Park et al. found the formation of Lewis acid–base adducts between DMSO and PbI_2 using Fourier transform infrared spectroscopy (FTIR). The perovskite film with high quality was attained based on

the stronger interaction between Pb^{2+} and DMSO [15]. Rong et al. reported the structure of the $MA_2Pb_3I_8 \cdot 2DMSO$ intermediate when DMF and DMSO were used as mixed solvents and inferred that the intermediate could slow down the crystallization process of perovskite, which was beneficial for the control of morphology and grain size of the perovskite film (Figure 7.2) [20]. Similar conclusions also apply to precursor with GBL, Pb^{2+} tends to coordinate with I^- or GBL according to the concentration of I^- in the precursor solution, which leads to the formation of the intermediate with different structures. The morphology and other properties of perovskite films would exhibit many differences due to the intermediate structures [17].
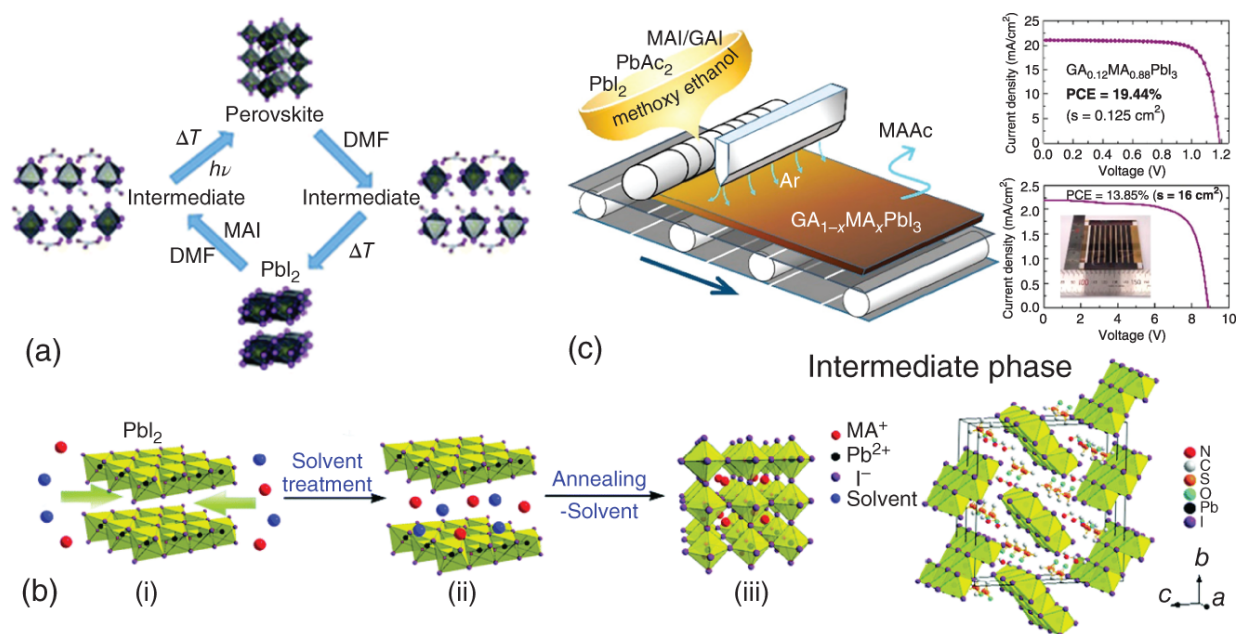
Figure 7.2 (a) Phase transformations between perovskite precursors and perovskite materials using DMF as the solvent. Source: Guo et al. [14]/Royal Society of Chemistry. (b) Scheme of the $MAPbI_3$ perovskite thin film forming process and crystal structure of the intermediate phase $MA_2Pb_3I_8 \cdot 2DMSO$. Source: Rong et al. [20]/Royal Society of Chemistry. (c) The air-knife-assisted D-bar coating process and performance of $GA_{0.12}MA_{0.88}PbI_3$-based perovskite solar cell and module using 2-methoxyethanol as the solvent. Source: Lee et al. [21], American Chemical Society.

Besides the property of coordination ability, the volatility and polarity of a certain solvent could also influence the quality of the perovskite film. Hendriks et al. adopted 2-ME as the solvent for the perovskite

precursor solution, which facilitated the rapid nucleation and grain growth of perovskite due to its higher volatility and lower polarity than DMF. The perovskite film fabricated with 2-ME exhibited improved surface coverage with less pinholes [22]. 2-ME could also be used in the preparation of large-area perovskite films due to its high volatility. In 2019, Lee et al. reported the preparation of large-area perovskite films with flat and uniform morphology based on 2-ME, which benefited from the rapid evaporation of solvent. Finally, the device employing a piece of large-area perovskite film (~46 cm^2) based on the $GA_{0.12}MA_{0.88}PbI_3$ achieved a PCE of 19.44% [21]. Moreover, Deng et al. reported a method of fast-blading large-area perovskite films. Combining volatile and low-volatile solvents could achieve both fast drying and large perovskite grains. The certified module PCE of 16.4% was achieved with an aperture area of 63.7 cm^2 based on the mixed solvent of ACN, 2-ME and DMSO [23].

In addition to the traditional liquid solvent, the MA gas could also be used as a special solvent in the fabrication of PSCs. Zhou et al. reported that $MAPbI_3$ perovskite crystals could turn to liquid phase when crystals were exposed to the MA gas, which could recrystallize after removing the MA gas. This recrystallization process could significantly reduce the surface roughness and pinhole of the perovskite film [24]. However, the liquid phase ($MAPbI_3 \cdot xMA$) formed by $MAPbI_3$ and MA has a high viscosity, which could not suitable for the fabrication of devices. Noel et al. developed a new low boiling point, low viscosity solvent system by combining ACN and MA, in which the perovskite film could be obtained under vacuum without thermal annealing. The devices also achieved a PCE of over 17% [25]. This solvent system also shows advantages for large-area fabrication. Jeong et al. prepared a perovskite film with a highly preferred orientation over an area of 100 cm^2 using ACN and MA mixed solvents, which facilitated an average PCE of 17.01% of resulting devices [25].

For printable mesoscopic PSCs, the selection of solvent could be relatively difficult because of the complexity of mesoscopic structure. Different from traditional PSCs, whether the perovskite materials could fill into the mesoscopic scaffold densely should be taken into consideration firstly for printable mesoscopic PSCs. Due to the large specific surface area of the mesopores, numerous and irregular interfaces exist among perovskite grains and other mesoporous layers in devices. The dense pore-filling determines good contact in the
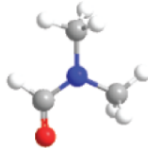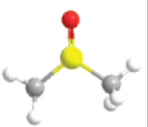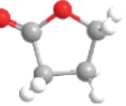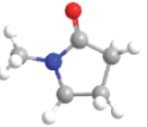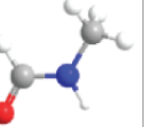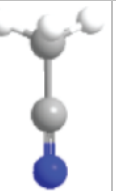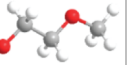
interface, which influences the light absorption and carrier transport inside devices. To achieve dense pore-filling, the solvent needs to meet several requirements in hydrophilic, viscosity, polarity, volatility, and so on.

The effect of solvent properties on perovskite crystallization in mesoporous structure was reported by Chen et al., who suggested that high viscosity and high polarity solvents are not conducive to the infiltration of the precursor solution into the hydrophobic C layer, but the solvent with high polarity helps the infiltration of hydrophilic TiO_2 layer. Among common solvents, DMF exhibits the smallest viscosity, GBL and NMP share a similar value, while DMSO owns the largest viscosity, and their polarity order is DMSO > NMP > DMF > GBL. After balancing the solvent viscosity and polarity, the perovskite precursor solution can be fully infiltrated into the printable triple-mesoporous scaffold using the mixed solvent consisting of DMF and DMSO with optimized ratio. In addition, compared to other solvents, $MAI \cdot PbI_2 \cdot DMSO$ intermediate could be more stable due to the stronger coordination between DMSO and PbI_2, which effectively slows down the crystallization process. The relatively slower crystallization process helps obtain high-quality perovskite crystals as well as uniform and dense pore-filling in printable mesoscopic structure [26]. N-methylformamide (NMF), which has a similar structure to DMF, can also be used as a perovskite precursor solvent. Compared with the above solvents, NMF has the highest PbI_2 solubility, which is related to the fact that NMF has a high solvent donor number and solvent hydrogen bond donor number. Liu et al. found that NMF does not strongly interact with MAI and PbI_2, allowing the direct formation of $MAPbI_3$ crystals from the precursor based on NMF. This facilitates the achievement of adequate growth of perovskite grains in mesoporous structures [27]. Other polar solvents such as methanol and ethanol can also effectively regulate the properties of precursor solutions. Printable mesoscopic PSCs have shown excellent stability, especially when the bifunctional additive 5-AVAI is introduced to the $MAPbI_3$ precursor. 5-AVAI and other similar bifunctional molecules only work when GBL is used as the solvent. However, some precipitate would appear due to relatively low solubility. The precipitate could change the stoichiometric of precursor components dissolved in the solution and further damage the performance of devices. Ming et al. introduced ethanol into such precursor solution to regulate the coordination between GBL and

PbI_2, which effectively improves the stability of the precursor solution as well as its wettability and thus facilitates the perovskite crystallization [28] (Table 7.1).

The liquid phase of $MAPbI_3 \cdot xMA$ exhibits a high viscosity which is not suitable for spin-coating method. For printable mesoscopic PSCs, $MAPbI_3 \cdot xMA$ could spread into the mesoscopic scaffold because of the gravity and capillary action of mesoporous. When the MA gas is removed from the $MAPbI_3 \cdot xMA$ phase, the change in volume is not obvious compared with the crystallization process using common polar solvents, which could be beneficial for the pore-filling inside the mesopores. Hong et al. treated the $MAPbI_3$ devices with MA gas to realize the recrystallization of perovskite in the mesoscopic scaffold. The posttreatment achieved a uniform and dense perovskite pore-filing with high crystallinity and reached a PCE of 15.26% in the printable mesoscopic PSCs. More importantly, this posttreatment strategy allows the regeneration of the photo-degraded PSCs via the crystal reconstruction and the PCE could recover to 91% of the initial value after two cycles of the photodegradation-recovery process, which extends the lifetime of perovskite solar cells [29]. Wagner et al. used MA gas and ACN to prepare a $MAPbI_3$ precursor solution and achieved dense filling and improved perovskite crystallization inside the triple-mesoporous scaffold. The printable mesoscopic PSCs obtained the open-circuit voltage (V_{OC}) of up to 1 V which was the highest V_{OC} reported at the time [30]. Based on the same interaction of methylamine gas and $MAPbI_3$, Guan et al. reported an in situ single-crystal transfer (ICT) process based on gas–solid interaction to deposit perovskite $MAPbI_3$ absorber in the scaffold. After exposure to methylamine atmosphere, the $MAPbI_3$ single crystal can change to liquid phase and then penetrate into the mesoporous scaffold, and after removing the MA gas, the liquid phase could recrystallize into the solid phase in the mesopores. Due to the dense filling, high crystallinity, and longer carrier lifetime, the champion device achieved a PCE of 15.87% with excellent stability in printable mesoscopic PSCs prepared by the ICT process [31].

Table 7.1 Typical physical and chemical properties of common organic solvents used for perovskite precursor solutions.

Solvent	DMF	DMSO	GBL	NMP	NMF	ACN	2-ME
Chemical structure							
Chemical formula	C_3H_7NO	C_2H_6OS	$C_4H_6O_2$	C_5H_9NO	C_2H_5NO	C_2H_3N	$C_3H_8O_2$
Boiling point (°C)	153	189	204	202	198	82	124
Vapor pressure (mmHg, 20 °C)	2.7	0.42	1.5	0.29	—	72.8	9.8
Viscosity (mPa s^{-1}, 20 °C)	0.92	1.996	1.75	1.67	1.732	0.369	1.72
Dielectric constants (20 °C)	38.3	47.2	41.7	32.2	—	36.6	—
Dipole moment (D)	3.86	3.96	4.27	4.09	3.83	3.92	—
Donor number (kcal mol^{-1})	26.6	29.8	17.8	27.3	27	14.1	—

Solvent engineering is critical to the formation of perovskite film with high crystallinity and excellent morphology by adjusting the properties of the precursor solution. Compared with the traditional PSCs, the growth of perovskite crystal is limited by mesopores in the printable mesoscopic PSCs. The perovskite materials need to contact the mesoscopic scaffold tightly, which requires dense pore-filling inside the device. Therefore, the viscosity, polarity, wettability of

precursor solution and the intermediate phases formed during annealing process significantly affect the perovskite crystals formed in the mesoscopic scaffold. The new MA gas-based solvent system has also been successfully applied in such mesoscopic structures and achieved high V_{OC} and PCE. Therefore, optimizing the quality of perovskite crystals through solvent engineering is the basis and the direction for further optimization of highly efficient printable mesoscopic PSCs.

7.2.2 Solvent Annealing

Besides properties of solvents, the annealing process could also influence the crystallization of perovskite. Through controlling the annealing temperature and solvent evaporation, we could regulate the nucleation and crystal growth of perovskite, which influence the grain size and morphology of perovskite films. The solvent atmosphere also plays an important role during the annealing process. The crystallization rate of perovskite could be effectively slowed down by providing a certain solvent atmosphere, which is called solvent annealing (SA) and has been widely applied in the fabrication of traditional PSCs.

SA was initially reported by Hang et al. who introduced the DMF vapor in perovskite annealing process, which significantly increased the grain size and improved the crystallinity and morphology of the perovskite film [32]. In the later research, Yang et al. explored the mechanism of grain growth during the SA process. They suggested that during the SA process, DMSO molecules could react with $MAPbI_3$ at the grain boundary to form the intermediate phase $MA_2Pb_3I_8(DMSO)_2$ in the DMSO atmosphere, which could reduce the activation energy of grain boundary migration and promote grain growth [33]. In addition, Gao et al. proposed an explanation of crystal growth based on Ostwald ripening model during SA. The smaller perovskite grains have a high chemical potential and are not as stable as the large grains because of the large specific surface area. In the solvent atmosphere, the small grains are easily dissolved by DMF molecules, so that the solute concentration around the small grains is always higher than that around the large grains, under this concentration gradient, solutes are transported from small grains to large grains, which promotes grain growth and size increase [19].

Consecutive morphology controlling operations
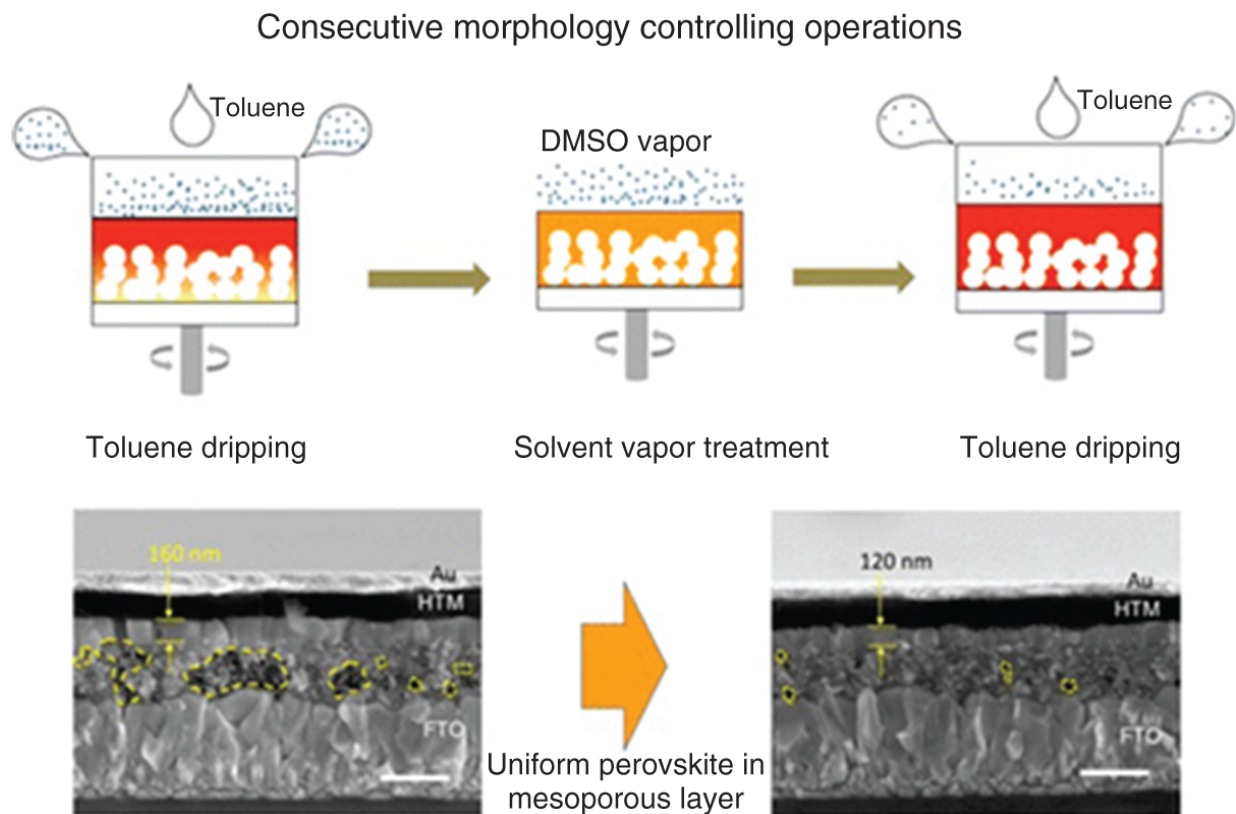
Figure 7.3 Illustration of consecutive morphology controlling operations and the cross-sectional scanning electron microscopy (SEM) images of corresponding devices. Source: Wu et al. [34]/American Chemical Society.

For printable mesoscopic PSCs, the slow crystallization process could be a benefit for the perovskite to fill the mesoscopic scaffold densely and the fast crystallization generally generates many small crystals due to rapid and uneven nucleation and leaves numerous voids. So, SA could be suitable for the uniform and continuous growth of perovskite crystals in mesoporous scaffolds. Wu et al. used DMSO vapor to treat the perovskite film during the spin-coating process, improved the uniformity of perovskite filling in the mesopores, and reduced the aperture gap as the shunt pathway (Figure 7.3) [34]. Hou et al. introduced DMF vapor during the annealing process and effectively increased the crystallinity of $Cs_{0.1}FA_{0.9}PbI_3$ perovskite and reduced defects in the 10 μm mesoporous scaffold [35].

Wang et al. introduced a solvent evaporation control crystallization (SECC) method, which can control the crystallization rate of perovskite in mesoporous by adjusting the evaporation rate of solvent. They also explained the crystallization process with a

proposed model. In the early stage of annealing, if the annealing process was not controlled by the SECC method, the solution was rapidly supersaturated due to the rapid evaporation of the solvent, which led to the uneven nucleation and rapid crystallization of the perovskite and thus formed small crystals spreading the whole triple-mesoporous scaffold. Lots of voids exist in mesoporous, which leads to weak light absorption and high defect density of the PSCs device. Under the SECC condition, the solvent vapor could slow down the further evaporation of the solvent, so that the precursor solution is concentrated on the bottom layer of the mesoporous scaffold, and the perovskite crystallization process is significantly slowed down promoting perovskite grain crystals can grow larger. If the petri dish is removed before the annealing is completed, the remaining solvent will evaporate quickly, resulting in rapid nucleation and crystallization, which causes many small crystal grains to appear in the middle of the large crystals again. When SECC is present during the entire annealing process, the crystal grains could grow slowly along the mesopores, and eventually achieve uniform and dense perovskite pore-filling. The high-quality perovskite film lays the foundation for mesoporous PSCs with excellent performance (Figure 7.4) [36].

SA also exhibited a significant positive effect in the crystallization process of perovskite with NMF as the solvent. Liu et al. combined the high boiling point and low saturation vapor pressure of NMF to design a low permeability annealing cover and low annealing temperature during device preparation, achieving slow removal of NMF and sufficient growth of perovskite grains. As shown in Figure 7.5, the nucleation of perovskite is severely inhibited due to the good precursor dissolution and slow solvent removal, while the grain growth is sufficient to eventually form large regions of several millimeters. The devices exhibited good filling of perovskite in the scaffold. They further demonstrated that the controlled crystallization process of nucleation inhibition and growth promotion can promote the orientation growth of perovskite as well as achieve the quasi-single crystal growth process of perovskite in the mesoporous scaffold by grazing-incidence wide-angle X-ray scattering (GIWAXS) analysis (Figure 7.6). Ultimately, the devices with controlled crystallization using NMF as the solvent obtained a PCE of 18.85%, which was the highest efficiency for the printable mesoporous devices at that time [27].

(a) ● FTO ● TiO$_2$ ● ZrO$_2$ ● Carbon ● Precursor solution ● Perovskite

(b)

(c)

FWHM = 0.189   120 min (SEC)

FWHM = 0.195   90 min (SEC) + 30 min (FEC)

FWHM = 0.213   60 min (SEC) + 60 min (FEC)

FWHM = 0.241   30 min (SEC) + 90 min (FEC)

10   20   30   40   50   60

Degree
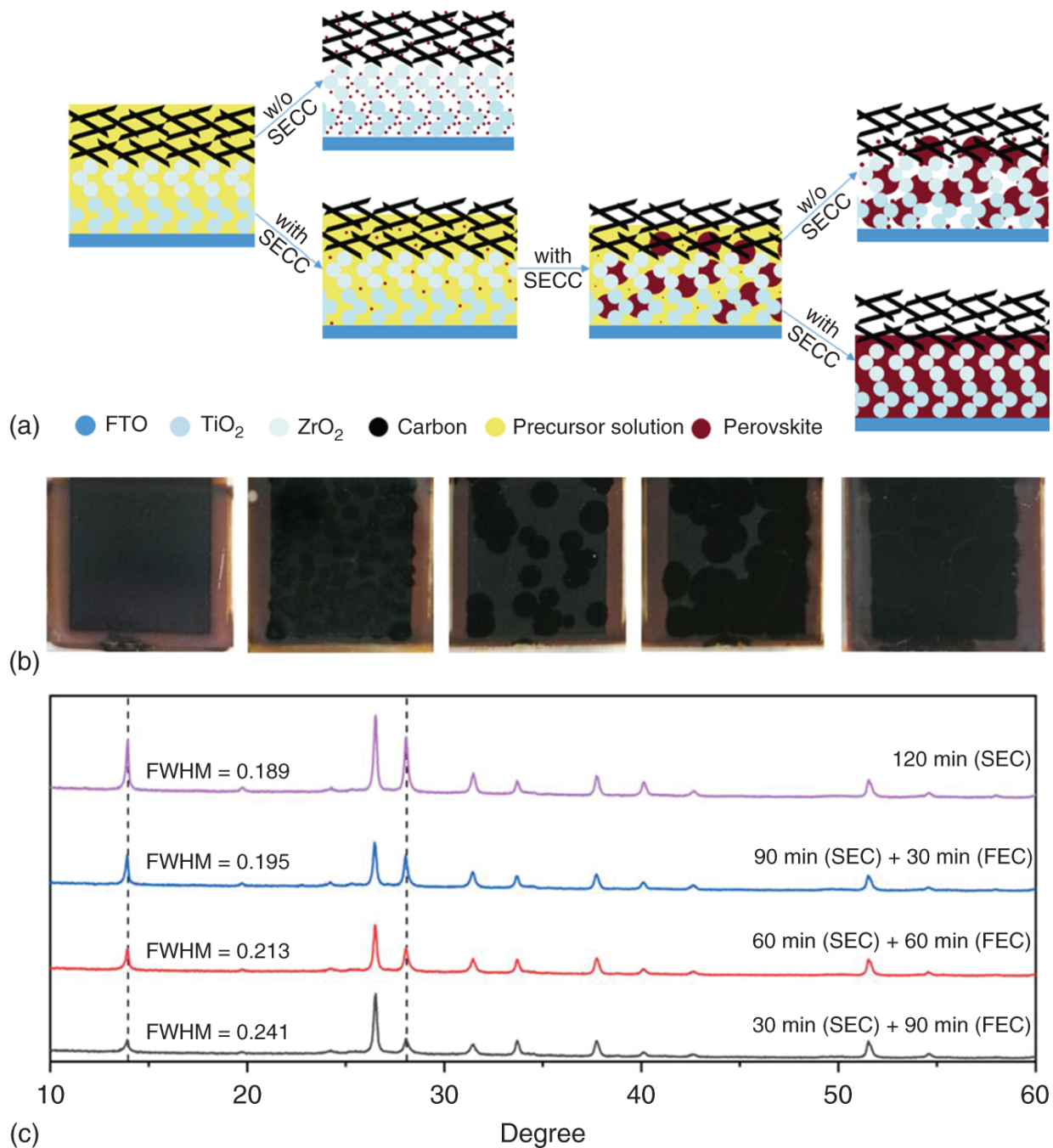
Figure 7.4 (a) The schematic diagram of perovskite crystallization in the mesoporous scaffold under different situations. The relationships between the color and the material are noted under diagrams. (b) The photographs of devices annealed under different situation and (c) the related XRD pattern of films on the substrate of glass/ZrO$_2$. Source: Wang et al. [36]/With permission of John Wiley & Sons.
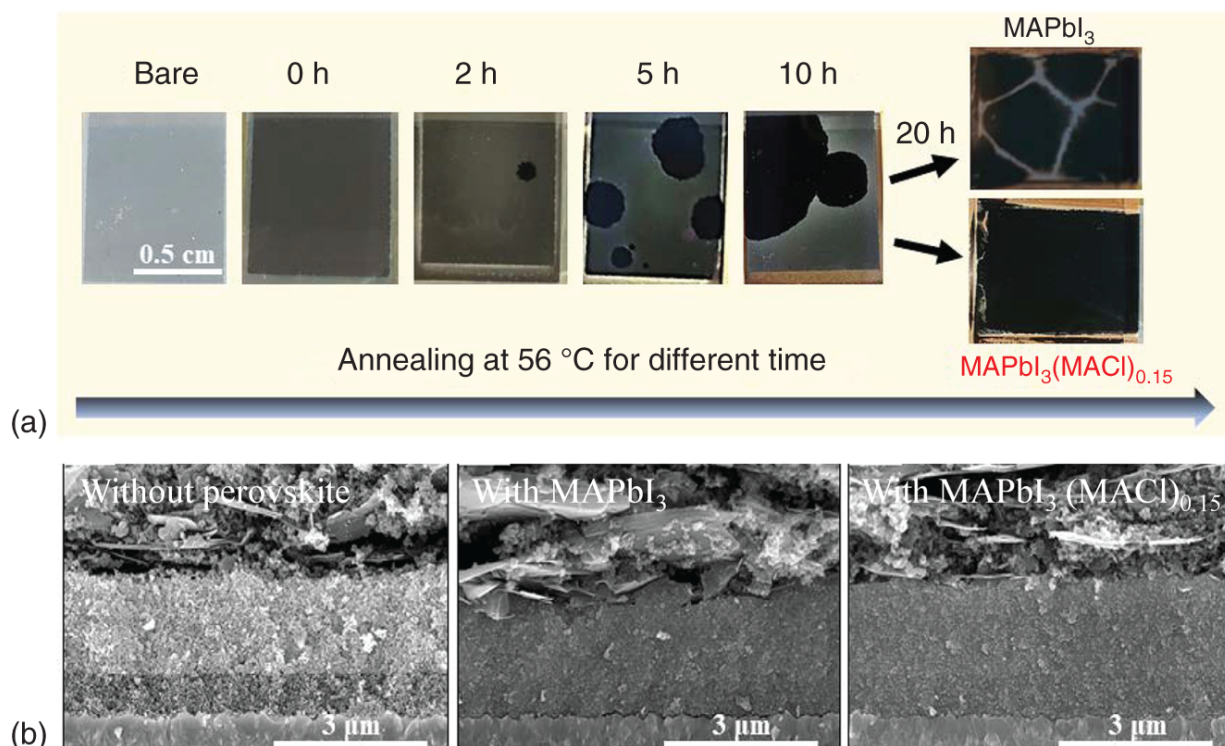
Figure 7.5 Growth of MAPbI$_3$ in mesoscopic layers. (a) Morphology evolution of perovskite in mesoscopic layers with different annealing time. (b) Cross-sectional SEM images of devices without perovskite, with MAPbI$_3$, and with MAPbI$_3$(MACl)$_{0.15}$. Source: Liu et al. [27], Elsevier.

From the current experimental results, we think that the slower crystallization process is conducive to the crystal growth and uniform filling of the perovskite in a thick mesoporous scaffold (>10 µm). Due to the limitation of mesoporous, too fast perovskite crystallization lead to poor crystallinity and pore-filling, which could lead to weak light absorption, severe non-radiative recombination caused by defects and poor carrier transport, and ultimately result in overall degradation of performance. SA could effectively control the perovskite crystallization rate, especially in the mesoporous structure, which is effective for the formation of perovskite films with high crystallinity and good morphology. Combined with solvent engineering, SA has greater potential to improve PCE by improving crystallization process and the resulting morphology.
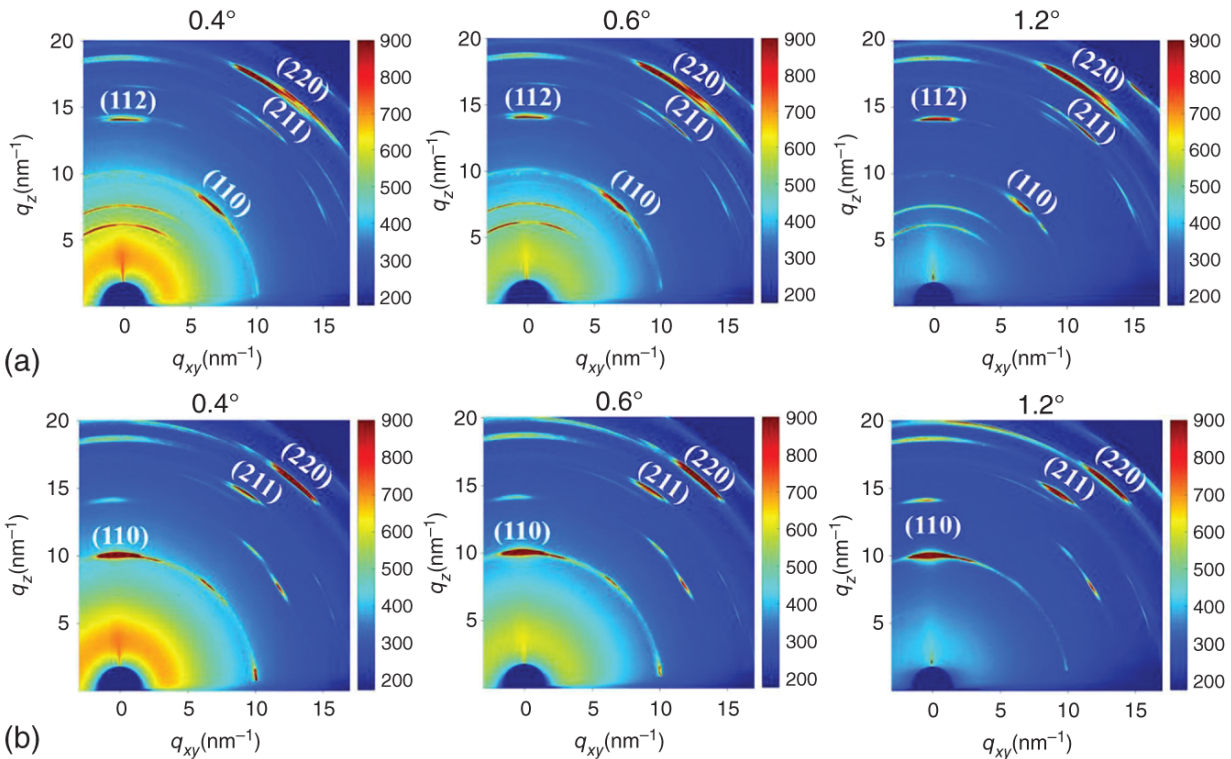
Figure 7.6 Crystallinity and film properties of MAPbI$_3$ in mesoscopic layers. the GIWAXS patterns of (a) MAPbI$_3$ and (b) MAPbI$_3$(MACl)$_{0.15}$ filled inside the mp-TiO$_2$ and mp-ZrO$_2$ layers with different incident angles. Source: Liu et al. [27], Elsevier.

7.3 Composition Engineering

In general, the organic–inorganic hybrid perovskites own a chemical structure of ABX$_3$ (A = Cs$^+$, CH$_3$NH$_3{}^+$, CH$_5$N$_2{}^+$; B = Pb^{2+}, Sn^{2+}; X = Cl$^-$, Br$^-$, or I$^-$). By changing the types and proportions of A, B, and X, the bandgap of perovskite can be adjusted continuously, which makes the perovskite meet different needs in specific application. Despite the fact that solar cells based on the MAPbI$_3$ perovskites have achieved PCE of more than 20%, the highest record efficiency of PSCs is achieved with the mixed perovskite based on the composition engineering. By rationally tuning the composition of cation or anion in organic–inorganic halide perovskites, the bandgap and Goldschmidt's tolerance factor of perovskite can be effectively regulated, which is in favor of improving the PCE and stability of PSCs [37].

7.3.1 The A-Site Cation

Goldschmidt's tolerance factor (τ) is a dimensionless number that measures the stability and distortion of perovskite crystal structures. Only when the τ is between 0.8 and 1, the perovskite could maintain a stable 3D structure, which makes only a few A-site cations, such as Cs^+, MA^+, and FA^+, have suitable size to be inserted into the inorganic framework and form a stable 3D structure. Among several kinds of perovskites, $MAPbI_3$ is first applied in the perovskite solar cells and has been extensively studied. At room temperature, the Goldschmidt's tolerance factor of $MAPbI_3$ is 0.91 [38], and it has a tetragonal crystal structure and a bandgap of about 1.56 eV [39–42]. Since $MAPbI_3$ changes from tetragonal to cubic phase at 330 K, which leads to poor stability of $MAPbI_3$ in the actual use, [43] it is necessary to develop more stable perovskites. It is reported that $FAPbI_3$ has good thermal stability because it has no phase change in a wide temperature range of 298–423 K. Compared with $MAPbI_3$, $FAPbI_3$ has a bandgap of about 1.45 eV, [42] which is closer to the optimal bandgap of single-junction solar cells based on the Shockley−Queisser limit [44, 45], and the lower bandgap allows photons to be effectively used in the near-infrared spectrum. The specific structure and ideal bandgap make it possible for $FAPbI_3$ to get excellent PCE and stability in PSCs. However, $FAPbI_3$ possesses two phases, (i) photoinactive non-perovskite, hexagonal δ-$FAPbI_3$ perovskite, and (ii) photoactive trigonal α-$FAPbI_3$ perovskite. Only the α-$FAPbI_3$ can be used as an excellent light-absorbing material in solar cells [46]. The presence of δ-$FAPbI_3$ could damage the performance of the device. Therefore, it is very important to stabilize the α-$FAPbI_3$ phase in the fabrication of PSCs by adjusting the Goldschmidt's tolerance factor of perovskite.

Incorporation of MA into $FAPbI_3$ resulted in a more stable $MA_xFA_{1-x}PbI_3$ perovskite structure [38, 47]. Binek et al. further studied the stability of $MA_xFA_{1-x}PbI_3$ perovskite, who suggested that the smaller MA^+ has a larger dipole and a stronger interaction with the PbI_6 octahedral inorganic framework, which is beneficial to the stability of α-$FAPbI_3$ [48]. Jeon et al. developed the $(FAPbI_3)_{1-x}(MAPbBr_3)_x$ perovskite, they suggested that MA^+ and Br^- could cooperate with each other to better stabilize α-$FAPbI_3$ [49]. In addition, smaller Cs^+ could also be used to stabilize α-$FAPbI_3$, it has

been suggested that the introduction of smaller Cs^+ could cause the shrinkage of the cubic octahedron and further enhances the interaction between FA and I, which could improve the $FAPbI_3$ light stability and phase stability [50, 51]. Despite few reports, Cs could also be introduced into $MAPbI_3$, which could improve the thermal stability of PSCs based on $MAPbI_3$ [52, 53]. The triple-cation perovskite also shows good phase stability and suitable bandgap, and more than PCE of 21% or excellent stability has been achieved in PSCs based on the triple-cation mixed perovskite $Cs_{0.1}FA_{0.75}MA_{0.15}PbI_{2.49}Br_{0.51}$ [54, 55].

In printable mesoscopic perovskite solar cells, the composition engineering is also an important method to improve the performance of PSCs. In 2014, Hu et al. prepared $MA_{0.4}FA_{0.6}PbI_3$ in a three-layer mesoporous structure by sequential deposition method to extend the light absorption spectrum to 840 nm, which significantly increased the short-circuit current density (J_{SC}) of the device without sacrificing the open-circuit voltage (V_{OC}), and achieved PCE of 12.9% [56]. In 2019, Hou et al. stabilized $FAPbI_3$ by introducing Cs^+, and improved the crystallization and morphology of perovskite in mesoporous through SA process. A PCE of 15% was obtained with a spectral response up to 840 nm in printable mesoscopic PSCs [35]. Subsequently, Wang et al. applied $Cs_{0.1}Rb_{0.05}FA_{0.85}PbI_3$ perovskite as a light absorber in printable mesoscopic PSCs, which stabilized the α-$FAPbI_3$ and obtained a PCE of 16.26% with good crystallization [36]. The above works exhibit that the composition control of the A-site cation could not only broaden the light absorption spectrum but also improve the PCE of printable mesoscopic PSCs (Figure 7.7).

Under the condition of good pore-filling inside the mesoscopic scaffold, adjusting the composition of A-site cation could change the bandgap of perovskite and further broaden the absorption spectrum of devices. In addition, compared with traditional PSCs, the α-$FAPbI_3$ with good stability and crystallization could be obtained at lower annealing temperature by adjusting the composition in printable mesoscopic PSCs.
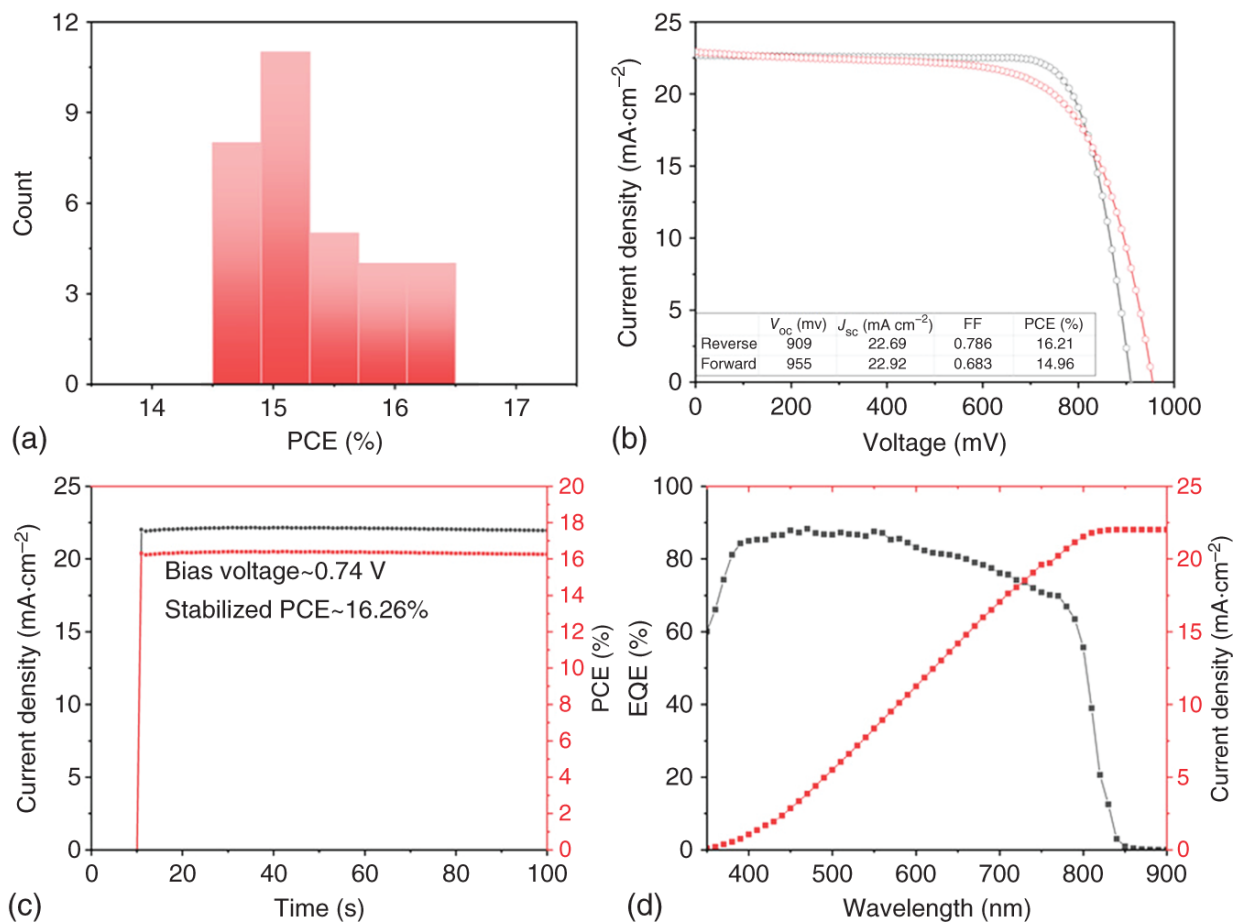
Figure 7.7 The performance parameters of devices based on $Cs_{0.1}Rb_{0.05}FA_{0.85}PbI_3$. (a) The distribution of PCE, there 32 pieces of device are taken into account. (b) The J–V curve of the champion device. (c) The stabilized output of the champion devices. (d) The IPCE spectrum of the champion device. Source: Wang et al. [36]/With permission of John Wiley & Sons.

7.3.2 The B-Site Cation and X-Site Anion

The B-site metal cation and X-site anion significantly affect the crystal and electronic structure of perovskite. For the $MAPbI_3$, the conduction band of the perovskite is mainly contributed by empty Pb p orbitals and I p orbitals, and the valence band is mainly contributed by I p orbitals and Pb s orbitals through the theoretical calculation. Considering that the bandgap of $MAPbI_3$ exceeds 1.45 eV, which is higher than the optimal range of SQ limit, [44, 45] we could directly adjust the band structure of perovskite through changing the composition of B-site cation and X-site anion. In addition, toxicity of Pb also has a negative impact on the commercialization of perovskite

solar cells. Therefore, it is very necessary to improve the quality and photoelectric characteristics of perovskite by adjusting the B-site and X-site components.

Since it is expected to further adjust the bandgap of perovskite and eliminate the toxicity of Pb, Sn halide perovskites have received widespread attention [57, 58]. In 2014, Noel et al. reported PCE of 6.4% based on $MASnI_3$ [59]. Subsequently, $CsSnI_3$ and $FASnI_3$ have also been applied to PSCs. Among several Sn-based PSCs, $FASnI_3$ has been studied intensively due to the higher performance and better repeatability. Adjusting the component and using additives could improve crystallinity and morphology of Sn-based perovskite and suppress the oxidation of Sn^{2+}, which leads to the improvement in the performance and stability of Sn-based PSCs. Currently, Ning et al. obtained the highest efficiency of 12.4% based $FASnI_3$ devices by optimizing ETL materials and improving the morphology of perovskite through additives [60]. Apart from Sn, Bi-based perovskite materials have also been used in photovoltaic due to their good stability. However, it is difficult for Bi-based materials to form a highly symmetric structure, and there could be numerous defects existing in the film of Bi-based perovskite films, which leads to the poor PCE of Bi-based PSCs [61]. Currently, Pai et al. reported highest PCE of 5.56% based on $Ag_3BiI_{5.92}S_{0.04}$ [62]. Another important direction of composition engineering based on B-site cations is the Pb–Sn mixing system. By adjusting the ratio of Pb and Sn in the metal halide perovskite, the bandgap of perovskite could be flexibly adjusted between 1.55 and 1.17 eV to match the optimal bandgap of the S–Q limit, which could be used in both single junction solar cells and tandem solar cells [58]. At present, Lin et al. introduced a metal Sn in the precursor solution to suppress the oxidation of Sn^{2+} and increase the carrier diffusion length to 3 µm. The device based on $FA_{0.7}MA_{0.3}Pb_{0.5}Sn_{0.5}I_3$ has obtained the PCE of 21.1% [63]. For the tandem solar cells based on the perovskite, In 2019, Lin et al. combined $FA_{0.7}MA_{0.3}Pb_{0.5}Sn_{0.5}I_3$ with wide bandgap $Cs_{0.2}FA_{0.8}PbI_{1.8}Br_{1.2}$ and obtained an impressive PCE of 24.8%, which also maintained good stability [63].

Apart from metal cation in the B-site, the X-site halogen anions, including I^-, Cl^-, and Br^-, also have a crucial impact on PSCs performance through changing the ratio or types [64, 65]. Cl^- could improve the photoelectric characteristics of perovskite, such as

increasing the carrier diffusion length, [66, 67] without influencing the spectral response [68]. By affecting the properties of the precursor solution, Cl^- could also improve the grain size and coverage of the perovskite film, and regulate the perovskite orientation growth [69–71]. Although it is still unknown whether Cl^- could insert into the perovskite lattice limited by the characterization method, Cl^- has been widely applied to improve the performance of PSCs [72]. On the contrary, Br^- could tune the bandgap of perovskite and improve the hole transportation and the wide bandgap $MAPbBr_3$ has good hole conduction characteristics [73, 74]. Br^- could generally lead to the enhancement of Goldschmidt's tolerance factor so the introduction of Br^- could stabilize the α-$FAPbI_3$ and further improve the PCE and stability of PSCs by adjusting the τ factor [49, 75]. Besides ions consisting of a single atom, F could be incorporated into the perovskite lattice through BF_4^- that has similar ionic radius to I^-, which could improve the conductivity of perovskite films [76, 77]. The introduction of SCN^- owning similar ionic radius with I^- could improve the crystallization and morphology of perovskite, enhancing the stability of PSCs and suppressing hysteresis [78–80].

Lead-free perovskite has also been applied in printable triple mesoporous structures. Li et al. reported a $C_6H_4NH_2CuBr_2I$ compound with excellent stability, extraordinary hydrophobicity, and a high absorption coefficient (Figure 7.8). They adopted $C_6H_4NH_2CuBr_2I$ as a light absorber in printable mesoscopic perovskite solar cells and obtained the PCE of 2% [81]. In addition, Li et al. explored the application of various organic–inorganic bismuth iodides in mesoporous structures. These compounds have a one-dimensional anionic chain built by edge-sharing BiI_6 octahedra. It is worth noting that the interaction of I...I, I...C, and hydrogen bonds between different chains make it possible for three-dimensional charge transport in one-dimensional organic–inorganic bismuth iodides and the printable mesoscopic PSCs achieved a PCE of 0.9% using the Bi-based perovskite [82, 83]. In addition, Sn-based perovskites are also used in mesoporous structures. Chen et al. firstly reported a low-dimensional halide perovskite $(4AMP)(FA)_{n-1}Sn_nI_{3n+1}$ based on Dion–Jacobson Sn (II), which shows the long PL lifetime and suitable bandgap. Printable mesoscopic PSCs obtained the PCE of 4.22% based on $(4AMP)(FA)_3Sn_4I_{13}$, which also exhibits good stability [84]. Although the performance of devices needs to be improved, the

development of these lead-free light-absorbing materials has demonstrated that many kinds of perovskite could be applied in the printable mesoscopic PSCs.
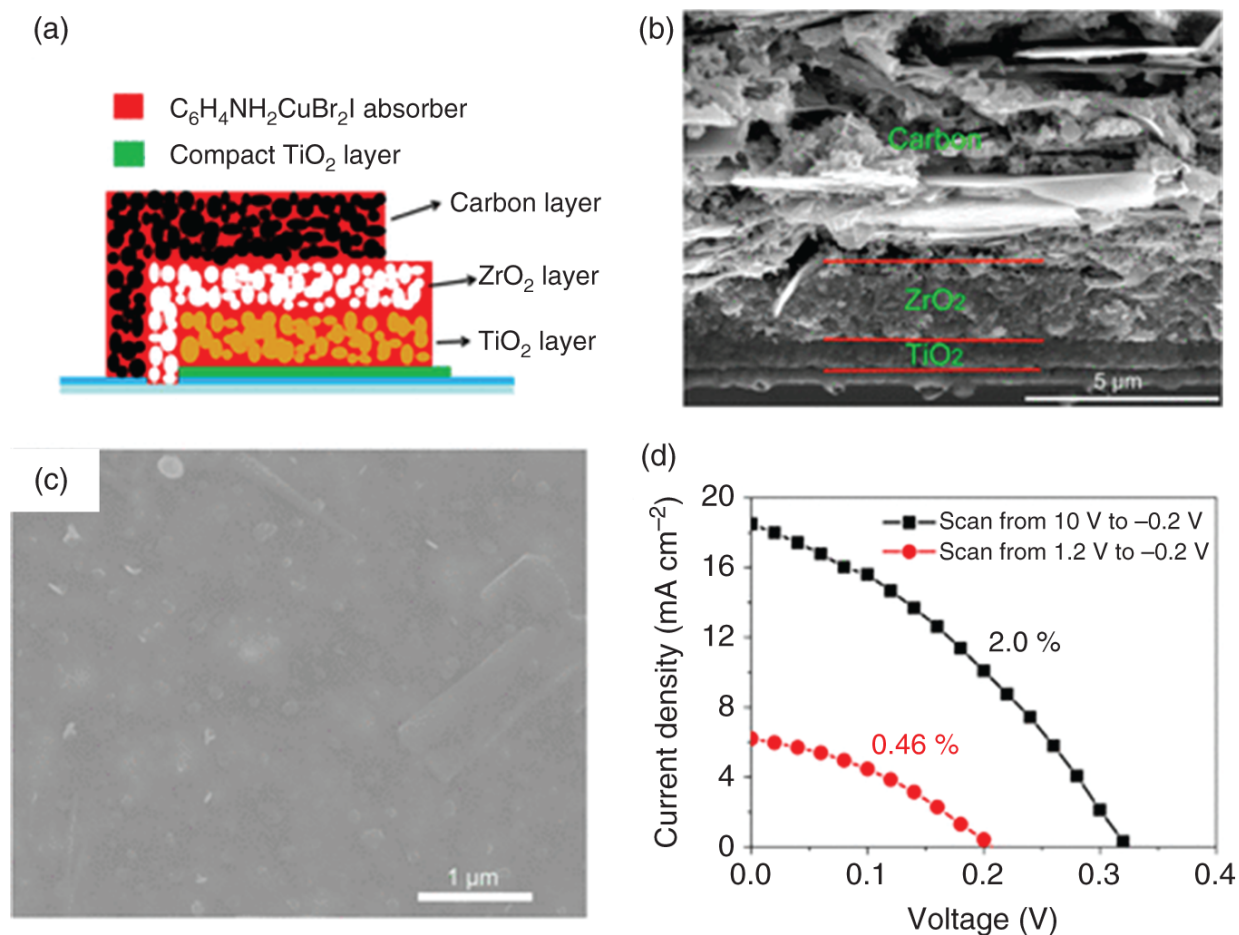
Figure 7.8 Scheme (a) and cross-section SEM image (b) of the Cu-based solar cell. (c) Top view SEM image of $C_6H_4NH_2CuBr_2I$ thin film. (d) *J*–*V* curves of the best performing device (reverse scan). Source: Li et al. [81]/American Chemical Society.

For the X-site anion, Chen et al. partially replaced I^- with BF_4^-, and applied the new $MAPbI_{2.95}(BF_4)_{0.05}$ perovskite in the printable mesoscopic PSCs and obtained the PCE of 13.24%. They inferred that the enhancement of V_{OC} and *FF* could be attributed to the increased interfacial and bulk recombination resistances for the BF_4^- could improve the electrical property of perovskite [76]. Subsequently, Sheng et al. introduced BF_4^- to $(5\text{-}AVA)_{0.034}MA_{0.966}PbI_3$, which could produce high-quality perovskite crystals and decrease the charge recombination rates and defect density. Devices obtained the PCE of

15.5% based on the mixed $(5\text{-}AVA)_x MA_{1-x} PbI_{3-y}(BF_4)_y$ perovskite and achieved the high V_{OC} of 0.97 V in the printable mesoscopic PSCs [85].

Similar to traditional PSCs, the composition engineering could also be applied to printable mesoscopic PSCs. The bandgap of Pb–Sn mixed perovskite is adjustable, and other metal cations also play an important role in the adjustment of the energy band, morphology, and defect density. Cl^- and Br^- could effectively improve the morphology, electrical properties, and stability of perovskite. Above all, B-site cation and X-site anion composition engineering have great potential on further improving performance of printable mesoscopic PSCs.

7.4 Additive Engineering

Many kinds of additives have been widely used in the fabrication of traditional PSCs. According to the different properties of additives, they could be applied to control the morphology of films, decreasing the defect density, adjusting the energy band, and improving the stability of perovskite. The additive engineering is an important strategy to obtain devices with high PCE and good stability in both traditional PSCs and printable mesoscopic PSCs. However, different from traditional PSCs in which interfaces are relatively clear, interfaces are pretty complex because of the mesoscopic scaffold in printable mesoscopic PSCs, which leads to different results when the same additive is applied in different device

7.4.1 Functional Molecular Additives

For a specific additive, the functional groups determine the effect that the additive could realize when it is applied. According to the type of functional groups that the additive owns, the additive could improve the morphology of films, passivate defects, reduce carrier recombination or promote charge carrier transport. Through combining different functional groups, a single functional molecular could realize more than one function.

Ammonium salts have been widely used as molecular additives because of their important role in controlling the perovskite morphology and improving the perovskite stability. Larger ammonium salts could not insert into the 3D perovskite lattice due to the limitation of tolerance factors, which leads to the formation of low-dimensional perovskites and exhibits excellent humidity stability [86–

88]. Similarly, the hydrophobic groups, such as tertiary and quaternary alkyl groups, could also improve the stability of PSCs, which are generally distributed on the surface of perovskite to block moisture [89]. In addition, $-NH_2$ in the ammonium salt could form the coordination bond with the uncoordinated Pb^{2+} so the halogen vacancy defects could be filled by the halogen ions in the ammonium salt, which could passivate defects existing in the perovskite grain boundaries and surface, suppress non-radiation recombination, and finally improve the performance of PSCs [90, 91]. In addition to ammonium salts, some additives containing acidic groups could also be used in perovskites. These acidic groups could passivate defects in perovskites and strengthen the contact between perovskite and charge-transporting materials by combining with metal oxides. Han group developed a series of bifunctional molecular additives with a terminal amino group and a terminal carboxyl group, which effectively improve the crystallization and the pore-filling of perovskites in the mesoscopic scaffold, and the printable mesoscopic PSCs achieved remarkable stability with the bifunctional molecule [9, 92]. Similarly, the molecules containing sulfuric acid and phosphoric acid groups could also be used to improve the crystallization and passivate the defects of perovskites, yielding an improved PCE and stability [34, 93]. A series of important additives that contain O, S, and N elements as electron donors, have also been widely used in PSCs. These additives could be used as a Lewis base to coordinate with Pb^{2+}. The formation of Lewis acid–base adducts could regulate the perovskite crystallization. In addition, the Lewis base additives could also passivate the defects of grain boundary and surface of perovskite by Lewis acid–base coordination [94]. Similar to the Lewis base, some molecular additives that could be used as Lewis acids could also coordinate with the halogen anions in perovskites and passivate hole defects [95, 96]. Polymer molecular additives have also received much attention due to the significant improvement in the stability of perovskite. After the annealing of the perovskite, the polymer molecules are spontaneously distributed on the grain boundaries or surface to passivate defects. The hydrophobic group of the polymer additive could protect the perovskite from the moisture. Typical polymer molecular additives mainly include poly(ethylene glycol) (PEG), poly(4-vinylpyridine) (PVP), and trimethylolpropane triacrylate (TMTA), which could improve the humidity and thermal stability of perovskite solar cells [97–99].

For printable mesoscopic PSCs, bifunctional molecular additives play a significant role in adjusting crystallization and improving stability of devices. In 2014, Mei et al. initially introduced 5-AVAI to prepare mixed cation perovskite $(5\text{-AVA})_x\text{MA}_{1-x}\text{PbI}_3$, which exhibited more dense and uniform pore-filling and lower defect density than MAPbI_3 in printable mesoscopic PSCs. In this work, researchers inferred that the –COOH of 5-AVAI molecule could contact with TiO_2 and ZrO_2 nanoparticles and the $-\text{NH}_3^+$ could participate in the crystallization of perovskite, as a nucleation site of perovskite and further improve the crystallization of perovskite inside the mesoscopic scaffold. The device shows a certified PCE of 12.8% and kept stable for >1000 hours in the ambient air under full sunlight [9].

In 2019, Filonik et al. observed the formation of perovskite inside the mesoscopic scaffold and further investigated the influence of 5-AVAI on perovskite crystallization with the GIWAXS. Such time-resolved measurement showed that the formation of large crystalline perovskite grains was suppressed in the early stage of perovskite crystallization when 5-AVAI was introduced, resulting in improving the perovskite pore-filling in the mesoscopic scaffold and enhancing the device performance, as shown in Figure 7.9 [100].

As an additive, the content of 5-AVAI needs to be precisely controlled, and high ratio of 5-AVAI could lead to the formation of 2D perovskite. Grancini et al. used 5-AVA to form an ultra-stable 2D/3D $(5\text{-AVA})_2\text{PbI}_4$ on the surface of MAPbI_3, which could act as a barrier to protect the 3D perovskite from moisture. Based on the 2D/3D $(5\text{-AVA})_2\text{PbI}_4$ layer, the printable mesoscopic PSCs achieved the PCE of 12.9%, and the $10 \times 10\,\text{cm}^{-2}$ module exhibited the PCE of 11.2% and remarkable long-term stability (>10 000 hours under the standard test conditions and no reduction, as seen in Figure 7.10) [101].

(a)

(b)

(c)

(d)
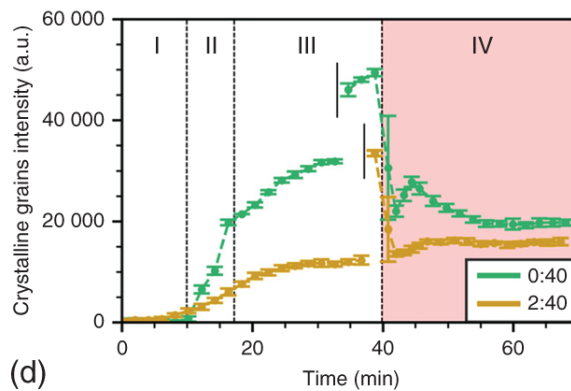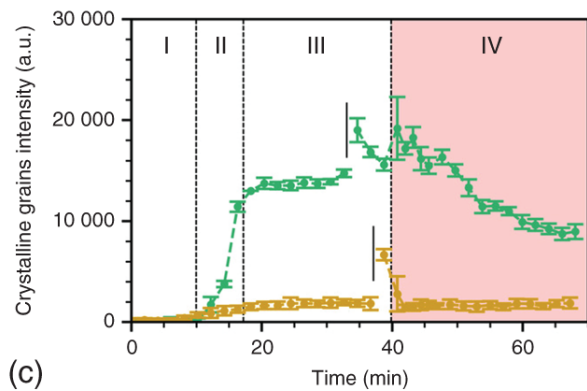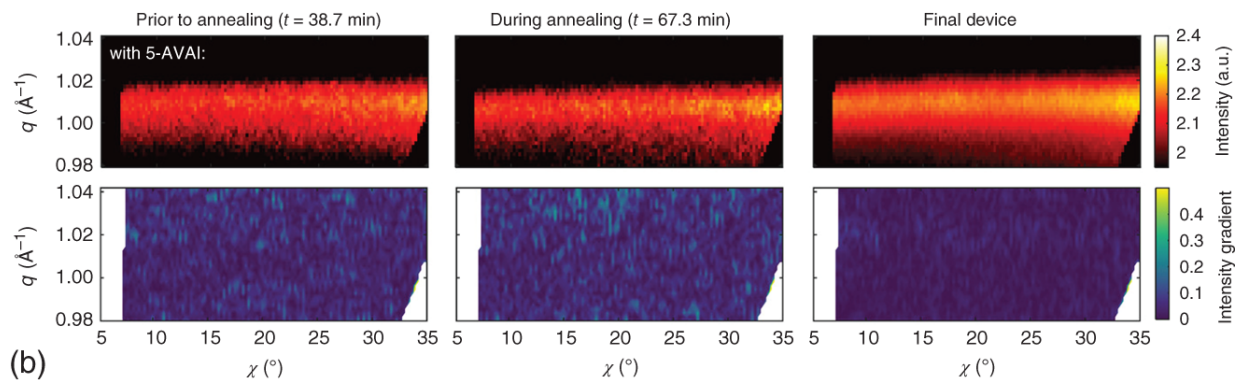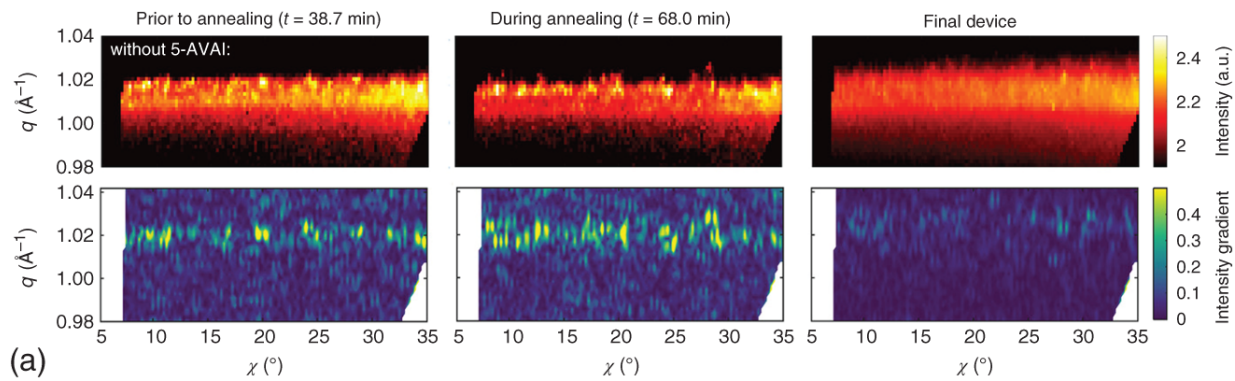
Figure 7.9 Selected diffraction pattern from time-resolved GIWAXS measurements (top) and corresponding directional intensity gradients along χ of the azimuthally integrated (002)/(110) reflex in the vertical direction (bottom). Pattern for selected time frames of samples (a) without 5-AVAI and (b) with $2:40$ molar ratio of 5-AVAI: MAI. Distinct diffraction peaks in the initial diffraction patterns are only detected for the reference sample. Intensity evolution from time-resolved GIWAXS measurements of the (c) crystalline grains and (d) dispersed crystallites for both cases with 5-AVAI in yellow and the reference without 5-AVAI in green during the solution infiltration (white background) and thermal annealing at $50\,^\circ\text{C}$ (light red background). The vertical solid lines mark the time of sample position change during the experimental procedure. Source: Filonik et al. [100]/With permission of John Wiley & Sons.

However, the insulating alkyl chain of 5-AVA could hinder the charge transport, which could damage the performance of printable mesoscopic PSCs. Therefore, Hu et al. designed a bifunctional conjugated organic molecule 4-(aminomethyl) benzoic acid hydroiodide (ABI). The ABI owns the same functional groups as 5-AVAI, which could improve the pore-filling of perovskite through similar mechanism. Different from the 5-AVAI, the ABI exhibits a conjugated molecular structure, which is beneficial for the transport of carriers. The printable mesoscopic PSCs based on AB-MAPbI$_3$ show good stability and excellent PCE of 15.6% [92].
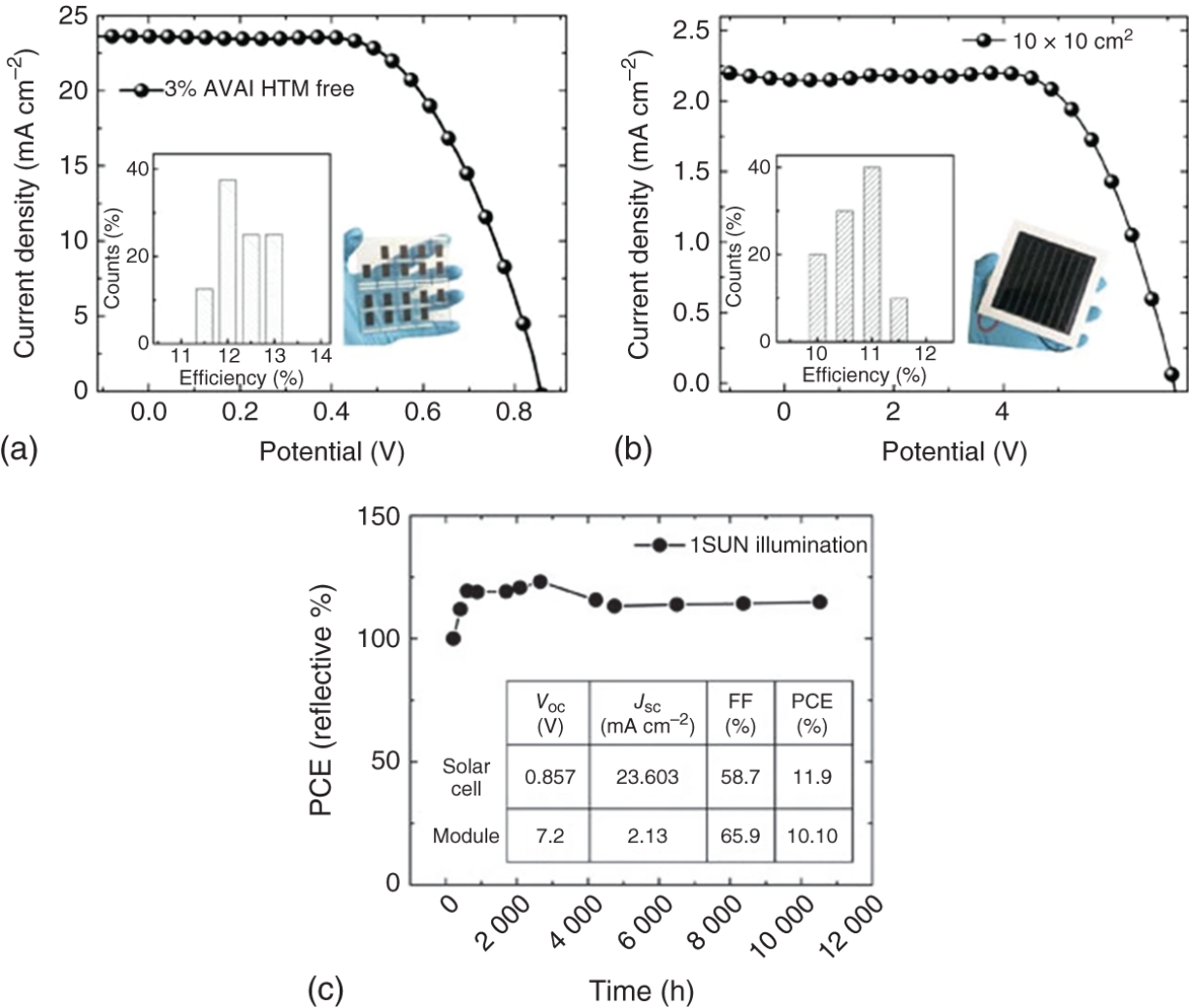
Figure 7.10 (a) *J–V* curve using the 2D/3D perovskite with 3%AVAI in HTM-free solar cell measured under Air Mass (AM) 1.5G illumination (device statistics and picture in the inset). (b) *J–V* curve using the 2D/3D perovskite with 3%AVAI in HTM-free $10 \times 10 \, cm^2$ module (device statistics and picture in the inset). (c) Typical module stability test under 1 sun AM 1.5G conditions at stabilized temperature of 55° and at short circuit conditions. Stability measurements done according to the standard aging conditions. Source: Grancini et al. [101], Springer Nature, CC BY 4.0.

Ammonium salt additives are widely used in perovskite solar cells due to the modulating effect of $–NH_2$ on crystallization processes and defects. In printable mesoscopic solar cells, Ammonium salt additives also exhibited significant positive effects in the printable mesoscopic PSCs. Xiao et al. introduced acetamidine hydrochloride (AceCl) and guanidine hydrochloride (GuaCl) as additives into the perovskite

precursor solution and found that the larger Ace and Gua cations could partially enter in the 3D perovskite lattice and significantly affect the electrical properties of perovskite. The mobility and conductivity of the Ace mixed perovskite are significantly enhanced (Figure 7.11). The printable mesoscopic devices based on Ace mixed perovskite obtain over 18% PCE (certified 17.7%). Liu et al. also found that melamine hydroiodide improves the filling and crystallization of chalcocite in mesoporous scaffolds [102].

Functional additives could improve the pore-filling and crystallization of perovskite in the mesoscopic scaffold and enhance the stability of devices, which indicates that functional molecular additives are essential for the performance improvement of printable mesoscopic PSCs. Through designing multifunctional additives with different functional groups, additives could also be used to passivate defects, promote carrier transport and reduce the carrier recombination in printable mesoscopic PSCs.
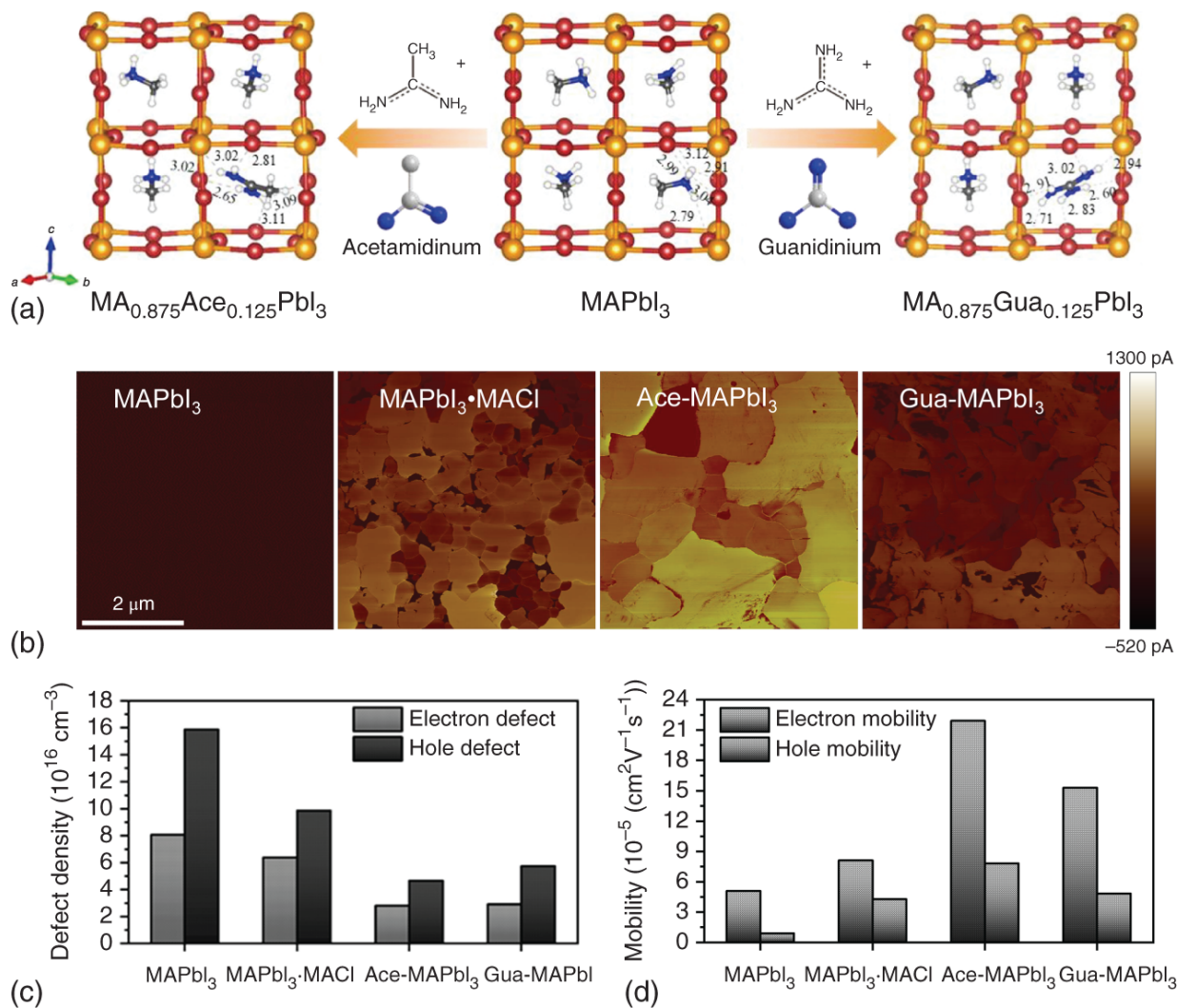
Figure 7.11 (a) Structure characterizations of different perovskite films. (a) The perovskite lattice of $MA_{0.875}Ace_{0.125}PbI_3$ (left), $MAPbI_3$ (middle), and MA $_{0.875}Gua_{0.125}PbI_3$ (right) with the density functional theory (DFT) calculated effective hydrogen bonds. (b) conductive atomic force microscope (c-AFM) images of different perovskite films. The Defect density (c) and carries mobility (d) calculated from SCLC measurements of different perovskites. Source: Xiao et al. [102]/With permission of Elsevier.

7.4.2 Other Additives

In addition to additives with functional groups, there are also some other additives applied to PSCs based on simpler molecular structures. This kind of additive could also influence the crystallization process of perovskite and improve the morphology of perovskite films. Exploring the behavior of these additives in the

formation of perovskite crystals could further reveal properties of perovskites.

Some additives could modulate the morphology of perovskite film by affecting the properties of the precursor solution. It has been proved that the perovskite precursor solution is colloid rather than true solution, and the size and morphology of the colloidal particles could influence the grain size and morphology of the final perovskite film. Extra MAI and MACl could change the size and morphology of colloidal particles by affecting the coordination form of the solute in precursor solution, which ultimately determines the grain size and morphology of the perovskite film [103, 104]. In addition, some acidic additives, such as HI and HBr, could promote the dissolution of large colloid particles in the precursor solution, which could further decrease nucleation sites in the solution and prolong the crystallization process of perovskite. With the slower crystallization, the perovskite film consists of crystals with larger grain sizes. However, too few nucleation sites could lead to loose contact between different grains in the perovskite film and the formation of undesirable pinholes, so it is necessary to adjust the properties of the perovskite precursor solution to balance the overall morphology of perovskite films and crystal grains size [73, 105]. Another way to improve the film morphology is to change the crystallization process of perovskite through the intermediate phase formed by additives and perovskite precursors. Typical additives are chlorides, such as MACl and $PbCl_2$, which could lead to the formation of Cl-containing perovskite. The Cl-contained intermediate could act as a template for the crystallization of perovskite, which could be transformed into the perovskite film with high crystallinity and dense morphology after thermal annealing [106, 107]. Other additives such as $Pb(Ac)_2$ and $Pb(SCN)_2$ have similar effects to improve morphology [78, 108, 109].

In printable mesoscopic PSCs, chloride additives are also widely used in improving the quality of perovskite. In 2016, Sheng et al. effectively improved perovskite crystallization and morphology in printable mesoscopic PSCs by adding LiCl into $MAPbI_3$. In addition, LiCl could also enhance the carrier concentration and electrical conductivity of the perovskite film [110]. Subsequently, $SrCl_2$ was also introduced into printable mesoscopic PSCs by Zhang et al. and improved the filling of perovskite materials in the mesoscopic scaffold. They also found that $SrCl_2$ could inhibit the non-radiative recombination through passivating defects inside the perovskite,

which resulted in V_{OC} up to 1.05 V and PCE of 15.9% in printable hole-conductor-free mesoscopic PSCs [111]. In addition, Rong et al. reported a method of improving crystallization and pore-filling of perovskite crystals in the mesoscopic scaffold based on the synergistic effect of NH_4Cl and moisture. As shown in Figure 7.12, during the crystallization process of perovskite, NH_4^+, precursor materials, and moisture could form the $MAI \cdot NH_4PbI(H_2O)_2$ intermediate phase, which could slow down the crystallization process and improve the crystal quality of perovskite in the mesoscopic scaffold. After annealing and exposing to the air, the moisture could induce the deprotonation of NH_4^+ in $MAI \cdot NH_4PbI(H_2O)_2$ leading to the formation of NH_3 and the intermediate phase change into $MAPbI_3$. Printable mesoscopic PSCs prepared based on this method achieved a PCE of 15.6% and excellent stability [112].
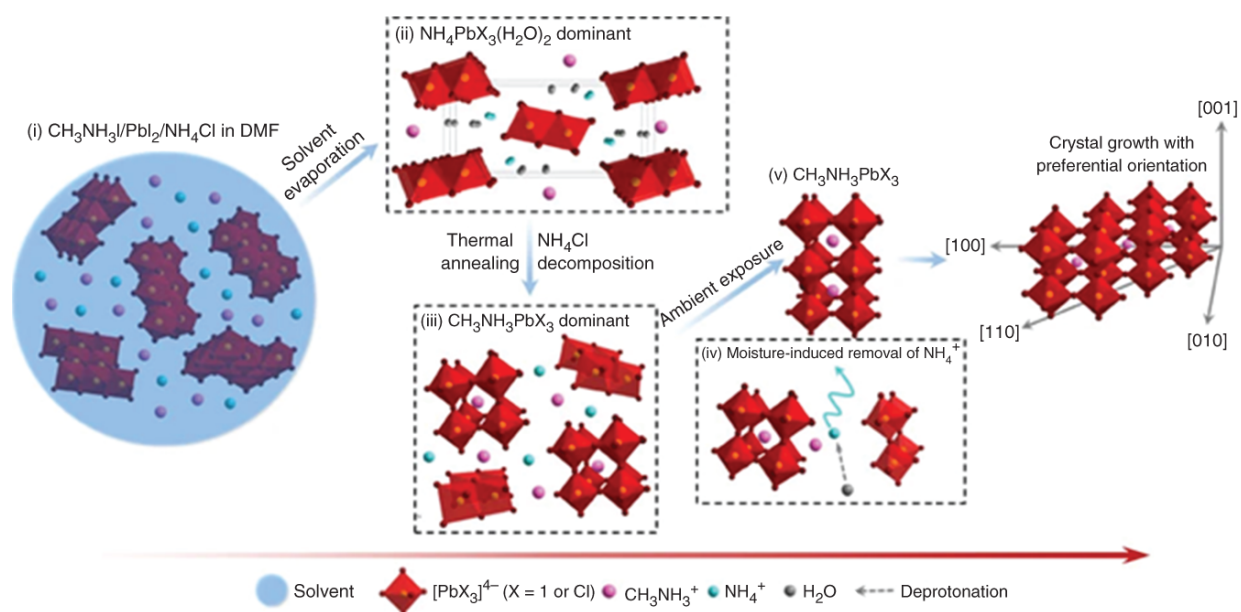
Figure 7.12 Schematic view of the crystal growth process of perovskite $CH_3NH_3PbX_3$ in the presence of ammonium and moisture. Source: Rong et al. [112]/Springer Nature/CC BY-4.0.

Schematic illustration of *in situ* GIWAXS

(a)

(b) MAPbI₃

(c) MAPbI₃·MACl
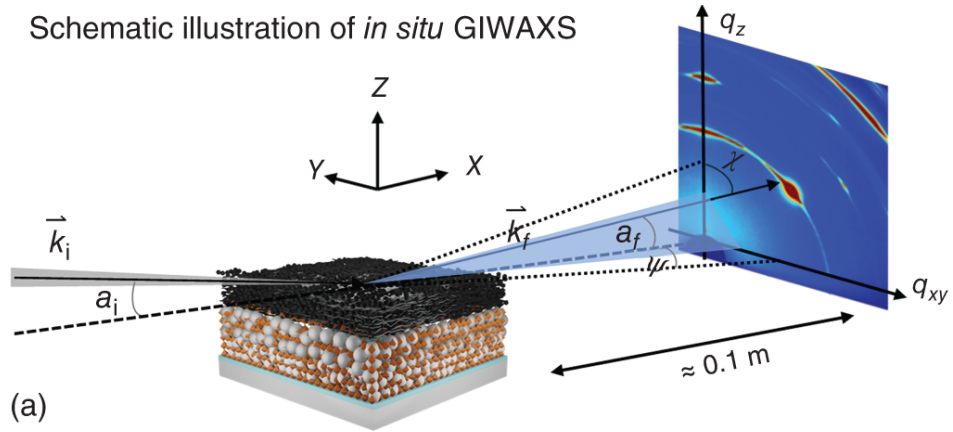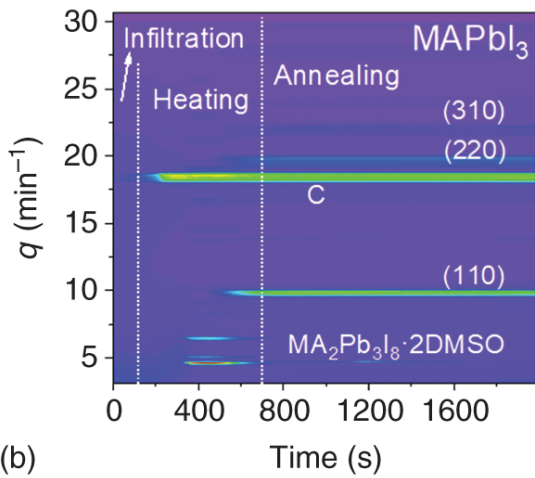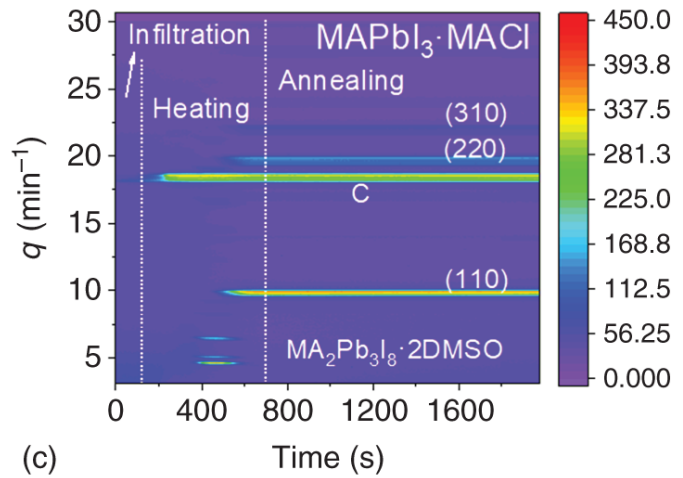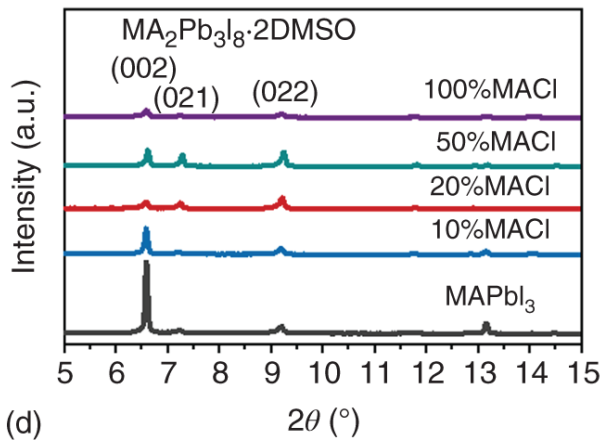
(d)
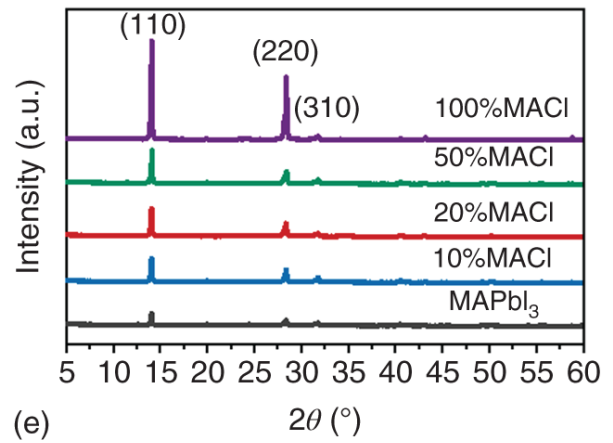
(e)

Figure 7.13 (a) Schematic illustration of in situ GIWAXS experimental setup. $\vec{k}_i$ is the incident beam, a_i the is shallow incident angle, $\vec{k}_f$ is the scattered wave, a_f is the in-plane exit angle, ψ is the out-of-plane angle, and χ is the azimuthal angle. The evolution of the scattering features with respect to the scattering vector q and the time for the MAPbI$_3$ perovskite (b) without and (c) with MACl in the DMF/DMSO solvent. The XRD patterns of (d) the precursor solution films after annealing at 100 °C for five minutes and (e) final perovskite films with different concentrations of MACl. Source: Xiao et al. [113]/With permission of American Chemical Society.

At present, introducing chloride additives (MACl, PbCl$_2$) has become a common way to improve the crystallization of perovskite in the printable mesoscopic PSCs. Xiao et al. revealed the Cl-assisted perovskite crystallization pathway in the mesoscopic scaffold by in situ GIWAXS (Figure 7.13a). The in situ characterizations suggest that Cl$^-$ ions can effectively delay the formation of the intermediate MA$_2$Pb$_3$I$_8$·2DMSO and shorten its existence time (Figure 7.13b), promote the conversion of the intermediate to perovskite, and ultimately significantly improve the morphology and crystallinity of the perovskite in the mesoscopic structure (Figure 7.13c) [113]. Xu et al. used TiO$_2$ nanoparticles loaded with commercial dye N719 as an additive to passivate shallow defects in perovskite, which promoted charge extraction and ultimately increased the short-circuit current of the device [114].

At present, a variety of additives have been applied to printable mesoscopic PSCs for efficiency enhancement. It is important to further explore the effects of different anions and cations of additives on the photovoltaic properties and film quality of perovskite. The selection of suitable additives could further improve the performance of printable mesoscopic PSCs in terms of crystal quality, defect passivation, energy band alignment, and further improve device stability.

7.5 Interfaces Engineering

Toward solar cells, no matter which type the solar cell is, the interface property could be of vital importance for devices. The exciton dissociation, carrier extraction, and transport as well as recombination could take place at the interface. Through interface

modification, researchers could adjust the energy level and banggap offset and improve the work function of materials, which could help enhance the quantum efficiency, accelerate the carrier transport and inhibit the non-radiative recombination [115–118]. In addition to electronic properties, the stability of perovskite could also be related to the properties of different interfaces. For instance, the moisture could react with the perovskite and lead to the decomposition of perovskite, which usually occurs at the surface of perovskite. Through modifying the surface with a hydrophobic layer, the moisture stability of devices could be improved. For traditional PSCs, the planar structure makes it relatively easier to realize the interface modification because interfaces are distinct. However, in the printable mesoscopic PSCs, the high specific surface area of mesoscopic scaffold brings more complex properties of interfaces. The perovskite crystals fill into the mesoscopic scaffold densely and contact each mesoporous layer so it could be difficult to modify the specific interface between perovskite and a certain layer. Here, we will introduce the interface engineering applied in both traditional PSCs and printable mesoscopic PSCs and compare differences between these two structures.

7.5.1 Interface of Perovskite and Electron Transport Materials

In traditional PSCs, the interface modification between perovskite and electron transport layer (ETL) could be used to decrease the defect density, adjust the band alignment and improve the contact of different layers. For the traditional PSCs are fabricated with the spin-coating method, in which materials are deposited layer by layer, the interface modification could also improve the film morphology of perovskite layer through modifying the surface of ETL in n-i-p structure PSCs. Ogomi et al. inserted a monolayer of HOOC–R–NH$_3^+$ between mesoporous TiO$_2$ layer and MAPbI$_3$. The organic monolayer could inhibit the recombination at the interface and improve the crystal growth of MAPbI$_3$. The COOH group was absorbed on the surface of TiO$_2$ and the NH$_3^+$ could anchor the perovskite through incorporating into the PbI$_2$, which could control the crystallization of perovskite. Under the modification of HOOC–R–NH$_3^+$, the perovskite could achieve the uniform crystals with large grain size [119]. Peng et al. deposited an ultrathin layer between the perovskite and TiO$_2$, which was consisted of a PMMA : PCBM mixture. This interlayer could

suppress the interfacial recombination and the champion device exhibit a V_{OC} of 1.18 V. The modified device achieved a negligible hysteresis, fast current and voltage response and finally attained a steady state PCE of 20.4% [120]. Besides organic molecules, Sargent et al. introduced $PbCl_2$ into the perovskite precursor solution to form the Cl-capped TiO_2. The interfacial Cl atoms could suppress deep trap states at the interface of the perovskite and TiO_2, which decreases the interfacial carrier recombination and improves the contact of perovskite and TiO_2 [121].

Different from traditional PSCs, interface modification strategies are relatively limited in printable mesoscopic PSCs. During the fabrication of printable mesoscopic PSCs, the modified ETL needs to be subsequently anneal at a temperature over 400 °C. The annealing process makes it difficult to introduce organic molecules into the interface for many organic molecules could decompose at the temperature. To prevent the decomposition of molecules used to modify TiO_2, one method is to immerse the annealed mesoscopic scaffold into the solvent of molecule. If the molecule could be selectively absorbed on the surface of TiO_2, the interface of TiO_2 and perovskite could be modified. Liu et al. inserted an organic silane self-assembled monolayer between TiO_2 and $MAPbI_3$ with the immersing method in printable mesoscopic PSCs. The monolayer could tune the interface electronic structure and inhibit the recombination process, which further improved the performance of devices (Figure 7.14a) [122]. Zhao et al. achieved surface modification of TiO_2 with ethanolamine by immersing the sintered blank devices in 2-ME solution. The ethanolamine located at the TiO_2/perovskite interface can reduce the interfacial energy barrier and passivate the unliganded Pb defects at the interface (Figure 7.14b) [123].

Another method is to modify the interface with materials owning good thermostability. Xiong et al. deposited a thin layer of metal Al on the surface of TiO_2 and the metal Al could be oxidized into Al_2O_3 through subsequent annealing process. The interfacial Al_2O_3 on the surface of TiO_2 could not only serve as an extra insulating layer but also modify the interface between TiO_2 and perovskite. To compare the recombination resistance of modified devices and original devices, EIS characterization was conducted and showed that modified devices could more effectively suppress the carrier recombination

inside devices through EIS spectrum ([Figure 7.15](#)). Finally, the V_{OC} of resulting devices was improved from 836 to 942 mV [124]. In the later research, Wang et al. used another method to modify the TiO_2 with Al_2O_3 in printable mesoscopic PSCs. Based on the spraying pyrolysis method, the precursor solution containing organic Al source was sprayed on the hot TiO_2 layer at 450 °C. The precursor decomposed and an ultrathin layer of Al_2O_3 was deposited on the surface of TiO_2. The modification could downshift the conduction band minimum (CBM) of TiO_2 and promote carrier transport, which leads to better performance [125]. Al_2O_3 is not the only choice to modify the TiO_2, several metal oxides, including La_2O_3 and MgO, could also be used to modify the energy bandgap and work function of TiO_2. Besides the metal oxides, C_{60} could stay stable at 400 °C and has been successfully used to adjust the energy band level in printable mesoscopic PSCs [126].

(a)

(b)
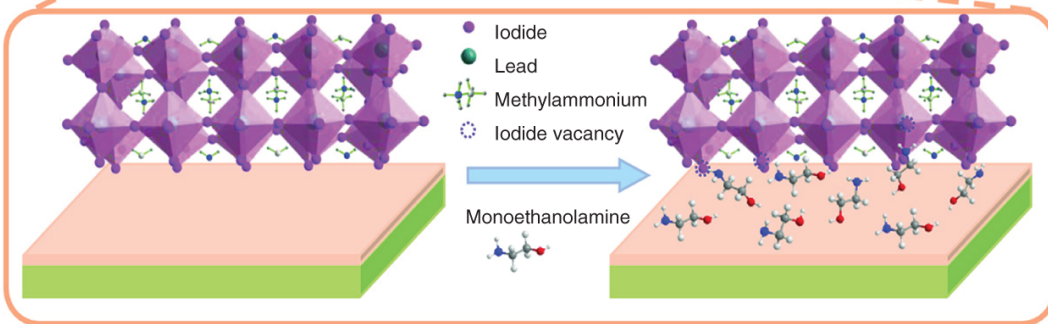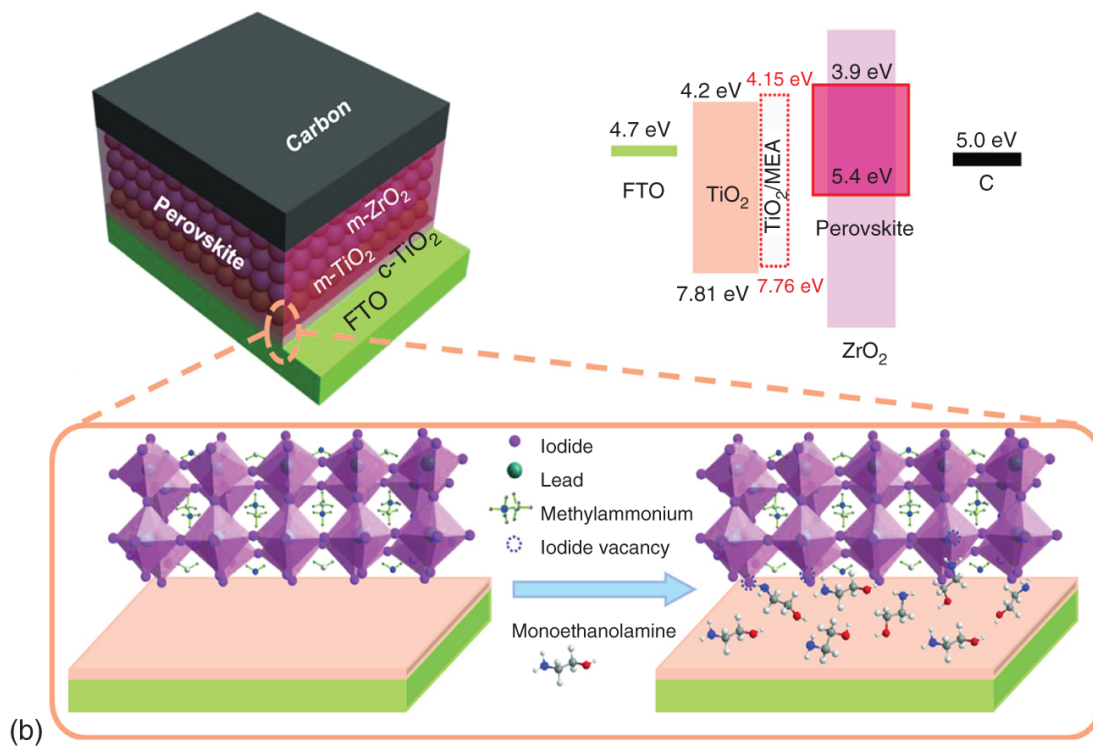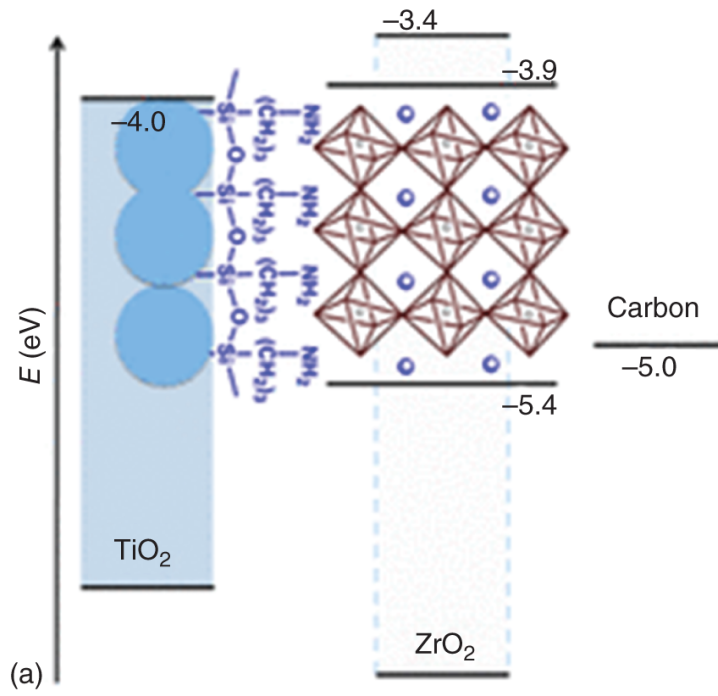
Figure 7.14 (a) Structure of the printable mesoscopic PSCs based on carbon. Source: Liu et al. [122]/With permission of American Chemical Society. (b) Structure of the printable mesoscopic PSC, the diagram of energy levels of each functional layer in the device with the MEA-passivated interface, and schematic representation of the PSC device modified with MEA. Source: Zhao et al. [123]/With permission of John Wiley & Sons.
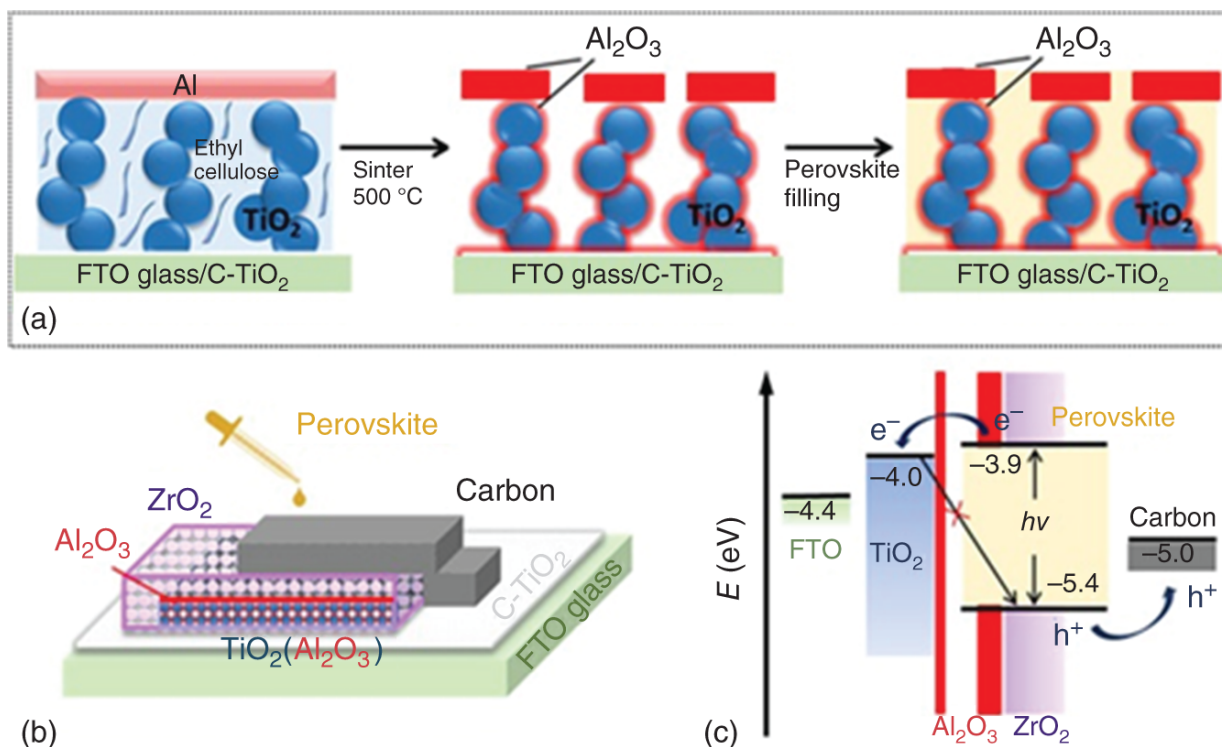
Figure 7.15 (a) Formation process of bifunctional Al_2O_3 interlayer; schematic structure (b) and energy band diagram (c) of hole-conductor-free C-PSCs with Al_2O_3 interlayer. Source: Xiong et al. [124]/With permission of John Wiley & Sons.

In summary, the interface modification at the interface of perovskite and ETL is widely used in adjusting the energy band structure, reducing defects, and suppressing carrier recombination. According to the structure of PSCs, the modification strategy and materials could be different, which depends on the fact whether the modified interface could maintain its properties when the fabrication of devices is finally completed.

7.5.2 Interface of Perovskite and Counter Electrode

To improve the hole extraction from perovskite to counter electrode, a layer of hole transport material (HTM) needs to be deposited between the perovskite and the counter electrode in traditional PSCs, which is important to achieve high PCE. For printable mesoscopic PSCs, NiO_x has been used as the HTL helping carrier transport [34]. However, the HTL is not so necessary in printable mesoscopic PSCs. The device could also achieve a PCE of 16.35% without HTL for the perovskite itself could also transport holes to the counter electrode in printable mesoscopic PSCs [127]. So, researchers could pay more attention to the perovskite/carbon interface in printable mesoscopic PSCs, which exhibits obvious differences between traditional PSCs and printable mesoscopic PSCs. In this chapter, we will concentrate on the interface of perovskite and carbon electrode in printable mesoscopic PSCs.

There are several methods to modify the perovskite/carbon interface. Li et al. introduced vanadium oxide (VO_x) to modify the interface of perovskite and carbon through the posttreatment. VO_x possesses a work function of approximate 5.39 eV, which is higher than carbon. With the modification of VO_x, the hole transport could be accelerated at the interface of perovskite and carbon. The V_{OC} of modified device increased from 892.73 to 922.86 mV, which leads to high PCE of 15.77% [128]. In addition to VO_x, adjusting the oxygen content of carbon electrode could also change the work function of carbon electrode (Figure 7.16a). Tian et al. proposed oxygen management of carbon black to improve the contact of perovskite/carbon interface and adjust the energy level alignment. Two kinds of carbon black were applied to the fabrication of printable mesoscopic PSCs, containing oxygen-rich carbon black (ORC) and oxygen-deficient carbon black (ODC). The carbon electrode made of ORC exhibited a p-type property and positive shift of work function, leading to efficient hole transport (Figure 7.16b). As a result, the PCE was improved from 13.6% to 15.7% with the ORC-based carbon electrode [129]. Boron doping is another method to enhance the work function of carbon electrodes. Duan et al. adopted boron-doped graphite to prepare the carbon electrode which exhibited enhanced work function. Through substituting part of carbon atoms with boron atoms in the graphite lattice, the modified graphite shows high graphitization, which is beneficial for improving the conductivity of carbon electrodes. The work function of carbon electrodes was

increased from 4.81 to 5.10 eV resulting in more efficient hole transport at the interface of perovskite/carbon [130].

The three layers mesoscopic structure of the printable mesoscopic devices makes the perovskite/carbon electrode interface unclear, leading to very difficult modulations of the interface. Therefore, the selection of a suitable solvent for posttreatment of the device after the preparation of the printable mesoporous device is a feasible option to regulate the perovskite/carbon electrode interface. Therefore, posttreatment of the device based on a suitable solvent after the preparation of the printable mesoporous device is an ideal solution for regulating the perovskite/carbon electrode interface. Chen et al. treated the devices by using fluorinated phenethylamine molecules and control the in situ formation of low dimensional perovskite with wide bandgap in carbon electrode (Figure 7.17a), which can form a type II energy band arrangement with 3D perovskite and facilitate directional charge transport and performance enhancement (Figure 7.17b) [131]. Xia et al. modulated the interfacial arrangement of the perovskite/carbon electrode by posttreatment of the devices with the p-type molecule 2,3,5,6-tetrafluoro-7,7,8,8-tetracyanoquinodimethane (F4TCNQ). This suppressed interfacial charge complexation and contributed to the highest open-circuit voltage (1044 mV) of the printable mesoscopic devices at that time (Figure 7.17c,d) [132].

(a)

Carbon
ZrO₂
persovskite
m-TiO₂
c-TiO₂
FTO-glass

(b)

VOₓ dispersed in IPA

VOₓ

(c)

−4.4 eV   −4.0 eV   −3.9 eV

FTO   TiO₂   perovskite   VOₓ   C

−5.4 eV   −5.4 eV

ZrO₂

(d)

Interface contact

Perovskite   ODC   ORC   Perovskite

Oxygen

Oxygen
management

5.0 eV

5.4 eV   5.2 eV   5.4 eV

Energy level alignment
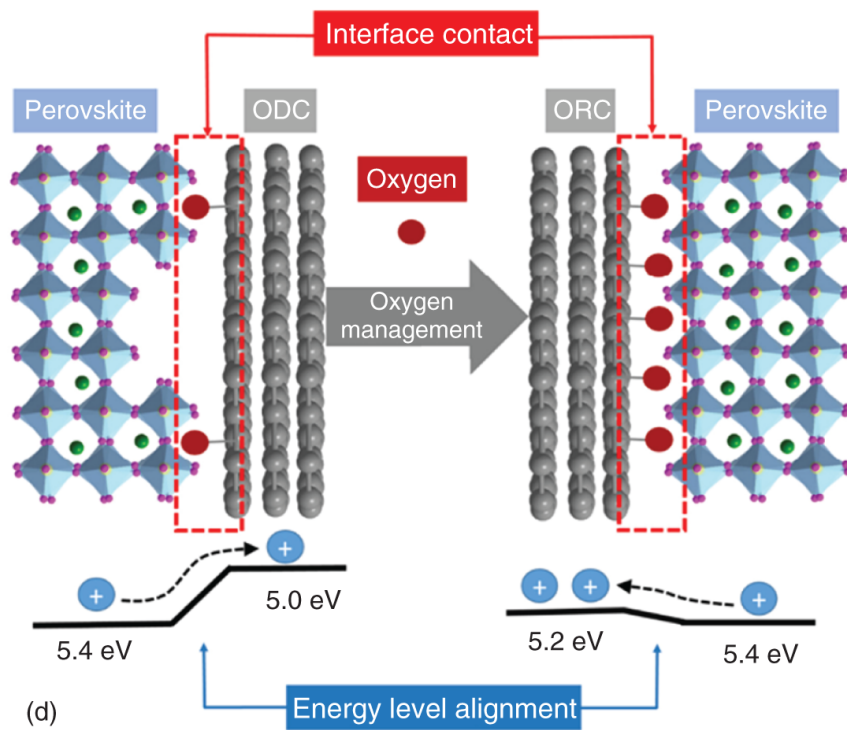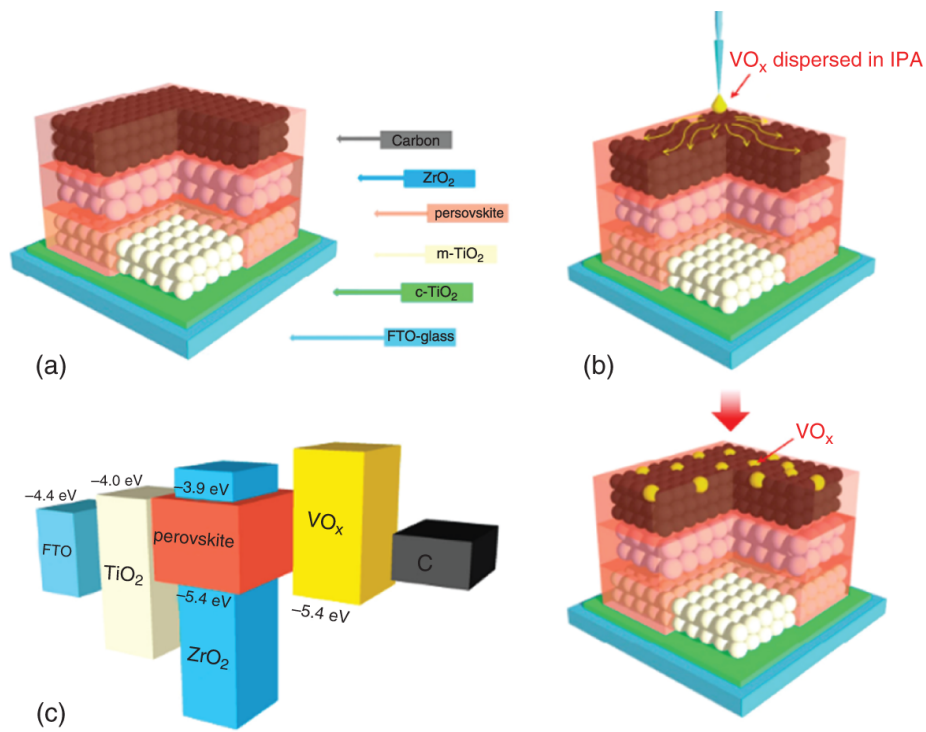
Figure 7.16 (a) the device structure of a typical printable PSC based on triple mesoscopic scaffold of TiO_2/ZrO_2/carbon. (b) schematic diagram of VO_x posttreatment of the interface of perovskite/carbon. (c) the energy levels and alignment of the components in printable PSCs. Source: Li et al. [128]/With permission of American Chemical Society. (d) The schematic of oxygen-deficient carbon black (ODC), oxygen-rich carbon black (ORC), interface contact, and energy level alignment of the materials. Source: Tian et al. [129]/With permission of Elsevier.
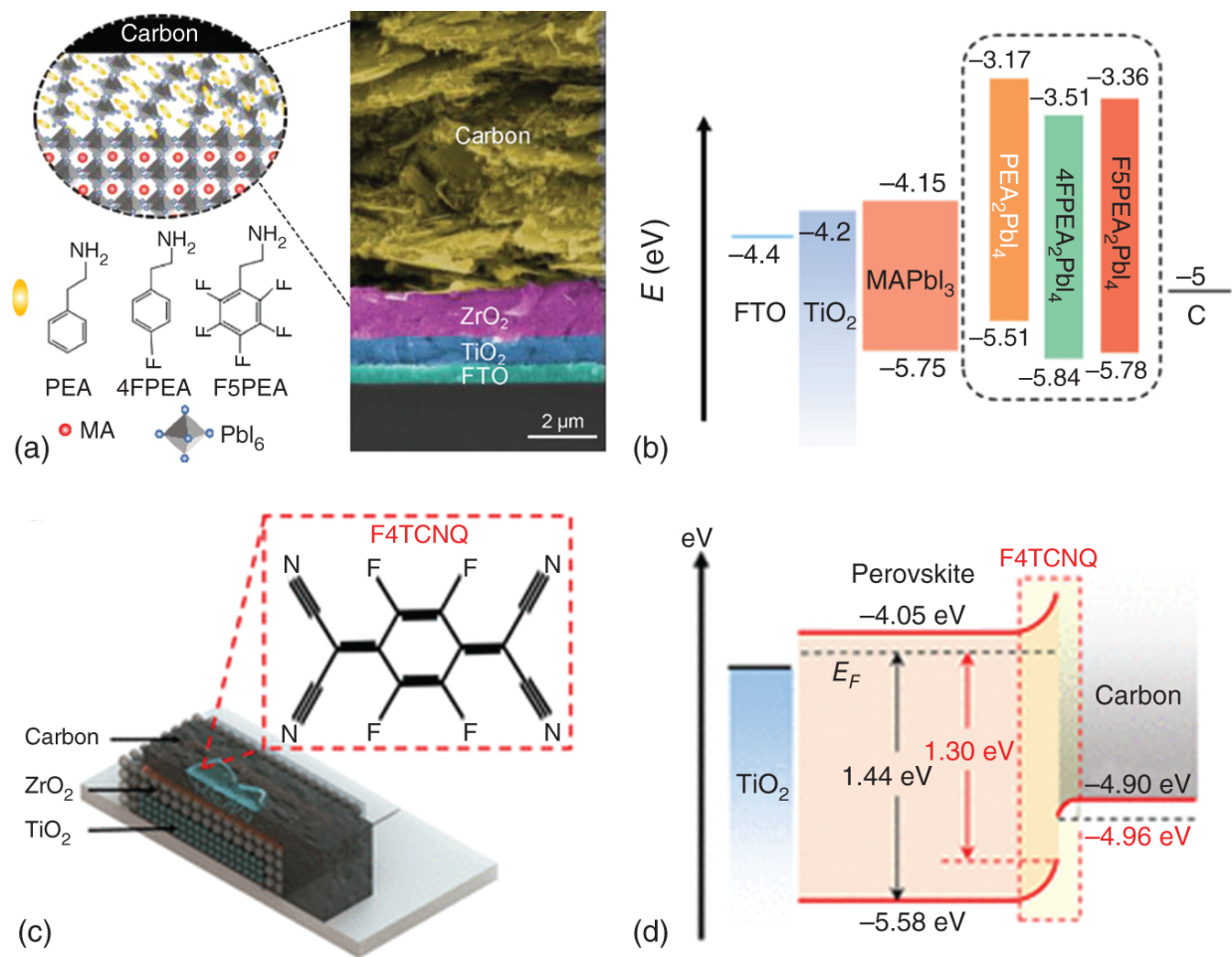
Figure 7.17 Posttreatment and in situ formation of 2D perovskites. (a) Scheme of constructing 2D perovskite at the interface between 3D perovskite and carbon and the cross-sectional SEM image of tripe-mesoscopic PSCs. (b) The energy level diagram of printable triple-mesoscopic PSCs with a 2D perovskite as an electron blocking layer at $MAPbI_3$/carbon interface. Posttreatment of F4TCNQ on printable mesoscopic PSCs. Source: Chen et al. [131]/With permission of John Wiley & Sons. (c) schematic diagram of printable mesoscopic PSC and molecular structure of F4TCNQ (d) energy band diagram of the F4TCNQ posttreated device. Source: Xia et al. [132]/With permission of American Chemical Society.

The two-step sequential deposition methods similar to posttreatment can also be used to tune the interfacial properties of printable mesoscopic devices. Du et al. prepared the like homogeneous structures of perovskite in the mesoporous scaffold by gradient self-doping. The difference in the work function of perovskite at different depths enhances the built-in electric field (Figure 7.18), which

improves the hole transport and extraction and significantly reduces carrier recombination losses in the device [133].

According to interface modification strategies mentioned above, the main purpose of the interface engineering is to improve the carrier transport at the interface. Doping in the ETL or carbon electrode or inserting an interlayer at the interface could help adjust the band alignment, leading to more efficient carrier transport and decreasing the carrier recombination. For different strategies applied in the fabrication of printable mesoscopic PSCs, on the one hand, the modification of ETL and carbon electrode should be adapted to the preparation process of the printable mesoscopic devices sintered at high temperature, and on the other hand, the interfacial modification should not affect the filling and crystallization process of perovskite in the mesoscopic scaffolds or cause perovskite decomposition. Modification of the mesoscopic scaffolds after sintering by some interfacial materials is a feasible method, but it is difficult to control which layer to modify and is less reproducible. Posttreatment of the prepared devices by selecting the appropriate solvent and material is a simpler and more efficient method. On the one hand, the strategy should not damage the perovskite materials which have been filled into the mesoscopic scaffold, on the other hand, the interface modification should not affect or damage the dense pore-filling morphology. Due to many modification methods that could lead to the decomposition of perovskite, directly modifying the ETL or carbon electrode before filling perovskite precursor solution could be a simpler method for the interface engineering in printable mesoscopic PSCs.
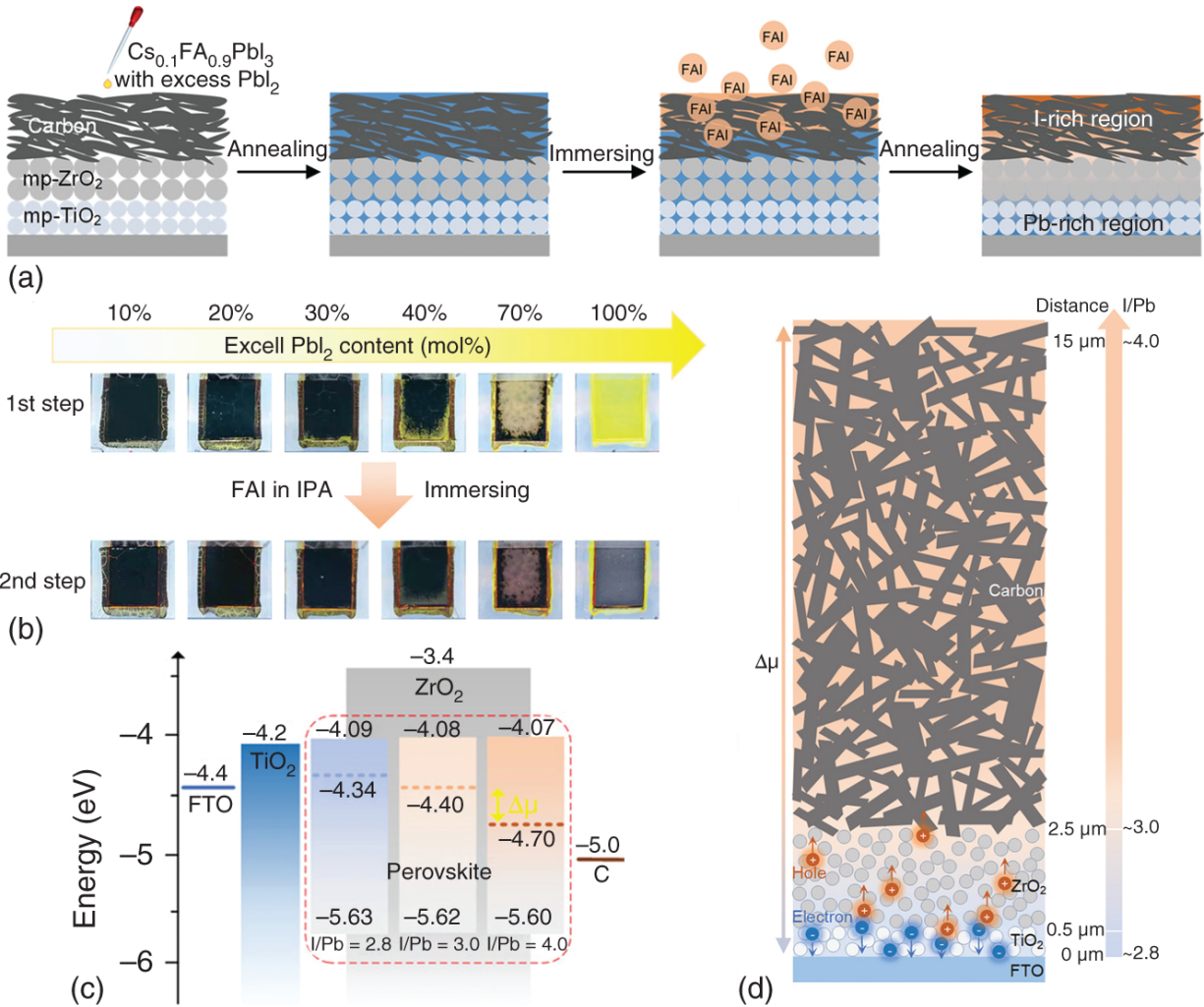
Figure 7.18 The schematic structure of printable mesoscopic PSCs with mp-TiO$_2$/mp-ZrO$_2$/porous carbon structure and the deposition process of perovskite absorber. Cs$_{0.1}$FA$_{0.9}$PbI$_3$ containing excess PbI$_2$ (20 mol%) was first deposited, then the device was immersed in IPA solution of FAI. (b) The digital photograph (from the glass side) of the device fabricated from perovskite precursor containing different contents of PbI$_2$ before and after treatment with FAI. (c) The energy level diagram of target printable mesoscopic PSCs device. (d) The schematic diagram of the change of perovskite composition along the longitudinal direction. Source: Du et al. [133]/ With permission of John Wiley & Sons.

7.6 Conclusion and Outlook

To achieve high performance of the printable mesoscopic PSCs, it is of vital importance to get a dense pore-filling inside the mesopores.

Selecting right solvents, regulating the annealing temperature, adjusting annealing methods and additive engineering could be helpful to achieve high crystallinity with favored orientation. In addition to improving the crystallization of perovskite, the additive could also be used to adjust the electronic and optical properties of perovskite to get better light absorbance and to improve carrier transport. Changing the ratio of different anions and cations in A, B, or X sites could also directly determine the bandgap of perovskite, which could help to achieve the proper absorption spectrum. However, the adjustment of perovskite compositions may lead to phase separation, which should be taken into consideration in the composition engineering. Besides the perovskite material itself, the interface of perovskite and other materials is also important to fabricate printable mesoscopic PSCs with high performance. Generally, adjusting the work function of ETL and carbon electrodes could be an effective strategy to improve the interface property through the interface engineering.

The unique structure and fabrication process bring printable mesoscopic PSCs with many advantages including the ease of large-scale fabrication, batter stability, and lower cost, which exhibit a great promise of commercialization. Combining different methods, printable mesoscopic PSCs could achieve both high PCE and long-term stability in the future.

References

1 Grätzel, M. and O'Regan, B. (1991). A low-cost, high-efficiency solar cell based on dye-sensitized colloidal TiO_2 films. *Nature* 353 (6346): 737–740.

2 Bach, U., Lupo, D., Comte, P. et al. (1998). Solid-state dye-sensitized mesoporous TiO_2 solar cells with high photon-to-electron conversion efficiencies. *Nature* 395 (6702): 583–585.

3 Kojima, A., Teshima, K., Shirai, Y., and Miyasaka, T. (2009). Organometal halide perovskites as visible-light sensitizers for photovoltaic cells. *Journal of the American Chemical Society* 131 (17): 6050–6051.

4 Kim, H.-S., Lee, C.-R., Im, J.-H. et al. (2012). Lead iodide perovskite sensitized all-solid-state submicron thin film mesoscopic solar cell

with efficiency exceeding 9%. *Scientific Reports* 2 (1): 1–7.

5 Lee, M.M., Teuscher, J., Miyasaka, T. et al. (2012). Efficient hybrid solar cells based on meso-superstructured organometal halide perovskites. *Science* 338 (6107): 643–647.

6 Rong, Y., Liu, L., Mei, A. et al. (2015). Beyond efficiency: the challenge of stability in mesoscopic perovskite solar cells. *Advanced Energy Materials* 5 (20): 1501066.

7 Burschka, J., Pellet, N., Moon, S.-J. et al. (2013). Sequential deposition as a route to high-performance perovskite-sensitized solar cells. *Nature* 499 (7458): 316–319.

8 Etgar, L., Gao, P., Xue, Z. et al. (2012). Mesoscopic $CH_3NH_3PbI_3/TiO_2$ heterojunction solar cells. *Journal of the American Chemical Society* 134 (42): 17396–17399.

9 Mei, A., Li, X., Liu, L. et al. (2014). A hole-conductor-free, fully printable mesoscopic perovskite solar cell with high stability. *Science* 345 (6194): 295–298.

10 Kim, H.S., Lee, C.R., Im, J.H. et al. (2012). Lead iodide perovskite sensitized all-solid-state submicron thin film mesoscopic solar cell with efficiency exceeding 9%. *Science Reports* 2: 591. https://doi.org/10.1038/srep00591.

11 Ku, Z., Rong, Y., Xu, M. et al. (2013). Full printable processed mesoscopic $CH_3NH_3PbI_3/TiO_2$ heterojunction solar cells with carbon counter electrode. *Science Reports* 3: 3132. https://doi.org/10.1038/srep03132.

12 US TNRELot (2022). Best research-cell efficiencies. https://www.nrel.gov/pv/assets/pdfs/best-research-cell-efficiencies-rev220126b.pdf (accessed 01 June 2022).

13 Ku, Z., Rong, Y., Xu, M. et al. (2013). Full printable processed mesoscopic $CH_3NH_3PbI_3/TiO_2$ heterojunction solar cells with carbon counter electrode. *Scientific Reports* 3 (1): 1–5.

14 Guo, X., McCleese, C., Kolodziej, C. et al. (2016). Identification and characterization of the intermediate phase in hybrid organic-inorganic $MAPbI_3$ perovskite. *Dalton Transactions* 45 (9): 3806–3813.

15 Ahn, N., Son, D.-Y., Jang, I.-H. et al. (2015). Highly reproducible perovskite solar cells with average efficiency of 18.3% and best efficiency of 19.7% fabricated via Lewis base adduct of lead (II) iodide. *Journal of the American Chemical Society* 137 (27): 8696–8699.

16 Jeon, N.J., Lee, J., Noh, J.H. et al. (2013). Efficient inorganic-organic hybrid perovskite solar cells based on pyrene arylamine derivatives as hole-transporting materials. *Journal of the American Chemical Society* 135 (51): 19087–19090.

17 Fateev, S.A., Petrov, A.A., Khrustalev, V.N. et al. (2018). Solution processing of methylammonium lead iodide perovskite from γ-butyrolactone: crystallization mediated by solvation equilibrium. *Chemistry of Materials* 30 (15): 5237–5244.

18 Jo, Y., Oh, K.S., Kim, M. et al. (2016). High performance of planar perovskite solar cells produced from PbI_2(DMSO) and PbI_2(NMP) complexes by intramolecular exchange. *Advanced Materials Interfaces* 3 (10): 1500768.

19 Cao, X., Zhi, L., Li, Y. et al. (2018). Fabrication of perovskite films with large columnar grains via solvent-mediated Ostwald ripening for efficient inverted perovskite solar cells. *ACS Applied Energy Materials.* 1 (2): 868–875.

20 Rong, Y., Tang, Z., Zhao, Y. et al. (2015). Solvent engineering towards controlled grain growth in perovskite planar heterojunction solar cells. *Nanoscale* 7 (24): 10595–10599.

21 Lee, D.-K., Jeong, D.-N., Ahn, T.K., and Park, N.-G. (2019). Precursor engineering for a large-area perovskite solar cell with >19% efficiency. *ACS Energy Letters* 4 (10): 2393–2401.

22 Hendriks, K.H., van Franeker, J.J., Bruijnaers, B.J. et al. (2017). 2-Methoxyethanol as a new solvent for processing methylammonium lead halide perovskite solar cells. *Journal of Materials Chemistry A* 5 (5): 2346–2354.

23 Deng, Y., Van Brackle, C.H., Dai, X. et al. (2019). Tailoring solvent coordination for high-speed, room-temperature blading of perovskite photovoltaic films. *Science Advances* 5 (12): eaax7537.

24 Zhou, Z., Wang, Z., Zhou, Y. et al. (2015). Methylamine-gas-induced defect-healing behavior of $CH_3NH_3PbI_3$ thin films for perovskite solar cells. *Angewandte Chemie (International Ed. in English)* 54 (33): 9705–9709.

25 Noel, N.K., Habisreutinger, S.N., Wenger, B. et al. (2017). A low viscosity, low boiling point, clean solvent system for the rapid crystallisation of highly specular perovskite films. *Energy & Environmental Science* 10 (1): 145–152.

26 Chen, J., Xiong, Y., Rong, Y. et al. (2016). Solvent effect on the hole-conductor-free fully printable perovskite solar cells. *Nano Energy* 27: 130–137.

27 Liu, S., Zhang, D., Sheng, Y. et al. (2022). Highly oriented $MAPbI_3$ crystals for efficient hole-conductor-free printable mesoscopic perovskite solar cells. *Fundamental Research.* 2 (2): 276–283.

28 Ming, Y., Xu, M., Liu, S. et al. (2019). Ethanol stabilized precursors for highly reproducible printable mesoscopic perovskite solar cells. *Journal of Power Sources* 424: 261–267.

29 Hong, L., Hu, Y., Mei, A. et al. (2017). Improvement and regeneration of perovskite solar cells via methylamine gas post-treatment. *Advanced Functional Materials* 27 (43): 1703060.

30 Wagner, L., Chacko, S., Mathiazhagan, G. et al. (2018). High photovoltage of 1 V on a steady-state certified hole transport layer-free perovskite solar cell by a molten-salt approach. *ACS Energy Letters* 3 (5): 1122–1127.

31 Guan, Y., Xu, M., Zhang, W. et al. (2020). In situ transfer of $CH_3NH_3PbI_3$ single crystals in mesoporous scaffolds for efficient perovskite solar cells. *Chemical Science* 11 (2): 474–481.

32 Xiao, M., Huang, F., Huang, W. et al. (2014). A fast deposition-crystallization procedure for highly efficient lead iodide perovskite thin-film solar cells. *Angewandte Chemie International Edition* 53 (37): 9898–9903.

33 Shuang Xiao, Y.B., Meng, X., Zhang, T. et al. (2017). Unveiling a key intermediate in solvent vapor postannealing to enlarge

crystalline domains of organometal halide perovskite films. *Advanced Functional Materials* 27: 1604944.

34 Wu, Y., Chen, W., Yue, Y. et al. (2015). Consecutive morphology controlling operations for highly reproducible mesostructured perovskite solar cells. *ACS Applied Materials & Interfaces* 7 (37): 20707–20713.

35 Hou, X., Xu, M., Tong, C. et al. (2019). High performance printable perovskite solar cells based on $Cs_{0.1}FA_{0.9}PbI_3$ in mesoporous scaffolds. *Journal of Power Sources* 415: 105–111.

36 Wang, Q., Zhang, W., Zhang, Z. et al. (2020). Crystallization control of ternary-cation perovskite absorber in triple-mesoscopic layer for efficient solar cells. *Advanced Energy Materials* 10 (5): 1903092.

37 Goldschmidt, V.M. (1926). Die gesetze der krystallochemie. *Die Naturwissenschaften* 14 (21): 477–485.

38 Weber, O.J., Charles, B., and Weller, M.T. (2016). Phase behaviour and composition in the formamidinium–methylammonium hybrid lead iodide perovskite solid solution. *Journal of Materials Chemistry A* 4 (40): 15375–15382.

39 He, C., Zha, G., Deng, C. et al. (2019). Refractive index dispersion of organic–inorganic hybrid halide perovskite $CH_3NH_3PbX_3$ (X   Cl, Br, I) single crystals. *Crystal Research and Technology* 54 (5): 1900011.

40 Shirayama, M., Kadowaki, H., Miyadera, T. et al. (2016). Optical transitions in hybrid perovskite solar cells: ellipsometry, density functional theory, and quantum efficiency analyses for $CH_3NH_3PbI_3$. *Physical Review Applied* 5 (1): 014012.

41 Jacobsson, T.J., Correa-Baena, J.-P., Pazoki, M. et al. (2016). Exploration of the compositional space for mixed lead halogen perovskites for high efficiency solar cells. *Energy & Environmental Science* 9 (5): 1706–1724.

42 Babu, R., Giribabu, L., and Singh, S.P. (2018). Recent advances in halide-based perovskite crystals and their optoelectronic applications. *Crystal Growth & Design* 18 (4): 2645–2664.

43 Leguy, A.M., Goni, A.R., Frost, J.M. et al. (2016). Dynamic disorder, phonon lifetimes, and the assignment of modes to the vibrational spectra of methylammonium lead halide perovskites. *Physical Chemistry Chemical Physics* 18 (39): 27051–27066.

44 Blakers, A.W., Wang, A., Milne, A.M. et al. (1989). Detailed balance limit of efficiency of pn junction solar cells. *Applied Physics Letters* 55 (13): 1363–1365.

45 Guillemoles, J.-F., Kirchartz, T., Cahen, D., and Rau, U. (2019). Guide for the perplexed to the Shockley–Queisser model for solar cells. *Nature Photonics* 13 (8): 501–505.

46 Stoumpos, C.C., Malliakas, C.D., and Kanatzidis, M.G. (2013). Semiconducting tin and lead iodide perovskites with organic cations: phase transitions, high mobilities, and near-infrared photoluminescent properties. *Inorganic Chemistry* 52 (15): 9019–9038.

47 Dai, J., Fu, Y., Manger, L.H. et al. (2016). Carrier decay properties of mixed cation formamidinium-methylammonium lead iodide perovskite $[HC(NH_2)_2]_{1-x}[CH_3NH_3]_xPbI_3$ nanorods. *Journal of Physical Chemistry Letters* 7 (24): 5036–5043.

48 Binek, A., Hanusch, F.C., Docampo, P., and Bein, T. (2015). Stabilization of the trigonal high-temperature phase of formamidinium lead iodide. *Journal of Physical Chemistry Letters* 6 (7): 1249–1253.

49 Jeon, N.J., Noh, J.H., Yang, W.S. et al. (2015). Compositional engineering of perovskite materials for high-performance solar cells. *Nature* 517 (7535): 476–480.

50 Li, Z., Yang, M., Park, J.-S. et al. (2015). Stabilizing perovskite structures by tuning tolerance factor: formation of formamidinium and cesium lead iodide solid-state alloys. *Chemistry of Materials* 28 (1): 284–292.

51 Lee, J.-W., Kim, D.-H., Kim, H.-S. et al. (2015). Formamidinium and cesium hybridization for photo- and moisture-stable perovskite solar cell. *Advanced Energy Materials* 5 (20): 1501310.

52 Choi, H., Jeong, J., Kim, H.-B. et al. (2014). Cesium-doped methylammonium lead iodide perovskite light absorber for hybrid

solar cells. *Nano Energy* 7: 80–85.

53 Niu, G., Li, W., Li, J. et al. (2017). Enhancement of thermal stability for perovskite solar cells through cesium doping. *RSC Advances* 7 (28): 17473–17479.

54 Singh, T. and Miyasaka, T. (2018). Stabilizing the efficiency beyond 20% with a mixed cation perovskite solar cell fabricated in ambient air under controlled humidity. *Advanced Energy Materials* 8 (3): 1700677.

55 Saliba, M., Matsui, T., Seo, J.Y. et al. (2016). Cesium-containing triple cation perovskite solar cells: improved stability, reproducibility and high efficiency. *Energy & Environmental Science* 9 (6): 1989–1997.

56 Hu, M., Liu, L., Mei, A. et al. (2014). Efficient hole-conductor-free, fully printable mesoscopic perovskite solar cells with a broad light harvester $NH_2CH=NH_2PbI_3$. *Journal of Materials Chemistry A* 2 (40): 17115–17121.

57 Tai, Q., Cao, J., Wang, T., and Yan, F. (2019). Recent advances toward efficient and stable tin-based perovskite solar cells. *EcoMat* 1 (1): e12004.

58 Gu, S., Lin, R., Han, Q. et al. (2020). Tin and mixed lead-tin halide perovskite solar cells: progress and their application in tandem solar cells. *Advanced Materials* 32 (27): e1907392.

59 Noel, N.K., Stranks, S.D., Abate, A. et al. (2014). Lead-free organic–inorganic tin halide perovskites for photovoltaic applications. *Energy & Environmental Science* 7 (9): 3061–3068.

60 Jiang X, Wang F, Wei Q, Li H, Shang Y, Zhou W, et al. Ultra-high open-circuit voltage of tin perovskite solar cells via an electron transporting layer design. *Nature Communications* 2020; 11(1):1-7.

61 Wu, C., Zhang, Q., Liu, G. et al. (2020). From Pb to Bi: a promising family of Pb-free optoelectronic materials and devices. *Advanced Energy Materials* 10 (13): 1902496.

62 Wu, C., Zhang, Q., Liu, Y. et al. (2018). The dawn of lead-free perovskite solar cell: highly stable double perovskite $Cs_2AgBiBr_6$ film. *Advanced Science* 5 (3): 1700759.

63 Lin, R., Xiao, K., Qin, Z. et al. (2019). Monolithic all-perovskite tandem solar cells with 24.8% efficiency exploiting comproportionation to suppress Sn(ii) oxidation in precursor ink. *Nature Energy* 4 (10): 864–873.

64 Albero, J., Asiri, A.M., and García, H. (2016). Influence of the composition of hybrid perovskites on their performance in solar cells. *Journal of Materials Chemistry A* 4 (12): 4353–4364.

65 Busipalli, D.L., Nachimuthu, S., and Jiang, J.C. (2019). Theoretical study on halide and mixed halide perovskite solar cells: effects of halide atoms on the stability and electronic properties. *Journal of the Chinese Chemical Society* 66 (6): 575–582.

66 Stranks, S.D., Eperon, G.E., Grancini, G. et al. (2013). Electron-hole diffusion lengths exceeding 1 micrometer in an organometal trihalide perovskite absorber. *Science* 342 (6156): 341–344.

67 Xing, G., Mathews, N., Sun, S. et al. (2013). Long-range balanced electron-and hole-transport lengths in organic-inorganic $CH_3NH_3PbI_3$. *Science* 342 (6156): 344–347.

68 Lee, B., Hwang, T., Lee, S. et al. (2019). Microstructural evolution of hybrid perovskites promoted by chlorine and its impact on the performance of solar cell. *Scientific Reports* 9 (1): 1–8.

69 Dong, Q., Yuan, Y., Shao, Y. et al. (2015). Abnormal crystal growth in $CH_3NH_3PbI_{3-x}Cl_x$ using a multi-cycle solution coating process. *Energy & Environmental Science* 8 (8): 2464–2470.

70 Fei, C., Guo, L., Li, B. et al. (2016). Controlled growth of textured perovskite films towards high performance solar cells. *Nano Energy* 27: 17–26.

71 Kim, D.H., Park, J., Li, Z. et al. (2017). 300% enhancement of carrier mobility in uniaxial-oriented perovskite films formed by topotactic-oriented attachment. *Advanced Materials* 29 (23): 1606831.

72 Odysseas Kosmatos, K., Theofylaktos, L., Giannakaki, E. et al. (2019). μethylammonium chloride: a key additive for highly efficient, stable, and up-scalable perovskite solar cells. *Energy & Environmental Materials.* 2 (2): 79–92.

73 Eperon, G.E., Stranks, S.D., Menelaou, C. et al. (2014). Formamidinium lead trihalide: a broadly tunable perovskite for efficient planar heterojunction solar cells. *Energy & Environmental Science* 7 (3): 982–988.

74 Noh, J.H., Im, S.H., Heo, J.H. et al. (2013). Chemical management for colorful, efficient, and stable inorganic–organic hybrid nanostructured solar cells. *Nano Letters* 13 (4): 1764–1769.

75 Min, H., Kim, M., Lee, S.-U. et al. (2019). Efficient, stable solar cells by using inherent bandgap of α-phase formamidinium lead iodide. *Science* 366 (6466): 749–753.

76 Jacobsson, T.J., Correa-Baena, J.-P., Halvani Anaraki, E. et al. (2016). Unreacted PbI_2 as a double-edged sword for enhancing the performance of perovskite solar cells. *Journal of the American Chemical Society* 138 (32): 10331–10343.

77 Zhang, J., Wu, S., Liu, T. et al. (2019). Boosting photovoltaic performance for lead halide perovskites solar cells with BF_4^- anion substitutions. *Advanced Functional Materials* 29 (47): 1808833.

78 Ke, W., Xiao, C., Wang, C. et al. (2016). Employing lead thiocyanate additive to reduce the hysteresis and boost the fill factor of planar perovskite solar cells. *Advanced Materials* 28 (26): 5214–5221.

79 Daub, M. and Hillebrecht, H. (2015). Synthesis, single-crystal structure and characterization of $(CH_3NH_3)_2Pb(SCN)_2I_2$. *Angewandte Chemie International Edition* 54 (38): 11016–11017.

80 Tai, Q., You, P., Sang, H. et al. (2016). Efficient and stable perovskite solar cells prepared in ambient air irrespective of the humidity. *Nature Communications* 7 (1): 1–8.

81 Li, X., Zhong, X., Hu, Y. et al. (2017). Organic-inorganic copper(II)-based material: a low-toxic, highly stable light absorber for photovoltaic application. *Journal of Physical Chemistry Letters* 8 (8): 1804–1809.

82 Li, T., Hu, Y., Morrison, C.A. et al. (2017). Lead-free pseudo-three-dimensional organic–inorganic iodobismuthates for photovoltaic applications. *Sustainable Energy & Fuels* 1 (2): 308–316.

83 Li, T., Wang, Q., Nichol, G.S. et al. (2018). Extending lead-free hybrid photovoltaic materials to new structures: thiazolium, aminothiazolium and imidazolium iodobismuthates. *Dalton Transactions* 47 (20): 7050–7058.

84 Min Chen, M.-G.J., Mingyu, H., Dai, Z. et al. (2019). Lead-free dion–jacobson tin halide perovskites for photovoltaics. *ACS Energy Letters* 4: 2.

85 Sheng, Y., Mei, A., Liu, S. et al. (2018). Mixed (5-AVA)$_x$MA$_{1-x}$PbI$_{3-y}$(BF$_4$)$_y$ perovskites enhance the photovoltaic performance of hole-conductor-free printable mesoscopic solar cells. *Journal of Materials Chemistry A* 6 (5): 2360–2364.

86 Zheng, H., Liu, G., Zhu, L. et al. (2018). The effect of hydrophobicity of ammonium salts on stability of quasi-2D perovskite materials in moist condition. *Advanced Energy Materials* 8 (21): 1800051.

87 Wang, Z., Lin, Q., Chmiel, F.P. et al. (2017). Efficient ambient-air-stable solar cells with 2D–3D heterostructured butylammonium-caesium-formamidinium lead halide perovskites. *Nature Energy* 2 (9): 1–10.

88 Luo, T., Zhang, Y., Xu, Z. et al. (2019). Compositional control in 2D perovskites with alternating cations in the interlayer space for photovoltaics with efficiency over 18. *Advanced Materials* 31 (44): e1903848.

89 Yang, S., Wang, Y., Liu, P. et al. (2016). Functionalization of perovskite thin films with moisture-tolerant molecules. *Nature Energy* 1 (2): 1–7.

90 Wu, W.-Q., Yang, Z., Rudd, P.N. et al. (2019). Bilateral alkylamine for suppressing charge recombination and improving stability in blade-coated perovskite solar cells. *Science Advances* 5 (3): eaav8925.

91 Jiang, Q., Zhao, Y., Zhang, X. et al. (2019). Surface passivation of perovskite film for efficient solar cells. *Nature Photonics* 13 (7): 460–466.

92 Hu, Y., Zhang, Z., Mei, A. et al. (2018). Improved performance of printable perovskite solar cells with bifunctional conjugated

organic molecule. *Advanced Materials* 30 (11): 1705786.

93 Saparov, B. and Mitzi, D.B. (2016). Organic-inorganic perovskites: structural versatility for functional materials design. *Chemical Reviews* 116 (7): 4558–4596.

94 Noel, N.K., Abate, A., Stranks, S.D. et al. (2014). Enhanced photoluminescence and solar cell performance via Lewis base passivation of organic–inorganic lead halide perovskites. *ACS Nano* 8 (10): 9815–9821.

95 Niu, T., Lu, J., Munir, R. et al. (2018). Stable high-performance perovskite solar cells via grain boundary passivation. *Advanced Materials* 30 (16): e1706576.

96 Niu, T., Lu, J., Tang, M.-C. et al. (2018). High performance ambient-air-stable $FAPbI_3$ perovskite solar cells with molecule-passivated Ruddlesden–Popper/3D heterostructured film. *Energy & Environmental Science* 11 (12): 3358–3366.

97 Zhao, Y., Wei, J., Li, H. et al. (2016). A polymer scaffold for self-healing perovskite solar cells. *Nature Communications* 7 (1): 1–9.

98 Zuo, L., Guo, H., deQuilettes, D.W. et al. (2017). Polymer-modified halide perovskite films for efficient and stable planar heterojunction solar cells. *Science Advances* 3 (8): e1700106.

99 Li, X., Zhang, W., Wang, Y.-C. et al. (2018). In-situ cross-linking strategy for efficient and operationally stable methylammonium lead iodide solar cells. *Nature Communications* 9 (1): 1–10.

100 Filonik, O., Thordardottir, M.E., Lebert, J. et al. (2019). Evolution of perovskite crystallization in printed mesoscopic perovskite solar cells. *Energy Technology* 7 (10): 1900343.

101 Grancini, G., Roldán-Carmona, C., Zimmermann, I. et al. (2017). One-year stable perovskite solar cells by 2D/3D interface engineering. *Nature Communications* 8 (1): 1–8.

102 Xiao, X., Chu, Y., Zhang, C. et al. (2021). Enhanced perovskite electronic properties via A-site cation engineering. *Fundamental Research* 1 (4): 385–392.

103 Yan, K., Long, M., Zhang, T. et al. (2015). Hybrid halide perovskite solar cell precursors: colloidal chemistry and coordination engineering behind device processing for high efficiency. *Journal of the American Chemical Society* 137 (13): 4460–4468.

104 Liu, D., Li, C., Zhang, C. et al. (2017). Blended additive manipulated morphology and crystallinity transformation toward high performance perovskite solar cells. *RSC Advances* 7 (82): 51944–51949.

105 McMeekin, D.P., Wang, Z., Rehman, W. et al. (2017). Crystallization kinetics and morphology control of formamidinium–cesium mixed-cation lead mixed-halide perovskite via tunability of the colloidal precursor solution. *Advanced Materials* 29 (29): 1607039.

106 Zhou, H., Chen, Q., Li, G. et al. (2014). Interface engineering of highly efficient perovskite solar cells. *Science* 345 (6196): 542–546.

107 Williams, S.T., Zuo, F., Chueh, C.-C. et al. (2014). Role of chloride in the morphological evolution of organo-lead halide perovskite thin films. *ACS Nano* 8 (10): 10640–10654.

108 Yu, Y., Wang, C., Grice, C.R. et al. (2017). Synergistic effects of lead thiocyanate additive and solvent annealing on the performance of wide-bandgap perovskite solar cells. *ACS Energy Letters* 2 (5): 1177–1182.

109 Tang, G., You, P., Tai, Q. et al. (2018). Performance enhancement of perovskite solar cells induced by lead acetate as an additive. *Solar RRl* 2 (6): 1800066.

110 Sheng, Y., Hu, Y., Mei, A. et al. (2016). Enhanced electronic properties in $CH_3NH_3PbI_3$via LiCl mixing for hole-conductor-free printable perovskite solar cells. *Journal of Materials Chemistry A* 4 (42): 16731–16736.

111 Jiang, F., Rong, Y., Liu, H. et al. (2016). Synergistic effect of PbI_2 passivation and chlorine inclusion yielding high open-circuit voltage exceeding 1.15 V in both mesoscopic and inverted planar $CH_3NH_3PbI_3$(Cl)-based perovskite solar cells. *Advanced Functional Materials* 26 (44): 8119–8127.

112 Rong, Y., Hou, X., Hu, Y. et al. (2017). Synergy of ammonium chloride and moisture on perovskite crystallization for efficient printable mesoscopic solar cells. *Nature Communications* 8 (1): 1–8.

113 Xiao, X., Zhang, W., Zhang, W. et al. (2022). Cl-assisted perovskite crystallization pathway in the confined space of mesoporous metal oxides unveiled by in situ grazing incidence wide-angle X-ray scattering. *Chemistry of Materials* 34 (5): 2231–2237.

114 Xu, L., Li, Y., Shi, J. et al. (2020). Suppressing shallow defect of printable mesoscopic perovskite solar cells with a N719@ TiO$_2$ inorganic–organic core–shell structured additive. *Solar RRL.* 4 (6): 2000042.

115 Zhao, X., Xu, C., Wang, H. et al. (2014). Application of biuret, dicyandiamide, or urea as a cathode buffer layer toward the efficiency enhancement of polymer solar cells. *ACS Applied Materials & Interfaces* 6 (6): 4329–4337.

116 Bao, X., Wang, J., Li, Y. et al. (2017). Interface engineering of a compatible PEDOT derivative bilayer for high-performance inverted perovskite solar cells. *Advanced Materials Interfaces* 4 (6): 1600948.

117 Jiang, L.-L., Cong, S., Lou, Y.-H. et al. (2016). Interface engineering toward enhanced efficiency of planar perovskite solar cells. *Journal of Materials Chemistry A* 4 (1): 217–222.

118 Agresti, A., Pazniak, A., Pescetelli, S. et al. (2019). Titanium-carbide MXenes for work function and interface engineering in perovskite solar cells. *Nature Materials* 18 (11): 1228–1234.

119 Ogomi, Y., Morita, A., Tsukamoto, S. et al. (2014). All-solid perovskite solar cells with HOCO-R-NH$_3^+$I$^-$ anchor-group inserted between porous titania and perovskite. *Journal of Physical Chemistry C* 118 (30): 16651–16659.

120 Peng, J., Wu, Y., Ye, W. et al. (2017). Interface passivation using ultrathin polymer–fullerene films for high-efficiency perovskite solar cells with negligible hysteresis. *Energy & Environmental Science* 10 (8): 1792–1800.

121 Tan, H., Jain, A., Voznyy, O. et al. (2017). Efficient and stable solution-processed planar perovskite solar cells via contact passivation. *Science* 355 (6326): 722–726.

122 Liu, L., Mei, A., Liu, T. et al. (2015). Fully printable mesoscopic perovskite solar cells with organic silane self-assembled monolayer. *Journal of the American Chemical Society* 137 (5): 1790–1793.

123 Zhao, J., Zhang, Y., Zhang, Q. et al. (2020). Efficient bifacial passivation enables printable mesoscopic perovskite solar cells with improved photovoltage and fill factor. *Solar RRL* 4 (11): 2000288.

124 Xiong, Y., Zhu, X., Mei, A. et al. (2018). Bifunctional Al_2O_3 interlayer leads to enhanced open-circuit voltage for hole-conductor-free carbon-based perovskite solar cells. *Solar RRL* 2 (5): 1800002.

125 Wang, Q., Liu, S., Ming, Y. et al. (2018). Improvements in printable mesoscopic perovskite solar cells via thinner spacer layers. *Sustainable Energy & Fuels* 2 (11): 2412–2418.

126 Tian, C., Zhang, S., Li, S. et al. (2018). A C60 modification layer using a scalable deposition technology for efficient printable mesoscopic perovskite solar cells. *Solar RRL* 2 (10): 1800174.

127 Wu, J., Zhang, W., Wang, Q. et al. (2020). A favored crystal orientation for efficient printable mesoscopic perovskite solar cells. *Journal of Materials Chemistry A* 8 (22): 11148–11154.

128 Li, D., Tong, C., Ji, W. et al. (2019). Vanadium oxide post-treatment for enhanced photovoltage of printable perovskite solar cells. *ACS Sustainable Chemistry & Engineering* 7 (2): 2619–2625.

129 Tian, C., Mei, A., Zhang, S. et al. (2018). Oxygen management in carbon electrode for high-performance printable perovskite solar cells. *Nano Energy* 53: 160–167.

130 Duan, M., Tian, C., Hu, Y. et al. (2017). Boron-doped graphite for high work function carbon electrode in printable hole-conductor-free mesoscopic perovskite solar cells. *ACS Applied Materials & Interfaces* 9 (37): 31721–31727.

131 Chen, X., Xia, Y., Huang, Q. et al. (2021). Tailoring the dimensionality of hybrid perovskites in mesoporous carbon electrodes for type-II band alignment and enhanced performance of printable hole-conductor-free perovskite solar cells. *Advanced Energy Materials* 11 (18): 2100292.

132 Xia, Y., Chen, X., Zheng, Z. et al. (2022). Interfacial energy band alignment enables the reduction of potential loss for hole-conductor-free printable mesoscopic perovskite solar cells. *Journal of Physical Chemistry Letters.* 13 (9): 2144–2149.

133 Du, J., Qiu, C., Li, S. et al. (2022). Minimizing the voltage loss in hole-conductor-free printable mesoscopic perovskite solar cells. *Advanced Energy Materials* 12 (1): 2102229.

8
Stability Issues and Solutions for Perovskite Solar Cells

Deyi Zhang, Anyi Mei, and Hongwei Han
Wuhan National Laboratory for Optoelectronics,
Huazhong University of Science and Technology, 1037
Luoyu Road, Wuhan, 430074, P.R. China

The levelized cost of energy (LCOE) for generating electricity by solar cells is determined by both the total life cycle cost and the total lifetime energy production [1, 2]. To realize low-cost photovoltaic technology, in addition to reducing the fabrication cost and improving the power conversion efficiency (PCE) of perovskite solar cells (PSCs), ensuring long-term duration is also very important. When PSCs were fabricated for the first time in 2009, they just survived for minutes [3]. Since then, various attempts have been made to study and improve the stability, and thousands of hours' lifetime has been widely obtained for PSCs now [4–8]. According to the current research, the stability of PSCs is influenced by various factors. Those factors could be summarized as chemical species including moisture and oxygen in the ambient conditions, illumination of sunlight, heat induced by light soaking, and electric field generated in the devices under light soaking. Those factors act on the functional layers including the electron transport layer (ETL), the halide perovskite light absorbing layer, the hole transport layer (HTL), the back electrode, and the interfaces between functional layers, leading to the degeneration of these layers and the performance decay of PSCs. Different functional layers and different functional materials are sensitive to different

factors. Some functional layers could also react with each other.

To achieve long-term stability of PSCs, one strategy is to block those adverse factors away from the devices. A typical method for this is encapsulation, which prevents the diffusion of moisture and oxygen into PSCs. However, some factors cannot be blocked. For example, light soaking is the basic requirement for the operation of solar cells and electric field is always generated in the device under working conditions. Therefore, constructing a tough PSC with tough and compatible materials and interfaces against those stimulations is the fundamental research direction for stable PSCs. In addition, the device configurations also influence the stability of PSCs. In this chapter, we discussed the stability concerns for each functional layer of PSCs and summarized those strategies for solving them.

8.1 Substrate

The substrates for conventional PSCs are commonly glass coated with transparent conductive oxides (TCO) such as fluorine-doped tin oxides (FTO) and indium tin oxides (ITO). For flexible PSCs, the glass is replaced with transparent polymers, such as polyethylene terephthalate (PET), to guarantee the flexibility and bending stability. The glass or polymers must endow PSCs with the mechanical strength against the mechanical shock, which can be caused in the transport and working conditions [4]. The breakdown of substrate would lead to rapid failure. Commercial TCO glass has been widely adopted in commercial thin film solar cells. Therefore, the mechanical strength of the substrate for PSCs can be well guaranteed. Except for the glass, the conductive layer must be stable for long-term applications. Meanwhile, perovskites are sensitive to some compounds including metal oxides.

Therefore, the conductive layer on the glass should be chemically inert and do not react with perovskites. Till now, FTO and ITO exhibit good compatibility with perovskites and do not cause obvious stability issues.

8.2 Electron Transport Layer

As introduced in the previous chapters, the electron transport materials (s) for PSCs are mainly n-type metal oxides such as TiO_2, ZnO, and SnO_2 that are inherited from the dye-sensitized solar cells and organic semiconductors, such as [6,6]-phenyl-C_{61}-butyric acid methyl ester (PCBM), which are inherited from the organic solar cells [9]. The surface defects on metal oxides cause the performance degradation of PSCs. Generally, the n-type property of metal oxides is induced by the oxygen vacancies (OVs), which are also located on the surface of the ETL [10]. Those surface OVs could be passivated spontaneously by oxygens in the ambient condition via physical adsorption during the fabrication of PSCs and do not cause serious adverse effects to the device performance for fresh cells. When the device is light-soaked continuously, photogenerated holes in TiO_2 react with the oxygen radicals, leading to the desorption of molecular oxygen and formation of positive charged OVs, which then serves as non-radiative recombination centers at the ETL/light absorber interface and degrades device performance [11, 12]. Meanwhile, the incomplete coordination of surface atoms would also lead to the existence of hydroxyl groups, which would react with halide perovskites such as by proton-transfer reactions and cause degradation [12, 13]. Surface modification is an effective strategy for solving the stability issue caused by the surface defects (Figure 8.1b), and Cl-terminated metal oxides reduced surface defects and helped realize enhanced stability [16]. Developing

suitable ETMs is also helpful [9]. SnO_2 was found to be a potential ETM for PSCs and widely adopted for efficient devices [17, 18]. Although SnO_2 was reported to be more stable than commonly used TiO_2 under light soaking, proper surface modification was generally developed and adopted for more efficient and stable devices [19]. Various chemicals including salts such as KCl, bases such as KOH, organic molecules such as ethylenediamine tetraacetic acid (EDTA), and polymers such as polyacrylic acid and polymethyl methacrylate (PMMA) have been applied as surface modulators for metal oxides to obtain stable PSCs (Figure 8.1a) [20]. Metal oxide ETMs with reduced intrinsic surface defects are also potential choices for stable PSCs. van der Waals materials have self-terminated crystal planes with reduced dangling bonds. Mixed valence tin oxides were noticed and developed as stable ETMs for PSCs (Figure 8.1c) [15]. Those special tin oxides are composed of Sn^{4+} and Sn^{2+}, and their crystal structure is a little bit such as 2.5D halide perovskites, making them two-dimensional materials. The mainly exposed crystal planes are terminated with Sn^{2+}, which are fully coordinated with no dangling bonds. The special structure and chemical components make mixed valence tin oxides of Sn_2O_3 and Sn_3O_4 well-performed and stable ETLs for PSCs. From this point of view, more materials with similar characteristics can be developed for stable PSCs. For organic ETLs, fullerene and its derivatives such as PCBM are the most widely adopted. They can be adopted alone or deposited on the metal oxide ETLs for interface passivation [21, 22]. It is not yet clear whether inorganic ETL or organic ETL is more tough for long-term lifespan and should be further clarified in the future, while organic ETLs are not suitable for p-MPSCs since it is challenging for them to tolerate high-temperature annealing.
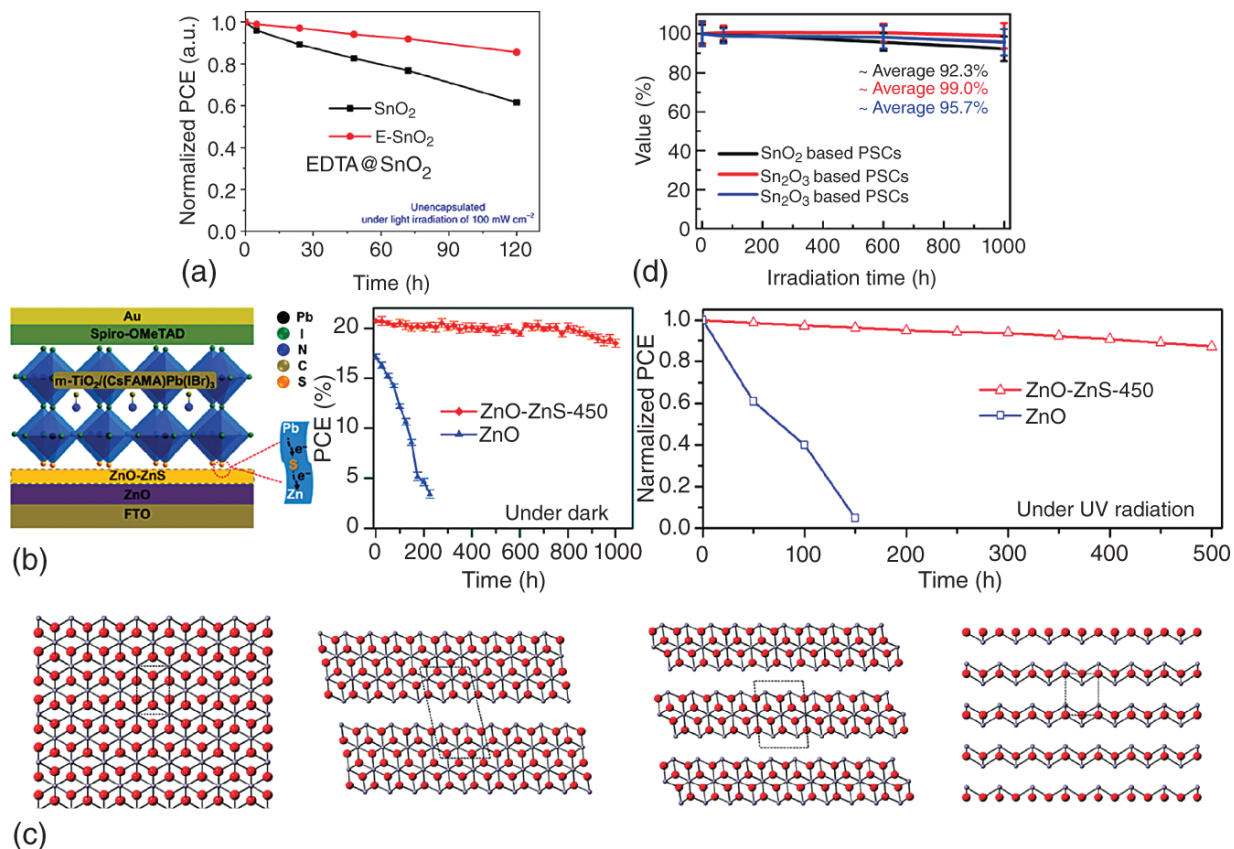
Figure 8.1 Stability concerns and solutions related to the ETL in PSCs. (a) Treating the surface of the SnO_2 ETL with EDTA enhanced the device stability. Source: Yang et al. [14]/Springer Nature/CC BY-4.0. (b) Sulfidation of the surface of the ZnO layer suppressed the adverse effect and enhanced device stability. The storage stability and the UV radiation stability of ZnO_2-based PSCs were significantly enhanced by the surface ZnS. Source: Reproduced with permission from Chen et al. [12]. Copyright 2018 American Chemical Society. (c) van der Waals mixed valence tin oxides of Sn_2O_3 and Sn_3O_4 possessed fewer intrinsic surface defects and brought enhanced interface stability under UV soaking. Source: Reproduced with permission from Li et al. [15]. Copyright 2020 American Chemical Society.

8.3 Hole Transport Layer

The degradation of HTL during the working period also brings stability issues. The popular organic HTL of Spiro-OMeTAD, which helps realize the highest reported PCE of 25.5% for PSCs, is not so tough under working conditions [23–25]. On one hand, Spiro-OMeTAD would undergo the morphology change due to crystallization or outgassing and creates pathways for the interaction of the back electrode and the perovskite, leading to performance decay (Figure 8.2a) [23–25]. Meanwhile, some studies found that migrated I^- from perovskite could reduce the oxidized Spiro-OMeTAD, which weakens the hole extraction ability of the HTL and reduces the device performance [27]. In addition, Li ions from the Li-TFSI salt additive, which is commonly required for organic HTL could migrate in the device and adsorb moisture, degrading the device's performance (Figure 8.2b) [26, 28]. Dopant-free HTLs or replacing Li-TFSI with other less-movable chemicals contributed to the stability enhancement of PSCs [29, 30]. Fluorinating Spiro-OMeTAD effectively enhanced the device stability along with improved PCE [31]. The replacement of polymer HTLs such as poly [bis(4-phenyl) (2,4,6-trimethylphenyl)amine] (PTAA) and poly-TPD [7, 23] or inorganic HTLs such as NiO and CuSCN have also demonstrated well-enhanced long-term stability [32, 33]. The device configuration of hole-conductor-free p-MPSCs completely removes the instability concerns induced by the HTL [34, 35].

8.4 Back Electrode

The back electrode for efficient PSCs including the metals of gold (Au), silver (Ag), and aluminum (Al) is another important component of PSCs and brings stability concerns

[36–38]. Although the metal electrode is separated from the perovskite layer by the charge transporting layer, Au or Ag atoms could diffuse in the popular Spiro-OMeTAD HTL and the popular [6,6]-phenyl-C_{61}-butyric acid methyl ester (PCBM) ETL (Figure 8.3) [36, 42]. Au was found to diffuse across the Spiro-OMeTAD HTL into the perovskite layer and accumulated close to the ETL, which leads to serious non-radiative recombination and irreversible performance degradation of PSCs [36]. Systematically evaluation of metal diffusion in PSCs based on first-principles calculations suggests that when a metal atom enters perovskite such as through the cracks or pinholes, it most likely diffuses through interstitial sites and may react with halide perovskites [39]. It is reported that Al can react with $MAPbI_3$, $CsPbI_3$, and $CsPbBr_3$ through redox reactions and Pb^0 can be formed as a result, leading to the degradation (Figure 8.2a) [38]. The reaction between silver and methyl ammonium lead perovskite has also been reported [37]. Although the gold electrode seems chemically inert, iodine/iodide could be utilized in microelectronics processing for gold etching [43].

The metal diffusion is influenced by their ion formation energy in perovskite. The calculated formation energies for those interstitial metal impurities are mostly low below 1 eV (Figure 8.3a). Ag_i^+ and Au_i^+ possess low diffusion barrier energy of about 0.27–0.42 eV and could diffuse at room temperature [39]. The formation energy for the metal impurities in perovskite is related to their charge state and a higher charge state tends to have a higher formation energy. Preparing a less-mobile chromium (Cr) layer below the Au electrode has been demonstrated to improve the stability of PSCs [36]. Bismuth (Bi) is also less mobile and works stably as the back electrode for PSCs (Figure 8.3b) [40]. The other chemically inert layer composed of metal

oxides including ZnO, ITO, and cerium oxide or carbon materials including graphene and its derivatives can also be prepared below the metal electrode to prevent the metal atom diffusion (Figure 8.3d) [33, 41, 42, 44].

(a)

HL38 w/ additives (LiTFSI and tBP)

Dashed lines: Fresh, 0 h
Solid lines: Aged, 1000 h at 85 °C

Cs^+
Pb^+
Li^+
Sn^+
Au^+

Intensity

Sputter time (S)

Spiro w/ additives (LiTFSI and tBP)

Perovskite

Intensity

Sputter time (S)

PCE(%)

HL38

spiro-MeOTAD

at 85 °C

Time (h)

(b)
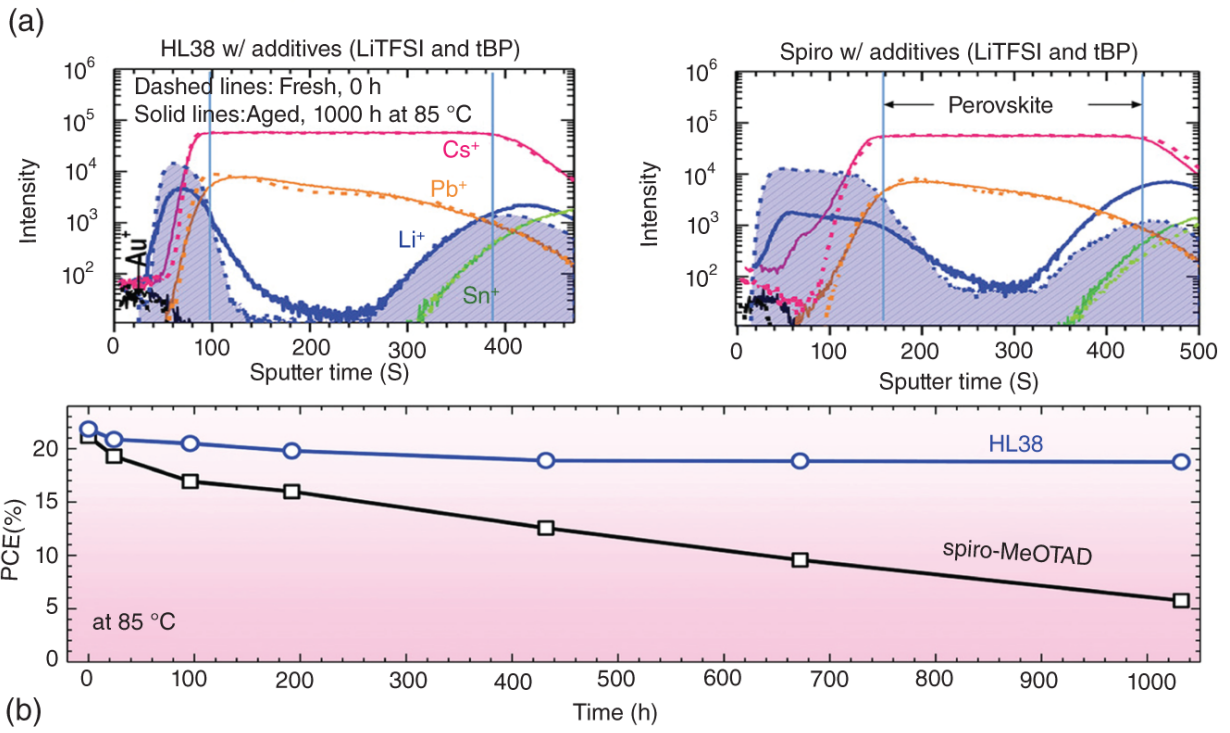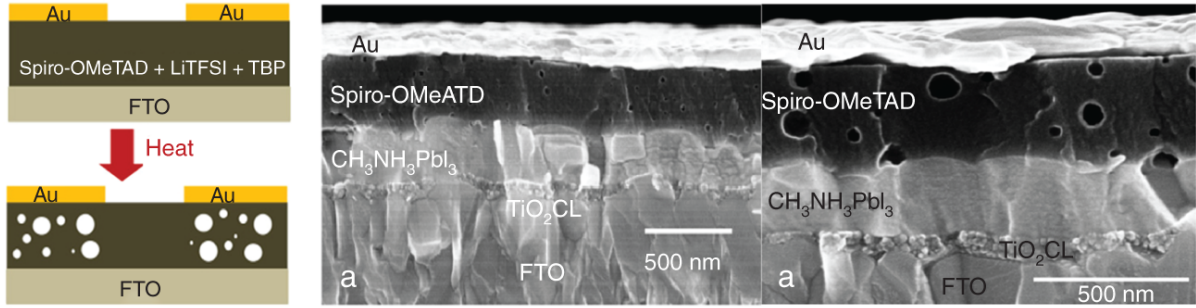
Figure 8.2 Stability concerns and solutions related to the HTL in PSCs. (a) Heat under working conditions made Spiro-OMeTAD undergo morphology change by forming voids. Source: Jena et al. [25], Reproduced with permission from American Chemical Society. (b) Li ions from the Li-TFSI dopant for Spiro-OMeTAD could migrate into halide perovskite in PSCs. The D–π–A–π–D hole transporter (HL38) based on thieno[3,4-c]pyrrole-4,6-dione (acceptor) and triphenylamine (donor) linked by thieno[3,2-b]thiophene as π-linker exhibited better chemical interaction between the Li ion by its carbonyl group together with the thiophene. PSCs with HL38 exhibited a much smaller portion of diffused Li ions and much-enhanced stability under aging at 85 °C for 1032 hours. Source: Reproduced with permission from Kim et al. [26]. Copyright 2021 Wiley.

Developing chemically inert back electrodes can also solve the above stability issues [45]. Conductive compounds including metal oxides such as ITO could also work as the stable back electrode for PSCs [43,46–48]. Carbon materials including graphite, carbon black, carbon nanotubes, and graphene are very promising electrode materials for PSCs [49, 50]. They do not react with halide perovskites and carbon atoms inside are immovable. The greatest challenge for carbon electrodes is that if they are deposited onto the top of perovskite films, it is difficult for them to form a tightly contacted interface due to the large size and rigidity of carbon particles, which is adverse to the stability and efficiency of PSCs [51–53]. p-MPSCs in which the porous carbon electrode is prepared before the filling of perovskite solved this concern [34, 35]. With this strategy, the perovskite grows on the surface of the carbon materials sufficiently with their oxygen-containing groups, resulting in well contacted interface and encouraging operational stability [5, 35, 54].

(a)

(b) Au⁻, 70 °C Au⁻, control I⁻, control Spiro + Au Spiro/Al₂O₃ + Au Spiro + Cr/Au

(c) Air Ag compact-B PCBM/BCP PVK NiMgLiO FTO Glass H₂O O₂ MA HI MAI

(d) Evap PCBM ITO on top and edge Top ITO SnOx Spun PCBM MAPbI₃ NiOx Bottom ITO 500 nm
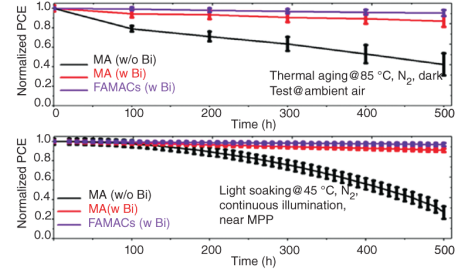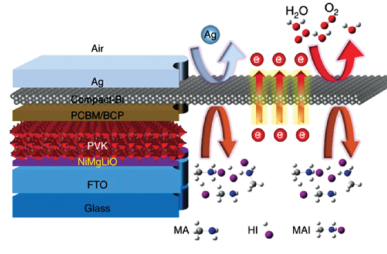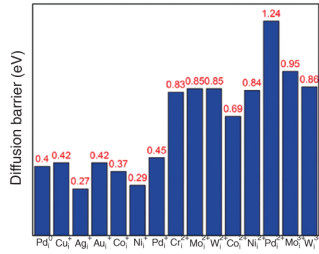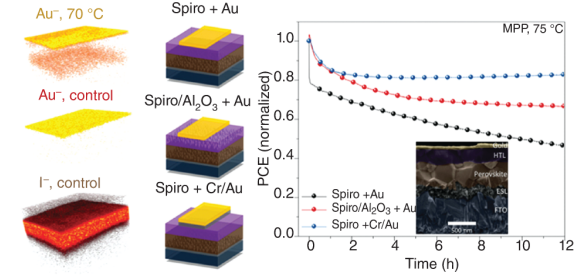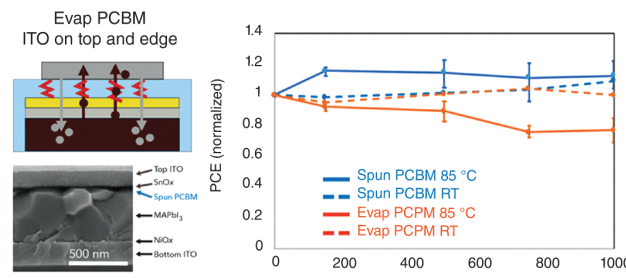
Figure 8.3 Stability concerns and solutions related to the back electrode in PSCs. (a) Metal atoms have low calculated diffusion barrier energies in halide perovskites. Source: Ming et al. [39]/John Wiley & Sons/CC BY-4.0. (b) TOF-SIMS measurement demonstrated the diffusion of gold atoms from the back electrode to the perovskite layer. Constructing a diffusion block layer composed of Al_2O_3 or less movable Cr below Au slowed down the diffusion and improved the device stability. Source: Domanski et al. [36], Reproduced with permission from American Chemical Society. (c) Bismuth was found to be chemical inert and the bismuth film acted well as a permeation barrier for atoms from the back electrode to the perovskite layer. The resulted inverted PSCs exhibited obviously enhanced thermal stability with 95% maintained initial PCE after aging at 85 °C for 500 hours and operational stability with 97% maintained initial PCE after aging under MPP at 45 °C for 500 hours. Source: Wu et al. [40]/Springer Nature/CC BY-4.0. (d) ITO barrier layer was designed to prevent the diffusion of metal atoms. It is found that the side edge of the perovskite film should also be considered when building the barrier layer. The designed inverted PSCs exhibited high tolerance against heat at 85 °C. Source: Boyd et al. [41], Reproduced with permission from American Chemical Society.

8.5 Encapsulant

Encapsulation, which isolates oxygen and moisture away from touching those functional layers in solar cells, is indispensable to guaranteeing long-term outdoor operational stability of PSCs [55]. An encapsulant layer such as composed of polymers or inorganic compounds including Al_2O_3 or MgF_2 can be prepared on top of PSCs to realize simple encapsulation (Figure 8.4a). To ensure

mechanical reliability and reliable long-term atmosphere resistance, a piece of glass or waterproof membrane can also be applied as the back cover for encapsulation. In this case, the back cover and the device are stuck together by the other encapsulant, mostly polymers, at the whole interface or at the edge of the interface between the two species (Figure 8.4b,c). When encapsulant is only at the edge, the existing chamber between the device and the back cover would trigger the fracture of the related glass and lead to poor mechanical stability. In addition, the encapsulation structure also influences the stability of perovskite, which will be discussed in the following section. Therefore, in typical application scenarios, both the whole interface and the edge are sealed (Figure 8.4c). The commonly used encapsulant polymers for the whole interface are hot melt adhesives including encapsulants (e.g. polyurethane [PU], polyolefin [POE], ethylene vinyl acetate [EVA], etc.), which can be processed for encapsulation via hot-pressing [56, 57]. Light-curable glue can also be adopted [58, 59]. The commonly used edge seal encapsulant is butyl rubber, epoxy resin, which is used to delay the moisture ingress. To avoid instability caused by the encapsulant, the applied encapsulant should be stable and will not react with halide perovskite [60]. A triple mesoscopic triple-mesoscopic PSC module encapsulated with PU maintained 97.52% of the initial PCE after 2136 hours under outdoor conditions and operated stably at maximum power point for more than 9000 hours at 55 ± 5 °C [61, 62].
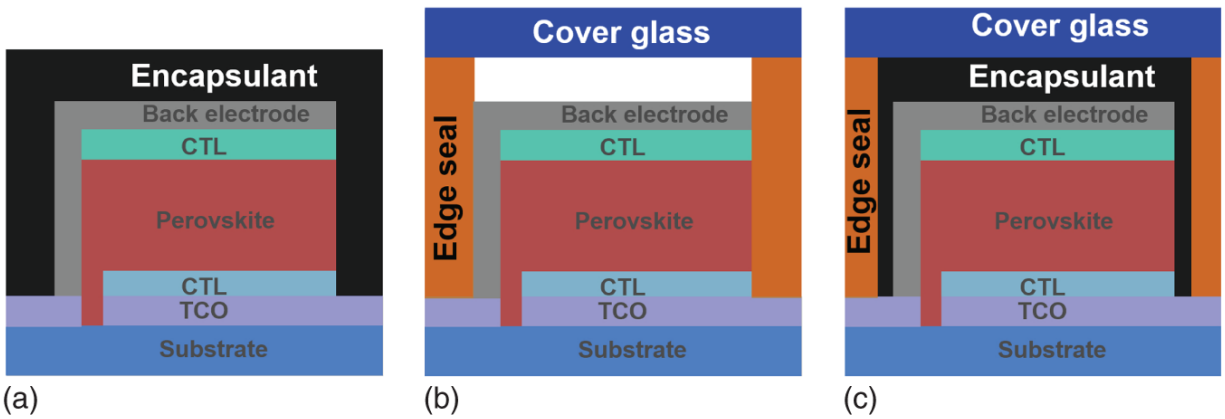
Figure 8.4 **Encapsulations for PSCs**. (a) Cover glass-free encapsulation by covering PSCs with encapsulant such as polymers or compact inorganic compound films. (b) Edge seal of PSCs with a piece of cover glass. (c) Edge and blanket encapsulation of PSCs with a piece of cover glass.

8.6 Halide Perovskite Light Absorbing Layer

Halide perovskite is the key component for PSCs and exhibited various stability issues. ABX_3 is the basic chemical formula for halide perovskites, which has been discussed in previous chapters. From the perspective of A cation, halide perovskites can be divided as the MA-based one, the FA-based one, the Cs-based one, and the mixed-cation one. From the perspective of B cation, halide perovskites can be divided into the Pb-based one, the Sn-based one, and the mixed Pb/Sn one. From the perspective of X anion, halide perovskites can be divided into the I-based one, the Br-based one, the Cl-based one, and the mixed-halide one.

8.6.1 Thermal Stability

Organic–inorganic hybrid halide perovskites including MA-based and FA-based ones face the thermal stability issue

[63]. From the thermogravimetric analysis, hybrid halide perovskites exhibited a high decomposition temperature of over 250 °C [64]. This temperature is much higher than the required 85 °C for terrestrial photovoltaic panels. However, decomposition of halide perovskites at 85 °C due to the volatilization and loss of organic species in the open space was reported [63]. The loss of organic salts from hybrid perovskites could happen in different pathways, which are determined by the components and heating temperature as reported. MAI or MABr could transform into NH_3 and CH_3I or CH_3Br under heating (Eqs. (8.1) and (8.3)), which is irreversible and detrimental [65, 66]. MAI or MABr could also undergo the reversible decomposition to MA and HI or HBr (Eqs. (8.4a) and (8.4b)). However, the decomposition products of MA and HI or HBr could undergo secondary reactions to form NH_3 and CH_3I or CH_3Br. FAI could transform into HCN, NH_3, and HI under heating (Eq. (8.2)). FAI could also transform into *sym*-triazine ($H_3C_3N_3$) together with NH_3 and HI (Eq. (8.7)). For mixed-cation perovskites, the formed HCN from FAX and formed CH_3X from MAX where X means halogen ions could further react with each other to generate CH_3CN and HX (Eq. (8.6)).

$$CH_3NH_3I(s) \xrightarrow{\Delta} CH_3I(g) + NH_3(g) \tag{8.1}$$

$$HC(NH_2)_2I(s) \xleftrightarrow{\Delta} HCN(g) + NH_3(g) + HI(g) \tag{8.2}$$

$$CH_3NH_3Br(s) \xrightarrow{\Delta} CH_3Br(g) + NH_3(g) \tag{8.3}$$

$$CH_3NH_3I(s) \xleftrightarrow{\Delta} CH_3NH_2(g) + HI(g) \tag{8.4a}$$

$$CH_3NH_3Br(s) \xleftrightarrow{\Delta} CH_3NH_2(g) + HBr(g) \qquad (8.4b)$$

$$(8.5)$$
$$CH_3NH_2(g)[Eq.(8.4b)] + HI(g)[Eq.(8.2)] \xrightarrow{\Delta} CH_3I(g) + NH_3(g)$$

$$HCN(g)[Eq.(8.2)] + CH_3X(g)[Eqs.(8.1), (8.3), or (8.5)] \qquad (8.6)$$
$$\longrightarrow CH_3CN(g) + HX(g), X = I \text{ or } Br$$

$$3HC(NH_2)_2I(s) \xrightarrow{\Delta} H_3C_3N_3(g) + 3NH_3(g) + 3HI(g) \qquad (8.7)$$
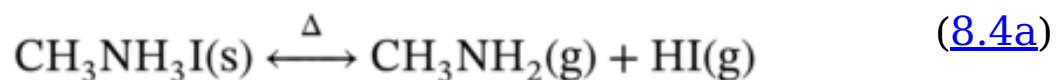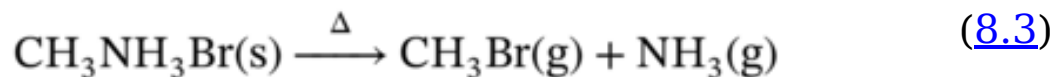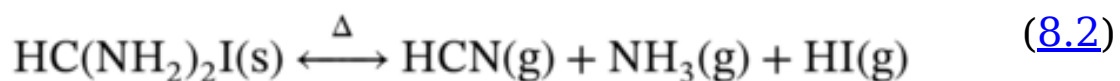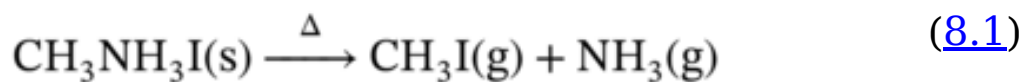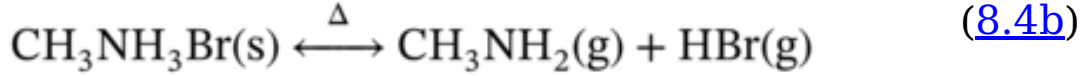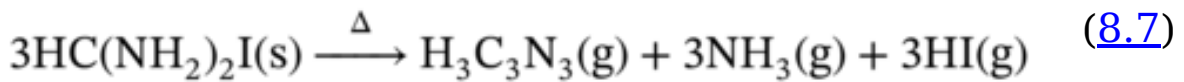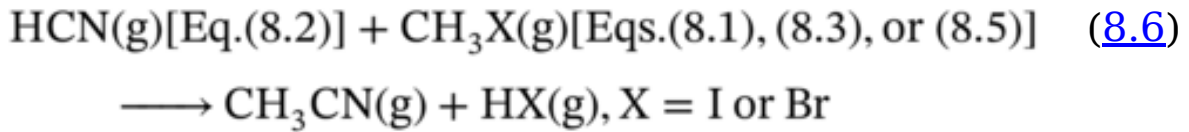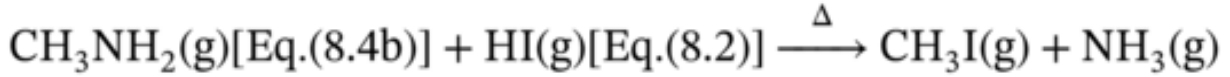
As described above, all the decomposition pathways induce the formation of gas products. When the release of the gas is blocked, the decomposition reaction tends to reach equilibrium before significant damage occurs to the perovskites. Therefore, constructing a pressure-tight environment could effectively suppress the decomposition of hybrid halide perovskites even when the decomposition pathway is not fully reversible. It has been found that the loss of MAI and formation of PbI_2 were inhibited when heating $MAPbI_3$ powders at 270 °C in a confined rather than in an open space [62]. Encapsulating perovskite solar cells with a piece of back cover glass and filling the space between the substrate and the back cover with the polymer of polyolefin (PO) or polyisobutylene (PIB) made MA-containing halide perovskite solar cells survive more than 1800 hours of Damp Heat test and 75 cycles of Humidity Freeze test exceeding the requirement of IEC61215:2016 standard [66]. Metal oxides such as the ITO were also used to form the pressure-tight coverage and inhibit the thermal decomposition of halide perovskites in a similar manner. In addition, the escape of MAI mainly starts with the grain boundaries and surfaces of halide perovskite films. Introducing excess chemicals such as the 5-

ammoniumvaleric acid hydroiodide (5-AVAI) that interact with perovskites at these locations to enhance the grain boundaries and surfaces were also found to reduce the loss of MAI and improve the stability [62]. From this point of view, atomic-level encapsulation can also be further developed to guarantee the thermal stability of halide perovskites.

8.6.2 Phase Stability

For chemicals with the formula of ABX_3, they do not always adopt the perovskite structure, which depends on the size and interaction of the ions as previously discussed. Goldschmidt tolerance factor (t) is generally used to evaluate whether the chemicals are preferentially formed in the perovskite structure or not. A suitable t for the perovskite phase is between 0.8 and 1.0, while the t for $CsPbI_3$ is 0.78, and the t for $FAPbI_3$ is 0.99 [67]. The near lower critical point t value of $CsPbI_3$ and the near upper critical point t value of $FAPbI_3$ make them tend to undergo a phase change from the black perovskite phase to the yellow non-perovskite phase at room temperature. Mixed-cation and mixed-anion strategies through partially substituting FA^+ with MA^+ and Cs^+ or partially substituting I^- with Br^- are the most widely demonstrated approaches for stabilizing the perovskite phase via amending the effective tolerance factor [68, 69]. In addition, rubidium (Rb) cations were also incorporated to promote the transition from yellow phase to black phase [67]. Although $FAPbI_3$ and $CsPbI_3$ can be stabilized as their perovskite phase via mixed-cation and mixed-anion strategies, they would undergo phase segregation under illumination due to the light-activated ion migration [70]. Some studies found that the phase segregation was triggered due to the inhomogeneous distribution of mixed species when

preparing the films due to their inhomogeneous distribution in the precursor. When the precursor was homogeneous, the phase segregation could be well suppressed. Some studies found that a properly optimized component can relieve the phase separation issue and ensure good stability.

The perovskite phase of $FAPbI_3$ or $CsPbI_3$ at room temperature can also be stabilized by additives [71]. Dimethylammonium iodide (DMAI), which can be obtained by adding hydroiodic acid (HI) into the precursor with DMF solvent, was found to stabilize both FA and Cs perovskites. Other long-chain alkyl or aromatic ammonium cations such as phenylethylammonium with size exceeding the tolerance of A site also stabilize the perovskite phase by decreasing the surface energy [72, 73]. In fact, surface energy can also be adjusted to stabilize the perovskite phase by changing the particle size such as making them as quantum dots [74, 75]. Similarly, strain, which affects localized energy distribution, was also applied to stabilize $CsPbI_3$ [76].

8.6.3 Ambient Stability

When halide perovskites are exposed to the ambient conditions, the chemicals, mainly including the moisture and oxygen in the air, can interact with halide perovskites and lead to the degradation [77]. Detailed studies demonstrated that moisture can induce reversible and irreversible changes of $MAPbI_3$ by forming hydrates and PbI_2 [78]. Hydrates of $MAPbI_3$ mainly include monohydrate of $MAPbI_3 \cdot H_2O$ and dihydrate of $MAPbI_3 \cdot 2H_2O$. $MAPbI_3 \cdot H_2O$ is constructed by one-dimensional isolated double PbI_3^- chains in which the PbI_6^{4-} octahedron is connected to two neighboring octahedra by a common corner, and H_2O molecules are inserted between the chains

via bifurcated hydrogen bonds between the H atoms of H_2O and N atoms of MA. Dihydrate of $MAPbI_3 \cdot 2H_2O$ was treated as a zero-dimensional network of isolated PbI_6^{4-} octahedra. The hydration reaction was a two-step process. When $MAPbI_3$ was exposed to airflow containing about 80% RH, monohydrate was firstly observed in the early one hour and dihydrate was observed in the next one hour. Firstly, one H_2O molecule was incorporated into one $MAPbI_3$ molecule until it was saturated. Monohydrate was metastable and could convert back to $MAPbI_3$ easily. Longer exposure led to the formation of the dihydrate, PbI_2, and release of H_2O. When exposing the hydrates to airflow with low humidity of 35% RH at 21 °C, dehydration reactions happened and the hydrates changed back to $MAPbI_3$. However, when $MAPbI_3$ was further exposed to excess moisture or liquid water, MA could be dissolved and irreversible degradation occurred. In addition, moisture also accelerates the phase instability of $FAPbI_3$ and $CsPbI_3$ from the perovskite phase to the non-perovskite phase. To improve the stability of halide perovskites against moisture, additives that could interact with halide perovskites and have the hydrophobic property were introduced to prevent the attack.

Oxygen in the ambient condition is also found to be adverse for the stability of halide perovskite by oxidizing its iodide. When perovskite was soaked under light, the electron was excited from the valence band (VB) to the conduction band (CB). The photogenerated electron in the CB could be then captured by molecular oxygen in the ambient condition and led to the formation of superoxide, which brought about deprotonation of the organic cation and formation of iodine. This adverse process is preferred to happen when the photogenerated carriers cannot be extracted immediately in PSCs. PSCs with more efficient electron extraction through mesoporous structure or well-designed charge

extraction materials possess enhanced stability. Inorganic monovalent cations such as cesium could also improve the stability. In addition, lowering the bandgap of halide perovskite to approach the ideal bandgap of 1.34 eV for the highest theoretical efficiency limit of a single-junction solar cell relies on the inclusion of divalent tin cations [79]. However, Sn^{2+} in low bandgap perovskites can be oxidized during processing, leading to restricted performance [80, 81].

For solar cells to operate over tens of years under harsh outdoor conditions, encapsulation is always essential no matter for the conventional silicon solar cells or the emerging solar cells. To obtain long-term stability of PSCs, compatible encapsulation technologies for PSCs have been developed as discussed above. Therefore, after effective encapsulation, ambient stability is well guaranteed for long-term application of PSCs.

8.6.4 Operational Stability

8.6.4.1 Degradation Pathways

In the above sections, we discussed the stability of halide perovskites in PSCs when they are even not under working conditions. When those stability concerns caused by intrinsic factors and extrinsic factors are well resolved, the remaining concern for PSCs is more and more related to the operating stability. In this section, the operating stability of PSCs, which is the combined results of light, heat, bias, and those functional materials mainly halide perovskites here in the devices, is discussed. The direct stress for operating stability of PSCs is the light soaking. Different from the adverse effect of ambient chemicals, light soaking is the basic requirement for PSCs to operate and cannot be sheltered. Therefore, PSCs must face the

challenge of light soaking when all the other components in the devices are made stable.

Generally, halide salts are light sensitive and undergo photodissociation at elevated temperatures (Figure 8.5a) [82]. It has been found that PbI_2, $PbBr_2$, $PbCl_2$, and even PbF_2 decompose and become black upon exposure to daylight. Light soaking with photoenergy over bandgaps excites the electron–hole pairs in lead halides. The holes diffuse to the crystal surface and grain boundaries and are trapped by the surficial halide ions, inducing the formation of intrinsic halide atoms. Two halide atoms further form a halogen molecule and generate anion vacancies in the crystals. Lead halides are also potential anion conductors. These surface anion vacancies could diffuse into the bulk of the crystals. The anion vacancy or the Pb^{2+} in the bulk could trap photoelectrons to form Pb^+ ions and lead atoms. These lead atoms aggregate to form lead nanoparticles, which have been demonstrated inside $PbCl_2$ and $PbBr_2$ crystals after relatively short-time UV irradiation [82]. As we see, the formation of I_2 or lead clusters, which offer impurity levels, is adverse for the performance of PSCs. Therefore, when excess PbI_2 is included in the perovskite films for PSCs, it may cause stability issues. On the other hand, the residual PbI_2 in halide perovskite may also promote ion migration. Studies have reported that the existence of excess PbI_2 led to the degradation of perovskite films under illumination in N_2 while perovskite films without PbI_2 are more stable [84–87].
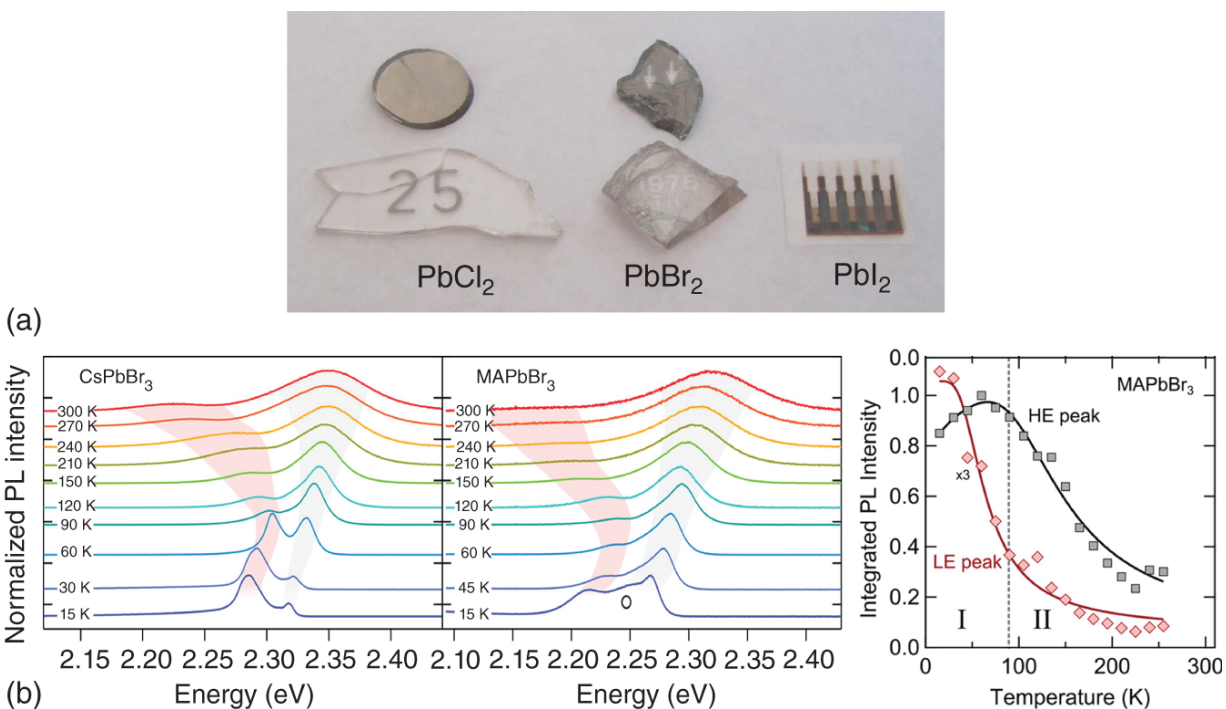
Figure 8.5 Phase stability of halide perovskites. (a) Light soaking led to the decomposition of lead halides of $PbCl_2$, $PbBr_2$, and PbI_2. Source: Schoonman et al. [82], Reproduced with permission from ELSEVIER. (b) Increased temperature broadened the PL peak and lowered the PL intensity of $MAPbBr_3$ single crystals. Source: Steele et al. [83]. Copyright 2019 American Chemical Society.

Halide perovskites are not as sensitive as lead halides since the photodissociation is highly correlated with the dynamic behavior of carriers. If photocarriers of electron–hole pairs recombine with each other such as by emitting photons, the degradation process will not happen. However, if the electrons and holes are trapped by the ions in the lead halide crystals before the radiative recombination, the above-discussed photodissociation will happen. Halide perovskites have very strong fluorescence effect and photogenerated carriers tend to recombine with each other or be extracted by selective contacts rather than interact with ions in the crystals. On the other hand, iodine ions in

lead iodides and in halide perovskites have different chemical environment, which also leads to a different behavior under light soaking. Therefore, current studies have not reported rapid photodissociation of halide perovskites. However, when all the other unstable concerns are well addressed, considering that the photogenerated carriers do not always recombine with each other or be extracted completely and iodide ions do not always locate at the lattice sites where they should be, light soaking will be the key threat for long-term applications for PSCs over tens of years. Light soaking would cause the degradation of halide perovskites at a slow and complicated process, which has not been comprehensively revealed and is generally affected by the combination of light and light-induced heat and electric field in PSCs. The challenge brought by light soaking to PSCs is discussed as follows.

An intuitive phenomenon is that the photoluminescence ability of halide perovskites would decrease obviously with the increased temperature in the temperature region when there is no phase transition (Figure 8.5b) [83,88–90]. The suppressed PL could be induced by the formation of non-radiative centers or by the electron–photon coupling (e–p coupling). Considering that the defect formation process maybe not so immediate along with the temperature, the latter process is probably responsible for this. When the temperature of PSCs is heated up by sunlight in hot weather, the lattice of halide perovskites will expand due to thermal expansion. The expansion reduces the space-filling factor of the unit cell and reduces the interaction strength of ions in the unit cell. The high space-filling factor of the unit cell could release the e–p coupling and enhance the PL. [91, 92] Therefore, the reduced space-filling by heat promotes the e–p coupling and suppresses PL. If no other process happens, the temperature-induced PL decay will be reversible. However, during the long-term outdoor

applications, the suppressed PL indicates that more photogenerated carriers interact with lattice ions, which would lead to the possible formation of I_2 and Pb in perovskite films although the process is not evident at present stage and should be deeply clarified in the future. In fact, studies have found that PSCs are more stable under light soaking at lower temperature, while increased temperature led to accelerated performance decay [93, 94].

Operational conditions also cause PCE decay of PSCs by inducing ion migrations. Light and heat reduce the activation energy for ion migrations in perovskites, making the ions more movable [95]. Meanwhile, the residual stress, especially the tensile stress in the perovskite film due to the fast crystallization process, also drives ion migrations and causes performance decay [96–98]. Taking I^- as an example, when I^- moves away from the lattice sites and to the interfaces or grain boundaries, they would capture holes and convert to I_2 as the manner in PbI_2. When I^- ions move to the interstitial sites especially when the lattice is expanded, they could also interact with holes and suppress the hole transportation [99]. The retarded hole transport leads to the accumulation of holes, which would lead to the generation of I_2. Light soaking not only generates heat but also voltage. The photogenerated electric field in the devices also promotes the migration and accumulation of ions especially. Ion migration can also be accelerated by accumulated charges originated from the insufficient and imbalanced charge extraction due to the poor interface contact or restricted charge extraction ability of charge transport layers. Those accumulated ions could interact with photogenerated holes and,form I_2, resulting in irreversible migration. In fact, even the migrated ions do not interact with photogenerated carriers, they can still not return to their original sites completely. As has

demonstrated, ions such as I⁻ from halide perovskites could diffuse into and react with the adjacent charge transport layer and the back electrode, leading to the performance degradation of PSCs by degrading the perovskite layer, the charge transport layer, and the back electrode.

8.6.4.2 Heat Management

As discussed above, eliminating thermal-induced heat will benefit the stability and promote the long-term application of PSCs effectively. On one hand, the heat is induced by the below-gap absorption, which enhances the lattice vibration. The entry of below-gap photons into the device could be reduced by optical films such as coating the infrared antireflection film onto the surface of the window glass substrate. The drawback for this is that the film will bring additional cost and the transmittance of the films is not 100% for those above-bandgap photons, which would lead to PCE loss. On the other hand, the heat is also induced by the above-bandgap absorption, which transmits excessive energy to the lattice via thermal relaxation. To relieve the thermal relaxation, hot carrier solar cells (HCSCs) is a good choice. However, although the lifetime of hot carriers in perovskites is found to be long [100], HCSCs have not been well realized experimentally, and extracting carriers before their cooling is quite challenging. Multi-junction solar cells are also potential choices for relieving the thermal effect by utilizing sunlight through stacking a series of solar cells with different absorption regions as a tandem device [101]. As a result, the below-gap and above-gap energy loss is reduced, and more sunlight can be converted to electricity, leading to a high theoretical efficiency limit and reduced thermal effect. At present, the obtained PCE for the monolithic perovskite/silicon tandem solar cell is boosted to 29.8%, higher than 25.7% of single-junction PSCs. The challenge for tandem solar cells is

probably that the spectra of sunlight on earth are changing on the whole day, which makes the match of current densities in all subcells challenging. The light-induced heat may also be utilized by integrating a thermoelectric device that improves the photo-to-electricity conversion efficiency and helps reduce the device temperature [102]. In addition, PSCs could be cooled under working conditions such as by water flow, realizing combined utilization of heat and electricity.

If the temperature of PSCs is increased under working conditions, suppressing the lattice expansion of halide perovskites would also benefit the long-term stability. One demonstrated strategy for this is burying halide perovskites in the mesoscopic layer. The p-MPSCs with a carbon electrode are a good embodiment for this. In p-MPSCs, perovskite is filled inside the triple mesoscopic scaffold of the mesoporous TiO_2 layer, the mesoporous ZrO_2 layer, and the porous carbon layer. There is no individual perovskite film in the device and the thermal expansion coefficient of halide perovskites is much larger than that of the scaffold. When the temperature is increased, the expansion of halide perovskites is limited by the expansion degree of the scaffold while the latter does not expand very much in the operating temperature region of PSCs. The space-confining effect induced by the scaffold helps p-MPSCs exhibit very encouraging stability result [5, 62]. Another potential strategy for this is designing a perovskite system, which does not expand significantly in the operating temperature region of PSCs. A probable condition for this is that halide perovskites would undergo phase transition in the operating temperature region of PSCs and the phase transition would affect the expansion behavior of halide perovskites [103]. Therefore, spacing confining engineering and phase transition engineering via

compositional engineering could be adopted to relieve the lattice expansion.

8.6.4.3 Grain Boundary Modification

Grain boundaries of halide perovskite films in PSCs should be taken care of to inhibit the ion migration and formation of I^0 and Pb^0. Suppressing the formation of I^0 and Pb^0 inside the grains or along the boundaries and interfaces in PSCs under working conditions also makes sense. The formation of I^0 and Pb^0 inside the grains would be reversible if they do not move away from the lattice sites. However, the formation of I_2 at the grain boundaries or interfaces is detrimental. To avoid the formation of I_2 at the grain boundaries or interfaces, the migration of ions such as I^- inside the grains, along and to the boundaries should be suppressed. The diffusion of ions inside the grains is accelerated by thermal-induced lattice expansion and defects such as vacancies. When I^- moves away from the lattice sites, more vacancies are formed and the diffusion of I^- would be further promoted. Therefore, preparing high-quality halide perovskite films with reduced defects, enlarged grain sizes, and released stress benefits the stability of PSCs. In addition, the diffusion of I^- to the boundaries and formation of I_2 can also be prevented by grain boundary modifications. Introducing proper additives to strengthen the boundaries by forming stable contact with lead could immobilize the ions, prevent the diffusion of I^- to the boundaries and inhibit the formation of I_2 at the boundaries (Figure 8.6). When the migration of I^- to the boundaries or interface is prevented, the migration inside the grains will also be inhibited. Therefore, boundaries strengthening strategies via suitable chemicals are very important for ensuring operating stability of PSCs. Present studies have reported that converting the surface of halide

perovskite to lead oxysalt, introducing the ionic liquid 1-butyl-3-methylimidazolium (BMIMBF$_4$), 1-butyl-1-methylpiperidinium tetrafluoroborate ([BMP]$^+$[BF$_4$]$^-$ or the 5-AVAI with bifunctional groups effectively stabilized the perovskite surface and enhanced the stability of PSCs [7, 62, 106].

8.6.4.4 Interface Strengthening

Constructing tough interfaces to extract photogenerated charges sufficiently and inhibit the ion migration in and across the interface is also very important for ensuring stability of PSCs. There are multiple interfaces in solar cells and they determine the PCE and stability. The interfaces in halide perovskite solar cells are of vital importance. Interfaces bring challenges mainly from two aspects. On one hand, halide perovskite is deposited on the as-prepared charge transport layer to form the buried interface [107]. When the related charge transport layer was crystalline inorganic semiconductors, it is challenging for perovskite to build a tough interface with the substrate [108, 109], which is probably due to the surface energy difference between the two related layers, as we know, the lattice constants of both layers are commonly not matched. The insufficient contact leads to interface voids, which lead to the accumulation of charges and promote ion migration, resulting in the formation of I$_2$. It has been reported that the interface between halide perovskite and the adjacent functional layers in the planar PSC is very brittle with toughness below 1.5 J m^{-2} [109]. Irreversible morphological degradation, formation of voids, delamination, and reconstruction at this interface under working conditions due to easy-triggered ion migration, mismatched thermal expansion efficient and weak bonding was reported and led to performance decay of PSCs. The deteriorated interface further slowed down charge extraction and accelerated the

deterioration. Constructing a well contacted interface with no interfacial voids could prevent such adverse process. Replacing inorganic charge transport materials with organic ones is an available solution to build a tougher interface, but the stability of the organic charge transport layer should be evaluated meanwhile. Developing more inorganic charge transport materials with appropriate specific surface energies to match the perovskite for tougher interfaces can also be attempted. Building an interface layer such as introducing chemicals including 5-AVAI, 3-iodopropyl trimethoxysilane [$Si(OCH_3)_3(CH_2)_3I$], which have bifunctional groups for bridging the substrate and the perovskite also works [62, 109]. In addition, a coherent interface layer of $FASnCl_x$ constructed by residual chloride on the surface of SnO_2 colloids was also proposed and realized for the interface modification [110].
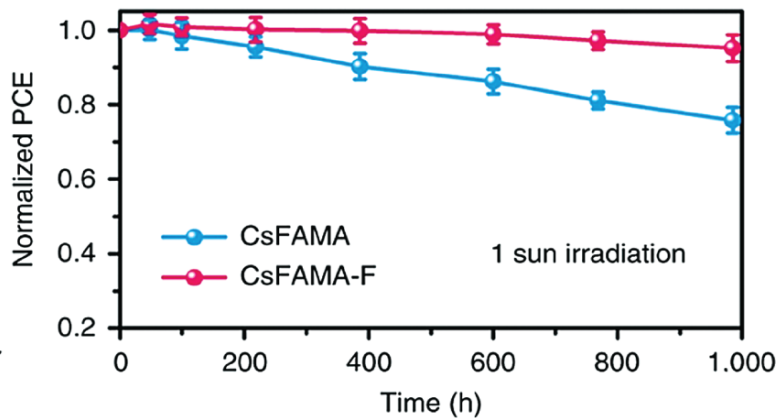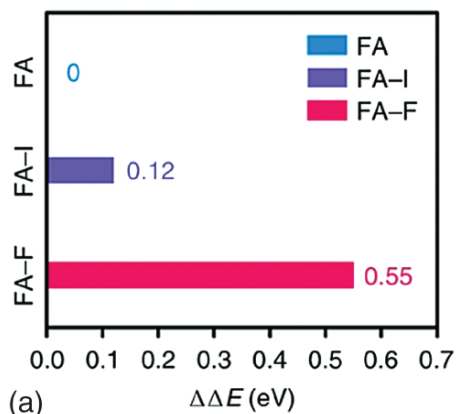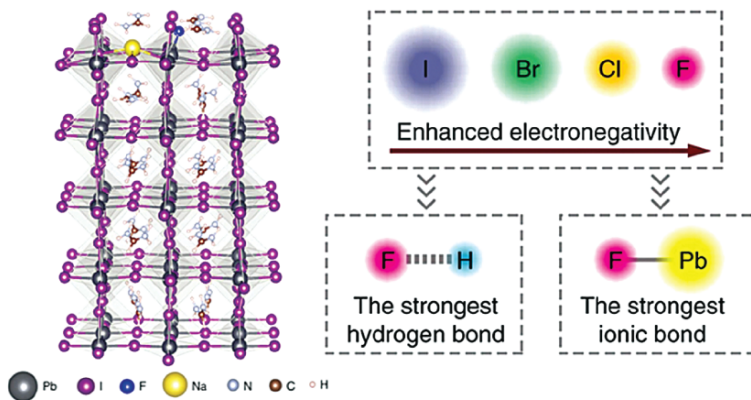
(a)
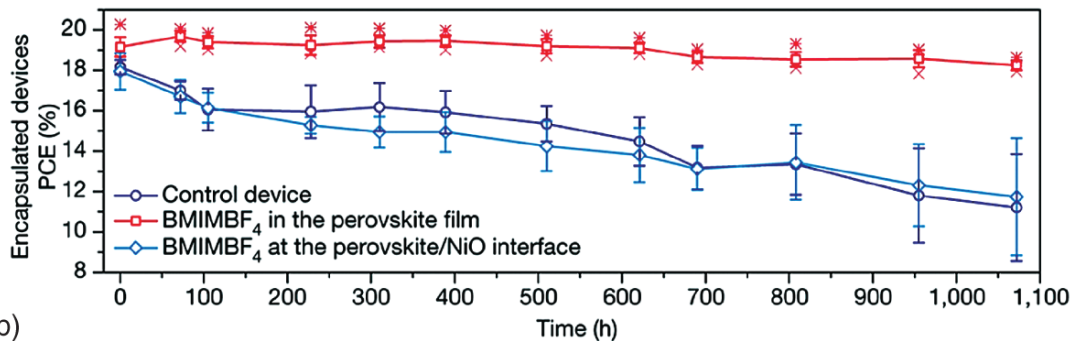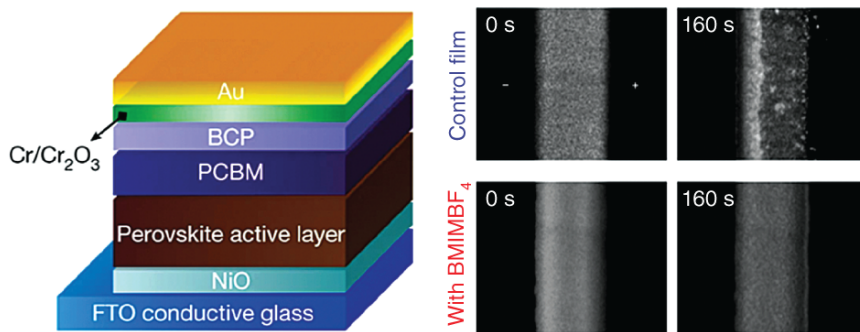
(b)

Figure 8.6 Grain boundary modification increased the stability of PSCs by inhibiting the degradation at the boundaries. (a) Immobilization of anions and cations at the grain boundaries by introducing fluorine anions into perovskite films. Fluorine anions with enhanced electronegativity could form a strong hydrogen bond with organic cations and a strong ionic bond with lead cations in halide perovskites. Calculations demonstrated that the introduction of fluorine cations increased the formation energy of the surface organic cation FA vacancy. The resulted PSCs with fluorine anions demonstrated well-improved stability under one sun irradiation. Source: Reproduced with permission from Li et al. [104]. Copyright 2019 Springer Nature. (b) Introducing the ionic liquid BMIMBF$_4$ into the halide perovskite films improved the stability of inverted PSCs by suppressing the undesired ion migration at the grain boundaries in the device. The resulted device exhibited very little degradation in the *J–V*-determined PCE, while the control device exhibited a faster degradation. Source: Bai et al. [105], Reproduced with permission from Springer Nature.

In addition to constructing a well-buried interface, the upper interface built by depositing the other charge transport layer on top of the perovskite layer should also be taken care of. Ions such as I$^-$ from halide perovskite could diffuse across the interface into the adjacent charge transport layer and further to the back electrode, leading to performance degradation by degrading the perovskite layer, the charge transport layer, and the back electrode. Replacing organic charge transport materials such as Spiro-OMeTAD that permits the penetration of ions with inorganic charge transport materials such as CuSCN in the n-i-p configuration or ZnO p-i-n configuration, which prevents the penetration of ions, enhanced the stability of PSCs [33, 111]. Constructing an interfacial layer such as by

sulfurizing the surface of perovskite film or introducing a chlorinated graphene oxide layer on top of the perovskite layer also helped solve this issue [8, 106, 112]. Device configuration could also contribute to solving this problem. In p-MPSCs, since no HTL was applied and carbon material was applied as the back electrode, the above adverse process was averted.

On the other hand, unmatched energy level alignment between halide perovskites and charge transport layers could also lead to the accumulation of charges, which promotes the ion migration in PSCs [94]. It is found that p-type metal oxides such as Ta–WO$_x$, NiO, and Sb–SnO$_x$ exhibited transient conductance and shifted work function with increased temperature. An energy barrier was then formed and slowed downhole extraction. As a result, PSCs based on those metal oxide HTL exhibited rapid PCE decay. When the HTL was replaced by a bilayer of dopant-free PDCBT and acid-doped PTAA–BCF, the hole extraction is very stable along the increased temperature and the related PSC retained almost 99% of its peak efficiency after 1450 hours of continuous operation at 65 °C in a N$_2$ atmosphere.

8.6.4.5 Defect Degeneration

When I^0 and Pb^0 are formed in PSCs, converting them back to Pb^{2+} and I$^-$ timely can also ensure the device's stability. A reported method for this is introducing a redox shuttle into the film. A typical shuttle is the Eu^{3+}–Eu^{2+} pair [113]. It is found that although the reaction between I^0 and Pb^0 could happen thermodynamically, a kinetic energy barrier existed in the reaction, which made the reaction complete. The introduced redox shuttle can effectively transfer electrons from Pb^0 to in a cyclical manner with the reduction of I^0 by Eu^{2+} and the oxidization of Pb^0 by Eu^{3+}.

As a result, the Pb^0 and I^0 were eliminated and the redox shuttle returned to its original state. When aging perovskite films under 1 sun illumination for more than 1000 hours, the $Pb^0/(Pb^0+Pb^{2+})$ ratio in the film with the redox shuttle was about 2.5%, while that in the control film was 7.4%. The introduction of Eu^{3+}–Eu^{2+} made PSCs retain 92% and 89% of the peak PCE under 1-sun continuous illumination or heating at 85 °C for 1500 hours. Gd^{3+}–Gd^{2+} could also work in a similar manner. In addition, the cheap metal element of iron was also designed to realize this [114]. Fe^{3+} is oxidative, while Fe^{2+} is reductive. The challenge is Fe^{3+} can not only oxidize Pb^0 but also oxidize I^-, which leads to the formation of I^0. Ferrocene (Fc) avoids such concern. Fc has been reported to react with I^0 to form FcI and FcI could react Pb^0 to form PbI_2 and convert back to Fc for improved stability of PSCs [114].

8.6.4.6 Reverse-bias Voltages

Compared with PSCs, perovskite solar modules (PSMs) suffer from an additional threat of the bias voltage, which would drive ion migrations as previously discussed and lead to decayed PCE [4, 115, 116]. Such adverse effects of voltage on PSMs are more significant when the cells in series or in parallel fail to work synchronously due to the performance difference or the shading effect (the hot spot effect). In photovoltaic systems, those cells or regions that fail to offer as high voltage as the parallel-connected ones or as high current density as the series-connected ones would serve as the load, generate heat and waste the electricity. The voltage together with the heat may lead to the decomposition of perovskites then. The generated heat could even melt the metal back electrode [116]. The reported breakdown voltage (V_{br}) for halide perovskites was −1 and −4 V [4]. The breakdown of halide perovskites

under voltage was reported to be triggered via tunneling first and then followed thermal runaway [117]. The voltage bias drives mobile ions from perovskite bulk to the interfaces, leading to the accumulation of holes in halide perovskites and resulting in the oxidation of iodide and creation of iodine vacancies and interstitials. The formed iodine interstitials then lead to the structural relaxations of compounds and formation of I_2. The heat induced by the bias voltage was also demonstrated in PSCs. A temperature close to 100 °C was demonstrated in PSCs under bias voltage and the active area turned yellow under high voltage. It was also found that the generation of heat was determined by the resistance in the device where the least resistance was. Single-cation and single-halide perovskite materials with no phase segregation concern, strengthened boundaries and interfaces for suppressing ion migration, nonmetal electrodes that will not react with halide perovskites and be melted by the generated heat and higher thickness of perovskites films for reduced electric field and electric potential gradients are beneficial to bias voltage stability of PSCs. The p-MPSCs have been reported to withstand reverse-bias voltages up to −9 V and surpass the IEC 61215:2016 international standard [117].

8.7 Summary

All the functional layers including ELT, HTL, the back electrode, the encapsulant, and the perovskite layer, together with those interfaces should be considered for improving the stability of PSCs. Various research has been made on these aspects and promoted the growing stability of PSCs. When the functional layers and the interfaces are well designed, encouraging stability could be obtained. For conventional PSCs, it has been demonstrated that through high throughput screening of stable perovskite

components, careful design of the ETL, the HTL, and the related interfaces, and sufficient encapsulation of the device via MgF_2, planar formal PSCs based on the mixed-cation perovskite kept 100% of their initial PCE and 99% of their peak PCE after aging at 60–65 °C under metal-halide lamps for 1400 hours. For p-MPSCs, the stability is also very encouraging. As discussed above, the special device configuration of p-MPSCs avoids the stability concern caused by the HTL and the metal back electrode. The thick and porous characteristics of p-MPSCs make perovskite more tough against ion migration induced by the electric field. Meanwhile, the introduced additive of 5-AVAI strengthened the grain boundaries of perovskite and the interfaces between perovskite and the metal oxide scaffolds. As shown in Figure 8.7, the device did not exhibit obvious degradation after 9000 hours operational tracking at MPP of 55 ± 5 °C. Studies on more detailed degradation behavior and in-depth understanding of PSCs and outdoor application demonstrations of PSMs will promote the formulation of stands for industrialization and commercialization of perovskite photovoltaics.
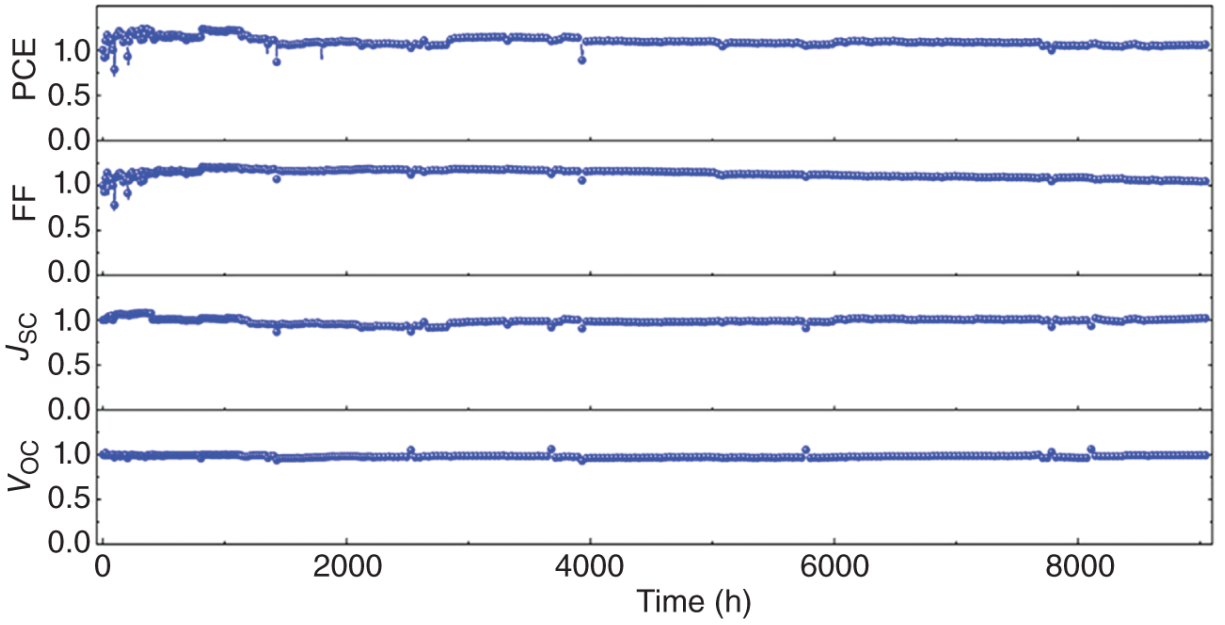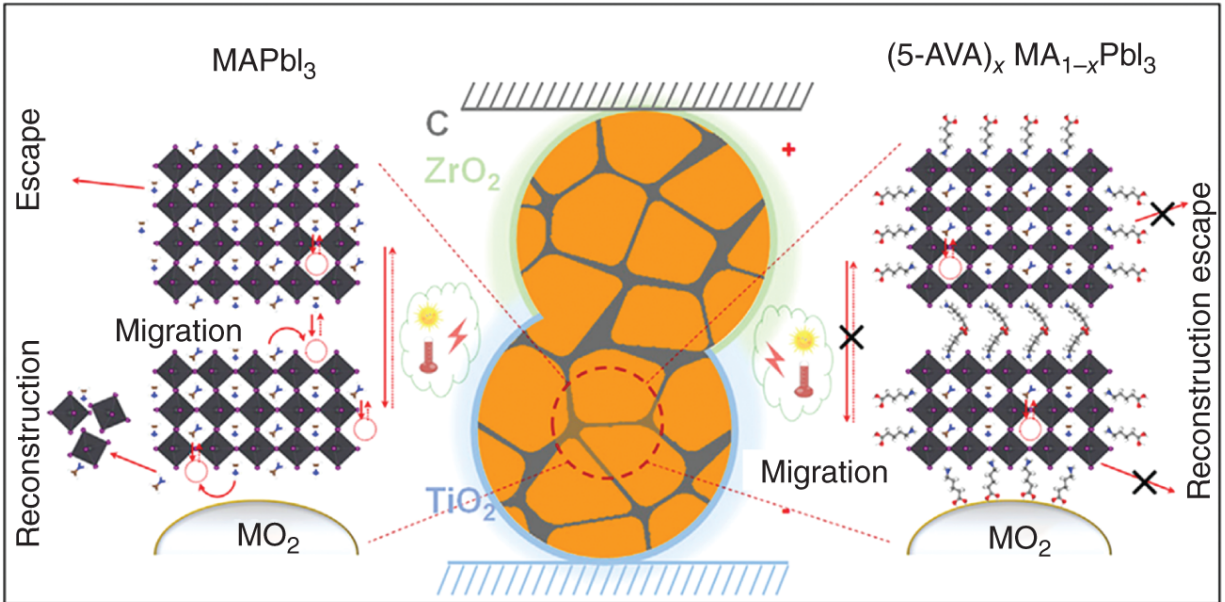
Figure 8.7 The long-term stability of p-MPSCs at MPP over 9000 hours. Source: Reproduced with permission from Fu et al. [61]/Elsevier.

References

1 Darling, S.B., You, F., Veselka, T., and Velosa, A. (2011). Assumptions and the levelized cost of energy for

photovoltaics. *Energy & Environmental Science* 4: 3133–3139.

2 Hernández-Moro, J. and Martínez-Duart, J.M. (2013). Analytical model for solar PV and CSP electricity costs: present LCOE values and their future evolution. *Renewable and Sustainable Energy Reviews* 20: 119–132.

3 Kojima, A., Teshima, K., Shirai, Y., and Miyasaka, T. (2009). Organometal halide perovskites as visible-light sensitizers for photovoltaic cells. *Journal of the American Chemical Society* 131: 6050–6051.

4 Rong, Y., Hu, Y., Mei, A. et al. (2018). Challenges for commercializing perovskite solar cells. *Science* 361: eaat8235.

5 Grancini, G., Roldán-Carmona, C., Zimmermann, I. et al. (2017). One-year stable perovskite solar cells by 2D/3D interface engineering. *Nature Communications* 8: 15684.

6 Jung, E.H., Jeon, N.J., Park, E.Y. et al. (2019). Efficient, stable and scalable perovskite solar cells using poly(3-hexylthiophene). *Nature* 567: 511–515.

7 Lin, Y.-H., Sakai, N., Da, P. et al. (2020). A piperidinium salt stabilizes efficient metal-halide perovskite solar cells. *Science* 369: 96.

8 Li, X., Zhang, W., Guo, X. et al. (2022). Constructing heterojunctions by surface sulfidation for efficient inverted perovskite solar cells. *Science* 375: 434–437.

9 Valadi, K., Gharibi, S., Taheri-Ledari, R. et al. (2021). Metal oxide electron transport materials for perovskite solar cells: a review. *Environmental Chemistry Letters* 19: 2185–2207.

10 Liu, J., Guan, Y., Liu, S. et al. (2021). Modulating oxygen vacancies in $BaSnO_3$ for printable carbon-based mesoscopic perovskite solar cells. *ACS Applied Energy Materials* 4: 11032–11040.

11 Leijtens, T., Eperon, G.E., Pathak, S. et al. (2013). Overcoming ultraviolet light instability of sensitized TiO_2 with meso-superstructured organometal tri-halide perovskite solar cells. *Nature Communications* 4: 2885.

12 Chen, R., Cao, J., Duan, Y. et al. (2018). High-efficiency, hysteresis-less, UV-stable perovskite solar cells with cascade ZnO-ZnS electron transport layer. *Journal of the American Chemical Society* 141: 541–547.

13 Yang, J., Siempelkamp, B.D., Mosconi, E. et al. (2015). Origin of the thermal instability in $CH_3NH_3PbI_3$ thin films deposited on ZnO. *Chemistry of Materials* 27: 4229–4236.

14 Yang, D., Yang, R., Wang, K. et al. (2018). High efficiency planar-type perovskite solar cells with negligible hysteresis using EDTA-complexed SnO_2. *Nature Communications* 9: 3239.

15 Li, S., Qin, F., Peng, Q. et al. (2020). van der Waals mixed valence tin oxides for perovskite solar cells as UV-stable electron transport materials. *Nano Letters* 20: 8178–8184.

16 Tan, H., Jain, A., Voznyy, O. et al. (2017). Efficient and stable solution-processed planar perovskite solar cells via contact passivation. *Science* 355: 722.

17 Ke, W., Fang, G., Liu, Q. et al. (2015). Low-temperature solution-processed tin oxide as an alternative electron transporting layer for efficient perovskite solar cells.

Journal of the American Chemical Society 137: 6730–6733.

18 Kim, M., Jeong, J., Lu, H. et al. (2022). Conformal quantum dot–SnO$_2$ layers as electron transporters for efficient perovskite solar cells. *Science* 375: 302–306.

19 Deng, K., Chen, Q., and Li, L. (2020). Modification engineering in SnO$_2$ electron transport layer toward perovskite solar cells: efficiency and stability. *Advanced Functional Materials* 30: 1–16. 2004209.

20 Uddin, A. and Yi, H. (2022). Progress and challenges of SnO$_2$ electron transport layer for perovskite solar cells: a critical review. *Solar RRL* 2100983.

21 Wang, J., Datta, K., Weijtens, C.H.L. et al. (2019). Insights into fullerene passivation of SnO$_2$ electron transport layers in perovskite solar cells. *Advanced Functional Materials* 29: 1–12. 1905883.

22 Hou, Y., Du, X., Scheiner, S. et al. (2017). A generic interface to reduce the efficiency-stability-cost gap of perovskite solar cells. *Science* 358: 1192.

23 Correa-Baena, J.-P., Saliba, M., Buonassisi, T. et al. (2017). Promises and challenges of perovskite solar cells. *Science* 358: 739.

24 Jena, A.K., Numata, Y., Ikegami, M., and Miyasaka, T. (2018). Role of spiro-OMeTAD in performance deterioration of perovskite solar cells at high temperature and reuse of the perovskite films to avoid Pb-waste. *Journal of Materials Chemistry A* 6: 2219–2230.

25 Jena, A.K., Ikegami, M., and Miyasaka, T. (2017). Severe morphological deformation of spiro-OMeTAD in $(CH_3NH_3)PbI_3$ solar cells at high temperature. *ACS Energy Letters* 2: 1760–1761.

26 Kim, S.G., Le, T.H., de Monfreid, T. et al. (2021). Capturing mobile lithium ions in a molecular hole transporter enhances the thermal stability of perovskite solar cells. *Advanced Materials* 33: e2007431.

27 Kasparavicius, E., Franckevicius, M., Malinauskiene, V. et al. (2021). Oxidized spiro-OMeTAD: investigation of stability in contact with various perovskite compositions. *ACS Applied Energy Materials* 4: 13696–13705.

28 Zhang, Z., Li, Z., Deng, L. et al. (2022). Hot-air treatment-regulated diffusion of LiTFSI to accelerate the aging-induced efficiency rising of perovskite solar cells. *ACS Applied Materials & Interfaces* 14: 4378–4388.

29 Zhang, W., Zhang, F., Xu, B. et al. (2020). Organic salts as p-Type dopants for efficient LiTFSI-free perovskite solar cells. *ACS Applied Materials & Interfaces* 12: 33751–33758.

30 Tan, B., Raga, S.R., Chesman, A.S.R. et al. (2019). LiTFSI-free spiro-OMeTAD-based perovskite solar cells with power conversion efficiencies exceeding 19%. *Advanced Energy Materials* 9: 1–10. 1901519.

31 Jeong, M., Choi, I.W., Go, E.M. et al. (2020). Stable perovskite solar cells with efficiency exceeding 24.8% and 0.3-V voltage loss. *Science* 369: 1615.

32 Chen, W., Wu, Y., Yue, Y. et al. (2015). Efficient and stable large-area perovskite solar cells with inorganic charge extraction layers. *Science* 350: 944.

33 Arora, N., Dar, M.I., Hinderhofer, A. et al. (2017). Perovskite solar cells with CuSCN hole extraction layers yield stabilized efficiencies greater than 20%. *Science* 358: 768–771.

34 Ku, Z., Rong, Y., Xu, M. et al. (2013). Full printable processed mesoscopic $CH_3NH_3PbI_3$/TiO_2 heterojunction solar cells with carbon counter electrode. *Scientific Reports* 3: 3132.

35 Mei, A., Li, X., Liu, L. et al. (2014). A hole-conductor–free, fully printable mesoscopic perovskite solar cell with high stability. *Science* 345: 295–298.

36 Domanski, K., Correa-Baena, J.-P., Mine, N. et al. (2016). Not all that glitters is gold: Metal-migration-induced degradation in perovskite solar cells. *ACS Nano* 10: 6306–6314.

37 Kato, Y., Ono, L.K., Lee, M.V. et al. (2015). Silver iodide formation in methyl ammonium lead iodide perovskite solar cells with silver top electrodes. *Advanced Materials Interfaces* 2: 1500195.

38 Zhao, L., Kerner, R.A., Xiao, Z. et al. (2016). Redox chemistry dominates the degradation and decomposition of metal halide perovskite optoelectronic devices. *ACS Energy Letters* 1: 595–602.

39 Ming, W., Yang, D., Li, T. et al. (2018). Formation and diffusion of metal impurities in perovskite solar cell material $CH_3NH_3PbI_3$: implications on solar cell degradation and choice of electrode. *Advanced Science* 5: 1700662.

40 Wu, S., Chen, R., Zhang, S. et al. (2019). A chemically inert bismuth interlayer enhances long-term stability of

inverted perovskite solar cells. *Nature Communications* 10: 1161.

41 Boyd, C.C., Cheacharoen, R., Bush, K.A. et al. (2018). Barrier design to prevent metal-induced degradation and improve thermal stability in perovskite solar cells. *ACS Energy Letters* 3: 1772–1778.

42 Liu, M., Chen, Z., Yang, Y. et al. (2019). Reduced open-circuit voltage loss for highly efficient low-bandgap perovskite solar cells via suppression of silver diffusion. *Journal of Materials Chemistry A* 7: 17324–17333.

43 Liang, L., Cai, Y., Li, X. et al. (2018). All that glitters is not gold: recent progress of alternative counter electrodes for perovskite solar cells. *Nano Energy* 52: 211–238.

44 Fang, R., Wu, S., Chen, W. et al. (2018). [6,6]-Phenyl-C61-butyric acid methyl ester/cerium oxide bilayer structure as efficient and stable electron transport layer for inverted perovskite solar cells. *ACS Nano* 12: 2403–2414.

45 Zhao, J., Zheng, X., Deng, Y. et al. (2016). Is Cu a stable electrode material in hybrid perovskite solar cells for a 30-year lifetime? *Energy & Environmental Science* 9: 3650–3656.

46 Bush, K.A., Bailie, C.D., Chen, Y. et al. (2016). Thermal and environmental stability of semi-transparent perovskite solar cells for tandems enabled by a solution-processed nanoparticle buffer layer and sputtered ITO electrode. *Advanced Materials* 28: 3937–3943.

47 Hou, Y., Aydin, E., De Bastiani, M. et al. (2020). Efficient tandem solar cells with solution-processed

perovskite on textured crystalline silicon. *Science* 367: 1135.

48 Wang, M., Fu, Q., Yan, L. et al. (2019). A Bi_2Te_3 topological insulator as a new and outstanding counter electrode material for high-efficiency and endurable flexible perovskite solar cells. *ACS Applied Materials & Interfaces* 11: 47868–47877.

49 Zhou, C. and Lin, S. (2019). Carbon-electrode based perovskite solar cells: effect of bulk engineering and interface engineering on the power conversion properties. *Solar RRL* 4: 1900190.

50 Fagiolari, L. and Bella, F. (2019). Carbon-based materials for stable, cheaper and large-scale processable perovskite solar cells. *Energy & Environmental Science* 12: 3437–3472.

51 Liang, Y., Wang, Y., Mu, C. et al. (2017). Achieving high open-circuit voltages up to 1.57 V in hole-transport-material-free $MAPbBr_3$ solar cells with carbon electrodes. *Advanced Energy Materials* 1701159.

52 Chen, H., Wei, Z., He, H. et al. (2016). Solvent engineering boosts the efficiency of paintable carbon-based perovskite solar cells to beyond 14%. *Advanced Energy Materials* 6.

53 Wei, H., Xiao, J., Yang, Y. et al. (2015). Free-standing flexible carbon electrode for highly efficient hole-conductor-free perovskite solar cells. *Carbon* 93: 861–868.

54 Hu, Y., Si, S., Mei, A. et al. (2017). Stable large-area ($10 \times 10 \, cm^2$) printable mesoscopic perovskite module exceeding 10% efficiency. *Solar RRL* 1: 1600019.

55 Dunfield, S.P., Bliss, L., Zhang, F. et al. (2020). From defects to degradation: a mechanistic understanding of degradation in perovskite solar cell devices and modules. *Advanced Energy Materials* 10: 1904054.

56 Cheacharoen, R., Boyd, C.C., Burkhard, G.F. et al. (2018). Encapsulating perovskite solar cells to withstand damp heat and thermal cycling. *Sustainable Energy & Fuels* 2: 2398–2406.

57 Cheacharoen, R., Rolston, N., Harwood, D. et al. (2018). Design and understanding of encapsulated perovskite solar cells to withstand temperature cycling. *Energy & Environmental Science* 11: 144–150.

58 Bi, E., Tang, W., Chen, H. et al. (2019). Efficient perovskite solar cell modules with high stability enabled by iodide diffusion barriers. *Joule* 3: 2748–2760.

59 Agresti, A., Pescetelli, S., Palma, A.L. et al. (2017). Graphene interface engineering for perovskite solar modules: 12.6% power conversion efficiency over 50 cm^2 active area. *ACS Energy Letters* 2: 279–287.

60 Matteocci, F., Cinà, L., Lamanna, E. et al. (2016). Encapsulation for long-term stability enhancement of perovskite solar cells. *Nano Energy* 30: 162–172.

61 Fu, Z., Xu, M., Sheng, Y. et al. (2019). Encapsulation of printable mesoscopic perovskite solar cells enables high temperature and long-term outdoor stability. *Advanced Functional Materials* 29: 1809129.

62 Mei, A., Sheng, Y., Ming, Y. et al. (2020). Stabilizing perovskite solar cells to IEC61215:2016 standards with over 9,000-h operational tracking. *Joule* 4: 1–15.

63 Conings, B., Drijkoningen, J., Gauquelin, N. et al. (2015). Intrinsic thermal instability of methylammonium lead trihalide perovskite. *Advanced Energy Materials* 5: 1500477.

64 Philippe, B., Park, B.-W., Lindblad, R. et al. (2015). Chemical and electronic structure characterization of lead halide perovskites and stability behavior under different exposures–a photoelectron spectroscopy investigation. *Chemistry of Materials* 27: 1720–1731.

65 Juarez-Perez, E.J., Hawash, Z., Raga, S.R. et al. (2016). Thermal degradation of $CH_3NH_3PbI_3$ perovskite into NH_3 and CH_3I gases observed by coupled thermogravimetry–mass spectrometry analysis. *Energy & Environmental Science* 9: 3406–3410.

66 Shi, L., Bucknall, M.P., Young, T.L. et al. (2020). Gas chromatography–mass spectrometry analyses of encapsulated stable perovskite solar cells. *Science* 368: eaba2412.

67 Saliba, M., Matsui, T., Domanski, K. et al. (2016). Incorporation of rubidium cations into perovskite solar cells improves photovoltaic performance. *Science* 354: 206–209.

68 Jeon, N.J., Noh, J.H., Yang, W.S. et al. (2015). Compositional engineering of perovskite materials for high-performance solar cells. *Nature* 517: 476–480.

69 Lee, J.-W., Kim, D.-H., Kim, H.-S. et al. (2015). Formamidinium and cesium hybridization for photo- and moisture-stable perovskite solar cell. *Advanced Energy Materials* 5: 1501310.

70 Slotcavage, D.J., Karunadasa, H.I., and McGehee, M.D. (2016). Light-induced phase segregation in halide-perovskite absorbers. *ACS Energy Letters* 1: 1199–1205.

71 Liu, S., Guan, Y., Sheng, Y. et al. (2019). A review on additives for halide perovskite solar cells. *Advanced Energy Materials* 1902492.

72 Li, N., Zhu, Z., Chueh, C.-C. et al. (2017). Mixed cation $FA_xPEA_{1-x}PbI_3$ with enhanced phase and ambient stability toward high-performance perovskite solar cells. *Advanced Energy Materials* 7: 1601307.

73 Fu, Y., Wu, T., Wang, J. et al. (2017). Stabilization of the metastable lead iodide perovskite phase via surface functionalization. *Nano Letters* 17: 4405–4414.

74 Wang, Y., Zhang, T., Kan, M., and Zhao, Y. (2018). Bifunctional stabilization of all-inorganic α-$CsPbI_3$ perovskite for 17% efficiency photovoltaics. *Journal of the American Chemical Society* 140: 12345–12348.

75 Swarnkar, A., Marshall, A.R., Sanehira, E.M. et al. (2016). Quantum dot–induced phase stabilization of α-$CsPbI_3$ perovskite for high-efficiency photovoltaics. *Science* 354: 92–95.

76 Steele, J.A., Jin, H., Dovgaliuk, I. et al. (2019). Thermal unequilibrium of strained black $CsPbI_3$ thin films. *Science*, eaax3878 .

77 Jena, A.K., Kulkarni, A., and Miyasaka, T. (2019). Halide perovskite photovoltaics: background, status, and future prospects. *Chemical Reviews* 119: 3036–3103.

78 Leguy, A.M.A., Hu, Y., Campoy-Quiles, M. et al. (2015). Reversible hydration of $CH_3NH_3PbI_3$ in films, single

crystals, and solar cells. *Chemistry of Materials* 27: 3397–3407.

79 Shockley, W. and Queisser, H.J. (1961). Detailed balance limit of efficiency of p-n junction solar cells. *Journal of Applied Physics* 32: 510–519.

80 Tong, J., Song, Z., Kim, D.H. et al. (2019). Carrier lifetimes of >1 µs in Sn-Pb perovskites enable efficient all-perovskite tandem solar cells. *Science* eaav7911.

81 Lee, S.J., Shin, S.S., Kim, Y.C. et al. (2016). Fabrication of efficient formamidinium tin iodide perovskite solar cells through SnF_2–pyrazine complex. *Journal of the American Chemical Society* 138: 3974–3977.

82 Schoonman, J. (2015). Organic–inorganic lead halide perovskite solar cell materials: a possible stability problem. *Chemical Physics Letters* 619: 193–195.

83 Steele, J.A., Puech, P., Monserrat, B. et al. (2019). Role of electron–phonon coupling in the thermal evolution of bulk rashba-like spin-split lead halide perovskites exhibiting dual-band photoluminescence. *ACS Energy Letters* 4: 2205–2212.

84 Liu, F., Dong, Q., Wong, M.K. et al. (2016). Is excess PbI_2 beneficial for perovskite solar cell performance? *Advanced Energy Materials* 6: 1502206.

85 Roose, B., Dey, K., Chiang, Y.H. et al. (2020). Critical assessment of the use of excess lead iodide in lead halide perovskite solar cells. *Journal of Physical Chemistry Letters* 11: 6505–6512.

86 Tumen-Ulzii, G., Qin, C., Klotz, D. et al. (2020). Detrimental effect of unreacted PbI_2 on the long-term

stability of perovskite solar cells. *Advanced Materials* 32: e1905035.

87 Zhao, L., Li, Q., Hou, C.H. et al. (2022). Chemical polishing of perovskite surface enhances photovoltaic performances. *Journal of the American Chemical Society* 144: 1700–1708.

88 Goetz, K.P., Taylor, A.D., Paulus, F., and Vaynzof, Y. (2020). Shining light on the photoluminescence properties of metal halide perovskites. *Advanced Functional Materials* 30: 1–35. 1910004.

89 Diroll, B.T., Nedelcu, G., Kovalenko, M.V., and Schaller, R.D. (2017). High-temperature photoluminescence of $CsPbX_3$ (X = Cl, Br, I) nanocrystals. *Advanced Functional Materials* 27.

90 Dobrovolsky, A., Merdasa, A., Unger, E.L. et al. (2017). Defect-induced local variation of crystal phase transition temperature in metal-halide perovskites. *Nature Communications* **8**: 34.

91 Shi, Z., Zhang, Y., Cui, C. et al. (2017). Symmetrization of the crystal lattice of $MAPbI_3$ boosts the performance and stability of metal-perovskite photodiodes. *Advanced Materials* 29: 1–6. 1701656.

92 Kubicki, D.J., Prochowicz, D., Hofstetter, A. et al. (2018). Formation of stable mixed guanidinium-methylammonium phases with exceptionally long carrier lifetimes for high-efficiency lead iodide-based perovskite photovoltaics. *Journal of the American Chemical Society* 140: 3345–3351.

93 Chen, B., Song, J., Dai, X. et al. (2019). Synergistic effect of elevated device temperature and excess charge

carriers on the rapid light-induced degradation of perovskite solar cells. *Advanced Materials* 31: e1902413.

94 Zhao, Y., Heumueller, T., Zhang, J. et al. (2021). A bilayer conducting polymer structure for planar perovskite solar cells with over 1,400 hours operational stability at elevated temperatures. *Nature Energy* 7: 144–152.

95 Zhang, T., Hu, C., and Yang, S. (2020). Ion migration: a "double-edged sword" for halide-perovskite-based electronic devices. *Small Methods* 4: 1900552.

96 Rolston, N., Bush, K.A., Printz, A.D. et al. (2018). Engineering stress in perovskite solar cells to improve stability. *Advanced Energy Materials* 8: 1802139.

97 Jones, T.W., Osherov, A., Alsari, M. et al. (2019). Lattice strain causes non-radiative losses in halide perovskites. *Energy & Environmental Science* 12: 596–606.

98 Zhu, C., Niu, X., Fu, Y. et al. (2019). Strain engineering in perovskite solar cells and its impacts on carrier dynamics. *Nature Communications* 10: 815.

99 Deng, Y., Xu, S., Chen, S. et al. (2021). Defect compensation in formamidinium–caesium perovskites for highly efficient solar mini-modules with improved photostability. *Nature Energy* 6: 633–641.

100 Fang, H.H., Adjokatse, S., Shao, S. et al. (2018). Long-lived hot-carrier light emission and large blue shift in formamidinium tin triiodide perovskites. *Nature Communications* 9: 243.

101 Wali, Q., Elumalai, N.K., Iqbal, Y. et al. (2018). Tandem perovskite solar cells. *Renewable and Sustainable Energy Reviews* 84: 89–110.

102 Xu, L., Xiong, Y., Mei, A. et al. (2018). Efficient perovskite photovoltaic-thermoelectric hybrid device. *Advanced Energy Materials*, 1702937.

103 Baikie, T., Fang, Y., Kadro, J.M. et al. (2013). Synthesis and crystal chemistry of the hybrid perovskite $(CH_3NH_3)PbI_3$ for solid-state sensitised solar cell applications. *Journal of Materials Chemistry A* 1: 5628.

104 Li, N., Chen, S., Mosconi, E. et al. (2019). Cation and anion immobilization through chemical bonding enhancement with fluorides for stable halide perovskite solar cells. *Nature Energy* 4: 408–415.

105 Bai, S., Tao, S., Chen, Y. et al. (2019). Planar perovskite solar cells with long-term stability using ionic liquid additives. *Nature* 571: 245–250.

106 Yang, S., Da, P., Li, C. et al. (2019). Stabilizing halide perovskite surfaces for solar cell operation with wide-bandgap lead oxysalts. *Science* 365: 473–478.

107 Yang, X., Luo, D., Xiang, Y. et al. (2021). Buried interfaces in halide perovskite photovoltaics. *Advanced Materials* 33: 2006435.

108 Chen, S., Dai, X., Xu, S. et al. (2021). Stabilizing perovskite-substrate interfaces for high-performance perovskite modules. *Science* 373: 902.

109 Dai, Z., Yadavalli Srinivas, K., Chen, M. et al. (2021). Interfacial toughening with self-assembled monolayers enhances perovskite solar cell reliability. *Science* 372: 618–622.

110 Min, H., Lee, D.Y., Kim, J. et al. (2021). Perovskite solar cells with atomically coherent interlayers on SnO_2

electrodes. *Nature* 598: 444–450.

111 You, J., Meng, L., Song, T.B. et al. (2016). Improved air stability of perovskite solar cells via solution-processed metal oxide transport layers. *Nature Nanotechnology* 11: 75–81.

112 Wang, Y., Wu, T., Barbaud, J. et al. (2019). Stabilizing heterostructures of soft perovskite semiconductors. *Science* 365: 687–691.

113 Wang, L., Zhou, H., Hu, J. et al. (2019). A $Eu^{3+}-Eu^{2+}$ ion redox shuttle imparts operational durability to Pb-I perovskite solar cells. *Science* 363: 265.

114 Chang, Q., Wang, F., Xu, W. et al. (2021). Ferrocene-induced perpetual recovery on all elemental defects in perovskite solar cells. *Angewandte Chemie International Edition* 60: 25567–25574.

115 Eames, C., Frost, J.M., Barnes, P.R. et al. (2015). Ionic transport in hybrid lead iodide perovskite solar cells. *Nature Communications* 6: 7497.

116 Bowring, A.R., Bertoluzzi, L., O'Regan, B.C., and McGehee, M.D. (2017). Reverse bias behavior of halide perovskite solar cells. *Advanced Energy Materials* 1702365.

117 Bogachuk, D., Saddedine, K., Martineau, D. et al. (2021). Perovskite photovoltaic devices with carbon-based electrodes withstanding reverse-bias voltages up to –9 V and surpassing IEC 61215:2016 international standard. *Solar RRL* 6: 2100527.

9
Manufacture, Modules, and Applications

Simone Meroni and Trystan Watson
SPECIFIC, Swansea University, Bay Campus, Swansea, SA1 8EN, UK

9.1 Introduction

The potential for high-power generation in large-area devices, the low cost, and the outstanding stability compared to the other perovskite architectures make the triple mesoscopic carbon perovskite solar cell (mCPSC) the front runner to early industrialization. In the transition between laboratory and factory production, a few aspects must be considered: the power generation of large area modules, which must be optimized with a maximized coverage of the total area with active materials (geometric fill factor); the low cost of production and materials; the stability, which is the result of the intrinsic long-term performance and of an effective encapsulation strategy. This chapter will focus on the engineering aspects of manufacture and module design of the mCPSC, and will give some examples of applications based on studies outdoors and indoors.

To achieve market penetration, the perovskite solar cell (PSC) must demonstrate high-power generation, low cost, and high stability. Probably, the closest architecture to achieving this is the triple mCPSC, which makes it the front runner to early industrialization [1–3]. This architecture is based on three screen-printed mesoscopic layers deposited sequentially on a conductive glass substrate of F:SnO$_2$ (FTO) and an electron transporting layer (ETL) on top (compact TiO$_2$ in case of mCPSC). The process to fabricate the mCPSC does not strictly require expensive equipment, thus, an eventual production line could be built with low-capital cost. As a result, the payback period can be expected to be very short and, more importantly, the initial investment risk can be very low. This unlocks the feasibility of affordable PV manufacture for any company size, from large multinationals to small enterprises wanting to expand to a high-tech market with low risk. An example of production of mCPSC with low-cost equipment is provided in Figure 9.1, where the deposition of the inorganic layers for the manufacture of mini-modules was carried out with a manual screen printer owned by a family-run company based in Mexico.

In terms of power conversion efficiency (PCE), mCPSC lags behind other PSC architectures when considering the results of small single cells. However, the power generation of a potentially commercial device is better tested for large-area modules. When considering small-scale devices, PSCs based on evaporated metal top electrodes demonstrate very high PCE, close to the best research single-crystal silicon solar cells (c-Si SC), i.e. over 25% [4]. The PCE of mCPSC was demonstrated to be up to 17% [5, 6]. However, in strong contrast to the other PSC architectures, PCE of mCPSC is not strongly affected by the device size. Figure 9.2 shows the performance of small devices with different PSC architectures on the left side and, on the right, the performance of the relative modules at different area sizes. All the architectures but mCPSC present a significant decrease in PCE during the scale-up. It should be noted that Figure 9.2 reports some outstanding modules as reported until 2018. Other important examples of modules can be found in [8–11]. Modules between 10% and 11% have been reported for the mCPSC architecture for between 50 and 70 cm^2 [12–14], and over 6% for 198 cm^2 mCPSC modules [15]. The consistent performance of mCPSC when device size is increased denotes the simple scalability of this architecture and places the technology close to the other expensive and less stable PSC in terms of PCE of larger modules.
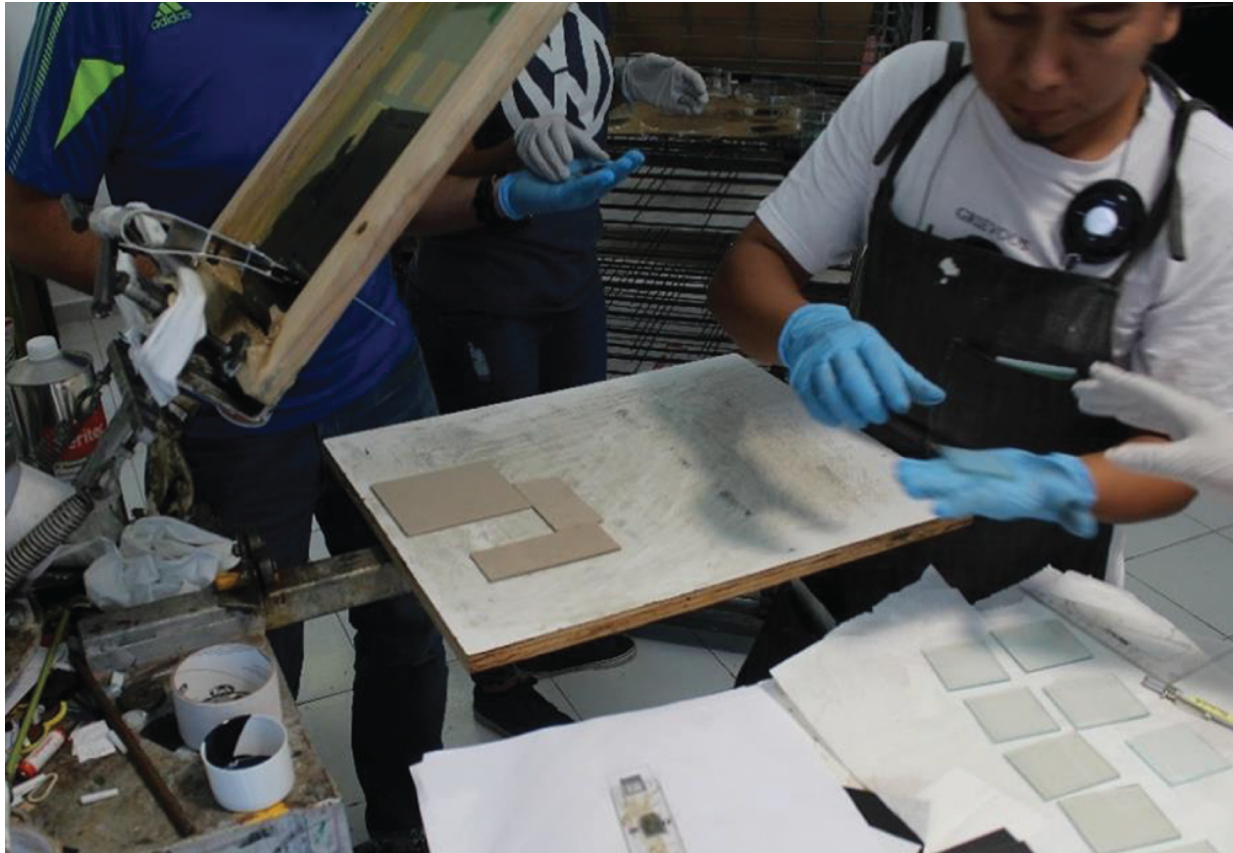
Figure 9.1 Manufacture of low-capital cost mCPSC mini-modules in "Serigrafía e impresos," a family-run company based in Mérida, (Yucatan, Mexico). Project within a Newton institutional link funding for the collaboration between SPECIFIC-Swansea University and CINVESTAV-Mérida.
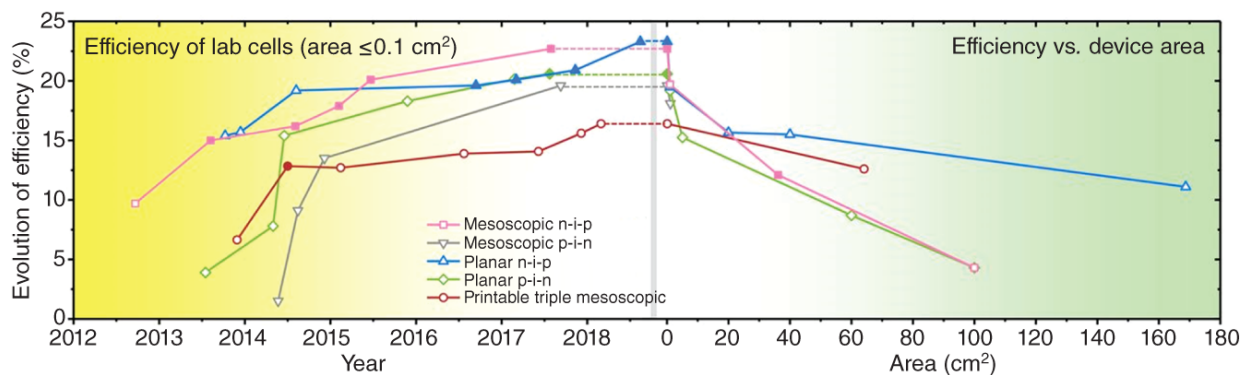
Figure 9.2 Evolution of the best-reported lab-cell ($\leq 0.1\,\text{cm}^2$) efficiencies and large-area ($\geq 1.0\,\text{cm}^2$) device efficiencies (2018). Source: Rong et al. [7]/With permission of American Association for the Advancement of Science.

A decrease in PCE can be expected in an up-scaled device because of two main factors:

- The higher probability of defects that can be found over a large area deposition, e.g. pinholes and variation in the layer thickness.

  The presence of pinholes and defects in layers can decrease the shunt resistance (G) of the device. This is the parallel parasitic resistance that bypasses the diode and

causes recombination phenomena in the device. A good working device should have a very high G. The presence of defects is likely to increase with device area but can be minimized with an appropriate layer deposition strategy. Screen printing, as a well-established industrial process, can be simply optimized to avoid the formation of defects in large-scale production.

Alongside pinholes, a defect specific to large-area devices is thickness variation, usually negligible for small devices. This kind of defect causes part of the device to work in unoptimized conditions. Variations of few tens of nm can be significant when working with thin layers of hundreds of nm, however, they are negligible when working with µm thick films. The mCPSC architecture is made of µm thick layers, much thicker than in other PSC architectures. Thick layers allow the deposition of consistent films with negligible thickness variation over large areas [16]. The thick screen-printed layers are likely to be one of the reasons for the reduced decrease in PCE during scale-up, compared to the other PSC architectures.

- Electrical resistance of the layers.

  The series resistance (R_s) is the parasitic resistance in series to the circuit and causes a drop in voltage equal to the product of current and R_s (iR drop). R_s increases with the substrate size, but a good working device should have a very low R_s. To limit this effect, electrical connections need to be placed as close as possible to the area where the charge is generated.

  A possible approach to reduce R_s is the application of a metallic grid that can be printed on one or both sides of the device. Screen-printed metallic grids are commonly used for silicon solar cells but conductive inks can chemically interact with the active layers. Perovskite, for example, can react with Ag, especially in the mCPSC architecture, where the conductive ink can penetrate through the porous carbon layer and enter into direct contact with the perovskite. An alternative approach to minimize the effect of R_s is the connection of single and narrow cells in parallel or in series. This is the case of modules, where R_s is small due to the small width of the single cells, but the size is large as the single cells can be printed on the same large substrate.

  The module design influences the device power generation as it dictates the coverage of the substrate with active material. PCE is commonly referred to as the power generation considering the active area, but a commercial device must be evaluated for the power generation of the total area that the device occupies. For this reason, it is crucial that the active layers have a high coverage of the entire area of the substrate. For example, a device with 20% PCE, but with coverage only at 40%, produces less power than a device with 15% PCE and 95% of coverage. Active areas can often be lost while creating space for module sealing and interconnects. This coverage is often defined as the geometric fill-factor (g-FF).

Another important characteristic of mCPSC is the low cost of:

- The materials. Expensive materials, such as noble metals and purified organic compounds, e.g. spiro-OMeTAD [17], are not used in this architecture.
- The manufacturing process. This is because all the layers are screen printed, including the top electrode, and the perovskite is simply infiltrated from the top, making the process fast and inexpensive.
- The initial investment. Screen printing is the main instrument used in production. While advanced screen printing equipment can be expensive in certain applications, it

is generally extremely inexpensive as only a plastic squeegee and a screen are required for the manual process.

A further advantage of mCPSC for industrial applications is the use of an inorganic stack as shell for the perovskite absorber material. In this way, it is possible to fabricate a large amount of inorganic stack on glass and then infiltrate the perovskite precursor solution on demand at a subsequent manufacturing stage. This characteristic allows the preparation of preassembled products for streamlined product delivery. Furthermore, there is potentiality for recycling the inorganic stack when the harvesting material is exhausted [18]. It may be possible to wash off the perovskite material and to re-infiltrate the inorganic stack with a fresh perovskite solution. This has the potential of increasing the lifetime of the device, thanks to the regeneration and recovery of toxic materials via simple washing.

9.2 Manufacture

The manufacture of mCPSC is mostly based on the screen-printing method, which is adopted for the deposition of the three mesoscopic layers. Although screen printing is by far the most used technique for the fabrication of mCPSC, other methods can be used instead, for example, doctor blading or inkjet. The inorganic stack is usually deposited via screen printing, making this deposition method key in the mCPSC manufacture. Due to the predominance of screen printing for the mCPSC, a particular focus is offered below.

Table 9.1 shows the different techniques that have been used to produce mCPSC in the literature. The inorganic stack is usually deposited via screen printing, making this deposition method key in the mCPSC manufacture. Due to the predominance of screen printing for the mCPSC, a particular focus is offered below.

9.2.1 Screen Printing

Screen printing is a very well-established technique that is widely used on an industrial scale. It is a versatile printing technique that allows a full two-dimensional patterning of the printed layers. The essential instruments are a squeegee and a screen. The screen is a mesh made with a woven material, which is glued in tension on a rigid frame (usually made in wood, cast iron, or aluminum). Common materials for the mesh include synthetic fiber or steel mesh. The mesh has an open area, or printing area, where the ink is forced to pass through. The printing area is created with the application of a light curable material, e.g. an emulsion or a capillary film, that is accurately applied onto the mesh. The pattern that is required is then printed in black on a transparent support and then placed on the mesh. After illumination, only the exposed area is cured, while the shadowed area can be easily removed, leaving the printing area open.

Table 9.1 Summary of techniques that have been used for the deposition of the mCPSC materials.

	Spray	Screen printing	Drop	Slot-die	Inkjet	Spin coating	Doctor-blading	FACVD	Vacuum deposition
Compact TiO$_2$		[19–21]			[22]	[23, 24]			[25]
Inorganic stack					[22]	[23, 24]	[23, 26, 27]		
Additional interlayers	[28]	[20, 29, 30]						[31]	[25, 32]
Perovskite deposition		(RbM) [15, 33, 34]		[21, 35]	[36]	[37, 38]			

Red, the most used deposition methods; Green, alternative methods for the material under consideration with reference of some examples; White, we are not currently aware of any work as applied to the mCPSC. Some examples of applications for the mCPSC are reported.

The screen-printing method suits either roll-to-roll (R2R) or sheet-to-sheet (S2S) production. R2R production can be performed via rotary screen printing, usually on flexible substrates, such as textiles. S2S production is preferred in many applications, especially on rigid substrates. To print, the screen is placed above the substrate. Screen and substrate are accurately registered, but they are not in contact as a gap of a few mm or less separates the two. At this point, the ink can be placed on the surface of the screen to be transferred to the substrate through the printing area. This is carried out with a squeegee that presses down the screen in contact with the substrate and forces the ink to transfer with a linear passage across the printing area (Figure 9.3a). There is essentially no loss or minimal loss of ink during printing as most of the unused ink can be collected. The squeegee is a piece of flexible material with at least one straight edge. The squeegee forces the ink through the mesh and ensures the screen–substrate contact during the printing passage.

After printing, only a small amount of ink is left in the mesh. The ink, therefore, must be spread again on the screen's surface. This can either be done with the same squeegee in a manual process or with a so-called flood coater in an automatic process. The flood coater is usually a blade that spreads the ink back without pressing on the screen (Figure 9.3b). Screen-printing instruments can be equipped with camera systems to improve registration accuracy, a vacuum table to hold the substrates, and other components to enhance printing consistency and speed. However, the essential parts of the instrument are the screen and the squeegee.
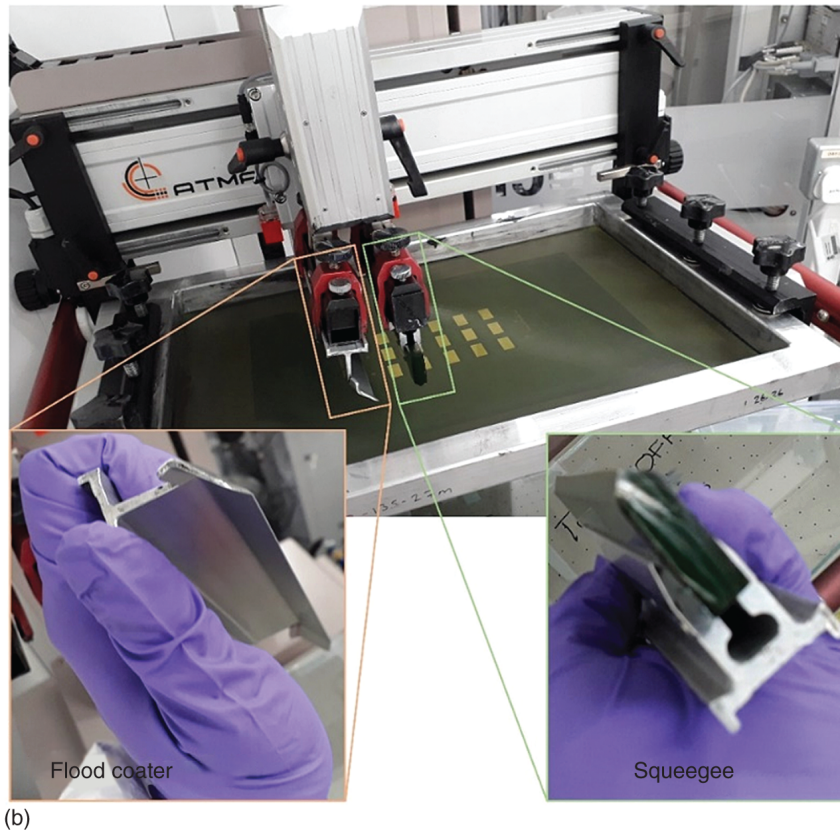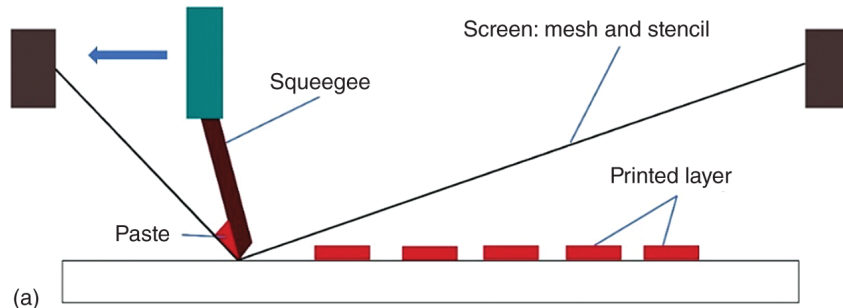
Figure 9.3 Screen printing. (a) A schematic of the process; (b) An example of automatic presser for screen printing. The essential components are a screen, in this case, covered with a green emulsion, and a squeegee. For automated processes, a flood coater is also necessary.

There are several parameters that can affect film quality. This section does not aim to substitute more specialistic books, therefore many aspects will not be presented here, such as the importance of the squeegee properties (hardness, shape, and angle), the effect of the thickness of the screen's emulsion, the effect of the pressure of the squeegee, the tension of the screen and many other printing parameters. Here, we aim to provide the basic concepts of screen printing and underline the most critical aspects for the deposition of the mesoscopic layers for mCPSC.

9.2.1.1 Ink Properties

This is the most critical parameter in every printing process. In the case of screen printing, the ink must be viscous enough to avoid slumping through the mesh during printing, but it must pass through the mesh when required. The rheology of the ink,

therefore, should be in a specific range depending on the characteristic of the mesh. To give an idea, it should be roughly such as honey, which is around 100 Pa s. This means that the viscosity is usually higher than for other printing methods, such as flexographic or inkjet. However, the viscosity range can be very large when using the appropriate mesh size for the given ink.

An ink is a dispersion (or a solution) of a pigment with a binder in a solvent. The pigment is the coloring agent or the active material in printed electronics. The solvent is not defined in a chemically rigorous way, as it could also be a mixture of chemicals, and it gives a striking effect on the final rheological properties. The rheology of the ink can change significantly during the printing process if a consistent amount of solvent evaporates. For this reason, high-boiling point solvents are typically used in inks. After printing, part of the solvent evaporates, leaving a dry film, which is made mostly of binder and active materials. Screen-printed films can be much thicker than other deposition techniques, in the range of few µm or tens of µm. Thicker layers in the mm range are also possible, as well as very thin layers of tens of nm. Very thin layers can be achieved when the solid content of the ink is very low. The wet film will be thick, but the dry film after the removal of the binder can be tens of nm thick, as in the case of the deposition of compact TiO_2 for mCPSC [19, 20]. In case of using particles in the ink, their size should be carefully considered in screen printing. The particles, including agglomerates of nanoparticles, must pass through the mesh without clogging it or affecting the printing process. An empirical rule is that the particle size should be a tenth of the mesh aperture area.

9.2.1.2 Mesh Characteristics

After the ink, the mesh characteristic is probably the most important parameter in screen printing. The aperture area between the threads and the thread diameter defines the volume of ink that is transferred to the substrate (Figure 9.4), thus, the thickness of the wet film. The thread diameter and the distance between threads or the mesh count can be used to calculate the mesh aperture area via simple geometric considerations:

$$D_T = \frac{1}{C_m} \tag{9.1}$$

$$G_T = \frac{1}{C_m} - \emptyset_T \tag{9.2}$$

$$A_{m\%} = \left(1 - \frac{D_T \cdot \emptyset_T + G_T \cdot \emptyset_T}{D_T^2}\right) \cdot 100 \tag{9.3}$$

$$V_{th} = A_{m\%} \cdot 2\emptyset_T \tag{9.4}$$

where C_m is the mesh count, D_T is the distance between two threads, $\emptyset_T$ is the diameter of the thread, G_T is the gap between two threads, $A_{m\%}$ is the aperture area in %, and V_{th} is the theoretical volume of ink per unit area. Factor "2" relates to the fact that the threads are woven on each other, so the height is twice the diameter of the single thread (Figure 9.4). As C_m and $\emptyset_T$ define the aperture area and the theoretical volume, these values should be mentioned in the nomenclature of the screen. An example of nomenclature can be 130-34, which refers to the mesh count (130 threads per cm in the example) and the thread diameter (34 µm in the example).
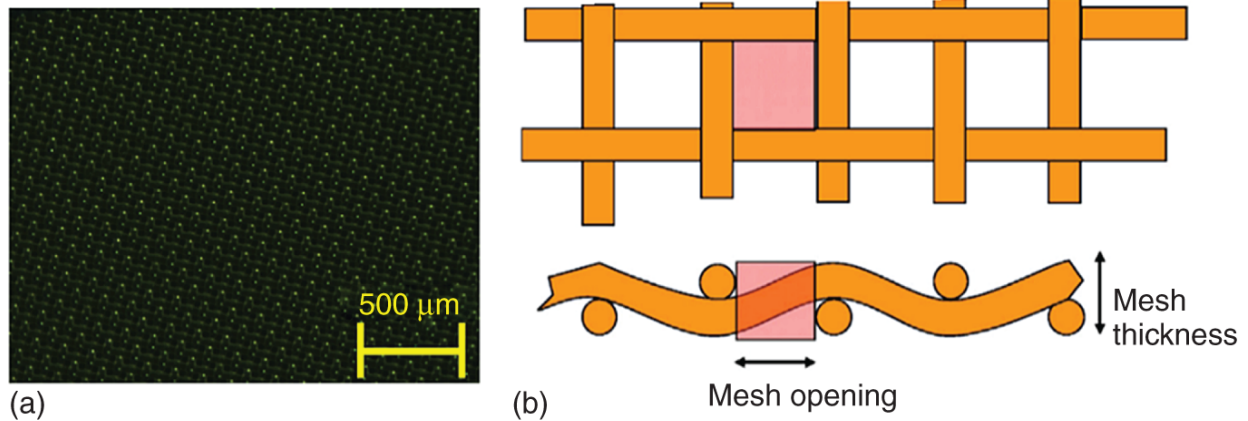
Figure 9.4 (a) A microscopic image of a 130-34 mesh, i.e. 130 threads per cm and 34 μm in diameter. (b) schematics (top and lateral view) of a mesh. Source: Philip et al. [39], Elsevier.

The volume of ink as expressed in V_{th} assumes that all the ink that is in the mesh is transferred to the substrate. However, part of it remains trapped in the mesh and V_{th} should be used only as a general idea of the potential wet film thickness when using a specific mesh. The actual volume of ink that is transferred to the substrate can be finely tuned also with other printing parameters, such as the gap between screen and substrate, the pressure of the squeegee, and the printing rate.

9.2.1.3 Gap Between Screen and Substrate

The optimization of the gap between screen and substrates during the print is crucial for good-quality prints. In the extreme case of no gap, the mesh is always in contact with the substrate. In this scenario, the ink can stick the mesh and the substrate together, leaving a very rough layer once the screen is removed. Moreover, the ink might float out of the printing area leaving an unpatterned layer. By increasing the gap, the contact time between screen and substrate becomes shorter and the layer deposition is simpler to control. However, in the extreme case of a very large gap, a high pressure of the squeegee is required to ensure screen–substrate contact. This might result in damage of the screen – if the mesh is in very high tension – or deformation of the printing image – if the tension of the screen is low. The deformation of the image is an effect that occurs when the angle between the screen and the substrate, in contact with the squeegee position, is very high. The original printing image follows the screen's deformation and the pattern of the film is therefore the projection of the printed image on the substrate.
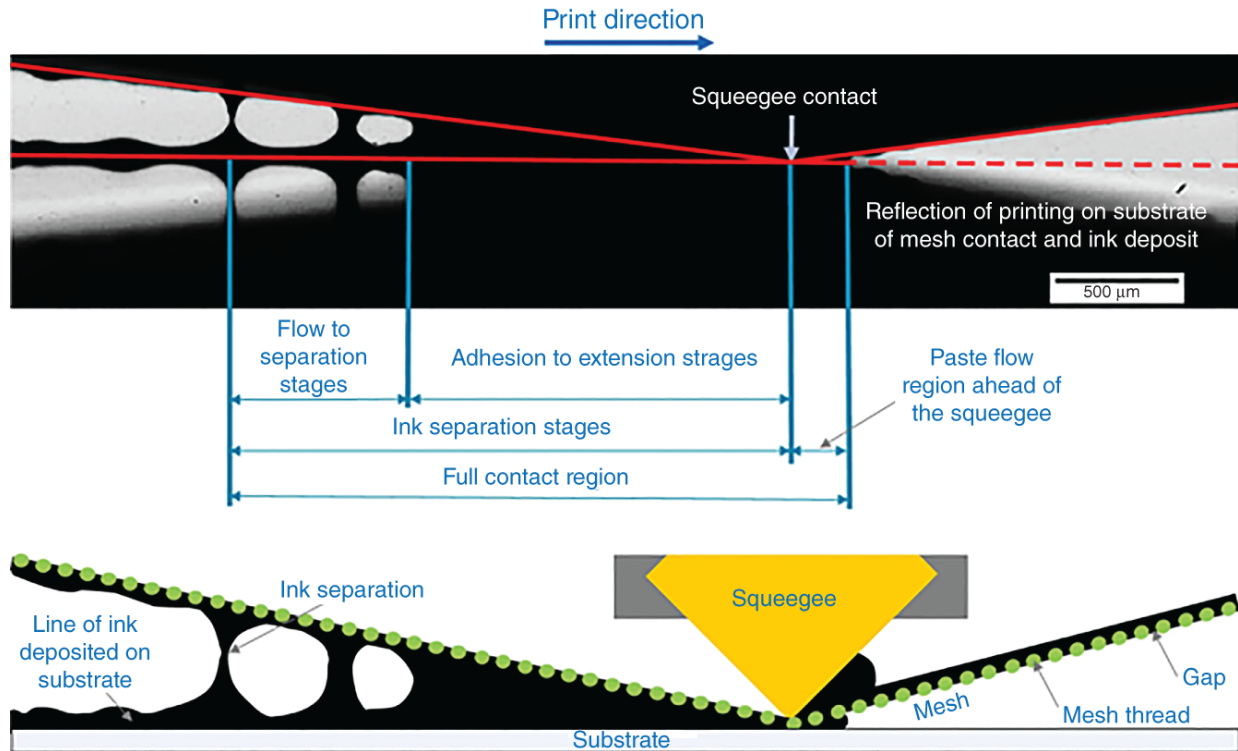
Figure 9.5 Labelled high-speed camera image of the squeegee forcing the mesh into contact with the substrate, where the ink is deposited from the mesh to the substrate as the squeegee flows across the screen (above) along with a cross-sectional schematic diagram of the process (below). Source: Potts et al. [40], Springer Nature, CC BY 4.0.

This process can be optimized empirically via a trial-and-error approach. However, an understanding of the process does speedup its optimization. The mechanism by which carbon ink wets the surface and releases during the printing process was studied via slow-motion camera by Potts et al. in 2020 [40]. The release of the ink in excess from the substrate occurs via a shearing action that causes the ink to split (Figure 9.5). The printing rate can affect the rheology of the ink, increasing or decreasing the elastic character. Therefore, the optimal gap depends on many factors, such as the printing rate, the rheology of the ink, and the angle of the squeegee.

9.2.1.4 A Case Study: TiO$_2$

Several parameters can affect the film characteristics of screen-printed layers. The special case of the mesoporous TiO$_2$ layer for mCPSC applications was investigated by Wan et al. and reported in 2019 [41]. To achieve thin layers via screen printing, the solid content of the ink must be reduced via dilution with α-terpineol. The lower amount of solid content reduces the amount of material that will remain in the film and, thus, the thickness. However, the viscosity is also affected (Figure 9.6a). For this reason, a very fine mesh is recommended, as low-viscosity ink might slough through a screen with a low mesh count and affect the printing process. Wan et al. used a 150-34 (150T) mesh, a very good choice for this system.

The viscosity can vary with the temperature (Figure 9.6b) and this can be one of the reasons for the thickness variation that sometimes can be observed between one print and another (Figure 9.6c). Because the viscosity changes also with the solvent content in the ink, and the solvent can evaporate during printing, it is recommended to use high-boiling point solvents. A short interval of time between prints is also recommended to reduce the

evaporation time. The solid content, then, dictates the thickness of the dried film, as shown in Figure 9.6d. The gap between the screen and the substrate, the pressure of the squeegee, and the printing speed can also affect the thickness of the final layer as shown in Figure 9.7. The operator should keep in mind that all the parameters should be measured and reproduced with high consistency.
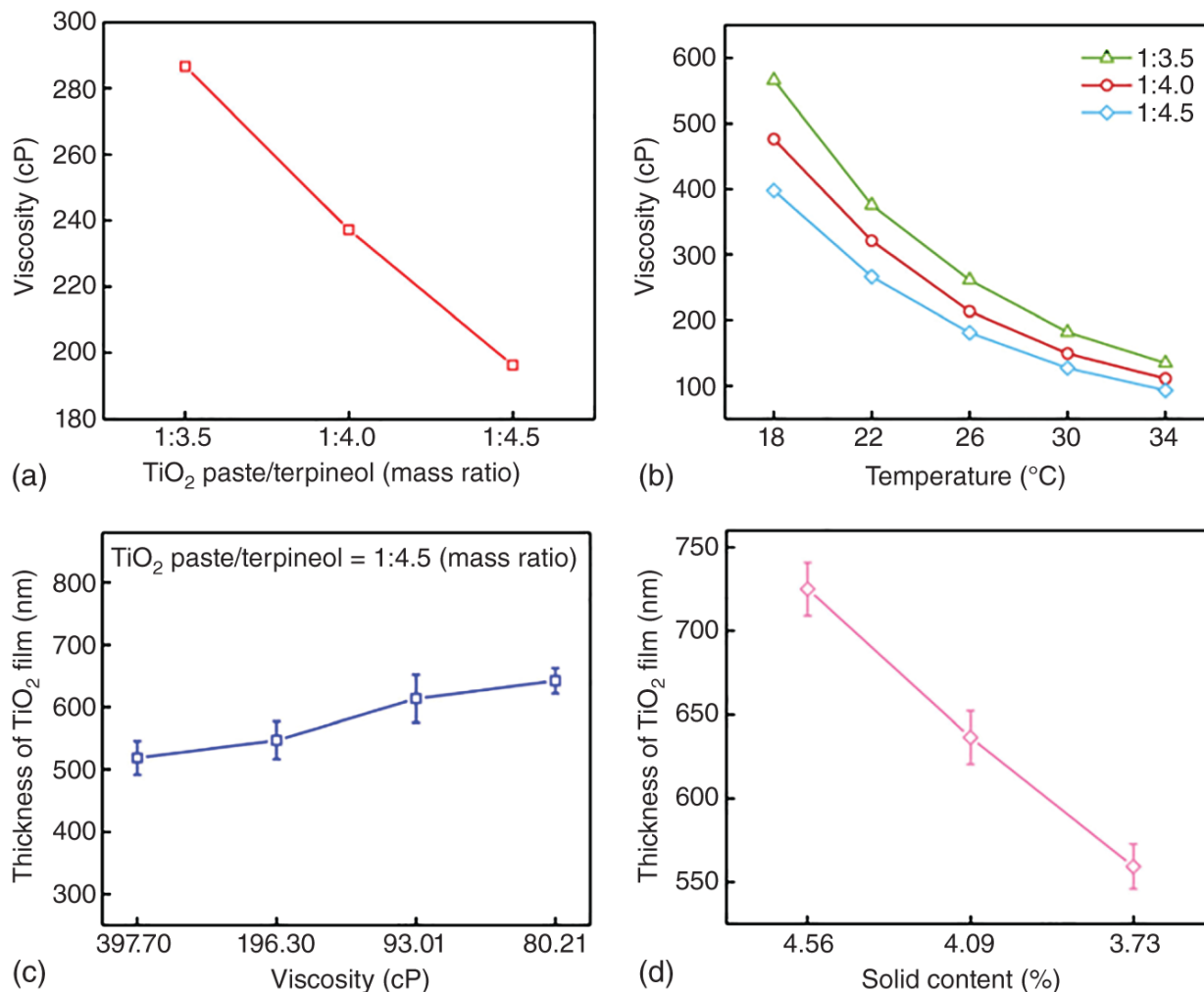
Figure 9.6 (a) Dependence of viscosity of the TiO_2 ink on paste:terpineol mass ratio; (b) dependence of viscosity of the TiO_2 ink on temperature; (c) dependence of the TiO_2 layer thickness on the viscosity; (d) dependence of the TiO_2 layer thickness on the solid content. Source: Rong et al. [37]/With permission of Springer Nature.

9.2.2 Deposition of the Compact TiO_2

The compact TiO_2 is used in many architectures as an ETL. Many materials have been reported as effective ETL, such as SnO_2 and ZnO_2 [42–44], but so far TiO_2 is the only reported ETL for mCPSC. The deposition can be carried out in many different ways, for example via atomic layer deposition (ALD) [45], sputtering [46], spray pyrolysis [47], spin coating [23], and many other deposition techniques (Table 9.1).

Spray coating is commonly used for mCPSC and has the advantage, as for screen printing, of being an established industrial technique. Spray coating can be also called spray pyrolysis in this context because a solution of TiO_2 precursor is sprayed at high

temperature and, then, a pyrolysis step ensures the chemical conversion and the formation of the inorganic layer. Spray pyrolysis is probably the best option to achieve high-quality thin films via a solution phase process, especially for devices >10 × 10 cm^2. Some disadvantages of the method include the consumption of materials, as most of the solution is vaporized, and the high temperature that is required during the deposition.
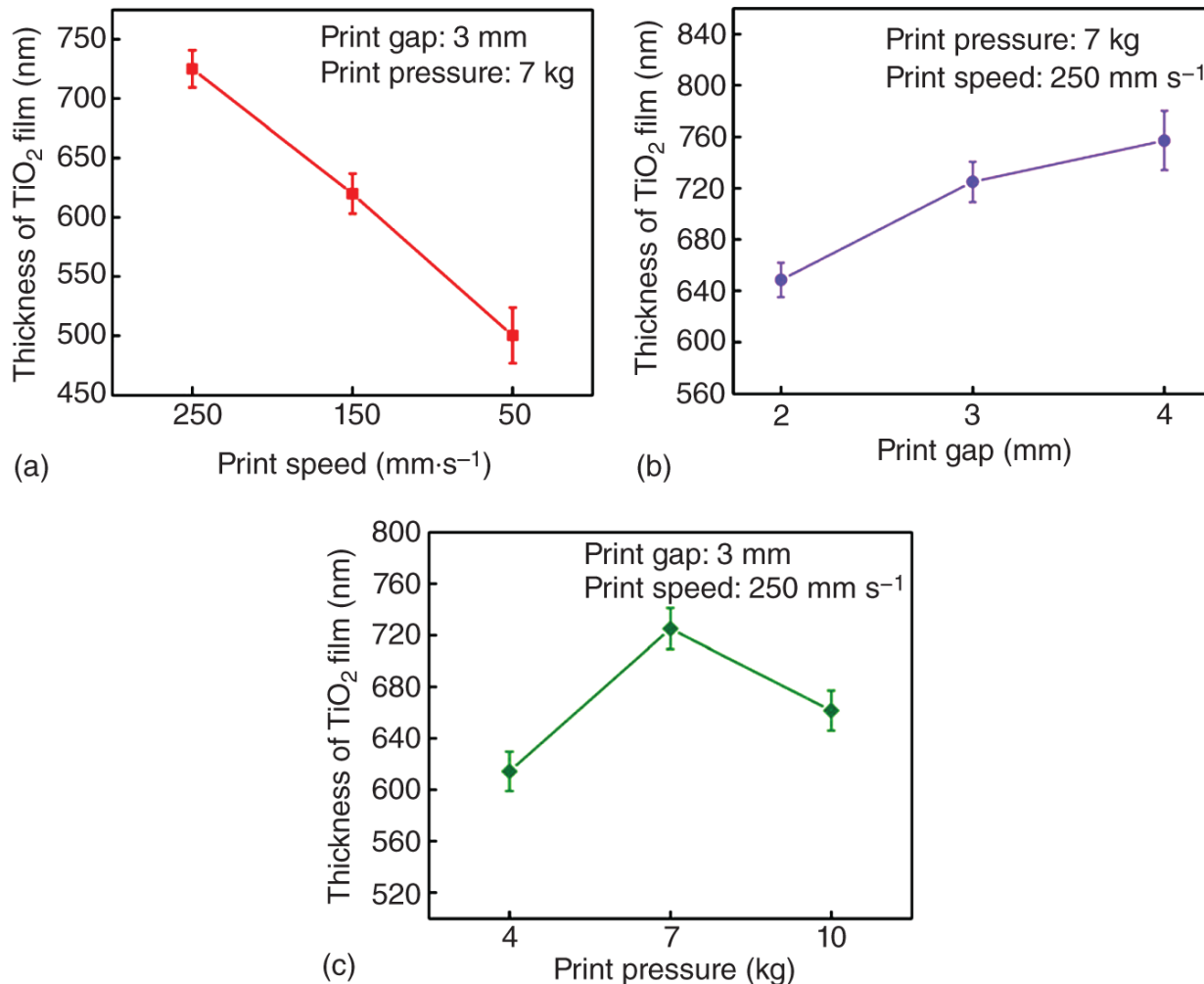
Figure 9.7 Dependence of the film thickness on: (a) the print speed; (b) the print gap; (c) the print pressure. Source: Rong et al. [37]/With permission of Springer Nature.

Spin coating is a valuable alternative to deposit the compact TiO$_2$, especially at labscale. The films can be very thin and homogenous, but the substrate size is normally restricted to no more than 10 cm^2. For larger substrate areas, spin coating is not recommended.

Screen printing can be used to deposit a compact and thin TiO$_2$ layer. The paste is based on TiO$_2$ nanoparticles mixed in a large quantity of binders. The very low amount of solid content allows the deposition of thick wet films, typical via screen printing, that shrink to tens of nm when the binder is removed. This method is promising for mCPSC because the same technique is then viable for all layers of the device.

Conformal films can also be achieved via vacuum deposition methods for very thin and conformal layers, such as ALD or sputtering. The resulting film quality can be ideal for the preparation of highly efficient devices. Although the cost of the process can be low, the

capital cost of the equipment, especially for very large devices, can be significant, and an accurate analysis of cost/benefit should be undertaken.

A potential solution to the requirements of compact layer deposition is to purchase substrates that already have a thin TiO_2 film applied via CVD during glass substrate manufacture. This would reduce the need for capital expenditure on compact layer deposition equipment. This approach has already been demonstrated for PSCs [48].

9.2.3 Deposition of the Mesoscopic Layers

Screen printing is the main deposition technique for the mesoscopic layers, but some alternatives can be found. Spin coating can be used for both the deposition of the mesoporous TiO_2 as well as the insulating layer (predominantly ZrO_2 but SiO_2 [23] and Al_2O_3 [24] have also been used). Spin coating allows the deposition of very consistent and thin layers, but the thick carbon layer is more challenging and as such screen printing or doctor blading is preferred. The doctor blade is a simple coating technique where a blade spreads ink on a surface. The method can be simply used for either lab or industrial-scale applications. A disadvantage of doctor blading compared to screen printing is the inability to produce any patterning.

An alternative approach to print the mesoscopic layers is via inkjet [22]. The method is simple and very versatile in the customization of the pattern and it can be used for all the layers, including the infiltration of perovskite [36]. The disadvantage compared to screen printing is the cost of the equipment and the production time. The deposition of a very large area film can be near-instantaneous by screen printing, whereas inkjet can take several minutes, depending on the number of nozzles present on the printing head.

The use of mesoporous layers requires high-temperature heat treatment, typically achieved in a furnace, to remove the organic binder and leave open pores. This crucial step can be time-consuming and requires significant consumption of energy [49]. Radiative annealing processes can speed up notably the heating step with lower energy consumption. Processes that last hours can be reduced to minutes, seconds, or even milliseconds. Such annealing processes have been already demonstrated for the annealing of the perovskite layers. The annealing of perovskite can be 90 minutes on conventional hot plate, but it can be reduced to 2.5 seconds via near-infrared radiation (NIR) [50] or even 1 ms via photonic [51]. The difference in speed between photonic and NIR is huge, although NIR is still fast enough for conventional production lines. NIR has already been demonstrated for the annealing of the inorganic triple stack of mCPSCs by Baker et al in 2017 [52]. In this case, the manufacture was sped up from a few hours to a few seconds with negligible effect on device performance.

9.2.4 Deposition of Additional Interlayers

The inorganic stack in mCPSC is typically based on three layers, but in some instances, an additional layer is used. For example, an inorganic and mesoporous hole transporting layer (HTL) can be added to enhance the hole extraction. The most common HTL is NiO [5, 21, 29] but other thermostable materials have been shown, such as Co_3O_4 [20]. In these cases, the layers are usually deposited via screen printing or doctor blade between the insulating and carbon layers. Alternatively, flame-assisted CVD (FACVD) can be a viable deposition method for NiO nanoparticles, as reported by Yates et al. in 2019 and 2020 [31, 53].

A further thin insulating layer between TiO_2 and the insulating layer can improve the performance of the device. This thin film, generally Al_2O_3, was shown to improve the V_{OC} compared to standard architectures. Its effect is so important that the mesoscopic insulating layer could even be removed, although the synergy of both thin Al_2O_3 and

mesoscopic ZrO_2 was reported to improve considerably the device performance. These thin layers were deposited via sputtering by Mathiazhagan et al. in 2020 [25], spray pyrolysis by Wang et al. in 2018 [28], or vacuum evaporation of Al and subsequent oxidation by Xiong et al. 2018 [32].

9.2.5 Infiltration of Perovskite

Many different perovskite formulations have been demonstrated for mCPSC. The first formulation was the methylammonium lead iodide perovskite ($CH_3NH_3PbI_3$, MAPI) in 2013 [2]. MAPI can be deposited via the one-step method, i.e. the infiltration of a solution with all the perovskite precursors, or the two-step, i.e. the infiltration of PbI_2 first and conversion into MAPI via dipping in a solution of methylammonium iodide (CH_3NH_3I, MAI). After this reported work in Ref. [2], improved performance and device stability was observed with the addition of 5-aminovaleric acid iodide ($NH_3(CH_2)_4COOHI$, AVAI) in the perovskite precursor solution, producing a 2D/3D perovskite structure ($AVA_xMA_{x-1}PbI_3$) [3, 12]. Other perovskite formulations with different or mixed cations, such as Cs^+ or formamidinium (($NH_2)_2CH^+$, FA^+), or different halides, such as Br^-, have been shown via either one-step or two-step methods.

The infiltration method itself can be considered one of the most straightforward steps of device fabrication, however, achieving appropriate drying and crystallization is complex. The process itself is simple, as the ink must only be added on top of the carbon surface to initiate infiltration. The solvent will evaporate with a gentle heating step leading to perovskite crystallization. This process is usually carried out via manual dropping at lab scale, resulting in very high-performance single-cell devices. As can be expected, the difficulty arises from the fact that if the infiltration is not complete or homogenous, the device will not function. The challenge increases over large area, where the dropping method is impractical and prone to inhomogeneities. Under these circumstances, the perovskite precursor solution in contact with the hydrophobic carbon layer can reorganize itself, resulting in an unwanted pattern. An approach developed to resolve this issue is the use of a robotic dispenser to continuously dispense the solution, and a fine mesh to control the infiltration (Figure 9.8a). This technique, named robotic mesh (RbM), was demonstrated for the infiltration of perovskite in the two-step method [33] and then also used for the one-step method [15, 34].

Alternative approaches to deposit perovskite can be used. Inkjet is an important example and it was demonstrated by Hashmi et al in 2017 for the infiltration of AVA-MAPI perovskite [36]. Slot-die was also employed for the infiltration of modules by Bashir et al in 2019 and Xu et al in 2020 [21, 35] (Figure 9.8b). A list of reports using different techniques to infiltrate perovskite in the mCPSC can be found in Table 9.1.
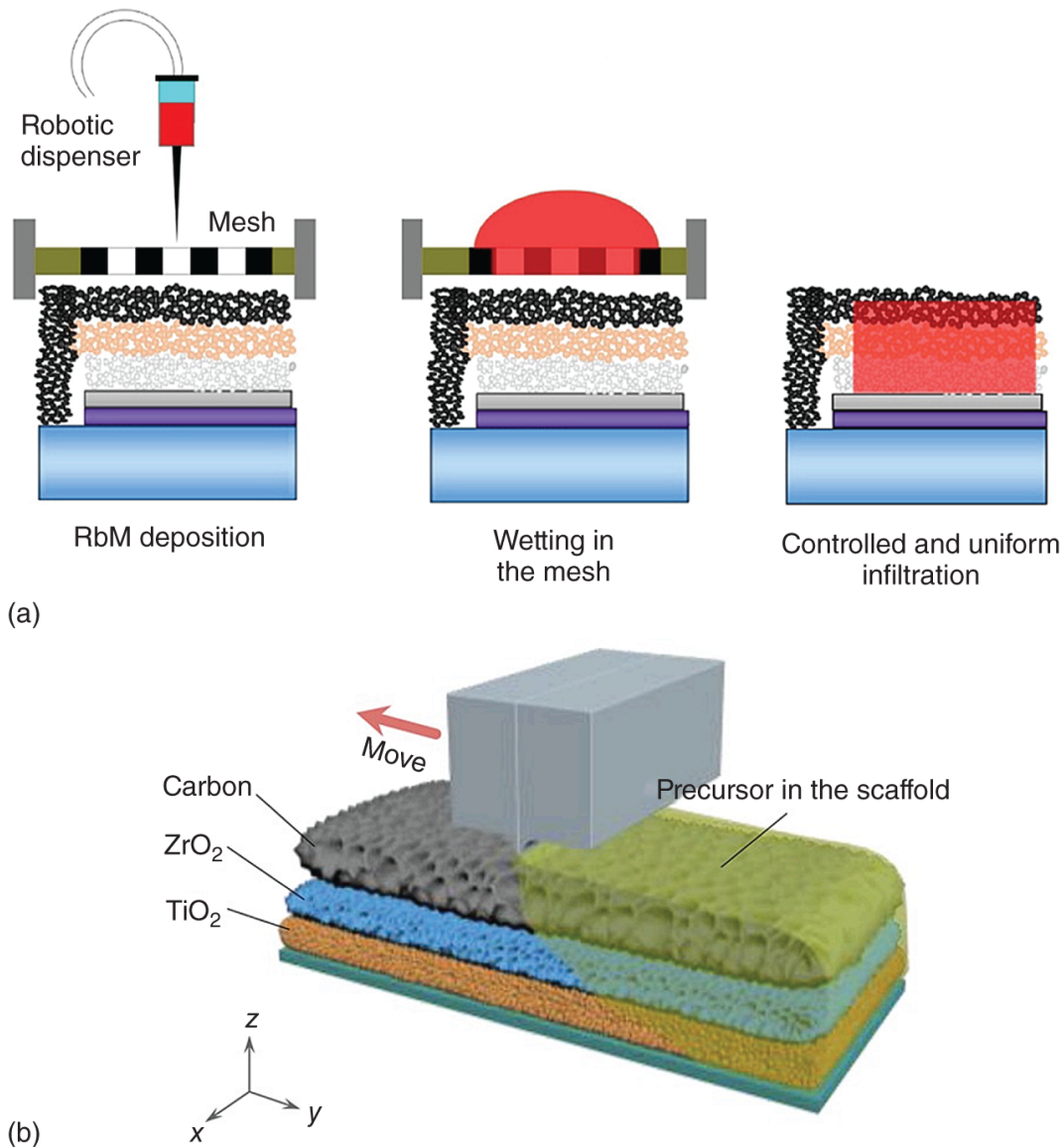
Figure 9.8 Infiltration methods for mCPSC. (a) Schematic representation of the RbM process. Source: Meroni et al. [33]/Taylor & Francis/CC BY-4.0. (b) Schematic representation of slot-die process. Source: Xu et al. [35]/With permission of Elsevier.

9.3 Modules

The resistance of the electrodes, especially of the transparent conductive layer, can make the fabrication of efficient large single cells impossible [54, 55]. To overcome the limits of electrode conductivity, parallel or series-connected modules can be designed. A typical design for a module is based on long and narrow single cells separated by a gap (Figure 9.9). These narrow single cells define the active area, and the width of each cell is called active area width (W_a). The gap between the cells is required to include interconnects, either bus bars to extract the current (see parallel connected modules) or the connection in series to allow the current to flow from one cell to another. From a current generation perspective, this area is called the dead area. The width of the dead area (W_d) defines the distance between the cells. The overall substrate area also includes

a lateral frame to place the electrical contacts or any other service space for the manufacture of the device, for example, the encapsulation. The aperture area is the area occupied by the active and dead areas.
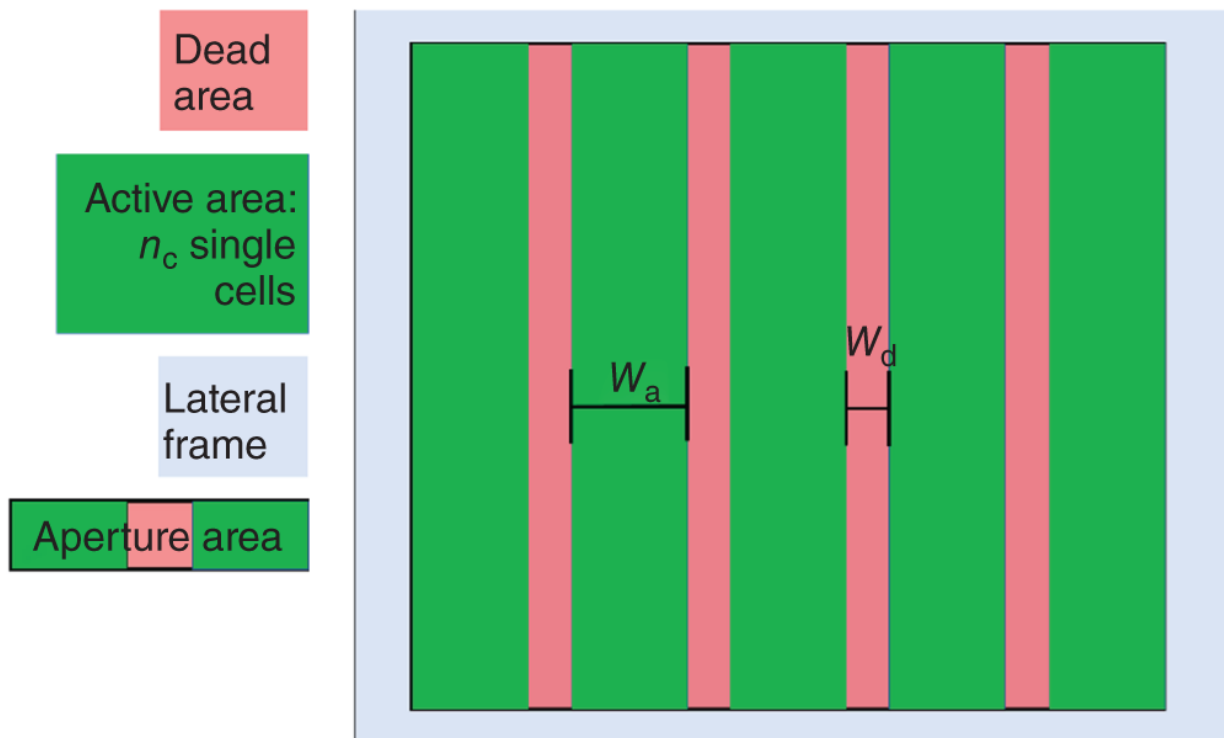
Figure 9.9 Generic schematic of a module with five single cells.

9.3.1 Designs

The single cells can be connected in parallel, for high-current devices, or in series, for high voltage modules. An example of a module in lateral view is shown in Figure 9.10a. A combination of parallel and series-connected modules can be used in certain circumstances to customize the current and voltage output of the device, either on the same substrate or via external connections.

The interconnects are crucial for the current flow between cells. In manufacturing terms, the interconnects can be created via registration of each layer, using printing technology, or via material removal (scribing method). The registration approach exploits the ability of the printing process to pattern each deposited layer. A very accurate registration between each layer can create the desired electrical connections in the substrates. For example, in mCPSC series-connected modules, the carbon layer must cover the ZrO_2 layer without touching the TiO_2 layer and connect the FTO of the following cell (see Figure 9.10b inset). The scribing method, by contrast, does not strictly require a printing process as all the layers are deposited on a solid area and the interconnects are created via removal of material on a specific location. The registration method is the most obvious approach for the mCPSC. Starting from a pre-patterned substrate, the three inorganic layers are printed sequentially with an increasing offset to create the interconnects via overlapping areas. The registration method is simple and allows the fabrication of efficient modules. The g-FF relies on the accuracy of the printing equipment on a pre-patterned substrate. This is because a safe area must be included to avoid mismatching between layers, thus, short circuits in the device. High accuracy allows a reduction of

these safe areas and increases space for active materials. Outstanding examples of mCPSC modules prepared via registration are from the following:
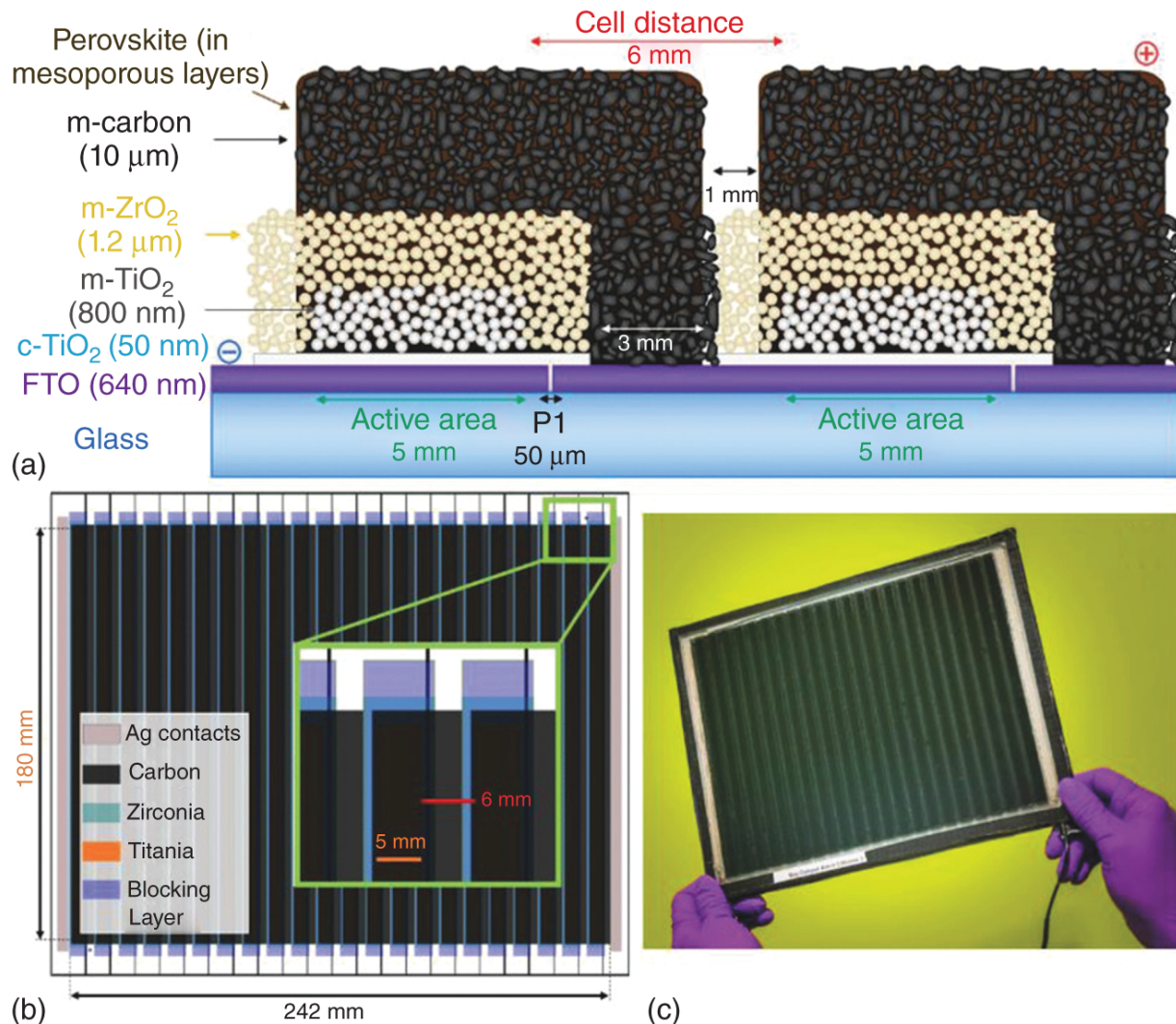
Figure 9.10 Example of modules prepared via the registration method. (a) Cross-section schematics of adjacent cells in a series-connected module. The single cells are defined by the presence of TiO_2. The distance between the cells is the result of the carbon/FTO contact area and the safe area to avoid mismatching between layers. (b) Module schematics, showing the different overlapping layers. In the inset, a blow-up of three single cells, showing the position of each layer. (c) Photo of a module. Source: De Rossi et al. [15], John Wiley & Sons.

- Grancini et al. in 2017 [12]. A module with more than 10.1% PCE was demonstrated on a 10× 10 cm^2 substrate and 46.7 cm^2 active area.
- Hu et al. in 2017 [13]. A module with more than 10.4% PCE was demonstrated on a 10× 10 cm^2 substrate and 49 cm^2 active area.
- De Rossi et al in 2018 [15]. A module with more than 6.6% PCE was demonstrated on a 27.5× 21 cm^2 substrate and 198 cm^2 active area (shown in Figure 9.10c).

The scribing method, by contrast, does not rely on the accuracy of the printing equipment, but on the alignment of the substrate relative to the scribing agents. The scribing agents can be anything that can remove materials, such as a blade – mechanical scribing – or a laser. The layers are printed or deposited on a solid area and the scribing process removes material, so that subsequent layers can be applied, to achieve the electrode-to-electrode interconnect. The scribes are named P1 on the transparent electrode, P2 on the active layers, and P3 on the top electrode (Figure 9.11). The g-FF can be much higher than in the registration method, as some waste of space, due to possible misalignments during the printing, can be removed. The approach is very simple and, when using blades, the cost of the equipment remains low, protecting the low-capital cost principle of the architecture. Examples of mCPSC modules prepared via the scribing method are given below:

- Meroni et al. in 2020 [34]. A module with more than 10.3% PCE on a $10 \times 10\,\mathrm{cm}^2$ substrate via the low-capital cost mechanical scribing.
- Xu et al. in 2020 [35]. A module with more than 12.8% PCE on a $10 \times 10\,\mathrm{cm}^2$ substrate via laser scribing.

9.3.2 Optimization

The dimensions of the single cells and the distance between them are key to optimizing module performance. Very large single cells can suffer from the high resistance at the electrode, while very narrow ones require a large number of interconnects, reducing the active area. The optimal design can be estimated with high accuracy via theoretical consideration.

The main parameters to define a design are W_a and W_d. W_d should be minimized as much as possible because it defines the dead area. However, the minimization of W_d is limited by the size of the interconnects, i.e. the area where top and bottom contacts overlap, as shown in Figure 9.12. The interconnects are crucial to ensure current flow in the device. A large W_a can be beneficial to reduce the number of interconnects. This is because a lower number of cells can fit on the same substrate when these are large, reducing also the number of interconnects between them. If the number of cells is n_c, the number of interconnects is $n_c - 1$. Thus, a lower number of interconnects increases the coverage of the substrate with active material (g-FF). However, large W_a can increase the resistance in the device with a considerable current–resistance (iR) drop effect. When W_a is large, the charge must travel for a long distance before being injected into the following single cell. A narrow W_a can reduce this distance and the resistance of the electrodes. Therefore, while W_d can be simply minimized provided that the interconnects are large enough to electrically connect the single cells, the optimal W_a is the result of a compromise between high g-FF and low resistance of the electrodes. To determine the optimal W_a, some theoretical considerations can be made.

9.3.2.1 A Simplified Approach

For small distances, the problem can be simplified with the consideration of constant resistance of the electrode (R_{el}) in relationship with the geometrical characteristic of the single cells without the use of any integral. This simple approach, proposed by Giordano et al. in 2011, was proved to be effective in double glass sealing modules and can give a good approximation for different design scenarios [56]. In short, the total R_s (series resistance) can be represented with an internal vertical resistance R_{vc}, which is constant, plus the resistance of the electrode R_{el}, which changes with the design geometry, i.e.:
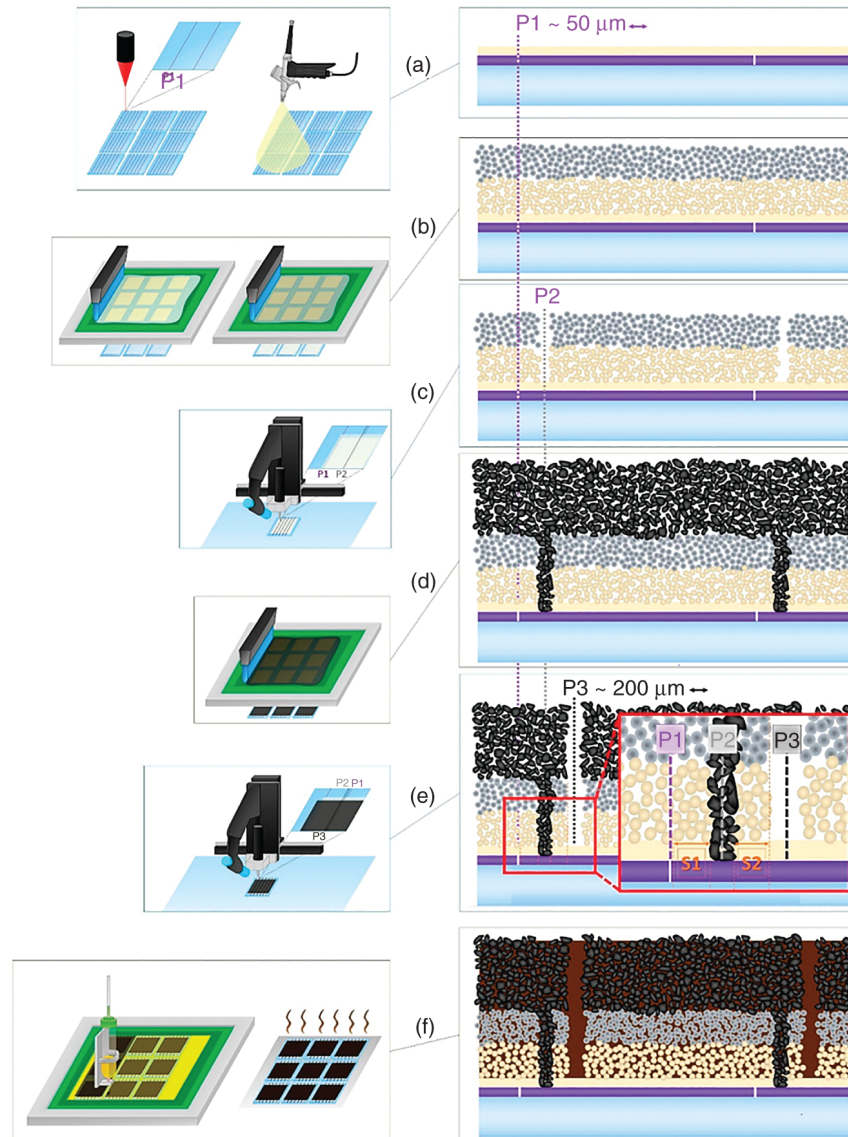
Figure 9.11 The mCPSC module based on the scribing method. (a) P1 on a substrate of glass/FTO/bLayer via laser scribing and then deposition of the bLayer. (b) Deposition of mesoporous TiO_2 and ZrO_2 via screen printing. (c) P2 via mechanical scribing to open an aperture for the interconnects. (d) Deposition of the top carbon electrode. (e) P3 to insulate the cells in series. In the inset, a magnification of the interconnection area shows the three scribes and the distance between them, i.e. S1 and S2. (f) Perovskite infiltration. Source: Meroni et al. [34]/MDPI/CC BY-4.0.

Figure 9.12 Schematic representation of a series-connected module with three single cells. Above, the top view; below, a lateral view.

$$R_s = R_{vc} + R_{el}; R_{el} = R_{sq} \frac{W_a + W_d}{H} \tag{9.5}$$

where R_{sq} is the sheet resistance of the transparent electrode, and H is the length of the single cell. This calculation assumes that one of the two electrodes can be considered unaffected by the design geometry, which is the case for most of the devices using metal contacts, e.g. Au or Ag. The calculated values are very close to the experimental ones, especially when W_a is very narrow, i.e. few mm wide (Figure 9.13). This method can closely predict the effect of the geometry on the single cell and on the module. The method has the advantage to be very simple and it does not require a high computing time. The tiny error that this method commits is largely compensated by the huge simplification of the problem.

9.3.2.2 2D Poisson's Equation

The simplified approach can be unsuitable for modules with very large cells and when the resistance of one of the two electrodes cannot be neglected. In case of mCPSC, no metal

contacts are utilized, and the carbon electrode is often more resistant than the FTO. More accurate models should include Poisson's equation. This was done by Galagan et al. in 2016 by solving the 2D Poisson's equation with the aid of COMSOL [57]. As for the simplified approach, the effect of the lateral resistance was taken into account starting from R_{sq} of the electrodes as:

$$\nabla \cdot \frac{1}{R_{sq}^{top}} \cdot \nabla V^{top} = J_p \Delta V \qquad (9.6)$$
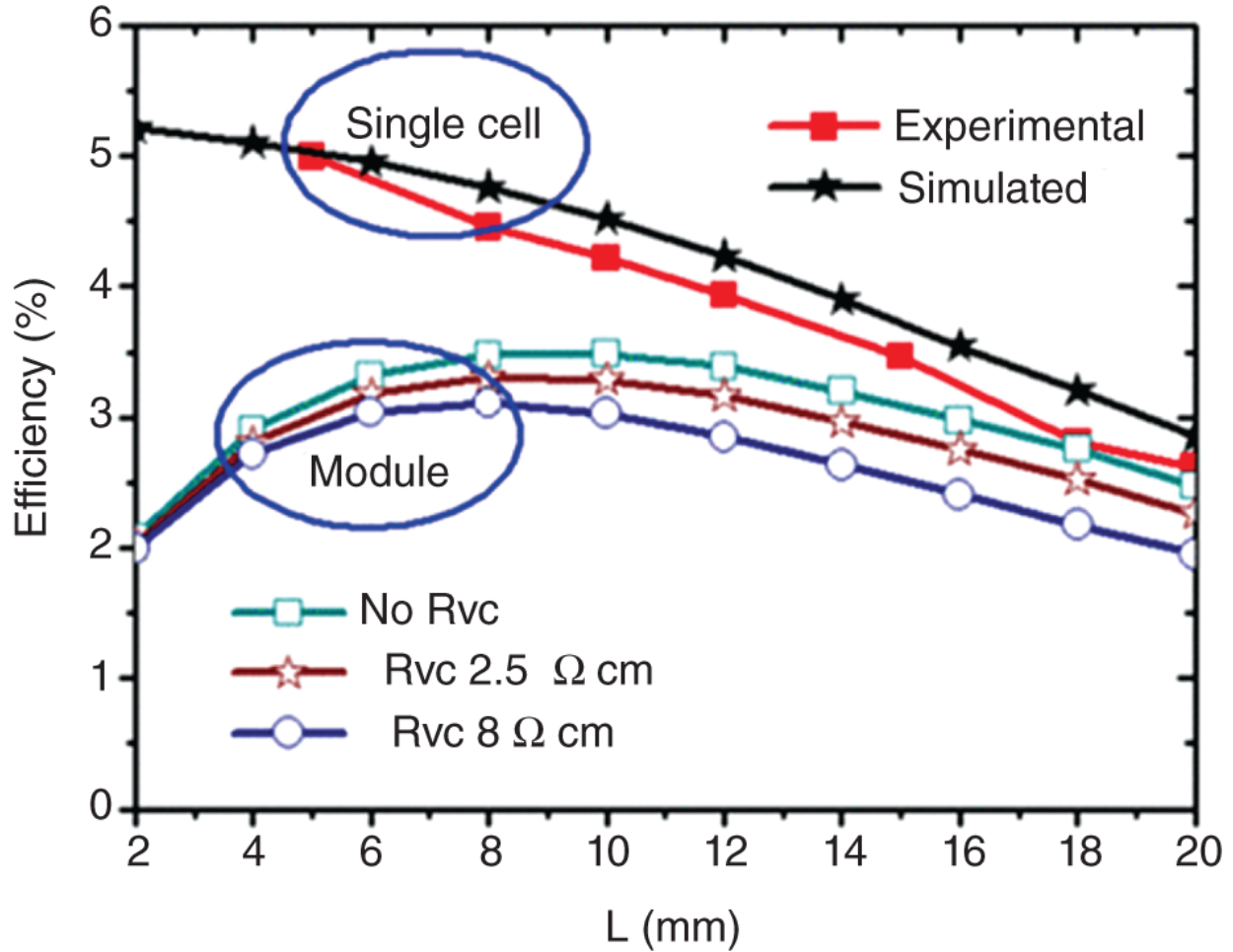
Figure 9.13 PCE of unit cells (experimental and simulated) and of Z modules. In case of modules, the PCE is referred to as the aperture area. R_{vc} is an additional internal resistance considering the vertical charge transfer and is independent from the module geometry. Source: Giordano et al. [56]/IEEE.

$$\nabla \cdot \frac{1}{R_{sq}^{bottom}} \cdot \nabla V^{bottom} = J_p \Delta V \qquad (9.7)$$

where R_{sq}^{top} and R_{sq}^{bottom} are the sheet resistance of the top and bottom electrodes, ∇V^{top} and ∇V^{bottom} are the voltage gradient at the top and bottom electrodes (in 2D) and ΔV is the electrical potential difference between the top and bottom electrodes. ΔV is the externally applied voltage when the edge of one of the electrodes is connected to the

ground and the edge of the other electrode is prescribed to a working V. J_p is the density of current at the different positions of the cell. The density of current of the device, J_{cell}, at given applied voltage is

$$J_{cell} = \frac{1}{A_{cell}} \cdot \int J_p dA_p \tag{9.8}$$

which is a normalized integral over the entire surface, or area, of the device.

The model was tested for a sandwich architecture with Au as top electrode (glass/ITO/TiO$_2$/perovskite/P$_3$HT/Au). The results can be represented as shown in Figure 9.14.

The results in Figure 9.14a show the gradient in generated power depending on the distance from the electrodes. It is evident that the size of the device becomes critical when the resistance of the electrodes increases. Figure 9.14b shows the effect of W_a and the resistance of the electrode. As one of the electrodes is Au, only the transparent electrode limits the geometry of the module. V_{OC} is completely unaffected from R_{sq} and W_a. J_{SC} is relatively low when W_a is low. This is because the current density is referred to the total area of the device and g-FF is low in this condition. In short, the low current is due to the low coverage of active material on the substrate and not by electrical issues. If J_{SC} was referred to the active area, the graph would show a plateau as the narrow single cells do not affect the current generation. J_{SC} is affected by the high resistance, as it is observed when W_a increases, especially with low conductive electrodes. The main parameter that is affected by the design is FF.
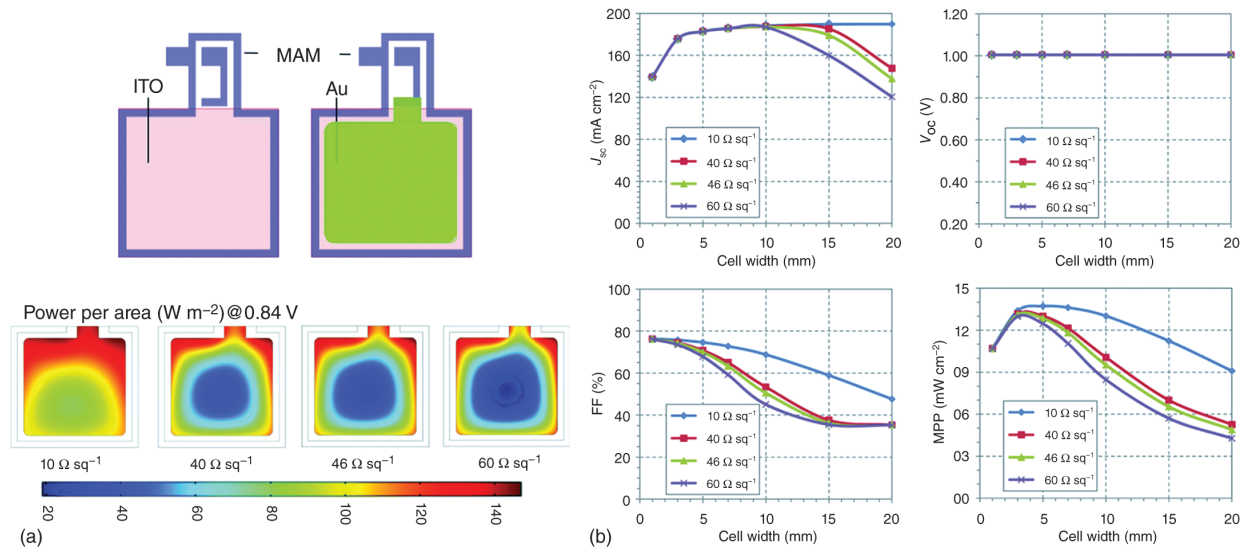
Figure 9.14 Reported results using Poisson's equation. (a) A study on single cells with a calculated power generation on the device area. (b) PV parameters of modules in different scenarios of W_a size and R_{sq} of the transparent electrode. The power density is referred to the device total area. Source: Galagan et al. [57]/With permission of Royal Society of Chemistry.
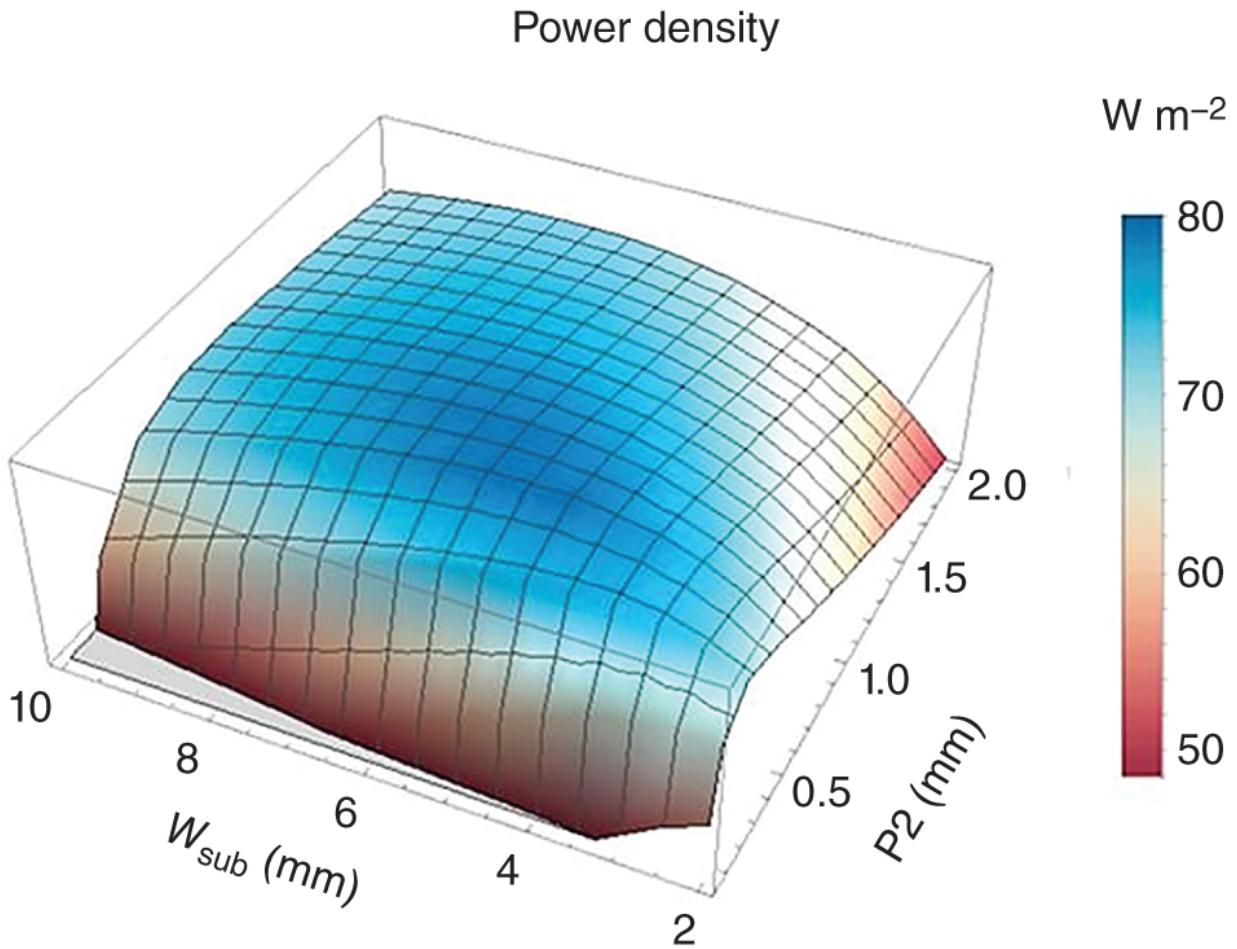
Figure 9.15 3D plot of generated power as function of P2 and W_a of a module made with 10 single cells connected in series for a carbon layer with $R_{sq} = 10\,\Omega_{sq}$ and $R_c = 60\,m\Omega$ at the interconnect. Source: Mouhamad et al. [58]/With permission of Elsevier.

9.3.2.3 Carbon Cells and Contact Resistance

The mCPSC can be quite different compared to the other PSC. The presence of a carbon electrode, which is comparable to the transparent electrode in terms of resistance, makes ineffective the use of the simplified method, as discussed above because the coupling effect of both top and bottom electrodes can affect device performance enormously. Furthermore, the contact resistance (R_c) can play an important role. R_c is the resistance element that connects two single cells and that is added to R_s. The presence of R_c can be usually neglected with metal contacts, as in [57]. However, a porous carbon electrode can affect R_c significantly, and the minimal contact area for effective interconnects must be determined. This is because, as discussed above, W_d must be minimized to maximize g-FF, but the dead area must contain the interconnects. The contact area is as large as the P2 in a series-connected scribed module (Section 9.3.1). The optimal contact area to achieve a compromise between high g-FF (or low W_d) and low R_c can be calculated with 2D Poisson's equation and was proposed by Mouhamad et al in 2019 [58]. Figure 9.15 shows a 3D plot of the module power density generation relatively to the device's total area and in function of both W_a and P2 (or contact area width), accounting for the effect of R_c.

According to these results, the optimal contact area (P2) is between 0.5 and 1 mm ([Figure 9.15](#)), much larger than typical interconnects, which are around 0.2 mm [59].

9.4 Applications

9.4.1 Modules Performance

Due to its low cost, good performance, and stability, the mCPSC is seen as the front-runner in the market [1]. To prove the effectiveness of the technology, mini-modules on 5 or $10\,cm^2$ substrates have been demonstrated in the literature. [Table 9.2](#) shows some examples of mCPSC modules reported in the literature.

[Table 9.2](#) Architecture, design, and performance of some of the most significant mCPSC modules reported in the literature.

References	Design: single cell/W_a (mm)/W_d (mm)	Area: active (cm^2)/substrate (cm^2)	g-FF: $(W_a/(W_a + W_d),$ %)	Scribing method?	PV parameters FF/Av$-V_{OC}$ (mV)/ Min$-J_{SC}$ $(mA\ cm^{-2})$
[14]	10 SC	**70/10 × 10**		No	**0.63**/963/**17.7**
[12]	**8 SC/7/3**	**48/10× 10**	70	No	**0.66**/900/17.0
[13]	**10 SC/5.3/5**	**49/10 × 10**	51.5	No	**0.56**/930/20.0
[15]	**22 SC/5.5/6**	**198/27.5 × 21**	47.8	No	**0.34**/895/21.3
[20]	10 SC	**70**		No	**0.57**/915/**22.1**
[60]	**9 SC/7.5/3**	**60/10 × 10**	71.4	No	**0.51**/844/23.4
[34]	**12 SC/5/2**	**50/10 × 10**	**71.4**	Yes, mechanical	**0.54**/866/22.2
[35]	**9 SC/7.5/2.5**	**60/10 × 10**	75	Yes, laser	**0.61/940/22.5**

Numbers in **bold** = stated in the article, in gray = calculated here from reported data. The g-FF is defined as $W_a/(W_a + W_d)$. Av-V_{OC} is the averaged V_{OC} of the single cells, i.e. the V_{OC} of the module divided by the number of cells. Min-J_{SC} is the minimal J_{SC} of the single cells, i.e. the current of the module referred to the area of a single cell in series connection in the module (see module design, [Section 9.3.1](#)).

Some modules have not been reported in the literature but illustrate outstanding examples of mCPSC modules. Wondersolar has fabricated 60× $60\,cm^2$ mCPSC modules with an active area of $2862.72\,cm^2$. Their preparation is based on the laser scribing method, proving the feasible fabrication of 71 series connected cells with a distance (W_d) of only 0.6 mm. With a W_a of 7.5 mm, the g-FF is nearly 93%. The performance of these modules is still undisclosed.

9.4.2 Encapsulation and Outdoor Performance

Device encapsulation is a key component of a completed mCPSC device. The encapsulation can act as a barrier from external agents, such as O_2 or moisture, but also as a protection from internal pollutants, such as Pb. A huge amount of work is still

necessary to prove the effectiveness of the encapsulation barrier, but some encouraging results have already been reported. Grancini et al reported one-year stability of devices kept under 1 sun illumination with UV filter and measured via regular JV scans [12]. Li et al reported high stability in outdoor conditions and hot weather, i.e. in Saudi Arabia, in 2015 [61]. Negligible degradation was observed after seven days of outdoor testing at above 40 °C. To study the device in more stressful conditions, some single cells were kept at 85 °C and regularly tested, showing negligible degradation after 90 days. Similarly, the devices were kept at 45 °C and continuously measured at maximal power point (MPP). The device showed no degradation after 44 days of test.

In terms of encapsulation, the mCPSC devices can be protected with similar strategies to other thin film devices. Glass–glass encapsulation is a common approach for PSC. This approach can be quickly summarized as having the device sandwiched between two glass sheets using a sealant. The sealants can be either thermo-curable, for example, ethylene vinyl acetate and surlyn ionomer, or UV-curable, for example, some epoxy resins [62]. Polymers can be also deposited directly on top of the device without the use of any glass sheet. This approach reduces the weight of the device and allows the encapsulation on flexible substrate. Some examples of polymers that can be deposited on the top of PSC without affecting the performance are poly(methyl methacrylate), polycarbonate, polyethylene naphthalate, and others [62]. Specifically for mCPSC, Fu et al reported the use of a polymeric film between the device and a top glass in 2019 [60] (Figure 9.16a,b). When using polyurethane (PU) films, the devices demonstrated high stability when kept at 85 °C for more than 300 hours.

An alternative approach adopted for mCPSC is the use of glass frit and laser ablation. Glass frit is a ceramic material that can be fused to obtain glass. A very accurate annealing step at a localized spot can fuse the frit to achieve a very good hermetic sealing around the device. The accurate annealing was achieved via laser (Figure 9.16c,d). The method was already proposed for DSSC [64] and used for mCPSC by Emami et al in 2020 [63]. The hermetically sealed mCPSC devices are not affected by the humidity of the external environment, as proven when the devices were aged in a humidity-air chamber. The humid air feed was produced by humidifying a 450 ml min^{-1} dry air feed to a cylindrical column filled with distilled water. Under these conditions, unencapsulated devices lost 100% of the original PCE in 50 hours, while the encapsulated devices did not show any degradation after 500 hours. This proved that the encapsulation strategy is very effective against humidity.
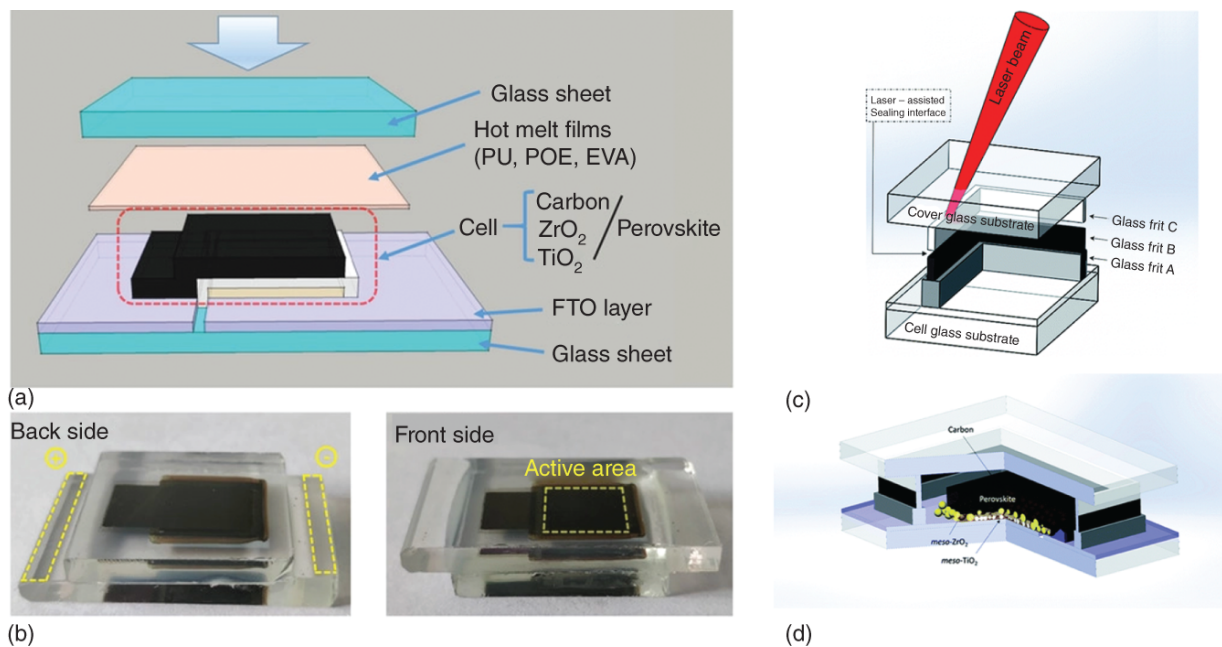
Figure 9.16 (a) The scheme of the encapsulation of mCPSCs based on hot melt films and glass sheets. (b) Images of the encapsulated cells. Source: Fu et al. [60]/With permission of John Wiley & Sons. Schematic view of (c) glass frit laser-assisted sealing configuration, and (d) encapsulated mCPSC device. Source: Emami et al. [63]/With permission of Royal Society of Chemistry.

9.4.3 Indoor Applications

The stability of mCPSC has been demonstrated as superior to a number of other PSC architectures for outdoor applications. The stability indoors can be expected to be even higher due to the lack of weathering stress, such as high illumination, high temperature, and high humidity. Perovskite is degraded by a combination of different factors, in particular O_2, moisture, high temperature, and UV light [65–69]. Factors like moisture and O_2 can be removed with a proper encapsulation strategy. UV light and temperature are related to the intrinsic stability of the device architecture or can be removed via approaches that can reduce the efficiency of the device, such as UV filters or energy-consuming chillers. The presence of UV light and high temperature can represent an issue outdoors but not indoors. UV light is not generated from indoor light sources, such as fluorescence lamps or LEDs. Light intensity is generally much lower, around 3 orders of magnitude lower, and no light-induced heating is expected indoors. The use of indoor PV systems is also promising for IoT (internet of things) applications, showing an interesting market for emerging PV. Due to the commercial value and the expected long-term stability indoors, Lee et al compared the performance of mCPSC with mesostructured and planar structures under fluorescence lamps in 2018 [70] (Figure 9.17). The mesoporous structures were nip devices with either spiro-OMeTAD or PTAA as HTL, while the planar structures were pin devices with either PEDOT:PSS or poly-TPD as HTL. The mCPSC was lower in performance compared with the other PSC architectures when tested under 1 sun illumination, but it showed much better results when measured under indoor illumination (1000 and 200 lx). When tested under 1 sun, the mCPSC generated only 60% of the power of the best PSC device (planar with poly-TPD 17.0%, mCPSC 11.2%) and it generated the least power compared to the other architectures (Figure 9.17). However, the situation was very different when the devices were measured under fluorescent lamps at 1000 lx. The mCPSC behaved much better than the device with PEDOT : PSS or PTAA

and generated nearly 80% of the power of the best device (in this case with Spiro-OMeTAD and poly-TPD). The trend was then confirmed at 200 lx when the mCPSC generated more than 80% of the power of the best devices in this experiment (Figure 9.17). The power generation of the mCPSC is comparable (or better in some instances) to the expensive PSC architecture, which is based on metal-evaporated electrodes. The indoor power generation of the mCPSC can reach the power generation of the best PSC devices and this can be explained by considering the conductivity of the top electrode. Carbon is not as conductive as metal (Au or Ag) contacts are. This means that it suffers from high resistance when the transported current is high due to the iR-drop. When the current is low, such as indoors, this resistance does not play a significant role, and the mCPSC recovers in performance. This opens opportunities in decreasing the carbon top contact resistance, for example, via applying metallic grids on top [71]. This experiment suggests that mCPSC is a technology ready for commercial (indoors) applications.
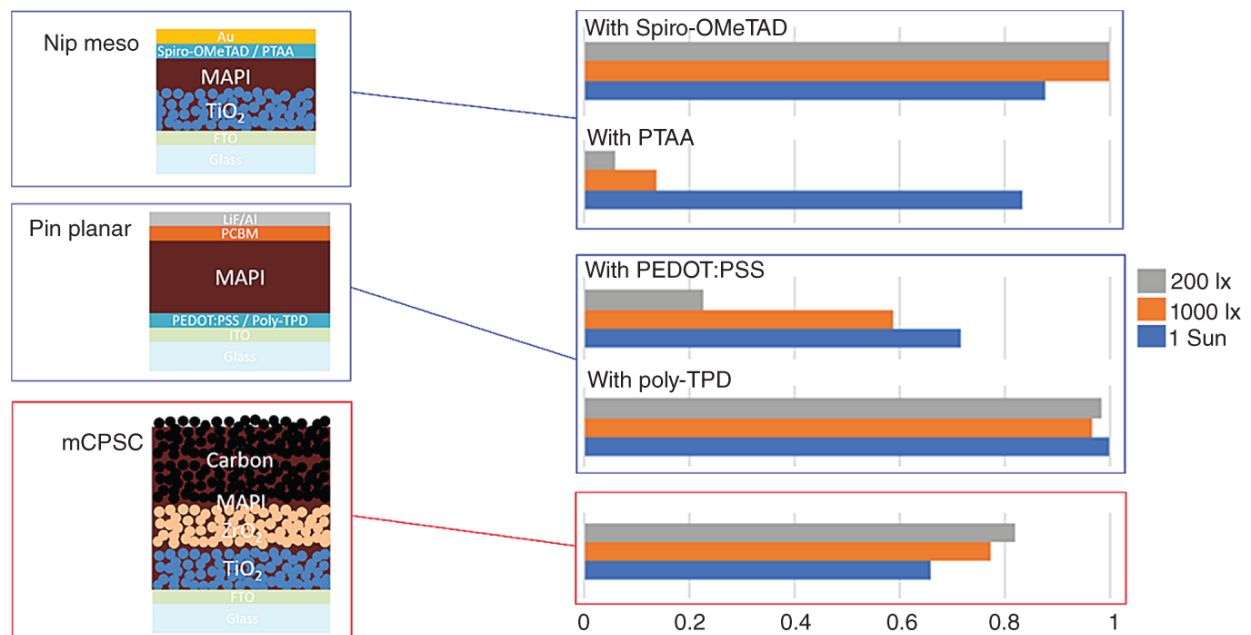
Figure 9.17 Comparison of device performance under different illumination conditions. The more expensive architectures of mesoscopic nip with Spiro-OMeTAD of PTTA as HTL and planar pin with PEDOT:PSS and poly-TPD were compared with the low cost and stable mCPSC. The power generation for each kind of device is shown as normalization to the highest-performing device in the illumination condition under study. The blue color shows the performance under 1 Sun (AM 1.5G), orange under 1000 lx, gray under 200 lx (fluorescent lamps). Source: Lee et al. [70]/With permission of John Wiley & Sons.

9.5 Summary

This chapter described three main engineering aspects of the fully printable triple mCPSC: the manufacture, the module design, and studies on the application of modules in outdoor and indoor conditions.

Manufacturing is the key to achieving the best compromise between high device performance and low-cost production. The low cost of the mCPSC is due to three main aspects: the low cost of the manufacture for high volume production; the low cost of the adopted materials; the low-capital cost that reduces the initial investment (due to the low cost of the equipment). All of this is possible, especially thanks to the industry-established

screen-printing method. The printing method is also key for the manufacture of large modules on a single substrate, i.e. without external connections. The performance of the devices was demonstrated to be relatively consistent at different sizes, proving that the up-scaling process is easily achievable.

The design of the module plays an important role in the final power generation of the device. An optimized design can reduce the effect of parasitic resistances such as series resistance (R_s) and contact resistance (R_c). Furthermore, a good working device has a high geometrical fill factor, i.e. a high coverage of the substrate with active materials, enhancing the exploitation of the available space for power generation.

The stability of the devices is outstanding compared to other PSCs. Still, plenty of work must be done to enhance the intrinsic stability of the devices and the effectiveness of the encapsulation strategy.

Considering its low cost, the good performance of its large area modules, and its stability, the mCPSC is an example of PSC capable of achieving market penetration in the near future.

References

1 Chen, H. and Yang, S. (2017). Carbon-based perovskite solar cells without hole transport materials: the front runner to the market? *Advanced Materials* 29 (24): 1603994. https://doi.org/10.1002/adma.201603994.

2 Ku, Z., Rong, Y., Xu, M. et al. (2013). Full printable processed mesoscopic $CH_3NH_3PbI_3/TiO_2$ heterojunction solar cells with carbon counter electrode. *Scientific Reports* 3 (1): 3132. https://doi.org/10.1038/srep03132.

3 Mei, A., Li, X., Liu, L. et al. (2014). A hole-conductor-free, fully printable mesoscopic perovskite solar cell with high stability. *Science* 345 (6194): 295–298. https://doi.org/10.1126/science.1254763.

4 NREL (2020). Best research-cell efficiency chart. https://www.nrel.gov/pv/assets/pdfs/best-research-cell-efficiencies.20200406.pdf (accessed 29 April 2020).

5 Liu, S., Huang, W., Liao, P. et al. (2017). 17% efficient printable mesoscopic PIN metal oxide framework perovskite solar cells using cesium-containing triple cation perovskite. *Journal of Materials Chemistry A* 5 (44): 22952–22958. https://doi.org/10.1039/c7ta07660f.

6 Wang, Q., Zhang, W., Zhang, Z. et al. (2020). Crystallization control of ternary-cation perovskite absorber in triple-mesoscopic layer for efficient solar cells. *Advanced Energy Materials* 10 (5): 1903092. https://doi.org/10.1002/aenm.201903092.

7 Rong, Y., Hu, Y., Mei, A. et al. (2018). Challenges for commercializing perovskite solar cells. *Science* 361 (6408): eaat8235. https://doi.org/10.1126/science.aat8235.

8 Hu, X., Huang, Z., Li, F. et al. (2019). Nacre-inspired crystallization and elastic 'brick-and-mortar' structure for a wearable perovskite solar module. *Energy & Environmental Science* 12 (3): 979–987. https://doi.org/10.1039/C8EE01799A.

9 Bu, T., Liu, X., Li, J. et al. (2020). Dynamic antisolvent engineering for spin coating of 10 × 10 cm^2 perovskite solar module approaching 18%. *Solar RRL* 4 (2): 1900263. https://doi.org/10.1002/solr.201900263.

10 Dai, X., Deng, Y., Van Brackle, C. et al. (2020). Scalable fabrication of efficient perovskite solar modules on flexible glass substrates. *Advanced Energy Materials* 10 (1): 1903108. https://doi.org/10.1002/aenm.201903108.

11 Bu, T. et al. (2018). Universal passivation strategy to slot-die printed SnO_2 for hysteresis-free efficient flexible perovskite solar module. *Nature Communications* 9 (1): 4609.

12 Grancini, G., Roldán-Carmona, C., Zimmermann, I. et al. (2017). One-year stable perovskite solar cells by 2D/3D interface engineering. *Nature Communications* 8 (14): 15684. https://doi.org/10.1038/ncomms15684.

13 Hu, Y., Si, S., Mei, A. et al. (2017). Stable large-area (10×10 cm^2) printable mesoscopic perovskite module exceeding 10% efficiency. *Solar RRL* 1 (2): 1600019. https://doi.org/10.1002/solr.201600019.

14 Priyadarshi, A., Haur, L.J., Murray, P. et al. (2016). A large area (70 cm^2) monolithic perovskite solar module with a high efficiency and stability. *Energy & Environmental Science* 9 (12): 3687–3692. https://doi.org/10.1039/c6ee02693a.

15 De Rossi, F., Baker, J., Beynon, D. et al. (2018). All printable perovskite solar modules with 198 cm^2 active area and over 6% efficiency. *Advanced Materials Technologies* 3 (11): 1800156. https://doi.org/10.1002/admt.201800156.

16 Meredith, P. and Armin, A. (2018). Scaling of next generation solution processed organic and perovskite solar cells. *Nature Communications* 9 (1): 8–11. https://doi.org/10.1038/s41467-018-05514-9.

17 Connell, A., Wang, Z., Lin, Y.-H. et al. (2019). Low cost triazatruxene hole transporting material for >20% efficiency perovskite solar cells. *Journal of Materials Chemistry C* 7 (18): 5235–5243. https://doi.org/10.1039/C8TC04231D.

18 Ku, Z., Xia, X., Shen, H. et al. (2015). A mesoporous nickel counter electrode for printable and reusable perovskite solar cells. *Nanoscale* 7 (32): 13363–13368. https://doi.org/10.1039/C5NR03610K.

19 Priyadarshi, A., Bashir, A., Gunawan, J. et al. (2017). Simplified architecture of a fully printable perovskite solar cell using a thick zirconia layer. *Energy Technology* 5 (10): 1866–1872. https://doi.org/10.1002/ente.201700474.

20 Bashir, A., Shukla, S., Lew, J.H. et al. (2018). Spinel Co_3O_4 nanomaterials for efficient and stable large area carbon-based printed perovskite solar cells. *Nanoscale* 10 (5): 2341–2350. https://doi.org/10.1039/c7nr08289d.

21 Bashir, A., Lew, J.H., Shukla, S. et al. (2019). Cu-doped nickel oxide interface layer with nanoscale thickness for efficient and highly stable printable carbon-based perovskite solar cell. *Solar Energy* 182 (December 2018): 225–236. https://doi.org/10.1016/j.solener.2019.02.056.

22 Verma, A., Martineau, D., Abdolhosseinzadeh, S. et al. (2020). Inkjet printed mesoscopic perovskite solar cells with custom design capability. *Materials Advances* 1: 153–160. https://doi.org/10.1039/D0MA00077A.

23 Liu, H., Yang, B., Chen, H. et al. (2018). Efficient and stable hole-conductor-free mesoscopic perovskite solar cells using SiO_2 as blocking layer. *Organic Electronics* 58 (February): 69–74. https://doi.org/10.1016/j.orgel.2018.04.008.

24 Zhou, L., Zuo, Y., Mallick, T.K., and Sundaram, S. (2019). Enhanced efficiency of carbon-based mesoscopic perovskite solar cells through a tungsten oxide nanoparticle additive in the carbon electrode. *Scientific Reports* 9 (1): 1–8. https://doi.org/10.1038/s41598-019-45374-x.

25 Mathiazhagan, G., Wagner, L., Bogati, S. et al. (2020). Double-mesoscopic hole-transport-material-free perovskite solar cells: overcoming charge-transport limitation by sputtered ultrathin Al_2O_3 isolating layer. *ACS Applied Nano Materials* 3 (3): 2463–2471. https://doi.org/10.1021/acsanm.9b02563.

26 Xu, X., Liu, Z., Zuo, Z. et al. (2015). Hole selective nio contact for efficient perovskite solar cells with carbon electrode. *Nano Letters* 15 (4): 2402–2408. https://doi.org/10.1021/nl504701y.

27 Cao, K., Zuo, Z., Cui, J. et al. (2015). Efficient screen printed perovskite solar cells based on mesoscopic TiO_2/Al_2O_3/NiO/carbon architecture. *Nano Energy* 17: 171–179. https://doi.org/10.1016/j.nanoen.2015.08.009.

28 Wang, Q., Liu, S., Ming, Y. et al. (2018). Improvements in printable mesoscopic perovskite solar cells: via thinner spacer layers. *Sustainable Energy & Fuels* 2 (11): 2412–2418. https://doi.org/10.1039/c8se00332g.

29 Liu, Z., Zhang, M., Xu, X. et al. (2015). NiO nanosheets as efficient top hole transporters for carbon counter electrode based perovskite solar cells. *Journal of Materials Chemistry A* 3 (47): 24121–24127. https://doi.org/10.1039/C5TA06458A.

30 Behrouznejad, F., Tsai, C.-M., Narra, S. et al. (2017). Interfacial investigation on printable carbon-based mesoscopic perovskite solar cells with NiO_x/C back electrode. *ACS Applied Materials & Interfaces* 9 (30): 25204–25215. https://doi.org/10.1021/acsami.7b02799.

31 Yates, H.M., Meroni, S.M.P., Raptis, D. et al. (2019). Flame assisted chemical vapour deposition NiO hole transport layers for mesoporous carbon perovskite cells. *Journal of Materials Chemistry C* 7 (42): 13235–13242. https://doi.org/10.1039/C9TC03922H.

32 Xiong, Y., Zhu, X., Mei, A. et al. (2018). Bifunctional Al_2O_3 interlayer leads to enhanced open-circuit voltage for hole-conductor-free carbon-based perovskite solar cells. *Solar RRL* 2 (5): 1800002. https://doi.org/10.1002/solr.201800002.

33 Meroni, S.M.P., Mouhamad, Y., De Rossi, F. et al. (2018). Homogeneous and highly controlled deposition of low viscosity inks and application on fully printable perovskite solar cells. *Science and Technology of Advanced Materials* 19 (1): 1–9. https://doi.org/10.1080/14686996.2017.1406777.

34 Meroni, S.M.P., Hooper, K., Dunlop, T. et al. (2020). Scribing method for carbon perovskite solar modules. *Energies* 13 (7): 1589. https://doi.org/10.3390/en13071589.

35 Xu, M., Ji, W., Sheng, Y. et al. (2020). Efficient triple-mesoscopic perovskite solar mini-modules fabricated with slot-die coating. *Nano Energy* 74 (March): 104842. https://doi.org/10.1016/j.nanoen.2020.104842.

36 Hashmi, S.G., Martineau, D., Li, X. et al. (2017). Air processed inkjet infiltrated carbon based printed perovskite solar cells with high stability and reproducibility. *Advanced Materials Technologies* 2 (1): 1600183. https://doi.org/10.1002/admt.201600183.

37 Rong, Y., Ku, Z., Mei, A. et al. (2014). Hole-conductor-free mesoscopic TiO_2 /$CH_3NH_3PbI_3$ heterojunction solar cells based on anatase nanosheets and carbon counter electrodes. *Journal of Physical Chemistry Letters* 5 (12): 2160–2164. https://doi.org/10.1021/jz500833z.

38 Barichello, J., Vesce, L., Matteocci, F. et al. (2019). The effect of water in carbon-perovskite solar cells with optimized alumina spacer. *Solar Energy Materials & Solar Cells* 197 (February): 76–83. https://doi.org/10.1016/j.solmat.2019.03.029.

39 Philip, B., Jewell, E., Greenwood, P., and Weirman, C. (2014). Material and process optimization screen printing carbon graphite pastes for mass production of heating elements. *Journal of Manufacturing Processes* 22: 185–191. https://doi.org/10.1016/j.jmapro.2016.03.001.

40 Potts, S.J., Phillips, C., Jewell, E. et al. (2020). High-speed imaging the effect of snap-off distance and squeegee speed on the ink transfer mechanism of screen-printed carbon pastes. *Journal of Coatings Technology and Research* 17 (2): 447–459. https://doi.org/10.1007/s11998-019-00291-6.

41 Wan, Z., Xu, M., Fu, Z. et al. (2019). Screen printing process control for coating high throughput titanium dioxide films toward printable mesoscopic perovskite solar cells. *Frontiers of Optoelectronics* 12 (4): 344–351. https://doi.org/10.1007/s12200-019-0904-7.

42 Tiwana, P., Docampo, P., Johnston, M.B. et al. (2011). Electron mobility and injection dynamics in mesoporous ZnO, SnO_2, and TiO_2 films used in dye-sensitized solar cells. *ACS Nano* 5 (6): 5158–5166. https://doi.org/10.1021/nn201243y.

43 Song, J., Zheng, E., Wang, X.-F. et al. (2016). Low-temperature-processed ZnO–SnO_2 nanocomposite for efficient planar perovskite solar cells. *Solar Energy Materials & Solar Cells* 144: 623–630. https://doi.org/10.1016/j.solmat.2015.09.054.

44 Luong, C.H., Kim, S., Surabhi, S. et al. (2015). Fabrication of undoped ZnO thin film via photosensitive sol–gel method and its applications for an electron transport layer of organic solar cells. *Applied Surface Science* 351: 487–491. https://doi.org/10.1016/j.apsusc.2015.05.170.

45 Hu, H., Dong, B., Hu, H. et al. (2016). Atomic layer deposition of TiO_2 for a high-efficiency hole-blocking layer in hole-conductor-free perovskite solar cells processed in ambient air. *ACS Applied Materials & Interfaces* 8 (28): 17999–18007. https://doi.org/10.1021/acsami.6b02701.

46 Rafieian, D., Ogieglo, W., Savenije, T., and Lammertink, R.G.H. (2015). Controlled formation of anatase and rutile TiO_2 thin films by reactive magnetron sputtering. *AIP Advances* 5 (9): 097168. https://doi.org/10.1063/1.4931925.

47 Lewis, A., Troughton, J., Smith, B. et al. (2020). In-depth analysis of defects in TiO_2 compact electron transport layers and impact on performance and hysteresis of planar perovskite devices at low light. *Solar Energy Materials & Solar Cells* 209 (February): 110448. https://doi.org/10.1016/j.solmat.2020.110448.

48 Smith, B., Troughton, J., Lewis, A. et al. (2019). Mass manufactured glass substrates incorporating prefabricated electron transport layers for perovskite solar cells. *Advanced Materials Interfaces* 6 (6): 1801773. https://doi.org/10.1002/admi.201801773.

49 Alberola-Borràs, J.-A., Baker, J., De Rossi, F. et al. (2018). Perovskite photovoltaic modules: life cycle assessment of pre-industrial production process. *iScience* 9: 542–551. https://doi.org/10.1016/j.isci.2018.10.020.

50 Troughton, J., Charbonnaeu, C., Carnie, M.J. et al. (2015). Rapid processing of perovskite solar cells in under 2.5 seconds. *Journal of Materials Chemistry A* 9123–9127. https://doi.org/10.1039/C5TA00568J.

51 Troughton, J., Carnie, M., Davies, M. et al. (2016). Photonic flash-annealing of lead halide perovskite solar cells in 1 ms. *Journal of Materials Chemistry A* 4 (9): 3471–3476. https://doi.org/10.1039/C5TA09431C.

52 Baker, J., Hooper, K., Meroni, S.M.P. et al. (2017). High throughput fabrication of mesoporous carbon perovskite solar cells. *Journal of Materials Chemistry A* 5 (35): 18643–18650. https://doi.org/10.1039/C7TA05674E.

53 Yates, H.M., Hodgkinson, J.L., Meroni, S.M.P. et al. (2020). Flame assisted chemical vapour deposition of NiO hole transport layers for planar perovskite cells. *Surface and Coatings Technology* 385 (January): 125423. https://doi.org/10.1016/j.surfcoat.2020.125423.

54 Gupta, D., Bag, M., and Narayan, K.S. (2008). Area dependent efficiency of organic solar cells. *Applied Physics Letters* 93 (16): 49–51. https://doi.org/10.1063/1.2998540.

55 Das, A.J. and Narayan, K.S. (2013). Retention of power conversion efficiency – from small area to large area polymer solar cells. *Advanced Materials* 25 (15): 2193–2199. https://doi.org/10.1002/adma.201204048.

56 Giordano, F., Petrolati, E., Brown, T.M. et al. (2011). Series-connection designs for dye solar cell modules. *IEEE Transactions on Electron Devices* 58 (8): 2759–2764. https://doi.org/10.1109/TED.2011.2158216.

57 Galagan, Y., Coenen, E.W.C., Verhees, W.J.H., and Andriessen, R. (2016). Towards the scaling up of perovskite solar cells and modules. *Journal of Materials Chemistry A* 4 (15): 5700–5705. https://doi.org/10.1039/c6ta01134a.

58 Mouhamad, Y., Meroni, S.M.P., De Rossi, F. et al. (2019). Geometrical optimization for high efficiency carbon perovskite modules. *Solar Energy* 187 (May): 129–136. https://doi.org/10.1016/j.solener.2019.05.047.

59 Palma, A.L., Matteocci, F., Agresti, A. et al. (2017). Laser-patterning engineering for perovskite solar modules with 95% aperture ratio. *IEEE Journal of Photovoltaics* 7 (6): 1674–1680. https://doi.org/10.1109/JPHOTOV.2017.2732223.

60 Fu, Z., Xu, M., Sheng, Y. et al. (2019). Encapsulation of printable mesoscopic perovskite solar cells enables high temperature and long-term outdoor stability. *Advanced Functional Materials* 29 (16): 1809129. https://doi.org/10.1002/adfm.201809129.

61 Li, X., Tschumi, M., Han, H. et al. (2015). Outdoor performance and stability under elevated temperatures and long-term light soaking of triple-layer mesoporous perovskite photovoltaics. *Energy Technology* 3 (6): 551–555. https://doi.org/10.1002/ente.201500045.

62 Corsini, F. and Griffini, G. (2020). Recent progress in encapsulation strategies to enhance the stability of organometal halide perovskite solar cells. *Journal of Physics: Energy* 2 (3): 031002. https://doi.org/10.1088/2515-7655/ab8774.

63 Emami, S., Martins, J., Ivanou, D., and Mendes, A. (2020). Advanced hermetic encapsulation of perovskite solar cells: the route to commercialization. *Journal of Materials Chemistry A* 8 (5): 2654–2662. https://doi.org/10.1039/c9ta11907h.

64 Sastrawan, R., Beier, J., Belledin, U. et al. (2006). A glass frit-sealed dye solar cell module with integrated series connections. *Solar Energy Materials & Solar Cells* 90 (11): 1680–1691. https://doi.org/10.1016/j.solmat.2005.09.003.

65 Saparov, B. and Mitzi, D.B. (2016). Organic–inorganic perovskites: structural versatility for functional materials design. *Chemical Reviews* 116 (7): 4558–4596. https://doi.org/10.1021/acs.chemrev.5b00715.

66 Frost, J.M., Butler, K.T., Brivio, F. et al. (2014). Atomistic origins of high-performance in hybrid halide perovskite solar cells. *Nano Letters* 14 (5): 2584–2590. https://doi.org/10.1021/nl500390f.

67 Aristidou, N., Sanchez-Molina, I., Chotchuangchutchaval, T. et al. (2015). The role of oxygen in the degradation of methylammonium lead trihalide perovskite photoactive layers. *Angewandte Chemie, International Edition* 54 (28): 8208–8212. https://doi.org/10.1002/anie.201503153.

68 Bryant, D., Aristidou, N., Pont, S. et al. (2016). Light and oxygen induced degradation limits the operational stability of methylammonium lead triiodide perovskite solar cells. *Energy & Environmental Science* 9 (5): 1655–1660. https://doi.org/10.1039/c6ee00409a.

69 O'Mahony, F.T.F., Lee, Y.H., Jellett, C. et al. (2015). Improved environmental stability of organic lead trihalide perovskite-based photoactive-layers in the presence of mesoporous TiO_2. *Journal of Materials Chemistry A* 3 (14): 7219–7223. https://doi.org/10.1039/c5ta01221j.

70 Lee, H.K.H., Barbe, J., Meroni, S.M.P. et al. (2019). Outstanding indoor performance of perovskite photovoltaic cells – effect of device architectures and interlayers. *Solar RRL* 3 (1): 1800207. https://doi.org/10.1002/solr.201800207.

71 Raptis, D., Stoichkov, V., Meroni, S.M.P. et al. (2020). Enhancing fully printable mesoscopic perovskite solar cell performance using integrated metallic grids to improve carbon electrode conductivity. *Current Applied Physics* 20 (5): 619–627. https://doi.org/10.1016/j.cap.2020.02.009.

10
Perspective

Xiayan Chen, Yue Hu, Anyi Mei, Yinhua Zhou, and Hongwei Han
Huazhong University of Science and Technology, Michael Grätzel Center for Mesoscopic Solar Cells, Wuhan National Laboratory for Optoelectronics, Wuhan 430074, Hubei, PR China

10.1 Commercializing

Further reducing the cost of solar cells is an inevitable trend and an eternal topic for the development of the photovoltaic industry. The first-generation solar cells represented by crystalline silicon solar cells based on bulk materials have made great progress. Their costs are mainly concentrated in silicon raw materials, which account for more than 60% of the total component cost. Due to the traditional p–n junction structure, the charge separation is realized by the built-in electric field. In this process, the silicon semiconductor material participates in both charge separation and photon capture. Therefore, high-purity materials are required, and silicon semiconductor materials with a high purity of 99.999% or even 99.9999% are used to obtain high-efficiency devices. Through the improvement of efficiency and fabrication processes, especially the progress of cutting technology, the thickness of silicon wafers has been reduced from the original millimeter level to the current 150~200 μm, and the peak watt cost of silicon photovoltaic devices has been reduced accordingly. In order to fundamentally reduce the consumption of raw materials, the second-generation photovoltaic technologies including CIGS, CdTe, and other types of solar cells based

on a few micron-scale thin-film technologies came into being. Traditional thin-film solar cells use expensive vacuum processes, so the fixed investment cost of equipment is still very high. Compared with the first-generation crystalline silicon photovoltaic technology, the cost advantage of the second-generation thin-film solar cells is not obvious, and the market share is less than 10%. Throughout the market development process of the photovoltaic industry, the essence is the cost advantage brought by technological iteration. The emergence of new technologies will defeat the old production capacity. There has never been a first-mover advantage or scale advantage.

In order to reduce the processing costs, the third-generation or the emerging photovoltaic devices based on solution-processable methods have been developed, while perovskite solar cells are a typical representative of such devices. Since perovskite was introduced into all-solid-state mesoscopic solar cells by Nam-Gyu Park and Professor Michael Grätzel in 2012, perovskite solar cells have achieved rapid development, and their highest certified power conversion efficiency has exceeded 25.7% now. Emerging technology companies have also begun the commercialization process of perovskite photovoltaic technologies. However, due to the uneven surfaces of glass and especially the bad points such as "burr" in the film prepared by the third-generation coating process, the uniformity of the film is seriously restricted, resulting in the imbalance of photon absorption and charge separation and transmission, which in turn leads to great reduction of efficiency when the device is scaled up. Unlike traditional p–n junction solar cells in which charge separation is achieved by the built-in electric field, charge separation is achieved by the kinetic competition of photosynthesis processes in mesoscopic solar cells. The mesoscale wide bandgap semiconductor material only participates in

charge separation, but not in photon capture. These have been demonstrated in dye-sensitized solar cells. Based on the printing technology and the mesoscopic triple-layer structure, the printable mesoscopic perovskite solar cell itself adopts an uneven mesoporous structure. The confinement of perovskite material in nanopores not only avoids the adverse influence of thermal expansion mismatch on the device's operational stability but also promotes the injection of photocarriers into the wide bandgap semiconductor, which essentially avoids the influence of uneven film on charge separation efficiency. As a result, the influence of the conductive glass unevenness on the performance of the device is avoided, and the performance of related large-area modules will exhibit enhanced tolerance to the fabrication process.

According to the light absorption characteristics of perovskite materials, the theoretical power conversion efficiency limit of single-junction perovskite solar cells could reach 32%. Due to the direct bandgap intrinsic characteristics of perovskite semiconductor materials, such as GaAs, the obtainable power conversion efficiency of single junction perovskite solar cells is expected to exceed 29%. However, how to exceed the Shockley–Queisser (SQ) limit of single-junction perovskite solar cells, especially whether the printable mesoscopic perovskite solar cells based on nano-mesoporous scale can break the SQ limit, is still a topic worthy of in-depth study.

10.2 Exceeding SQ Limit

In the recent publication [1], we have updated the power conversion efficiency of the fully printable mesoscopic perovskite solar cells to 18.82% with a perovskite's bandgap of 1.62 eV, where $V_{oc} = 1.03\,\text{V}$, $J_{sc} = 22.82\,\text{mA}$

cm^{-2}, and FF = 0.80. How far can the efficiency go for these fully printable mesoscopic perovskite solar cells?

It is straightforward to compare the efficiency of the fully printable mesoscopic cells and the cells with regular structure including hole-transporting layer, vacuum-deposited metal electrode, and spin-coated perovskite layers. Recently, in early 2021, cells with the regular structure deliver power conversion efficiency of 25.2%, with V_{oc} = 1.18 V, J_{sc} = 25.14 mA cm^{-2}, and FF = 0.85, where the perovskite's bandgap is 1.56 eV [2] (Table 10.1).

Table 10.1 Photovoltaic parameters of the state-of-the-art fully printable mesoscopic perovskite solar cells, regular perovskite solar cells, and GaAs solar cells.

Device type	E_g of the absorber (eV)	PCE (%)	V_{oc} (V)	J_{sc} (mA cm^{-2})	FF
Perovskite (mesoscopic triple-layer)	1.62	18.82	1.03	22.82	0.80
Perovskite (regular)	1.56	25.2	1.18	25.14	0.85
GaAs	1.43	29.1	1.13	29.78	0.87

The GaAs cells hold the highest efficiency among all-type single-junction perovskite solar cells.

Furthermore, for a semiconductor-based single-junction photovoltaic device, its efficiency always follows the SQ efficiency limit, initiated by Shockley and Queisser in 1961 [3]. It describes the efficiency limit of single-junction solar cells. The limit as a function of bandgap (E_g), resulting from absorption loss (due to the photons having energy lower than bandgap), thermalization loss (due to the photons having energy higher than bandgap that will excite

electrons to a higher energy level and then the electrons will relax to the edge of the bandgap), and radiative recombination loss (equivalent to blackbody emission having a temperature over 0 K).

The power conversion efficiency (PCE) of the fully printable cells is within the range between 50% and 75% of the SQ limit, while that of the regular perovskite solar cells is within the range between 75% and 100% of the SQ limit. The trend of regular perovskite solar cells is approaching GaAs solar cells. It is amazing that the solution-coated perovskite solar cells can deliver comparable performance to the GaAs cells fabricated by delicate metal–organic chemical vapor deposition.

From each photovoltaic parameter to the SQ limit, we understand the reason causing the efficiency difference and the gap to the SQ limit. For J_{sc}, the three-type of cells are very close to the SQ limit. For the fully printable cells, the J_{sc} is even closer to the limit that the other two cells, which might be associated with the thicker perovskite absorber layer (around 1–2 µm). That suggests sufficient light harvest in the fully printable cells. The shortage of fully printable cells is the FF and V_{oc}. Both FF and V_{oc} are correlated to the charge carrier management [4], i.e. nonradiative recombination.

Actually, for the recently reported 25.2% cells with regular structure, high efficiency was obtained via improved charge carrier management. [2] Therefore, they fabricated an electron transport layer (SnO_2) with sufficient film coverage and composition by tuning the chemical bath deposition. Combined with the decoupled passivation strategy between the bulk and the interface, a high efficiency of 25.2% was obtained. That reaches 80.5% of the theoretical SQ limit efficiency. The ratio of V_{oc} to the

radiative V_{oc} limit reaches 96.5%. Such a low V_{oc} deficit suggests that almost all nonradiative recombination pathways have been efficiently eliminated. A high electroluminescence external quantum efficiency (EQE) of up to 17.2% confirms the elimination of nonradiative recombination.

This tells charge carrier management is the direction to overcome the loss of V_{oc} and FF to enhance the efficiency of the fully printable mesoscopic perovskite solar cells. But the methods of carrier management for the printable cells can be different from the cells with regular structure. It is related to two major differences between the regular device and fully printable devices:

(1) **Device structure**: The fully printable cells are hole-transporting layer free. The hole-transporting interface between the perovskite film and the top electrode is completely different for the two types of cells. For example, according to the reported literature, surface passivation and modification are very important to charge recombination and V_{oc} loss. In regular cells, coating a large-sized cation to construct 2D perovskite structure at the interface between the hole-transporting layer (HTL) and 3D perovskite absorber is a very effective strategy to suppress nonradiative recombination. But this method is not applicable in our fully printable cells due to the complete device structure and processing sequence of layers of the cells.

(2) ***Processing method and thickness/crystallinity of the perovskite absorber***: For the regular structure, the cells are fabricated layer by layer from the bottom to the top. The perovskite layer is coated on top of the transparent electrode/electron-transporting

layer. HTL and top electrodes are then deposited on the perovskite layer. The processing step of the perovskite layer is between the bottom electrode/ETL and HTL/top electrode. For fully printed cells, the bottom electrode/ETL, scaffold layer, and top electrode are fabricated first. After sintering, mesoscopic pores form a continuous path: from the top carbon electrode, across the scaffold layer, to the ETL. The dropping or coating of the perovskite layer is the final step of the fabrication.

In regular structure, thickness of the perovskite absorber is typically 300–500 nm; the thickness of the fully printable cells is typically 1–2 µm.

In regular structure, the perovskite crystalizes freely in a 300–500 nm film; in fully printable cells, the process of perovskite crystallization is confined in mesoscopic pores.

Thus, both the bulky crystallinity and interface structure in fully printable solar cells are different from those in regular structures. It is known that the charge recombination occurs exactly in the bulky absorber as well as at the interfacial contact (perovskite/anode or HTL). Thus, the charge recombination behavior and strategies to suppress the charge behavior can be completely different. The thicker perovskite absorber and HTL-free structure would turn out more difficult to suppress the nonradiative recombination in fully printable perovskite solar cells than in regular structures.

Strategies to improve perovskite crystallinity grown inside the mesoscopic pores can be effective to reduce traps in the bulky films and therefore suppress the bulky charge carrier recombination. Materials and mesoscopic structures to improve the contact between the perovskite absorber and the anode are also to be developed to suppress the

charge recombination at the interface. After understanding and well manipulating the charge recombination, efficiency of the fully printable mesoscopic solar cells can catch that of their compartments in regular structure by about 25%. It can also be further enhanced to that of GaAs solar cells by 28%–29%, approaching the SQ theoretical limit, considering the excellent optoelectronic properties of metal halide perovskite absorbers.

10.3 Efficiency Breaking Out of SQ Limit

The above discussion is based on a general single-junction solar cell, whose efficiencies are below the SQ theoretical limit due to the trade-off between light harvest and thermalization of excess energy over bandgap.

In the past years, the community has been seeking methods to surpass the SQ limit and achieve very high efficiency. The calculation of the SQ limit is based on the following assumptions:

(1) Concentration of one sun;

(2) Sun and cells are considered as blackbodies;

(3) Absorption is in step function, photons only with energy over E_g can be absorbed by the cell, and band tails of semiconductor are not considered;

(4) An absorbed photon only creates an electron–hole pair;

(5) Recombination is radiative and nonradiative recombination is not considered.

Once these assumptions are broken up, it is possible to surpass the SQ limit. Typically, the following strategies are

expected and some of them are experimentally confirmed to surpass the SQ limit:

(1) Building tandem structure;

(2) Concentration of sunlight up to hundred times of intensity;

(3) One photon produces multiple electron–hole pairs (excitons).

First, the community fabricates multijunction structure. The SQ limit is for single-junction devices. The multijunction overcomes the trade-off between the light harvest and the thermalization of excess energy over bandgap. Thus, it can break the limit for single-junction photovoltaic devices. Indeed, in the reality, the highest efficiency of all types of photovoltaic cells is in multijunction tandem structures. A 6-junction solar cell delivers an efficiency of 39.2% under one-sun illumination reported by National Renewable Energy Laboratory (NREL) [5]. This number is higher than the theoretical SQ limit of 33% for single-junction solar cells.

Second, under illumination of concentrated sunlight, the efficiency can be future enhanced. That is because the ratio of photocurrent over current produced from radiative illumination is significantly enhanced, thus leading to an effectively enhanced V_{oc} and efficiency. For the 39.2% 6-junction solar cell (under one sun), its efficiency reaches 47.1% under illumination of $143 \times$ sunlight.

Thus, the dual strategies of multijunction structure and concentrated sunlight can yield an efficiency much higher than the SQ limit for single-junction cells.

For perovskite cells, the demonstrated efficiency of two-junction structure reaches 26.4%, which is also higher than the reported single-junction cells of 25.5%. This is also an

example showing the multijunction strategy to improve efficiency. The demonstrated two-junction solar cells are based on regular structure. For fully printable mesoscopic perovskite solar cells, it is difficult to fabricate tandem structures. The current top electrode, sintering process, and coating perovskite as the final processing steps are hurdles for fabricating the multijunction structure. It might also be possible if porous tunneling junction materials are developed and new methods can be developed to manipulate bandgaps of the junctions through coating time offset or if other new materials and processing methods can be produced. With the multijunction structure, efficiency of the fully printing perovskite solar cells can potentially be enhanced.

Another strategy that is possible to surpass the SQ limit and enhance device efficiency to obtain multiple exciton generation (MEG) effects that spawns two or more electron–hole pairs from an absorbed high-energy photon (larger than two times bandgap energy). The MEG effect utilizes excess photon energy to create additional electron–hole pairs that can increase the thermodynamically allowed PCE to ~44% for unconcentrated light [6]. It is a very good model to bypass the SQ limit. The MEG effect has been widely studied in quantum dots (QDs) photovoltaic system. In 2011, Beard et al. reported MEG effect in PbSe QD-based solar cells that can successfully produce quantum efficiency over 100%: external quantum efficiency of 114% and internal quantum efficiency of 130% [7].

For perovskite, some reports have shown MEG effect can be produced in metal halide perovskite nanocrystals [8, 9]. The MEG contribution to solar cell efficiency enhancement has not been observed. The MEG is a promising strategy to enhance the device efficiency, but it is also a very difficult one based on the present material structure and crystallinity of perovskites. The mesoscopic or microscopic

pores might have some unique advantages in producing the MEG or others compared with the traditional and widely studied thin films. It is a great adventure that is worth pursuing.

References

1 Liu, S., Zhang, D., Sheng, Y. et al. (2021). Highly oriented $MAPbI_3$ crystals for efficient hole-conductor-free printable mesoscopic perovskite solar cells. *Fundamental Research* 2 (2): 276.

2 Yoo, J.J., Seo, G., Chua, M.R. et al. (2021). Efficient perovskite solar cells via improved carrier management. *Nature* 590 (7847): 587–593.

3 Archard, G.D. (1961). Back scattering of electrons. *Journal of Applied Physics* 32 (8): 1505–1509.

4 Polman, A., Knight, M., Garnett Erik, C. et al. (2016). Photovoltaic materials: present efficiencies and future challenges. *Science* 352 (6283): aad4424.

5 NREL. (2022) Best research-cell efficiency chart. https://www.nrel.gov/pv/cell-efficiency.html2022.

6 Hanna, M.C. and Nozik, A.J. (2006). Solar conversion efficiency of photovoltaic and photoelectrolysis cells with carrier multiplication absorbers. *Journal of Applied Physics* 100 (7): 074510.

7 Semonin Octavi, E., Luther Joseph, M., Choi, S. et al. (2011). Peak external photocurrent quantum efficiency exceeding 100% via MEG in a quantum dot solar cell. *Science* 334 (6062): 1530–1533.

8 Manzi, A., Tong, Y., Feucht, J. et al. (2018). Resonantly enhanced multiple exciton generation through below-band-gap multi-photon absorption in perovskite nanocrystals. *Nature Communications* 9 (1): 1518.

9 Li, M., Begum, R., Fu, J. et al. (2018). Low threshold and efficient multiple exciton generation in halide perovskite nanocrystals. *Nature Communications* 9 (1): 4197.

Index

WILEY END USER LICENSE AGREEMENT

Go to www.wiley.com/go/eula to access Wiley's ebook EULA.